GEORGIA INSTITUTE OF TECHNOLOGY — OFFICE OF CONTRACT ADMINISTRATION

PROJECT ADMINISTRATION DATA SHEET

[X] ORIGINAL [ ] REVISION NO. ____

Project No. E-16-620 (R6026-0A0) GTRC/~~GIT~~ DATE 9 / 18 / 85

Project Director: D. A. Peters School/~~AXX~~ Aerospace Engineering

Sponsor: U. S. Army Research Office
Research Triangle Park, NC

Type Agreement: SFRC DAAG29-85-K-0225 9-30-86

Award Period: From 9/1/85 To ~~8/31/86~~ (Performance) 10/31/86 (Reports)

Sponsor Amount:	This Change	Total to Date
Estimated:	$ 119,489	$ 119,489
Funded:	$ 119,489	$ 119,489

Cost Sharing Amount: $ 11,949 Cost Sharing No: E-16-376

Title: Effect of Dynamic$ Stall and Elastic Parameters on the Fundamental Mechanisms of Helicopter Vibrations

ADMINISTRATIVE DATA OCA Contact William F. Brown X4820

1) Sponsor Technical Contact:

Dr. Gary L. Anderson
Engineering Services Division
U. S. Army Research Office
P. O. Box 12211
Research Triangle Park, NC 27709-2211

2) Sponsor Admin/Contractual Matters:

~~T. A. Bryant~~
ONR RR
Georgia Tech

Defense Priority Rating: None Shown Military Security Classification: Unclassified
(or) Company/Industrial Proprietary: N/A

RESTRICTIONS

See Attached Gov't Supplemental Information Sheet for Additional Requirements.

Travel: Foreign travel must have prior approval – Contact OCA in each case. Domestic travel requires sponsor approval where total will exceed greater of $500 or 125% of approved proposal budget category.

Equipment: Title vests with GIT; Requires prior approval to buy any equipment not in the proposal budget, any ADFE item; and equipment item with unit cost $10,000 or more.

COMMENTS:

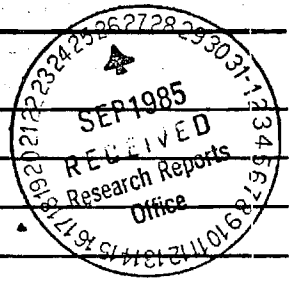

COPIES TO:

SPONSOR'S I. D. NO. 02.102.001.85.014

Project Director
Research Administrative Network
Research Property Management
Accounting
Procurement/GTRI Supply Services
Research Security Services
Reports Coordinator (OCA)
Research Communications (2)
GTRC
Library
Project File
Other A. Jones

FORM OCA 65:285

GEORGIA INSTITUTE OF TECHNOLOGY OFFICE OF CONTRACT ADMINISTRATION

SPONSORED PROJECT TERMINATION/CLOSEOUT SHEET

Date 12/12/86

Project No. E-16-620 School/~~XXX~~ AE

Includes Subproject No.(s) N/A

Project Director(s) D. A. Peters GTRC /~~XXX~~

Sponsor U. S. Army Research Office

Title Effect of Dynamic Stall and Elastic Parameters on the Fundamental Mechanisms of Helicopter Vibrations

Effective Completion Date: 9/30/86 (Performance) 11/30/86 (Reports)

Grant/Contract Closeout Actions Remaining:

- [ ] None
- [X] Final Invoice or Final Fiscal Report
- [X] Closing Documents
- [ ] Final Report of Inventions - already submitted.
- [X] Govt. Property Inventory & Related Certificate
- [ ] Classified Material Certificate
- [ ] Other

Continues Project No. Continued by Project No.

COPIES TO:

Project Director
Research Administrative Network
Research Property Management
Accounting
Procurement/GTRI Supply Services
Research Security Services
Reports Coordinator (OCA)
Legal Services

Library
GTRC
Research Communications (2)
Project File
Other I. Lashley
A. Jones
R. Embry

FORM OCA 69.285

Reprinted from the Journal of the AMERICAN HELICOPTER Society, April, 1986

Effectiveness of Current Dynamic-Inflow Models in Hover and Forward Flight

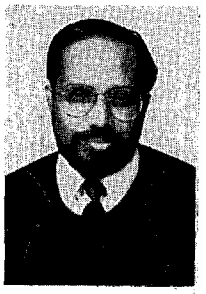

Gopal H. Gaonkar
Professor
Department of Mechanical Engineering
Florida Atlantic University
Boca Raton, Fla.

David A. Peters
Professor
School of Aerospace Engineering
Georgia Institute of Technology
Atlanta, Ga.

A brief overview of dynamic inflow theory is given, including its history and its dependence on experimental data. Some of the most extensive of this data, flapping response derivatives obtained in 1972–1974, indicated that theoretical predictions which included the best dynamic-inflow models of that time were qualitatively as well as quantitatively inaccurate. In this paper, these original flapping data (some of which have never been compared to theory in the literature) are compared with theory which includes a more recently developed model of dynamic inflow. The correlation is excellent at most frequencies and advance ratios, and the new model brings the theory into qualitative agreement with experiment in all conditions.

Notation

a = slope of lift curve, rad^{-1}
B = tip loss factor
C_L = roll-moment coefficient perturbation
C_M = pitch-moment coefficient perturbation
C_T = thrust coefficient perturbation
e_{pc} = root cut-out normalized by R
k = reduced frequency based on free-stream velocity, ω/V
K_m = normalized apparent mass
K_I = normalized rotary inertia
L = inflow gain, Ref. 14
$[L]$ = matrix of inflow gains
$[L(k)]$ = complex $[L]$ matrix
$[M]$ = apparent mass matrix
p = flapping frequency, per revolution
r = distance from rotor center, m
R = rotor radius, m
t = time, sec
V = inflow mass-flow parameter, Eq. (6)
α = wake angle at rotor, rad, Eq. (5)
α_s, α_c = shaft tilt, lateral and longitudinal, rad
β = flapping angle, rad
γ = Lock number
θ_o, θ_s, θ_c = collective and cyclic pitch, rad
λ = normalized free-stream velocity perpendicular to rotor disk
μ = normalized free-stream velocity in the plane of rotor disk
ν = induced flow perturbation, $\nu = \nu_o + \nu_s \frac{r}{R} sin\psi + \nu_c \frac{r}{R} cos\psi$
$\bar{\nu}_o$ = steady part of induced flow
ν_o, ν_s, ν_c = induced flow perturbation harmonics
σ = blade solidity
τ = inflow time constant, Ref. 14
$[\tau]$ = matrix of time constants
ψ = blade azimuth angle, rad
ω = frequency of oscillations, per revolution
Ω = rotor speed, rad/sec
$(*)$ = $d(\ )/d\psi$

Presented at the American Helicopter Society Second Decennial Specialists' Meeting on Rotorcraft Dynamics, NASA Ames Research Center, Moffett Field, Calif., Nov. 1984.

Introduction

From its inception over 30 years ago, the theory of dynamic inflow has been driven constantly by the impetus of experimental data. In 1950, Amer observed that the theoretical pitch-roll damping of helicopters did not agree with flight measurements, Ref. 1. Although most of the differences could be attributed to the angle between thrust and tip-path plane, there remained a discrepancy that Amer attributed to a variation in inflow over the rotor disk. Sissingh provided a mathematical model to explain this phenomenon (Ref. 2) and his model initiated the study of dynamic (or variable) inflow. In short,

Sissingh showed that the side-to-side thrust perturbation created by a roll rate could create perturbations in the induced flow field that substantially affect roll damping. It was essentially this inflow model that was later clarified and extended by Curtiss and Shupe and applied extensively to problems of flight dynamics via an "equivalent Lock number" to account for induced flow perturbations (Refs. 3 and 4).

In 1971–1972, Lockheed performed some wind tunnel tests that changed the course of the theory of dynamic inflow. These tests, on a 7.5 ft. diameter rotor in NASA's 7×10 ft. wind tunnel, measured 15 static rotor derivatives (C_T, C_L, C_M, with respect to θ_o, θ_s, θ_c, α_s, α_c) as functions of advance ratio from $\mu = 0$ to 1.4 (Ref. 5). The results revealed major qualitative differences between conventional rotor theory (i.e., static, nonuniform induced flow) and the experimental data. Most importantly, these differences could not be attributed to classical explanations (reversed flow, blade elasticity, dynamic stall, etc.). As a result of this comparison, a variable-inflow theory was included in the blade flapping equations, based on momentum developments similar to those in Refs. 2–4. In this theory, induced-flow distributions were allowed to vary in a quasi-static manner as blade loads were perturbed. The results were very interesting. In hover, the momentum-theory model of dynamic inflow provided good correlation with the data. In forward flight, however, the model did not improve the correlation. As a result, the authors of Ref. 5 formulated other theories in forward flight based on simple vortex considerations. Finally, they formulated an empirical inflow model based on the best fit of the quasi-static data.

The above narrative describes the development of the quasi-static theory of variable inflow. In 1953, Carpenter and Fridovitch noticed that there was a time delay in the development of induced flow following rapid changes in blade collective pitch, Ref. 6. They formulated a time constant for uniform induced flow that was based on the apparent mass of an impermeable disk, and they showed that this time constant accounted for the measured transients in induced flow. In 1972, new experimental data (Ref. 7) spurred the incorporation of time delays for both uniform and gradient induced flow into the variable inflow theories, Ref. 8. Reference 8 compares theory and experiment for the oscillatory response (magnitude and phase) of roll and pitch moments due to oscillations of θ_o, θ_s, θ_c, α_s, and α_c. These results show that the variable inflow theories of Ref. 5, while giving good static correlation, give poor correlation as ω is increased. Furthermore, the data show that the cause of the poor correlation is that the effect of variable inflow decreases with increasing ω. In other words, the induced flow does not have time to respond to rapid changes in loads, which points back to the need for time delays such as those in Ref. 6. As a result of this new information, the apparent mass terms were incorporated into both the empirical and momentum-theory variable inflow models, thus creating dynamic inflow theory (Ref. 8).

Background

Before going on to correlation of the data in Ref. 5, the form of dynamic inflow theory will be defined. First, dynamic inflow assumes a limited number of induced flow distributions of unspecified magnitude. The relative amounts of each distribution (that might be present at a particular instant in time) become degrees of freedom in the dynamic analysis. Although several alternatives have been tried through the years, the best results have been obtained with the following formulation.

$$v(r,\psi) = v_o + v_s \frac{r}{R} \sin\psi + v_c \frac{r}{R} \cos\psi \qquad (1)$$

Some investigators have used only the v_s and v_c terms, Refs. 9–10, and some have added second-harmonic terms, Refs. 11–12. However, in forward flight for rotors with three or more blades, the model in Eq. (1) is both necessary and sufficient to model the phenomenon.

In dynamic inflow theory, the induced flow coefficients, that is, the air-mass degrees of freedom (v_o, v_s, v_c), are described by differential equations as follows:

$$[\tau] \begin{Bmatrix} \overset{*}{v_o} \\ \overset{*}{v_s} \\ \overset{*}{v_c} \end{Bmatrix} + \begin{Bmatrix} v_o \\ v_s \\ v_c \end{Bmatrix} = [L] \begin{Bmatrix} C_T \\ C_L \\ C_M \end{Bmatrix}_{aero} \qquad (2a)$$

or

$$[M] \begin{Bmatrix} \overset{*}{v_o} \\ \overset{*}{v_s} \\ \overset{*}{v_c} \end{Bmatrix} + [L]^{-1} \begin{Bmatrix} v_o \\ v_s \\ v_c \end{Bmatrix} = \begin{Bmatrix} C_T \\ C_L \\ C_M \end{Bmatrix}_{aero} \qquad (2b)$$

Several explanations are in order for Eq. (2). First, the quantities in Eq. (2) are perturbation values (v_o, v_s, v_c, C_T, C_L, C_M). Thus, the theory is formulated for a linearized analysis, although a nonlinear version is also given in Ref. 13. Second, the thrust, roll, and pitch coefficients refer to the aerodynamic components only. Thus, they may be obtained from integrated air loads, or they may be obtained by correction of total hub loads for inertial effects. The matrix $[L]$ is the static coupling matrix between induced flow and aerodynamic loads. The matrix $[M]$ assumes the role of an inertia of the air mass, and $[\tau] = [L]\,[M]$ is a matrix of time constants.

It is interesting to note that most general-purpose rotor loads programs do have some type of nonuniform wake included in the analysis. However, this wake is not generally allowed to fluctuate dynamically as rotor thrust, roll moment, and pitch moment change in a transient manner. It is true that some programs do allow a timewise variation of inflow (uniform flow and fore-to-aft gradient), due to changes in thrust *only* and some (such as MOSTAB) even have a time delay on this variation. However, the codes do not allow for dynamic variations due to oscillations in roll and pitch moments, which are the most important ones.

Correlation with Flapping Data

With the form of dynamic inflow theory now set forth, we can proceed to further define the elements of the $[L]$ and $[M]$ matrices. In Ref. 8, the experimental data from Ref. 7 are compared with results calculated from dynamic inflow theory (including both $[L]$ and $[M]$). In hover, $[L]$ and $[M]$ are taken from momentum theory and are diagonal matrices.

$$[L] = \frac{1}{V} \begin{bmatrix} \frac{1}{2} & 0 & 0 \\ 0 & -2 & 0 \\ 0 & 0 & -2 \end{bmatrix} \qquad (3a)$$

$$[\mathrm{M}] = \begin{bmatrix} \frac{8}{3\pi} & 0 & 0 \\ 0 & \frac{-16}{45\pi} & 0 \\ 0 & 0 & \frac{-16}{45\pi} \end{bmatrix} \qquad (3b)$$

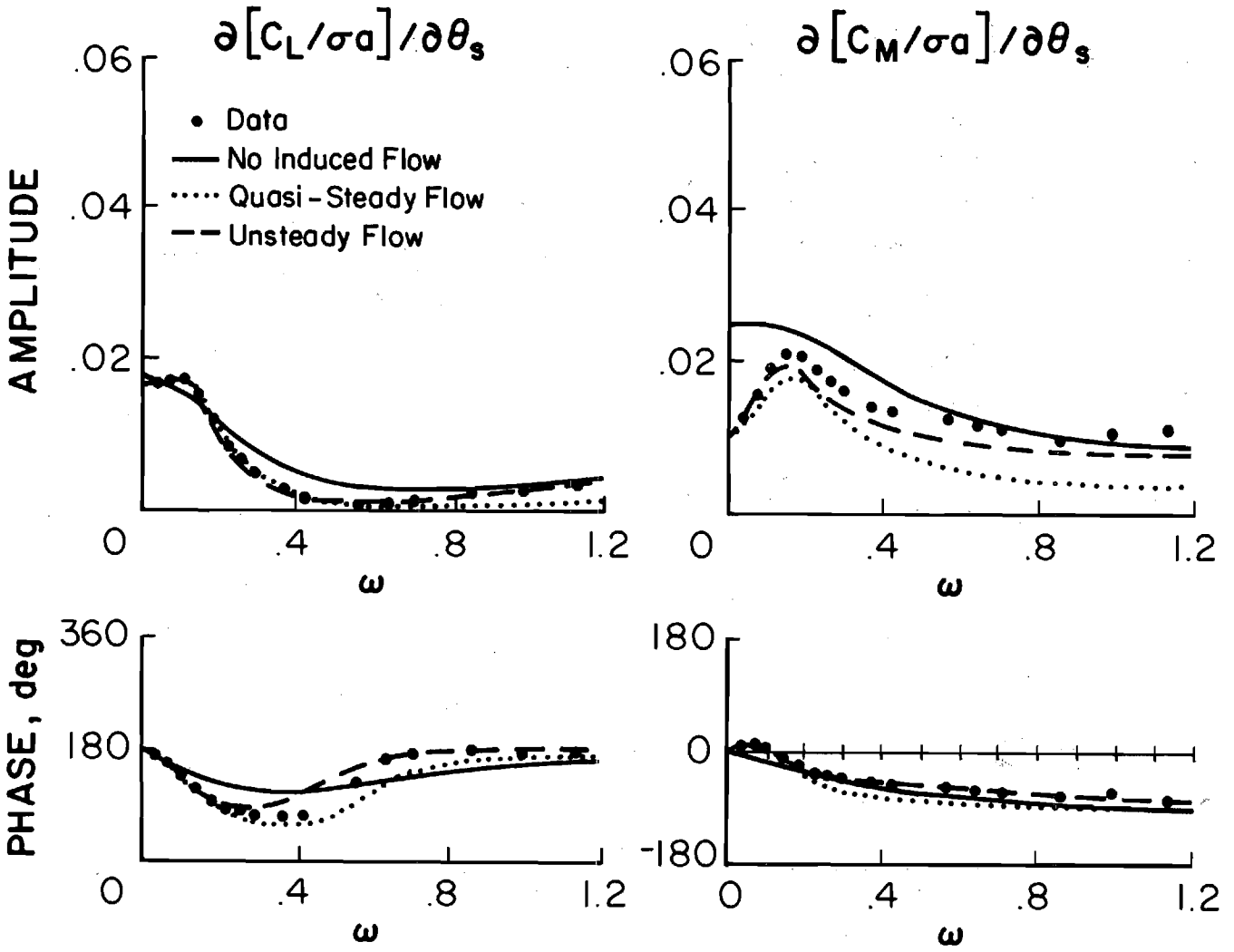

Fig. 1 Rotor response to cyclic pitch in hover; $p = 1.15$, $\gamma = 4.25$, $B = 0.97$, $e_{pc} = 0.25$, $\mu = 0$, $\sigma a = 0.73$, $\bar{\nu}_o = 0.03$, $\theta_o = 4°$, $\lambda = 0$; momentum theory, single rotating mode.

The results are extremely interesting. Figure 1 gives the magnitude and phase of both roll and pitch moments in hover due to oscillations in θ_s. The frequency of excitation is given in cycles per revolution. To put the frequency scale in physical perspective, stability and control of rotors involves the frequency range $0 < \omega < 0.3$; air and ground resonance, the range $0.3 < \omega < 0.7$; rigid-blade flapping, the range $0.7 < \omega < 1.2$; and blade elastic modes, generally, $\omega > 2.0$.

The theory without dynamic inflow is not even qualitatively accurate. When quasi-steady inflow is included (no apparent mass) the data are well-matched for $\omega < 0.2$. For larger ω, the quasi-steady theory is inaccurate, but the unsteady theory (with apparent mass) models the effect. Figure 2 presents a similar plot from Ref. 8 but for oscillations of shaft angle. Because of the theoretical symmetry in roll and pitch oscillations, data for both excitations are presented together. Above $\omega = 0.3$, the two sets of data diverge due to stand resonances. For $\omega < 0.3$ both agree. Once again, the theory with no dynamic inflow is qualitatively in error; but momentum theory completely predicts the response for $\omega < 0.3$. Figures 1 and 2 clearly demonstrate that dynamic inflow is well-modeled in hover by momentum theory with apparent-mass time delays.

At the same time as Refs. 7 and 8 were showing that dynamic inflow was necessary to correlate the Lockheed data, the same conclusion was being made in an entirely different test (Ref. 14). Figure 3 presents the data of Hohenemser and Crews for pitch stirring excitation. Rather than momentum theory, they used parameter identification to determine a gain L and a time constant τ for an inflow theory. Interestingly, the values of L and τ they obtained turned out to be within a few percent of the similar values from momentum theory; and the correlation with data was excellent. This is further verification of the validity of dynamic inflow. It should be noted that the researchers in Ref. 14 (along with D. Banerjee) also attempted to identify a full $[L]$ matrix from transient blade dynamics. However, because their rotor could not be excited in collective pitch, they were unable to develop an adequate response to identify $[L]$.

The first conclusion from the experiments in Refs. 7 and 14 was that momentum theory is completely adequate in hover. The second conclusion was that it is ineffective in forward flight. To be more specific, experimental data in forward flight also showed large deviations from conventional theory, but momentum theory could not make up the difference. There was one optimistic note, however. The empirical model, which had been identified based on static ($\omega = 0$) derivatives, gave very good agreement with dynamic data for all ω, provided that the apparent mass terms were added to give appropriate time delays in thrust, pitch, and roll. This implies that the same apparent

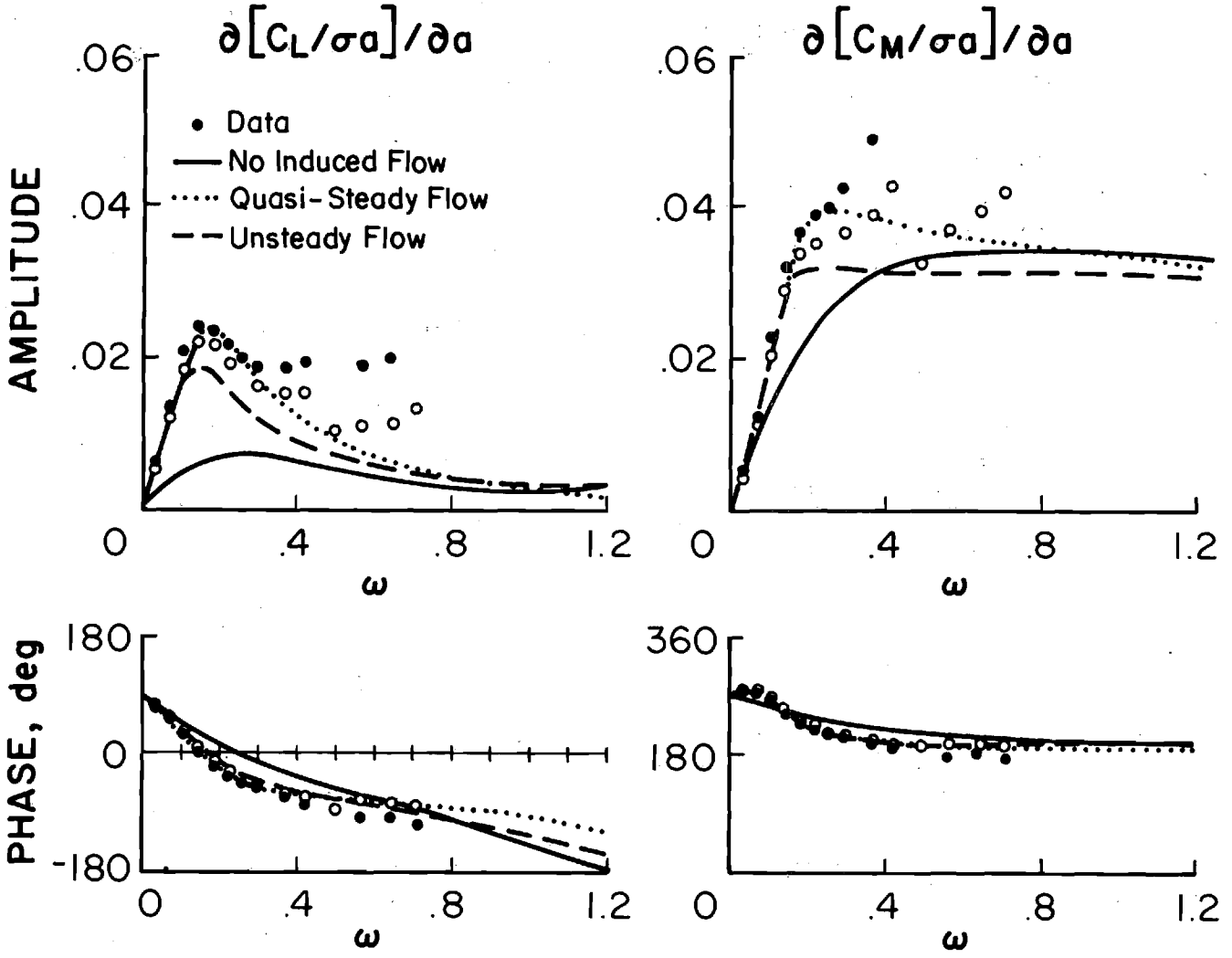

Fig. 2 Rotor response to hub motions in hover; $p = 1.15$, $\gamma = 4.25$, $B = 0.97$, $e_{pc} = 0.25$, $\mu = 0$, $\sigma a = 0.73$, $\bar{v}_o = 0.03$, $\theta_o = 4°$, $\lambda = 0$; momentum theory, single rotating mode.

mass terms are valid at all advance ratios. There are, however, several major problems with the empirical model. First, it is inconveniently formulated in terms of tabulated coefficients. Second, it has no fundamental basis in aerodynamics. Third, the $[L]$ matrix shows singularities at $\mu = 0.32$ and $\mu = 0.80$. Fourth, and the most serious, the empirical model is formulated only for edgewise flow. Therefore, there is no accounting for the transition from hover to forward flight.

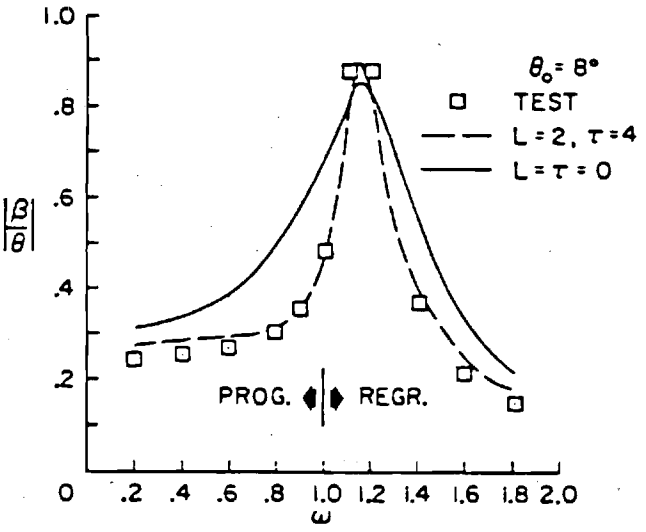

Fig. 3 Rotor response to pitch stirring, $p = 1.21$, $\gamma = 4.0$, $\mu = 0$, $B = 0.97$.

Pitt Model

The first attempt to develop a forward-flight dynamic inflow theory from first principles is found in Ref. 16. Here, Ormiston began to sort out the various induced-flow components of an actuator disk. The effort was not fully successful due to the complexities of blade motion that are coupled into the lift-flow problem. It became clear that one would have to isolate the induced flow from the blade dynamics in order to solve the problem. This was soon done; and, in 1981, Pitt and Peters introduced a new formulation of dynamic inflow, based on a rigorous solution to actuator-disk theory, Ref. 11.

This theory provides a smooth transition from hover to forward flight and has no singularities. In hover, it is identical to classical momentum theory (both for $[M]$ and $[L]$), and in forward flight, it develops characteristics similar to those of the empirical model. In the absence of direct experimental inflow measurements, the model has been compared to numerical wake computations, Ref. 17. For the static case, comparisons are made with the Landgrebe prescribed wake model

applied to a four-bladed lifting rotor, Ref. 18. Figures 4 through 6 show this comparison for the nine inflow derivatives, L_{ij}, as functions of disk angle of attack (0° = edgewise flow, 90° = hover). Results from Landgrebe's computer program are labeled "WAKE" on the figures. Clearly, the Pitt model gives results for [L] that agree with Landgrebe's at all disk angles.

For the dynamic case, the Pitt model is compared with a Theodorsen-type actuator-disk theory for frequency-response calculations in Fig. 7. In the results of the Pitt model, labeled "superposition of pressures," the formulation assumes that the harmonic induced *velocities* are all in phase. Consequently, these velocities create pressures that add as in Eq. (2b): 1) in phase loads due to L, and 2) out-of-phase loads due to M. In the other results, labeled "superposition of velocities," the formulation assumes that the oscillatory *loads* are all in phase. The resultant induced velocities are then calculated by an involved, Theodorsen-type integration over the entire wake, Ref. 17. One would assume that true rotor behavior would be some mixture of the two results. Therefore, the agreement between the two results is confirmation that the simple formulation of Eq. (2b) is adequate. Thus, Figs. 4–7 attest to the reasonableness of the actuator-disk model for modeling a four-bladed rotor with flapping dynamics and wake contraction.

The formulation of the Pitt model is given below.

$$[L] = \frac{1}{V}\begin{bmatrix} \frac{1}{2} & 0 & \frac{15\pi}{64}\sqrt{\frac{1-\sin\alpha}{1+\sin\alpha}} \\ 0 & \frac{-4}{1+\sin\alpha} & 0 \\ \frac{15\pi}{64}\sqrt{\frac{1-\sin\alpha}{1+\sin\alpha}} & 0 & \frac{-4\sin\alpha}{1+\sin\alpha} \end{bmatrix} \tag{4a}$$

$$[M] = \begin{bmatrix} \frac{128}{75\pi} & 0 & 0 \\ 0 & \frac{-16}{45\pi} & 0 \\ 0 & 0 & \frac{-16}{45\pi} \end{bmatrix} \tag{4b}$$

Several comments are in order. First, α is the wake angle at the rotor.

$$\alpha = \tan^{-1}\left(\frac{\lambda+\bar{v}_o}{\mu}\right) \tag{5}$$

Therefore, $\alpha = 0°$ corresponds to edgewise flow and $\alpha = 90°$ to hover or axial flight. Second, the V parameter is taken from momentum theory.

$$V = \frac{(\lambda+\bar{v}_o)(\lambda+2\bar{v}_o)+\mu^2}{\sqrt{(\lambda+\bar{v}_o)^2+\mu^2}} \tag{6}$$

Thus, in edgewise flow $V = \mu$ and in axial flow $V = \lambda + 2\bar{v}_o$. Because of this, the [L] matrix in Eq. (4a) exactly reduces to momentum theory at $\alpha = 90°$. The elements for $\alpha = 90°$ are consequently identical to the previous work in dynamic inflow, Refs. 2, 3, 4, 5, 8, and 9. It follows that the Pitt model provides the same good correlation as momentum theory in hover.

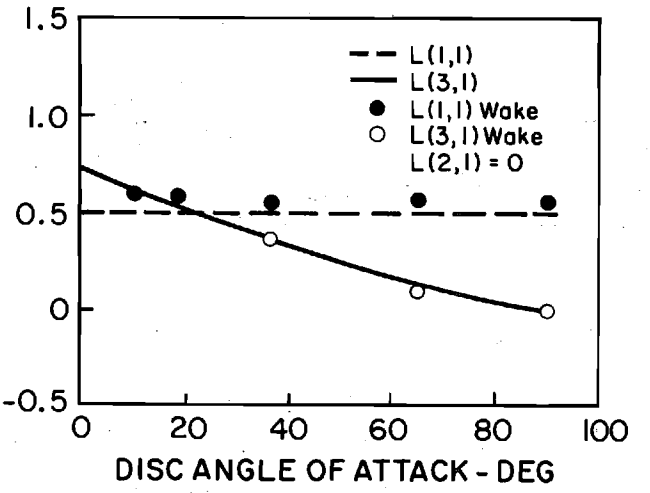

Fig. 4 Verification of first column of L.

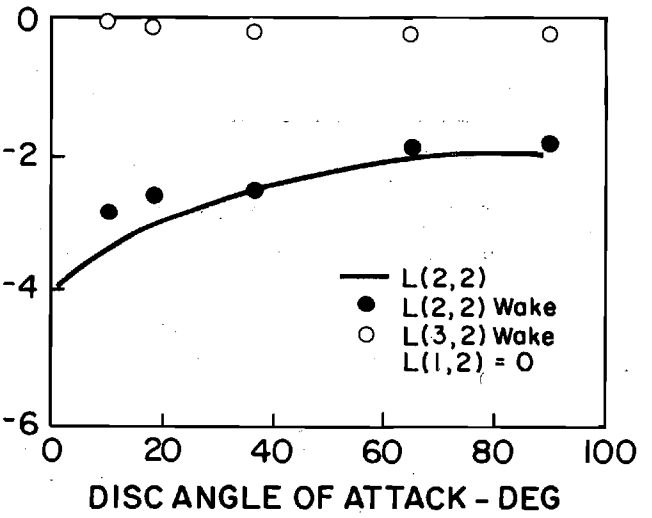

Fig. 5 Verification of second column of L.

Another interesting aspect of Eq. (4a) is the (3, 1) element of [L]. This element provides for a fore-to-aft gradient in induced flow due to thrust and is identical to the Coleman equation for the classical Glauert constant, Ref. 19. This L_{31} term is also one of the more important coupling terms found in the empirical model. The other elements of [L] also behave similarly to the empirical model. Of special importance is the fact that $L_{33} = 0$ at $\alpha = 0$ for both models.

With respect to the [M] matrix, the elements in Eq. (4b) are also derived from the unsteady, actuator-disk theory. When a uniform lift distribution is used for C_T, the elements are identical to those of momentum theory. When the lift is forced to be zero at the rotor center, however, then M_{11} becomes $\frac{128}{75\pi}$ ($=0.54$) rather than $\frac{8}{3\pi}$ ($=0.85$); while M_{22} and M_{33} remain identical to the values from momentum theory (i.e., from an impermeable disk).

Thus, the Pitt model provides all of the important ingredients for a good dynamic inflow model: 1) simplicity of closed-form expressions, 2) recovery of momentum theory in axial flow,

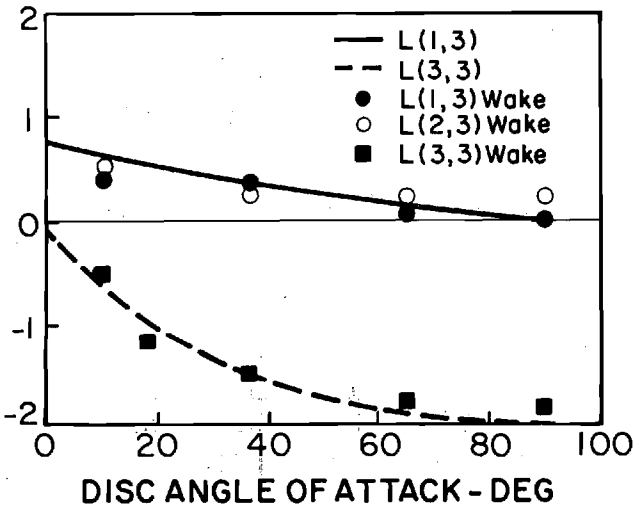

Fig. 6 Verification of third column of L.

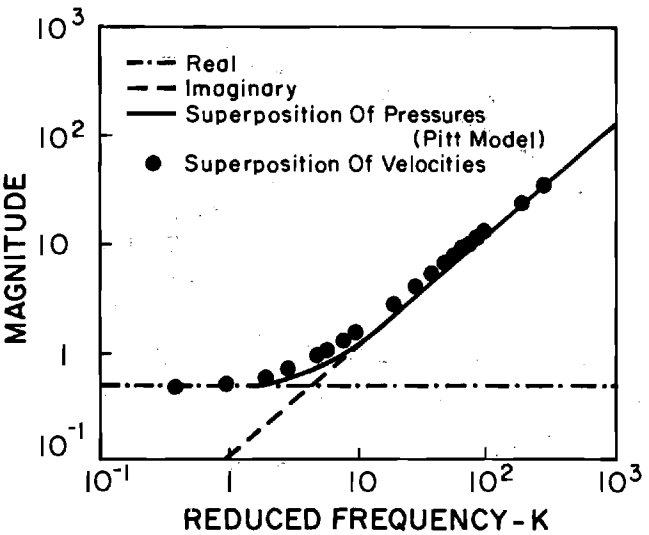

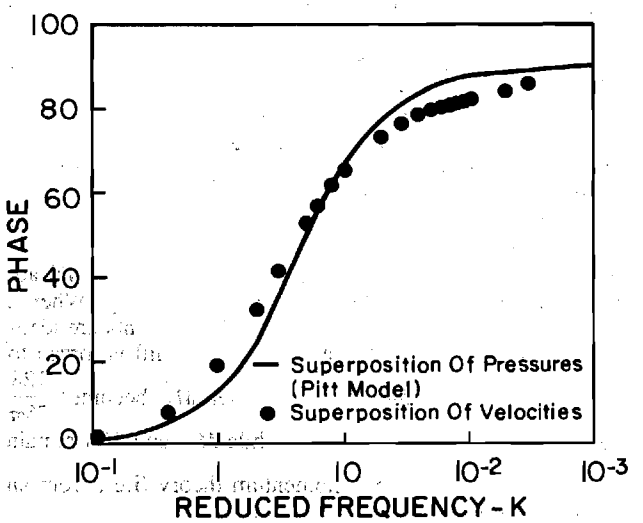

Fig. 7 Comparison of harmonic pressure distributions as calculated by the Pitt model (superposition of apparent-mass pressure) with those of an unsteady wake calculation (superposition of velocities).

3) reasonable behavior for edgewise flow, and 4) correlation with wake calculations.

The major task remaining to complete validation of the Pitt model is a direct comparison with experimental flapping data, and that will be given in the following two sections.

Comparison of Pitt Model with Static Data

In this section, we compare the Pitt model to the Lockheed-Ames data of Ref. 7. The first comparison concentrates on the nine static derivatives analyzed in Ref. 5. The derivatives are for $p = 1.17$ and are given as functions of advance ratio for $0 < \mu < 0.5$. Comparison is made of the theory without dynamic inflow, momentum theory, the Pitt model, and the experimental data. All coefficients are normalized on σa.

We begin with the C_T derivatives, Figs. 8a–c. For C_T/θ_o, momentum theory and the Pitt model give equally good data correlation. For C_T/θ_s, the data show an initial sign reversal followed by a return to a more conventional response. The Pitt model also gives this sign reversal, which is not predicted by momentum theory. For $\mu \geq 0.2$, however, momentum theory is a little better. For C_T/θ_c, only the Pitt model gives any derivative, but no data is available for comparison. We now turn to the C_L derivatives, Figs. 9a–c. For C_L/θ_o, momentum theory is little different from the no-inflow theory, and neither gives even a qualitative correlation. The Pitt model, however, is much better. For C_L/θ_s, momentum theory is again inadequate while the Pitt model is very good. In C_L/θ_c, both inflow models do fairly well for $\mu < 0.4$. The theory without dynamic inflow is not satisfactory. Next, we consider the C_M derivatives, Figs. 10a–c. For C_M/θ_o, only the Pitt model predicts the large increase in the derivative for $\mu < 0.2$, but momentum theory does better at higher μ. For C_M/θ_s, momentum theory is slightly better than the Pitt model, and, for C_M/θ_c, the Pitt model correctly predicts the increase in derivative for $\mu > 0.1$. For $\mu \leq 0.1$, however, momentum theory seems better.

The above static comparisons contain a mixture of judgments with momentum sometimes "better" and the Pitt model sometimes "better." However, a study of Figs. 8–10 shows that "better" for the Pitt model usually means a qualitative improvement in correlation, whereas "better" for momentum theory is, at best, only slightly better. In other words, the Pitt model is never qualitatively wrong and is seldom quantitatively wrong, while momentum theory is qualitatively wrong on three of eight derivatives.

Comparison with Dynamic Data

We are now ready to compare the Pitt model with the dynamic measurements of Ref. 7. This data, at $p = 1.15$, is for nearly the same configuration as that of the static data. Thus, the $\omega = 0$ results closely resemble the static data of Figs. 8–10. The original dynamic data in Ref. 8 were presented only for $\mu = 0.51$. Here, we expand the data base to include three advance ratios: $\mu = 0.27$, 0.36, and 0.51. Thus, we present entirely new data correlations and provide a broader comparison. Only roll and pitch moments are given because no dynamic thrust measurements were made. Consequently, the following figures are for the six dynamic roll and pitch moment derivatives (magnitude and phase). For the sake of brevity, phase angles are not presented for all derivatives. However, the phase angles that are given are representative of those omitted.

Figures 11–13 give $C_L/\sigma a$ due to θ_o at three advance ratios. The points near $\omega = 0$ correspond to the static data in Fig. 10. We give the magnitude of the response as a function of ω. Several items are noteworthy. First, the static results at $p = 1.15$ (inferred from $\omega = 0$) show the same deviations as do the derivatives in Fig. 9a. In particular, the derivative from the Pitt model is smaller than the data, and the null point is shifted. Despite this, however, the theory does a good job of data correlation as ω is increased. For example, at all three values of μ, the no-inflow and momentum theories show a nearly null

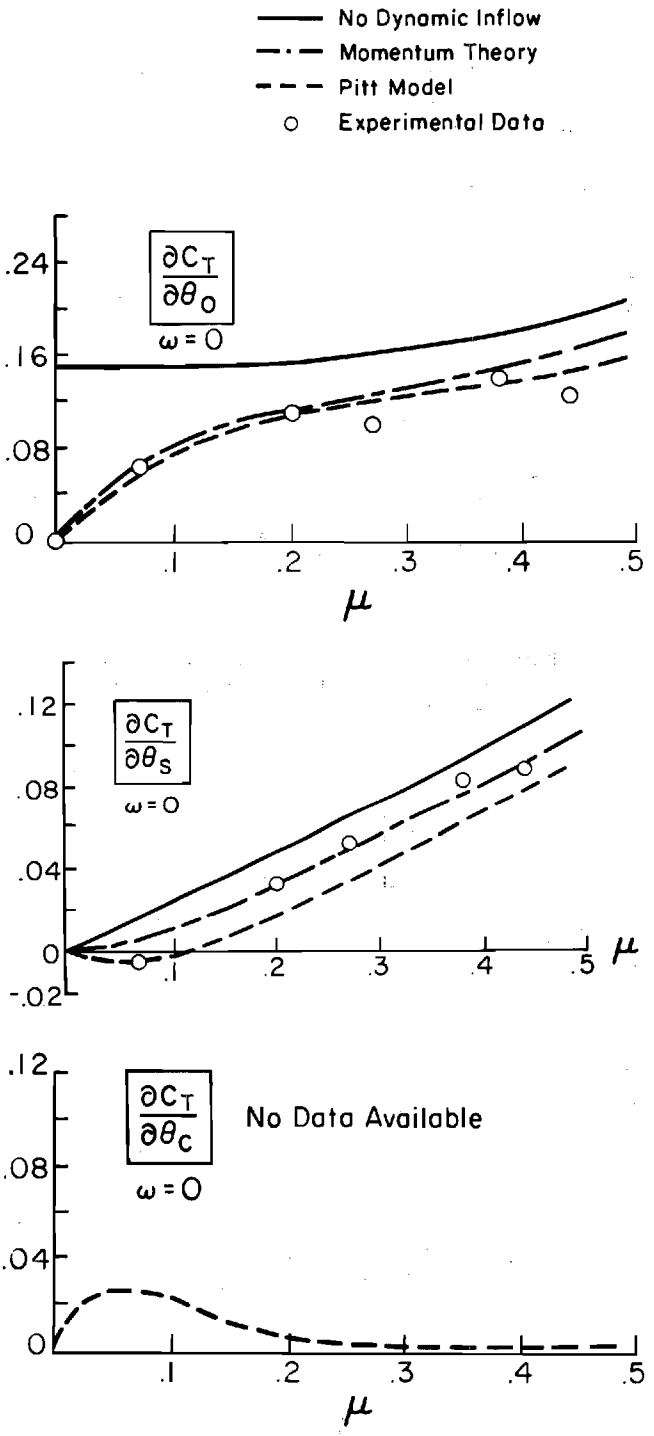

Fig. 8 Rotor thrust response for $\omega = 0$, $p = 1.17$, $\gamma = 4.2$, $B = 0.97$, $e_{pc} = 0.25$, $\sigma a = 0.73$, $\bar{v}_o = \lambda = 0$; all coefficients normalized on σa.

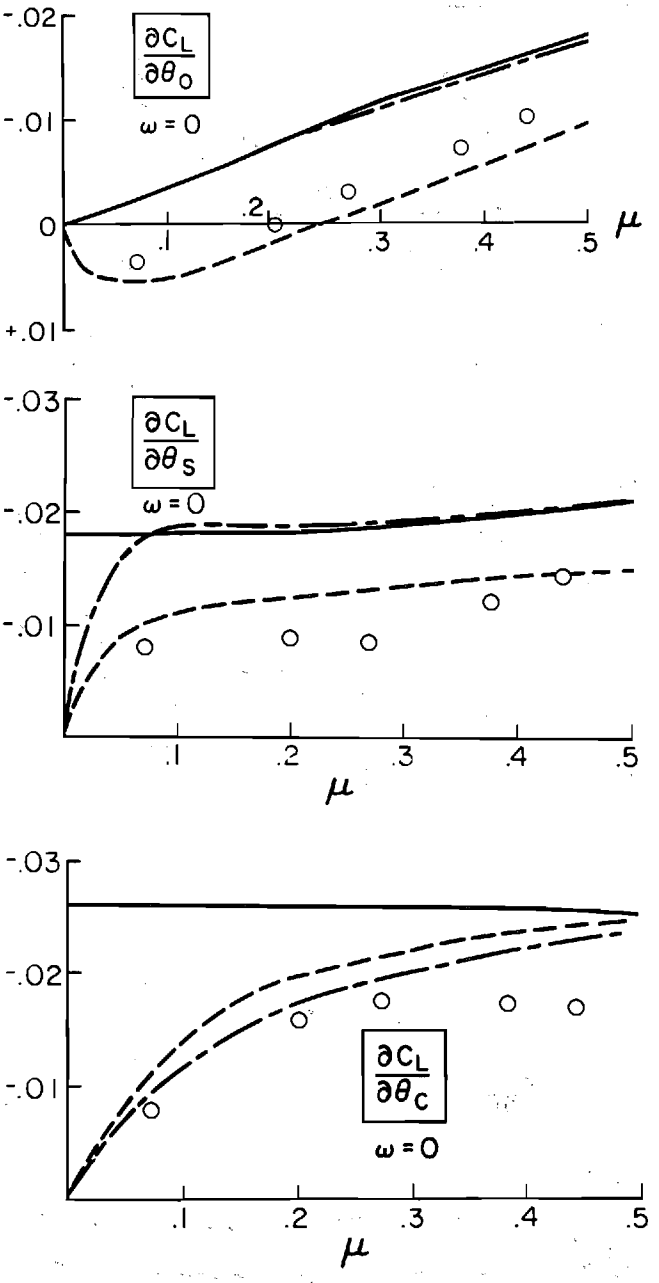

Fig. 9 Rotor roll moment response for $\omega = 0$, $p = 1.17$, $\gamma = 4.2$, $B = 0.97$, $e_{pc} = 0.25$, $\sigma a = 0.73$, $\bar{v}_o = \lambda = 0$; all coefficients normalized on σa.

point at $\omega = 0.4$ accompanied by a near discontinuity in phase from 90° to 270°. The data and the Pitt model, however, do not follow this pattern and show a level amplitude and smooth phase change through the region. (Recall that $\theta = 0°$ and $\theta = 360°$ are identical.) Another note here is that momentum theory provides virtually no improvement in correlation, whereas the Pitt model provides a definite improvement.

In Figs. 14–16, we examine $\partial C_L/\partial\theta_s$ at the same three advance ratios. The phase at $\mu = 0.36$ is representative. One can also use Fig. 1 in this comparison, since it is the C_L/θ_s derivative in hover, $\mu = 0$. In hover, momentum theory and the Pitt model are identically good. As advance ratio increases, however, the data begin to change dramatically while the no-inflow and momentum theories remain stationary. The actuator-disk model on the other hand changes with advance ratio and provides good static correlation ($\omega = 0$). Similarly, as ω increases, results with the Pitt model follow the data well up to $\omega = 0.6$. Beyond that, the data lie below all three theories. In terms of phase, the Pitt model does well except for the rapid change in phase at $\omega = 0.4$ associated with antiresonance. Thus, the Pitt model does well at all advance ratios from 0 to 0.51.

For the remainder of the derivatives, we will present only the $\mu = 0.36$ correlations since these are fairly representative. Figure 17 gives $\partial C_L/\partial\theta_c$. For comparison purposes we can again refer to Fig. 1 since, in hover, C_L/θ_c is analogous to $\partial C_M/\partial\theta_s$. At $\mu = 0$, the momentum theory and Pitt model are equally good (being identical), and they show the large drop in static

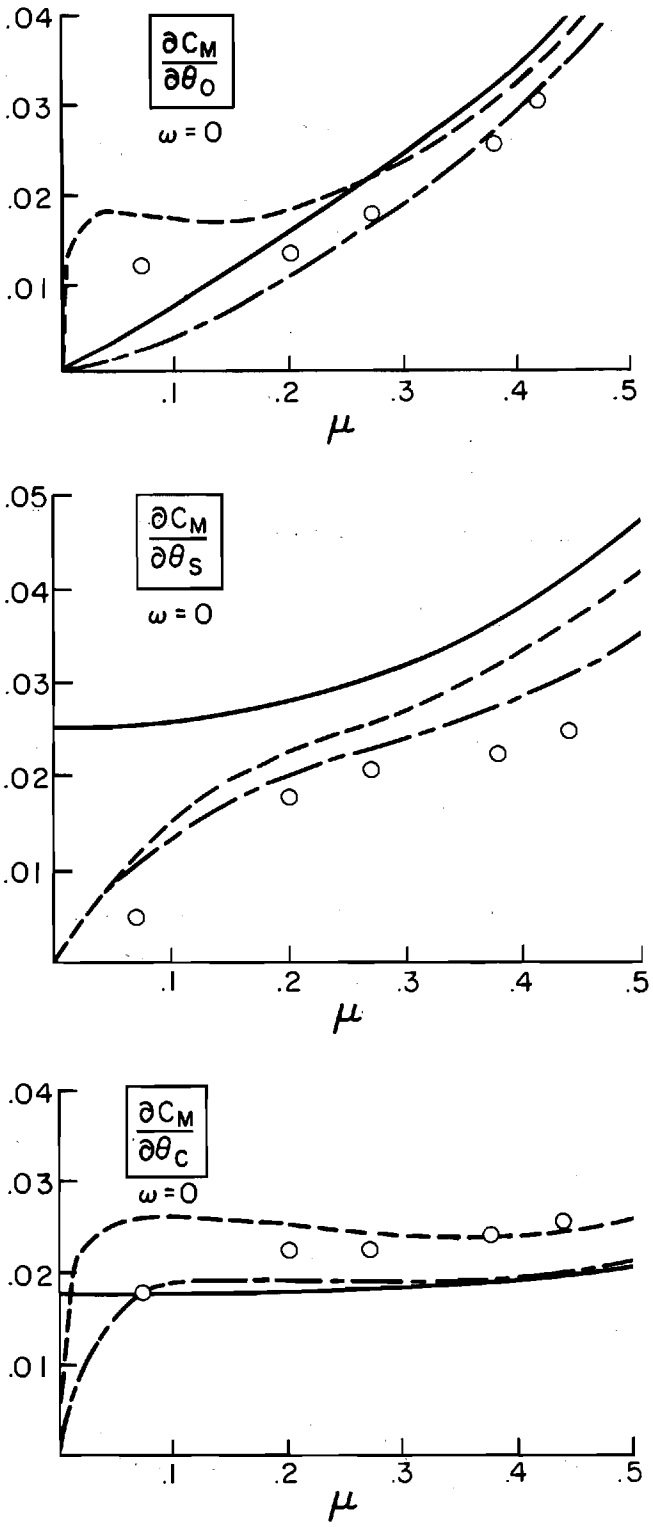

Fig. 10 Rotor pitch moment response for $\omega = 0$, $p = 1.17$, $\gamma = 4.2$, $B = 0.97$, $e_{pc} = 0.25$, $\sigma a = 0.73$, $\bar{\nu}_o = \lambda = 0$; all coefficients normalized on σa.

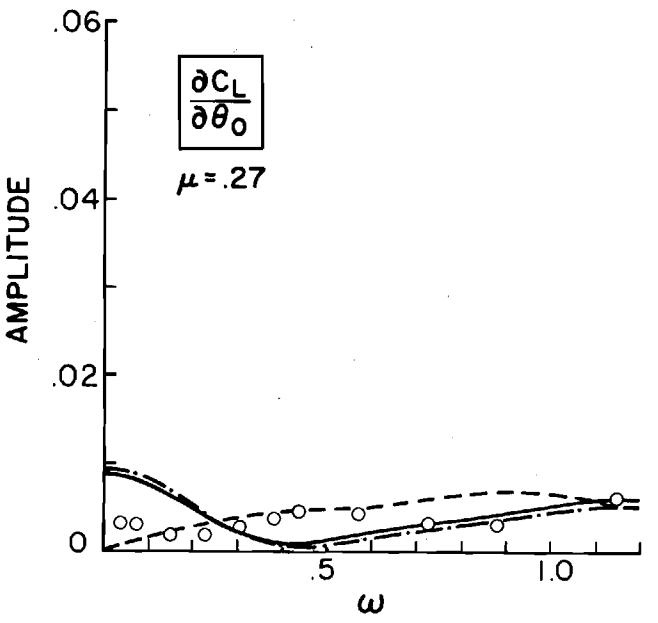

Fig. 11 Rotor response in forward flight, $C_L/\sigma a$ due to θ_o for $\mu = 0.27$, $p = 1.15$, $\gamma = 4.25$, $B = 0.97$, $e_{pc} = 0.25$, $\sigma a = 0.73$, $\bar{\nu}_o = \lambda = 0$. (See Fig. 8 for legend.)

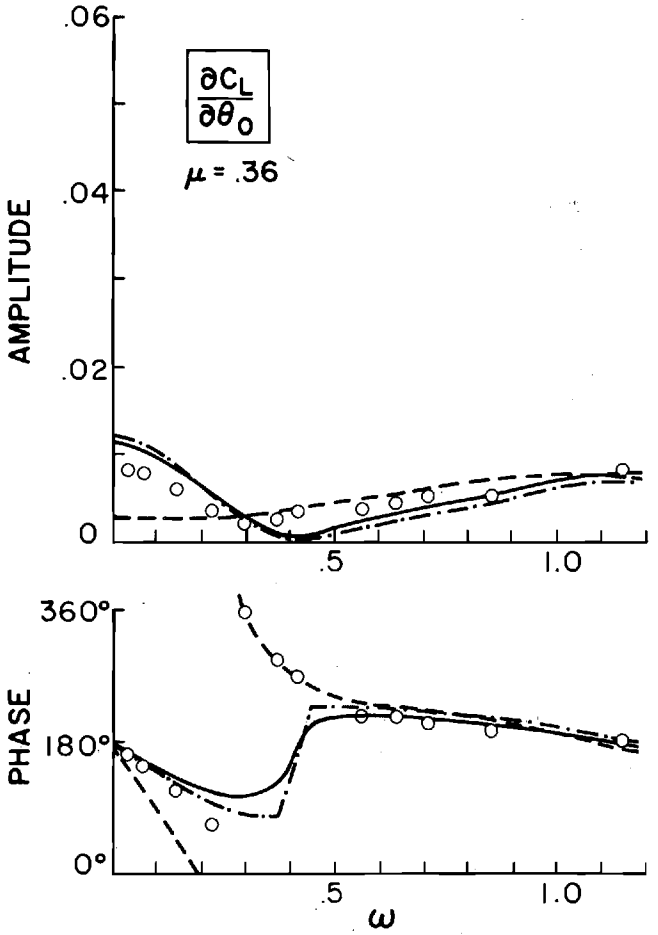

Fig. 12 Rotor response in forward flight, $C_L/\sigma a$ due to θ_o for $\mu = 0.36$, $p = 1.15$, $\gamma = 4.25$, $B = 0.97$, $e_{pc} = 0.25$, $\sigma a = 0.73$, $\bar{\nu}_o = \lambda = 0$. (See Fig. 8 for legend.)

derivative followed by a peak and return to no-inflow values. At $\mu = 0.36$, both theories still show the proper reduction in static value, but the Pitt model does better at reproducing the return to no-inflow theory. Both theories do well on phase angle (not shown).

We now turn to pitch-moment data. Figure 18 provides $C_M/\sigma a$ with θ_o. This derivative is zero in hover but is quite large at $\mu = 0.36$. In this case, momentum theory shows too much reduction in the static value while the Pitt model is very good. (Recall that the momentum theory was slightly better at $p = 1.17$.) One notices two ripples in the data (at $\omega = 0.4$ and ω

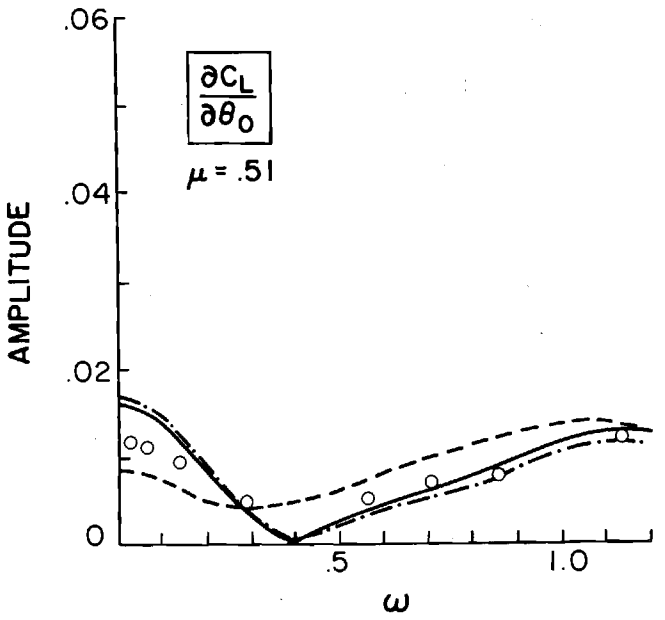

Fig. 13 Rotor response in forward flight, $C_L/\sigma a$ due to θ_o for μ = 0.51, p = 1.15, γ = 4.25, B = 0.97, e_{pc} = 0.25, σa = 0.73, $\bar{v}_o = \lambda$ = 0. (See Fig. 8 for legend.)

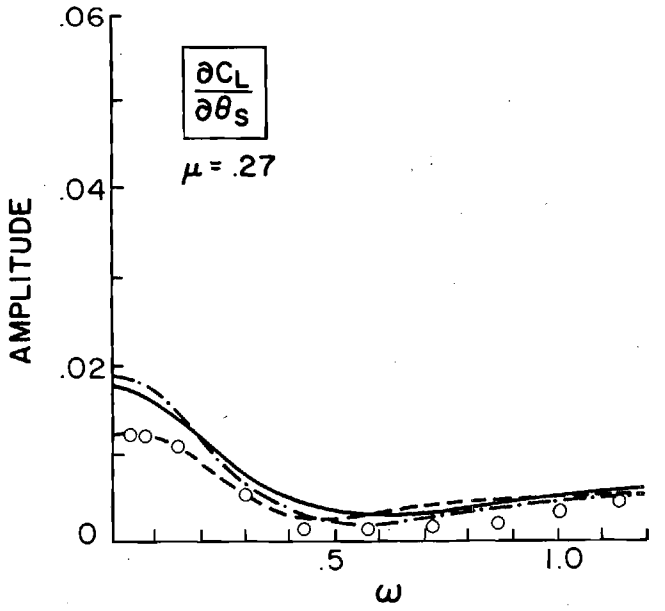

Fig. 14 Rotor response in forward flight, $C_L/\sigma a$ due to θ_s for μ = 0.27, p = 1.15, γ = 4.25, B = 0.97, e_{pc} = 0.25, σa = 0.73, $\bar{v}_o = \lambda$ = 0. (See Fig. 8 for legend.)

= 0.7). These are stand resonances and introduce some contamination of the data. It is possible that these resonances account for some deviations in roll-moment data, especially the null point in $\partial C_L/\partial\theta_s$. The phase angle for $\partial C_M/\partial\theta_c$ (not shown) is insensitive to inflow model, and all models show equally good correlation.

In Fig. 19, we have $\partial C_M/\partial\theta_s$ at μ = 0.36, which can be compared with the hover value in Fig. 1. The stand resonance is clearly seen at ω = 0.4.

Both the Pitt model and the momentum theory do well at μ = 0.36 with the momentum theory being slightly better. C_M with θ_s is the only derivative for which momentum theory is consistently better than the empirical and the Pitt models. Once again, all models give good phase correlation.

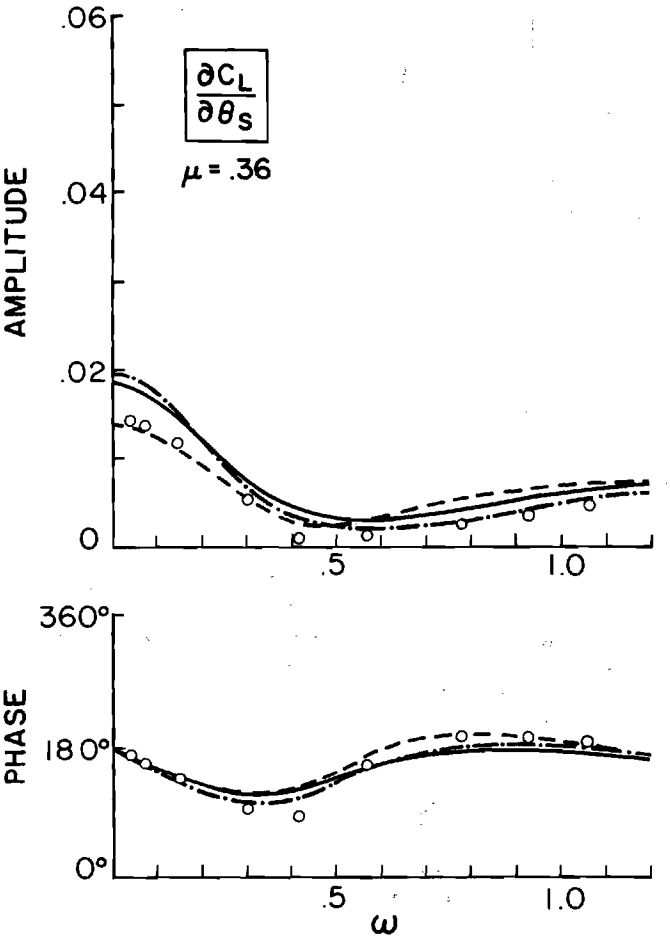

Fig. 15 Rotor response in forward flight, $C_L/\sigma a$ due to θ_s for μ = 0.36, p = 1.15, γ = 4.25, B = 0.97, e_{pc} = 0.25, σa = 0.73, $\bar{v}_o = \lambda$ = 0. (See Fig. 8 for legend.)

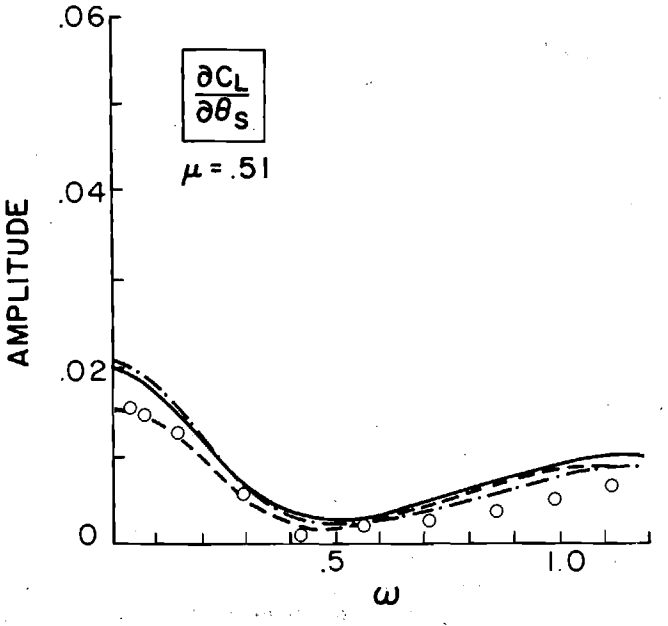

Fig. 16 Rotor response in forward flight, $C_L/\sigma a$ due to θ_s for μ = 0.51, p = 1.15, γ = 4.25, B = 0.97, e_{pc} = 0.25, σa = 0.73, $\bar{v}_o = \lambda$ = 0. (See Fig. 8 for legend.)

The final figure to be presented is $C_M/\sigma a$ with θ_c, Fig. 20. Both magnitude and phase are shown, and the corresponding hover results are $\partial C_L/\partial\theta_s$, Fig. 1. The Pitt model predicts the

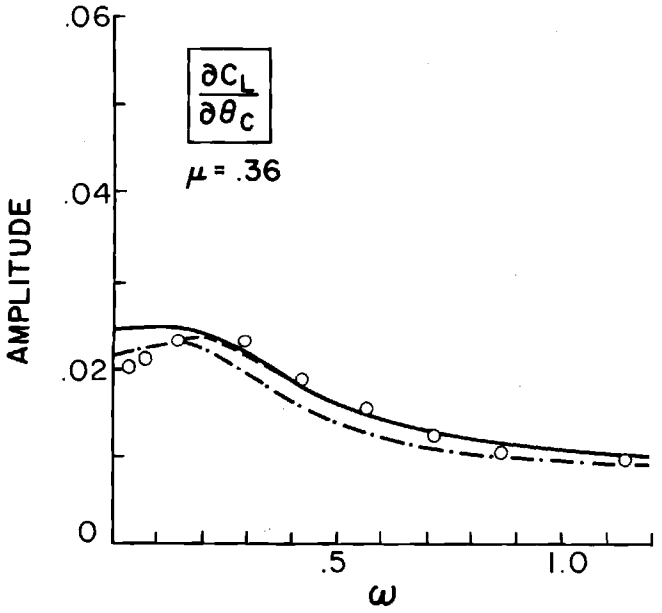

Fig. 17 Rotor response in forward flight, $C_L/\sigma a$ due to θ_c for μ = 0.36, p = 1.15, γ = 4.25, B = 0.97, e_{pc} = 0.25, σa = 0.73, $\bar{v}_o = \lambda$ = 0. (See Fig. 8 for legend.)

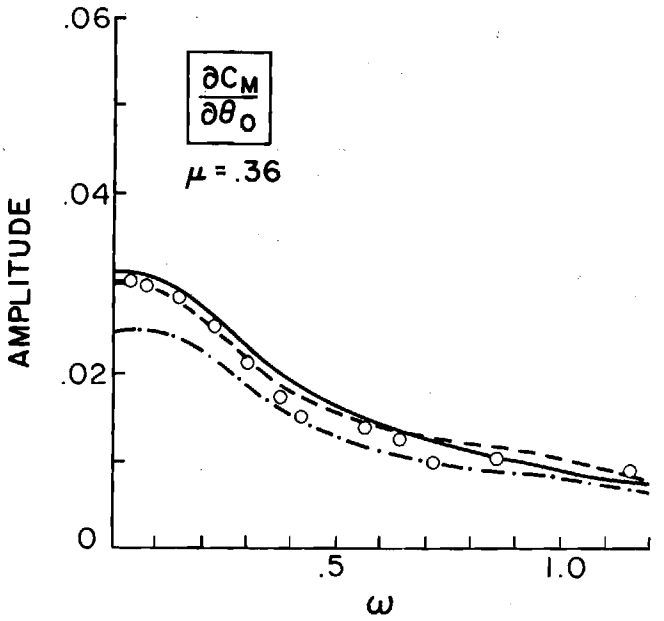

Fig. 18 Rotor response in forward flight, $C_M/\sigma a$ due to θ_o for μ = 0.36, p = 1.15, γ = 4.25, B = 0.97, e_{pc} = 0.25, σa = 0.73, $\bar{v}_o = \lambda$ = 0. (See Fig. 8 for legend.)

increased static derivative (ω = 0), and the model does well for $\omega < 0.5$. For larger values of ω, it is hard to distinguish the best theory.

Once again, we notice dramatic improvement in correlation when the Pitt model is used. Although momentum theory is sometimes helpful, most of the time the inclusion of momentum-theory inflow does no better than the theory with no dynamic inflow. On the other hand, the Pitt model usually produces a substantial improvement in correlation.

Conclusions

Over the past thirty years, the theory of dynamic inflow has developed in response to experimental data. The preponderance

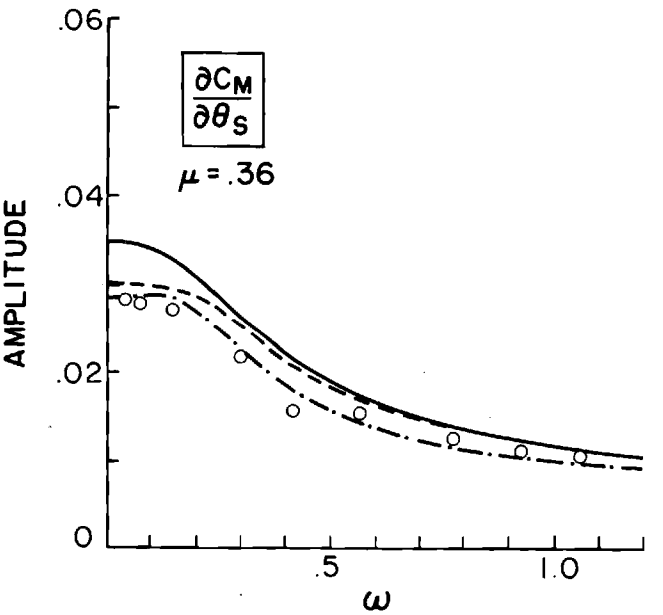

Fig. 19 Rotor response in forward flight, $C_M/\sigma a$ due to θ_s for μ = 0.36, p = 1.15, γ = 4.25, B = 0.97, e_{pc} = 0.25, σa = 0.73, $\bar{v}_o = \lambda$ = 0. (See Fig. 8 for legend.)

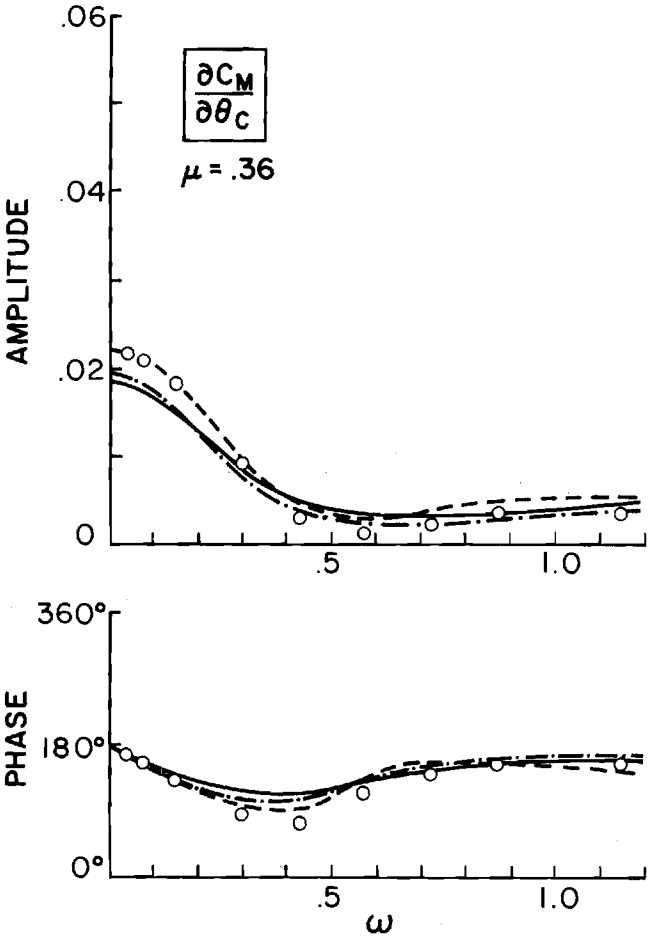

Fig. 20 Rotor response in forward flight, $C_M/\sigma a$ due to θ_c for μ = 0.36, p = 1.15, γ = 4.25, B = 0.97, e_{pc} = 0.25, σa = 0.73, $\bar{v}_o = \lambda$ = 0. (See Fig. 8 for legend.)

of data correlations over that time and the new comparisons presented here lead to the following conclusions:

1) Dynamic inflow has been demonstrated to be a valid physical phenomenon that changes the qualitative nature of rotor response in hover and forward flight.
2) In hover, dynamic inflow is represented extremely well by momentum theory coupled with apparent mass terms (three first-order equations).
3) In forward flight, momentum theory does poorly and cannot predict the major effects of dynamic inflow.
4) The Pitt model, developed from first principles, provides excellent data correlation in forward flight and is identical to momentum theory in hover. Thus, it appears to be the best currently available model for rotor analysis.

Acknowledgment

This work was sponsored by the U.S. Army Research Office, Grant No. DAAG-29-80-C-0092.

References

[1]Amer, K. B., "Theory of Helicopter Damping in Pitch or Roll and a Comparison with Flight Measurements," NACA TN-2136, Oct. 1950, p. 11.

[2]Sissingh, G. J., "The Effect of Induced Velocity Variation on Helicopter Rotor Damping in Pitch or Roll," Aeronautical Research Council Paper No. 101, Technical Note No. Aero 2132, Nov. 1952.

[3]Shupe, N. K., "A Study of the Dynamic Motions of Hingeless Rotored Helicopters," Ph.D. Thesis, Princeton, Sept. 1970.

[4]Curtiss, H. C., Jr. and Shupe, N. K., "A Stability and Control Theory for Hingeless Rotors," *Proceedings of the 27th Annual Forum of the American Helicopter Society*, May 1971, Paper No. 541.

[5]Ormiston, R. A. and Peters, D. A., "Hingeless Rotor Response with Nonuniform Inflow and Elastic Blade Bending," *Journal of Aircraft*, Vol. 9, No. 10, Oct. 1972, pp. 730–736.

[6]Carpenter, P. J. and Fridovitch, B., "Effect of Rapid Blade Pitch Increase on the Thrust and Induced Velocity Response of a Full Scale Helicopter Rotor," NACA TN-3044, Nov. 1953.

[7]Kuczynski, W. A. and Sissingh, G. J., "Characteristics of Hingeless Rotors with Hub Moment Feedback Controls Including Experimental Rotor Frequency Response," NASA CR 114427, Jan. 1972.

[8]Peters, D. A., "Hingeless Rotor Frequency Response with Unsteady Inflow," *Rotorcraft Dynamics*, NASA SP-352, Feb. 1974, pp. 1–13.

[9]Ormiston, R. A., "Application of Simplified Inflow Models to Rotorcraft Dynamic Analysis," *Journal of the American Helicopter Society*, Vol. 21, No. 3, July 1976, pp. 34–39.

[10]Gaonkar, G. H., Mitra, A. K., and Reddy, T. S. R., "Feasibility of a Rotor Flight Dynamics Model with First-Order Cyclic Inflow and Multi-Blade Modes," *Proceedings of the AIAA Dynamics Specialists' Meeting*, Atlanta, Georgia, April 1981, p. 15.

[11]Pitt, D. M. and Peters, D. A., "Theoretical Predictions of Dynamic Inflow Derivatives," *Vertica*, Vol. 5, No. 1, March 1981.

[12]Gaonkar, G. H. et al., "The Use of Actuator-Disc Dynamic Inflow for Helicopter Flap-Lag Stability," *Journal of the American Helicopter Society*, Vol. 28, No. 3, July 1983, pp. 79–88.

[13]Peters, D. A., "The Importance of Steady and Dynamic Inflow on the Stability of Rotor-Body Systems," Proceedings of the ITR Methodology Workshop, NASA-Ames Research Center, June 21–22, 1983.

[14]Crews, S. T., Hohenemser, K. H., and Ormiston, R. A., "An Unsteady Wake Model for a Hingeless Rotor," *Journal of Aircraft*, Vol. 10, No. 12, Dec. 1973, pp. 758–760.

[15]Azuma, A. and Nakamura, Y., "Pitch Damping of Helicopter Rotor with Nonuniform Inflow," *Journal of Aircraft*, Vol. 11, No. 10, Oct. 1974, pp. 639–646.

[16]Ormiston, R. A., "An Actuator Disk Theory for Rotor Wake Induced Velocities," AGARD Specialists Meeting on the Aerodynamics of Rotary Wings, Marseille, France, Sept. 1972.

[17]Pitt, D. M. and Peters, D. A., "Rotor Dynamic-Inflow Derivatives and Time Constants from Various Inflow Models," *Proceedings of the Ninth European Rotorcraft Forum*, Stresa, Italy, Sept. 1983.

[18]Landgrebe, A. J., "An Analytical Method for Predicting Rotor Wake Geometry," *Journal of the American Helicopter Society*, Vol. 14, No. 4, Oct. 1969.

[19]Coleman, R. P., Feingold, A. M., and Stempin, C. W., "Evaluation of the Induced Velocity Field of an Idealized Helicopter Rotor," NACA WRL-126, June 1945.

AIAA'86

AIAA-86-0845-CP

Review of Dynamic Inflow Modeling for Rotorcraft Flight Dynamics

G.H. Gaonkar, Florida Atlantic Univ., Boca Raton, FL; and D.A. Peters, Georgia Institute of Technology, Atlanta, GA

AIAA/ASME/ASCE/AHS 27th Structures, Structural Dynamics and Materials Conference

May 19-21, 1986/San Antonio, Texas

REVIEW OF DYNAMIC INFLOW MODELING FOR ROTORCRAFT FLIGHT DYNAMICS

G.H. Gaonkar
Florida Atlantic University
Boca Raon, FL 33431

David A. Peters
Georgia Institute of Technology
Atlanta, GA 30332

Abstract

Dynamic inflow and its influence on some problems of rotorcraft flight dynamics are briefly introduced under transient conditions, as required in flight dynamics. The bases of modeling range from a simple empirical formulation to an involved prescribed-wake, discrete-vortex analysis of a four-bladed rotor. The emphasis is on perturbed linear versions of inflow in matrix form and on the sensitivity of low-frequency stability and response to inflow. However, non-linear versions for use in time-history solutions are presented. Coverage also includes the areas of weakness, controversial notions, and the need for additional test data on rotor-body damping in forward flight for a better appreciation of the developments in modeling dynamic inflow.

Nomenclature

a	slope of lift curve
B	tip loss factor
C_T	thrust coefficient
C_L, C_M	roll and pitch moment coefficients
C_{2L}, C_{2M}	second-harmonic lift coefficients
C_d, C_d^*	drag coefficient, equivalent drag coefficient
C_Q	power coefficients
$\bar{f}$	fuselage drag coefficient
h	wake spacing
I_A	apparent inertia
k	Sissing factor, reduced frequency
K_m	apparent mass coefficient
K_I	apparent inertia coefficient
$[L]$	matrix of inflow gains
$[M]$	matrix of apparent mass terms
M_A	apparent mass
N	number of blades
P	flap frequency, per/rev
q	roll rate, per rotor revolution
r	radial position
R	blade radius
V	mass-flow parameter
α, α_s	rotor shaft angle
γ, γ^*	Lock number, equivalent Lock number
δ	perturbation
$\theta_o, \theta_s, \theta_c$	collective and cyclic pitch ($\theta_o = \bar{\theta}$)
$\bar{\lambda}$	total inflow ratio, $\gamma + \bar{\nu}$
μ	advance ratio
$\bar{\nu}$	steady induced flow
$\nu_o, \nu_s, \nu_c, \nu_{2s}$	perturbation induced flow
ρ	density of air solidity
σ	solidity
$[\tau]$	matrix of time constants
ψ	azimuth angle ($=\Omega t$)

I. INTRODUCTION

1. Background

Dynamic inflow modeling in rotorcraft flight dynamics is a means of accounting for the low-frequency wake effects under unsteady or transient conditions. Here, we distinguish between the two facets of unsteady aerodynamics --- dynamic inflow that is viewed globally as rotor-disk downwash dynamics under unsteady flight conditions, and the classical unsteady rotor aerodynamics that is viewed locally as airfoil aerodynamics under steady flight conditions. In other words, inflow is treated globally more as a large mass of air rather than being treated locally as individual vortices. For convenience, this second facet, extended to unsteady flight conditions, is referred to as extended unsteady aerodynamics. It is used to examine critically the assumptions in modeling dynamic inflow that

are based on global approximations. Thus, this review refers primarily to the first facet of transient downwash dynamics and marginally to the second facet of extended unsteady aerodynamics. Elaborating, we spell out the reasons for such an approach. First, even for steady flight conditions, the rotor wake is complex and is not well understood, though it has been the subject of extensive research and reviews during the past years.[1] Further, this research is generally oriented towards high frequency phenomena such as flutter and loads analyses or towards performance analysis. A state-of-the-art summary is available in the monographs of Johnson[1] and Baskin[2]. A good account of induced flow under steady conditions is given in Heyson's review[3] and in Bramwell's text[4] as well. Second, dynamic inflow modeling per se can be treated as an open-loop problem, for example, as treated by Joglekar and Loewy (5,6) under steady flight conditions and by Pitt and Peters (6-8) under unsteady flight conditions. As shown in Figure 1, dynamic inflow introduces perturbations in rotor-disk loading which, in turn, affect dynamic inflow. Thus dynamic inflow in flight dynamics applications is a closed-loop problem, for example, as treated by Gaonkar et al., (9-16) and Johnson. (17) Recently, Pitt and Peters[6,8] used Landgrebe's prescribed wake, discrete-vortex analysis of a four-bladed rotor to assess the adequacy of an actuator-disk inflow model. Most rotor wake analyses are intrinsically keyed to vortex element representations of one form or the other, under steady flight conditions. (18-20). When extended to unsteady flight conditions as a closed-loop problem, they become over sophisticated or hopelessly complicated. (19,20) Third, since the early 1950's, considerable experience has been accumulated in dynamic inflow modeling and in recognizing dynamic inflow as an important ingredient in improving the correlation between predicted and measured data. As a matter of fact, two fundamental concepts of inflow modeling were available some thirty years ago. In particular, both change in induced flow due to perturbations in lift and the time lag for this change can be respectively traced back to the pioneering work of Sissingh, (21) and of Carpenter and Fridovich. (22) Moreover, Sissingh's work was motivated by Amer's observation (23) that part of the difference between predicted and measured pitch-roll damping is due to dynamic inflow effects.

2. Recent Developments

With this as background, we come to dynamic inflow research of the past 15 years, particularly with the advent of non-articulated rotorcraft. In 1970, Curtis and Shupe (24,25) initiated this research by refining Sissingh's quasi-steady formulation (no time lag) to include induced flow perturbations in pitch and roll moments. Their reformulation (24,25) shows that the quasisteady effect of dynamic inflow in pitch and roll can be accounted for with a reduced Lock number, γ^*. It is significant that γ^* can be identified with the lift deficiency function from Loewy's shed vorticity theory and Miller's vorticity tube theory. (26-29) The fact that dynamic inflow can be recovered in good measure from sophisticated vorticity theories, gives considerable viability and credance to dynamic inflow formulation. During 1972-1976, Ormiston and Peters (30-32) gave a state variable formulation of unsteady inflow in which the three uncoupled inflow components (uniform, side-to-side and fore-to-aft) assume the role of degrees of freedom. Following Carpenter and Fridovich, they (30-32) introduced the time lag (or the effects of apparent mass) of inflow which is approximated by the apparent mass of an impermeable disk. The result was the unsteady momentum theory model which gave excellent correlation with Kuczynski's measured control derivatives in hover, but not in forward flight. (30,32-35). Therefore, during 1972-1979, the search for a viable alternative to the momentum theory led to the development of empirical models by Ormiston and Peters (30-31) and to tests by Hohenemser et al. (36-40) to identify inflow parameters. The identified time-lag parameter in roll and pitch superbly agreed with the impermeable disk value (36).

Since the 1980's, dynamic inflow has been one of the intensely pursued areas of research which, in good measure, was spurred by Bousman's test data (41) on aeromechanical stability in hover. One aspect of that research concerns a series of direct and indirect correlations with Bousman's data, (12,17,42-47) which established the role of dynamic inflow. It would seem that dynamic inflow "has been driven constantly by the impetus of experimental data," (46) as was the case in 1948 when Amer presented his correlation studies on pitch-roll damping and in 1970 when Kuczynski presented his test data on control derivatives. (33-35) Another aspect of that research brings dynamic inflow to its development today---the Pitt model, its validation on the basis of pure flap-response data and its application to help predict damping and response in forward flight. (6-8, 42-52)

The crux of the matter, however, lies in assessing how far the verified Pitt model improves correlation with the measured damping data in forward flight. Here, only the barest beginnings have been made, as seen from a recent correlation study of Gaonkar et al. on lag damping of isolated rotors. (48) Nor is the dynamic inflow literature without controversial notions on several aspects of inflow modeling. (17, 42-48). Yet, very little information is available on a unified basis. Accordingly, this review appraises different linear dynamic-inflow models with the benefit of 'extended' unsteady aerodynamics and test data, and discusses non-linear versions in time history solutions. The areas of weakness and controversial notions are covered as well.

II. BASIS OF MODELING

We now come to the developments of modeling dynamic inflow. The related efforts are presented in a sequential and integrated manner toward facilitating an appreciation of the degree of sophistication that can be built into globally

approximated inflow models. We also emphasize the strengths and weaknesses of such models and, accordingly, consider eight widely used bases of modeling, some of them being interrelated. These bases are: 1) simple momentum and vortex theories (without time delay or apparent mass effects), 2) empirical models, 3) extended momentum theory, 4) mass effects or time delay, 5) equivalent Lock number and profile drag coefficient, 6) unsteady actuator disk theory, and 7) prescribed wake theory, and 8) higher harmonic models.

1. Simple Momentum and Vortex Theories:

Some thirty five years ago, Amer (23) analyzed the problem of rotor damping in roll and correlated the predicted data with flight test measurements in hover and forward flight. His investigation showed that the damping decreases with increasing pitch. As for the discrepancy between the predicted and measured data, Amer succinctly observes that this discrepancy is "due primarily to changes in induced velocity which occur during rolling (or pitching) because of changes in the distribution of thrust around the rotor disk". (23) This observation more or less forms the stimulus for most of the subsequent dynamic inflow work. It fell to Sissingh,[21] however, to explain this discrepancy by quantifying Amer's work with the inclusion of variable inflow or, more precisely, of changes in induced velocities caused by transient changes in rotor disk loading. Starting from Glauert's classical momentum theory postulate, Sissingh (21) gives the formula

$$k\,(\delta\lambda/\lambda) = \delta C_T/C_T \qquad (1)$$

where $k = 2$ in hovering and $k = 1$ in forward flight with $V > 40$ mph ($\mu \gg \lambda$). For transitional flight conditions when induced flow λ cannot be neglected in comparison to μ, Sissingh suggests an "appropriate" value for k ($1 \le k \le 2$) on an ad hoc basis.

It is easily seen that equation (1) follows from the classical results

$$\lambda = \sqrt{C_T/2}, \quad \mu = 0 \qquad (2a)$$

$$\lambda = C_T/2\mu, \quad \mu \gg \lambda \qquad (2b)$$

Sissingh was probably the first to initiate a systematic exposition that established a relation between instantaneous perturbations (or transients) in thrust δT, and perturbations in induced flow, $\delta\lambda$. The induced flow λ is an involved function of radius r and spatial azimuth position ψ. To arrive at a tractable model, he uses a first harmonic inflow and lift distribution, without radial variation,

$$\lambda = \lambda_0 + \lambda_s \sin\psi + \lambda_c \cos\psi \qquad (3)$$

Here, λ_0 is the uniform inflow, while λ_s and λ_c are side-to-side and fore-to-aft inflow variations. His analysis convincingly shows that the predicted damping values with the inclusion of induced velocity perturbations, as typified in equation (1), improves correlation with the flight test data of Amer (23). In figure 2, we have shown the ratio between the thrust-vector tilt and the tip-path-plane tilt without the inclusion of $\delta\lambda$ and δC_T effects, as was done by Amer (dotted lines) and with the inclusion of $\delta\lambda$ and δC_T effects as was done by Sissingh (full line) for the hovering condition. The appreciable effect of inflow perturbations is clearly evident.

The matter rested here for almost twenty years, till this was further refined by Curtiss and Shupe (24,25) on the basis of first harmonic inflow distribution, used by Sissingh, equation (3). The refinement basically pertains to expression of equation (1) as the perturbation rolling moment δC_L and the perturbation pitching moment δC_M due to perturbation inflow gradients $\delta\lambda_s$ and $\delta\lambda_c$. This work was further continued by Ormiston and Peters (30) who expressed the dynamic inflow relation in a matrix context such that the perturbation inflow components ($\delta\lambda_0$, $\delta\lambda_s$, $\delta\lambda_c$) can be identified with a state variable vector as a feedback system. When equation (3) is substituted into equations (2a) and (2b), the corresponding perturbation relation is

$$\begin{Bmatrix} \delta\lambda_o \\ \delta\lambda_s \\ \delta\lambda_c \end{Bmatrix} = \frac{1}{C} \begin{bmatrix} \frac{1}{2} & 0 & 0 \\ 0 & -\frac{3}{2} & 0 \\ 0 & 0 & -\frac{3}{2} \end{bmatrix} \begin{Bmatrix} \delta C_T \\ \delta C_L \\ \delta C_M \end{Bmatrix}_{aero} \qquad (4a)$$

With $\mathscr{L}$ representing the matrix of dynamic inflow gains. Symbolically, equation [4] is expressed as

$$\{\delta U\} = \frac{1}{C}\,[\mathscr{L}]\,\{\delta F\} \qquad (4b)$$

aerodynamic only

where $C = 2\lambda_o$ in hover and $C = \mu$ in forward flight. The subscripted statement "aerodynamic only" implies that only aerodynamic contributions are included, since rotor wake is not affected by inertial loads. As observed in reference 30, equation (4) demonstrates that the higher the thrust or the higher the forward velocity, the lower is the perturbation inflow $\delta\lambda$, an observation consistent with Sissingh's study based on equation (1). It should also be noted that the 2nd two equations in matrix equation (4) can be identified with Sissingh's equation (1) for both hovering and forward flight conditions when λ is measured at the 3/4 radius.

When correlated with Kuczynski's test data, (33-35), the simple momentum theory, typified by equation (4), was found to be fairly viable in hover but not in forward flight. To alleviate this situation, Ormiston and Peters (30) develop two versions of the L-matrix. The first one is a combination of the vortex and simple momentum theories, and the second one is an empirical one. The result is (6)

$$L = \frac{1}{\mu}\begin{bmatrix} 1/2 & 0 & 1 \\ 0 & -8/3 & 0 \\ 1/2 & 0 & 0 \end{bmatrix} \quad (5a)$$

Based on the best fit of data, the combined[L] matrix from equations (4a) and (5a) is (6,30)

$$L = \frac{1}{\mu}\begin{bmatrix} 1/2 & 0 & 0 \\ 0 & -3/2 & 0 \\ 1/2 & 0 & 0 \end{bmatrix} \quad (5b)$$

That [L] combined is singular could be an anomaly in the inflow representation or it could be a physically realizable phenomenon associated with a radial shift in the lift distribution of the type described in reference 53. However, we are inclined to suspect that an anomaly is more likely. Moreover, the experimental correlation with the combined theory indicated two things. First, the combined theory is at best marginally better than the simple momentum theory, equation (4). Second, a need exists for a better model in forward flight.

2. Empirical Models

In the absence of a viable alternative model in forward flight, a quasisteady empirical model was postulated in reference 30. It was subsequently extended to the unsteady case with the inclusion of apparent mass or time delay effects (32). The nine elements of the inflow-gains matrix L_E were determined by a least square method, since at each advance ratio μ, more than nine flap response derivatives were measured. The test data were for a static condition (ω=0) and for edgewise flow when the tip-path plane is horizontal. Therefore, the transition condition from hover to forward flight is not accounted for. Further, the model has no rational basis in aerodynamics. It is also rather inconvenient to use, since the elements of L_E are tabulated for different advance ratios. Significantly enough, the L_E matrix exhibits singularities at μ = 0.32 and 0.8. (14)

In spite of such limitations, the unsteady model gave good correlation in forward flight for a comprehensive set of dynamic data (frequency $\omega \neq 0$). Such a correlation over a wide range of frequencies and advance ratios showed that the unsteady empirical model must not be too far from the true aerodynamic behavior. Three striking features that became evident during correlation merit special mentioning, features that provided insights into the development of future viable models. First, the correlation with the quasisteady model was degrading with increasing frequency, since the true induced flow does not have time to respond to rapid changes in disk loading. This feature demonstrates the necessity of including time lag effects, as was pointed out by Carpenter and Fridovich in 1953. Second, the improved correlation with time delay showed that the apparent mass terms are virtually constant for all advance ratios. Third, the elements of L_E vary with advance ratio, and the off-diagonal elements are not equal to zero. This is a desirable feature since the unsymmetrical flow (dependent on μ) and the tip-path plane tilt both introduce off-diagonal coupling between inflow and disk-loading perturbations.

3. Extended Momentum Theory

The inflow distribution $\lambda(r,\psi)$ over the rotor disk is an involved function of both the radial coordinate r and the spatial azimuthal position ψ. Sissingh was probably the first to suggest the distribution given by equation (3) which was used by several other investigators (20,24,25,30,36). As seen from this equation, the distribution has two disadvantages. First, it neglects the effects of radial variation completely. Second, it exhibits discontinuity. As a means of improving the inflow distribution to account for radial variation to some degree and to avoid discontinuity, Peters (32) approximates dynamic inflow perturbations in induced flow by a truncated Fourier series with a prescribed radial distribution. The dynamic inflow ν is perturbed with respect to the steady inflow $\bar{\lambda}$ such that the total inflow is

$$\lambda = \bar{\lambda} + \nu \quad (6)$$

and dynamic inflow is

$$\nu = \nu_0 + \nu_s \frac{r}{R}\sin\psi + \nu_c \frac{r}{R}\cos\psi \quad (7)$$

Similar to the development of equation (4a), according to the inflow distribution in equation (3) that completely neglects radial variation, the improved L matrix in combination with equation 7 takes the form (14,32)

$$\begin{Bmatrix} \nu_0 \\ \nu_s \\ \nu_c \end{Bmatrix} = \frac{1}{v}\begin{bmatrix} 1/2 & 0 & 0 \\ 0 & -2 & 0 \\ 0 & 0 & -2 \end{bmatrix}\begin{Bmatrix} \delta C_T \\ \delta C_L \\ \delta C_M \end{Bmatrix} \quad \text{aerodynamic only} \quad (8)$$

where the mass-flow parameter, v, is obtained from momentum theory as

$$v = \frac{\mu^2 + \bar{\lambda}(\bar{\lambda} + \bar{\nu})}{\{\mu^2 + \bar{\lambda}^2\}^{1/2}} \quad (9)$$

Equation (8) is an improved version of equation (4a). Therefore, in the subsequent comparison of inflow models, only equation (8) together with (9) is referred as the quasisteady momentum theory model.

It is good to note that in the literature there are several formulae of the mass flow parameter ν as noted in table I (43). It appears that some of these are ad hoc formulae and some of the approximations used in such formulae seem to warrant a critical examination. Table 1 gives a comparison of mass flow parameter values for different flight conditions and the subsequent section IV entitled "Philosophical Aspects" contains such an examination.

4. Mass Effects or Time Delay

The preceding development of equation (4b) implies that perturbations in disk loading (δC_T, δC_L, δC_M) follow instantaneously perturbations in inflow (ν_0, ν_s, ν_c) which in turn affect disk-loading perturbations. In other words, the feedback between changes in disk loading and inflow takes place without time lag. However, in transient downwash dynamics, a large mass of air is involved and it is natural to expect that mass effects will have an influence on the complete build up of inflow perturbations due to disk-loading perturbations and vice versa. That is, the feedback will have some form of time delay due to mass effects. This aspect of the problem was investigated by Carpenter and Fridovich (22) during the early 1950s and by Rebont et al. (54-56) during the early 1960s. The inclusion of the mass effects forms an integral part of the development of unsteady inflow models as an extension of the quasisteady inflow treated in the preceding sections. Substantial data-correlation experience with the quasisteady momentum and empirical models clearly demonstrates that unsteady wake effects (not quasisteady alone) play a dominant role in hover, in transitional flight and at low collective pitch (30,32). We will bypass the mathematical details (6,8) and include the rate terms to quasisteady equation:

$$[M]\begin{Bmatrix}\dot{\nu}_0\\ \dot{\nu}_s\\ \dot{\nu}_c\end{Bmatrix} + [L]^{-1}\begin{Bmatrix}\nu_0\\ \nu_s\\ \nu_c\end{Bmatrix} = \begin{Bmatrix}\delta C_T\\ \delta C_L\\ \delta C_M\end{Bmatrix} \qquad \text{(10a)}$$

aerodynamic

Table 1. Comparison of Mass Flow Parameters

Condition	Ref. 32	Ref. 25	Ref. 1, C_T	Ref. 1, C_L and C_M
Hover, $\mu = \lambda = 0$	$2\bar{\nu}$	$2\bar{\nu}$	$2\bar{\nu}$	$\bar{\nu}$
Zero lift, climb $\bar{\nu} = 0$, $\mu = 0$	λ	λ	2λ	λ
Climb, $\mu = 0$	$\lambda + 2\bar{\nu}$	$\lambda + 2\bar{\nu}$	$2\lambda + 2\bar{\nu}$	$\lambda + \bar{\nu}$
Zero lift, edgewise $\bar{\nu} = 0$, $\lambda = 0$	μ	μ	μ	μ
Lifting, edgewise $\lambda = 0$	$\dfrac{\mu^2 + 2\bar{\nu}^2}{\sqrt{\mu^2 + \bar{\nu}^2}}$	μ	$\sqrt{\mu^2 + \bar{\nu}^2} + \bar{\nu}$	$\sqrt{\mu^2 + \bar{\nu}^2}$
Zero lift $\bar{\nu} = 0$	$\sqrt{\mu^2 + \lambda^2}$	$\sqrt{\mu^2 + \lambda^2}$	$\sqrt{\mu^2 + \lambda^2} + \lambda$	$\sqrt{\mu^2 + \lambda^2}$
No normal flow, $\lambda = -\bar{\nu}$ (descent)	μ	$\dfrac{\mu^2 - \lambda^2}{\sqrt{\mu^2 + \lambda^2}}$	μ	μ

or symbolically

$$[M]\{\dot{U}\} + [L]^{-1}\{U\} = \{\delta F\} \qquad (10b)$$

Premultiplying by [L], equation (10b) takes the form

$$[\tau]\{\dot{U}\} + \{U\} = [L]\{\delta F\} \qquad (10c)$$

where $[\tau] = [L][M]$.

In equation (10c), $[\tau]$ and $[L]$ have the physical significance of time constants and gain respectively. The elements of $[\tau]$ in equation (10c) can also be treated as filter constants. This means, unsteady inflow can be simulated by passing the quasisteady inflow through a low-pass filter. According the Hohenemser (20), a somewhat analogous procedure is used in Bell C-81 and Lockheed Rexor global programs.

We now turn to the problem of evaluating the apparent mass terms, also referred to as time-lag factors. (17) This problem has been the subject matter of extensive studies, (6,7,22,32,36-40, 54-56) motivated by the experimental studies of Carpenter and Fridovich (22) and of Rebont et al. (54-56) in hover. Notwithstanding the quantitative differences in the measured values, (22,54-56) a significant finding did emerge in that there is measurable time-lag between the input of rapid collective pitch and the subsequent build-up of inflow perturbations to the full value. In reference 22, apparent mass terms are identified in terms of reaction forces (or moments) of an impermeable disk which undergoes instantaneously acceleration (or rotation) in still air. A somewhat similar concept is present in the work of Potthast, also (57). The problem of finding reactions on an impermeable disk basically leads to the solution of a potential flow problem in terms of elliptic integrals as was done in the classical studies of Tuckerman (58) and Munk (59). The values for apparent mass of air m_A and apparent inertia of air I_A are (6,8,32):

$$m = \frac{8}{3}\rho R^3 \quad \text{and} \quad I_A = \frac{16}{45}\rho R^5 \qquad (11)$$

In other words, these values represent 64 per cent of the mass and 57 per cent of rotary inertia of a sphere of air of radius R, and we have

$$m_{11} = m_A/\rho\pi R^3 = 8/3\pi = 8/3\pi \text{ and } m_{22} = m_{33} = -I_A/\rho\pi R^5 = -16/45\pi \qquad (12)$$

which give time constants of $0.4244/v$ for δC_T and $0.2264/v$ for δC_L or δC_M. Given the complexity of the actual apparent mass terms of a lifting rotor, it would seem that the methodology adopted to arrive at the time constants is at best a crude approximation. Surprisingly, tests of Hohenemser et al. (36-40) and recent more elaborate analytical studies of Pitt and Peters (6,7) arrive at time constants or mass terms which are surprisingly close to those given by equation (12). From the symmetry of the flow problem in hover, it is clearly seen that M is a diagonal matrix with $m_{22} = m_{33}$. Therefore, we have

$$[M] = \begin{bmatrix} 8/3\pi & 0 & 0 \\ 0 & -16/45\pi & 0 \\ 0 & 0 & -16/45\pi \end{bmatrix} \qquad (13)$$

Thus, we now have two unsteady inflow models in combination with the apparent mass matrix [M] given by equation (13). For the momentum theory, the inflow gains matrix [L] is typified by equation (8) according to the improved inflow distribution given by equation (7). For the empirical model the elements of $[L]_E$ are tabulated for different advance ratios, for example, see references 6 and 14.

5. Equivalent γ^* and C_d^*

One of the most subtle and interesting aspects of the dynamic inflow theory refers to the formulation of equivalent Lock number and drag coefficient (γ^* and C^*_d).[14] This formulation reveals the intrinsic correlation between the transient downwash dynamics and unsteady airfoil aerodynamics. After all, any three-dimensional, unsteady vorticity theory automatically includes induced flow theory as a local approximation to transient downwash dynamics (60). Further, dynamic inflow decreases lift and increases profile drag. Therefore, we should expect an equivalent γ (or γ^*) that is lower than γ and an equivalent C_d^* that is higher than C_d. Thus, the 'γ^*-C_d^*' concept leads to one of the simplest methods of crudely accounting for dynamic inflow in the conventional 'no-inflow' programs simply by changing γ to γ^* and C_d to C_d^*. (61) Furthermore, it brings out the physics of dynamic inflow in a simple and visible manner.

In quasisteady inflow theory, apparent mass effects are neglected. Therefore, the inflow differential equations reduce to algebraic equations which can be absorbed into the rotorcraft dynamics equations without increasing the system dimension. If we further stipulate the condition of axial flow (e.g. $\mu = 0$) in the quasisteady formulation, we get γ^* and C^*_d, as

detailed in references 14 and 12 in the rotating and non-rotating frames respectively. It is essential to mention that a consistent (γ^*, c_d^*) formulation is possible only to isolated rotors and not to coupled rotor-body systems (61). For simplicity, we will consider zero pitch-flap coupling and consider only cyclic inflow components ν_s and ν_c. The formulae are:

$$\gamma^* = \gamma/(1 + \frac{a\sigma}{8v}) \qquad (14a)$$

and

$$(C_d/a)^* = \frac{C_d}{a}(1 + \frac{a\sigma}{8v}) + \frac{a\sigma}{8v}(\bar{\theta} - \phi)^2 \qquad (14b)$$

In equation (14b), $(\theta - \phi)^2$ can be well approximated by $6\,C_T/a\sigma + 1/8\,\phi$. Figure 3 shows graphically γ^* and C_d^* values for datum values of $\gamma = 4$ and $C_d = 0.01$. It is clearly seen that at $\mu = 0$ and for near hovering modes ($\mu < 0.15$ or so) the inflow is highly unsteady. For increasing μ, as noted earlier, the inflow becomes quasisteady and asymptotically reaches 4 and $0.01/2\pi$ values. Ref. 11 further shows that the derivations need not be restricted to rigid flap-lag blades and are applicable to elastic blades as well. A revealing aspect of γ^* is that it is identical to the Loewy lift deficiency function (24-29) at integer-multiple frequency

$$C = \frac{h}{h+\pi} = \frac{1}{1 + \frac{\sigma\pi}{4\bar{\lambda}}} \qquad (15)$$

Where h represents the wake spacing in the two-dimensional model of a hovering rotor. Note that the ratio "$\bar{h}$/semi-chord" refers to the pitch of the helix of vortex sheets. While the first expression on the right hand side of equation (15) is due to Loewy, (27), the second expression, in which the number of blades and wake pitch appear, is due to Miller. (28-29) As pointed out by Jones, (26)

$$\bar{h}/\text{semi-chord} = \frac{4\bar{\lambda}}{\sigma}$$

In hover, the mass flow parameter (see table 1), $v = 2\bar{\lambda}$ and $\frac{8v}{a\sigma} = \frac{h}{\pi}$ and consequently,

$$C = \gamma^* = \frac{1}{1 + \frac{a\sigma}{8v}}\gamma = \frac{1}{1 + \frac{a\sigma}{16\bar{\lambda}}}\gamma \qquad (16)$$

What is striking about equations (15) and (16) is that the same result is obtained by three independent approaches. Such an agreement is more than a coincidence and is a satisfying feature of the γ^* formulation. It is good to reiterate that in hover $v = 2\bar{\lambda}$ with respect to cyclic components λ_c and λ_s. However, according to Johnson, as noted in table I, $v = \bar{\lambda}$. This means, if we use Johnson's formulae (column four in table I) in hover, we have

$$\bar{\lambda}^* = \frac{1}{1 + \frac{a\sigma}{8\bar{\lambda}}}\lambda \qquad (17)$$

That is, equation (16) which agrees with all the earlier work on λ^* due to Shupe and others, will have a factor-of-2 discrepancy when compared to equation (17) in hover. However, this discrepancy disappears for zero-lift climb. This fact partly explains why, in some studies, (1,17,45) equation (17) is explained on the basis of Loewy's theory which is for low-lift climb. The source of the discrepancy vis-a-vis the mass flow parameter v is briefly given in section IV, following reference 43.

6. Unsteady Actuator-Disk Theory

As a viable alternative to the unsteady momentum and empirical models, an unsteady actuator-disk theory has been exercised to derive the [M] and [L] matrices in references 6 to 8. As in the momentum theory, here also, the same improved inflow distribution of equation (7) is used. The resulting model is widely referred to as the Pitt model (46) for which

$$M = \begin{bmatrix} \frac{128}{75\pi}^* & 0 & 0 \\ 0 & \frac{-16}{45\pi} & \\ 0 & 0 & \frac{-16}{45\pi} \end{bmatrix} \qquad (18a)$$

* or $M_{11} = 8/3\pi$

and

$$L = \frac{1}{v}\begin{bmatrix} \frac{1}{2} & 0 & \frac{15\pi}{64}\sqrt{\frac{1-\sin\alpha}{1+\sin\alpha}} \\ 0 & \frac{-4}{1+\sin\alpha} & 0 \\ \frac{15\pi}{64}\sqrt{\frac{1-\sin\alpha}{1+\sin\alpha}} & 0 & \frac{-4\sin\alpha}{(1+\sin\alpha)} \end{bmatrix} \qquad (18b)$$

In equation (18b), v is the inflow mass-flow parameter used in the momentum theory, see equation (9). The other parameter α is the wake skew angle at the disk, that is

$$\alpha = \arctan\left|\frac{\bar{\lambda}}{\mu}\right| \qquad (18c)$$

In hover, $\alpha = 90$; and, in steady cruising, α varies from 5° to 10° for conventional pure helicopters. Figures 4 shows a typical variation of α as a function of advance ratio μ, while the inset figure shows $\bar{\lambda}$ verses μ for the untrimmed condition ($\bar{f} = 0$) and for the two moment trimmed conditions ($\bar{f} = 0$ and $\bar{f} = 0.01$). Comparing equations (18) with the corresponding momentum theory expression in equation (13), we see that the [M] matrix is almost identical in both the theories except for the M_{11} term which is $8/3\pi$ for an elliptical pressure (blade lift $\cong r\sqrt{1-r^2}$) but is reduced to $128/75\pi$ for a cubic blade lift ($\cong r^3\sqrt{1-r^2}$). The marked difference between the two theories is reflected in the L-matrix; compare equation (18b) with equation (8). A significant aspect of the Pitt model is that its L-matrix correlates extremely well with an elaborate prescribed wake analysis taken up next.

7. Prescribed Wake Theory

In the unsteady actuator disk theory two assumptions are tacitly implied. First, the rotor-disk is modeled as an actuator-disk (infinite number of blades); and the vorticity shed from each blade spread over the disk. Second, the rate terms are superimposed on the quasisteady formulation - - a form of superposition that is equivalent to the assumption that all inflow velocities are in phase (6,8). These two assumptions are examined in reference 6 and 8 by comparison with Landgrebe's prescribed-wake, lifting-line, discrete-vortex analysis of a four bladed rotor in a steady flight condition (wake analysis for short), (6-8). Based on the wake analysis, the elements of the gains matrix of the Pitt model are compared with the actuator-disk theory data, as shown in figure 5. The L_{12} and L_{21} terms are zero for both the actuator-disk and wake theories. A noteworthy discrepancy between the two theories concerns L_{32} (shown by open circle) which reflects the fore-to-aft inflow due to roll. While $L_{32} = 0$ for the actuator-disk theory, it shows a non-zero value ($\cong -0.2 = L_{23}$) from the wake analysis. This discrepancy is of minor importance (6,8,43). Actually, it is a consequence of the wake rotation which is not accounted for by actuator disk theory. Thus, overall, excellent correlation is obtained with the wake theory when the mass flow parameter v is given by equation (9) and when α is identified with the wake skew angle at the rotor given by equation (18c).

8. Higher Harmonic Models

Now it is good to consider why an improved inflow distribution does not necessarily mean an improved dynamic inflow model.

By adding second harmonic Fourier terms for the inflow distribution in equation (7) , we obtain

$$\nu = \nu_0 + \nu_s \frac{r}{R}\sin\psi + \nu_c\left(\frac{r}{R}\right)\cos\psi + \nu_{2c}\left(\frac{r}{R}\right)^2\cos 2\psi + \nu_{2s}\left(\frac{r}{R}\right)^2\sin 2\psi \qquad (19)$$

With the above distribution, the actuator-disk theory leads to a series of 5x5-type models among which we will consider the 5x5-analogue of the Pitt model:

$$\left[\begin{array}{c|c} M_{3x3} & 0 \\ \hline 0 & M_{2x2} \end{array}\right]\left\{\begin{array}{c} \nu_0 \\ \nu_s \\ \nu_c \\ \hline \nu_{2s} \\ \nu_{2c} \end{array}\right\}^{\bullet} + \left[\begin{array}{c|c} L_{3x3} & L_{3x2} \\ \hline L_{2x3} & L_{2x2} \end{array}\right]\left\{\begin{array}{c} \nu_0 \\ \nu_s \\ \nu_c \\ \hline \nu_{2s} \\ \nu_{2c} \end{array}\right\} = \left\{\begin{array}{c} C_T \\ -C_L \\ -C_M \\ \hline -C_{2L} \\ -C_{2M} \end{array}\right\} \qquad (20)$$

The elements of M_{3x3} and L_{3x3} are given by equation (18). For a complete description of a hierarchy of 5x5 M and L matrices, see references 13,15,16 and 61.

Figure (6a), shows the body roll made damping of a coupled rotor-body system from the 3x3 and the 5x5 inflow models (16,61). The "5x5 CCA" implies that the data refers to the 5x5 inflow model in which constant-coefficient approximation is used in calculating the perturbed aerodynamic disk loading components. The rotor has three blades (N=3) and the rotor support system is idealized as a rigid body executing roll and pitch motions. The dimensionless ($1/\Omega$) roll mode frequency is close to 0.3. Therefore, there should be hardly any appreciable difference between the 3x3 and 5x5 models, which are respectively based on the first and second harmonic inflow distributions. Further, with increasing advance ratio, the downwash should "wash out"; and, consequently, the data with inflow should approach the no-inflow data (without dynamic inflow). Given these physical considerations, the data in Figure 6a is quite instructive. With increasing advance ratio μ, the 3x3 data approaches the no-inflow data, but the difference between the 3x3 and 5x5 data increases with increasing μ. Moreover, even in hover (zero advance ratio) when the three-bladed system has polar symmetry, the equations for C_{2L} and C_{2M} contain extraneous or spurious periodic terms (13,15,16,61). The effects of such spurious terms increases with increasing μ, as depicted by the comparison between the 5x5 CCA data in which such terms are eliminated and the 5x5 data in which all periodic terms are retained. Thus, the 5x5 data lead to an inconsistent damping description and places doubts on the consistency of the wake description by the 5x5 model for the three-bladed rotor. Therefore, further study is warranted, as outlined below.

In flight dynamics applications, finite blade loading rather than disk loading must be defined, although momentum and actuator-disk theories assume infinite number of blades. Therefore, the process of discretizing the disk loading is inevitable. The rotor/body/inflow system with $n \geq 3$ always leads to a constant parameter system for $\mu = 0$ for the 3x3 models from both the momentum and actuator-disk theories. However, when the 5x5 models are used for 3 and 4 bladed systems (13,15,16,61), the system equations exhibit periodicity even for $\mu = 0$, an apparent inconsistency for a system with polar symmetry. It is good to reiterate that for rotors with five or more blades, such inconsistencies disappear, as depicted in figure 6b. The small difference between the 3x3 and 5x5 data in figure 6b is due to the effects of legitimate periodic terms as a consequence of 2/Rev variations in the inflow distribution of the 5x5 model.

Under unsteady flight conditions, the 3x3 model requires instantaneous thrust, roll moment and pitch moment. Similarly, the 5x5 model requires instantaneous thrust, roll moment, pitch moment, second harmonic roll, and second harmonic pitch. For a three-bladed rotor in a cyclic mode C_{2L} and C_{2M} vary at 3/rev yielding strong periodic coefficients even in axial flight, the effects of which increase with increasing advance ratio. In contrast, a five-bladed rotor in a regressing mode cannot excite C_{2L} or C_{2M} at all (although the 2/rev warping mode would excite C_{2L} and C_{2M}). In other words, as a result of trying to represent a continuous lift distribution by discrete blade loadings, the discretized loading has only three discrete points for a three-bladed rotor and 5 discrete points for a five-bladed rotor over one rotor revolution ($0 \leq \psi \leq 2\pi$). When the 5x5 model is applied to a three-bladed rotor, the instantaneous calculation of the five disk loading components gives rise to periodic terms both in hover and forward flight.

Since the problem is due to high-frequency excitation, it appears that the sensitivity of the 3-bladed rotor to 2nd harmonic inflow might disappear if that lift distribution had a higher apparent mass. The apparent mass of the r^2 distribution, equation (19), yields a time constant of only .155 rad. In contrast, a 2nd-harmonic distribution with a more uniform inflow distribution could have a time constant as high as .242, which could eliminate the problem. Similarly, one might infer that the 3x3 model would give inconsistent results for rotors with less than 3 blades. However, the time constant for the radial 1/rev distributions is .226, which seems large enough to prevent this. Furthermore, 2-bladed rotors do lack polar symmetry and periodic coefficients in hover are to be expected (62).

Thus, the 3x3 model is consistent for rotors with three and more blades, (and it is an excellent approximation to the 5x5 model as well). On the other hand, the 5x5 model seems valid for rotors with five and more blades (13,15,16,61).

III. MODEL VALIDATION

1. Background

Given the complexity of transient downwash, experimental corroboration is practically the raison d'etre of a dynamic inflow model. Therefore, model validation involves correlation of test data with predicted data to isolate the dynamic inflow effects that contribute to improving the correlation. Thus, predicted data without and with dynamic inflow are required, and the goodness of the validation would depend upon the extent to which inflow effects are uniquely isolated. Here, three points merit special mentioning. First, such a correlation cannot isolate dynamic inflow as a phenomenon per se, though in some cases we observe coupled modes in which inflow components are discernibly dominant (17,43-46). Still, it provides a viable means of accounting for dynamic inflow effects. Second, a reliable data base is required to pass a judgement on a particular inflow model. That means, we need a data base which includes a fair measure of dynamic inflow effects and for which our predictive capabilities are refined enough to isolate such effects. The tacit assumption is that the prediction process is not overly sensitive to several "other unknowns" which contaminate the predicted values. Third, once a model is verified, it can be used to help predict the other data concerning which our predictive capabilities merit further refinement, and to assess other simplified approaches such as the "γ^*-$c\bar{d}^*$" approach. Though we have earlier pointed out several limitations of the empirical model, we will consider it in the validation process, since it has the benefit of extensive test data. Moreover, we have also included the momentum theory model, though it can be recovered from the Pitt model in axial flight. Its inclusion provides a better appreciation of the comparison between different models, since considerable experience of the past years centers around the momentum theory.

2. Wake Instability

An interesting validation of dynamic inflow theory is that it predicts an instability in the wake when V becomes negative. From equation (9), we see that this occurs for

$$\mu^2 + \bar{\eta}^2 + 3\bar{\eta}\bar{\nu} + 2\bar{\nu}^2 < 0 \qquad (21)$$

Equation (21) can be combined with basic momentum theory

$$C_T = 2\bar{\nu}\sqrt{\mu^2 + (\bar{\eta} + \bar{\nu})^2} \qquad (22)$$

to give a criterion for the instability region for wake dynamics, Reference 62.

$$\mu^2 < \frac{(C_T/2)^2}{\bar{\nu}^2} - \frac{(C_T/2)^4}{\bar{\nu}^6} \qquad (23a)$$

$$\bar{\eta} = \bar{\nu} + \frac{(C_T/2)^2}{\bar{\nu}^3} \qquad (23b)$$

Equations (23) show that a wake instability occurs for certain momentum-theory, equilibrium solutions of momentum theory that represent a rate of descent (autorotation).

Figure 7 illustrates momentum-theory solutions for various power coefficients and advance ratios. (All inflow parameters, $(\mu,\bar{\lambda},\bar{\eta},\bar{\nu})$ are normalized on $\sqrt{C_T/2}$.) The μ=0 curve is the well-known momentum-theory solution for axial flight. For $\bar{\eta} < -2$, there are three branches of $\bar{\nu}$ solutions. The middle branch, $1<\bar{\nu}<-\bar{\eta}$, is known to be physically unrealizable. As μ increases, however, this middle branch becomes shorter and shorter and disappears for $\mu > .62/\sqrt{C_T/2}$. The interesting aspect here is that the formula for this physically unrealizable branch is exactly the formula of equation (23). In other words, dynamic inflow theory predicts that this branch is unrealizable due to a negative eigenvalue of the inflow system. Thus, dynamic inflow also predicts the autorotational boundary of the vortex-ring state. Certainly this is a strong argument in favor of both dynamic inflow and the mass-flow formula of equation (9).

3. Use of Lag-Damping Results to Identify a Model

Now we come to discussing why lag damping data (usually of the lag regressing mode) do not provide a reliable data base to identify an inflow model, though such data has been profitably used to demonstrate that the inclusion of dynamic inflow significantly improves correlation (17,42-48). This improvement is concomitantly keyed to the reliability and sensitivity of the predicted data, and to the quantum of improvement that can be reasonably identified with dynamic inflow. Concerning dynamic inflow effects on lag damping, the predicted data are often qualitatively affected by modeling assumptions such as of blade elasticity, (39,64,65) hinge offset,[61] thrust levels, (61) etc. It is also expected that such measured and predicted data are sensitive to several 'other unknowns', possibly to the effects of high frequency aerodynamics, low - Reynolds - number et cetera. Extensive correlations between the predicted and measured lag damping data of isolated rotors in hover and forward flight (48) and of coupled rotor-body systems in hover (41,47) point towards this expectation. Concerning the quantum of improvement for isolated rotors, dynamic inflow explains only a part of the difference between predicted and measured data, and hardly influences some configurations, (48). Concerning dynamic inflow effects on rotor-body systems, (unlike body damping) the predicted lag damping often exhibits erratic trends in hover and forward flight with respect to changes in system parameters, (61). As is evident from Bousman's comprehensive correlation study of coupled rotor-body systems in hover, (47), dynamic inflow "only slightly" improves correlation for lag damping, though it significantly improves correlation for the body damping (roll and pitch). We touch upon this point here with the help of predicted data on rotor body damping in hover and forward flight. Particularly in forward flight, we intend to emphasize the necessity of a set of test data on body damping in forward flight. Such a data base could provide a better appreciation of the role of the Pitt model in improving correlation. Figure 8 shows the damping levels of the lag regressing and body roll modes in forward flight for two cases of thrust levels, C_T/σ = 0.05 and 0.20. The other parameters are typical of hingeless rotors, as identified in the figure. The predicted data are somewhat comprehensive in that they apply to all rotors with polar symmetry ($N \geq 3$). Concerning dynamic inflow effects, the lag damping exhibits qualitative differences between the two cases. On the other hand, the roll mode damping depicts essentially the same trend, and the pitch mode damping (not shown) behaves very much like the roll mode damping. Compared to lag mode damping, the body damping levels are far less sensitive to modeling assumptions and parameter variations such as of hinge offset and thrust levels and are far more affected by dynamic inflow.

It is thus seen that measured body-damping levels of conceptual models could serve as a data base. A good example is configuration 1 of reference 41, the configuration having zero blade pitch (effective pitch is 1.5°) with minimized coupling between dynamic modes. Such configurations are relatively less demanding for predicting damping. (47) Further, the quantum of improvement in correlation with the inclusion of dynamic inflow is substantial for the body modes, particularly for the roll mode. (17,42-47) Unfortunately, body damping data from conceptual models are presently restricted to hovering conditions (41,47) and those based on complex global models[61] are not suited to inflow-model validation.

4. Use of Flapping Data to Identify an Inflow Model

However, another category of test data which provides a reliable data base for model validation refers to pure flap-response data, (43,46). Compared to even body damping, our predictive capabilities of pure flap-response under low-thrust conditions are relatively better, and trends established from such response data are virtually unaffected by small differences in aerodynamic and structural modeling. Therefore, flap response data have been widely used to validate inflow models by parameter identification and direct correlation. (30,32,36-40,43,46) Accordingly, we review model validation on the basis of flap response data.

Coming to parameter identification, we begin with Figure 9 which shows amplitude ratio and phase variation, (36). The data refer to a small scale two-bladed model with a 20-inch diameter rotor in hover. Progressing and regressing cyclic pitch excitations of the type $\theta = \| \theta \| \exp i(1 + \omega)t$ in the rotating frame are provided by an eccentric mechanism. Zero values of inflow gain ($L = L_{22} = L_{33} = 0$) and time lag ($\tau = 0$) refers to no-inflow. The values of ($L = 4$, $\tau = 8$) and ($L = 2$, $\tau = 4$) are selected to give the best fit of data. It is seen that the momentum theory or the Pitt model in hover completely captures the test results of amplitude ratio $\| \beta / \theta \|$ for both the regressing and progressing cases. What is rather striking is that the identified time lag or equivalently the $m_{22} \cdot L_{22}$ ($= m_{33} \cdot L_{33}$) parameter is almost identical to the analytical value. For example, for the case with $\tau = 8$, $\nu = 0.014$, we have $m_{22} = m_{33} = 0.112$, the analytical value being $16/45\pi$ ($\cong 0.1132$); also see equation (12). (36,43,46) As for the phase variation, fairly good correlation is observed only for the progressing mode. As a matter of fact, the degradation in correlation for the regressing mode increases with increasing collective, a situation that merits further investigation; see phase variations in figures 9a and 9b.

Concerning the apparent mass term m_{22} or m_{33}, also referred to as inflow time-lag factor,[17] the impermeable disk value is $16/45\pi$ which is supported by several independent experimental and related correlation studies. (22,32,36-40,45) However, it is good to mention that a higher value is indicated by the experimental studies of Rebont et al. (54-56) Such a variation is not unexpected, since the apparent mass terms depend upon the rotor loading distribution. An elaborate actuator-disk analysis for different loading distributions supports the lower value of $16/45\pi$ for realistic rotor loading conditions and that is the value used in the Pitt model. (6-8,46)

Now, we return to discussing model validation on the basis of flap-response data due to Kuczynski, (33-35). The data comprises nearly 200 test points, each under static ($\omega = 0$) and dynamic ($\omega \neq 0$) conditions. For the dynamic data, the swashplate oscillation frequency ω varies from 0 to 1.2 per revolution. The data refer to a 7.5 ft. diameter rotor with a flapping frequency close to 1.15 and they were generated in the NASA-Ames 7x10 ft. wind tunnel. The data are basically comprised of 15 rotor derivatives (C_T, C_L, C_M with respect to θ_0, θ_s, θ_c, α_s), and for advance ration varying from 0 to 1.4. The predicted data are virtually unbiased by modeling limitations, since the blade is well represented both structurally and aerodynamically in substall for a steady collective pitch of 4°. For such low-frequency response data, the usual modeling limitations cease to be the issues, and the improvement in correlation with the inclusion of dynamic inflow effects can be well identified with dynamic inflow.

For Figure 10, we have selected only two typical derivatives --- $\partial[C_m/\sigma a]\,\partial\theta_s$ in hover and $\partial[C_L/a\sigma]\partial\theta_s$ in forward flight --- to demonstrate that the momentum theory, though nearly perfect in hover, is nearly useless in forward flight. On the other hand, the unsteady empirical model, though deficient in several respects (see section II-2) is quite viable in forward flight. The results are rather revealing. In Figure 10a, the pitch moment derivative with respect to the lateral cyclic pitch in hover is shown. Up to $\omega \geq 0.2$, both the unsteady and quasisteady momentum theories beautifully capture all the subtleties of the test data in amplitude as well as in phase. By comparison, the no-inflow prediction fails to capture the data even qualitatively. As expected, for $\omega \geq 0.2$ or so, the correlation with the quasisteady momentum theory degrades with increasing ω, and the unsteady momentum theory correlates well throughout the frequency range. That comparison reveals the importance of apparent mass with increasing ω in that the inflow responds with time lag.

In Figure 10b, we study the unsteady momentum theory vs. the unsteady empirical model at an advance ratio $\mu = 0.51$; the data refer to the roll moment derivative with respect to the lateral cyclic pitch. Here, the momentum theory results fare no better than the 'no-inflow' results for either the amplitude or phase measurements; but, the empirical model completely captures all the qualitative features of the data. That the momentum theory and empirical models give good correlation respectively in hover and forward flight, gave considerable insights into the development of the Pitt model which reduces to the momentum theory model in axial flight (e.g. hover). As a matter of fact, the correlation with the Pitt model shown in Figure 11 is almost identical to that with the empirical model. (32,46) Therefore, for clarity, we have shown only the unsteady momentum and the Pitt models in Figure 11. A detailed comparison between the empirical and momentum theory models is given in reference 32.

Coming to Figure 11, we show four typical rotor derivatives from reference 46 under static and dynamic conditions ... $\partial C_L/\partial\theta_0$, $\partial C_L/\partial\theta_s$, $\partial C_M/\partial\theta_s$ and $\partial C_M/\partial\theta_c$. For the static condition, advance ratio μ varies from 0 to 0.5 and for the dynamic condition, the frequency ω varies from 0 to 1.2 in combination with $\mu = 0.27$, 0.36 and 0.51. The data are self explanatory. Further, the extensive correlation of reference 46 shows that the Pitt model, and also the empirical model (32), fare far better than the momentum theory model, figure 11 serving only as a sample representation. However, there are cases when the momentum theory is better than the Pitt model over a whole or part of the spectrum of the data base with respect to frequencies and advance ratios. For example, for the $\partial C_M/\partial\theta_s$ derivative under static and dynamic conditions, the momentum theory is better than the Pitt model for all frequencies and advance ratios. As for the $\partial C_M/\partial\theta_c$ derivative, we have a mixture of correlations with momentum theory sometimes better and with the Pitt model sometimes better. For an objective measure

of comparison, ref. 46 adopts a rating scheme to quantify the correlations from the empirical, Pitt, and momentum theory models for nearly 200 test points in static and dynamic conditions. That rating scheme and the resulting quantitative measure of the relative merits of the models are given in table 2.

It is thus seen that the Pitt model with a sound analytical basis (actuator-disk theory and correlation with prescribed wake analysis) is as good as the empirical model which is based on data under static ($\omega = 0$) and edgewise flow ($\alpha = 0$) conditions. The Pitt model is applicable both in axial flight ($\alpha = 90^{o}$) when it reduces to the momentum theory model, and in forward flight. Further, it is very convenient to use in flight dynamics applications, since its M and L matrices are known in closed form. Above all, correlation from a data base that is reliable and comprehensive validates the Pitt model. Given the complexity of dynamic wake, the Pitt model seems to contain the most sophistication that can be introduced within the framework of a simple global approximation.

5. Use of Inflow Model to Improve Damping Correlations

With an identified dynamic inflow model, the next step then is to study the role of that model in our flight-dynamics analysis packages. We study that role in two phases on the basis of correlating measured damping with theory. In the first phase, the predicted rotor-body damping in hover is compared with Bousman's test data.[41,47] That comparison demonstrates the importance of dynamic inflow in improving the correlation and the need for an improved predictive capabilities of rotor-body damping. Concerning dynamic inflow models in hover, two competing models are used. (1,6-17, 24,25,30-32,42-46,48-52,61-64) For the first type, (1,17,42,45) the mass-flow parameter is taken as $v = \nu$, as proposed in reference 1. For the second type, (6-16,24,25,30-32,43-46, 48-52,61-64) the mass flow parameters in hover is taken as $v = 2\nu$. This second model is by far the most commonly used. For completeness and

TABLE II: Quantifying Relative Merits of Models in Forward Flight

Scoring System		Comparison of Models: Type of Data		
	Type of Model	Static Data p=1.17	Dynamic Data p=1.15	
0	No better than no dynamic flow	Unsteady Momentum Theory Model	1.6	0.8
1	Moves theory in correct qualitative direction	Pitt Model	2.5	2.1
2	Substantially improves data correlation	Unsteady Empirical Model	2.7	2.2
3	Excellent correlation with data			

preparatory to discussing the pedagogical aspects of v in the next section, we include the predicted data from both the cases with $v = \bar{\nu}$ and $v = 2\bar{\nu}$. In the second phase, the predicted lag damping of a three-bladed isolated rotor is compared with McNulty's test data[48] in hover and forward flight. Here we use the predicted data based on the Pitt model which is applicable to both the hover and forward flight conditions.

In reference 47, comparative correlations of rotor-body damping are presented for three test configurations of hingeless rotor-body systems. In that reference, the major state-of-the-art computer programs of stability analysis are independently exercised. However, for only two computer programs --- the Bell Helicopter DRAV21 code and the NASA-Ames CAMRAD code --- dynamic inflow was included and data without and with dynamic inflow were predicted. The comparison of results shows significant deviations between the various analyses. Such deviations are due to differences in modeling the test configurations and are not related to dynamic inflow. Further, we are discussing the role of dynamic inflow, in particular of the Pitt model, in improving the damping-data correlation. In other words, the issue is the overall improvement in correlation that includes dynamic inflow when compared to the corresponding correlation that does not include dynamic inflow. Therefore, the established trends on the role of dynamic inflow will remain valid, in spite of such deviations between the analyses.

Among the three cases of reference 47, we select the simplest one with zero pitch setting (1.5° camber) and zero aeroelastic couplings. (The other two cases have 9° blade pitch without and with negative pitch-lag coupling). The model simplicity and low-thrust conditions simplify the study of dynamic inflow effects. The predicted and test data (stippled area) in figures 12 to 14 refer to the damping levels of the lag, body roll. and body pitch modes. The labels 'BH' and 'NA' indicate that the data were predicted from the Bell DRAV21 and NASA CAMRAD codes respectively. While the mass flow parameter is taken as $v = 2\bar{\nu}$ for the BH - analysis, it is taken as $v = \bar{\nu}$ for the NA-analysis. Figure 12 shows that dynamic inflow improves the overall correlation only slightly for the lag mode damping. By comparison, dynamic inflow significantly improves the correlation for the body pitch and roll modes. Particularly for the roll mode, the quantum of improvement with dynamic inflow is significant. Figures 12 to 14 also show that dynamic inflow does not explain all the differences between theory and data, a fact that shows that "other unknowns" not related to dynamic inflow are involved in the prediction process.

Coming to phase two, we begin with figure 15 which shows the lag mode damping of a soft-inplane, three-bladed rotor in hover for blade collective pitch of 0° and 8°. The results are from reference 48 which includes a similar correlation. For $\theta_o = 0^\circ$, the correlation is very good, which attests to the overall adequacy of the analytical model. For this particular case, the role of dynamic inflow is negligible. However, with increasing collective, the discrepancy between the test data and theory increases, so does the quantum of improvement due to including dynamic inflow, as typified for the case with $\theta_o = 8^\circ$. Moreover, with increasing rotor speed Ω (particularly for $\Omega > 700$ rpm) the difference between data and theory also increases for $\theta_o = 8^\circ$. This difference, which consistently increases with increasing values of θ_o and Ω, merits further study.

Thus far, we discussed the correlation of damping of rotor-body and isolated rotors in hover. By comparison, the measured damping of simplified models in forward flight is limited to isolated rotors, (48). The results shown in figure 16 are also from reference 48 in which the predicted data are based on linear quasisteady aerodynamics. In that reference, a comprehensive data-base of nearly 1200 test points at different pitch settings is discussed for advance ratios as high as 0.55. The rotor is untrimmed with an essentially unrestricted tilt of the tip-path plane, as is typical of tail rotors. As seen from figure 16, the correlation is given for two advance ratios; $\mu = 0.15$ and 0.25. The blade pitch is zero (1.5 camber) and the rotor rotational speed Ω is 1000 rpm. Thus, the effective blade pitch is 1.5° and the free stream inflow is equal to $\mu\tan\alpha_s$, where α_s is the shaft tilt. Therefore, with increasing values of μ and α_s (that is for high $\mu\alpha_s$ values), the angle of attack α also exceeds the stall limit value of -12°. Thus, a portion of the data-base is under stall conditions. For example, for $\mu = 0.25$, the stall areas are approximately equal to 10% and 25% for $\alpha_s = 10^\circ$ and 20° respectively. Figure 16 shows that in substall (say, $\alpha_s \leq 10^\circ$ for $\mu = 0.25$), the correlation is very good, though dynamic inflow hardly influences the predicted data. However, in stall, the correlation merits additional comments, although the predicted data from the linear theory are suspect. A striking feature is that the theory without dynamic inflow which also does not account for stall, shows relatively "good" correlation with the test data. The predicted data without dynamic inflow are anomalous in stall. This does not mean, in general, however, that the inclusion of dynamic inflow degrades correlation. The fact is that the predicted values based on linear aerodynamic theory with or without dynamic inflow need to be appropriately resolved for stall conditions. If blithely applied, such results masked by stall effects, may lead to incorrect conclusions, (48).

IV. Philosophical Aspects

1. Misconceptions

Through the history of the development of dynamic-inflow theory, several misconceptions about dynamic inflow have entered the literature, and some still remain. For example, we have already mentioned that alternate formulas have existed for the mass flow parameter in forward flight (Table 1), and that one of these, Ref. 1, disagrees with all other formulations even in hover. In particular, Ref. 1 gives the mass-flow parameter for roll and pitch as $\bar{\nu}$ in hover, whereas all other investigators give $2\bar{\nu}$. The source of this discrepancy is simply the fact that Ref. 1 has omitted ν_s and ν_c from the "$\dot{m}$" part of $\dot{m}\Delta v$ in momentum theory. That $2\bar{\nu}$ is correct is well-documented from a theoretical standpoint in Ref. 43. Similarly, Curtiss argues effectively that (especially at zero thrust) the local $\dot{m}$ must be used including radial and azimuthal variations, Reference 66. Here, however, we wish to make a strong experimental argument in favor of $2\bar{\nu}$.

Perhaps the most direct way to resolve this question is to go back to the parameter-identification work of Reference 9, from which V and K_I can be inferred directly. The rotor in those tests was 16.5 inches in diameter with a Lock number of $\gamma = 3.8$, a flapping frequency of $p = 1.18$, and a solidity ratio resulting in $\sigma a = .85$. The aerodynamic parameter $A = B^4\gamma/8$ was identified as 0.391 at $\theta = 6.3°$, which implies a tip-loss factor of $B = .953$. Measurements of blade transients were obtained for 6 different collective-pitch settings and at various ground heights. From these transients, values of inflow gains (L) and time constants (τ) were obtained by parameter identification. These can easily be converted to k and K_I by the following formulas, and it is amazing that we have not made this calculation long ago.

$$k = \frac{\sigma a}{\gamma L \nu} = \frac{.224}{L\nu} \qquad (24a)$$

$$K_I = \frac{\sigma a}{2\gamma}\,\frac{\tau}{L} = \frac{.112\tau}{L} \qquad (24b)$$

Values of K_I are easily calculated from τ and L; but values of k depend also on the steady inflow, $\bar{\nu}$, which can be a problem to calculate. However, $\bar{\nu}$ was measured in Reference 38 by means of hot-wire anemometry for the case of the highest rotor height above ground, $\frac{h}{R} = 1.28$. Therefore, we have an almost indisputable measurement of k and K_I. The data are summarized in the following Table III.

It is extremely interesting to compare these identified values with those of momentum theory. First, we consider the possible differences between the conditions of the experimental procedure and the assumptions of momentum theory. We have already ruled out large errors in $\bar{\nu}$, since $\bar{\nu}$ is measured to within 5-10%. There could be an effect of the ground plane since the rotor at h/R = 1.28 is still in ground effect. However, the data in Reference 38 at several rotor heights show that the ground plane is not significant for L and τ except in that it impacts ν (and thus affects L but not k). Therefore, no more than a few percent error could be attributed here. Third, one might feel that B = .953 (the identified value of tip loss) is a little small. However, a change to B = .97 would make at most a 10% shift in k and K_I, as shown in the table.

Table III: Identified Parameters, Reference 38

θ_o	ν	L	τ	k	K_I
1.5	.014	6.7	6.2	2.4	.104
3.4	.019	5.6	5.3	2.1	.111
4.4	.022	4.0	4.4	2.5	.123
6.3	.027	4.5	2.0	2.0	.120
7.6	.031	3.1	4.2	2.3	.152
9.4	.036	3.1	3.0	2.0	.108
Experimental Average (B=.953)				2.2	.120
Experimental Average (B =.97)				2.0	.109
Conventional Momentum Theory				2.0	.113

Consequently, we conclude that k lies between 2.0 and 2.2 and that K_I lies between .109 and .120 for this data. This compares very favorably with k = 2.0 and K_I = .113 from momentum theory. In fact, the difference (about 5%-10%) is exactly in the range of the expected experimental error. On the other hand, if one takes k = 1.0, as suggested in Reference 1, it is obvious that this assumption differs from the identified k data by a factor of 100%; and no conceivable experimental variations warrant such a difference. Therefore, it seems fairly clear from this data that the conventional theory is correct, that v_s and v_c should be included in $\bar{m}$, and that the theory in Reference 1 is inaccurate.

Another misconception about dynamic inflow is that it is only important for rotors with high flap frequencies, Refs. 1, 6, 20, and 30. The rationale for this conclusion is that only hingeless rotors develop hub moments; and, if there are no hub moments, there are no moments on the air mass. In fact, however, it is only the aerodynamic portion of the hub moment that acts on the air. Thus, even for a centrally-hinged blade (p=1.0), there can be strong aerodynamic moments that are cancelled by gyroscopic moments at the hub; but which definitely affect the flow field.

For example, Figure 17 shows cyclic flapping due to cyclic pitch, θ_s and roll rate, q. The solid line is the theory without dynamic inflow; the dash-dot line is the theory with dynamic inflow ($\nu=2\bar{\nu}$); the short-dash line is the theory with $\nu=\bar{\nu}$, Ref. 1; and the solid dot is a data point from Reference 32. Clearly the effect of dynamic inflow is large at all values of flap frequency, with the greatest effect being at p = 1.05, a moderate frequency. The curve also shows the extent to which the alternate formula ($\bar{V}=\nu$) overpredicts this effect and the excellent correlation between test data and the conventional theory ($V=2\bar{\nu}$).

A third misconception, about dynamic inflow has been the manner in which it relates to the Loewy lift-deficiency function, Ref. 27. In general, it has been assumed that dynamic inflow would automatically be included if one used the Loewy function. For example, Reference 1 points out that (at a collective frequency that is any integer multiple of blade number, $\omega=m=nN$) the Loewy function reduces to $\frac{h}{h+\pi}$ which is the same result as dynamic inflow, equation (15). In fact, however, this equivalence does not hold for the zero harmonic, which is the basis of dynamic inflow for thrust.

In order to facilitate a true comparison of Loewy theory with dynamic inflow, we write the Loewy function for small reduced frequency k, but not necessarily small per/rev frequency ω. (Since $k = \frac{\omega c}{2r}$, this implies high aspect ratio.) The Loewy lift-deficiency function becomes

$$C' = \frac{1}{1+\pi k(\frac{1}{2}+w)} = 1 - \frac{1}{1+\frac{1}{\pi k(\frac{1}{2}+w)}} \qquad (25a)$$

$$\frac{1}{2}+w = \frac{1}{2}\,\frac{e^{kh}e^{2\pi i\omega/N}+1}{e^{kh}e^{2\pi i\omega/N}-1} \qquad (25b)$$

Near an integer multiple of blade number, $\omega = nN+\Delta\omega$, equation (25) can be approximated by

$$\frac{1}{\pi k(\frac{1}{2}+w)} = \frac{n}{\pi} + i\,\frac{2\Delta\omega}{Nk} = \frac{8}{\sigma a}\left(\bar{\lambda} + \frac{i\Delta\omega}{m}\,r\right) \qquad (26)$$

The term $\frac{8\bar{\lambda}}{\sigma a}$ is the reduction term mentioned earlier (identical to dynamic inflow), and the term $\frac{r}{m}$ is a time constant of the mth harmonic.

Similarly, dynamic-inflow theory for an N-bladed rotor can be expressed as a lift deficiency function in terms of all blade-passage harmonics for a collective mode.

$$C' = 1 - \sum_{n=-\infty}^{+\infty} \frac{1}{1+\frac{8}{\sigma a}\left[\bar{\lambda} + B_m(\omega-m)i\right]} \qquad (27)$$

$$(m = nN)$$

For $\omega = m + \Delta\omega$, equation (29) is dominated by the nth term which is identical in form to equations (27a) and (28). However, the time constants in dynamic-inflow theory are 3-dimensional and depend on the loading distribution. For example, for blade loading proportional to $r^{m+1}\sqrt{1-r^2}\cos(m\psi)$

$$B_m = \frac{4}{(2m+3)\pi}\,\frac{2^{2m}(m)!\,(m+1)!}{[(2m+1)!!]^2} \qquad (28a)$$

and for a loading distribution proportional to $r\sqrt{1-r^2}\cos(m\psi)$, we have the approximation

$$B_m \cong \frac{(m+2)^2}{(2m+3)(m+1)\pi} \qquad (28b)$$

In comparison, the 2-dimensional Loewy theory gives (at the 3/4 radius)

$$B_m = \frac{3}{4m} \qquad (28c)$$

A comparison of time constants in equation (28) reveals an important factor that has not been noted before. Namely, while both theories give a B_m that decrease as m increases, dynamic inflow and Loewy theory differ greatly for quasisteady motions, m=0. In fact, equation (28c) gives an infinite apparent mass at m = 0. As a result, equation (27a) does not go to $\frac{h}{h+\pi}$ as $\omega \to 0$.

Instead, equation (26) becomes

$$\lim_{k\to 0}\left[\frac{h}{\pi} + i\,\frac{2\Delta\omega}{Nk}\right] = \frac{8}{\sigma a}(\bar{\lambda} + ir) \qquad (26)$$

There is a finite imaginary part of C' that remains even at $\omega=k=0$ due to the infinite apparent mass. (The flow is "stuck" with a phase lag). The cause of this anomaly is that, for $\omega<1$, the Loewy assumption of infinite vortex sheets at each layer counts the kinetic energy of a single cycle an infinite number of times as apparently different vortex oscillations in successive layers. Figure 18 illustrates the relationship between Loewy theory and dynamic inflow by a comparison of real and imaginary parts for N=4, C_T = .005, σ = .06. We see an excellent correlation near 4/rev (due to the close values of apparent mass); but the Loewy theory breaks down for $\omega<1$/rev. The real part does not go to $\frac{h}{h+\pi} = \frac{1}{2}$ (as previously thought), and the imaginary part goes to .063 (rather than 0) as $\omega \to 0$. Figure 12 gives insight as to why Reference 67 calculates such large discrepancies between the two theories at 0.5/rev.

(We also note that Loewy theory also has terms of the form $k\ln(k)$ which we have neglected in Equation (27) and Figure 18. Again, these terms arise from integrals over an infinite wake; but they are not physically realized due to the fact that the rotor wake wraps around in only a partial cycle at $\omega<1$/rev.)

As a final item under "misconceptions", we note that tip-loss effects are not really an issue for dynamic-inflow theory. In the actuator-disc formulations of References 6-8, as typified by equations (18a-18c), the lift distribution is prescribed as zero at the blade tip (or, more precisely at the edge of the disc), which is an implicity accounting of tip loss. Nevertheless, the results in hover agree exactly with momentum theory for which there is no tip loss. The reason for this is that tip "loss" refers to loss of lift not to loss of induced flow. Induced flow continues out to the tip and beyond.

2. Limitations

Time-history solutions are usually adopted as the solution strategy in large scale global models. For such cases, it is necessary to treat the inflow components (ν_0, ν_s, ν_c) and disk loading components (C_T, C_L, C_M) as total quantities rather than as perturbation quantities. Following references 43 and 46, we introduce the following definitions:

$$V_T = \mu^2 + \bar{\lambda}^2, \quad v = \frac{d}{d\bar{\nu}}(\bar{\nu}\, v_T) \text{ and } [L] = \frac{1}{v}[\mathcal{L}] \qquad (29a)$$

where v_T is the normalized (1/ΩR) flow at the rotor and v has now the connotation of a weighted downstream velocity. Then, the correspondent inflow gains matrix can be expressed as

$$[L] = [\mathcal{L}]\begin{bmatrix} V_T & 0 & 0 \\ 0 & v & 0 \\ 0 & 0 & v \end{bmatrix}^{-1} \qquad (29b)$$

In combination with an appropriate apparent mass matrix, the above equation provides the essence of the nonlinear version. It also reveals the feature that the flow parameter associated with the thrust equation is different from the flow parameter associated with the roll and pitch equations in the nonlinear case.

It should be noted here what the nonlinear version does (and does not) contain. It is completely nonlinear in C_T and ν_0, but it is nonetheless linearized in C_L and C_M. Thus, it will not give the nonlinear-curve, roll-moment control-power with cyclic pitch at zero thrust. Also, it has as an implicit assumption that ν_0 is everywhere the same sign. Thus, it does not include the type of nonlinearity that would account for twisted blades at zero thrust, Reference 66. However, it does allow for negative μ, η, and $\bar{\nu}$. Since α is always taken as between 0° and 90°. Third, the model explicitly accounts for hub translations (as dynamic changes in η and μ). However, it does not account for the fact that the actuator disc might have dynamic motion due to blade dynamics, Reference 22. However, one can show that dynamic motions of the disc are generally negligible. The maximum effect is for the collective mode at 0.7/rev for which the effect is less than 10%.

Given the limitations of the nonlinear model, it is interesting to identify the limitations of the linearized model, equations (10) and (18). First of all, this linearized model is a perturbation model. Thus, it assumes small oscillations in induced flow about ν_0, ν_c, ν_s. Second, the model in equation (10) does not include perturbations in hub translations u, v and w. However, these can be obtained from the model in equations (29). The result is:

$$[\tau]\begin{Bmatrix}\dot{\nu}_o\\ \dot{\nu}_s\\ \dot{\nu}_c\end{Bmatrix} + V\begin{Bmatrix}\nu_o\\ \nu_s\\ \nu_c\end{Bmatrix} = \left[\mathcal{L}\right]\begin{Bmatrix}C_T\\ C_L\\ C_M\end{Bmatrix}$$

$$-\{\mathcal{L}\}_1 \langle 2U\ 0\ 2W\rangle \begin{Bmatrix}\dot{u}\\ \dot{v}\\ \dot{w}\end{Bmatrix} + V\begin{Bmatrix}0\\ 0\\ 1\end{Bmatrix}\langle A\ 0\ -B\rangle \begin{Bmatrix}u\\ v\\ w\end{Bmatrix} \qquad (30a)$$

or, in alternate form

$$[M]\begin{Bmatrix}\dot{\nu}_o\\ \dot{\nu}_s\\ \dot{\nu}_c\end{Bmatrix} + V[\mathcal{L}]^{-1}\begin{Bmatrix}\nu_o\\ \nu_s\\ \nu_c\end{Bmatrix} = \begin{Bmatrix}C_T\\ C_L\\ C_M\end{Bmatrix} -$$

$$\begin{Bmatrix}1\\ 0\\ 0\end{Bmatrix}\langle 2U\ 0\ 2W\rangle \begin{Bmatrix}\dot{u}\\ \dot{v}\\ \dot{w}\end{Bmatrix} + \begin{Bmatrix}\mathcal{X}^{-1}\\ \end{Bmatrix}_3\langle A\ 0\ -B\rangle \begin{Bmatrix}u\\ v\\ w\end{Bmatrix} \qquad (30b)$$

The terms U and W are the primary contributors to the effect of lateral translation (in the direction of flight) and vertical translation (normal to the rotor plane). They account for the motion of the actuator disc due to u and w. The terms A and B are secondary effects that account for oscillations in the disc angle, α, during oscillations in C_T. These terms are given by:

$$U = \frac{\partial}{\partial\mu}(\nu V_T) = \bar{\nu}\mu/V_T \qquad (31a)$$

$$W = \frac{\partial}{\partial\eta}(\nu V_T) = (\bar{\nu}+\eta)\bar{\nu}/V_T \qquad (31b)$$

$$A = \frac{15\pi}{64}\cdot\frac{\sin^2\alpha}{1+\sin\alpha}\left(\frac{2\bar{\nu}}{\eta+\bar{\nu}}\right) \qquad (31c)$$

$$B = \frac{15\pi}{64}\cdot\frac{\sin\alpha\cos\alpha}{1+\sin\alpha}\left(\frac{2\bar{\nu}}{\eta+\bar{\nu}}\right) \qquad (31d)$$

For rotors where most of the normal flow is from advance ratio and shaft tilt (not from thrust, $\bar{\nu}<<\eta$), the secondary effects are zero. In transition, however, where $\frac{\bar{\nu}}{\eta+\bar{\nu}} \cong 1$, they must be accounted for.

It should also be pointed out that there is an effect of α oscillations in $\mathcal{L}_{31}$ and this effect has not appeared in previous dynamic inflow theories. In particular, we have

$$\mathcal{L}_{31} = \frac{15\pi}{64}\sqrt{\frac{1-\sin\alpha}{1+\sin\alpha}}\cdot\left[1+\left(\frac{\bar{\nu}}{\eta+\bar{\nu}}\right)\sin\alpha\right] \qquad (32a)$$

$$\left(\text{Note: }\sqrt{\frac{1-\sin\alpha}{1+\sin\alpha}} = \frac{\cos\alpha}{1+\sin\alpha}\right) \qquad (32b)$$

The $\frac{\bar{\nu}}{\eta+\bar{\nu}}$ term has not been included before. It has no effect either in hover, in edgewise flow ($\mu/\sqrt{C_T} > 2$, $\eta = 0$), or at low thrust ($\bar{\nu}<<\eta$); but it can have an effect in transition. However, since the aerodynamics of transition are probably not well approximated by actuator disc theory, it is premature to add this term to perturbation dynamic inflow theory. More experimental data must be obtained in transition before a decision is made. The same can be said of the U, A, and B terms above. As for the W term, numerical studies indicate that W is most important in hover for vertical oscillations near 0.13/rev and for vertical amplitudes greater than one rotor radius (peak-to-peak). Thus, it may have an applicability in stability and control.

V. Concluding Remarks

We have reviewed dynamic inflow models and their relation to the prediction of low-frequency response and damping. Given the complexity of the dynamic wake, the Pitt model stands out as a premier dynamic inflow model within the conceptual framework of a global approximation. It is derived from first principles and leads to a consistent rotor wake description for rotors with any number blades. Its inflow-gain matrix has been substantiated with a prescribed wake analysis, and it reduces to the momentum theory model in hover. It has been verified on the basis of flap response data, since pure flap data provides a data base to pass a judgement on particular inflow model. It can be easily adapted in nonlinear version for use in time history solutions.

Understanding is far from complete. The correlations between the measured data from conceptual models and predicted data lead to the following specific remarks:

1) Dynamic inflow in hover improves lag-damping correlations of rotors with (47) and without (48) body coupling. However, the varying extent of dynamic inflow effects for certain combinations of system and flight parameters merits further study

2) The damping-data correlations in forward flight are presently limited to lag regressing mode damping of isolated rotors in substall, and the improvement due to dynamic inflow is at best marginal. The prediction needs to be appropriately resolved for stall effects to fully exploit the available data base at shaft angles as high as 20, (48). Such a correlation in stall should promote further insights into the role of dynamic inflow effects on lag damping.

3) Dynamic inflow significantly improves body damping (roll and pitch mode) correlation (47) and is a dominant factor in aeromechanical stability during autorotation. (32,61) Test data on body-damping provides a data base in forward flight as well, though not presently available. Therefore, correlations of body damping in forward flight including autorotation offer promise for a better and improved appreciation of the Pitt model.

4) More work needs to be done on application of higher-harmonic dynamic inflow to improve lift-deficiency functions and finite-state models.

REFERENCES

1. Johnson, W., Helicopter Theory, Princeton University Press, 1980, Chapter 10.

2. Baskin, V. YE, Veldgrube, L.S., Vozhdayey, YE.S. and Maykapar, G.I., Theory of Lifting Airscrews , NASA TTF - 823, 1975.

3. Heyson, H. H., "A Brief Survey of Rotary Wing Induced Velocity Theory", NASA, TM 78741, June 1978.

4. Bramwell, A.R.S., Helicopter Dynamics, John Wiley and Sons, New York, 1976.

5. Joglekar, M. and Loewy, R., " An Actuator-Disc Analysis of Helicopter Wake Geometry and the Corresponding Blade Response", USAAVLABS, Technical Report, 69-66, 1970.

6. Pitt, D. M., "Rotor Dynamic Inflow Derivatives and Time Constants from various Inflow Models", USATSARCOM, TR81-2, December, 1980.

7. Pitt, D. M., and Peters, D. A., "Theoretical Prediction of Dynamic Inflow Derivatives", presented at the Sixth European Rotorcraft and Powered Lift Aircraft Forum, Bristol, England, September, 1980. (Vertica, Vol. 5, No.1,) March 1981, pp.21-34.

8. Pitt, D. M., and Peters, D.A., "Rotor Dynamic Inflow Derivatives and Time Constants from Various Inflow Models", Ninth European Rotorcraft Forum, Stresa, Italy, September 13 -15, 1983, Paper No. 55.

9. Gaonkar, G. H., and Peters, D.A., "Flap-Lag Stability with Dynamic Inflow by the Method of Multiblade Coordinates", AIAA paper No. 79-0729, April, 1979.

10. Gaonkar, G. H., and Peters, D. A., "Use of Multiblade Coordinates for Helicopter Flap-Lag Stability with Dynamic Inflow", Journal of Aircraft, Vol. 17, No. 2, February, 1980.

11. Gaonkar, G. H., Mitra, A. K., and Peters, D.A., "Feasibility of a Rotor Flight-Dynamics Model with First-Order Cyclic Inflow and Multiblade Modes"; AIAA paper No. 81-0611-CP, April 1981. Presented at the AIAA Dynamics Specialists Meeting, Atlanta, Georgia, April 9-10, 1981.

12. Gaonkar, G. H., Mitra, A. K., Reddy, T. S. R., and Peters, D. A., "Sensitivity of Helicopter Aeromechanical Stability to Dynamic Inflow", Vertica, Vol. 6, No. 1, 1982, pp. 59-75.

13. Gaonkar, G. H., Sastry, V. V. S. S., Reddy, T. S. R., and Peters, D. A. "On the Adequacy of Modeling Dynamic Inflow for Helicopter Flap-Lag Stability", Eighth European Rotorcraft Forum, Aix-En-Provence, France, August 31-September 3, 1982, paper No.3. 11.

14. Peters, D.A., and Gaonkar, G. H. "On Theoretical Flap-Lag Damping with Various Dynamic Inflow Models", Journal of the American Helicopter Society, Vol. 21, No. 3, July 1980, p.p. 29 - 36.

15. Gaonkar, G. H., Sastry, V. V. S. S., Reddy, T. S. R., Nagabhushanam J, and Peters, D. A., "The Use of Actuator-Disc Dynamic Inflow for Helicopter Flap-Lag Stability", Journal of the American Helicopter Society, Vol. 28, No. 3, July 1983, pp. 79-88.

16. Nagabhushanam, J., and Gaonkar, G. H., "Rotorcraft Air Resonance in Forward Flight with Various Dynamic Inflow Models and Aeroelastic Couplings", Vertica, Vol. 8, No. 4, December 1984, pp. 373-394.

17. Johnson, W., "Influence of Unsteady Aerodynamics on Hingeless Rotor Ground Resonance", Journal of Aircraft, Vol. 29, No. 9, August 1982, pp. 668 -673.

18. Cheeseman, I.C., "Developments in Rotary Wing Aircraft Aerodynamics", Proceedings of the Seventh European Rotorcraft Conference, Garmisch-Partenkirchen, Federal Republic of Germany, September 1981, paper No. 1.

19. Ormiston, R. A., "An Actuator Disc Theory for Rotor Wake Induced Velocities," Agard CP-111, September, 1972, pp.2-1 to 2-19.

20. Hohenemser, K. H.,"Hingeless Rotorcraft Flight Dynamics", Agard-AG-197, 1974.

21. Sissingh, G. J., "The Effect of Induced Velocity Variation on Helicopter Rotor Damping in Pitch or Roll", Aeronautical Research Council (Great Britain), A.R.C. Technical Report G. P. No. 101 (14, 757), 1952.

22. Carpenter, P. J., and Fridovich, B., "Effect of a Rapid Blade Pitch Increase on the Thrust and Induced Velocity Response of a Full Scale Helicopter Rotor" NASA,TN 3044, November 1953.

23. Amer, K. B., "Theory of Helicopter Damping in Pitch or Roll and Comparison with Flight Measurements", NACA, TN 2136, October 1948.

24. Shupe, N. K., A Study of the Dynamic Motions of Hingeless Rotored Helicopters, Ph. D. Thesis, Princeton University, 1970.

25. Curtiss, H. C., Jr. and Shupe, N. K., "A Stability and Control Theory for Hingeless Rotors", Annual National Forum of the American Helicopter Society, Washington, D.C., May 1971.

26. Jones, J. P., "An Actuator Disc Theory for the Shed Wake at Low Tip Speed Ratios", MIT Aeroelastic and Structures Laboratory", Technical Report 133-1, 1965.

27. Loewy, R. G., "A Two Dimensional Approach to the Unsteady Aerodynamics of Rotary Wings", Journal of Aerospace Science, Vol. 24, 1957, pp. 82-98.

28. Miller, R. H., "Rotor Blade Harmonic Air Loading", AIAA Journal, Vol. 2, No.7, July 1964, pp. 1254-1269.

29. Miller, R. H., "Unsteady Air Loads on Helicopter Rotor Blades", Journal of the Royal Aeronautical Society, Vol. 68, No. 640, April 1964 (The Fourth Cierva Memorial Lecture), pp. 217-229.

30. Ormiston, R. A. and Peters, D. A., "Hingeless Helicopter Rotor Response with Non-Uniform Inflow and Elastic Blade Banding", Journal of Aircraft, Vol. 9, No. 10, Oct. 1972, pp.730-736.

31. Ormiston, R. A., "Application of Simplified Inflow Models to Rotorcraft Dynayic Analysis", Journal of the American Helicopter Society, Vol. 21, No. 3, July 1976, pp. 34-39.

32. Peters, D. A., "Hingeless Rotor Frequency Response with Unsteady Inflow", presented at the AHS/NASA Ames Specialists Meeting on Rotorcraft Dynamics, NASA SP-362, February 1974.

33. Kuczynski, W. A. and Sissingh, G. J., "Research Program to Determine Rotor Response Characteristics at High Advance Ratios", NASA CR 114290 (LR 24122), February 1971.

34. Kuczynski, W. A. and Sissingh, G. J., "Characteristics of Hingeless Rotors with Hub Moment Feedback Controls including Experimental Rotor Frequency Response", NASA CR 114427 (Vol. I) and NASA CR 114428 (Vol II), 25048, January, 1972

35. Kuczynski, W. A., et al. "Experimental Hingeless Rotors Characteristics at Full Scale First Flap Mode Frequencies", NAS2-5419, LR 25451, October 1972. (Also see - 28th Annual National Forum, American Helicopter Society, May 1972 Preprint No. 512).

36. Crews, S. T., Hohenemser, K. H., and Ormiston, R.A. "An Unsteady Wake Model for a Hingeless Rotor", Journal of Aircraft, Vol. 10, No. 12, December 1973, pp. 758-760.

37. Crews, S. T., Unsteady Hovering Rotor Wake Parameters Identified from Dynamic Model Tests, D.Sc. Thesis, Washington University, St. Louis, 1977.

38. Banerjee, D., Crews, S. T., Hohenemser, K. H., and Yin, S. K., "Identification of State Variables and Dynamic Inflow from Rotor Model Dynamic Tests", Journal of the American Helicopter Society, Vol. 22(2), April 1977, pp. 28-36.

39. Banerjee, D., Application of System Identification to Analytic Rotor Modeling from Simulated and Wind Tunnel Test Data , D.Sc., Thesis, Washington U niversity, May 1977.

40. Banerjee, D., Crews, S. T., and Hohenemser, K. H., "Parameter Indentification Applied to Analytic Hingeless Rotor Modeling", Journal of the American Helicopter Society, vol. 24, no.I, January 1979, pp. 26-32.

41. Bousman, W. G., "An Experimental Investigation of the Effects of Aeroelastic Couplings on Aeromechanical Stability of a Hingeless Rotor Helicopter", Journal of the American Helicopter Society, Vol. 26, No. 1, January 1981, pp. 46-54.

42. Johnson, Wayne, "Development of a Comprehensive Analysis for Rotorcraft II. Aircraft Model, Solution Procedure and Applications", Vertica, Vol.5, 1981, pp.185-216.

43. Peters, D. A., "The Importance of Steady and Dynamic Inflow on the Stability of Rotor-Body Systems", ITR Methodology Assessment Workshop, NASA-AMES Research Centre, June 21-22, 1983.

44. Friedman, P. P., and Venkatesan, C., "Comparison of Experimental Stability Results with a Simple Analytical Model", presented at the Integrated Technology Rotor (ITR) Methodology Assessment Workshop, NASA, AMES Research Center, Moffett Field CA, June 21-22, 1983.

45. Friedman, P. P., and Venkatesan, C., "Influence of Various Unsteady Aerodynamic Models on the Aeromechanical Stability of a Helicopter in Ground Resonance", Second Decennial Specialist's Meeting on Rotorcraft Dynamics, AHS-NASA Ames. Moffett Field, California, November 7-9, 1984.

46. Gaonkar, G. H., and Peters, D. A., "A Review of Dynamic Inflow and Its Effect on Experimental Correlations", Second Decennial Specialist's Meeting on Rotorcraft Dynamics, AHS-NASA, Ames, Moffett Field, California, November 7-9, 1984.

47. Bousman, William G., " A comparison of Theory and Experiment for Coupled Rotor-Body Stability of a Hingeless Rotor Model in Hover," ITR Methodology Assessment Workshop, NASA-Ames Research Centre, June 21-22, 1983.

48. Gaonkar, G. H., McNulty, M.J., and Nagabhushanam, J., "An Experimental and Analytical Investigation of Isolated Rotor Flap-Lag Stability in Forward Flight". The 11th European Rotorcraft Forum, London, September 10-13, 1985, paper no.66.

49. Reddy, T. S. R. and Warmbrodt, W., "The Influence of Dynamic Inflow and Torsional Flexibility on Rotor Damping in Forward Flight from Symbolically Generated Equations", Second Decennial Specialist's Meeting on Rotorcraft Dynamics, AHS-NASA, AMES, Moffett Field, California, November 7-9, 1984.

50. Panda, B. and Chopra, I., "Flap-Lag-Torsion Stability in Forward Flight", Second Decennial Specialist's Meeting on Rotorcraft Dynamics, AHS-NASA,Ames, Moffett Field, California, November 7-9, 1984.

51. Panda, B. and Chopra, I. ,"Dynamic Stability of Hingless and Bearingless Rotors in Forward Flight", presented at the International Conference on Rotor craft Basic Research, American Helicopter Society and Army Research Office, Research Triangle Park, North Carolina, February 19-21, 1985.

52. Bir, G.S. and Chopra, I., "Gust Response of Hingless Rotors", presented at the 41st Annual Forum of the American Helicopter Society, Fort Worth, May 15-17, 1985, paper no. 4.

53. McHugh, F. J., " What are the Lift and Propulsive Force Limits at High Speed for the Conventional Rotor?", Proceedings of the 34th Annual National Forum of the American Helicopter Society, Washington, D.C. May 15-17, 1978.

54. Rebont, Jean, Valensi, Jacques and Soulez-Lariviere, Jean, "Wind Tunnel Study of the Response in Lift of a Rotor to an Increase in Collective Pitch in the Case of Vertical Flight near the Autorotative Regime", NASA, TTF-17, 1960.

55. Rebont, Jean, Valensi, Jacques and Soulez-Lariviere, Jean, "Response of Rotor Lift to an Increase in Collective Pitch in the Case of Descending Flight, the Regime of the Rotor Being Near Autorotation", NASA, TTF-18, 1960.

56. Rebont, Jean, Valensi, Jacques and Loulez-Lariviere, Jean, "Response of a Helicopter Rotor to an Increase in Collective Pitch for the case of Vertical Flight", NASA TTF-55, 1961.

57. Potthast, A.J., "Lockheed Hingeless Rotor Technology Summary Flight Dynamics", Lockheed Report, LR-25987, June, 1973.

58. Tuckerman, L., B., "Inertia Factors of Ellipsoids for Use in Airship Design." NACA Report No. 210, 1925.

59. Munk, Max, M., "Some Tables of the Factor of Apparent Additional Mass", NACA Report TN-197, 1924.

60. Landgrebe, A. J., "An Analytical Method for Predicting Rotor Wake Geometry", Journal of the American Helicopter Society, Vol. 14, No. 4, Oct. 1969, pp. 20-32.

61. Nagabhushanam, J., Rotocraft Aeromechanical Instability in Forward Flight with Various Dynamic Inflow Models and Aeroelastic Couplings , Ph.D. Thesis, Indian Institute of Science, Bangalore, India, October, 1984.

62. Chen Shyi-Yang, Stability and Vibration of Two-Bladed Aeroelastic Rotors on Flexible Supports, D.Sc. Dissertation, Sever Institute Technology of Washington University, August 1981.

63. Peters, D. A. and Chen S.Y.", Momentum Theory, Dynamic Inflow, and Vortex-Ring State", Journal of the American Helicopter Society, Vol. 27, No.3, July 1982, pp. 18-24.

64. Reddy, T.S.R., " Flap-lag Damping of an Elastic Rotor Blade with Torsion and Dynamic Inflow in Hover from Symbolically Generated Equations," AIAA/ASME/ASCE/AHS 25th Structures, Structural Dynamics and Materials Conference, Palm Springs, California, May 14-16, 1984, AIAA paper no. 84-0989.

65. Nilakantan, G.R. and Gaonkar, G.H., "Feasibility of Simplifying Coupled Flap-Lag Torsional Models for Rotor Blade Stability in Forward Flight", Tenth European Rotorcraft Forum, The Hague, The Netherlands, August 28-31, 1984, paper no. 53 (Vertica, vol 9, no. 3, 1985, pp. 241-256).

66. Curtiss, H.C., Jr. and Sumantran, V., "Stability and Control of VTOL Capable Airships in Hovering Flight," AIAA Ligher-than-Air Systems Conference, Anaheim, CA, July 25-27, 1983, AIAA Paper No. 83-1987-CP.

67. Friedmann, P.P. and Vankatesan, C., "Finite State Modelling of Unsteady Aerodynamics and Its Application to a Rotor Dynamic Problem," Eleventh European Rotorcraft Forum, London, Sept. 10-13, 1985, Paper No. 72.

Acknowledgement

This work was sponsored, in part, by the United States Army Research Office, Grant No. DAAG29-85-K-0228. The views, opinions, and/or findings of this report are those of the authors and should not be construed as an official Department of the Army position, policy, or decision, unless so designated by other documentation.

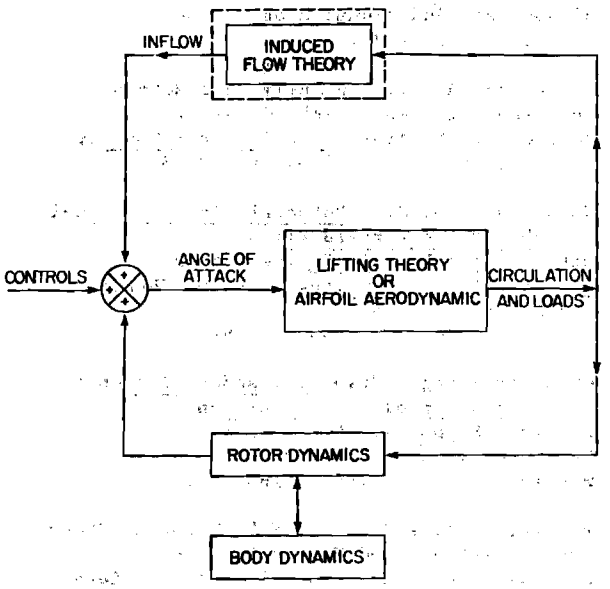

Fig.1 BLOCK DIAGRAM OF INFLOW DYNAMICS AS OPEN LOOP (---) AND CLOSED LOOP (—) SYSTEMS

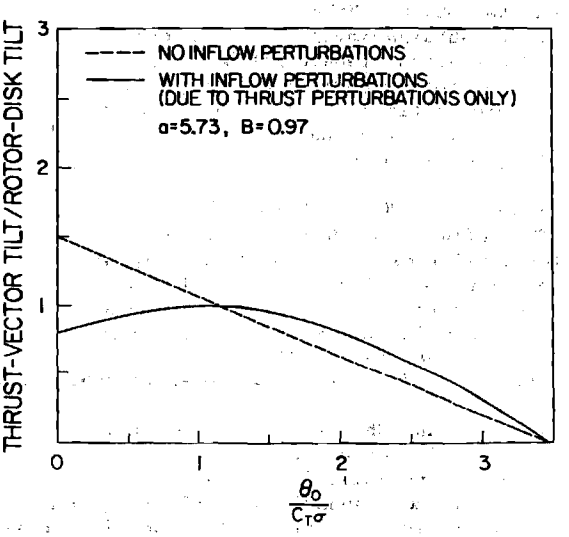

Fig.2 RATIO OF THRUST-VECTOR TILT TO DISC TILT DURING STEADY ROLLING VELOCITY IN HOVER.

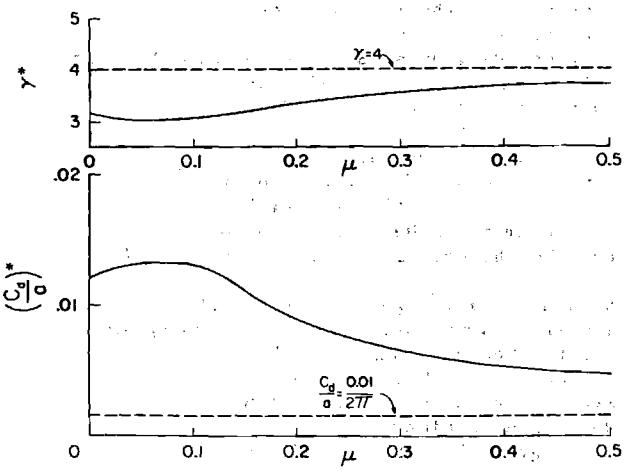

Fig.3 EQUIVALENT γ AND C_d

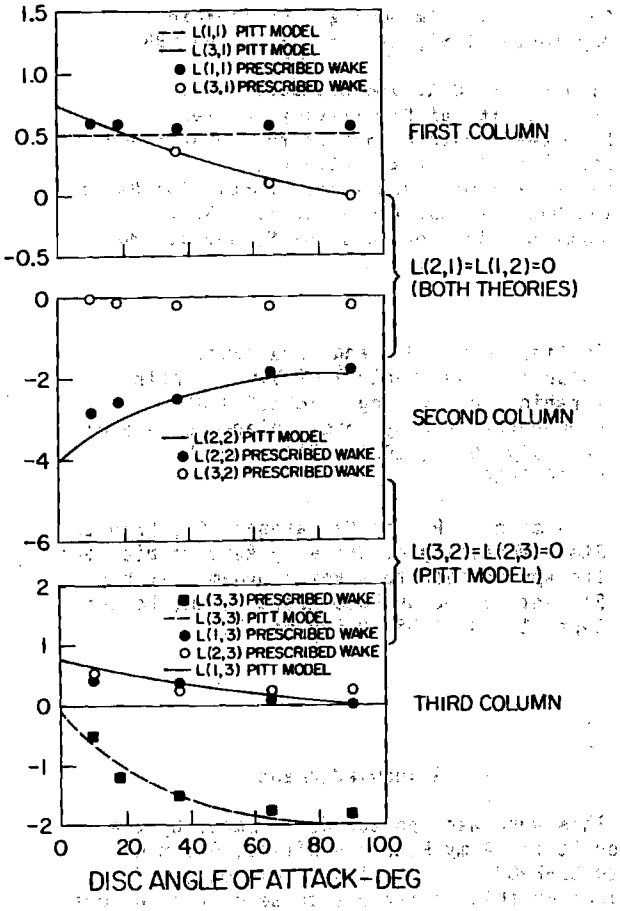

Fig.5 VERIFICATION OF THE L-MATRIX OF THE PITT MODEL FROM A PRESCRIBED WAKE ANALYSIS

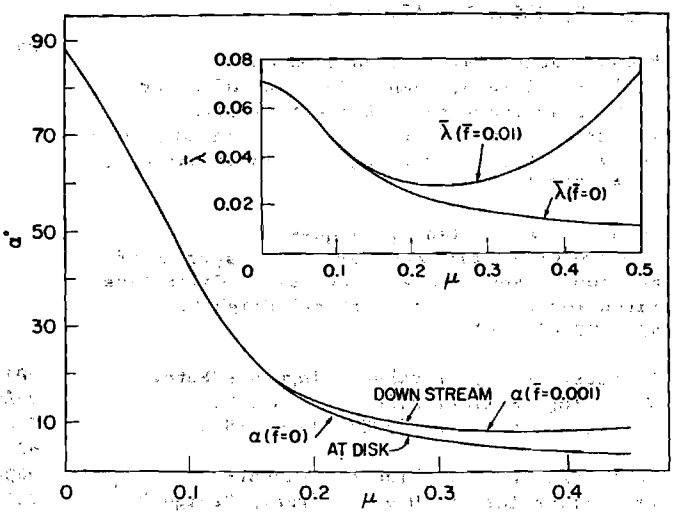

Fig.4 STEADY INFLOW AND DISK ANGLE OF ATTACK AS A FUNCTION OF ADVANCE RATIO (P=1.15, γ=5, ω_ζ=0.7, C_T/σ=0.2, σ=0.05)

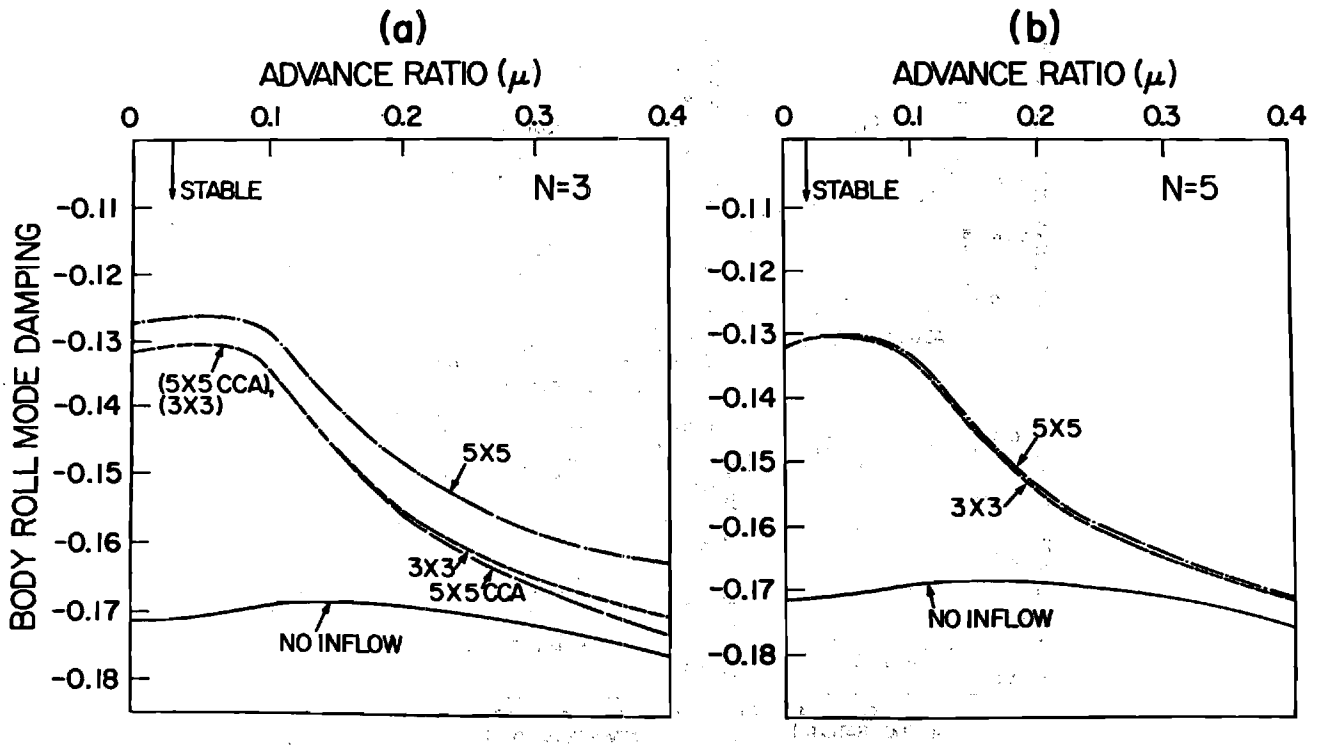

Fig.6 BODY ROLL MODE DAMPING FOR THREE AND FIVE BLADED ROTOR-BODY SYSTEMS WITH THE 3X3 AND 5X5 INFLOW MODELS (MOMENT TRIM, $C_{T/\sigma}$=0.2, P=1.15, ω_ζ=0.7, τ_c=0.4, τ_s=0.2, m_μ=0.1, h=0.4)

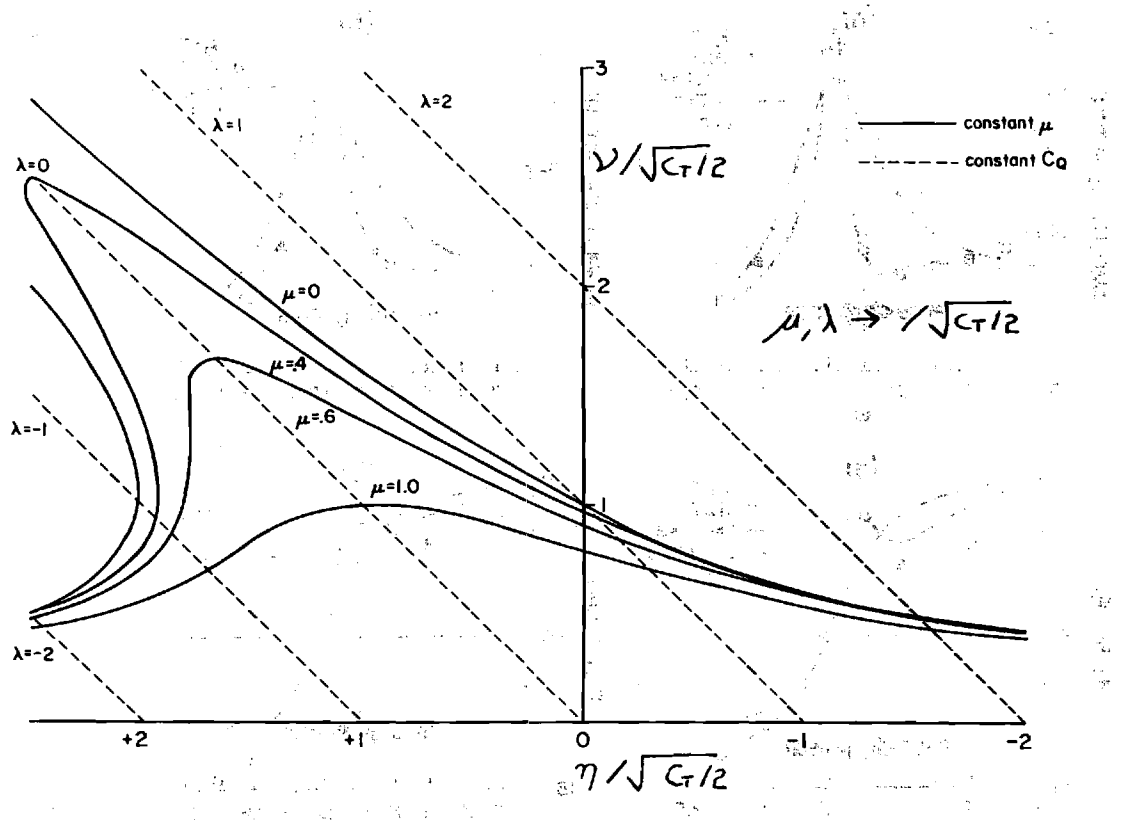

Figure 7. Induced flow versus rate of descent for various normalized inplane flows.

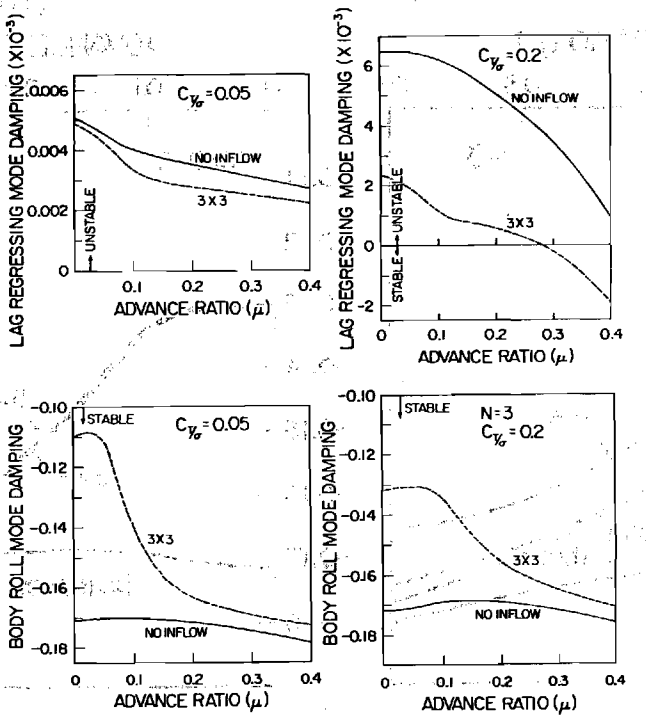

Fig.8 DAMPING LEVELS OF LAG AND BODY ROLL MODES OF ROTOR-BODY SYSTEMS (N≥3, OTHER PARAMETERS AS IN Fig.6)

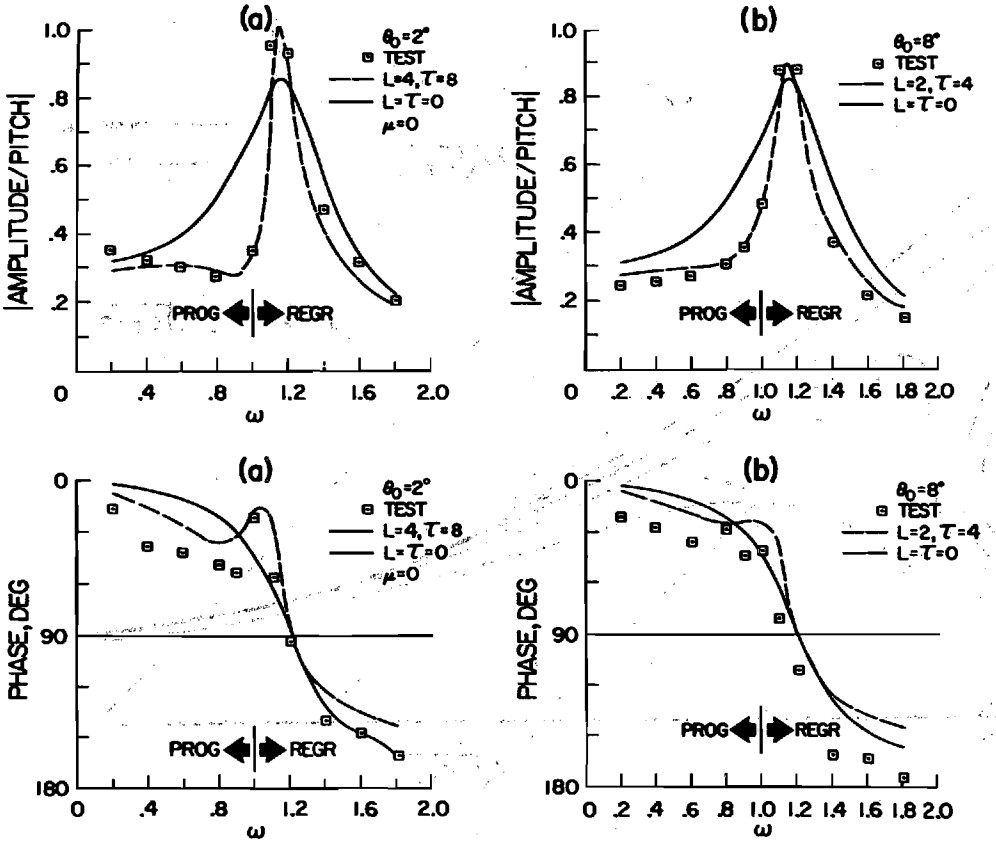

Fig.9 AMPLITUDE AND PHASE VARIATIONS vs. FREQUENCY FOR IDENTIFIED INFLOW PARAMETERS IN HOVER

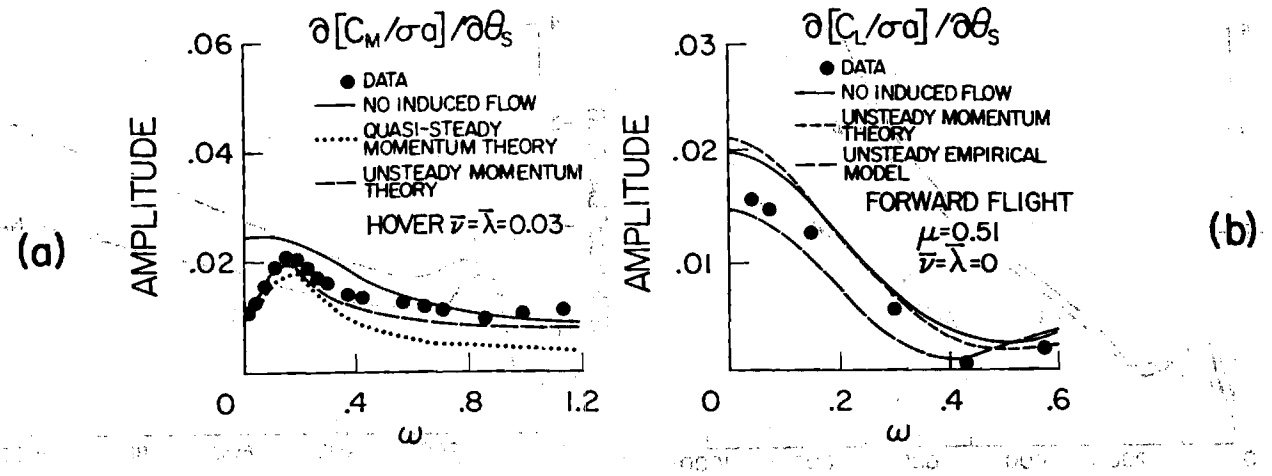

Fig.10 ROTOR RESPONSE TO CYCLIC PITCH IN HOVER AND FORWARD FLIGHT ($P=1.15, \gamma=4.25, B=.97, \sigma a=.7294, \theta_0=4^\circ$ SINGLE ROTATING MODE)

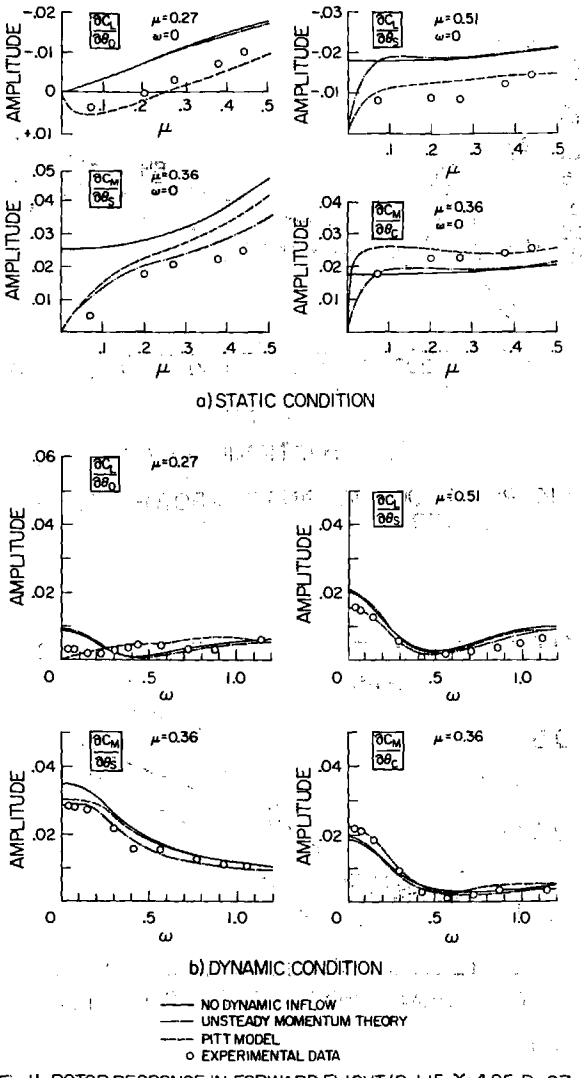

Fig.11 ROTOR RESPONSE IN FORWARD FLIGHT ($P=1.15, \gamma=4.25, B=.97, \sigma a=.73, \bar{\nu}=\bar{\lambda}=0$, ALL COEFFICIENTS NORMALIZED ON σa)

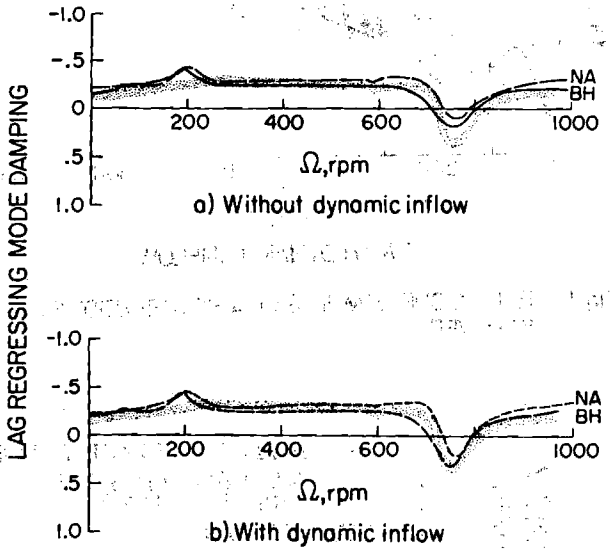

Fig.12 LAG MODE DAMPING OF A ROTOR-BODY SYSTEM IN HOVER

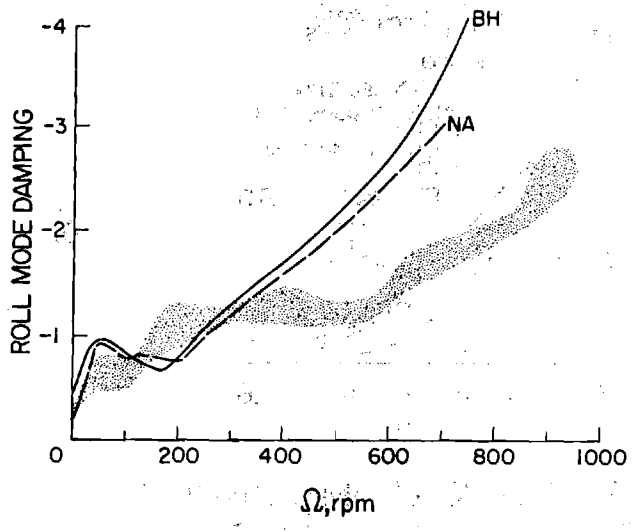

a) WITHOUT DYNAMIC INFLOW

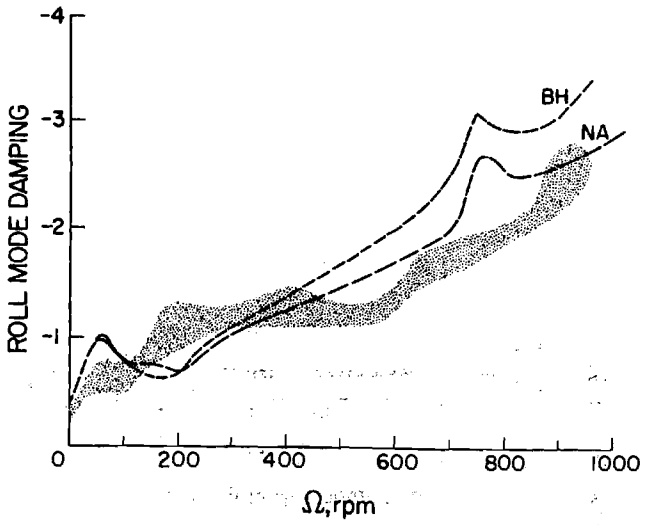

b) WITH DYNAMIC INFLOW

Fig. 13 ROLL MODE DAMPING OF A ROTOR-BODY SYSTEM IN HOVER

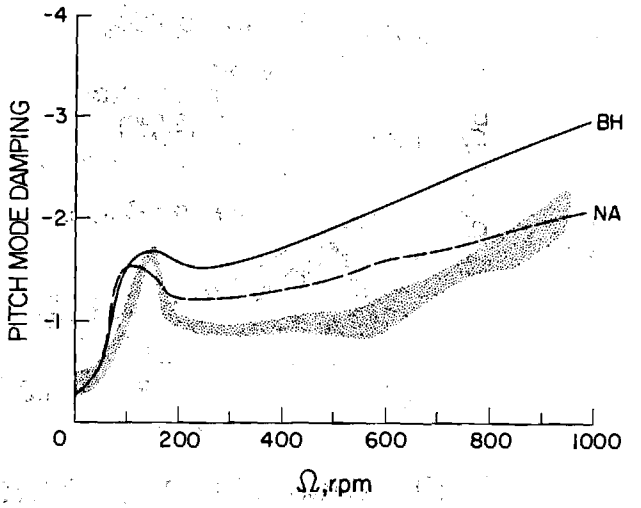

a) WITHOUT DYNAMIC INFLOW

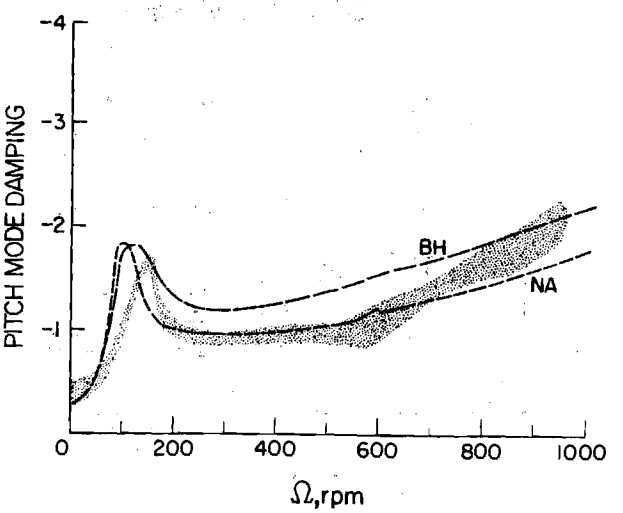

b) WITH DYNAMIC INFLOW

Fig. 14 PITCH MODE DAMPING OF A ROTOR-BODY SYSTEM IN HOVER

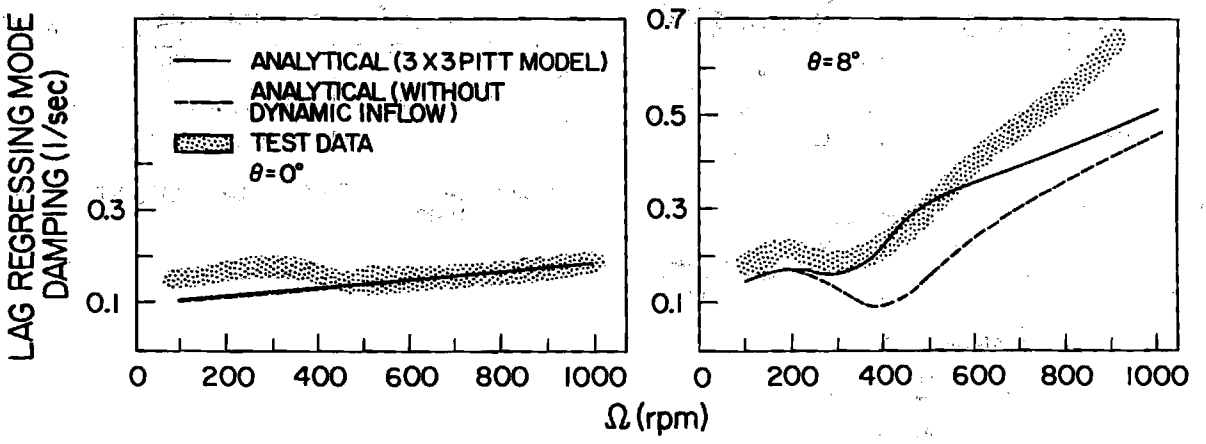

Fig. 15 CORRELATION OF MEASURED LAG MODE DAMPING WITH PREDICTED VALUES IN HOVER

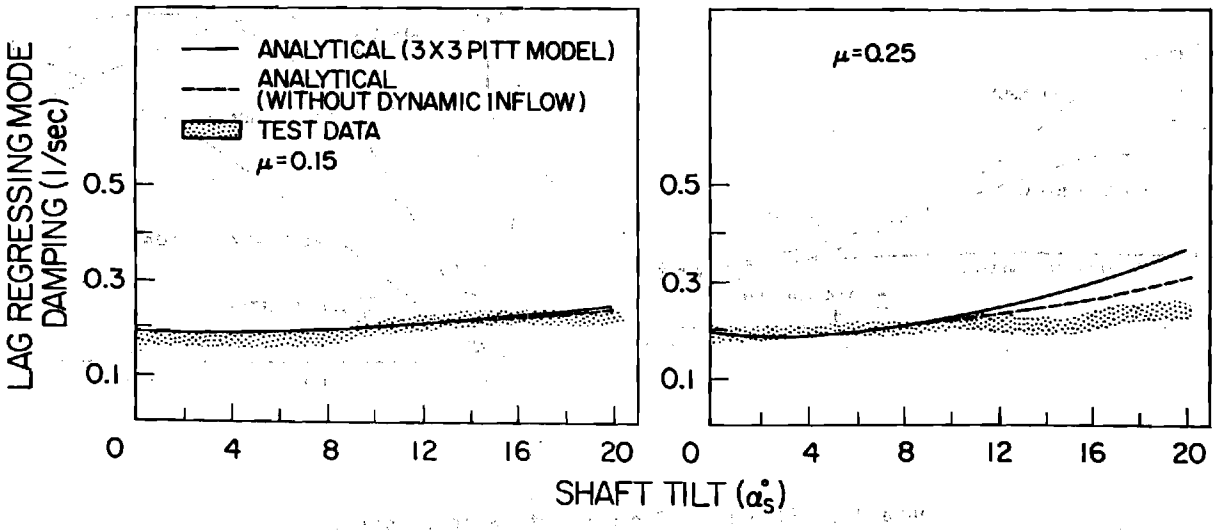

Fig.16 CORRELATION OF MEASURED LAG MODE DAMPING WITH PREDICTED VALUES ($\theta=0^\circ, \Omega=1000$ RPM)

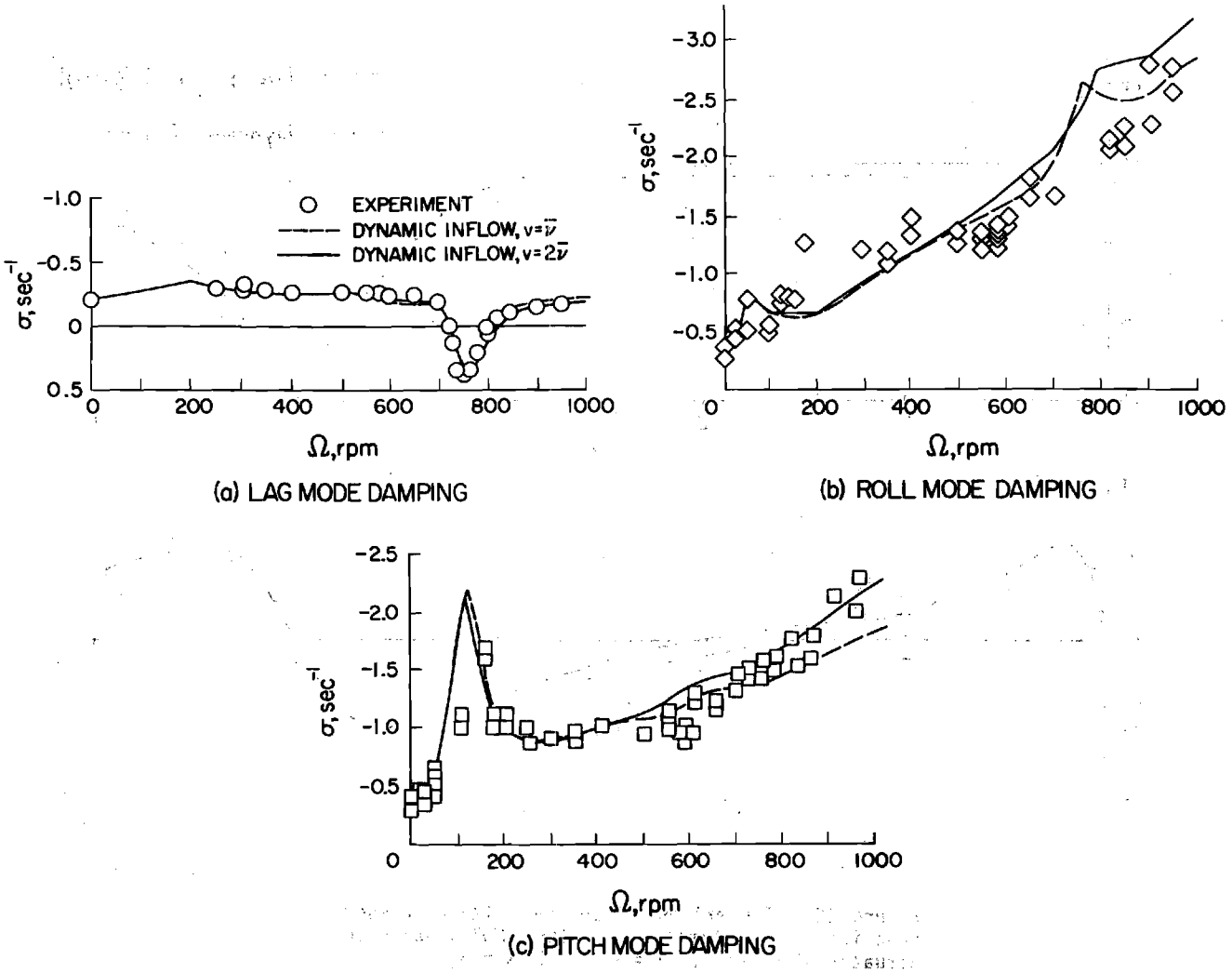

Fig.17 SENSITIVITY OF DAMPING DATA CORRELATIONS IN HOVER TO INFLOW MASS-FLOW PARAMETER

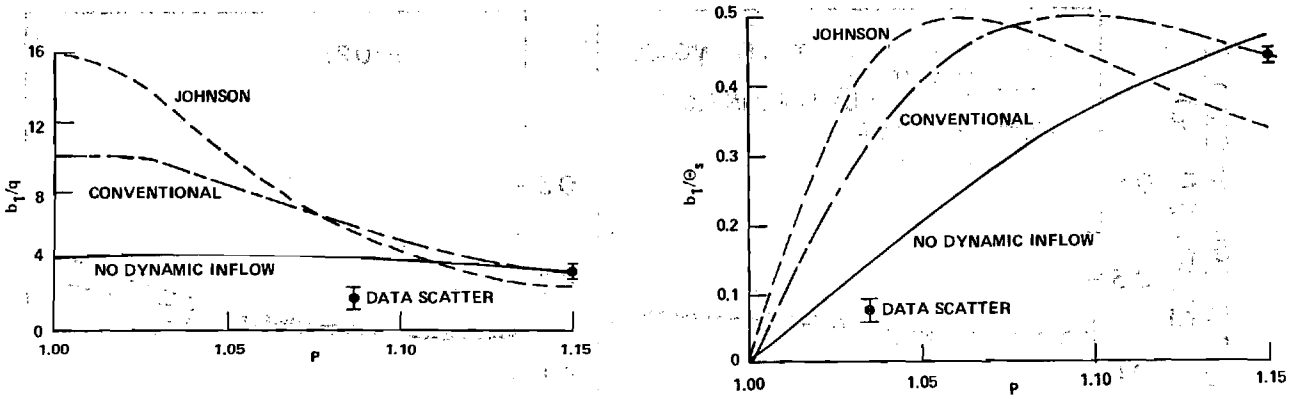

Figure 18. Effect of Dynamic Inflow on Flapping Response as a Function of Flap Frequency, γ = 4.25, σa = .729, β = .97, Data Point at p = 1.15.

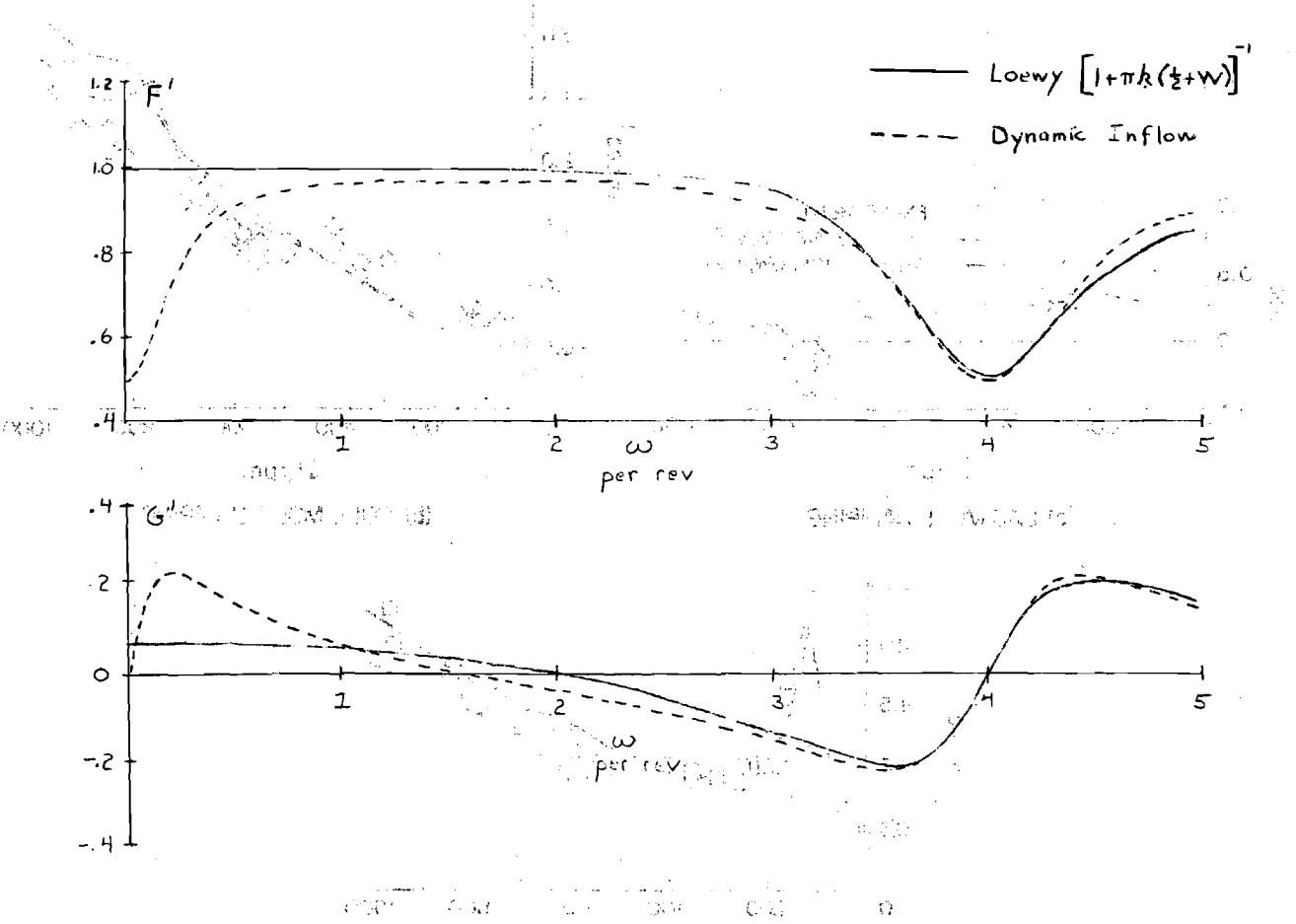

Figure 19. Comparison of Loewey Lift-Deficiency Function (for Small k) with Multi-Harmonic Actuator-Disc Theory, $\lambda = \eta = .05$, N = 4, $\sigma = .061$, h = 3.27, Collective Mode.

P-VERSION FINITE ELEMENTS FOR THE SPACE-TIME DOMAIN

by

David A. Peters
Professor

and

Amir P. Izadpanah
Research Assistant

School of Aerospace Engineering
Georgia Institute of Technology
Atlanta, Georgia 30332

Submitted to Computational Mechanics
An International Journal

June 17, 1986

Abstract

A bilinear formulation of elasto-dynamics is offered which includes, as a special case, Hamilton's Law of Varying Action. However, the more general bilinear formulation has several advantages over Hamilton's Law. First, it admits a larger class of initial-value and boundary-value problems. Second, in its variational form, it offers physical insight into the so-called "trailing terms" of Hamilton's Law. Third, numerical applications (i.e., finite elements in time) can be proven to be convergent under correct application of the bilinear formulation, whereas they can be demonstrated to diverge for specific problems under Hamilton's Law. Fourth, the bilinear formulation offers automatic convergence of the "natural" velocity end conditions; while these must be constrained in present applications of Hamilton's Law. Fifth, the bilinear formulation can be implemented in terms of a Lagrange multiplier that gives an order of magnitude improvement in the convergence of velocity. This implies that, in this form, the method is a hybrid finite-element approach.

Notation

a	- action density along edges (N-m on space boundary, N-sec on time boundary)
A	- cross-sectional area, m^2
A_i	- vector of integrals
$A(v)$	- linear operator on v
$\bar{A}(v)$	- Hamilton's form of A
$B(u,v)$	- bilinear operator on u,v
$\bar{B}(u,v)$	- Hamilton's form of B

B_{ij}, $\bar{B}_{ij}$, $\hat{B}_{ij}$ - matrix of integrals

C - constant, N/m

E - Young's modulus, N/m^2

f(x), f(x,t) - force per unit length, N/m

F_B - normalized aerodynamic force

F, F_0, F_L - forces, N

J - number of functions in series for $\hat{u}$

k - spring rate per unit length, N/m^2

K - spring rate, N/m

K_{max} - maximum value of K

L_a - Lagrangian, nondimensional

L - length of beam, m

$\mathcal{L}$ - Lagrangian density, N-m/unit volume

m - mass per unit length, kg/m

M - mass, kg

M_{max} - maximum value of M

n - number of functions in series for $\hat{v}$

N - number of elements in domain

p, p_0, p_T - momentum density, kg/sec

P, P_0, P_T - momentum, kg-m/sec

[Q] - Floquet Transition Matrix

q_i - generalized coordinates

t - time, sec

T - end of time period, sec

T_E - kinetic energy, nondimensional

u - solution for displacement, m

$\hat{u}$ - approximation to u, m

u_o - initial value for u, m

V_E - potential energy, nondimensional

v - test function, m

$\hat{v}$ - limited class of v, m

x - spacial coordinate, m

β - flapping angle, rad

γ - Lock number

λ - Lagrange multiplier

μ - longitudinal stiffness EA, N (equations 1-18)

μ - advance ratio of rotor, (equations 33-34 and Figures)

ϕ_j, ψ_j - polynomial functions

Σ - boundary of space-time domain

Ω - space-time domain

$\delta()$ - variation of ()

$()'$ - d()/dx

$(\dot{})$ - d()/dt

Δ - time increment, sec

δW - virtual work

δw - virtual work per unit volume (or virtual action density)

$(*)$ - $d/d\psi$

ψ - nondimensional time, azimuth angle

[ ] - matrix

{ } - column vector

< > - row vector

1. Introduction

1.1 Background

In Reference 1, Cecil Bailey offered a new look at Hamilton's Principle which he called Hamilton's Law of Varying Action.

$$\delta \int_{t_1}^{t_2} L_a dt - \left. \frac{\partial L_a}{\partial \dot{q}_i} \delta q_i \right|_{t_1}^{t_2} + \int_{t_1}^{t_2} \delta W dt = 0$$

The trailing terms, $\left. \frac{\partial L_a}{\partial \dot{q}_i} \delta q_i \right|_{t_1}^{t_2}$, cancel the other trailing terms that come from integration by parts of the variational of L_a. Therefore, they are usually of only academic interest and do not affect the equations of motion. However, Bailey noted that if the above equation is to be solved numerically, then the trailing terms must be included in order to obtain correct answers.

It was not long after this that other authors were attacking the direct numerical solution of Hamilton's Law. In Reference 2, the method is applied to problems of celestial mechanics. In Reference 3, the author notes that, by breaking the domain into small segments, the numerical application of Hamilton's Law gives rise to h-version "finite-elements" in the time domain. In Reference 4, the authors take the limit of very small elements and arrive at a marching algorithm, thus closing the gap between numerical integration and timewise finite elements. In Reference 5, however, the same authors note that (under certain conditions) the finite-element formulation can become numerically unstable; and this instability is demonstrated mathematically. As a solution to the stability problem, the authors replace δq, which appears in Hamilton's Law, with $\delta \ddot{q}$.

They make the very important observation that "δq" in the formulation does not need to be resricted to a literal variation of q. Instead, Hamilton's Law must hold true for all functions δq, regardless of their origin. Thus, in essence, Baruch and Riff offer a bilinear (rather than variational) form of Hamilton's Law. These ideas are further developed and applied in Reference 6.

Recently, the method of finite elements in time has also been applied to systems of equations with periodic coefficients, such as are present in the modeling of helicopter dynamics, References 7-9. In Reference 7, Borri applies a time-marching version of Hamilton's Law (analogous to Euler integration) to helicopter problems. However, in contrast to References 4 and 5, he notes that the trailing terms in Hamilton's Law should be written in terms of unknown momenta (P_{1i} and P_{2i}) rather than explicitly in terms of $\partial L_a / \partial \dot{q}_i$.

$$\delta \int_{t_1}^{t_2} L_a \, dt - P_{2i} \, \delta q_i(t_2) + P_{1i} \, \delta q_i(t_1) + \int_{t_1}^{t_2} \delta W \, dt = 0$$

This allows a natural convergence to $\dot{q}_i \, (t_1)$ rather than a constraint of $\dot{q}_1 \, (t_1)$. This concept is further developed in Reference 8.

In Reference 9, a complete bilinear formulation of Hamilton's Law is presented giving rise to p-version finite elements in time. Thus, h-version time-wise finite elements (as well as time-marching versions) fall out as special cases of this more generalized formulation. Reference 9 also investigates the convergence properties of the generalized formulation and conjectures that convergence is guaranteed only when certain restrictions are placed on the test functions of the bilinear

formulation. Numerical examples verify that problems which diverge under previous application of Hamilton's Law converge under the correct formulation. The work here is a continuation of the work in Reference 9.

1.2 Scope of Work.

In this paper, we offer an even more general formulation of elasto-dynamics than that presented in Reference 9. In particular, we present a bilinear formulation that is applicable to boundary-value, initial value, and periodic problems of elasto-dynamics. This more general formulation is stated in a completely generic way, but specific examples are given for beams and spring-mass systems to illustrate the implementation. The development here leads to several important advantages of the present formulation over Hamilton's Law. Of primary importance is the establishment of a convergence proof for the new formulation as well as the demonstration that numerical applications of Hamilton's Law can (and often do) fail to converge. Applications of the new and old methods to problems of helicopter stability are also presented for the case of simple blade flapping, and these yield insight into the numerical effectiveness of the method.

1.3 Philosophy and Justification

In a search for a new type of solution method, we wish to investigate solutions based not on the differential equations, but based on the original variational formulation from which the equations come (i.e., finite elements in time). However, there are two very good reasons for believing that finite elements in time would not be competitive with conventional methods. Therefore, we need first to provide some justification for the pursuit of this investigation.

We begin by recalling that the finite element approach was developed for the space domain in which two important factors exist that are not present in the time domain. First, the space problem is usually a boundary-value problem for which the displacement at a given value of x (the independent variable) depends on the entire solution for both smaller and larger values of x. For time, however, the solution for most problems depends only on the solution at smaller values of t (the independent time variable). Thus, we can develop a solution by marching in time, with the solution as accurate as we please at any given t. Therefore, finite element approaches would seem to be unnecessary in the time domain.

Second, and even more important, the space problem generally involves several independent variables that interact only at isolated nodes. Therefore, any marching algorithm would be too complex for intricate structures; and finite elements are required. On the other hand, for spatial boundary-value problems with only <u>one</u> spatial dimension, one can march (i.e., integrate) over the domain once for each independent end condition and then superimpose those solutions to obtain an exact solution to the boundary-value problem. It follows that, even for structural problems (with only one spatial dimension), finite elements are not needed. For a complex structure, however, the number of integration paths becomes staggering; and finite elements are necessary. Now, in the time domain, we have both an initial-value problem and a problem with only one integration path. Therefore, it would seem extremely doubtful at first consideration that a finite-element approach could rival time-marching for efficiency in the time domain.

In this paper, however, we consider another factor. The finite-element method is applied to the energy (or action) form of the equations. The time-marching algorithms, on the other hand, must be applied to the differential equations themselves. Because there is a considerable effort involved in obtaining the differential equations from the energy (whether it be by hand or by computer algebra), the finite element method has a "head start" over the marching algorithms. Therefore, if a finite element approach in time can be shown to be at least competitive with time-marching, then it has the potential of being a viable solution technique for some problems. Furthermore, we note that not all time-domain problems are initial-value problems. Many problems in optimal control are boundary-value problems in which some of the state variables are constrained at the end of the time domain. Thus, finite elements could be applicable if computationally competitive.

This brings us to the question, "To what extent might finite elements be competitive in time?" There are several reasons to believe that they could be competitive for the type of problem we consider. First, we are generally interested in a solution over a fixed period of time; and, for many problems, the solution at $t = T$ is the most important point. Thus, we are interested in a very specific solution at a specific point in time. Second, we notice that the most efficient time-marching techniques seem to be fourth-order predictor-correctors. These do not simply step through time, but they utilize the solution at four previous points. Therefore, it is not unreasonable that a finite element solution (which similarly requires past and future points) could be competitive. Third, we notice that for <u>periodic</u> solutions in time (which corresponds to a boundary-value

problem in time), Fourier analysis is considered to be competitive with marching even when there are many degrees of freedom. It follows that p-version finite elements in time (which are analogous to a Fourier series) could be competitive. Fourth, in time marching, we deal with two state variables for every second-order degree of freedom. In the finite element approach, however, only a single constraint (the initial displacement) need be applied for each second-order variable, provided we utilize the correct bilinear formulation. Thus, the initial velocity can be made to converge automatically, provided one follows the generalizations to be developed in this paper. As a result, we can effectively reduce the size of the problem and then use extraction techniques to aid velocity convergence.

In summary, we believe that the use of finite elements in time deserves at least a fair evaluation. Although we realize that there is some risk that the method may not prove economical, there is also a high potential benefit should the method be found to be at least competitive.

2. Formulation

2.1 Special Case of Spring-Mass System

Perhaps the best way to introduce the bilinear formulation of dynamic systems is to compare it with the standard, bilinear formulation of elasticity. We begin with the governing equation for a uniform beam-segment of length L on elastic foundation, Figure 1.

$$ku - \mu u'' = f \tag{1a}$$

$$F_L = \mu u'(L), \; F_0 = \mu u'(0) \tag{1b,c}$$

$$u(0) = u_o, \; u(L) = u_L \tag{1d,e}$$

We consider the segment to be an isolated free-body element so that F_0, F_L, u_0, and u_L may or may not be known, depending on the problem. Next, we compare equation (1) with the equation of motion for a simple spring-mass oscillator over a given length of time $0 < t < T$, Figure 2,

$$Ku + M\ddot{u} = F \tag{2a}$$

$$P_T = M\dot{u}\ (T),\ P_0 = M\dot{u}(o) \tag{2b,c}$$

$$u(T) = u_T\ ,\ u(o) = u_o \tag{2d,e}$$

where P_0, P_T, u_0, and u_T may or may not be given, depending on the problem. Except for the sign of the second-derivative term, equations (1) and (2) are an exact mathematical analogy.

Now the bilinear formulation of the spatial problem, equation (1), is well known, References (9-10), and can be written in operator notation as

$$B(u,v) = A(v) \quad \text{for all } v \tag{3}$$

where

$$B(u,v) = \int_0^L (kuv + \mu u'v')dx \tag{4a}$$

$$A(v) = \int_0^L fvdx + F_L v(L) - F_0 v(0) \tag{4b}$$

That equations (3) and (4) are equivalent to equation (1) is easily seen from integration by parts

$$B(u,v) - A(v) = \int_0^L (ku-\mu u''-f)v\,dx$$

$$- \left[F_L-\mu u'(L)\right] v(L) + \left[F_0-\mu u'(0)\right] v(0) = 0 \qquad (5)$$

For equation (5) to equal zero for all v(x), clearly each of equations (1a) - (1c) must hold.

By analogy, it would seem that a bilinear formulation of dynamics could be set in the same way as equation (3) with

$$B(u,v) = \int_0^T (Kuv-M\dot{u}\dot{v})dt \qquad (6a)$$

$$A(v) = \int_0^T Fvdt - P_T v(T) + P_0 v(0) \qquad (6b)$$

Again, integration by parts shows that equations (3) and (6) are equivalent to equation (2).

$$B(u,v) - A(v) = \int_0^T (Ku+M\ddot{u}-F)vdt$$

$$+ \left[P_T-M\dot{u}(T)\right] v(T) - \left[P_0-M\dot{u}(0)\right] v(0) = 0 \qquad (7)$$

For equation (7) to be valid for all v(t), clearly each of equations (2a) - (2c) must hold. Therefore, equations (3) and (6) comprise a bilinear formulation of the dynamics of a spring-mass system.

2.2 Variational Form

In order to obtain greater insight into the nature of this formulation, it is instructive to consider a special case which has

importance in the spatial problem. In particular, we refer to the case $v = \delta u$, in which v is taken as the variation of the displacement. In that case, the spatial problem, equations (3) and (4), reduces to

$$\delta \int_0^L \left[\frac{1}{2} ku^2 + \frac{1}{2} \mu u'^2 \right] dx =$$

$$\int_0^L f\delta u dx + F_L \delta u(L) - F_0 \delta u(0) \tag{8}$$

Equation (8) has important physical significance in that it equates the variation of the potential energy to the virtual work done on the system by $f(x)$, F_L, and F_0. This, then, is a variational (or energy) formulation of the spatial problem.

By analogy, we can write a variational formulation of the temporal problem, equations (3) and (6), when $v = \delta u$.

$$\delta \int_0^T \left[\frac{1}{2} Ku^2 - \frac{1}{2} M\dot{u}^2 \right] dt = \int_0^T F\delta u dt - P_T \delta u(T) + P_0 \delta u(0) \tag{9}$$

Equation (9) also has a direct physical interpretation. The bracketed term on the left-hand side is the negative of the Lagrangian. Therefore, the integral term is the negative of the dynamical quantity known as the "action"; thus, the left-hand term is the negative variation of action. The integral term on the right-hand side can be thought of as the "virtual action"; applied to the system over the time interval $0 < t < T$. Here, "virtual action" has the precise definition of the time-integral of virtual work. This definition of virtual action leads to a physical interpretation of the last two terms in equation (9). Consider the following manipulation.

$$\text{Virtual Action} = \int_0^T \delta u(t) F dt = \int_0^T \delta u(t) \frac{dP}{dt} dt \tag{10a}$$

$$\text{Virtual Action} = \int_{P_0}^{P_T} \delta u dP \tag{10b}$$

where P is the momentum.

A comparison of equation (10b) with equation (9) identifies the last two terms in equation (9) as the virtual action entering ($P_0 \delta u_0$) and leaving ($P_T \delta u_T$) the system at the boundaries of the time interval. Therefore, just as the right-hand side of equation (8) contains both the virtual work done on the spatial domain $0 < x < L$ and the virtual work done across the boundaries, the right-hand side of equation (9) represents both the virtual action done during the time domain and the virtual action that crosses the boundaries. Thus, we interpret equation (9) as a variational statement of dynamics. Namely, the variation of the action plus the virtual action over any time interval $0 < t < T$ must sum to zero.

2.3 Comparison with Hamilton's Law

It is now interesting to compare this variational formulation of dynamics (which is a special case of the bilinear formulation) with Hamilton's Law of Varying Action as applied in References (1) - (7). Hamilton's Law can be placed in the framework of equation (3) with $v = \delta u$ as

$$\bar{B}(u, \delta u) = \bar{A}(\delta u) \tag{11a}$$

$$B(u, \delta u) = \int_0^T \left[\frac{1}{2} K u^2 - \frac{1}{2} M \dot{u}^2 \right] dt + M\dot{u}(T)\delta u(T) - M\dot{u}(0)\delta u(0) \tag{11b}$$

$$\bar{A}\ (\delta u) = \int_0^T F\delta u dt \qquad (11c)$$

Two observations about Hamilton's Law are noteworthy. First, equation (11b) (in contrast to equation (6)) replaces P_0 and P_T with their $M\dot{u}$ formulas, thus making these terms bilinear in u and v. Therefore, the terms move from A(v) to B(u,v). It follows that $\bar{B}$ $(u,\delta u)$ is no longer a symmetric operator as was B(u,v). This is also pointed out in References 7 and 8, in which Borri notes that the exact momentum should be used in the operator.

Second, integration by parts of equations (11) yields an equivalent form of Hamilton's Law

$$\bar{B}(u,\delta u) - \bar{A}(\delta u) = \int_0^T (Ku + m\ddot{u} - F)\ \delta u dt = 0 \qquad (12)$$

A comparison with equation (7) gives an important insight. Hamilton's Law, as used in Reference (1) - (7), implies satisfaction of the differential equation (2a); but it does not enforce the natural end conditions, equations (2b) - (2c). Therefore, one must constrain $\dot{u}$ in Hamilton's Law; whereas, in the present formulation, $\dot{u}$ automatically approaches P/M (as we will see in the following sections). This distinction is similar to that between the Rayleigh-Ritz and Galerkin methods in the space domain.

2.4 Generalization

In the above development, we have considered only the special cases of a beam and spring-mass system. However, this is easily generalized to a complete theory of elastodynamics. As a conceptual step in this

generalization, we consider the system in Figure 1 but with f, F_0, F_L, and u functions of space and time. The mass per unit length of the beam is taken as m. The equation of motion and end conditions are, therefore

$$ku - \mu u'' + mu = f(x,t) \tag{13a}$$

$$F_L(t) = \mu u'(L,t) \tag{13b}$$

$$F_0(t) = \mu u'(0,t) \tag{13c}$$

For all t

$$p_T(x) = m\dot{u}(x,T) \tag{13d}$$

$$p_0(x) = m\dot{u}(x,0) \tag{13e}$$

For all x

Equations (13b-e) represent edge conditions on the boundaries of the domain, Figure 3.

The bilinear formulation of this elasto-dynamical problem can be stated as follows.

$$B(u,v) = \int_0^T \int_0^L \left[kuv+\mu u'v' - m\dot{u}\dot{v}\right] dxdt \tag{14a}$$

$$A(v) = \int_0^T \left[-F_0(t)v(0,t) + F_L(t)v(L,t)\right] dt$$

$$+ \int_0^L \left[P_0(x)v(x,0) - P_T(x)v(x,T)\right] dx$$

$$+ \int_0^T \int_0^L fvdxdt \tag{14b}$$

$$B(u,v) - A(v) = 0 \tag{14c}$$

Integration by parts over time and space leads directly to

$$0 = B(u,v) - A(v) = \int_0^T \int_0^L \left[ku-\mu u''+m\ddot{u}-f\right] v\,dx - \int_0^T \left[F_L-\mu u'(L,t)\right] v(L,t)\,dt$$

$$+ \int_0^T \left[F_0-\mu u'(0,t)\right] v(0,t)\,dt + \int_0^L \left[P_T-m\dot{u}(x,T)\right] v(x,T)\,dx \qquad (15)$$

$$- \int_0^L [P_0 - m\dot{u}\,(x,o)]v(x,o)\,dx$$

Thus, if the bilinear formulation is true for all v(x,t), then u must satisfy the differential equation and all four edge conditions.

With v= δu, equation (15) can be expressed as follows:

$$-B(u,\delta u) + A(\delta u) = 0 \qquad (16)$$

Equations (15 and 16) state that the variation of the action plus the virtual action done on the domain plus the virtual action crossing the boundaries of the space-time domain must sum to zero. On the spatial boundaries, [(x = 0, L), (0 < t < T)], the "virtual action" is the temporal integral of the virtual work. On the time boundaries, [(t = 0, T), (0 < x < L)], the "virtual-action" is taken to mean the spatial integral of virtual-action density which is defined as pδu, momentum times virtual displacement.

We can now completely generalize to all problems of elasto dynamics by the statement:

$$\text{Variation of (Action)} + \text{Virtual Action} = 0 \qquad (17)$$

Or, if we call $\mathcal{L}$ the Lagrangian density, δw the virtual-action density within the domain (i.e., virtual work per unit volume), and δa the virtual-action density along a space-time boundary, then a general formulation of dynamics is

$$\delta \int_{\Omega} \mathcal{L}\, d\Omega + \int_{\Omega} \delta w d\Omega + \int_{\Sigma} \delta a d\Sigma = 0 \tag{18}$$

where Ω is the space-time domain and Σ is the boundary of that domain. Equation (18) is a general statement of elasto-dynamics. If $\mathcal{L}$, δw, and δa depend on generalized coordinates q_i, then the bi-linear formulation is obtained by setting $\delta q_i = v_i(x,t)$.

3. Convergence

3.1 Approximate Solutions

The development in the previous section is mainly a conceptual one. That is, we have merely looked at dynamical equations in a slightly different way. Taken by itself, however, that formulation would probably make no change at all in the way that one derives differential equations of motion for dynamical systems. However, once we make the transition to approximate solutions of dynamical problems, the above development becomes of very practical interest. In the numerical formulation of the problem, we assume a solution for u from some limited class of functions ϕ_j, $j = 1, J$.

$$\hat{u}(x) = \sum_{j=1}^{J} \phi_j(x)\, q_j \tag{19a}$$

or

$$\hat{u}(t) = \sum_{j=1}^{J} \phi_j(t)\, q_j \tag{19b}$$

Now, $\hat{u}$ is only an approximation to u (except in the limit as $J \to \infty$) and can exactly satisfy neither the differential equations and boundary conditions of equation (1) nor those of equation (2). Similarly, $\hat{u}$ cannot satisfy the bilinear formulation, $B(\hat{u},v) = A(v)$, for all possible v. A numerical solution can be obtained, however, if one restricts the class of v to some subspace, $\hat{v}$, such that $B(\hat{u},\hat{v}) = A(\hat{v})$ for all $\hat{v}$ in the subspace. For example, we can write

$$\hat{v}(x) = \sum_{i=1}^{n} \psi_i(x)\, r_i \tag{20a}$$

or

$$\hat{v}(t) = \sum_{i=1}^{n} \psi_i(t)\, r_i \tag{20b}$$

Any mathematical proof for the numerical solution for u(t) must show that, as $\hat{v}$ is expanded to cover more and more of the space of admissable functions, then $\hat{u}$ will converge to u.

Clearly, the choice of ϕ_i and ψ_i is related to the convergence in a very direct way. In the bilinear formulation, ψ_i and ϕ_i are completely independent. In the variational case, however, $\psi_i = \phi_i$, and $r_i = \delta q_i$. Clearly, then, the convergence will be affected by the choice of bilinear formulation. In this section, we wish to address this convergence.

3.2 Classes of Solution

Before looking at sufficient conditions for convergence of a bilinear formulation, we need to look first at some necessary conditions for certain classes of problems. For our purposes here, three types of solutions are considered.

3.2.1 Boundary-Value Problems

The first class of solutions is that of boundary-value problems. For the spatial example, these are problems for which either displacement, force, or some linear combination of them (such as with an end spring) is specified at each end of the segment ($x = 0, L$). For simplicity, we will consider only three possibilities within this first class of problems:

1.) Free-free: F_0 and F_L given, $u(0)$ and $u(L)$ unknown,

2.) Fixed-free: $u(0)$ and F_L given, F_0 and $u(L)$ unknown

3.) Fixed-fixed: $u(0)$ and $u(L)$ given, F_0 and F_L unknown.

Equation (5) immediately suggests some limitations on v if the solution is to converge. For example, in the free-free case neither $\hat{v}(0)$ nor $\hat{v}(L)$ can be zero. Otherwise, setting $B(\hat{u},\hat{v}) - A(\hat{v}) = 0$ would not ensure that $\mu\hat{u}'$ converges to F_0 or F_L. The only alternative to this condition would be to constrain $\hat{u}'$ at the end points. For example, if the ϕ's and q_i's are constrained either by choice of ϕ or by Lagrange multipliers (as will be discussed later) such that $\mu\hat{u}'(o) = F_0$, then $\hat{v}(0)$ could be set to zero without loss of this end condition. Similarly, in the fixed-free case, one must insure $\hat{v}(L) \neq 0$ so that the F_L boundary condition is enforced. However, for this fixed-free condition, one must apply two additional constraints. First, the ϕ's and q's need to be chosen such that $\hat{u}(0)$ equals the desired value u_o. Second, one must set $\hat{v}(0) = 0$ by choice of ψ_i and r_i, so that the unknown F_0 does not enter the formulation. Finally, in the fixed-fixed case, both $\hat{v}(0)$ and $\hat{v}(L)$ must be set to zero and $\hat{u}(0)$ and $\hat{u}(L)$ must be constrained to be u_o and u_L, the specified values.

The identical three boundary-value problems can be formulated for the time domain as shooting problems. That is, either the displacement or velocity (i.e., momentum, P) is specified at t = 0; and the other initial condition (u_o or $\dot{u}_o$) is chosen such that u reaches a desired value (u or $\dot{u}$) at the end of time, T. Such problems are common in dynamics and especially in optimum control. As with spatial problems, $\hat{v}$ must be set to zero at the end-point for which the momentum (P_0 or P_T) is not known.

In the variational statement of the problem, this requirement on $\hat{v}$ is automatically fulfilled in either the spatial or the temporal formulation. This is because a constraint on u(0) or $\hat{u}(T)$ automatically ensures that $\hat{v}= \delta\hat{u} = 0$ at that point. This is one of the aesthetic attributes of the variational formulation, equations (8) and (9). However, we must point out that this attribute is not present in Hamilton's Law, equation (11). In that formulation, enforcement of $\delta\hat{u} = 0$ at either end does nothing to improve the attractiveness of the operator. In fact, due to the lack of boundary terms in equation (11c), displacements and velocities must <u>both</u> be constrained to be equal to their desired values as specified at either end; and $\delta u = 0$ gives no particular advantage.

3.2.2 Periodic Problems

A second class of problems is the case of periodic solutions. For the beam, this could be a solution for a circular ring that comes back on itself; or, when f(t) is periodic for the spring-mass system, it could be a classical periodic-response problem. Here, the conditions are

$$u(0) = u(L),\ u'(0) = u'(L),\ F_0 = F_L \qquad (21a\text{-}c)$$

or

$$u(0) = u(T),\ \dot{u}(0) = \dot{u}(T),\ P_0 = P_T \qquad (21d\text{-}f)$$

Neither $u(0)$, $\dot{u}(0)$, nor F_0 is known. From the bilinear formulation, equation (4) or (6), we see that we must choose $\hat{v}(0) = \hat{v}(L)$ in order to eliminate the unknown F's and P's from the formulation. Thus, $\hat{v}$ must be chosen to be periodic. The periodic condition on $\hat{u}'$ will thus converge automatically due to equation (5) or equation (7),

$$\hat{v}(0)\left[\mu\hat{u}'(L)-\mu\hat{u}'(0)\right] = 0 \tag{22a}$$

$$\hat{v}(0)\left[M\dot{u}(0) - M\dot{u}(T)\right] = 0 \tag{22b}$$

provided that $\hat{v}(0) \neq 0$. However, we must also constrain $\hat{u}(0) = \hat{u}(L)$, or $\hat{u}(0) = \hat{u}(T)$, through the choice of ϕ's and q's.

For the variational formulation of periodic problems, again we have an aesthetically pleasing formulation. The geometric constraint $\hat{u}(0)= \hat{u}(T)$ automatically ensures that $\delta\hat{u}(o) = \delta\hat{u}(T)$ or, more explicitly, $v(0) = v(T)$. In contrast, for Hamilton's Law of Varying Action in equation (11), although we have $\hat{u}(0) = \hat{u}(T)$ as in the above argument, this does <u>not</u> ensure that $\hat{u}'(0) = \hat{u}'(T)$ since these terms are not present in $\bar{A}(\delta u)$. Thus, one must also constrain $\hat{u}'(0) = u'(T)$. However, such a constraint is not difficult; and, often, both the $\hat{u}$ and $\hat{u}'$ constraints are handled simultaneously by choice of the ϕ_i as elements of a Fourier series.

<u>3.2.3 Initial-Value Problems</u>

We have just seen that for boundary-value (or shooting) problems and for periodic problems: 1) the bilinear formulation implies restrictions on $\hat{u}$ and $\hat{v}$, 2) the variational version <u>automatically</u> gives the correct restrictions on $\hat{v} = \delta\hat{u}$ when $\hat{u}$ is properly restricted, and 3) Hamilton's Law

will not converge to the correct timewise solution unless desired values for $P = M\dot{u}$ are enforced by additional constraints on u. In other words, numerical application of Hamilton's Law takes on the flavor of a Galerkin method (in which geometric and natural boundary conditions are enforced) whereas numerical application of the present variational statement takes on the flavor of a Rayleigh-Ritz method (in which only geometric conditions need be enforced).

Now, we wish to consider a third class of problems which is of great importance in the time domain, the class of initial value problems. Within the time domain, these comprise by far the most common types of solutions. In such cases, u and $\dot{u}$ (i.e. P_o) are prescribed at t = 0 but are unknown at t = T. The analogous spatial problem is also well-formulated (although little used) as a semi-infinite rod for which force and displacement are measured at one end and the solution for the rest of the rod is desired. Both problems always have solutions that can be obtained numerically by Runge-Kutta or similar marching methods. The interest here, however, is in obtaining such a solution from the bilinear formulation.

Equations (4)-(7) immediately provide necessary conditions on $\hat{v}$. Clearly $\hat{v}(L)$ or $\hat{v}(T)$ must be set to zero to eliminate the unknown F_L or P_T from the formulation. Furthermore, $\hat{v}(0)$ must not be set to zero. Otherwise the natural convergence of $M\dot{u}(0)$ to P_0 (or of $\mu u'$ to F_0) will not occur. It follows that the variational version ($v=\delta u$) fails to provide an adequate formulation of initial-value problems. First, the constraint of $u(0) = u_0$ automatically forces $\hat{v}(0) = \delta\hat{u}(0) = 0$ which destroys velocity convergence. Second, the fact that $\hat{u}(T)$ is unknown eliminates all possibility of enforcement of $\hat{v}(T) = \delta\hat{u}(T) = 0$. (On the other hand, Hamilton's Law, in which the $\dot{u}(0)$ condition is constrained is apparently

applicable, although it requires constraints on both $u(0)$ and $\dot{u}(0)$.) Thus, initial-value problems (whether in time or space) are not well-suited to the classical variational formulation because the virtual work (or the virtual action) at $x = L$ (or $t = T$) is not known. However, initial-value problems are well-suited to the general bilinear formulation presented here.

3.3 Sufficient Proof of Convergence

This section is perhaps the most crucial of this development. Thus far, we have seen from the bilinear formulation that certain explicit restrictions must be made on $\hat{u}$ and $\hat{v}$, the trial and test functions. We have also seen that the variational approach automatically gives the correct $\hat{v}$ conditions for boundary-value and periodic problems, but that it fails on initial-value problems. Third, we have seen that Hamilton's Law is a variational formulation that overcomes the problem of $\hat{v}$ constraints but at two costs: 1) the loss of natural $\dot{u}$ convergence, and 2) the introduction of nonsymmetric terms into $\bar{B}(u,v)$, equation (11b).

In this section, we deal the coup de grace to Hamilton's Law (as a computational tool) by showing that: 1) the nonsymmetric terms in $\bar{B}(\hat{u},\hat{u})$ preclude proof of convergence, and 2) specific cases of divergence can be demonstrated for well-formulated problems. On the other hand, the bilinear formulation can be <u>proven</u> to converge; and specific numerical examples will be given for which the bilinear formulation eliminates the divergence found with Hamilton's Law.

3.3.1 Proof for Bilinear Formulation

For spatial boundary-value problems, convergence can be proven rather simply based on the following properties of $B(u,v)$ and $F(v)$. (References 10-11)

1.) $F(v)$ linear: $F(\lambda v) = \lambda F(v)$

2.) $B(u,v)$ bilinear: $B(\lambda u,v) = B(u,\lambda v) = \lambda B(u,v)$

3.) $B(u,v)$ symmetric: $B(u,v) = B(v,u)$

4.) $B(u,v)$ positive definite, i.e.

$$B(u,u) > 0 \text{ if } \int_0^T u^2 dt > 0$$

For the temporal problem, the positive-definite property is lost; but convergence can be proven for initial-value and boundary-value problems (even for a nonsymmetric B) provided that an alternative property holds in lieu of numbers 3) and 4) above. This property is the Lax-Milgram Lemma. Reference 10-12. It is a sufficient condition for convergence and is given by

$$|B(u,v)| \leq$$

$$C\left[\int_0^T (u^2 + \dot{u}^2)dt\right]^{1/2} \cdot \left[\int_0^T (v^2 + \dot{v}^2)dt\right]^{1/2} \qquad (23)$$

$$= C \left|\left|u,\dot{u}\right|\right| \cdot \left|\left|v,\dot{v}\right|\right|$$

Where C is a constant independent of u and v. The above condition ensures that small perturbations in problem parameters will result in small perturbation to the generalized solution, (References 10 - 12).

The verification of equation (23) for the bilinear formulation given in this paper, Equation 6, follows from the Schwarz inequality:

$$|B(u,v)| \leq \int_0^T K|u|\cdot|v| \; dt + \int_0^T M|\dot{u}|\cdot|\dot{v}|dt$$

$$\leq K_{max} \int_0^T |u|\cdot|v| \; dt + M_{max} \int_0^T |\dot{u}|\cdot|\dot{v}|dt$$

$$\leq K_{max} \left[\int_0^T u^2 dt \right]^{1/2} \cdot \left[\int_0^T v^2 dt \right]^{1/2}$$

$$+ \; M_{max} \left[\int_0^T \dot{u}^2 dt \right]^{1/2} \cdot \left[\int_0^T \dot{v}^2 dt \right]^{1/2}$$

$$\leq \sqrt{K^2_{max} + M^2_{max}} \left[\int_0^T (u^2 + \dot{u}^2)\, dt \right]^{1/2} \cdot \left[\int_0^T (v^2 + \dot{v}^2) dt \right]^{1/2} \quad (24)$$

Thus, the property is demonstrated to hold if we take

$$C = \sqrt{K^2_{max} + M^2_{max}}$$

3.3.2 Failure of Hamilton's Law

In contrast, in the formulation of Hamilton's Law, $\bar{B}(u,v)$ has two extra bilinear terms that prevent the establishment of the above property

$$|\bar{B}(u,v)| \leq |B(u,v)| + \underline{M|\dot{u}(0)|\cdot|v(0)|} + \underline{M|\dot{u}(T)|\cdot|v(T)|} \quad (25)$$

The two underlined terms in $|\bar{B}(u,v)|$ cannot be limited to be less than the norm in the above equation. For example, consider

$$v(t) = 1,\ \dot{v}(t) = 0 \qquad \text{for all } t \tag{26a}$$

$$\dot{u}(t) = \begin{cases} 0\ , & 0 \le t \le T - \Delta \\ 1 - \dfrac{T-t}{\Delta}\ , & T-\Delta < t \le T \end{cases} \tag{26b}$$

$$\dot{u}(t) = \begin{cases} 0\ , & 0 \le t \le T - \Delta \qquad (26c) \\ \dfrac{1}{\Delta}\ , & T - \Delta < t \le T \qquad (26d) \end{cases}$$

It follows that

$$|\dot{u}(T)| \cdot |v(T)| = \frac{1}{\Delta} \tag{26e}$$

$$\left[\int_0^T (v^2 + \dot{v}^2)dt \right]^{1/2} = T^{1/2} \tag{26f}$$

$$\left[\int_0^T (u^2 + \dot{u}^2)dt \right]^{1/2} = \left[\int_{T-\Delta}^T \frac{1}{\Delta^2}\ dt \right]^{1/2} = \sqrt{\frac{1}{\Delta}} \tag{26g}$$

Thus, no matter how large one makes C, there is always a Δ small enough such that

$$M|\dot{u}(T)||v(T)| = \frac{M}{\Delta} > ||u,\dot{u}||\ ||v,\dot{v}\ || = \frac{CT}{\sqrt{\Delta}}^{1/2} \tag{26h-i}$$

This does <u>not</u> imply that numerical application of Hamilton's Law will <u>never</u> converge, as convergence has been demonstrated in a great number of cases. However, it <u>does</u> imply that one can find individual examples for which convergence will not occur. In fact, divergence has occurred in at

least two instances in the literature, References (5) and (9). In the first case, the divergence was eliminated by replacement of ($\hat{v} = \delta\hat{u}$) by ($\hat{v} = \delta\ddot{u}$). From our previous development, we see that this is a step in the right direction since it eliminates $\delta\hat{v}(0) = 0$. However, it is still not sufficient to provide convergence in all cases because the troublesome trailing terms still occur. The only sure way is to convert to the bilinear formulation with $\hat{v}(T) = 0$.

3.4 Summary of Convergence Conditions

Based on the above development, we find that the following items are necessary and sufficient conditions for convergence of the initial value problems to the solution (including $\dot{u}$) in all cases, with the bilinear form chosen as in equations (14a, b).

a) Trailing terms in "Action" statement of dynamics must be written in terms of momenta, P (whether known or unknown), and not in terms of $M\dot{u}$. (Ref. 7, 9)

b) The normally used variation, $\delta\hat{u}$, must be replaced by a general test function, $\hat{v}$, (Ref. 5, 10).

c) The constraint on $\hat{u}$ should be $\hat{u}(0) = u_o$, but the constraint on $\hat{v}$ should be $\hat{v}(T) = 0$.

This last point has apparently escaped other investigators. Although one can converge without c) in some cases, the proofs here show c) to be necessary to ensure convergence in all cases. Robustness of this type is absolutely necessary for a numerical method. Furthermore, the procedure outlined above opens the way for a p-version finite element in time, whereas the other approach has lead more to h-versions, Ref. 10.

4. Numerical Applications

4.1 Matrix Formulation

Numerical solutions to dynamics problems by use of the above, bilinear formulation can be couched in a matrix framework. We consider an approximate solution, $\hat{u}$, as in equation (19b) with a restricted class of test functions, $\hat{v}$, as in equation (20b). Substitution into equations (3) and (6) gives a matrix formulation of an approximate solution for a temporal problem.

$$< r_i > \left[B_{ij} \right] \left\{ q_j \right\} = < r_i > \left\{ A_i \right\} \tag{27a}$$

where

$$B_{ij} = \int_0^T (K \psi_i \phi_j - M\dot{\psi}_i \dot{\phi}_j)dt \tag{27b}$$

$$A_i = \int_0^T F\psi_i dt - P_T\psi_i(T) + P_0\psi_i(0) \tag{27c}$$

Since equation (27a) must be valid for all r_i, we can eliminate r_i from the equation to obtain n equation in J unknowns.

The constraints on $\hat{u}$ and $\hat{v}$ must now be included, and this can be handled in a variety of ways. For example, for an initial-value problem we have $\hat{u}(0) = u_o$, $M\dot{u}(0) = P_0$ as given, with $\hat{u}(T)$ and P_T unknown. Thus, we have two constraints, as outlined in section 3.2.3.

$$\hat{u}(0) = \sum_{j=1}^{J} \phi_j(0)q_j = u_o \tag{28a}$$

$$\hat{v}(T) = \sum_{i=1}^{n} \psi_i(T) r_i = 0 \tag{28b}$$

Equation (28a) can be included in equation (27a) as an augmented equation. Equation (28b) can be included in equation (27a) by multiplication by an aribitrary Lagrange multiplier, λ, and then by addition of that term to the equation on the left-hand side. This gives, as a constrained equation,

$$\begin{bmatrix} [B_{ij}] & \{\psi_i(T)\} \\ \langle \phi_j(0) \rangle & 0 \end{bmatrix} \begin{Bmatrix} \{q_j\} \\ \lambda \end{Bmatrix} = \begin{Bmatrix} \{\hat{A}_i\} \\ u_o \end{Bmatrix} \tag{29a}$$

$$\hat{A}_i = \int_o^T F\psi_i \, dt + P_0\psi_i(0) \tag{29b}$$

where $\psi_i(T)\ P_T$ has been eliminated from $\hat{A}$ due to the constraint $v(T) = 0$. Equation (29) is taken with J=n (the same number of functions in $\hat{u}$ and $\hat{v}$) to yield n + 1 equations in n + 1 unknowns to be solved for q_j and λ. However, care must be taken, since Lagrange multipliers have been known to create numerical problems, Ref. 13.

Of course, there are other ways to do this besides use of the Lagrange multiplier. For example, if we take

$$\phi_1(0) = 1, \qquad \phi_j(0) = 0 \qquad j \neq 1 \tag{30a}$$

$$\psi_1(T) = 1, \qquad \psi_i(T) = 0 \qquad i \neq 1 \tag{30b}$$

Then the constraints become trivial

$$q_1 = u_o, \quad r_1 = 0 \tag{30c}$$

The Lagrange multiplier is, then, effectively eliminated from equation (29); and we have n - 1 equations in n - 1 unknowns

$$\left[\hat{B}_{ij}\right]\begin{Bmatrix} q_2 \\ q_n \end{Bmatrix} = \begin{Bmatrix} A_2 \\ A_n \end{Bmatrix} - \begin{Bmatrix} B_{21} \\ B_{n1} \end{Bmatrix} u_o \tag{31a}$$

where $\hat{B}_{ij}$ is B_{ij} with the first row and column removed, and where

$$\lambda = A_1 - B_{11}u_o - < B_{12} \text{ --- } B_{1n} > \begin{Bmatrix} q_2 \\ q_n \end{Bmatrix} \tag{31b}$$

In contrast, the same development for Hamilton's Law differs slightly (but significantly) in its numerical formulation. Equations (27b) and (27c) become:

$$\bar{B}_{ij} = \int_0^T (K\phi_i\phi_j - M\dot{\phi}_i\dot{\phi}_j)dt + M\phi_i(T)\dot{\phi}_j(T) - M\phi_i(0)\dot{\phi}_j(0) \tag{32a}$$

$$\bar{A}_i = \int_0^T F\phi_i dt \tag{32b}$$

Furthermore, an initial-velocity constraint must be added to Hamilton's Law which implies a second auxillary equation. Also, the relation $v=\delta u$ implies constraints on both $v(0)$ and $\dot{v}(0)$ which implies two Lagrange multipliers.

$$\begin{bmatrix} \left[\bar{B}_{ij}\right] & \{\phi_i(0)\} & \{\dot{\phi}_i(0)\} \\ < \phi_j(0) > & 0 & 0 \\ < \dot{\phi}_j(0) > & 0 & 0 \end{bmatrix} \begin{Bmatrix} \{q_j\} \\ \lambda_1 \\ \lambda_2 \end{Bmatrix} = \begin{Bmatrix} \{A_i\} \\ u_0 \\ P_o/M \end{Bmatrix} \tag{33}$$

A comparison of equations (29) and (33) reveals the similarities and differences in the two formulations. Again, λ_1 and λ_2 can be eliminated, if desired, by judicious choice of ϕ, q_1, and q_2. Thus, the Hamilton's formulation results in a form similar to that of the bilinear formulation but with differences in numerical details. However, it is exactly these details that cause equation (29) to converge unconditionally whereas equation (33) can cause divergence.

A similar development occurs for other choices of end conditions or for other constraints on $\hat{u}$. For multiple elements (i.e., many finite-elements in time over a domain), each solution is applied sequentially, exactly as above, over the time domain of interest, with the end values of one segment (u and $\dot{u}$)used as the initial conditions for the next.

4.2 Significance of Lagrange Multipliers

Lagrange multipliers, such as those introduced in equations (29)-(33), often have important physical meaning; and this is the case in the present formulation. A comparison of equations (27) and (29) reveals that $\lambda = P_T$, the final momentum. This fact provides us with an extraction technique to obtain an improved estimate of $\dot{u}(T)$. In particular, equation (7) shows that P_T must approach $M\dot{u}(T)$ as the number of functions, n, is increased. However, one would expect P_T/M to converge much more rapidly to $\dot{u}(T)$ than does the actual time derivative of $\hat{u}$,

$$\dot{\hat{u}}(T) = \sum_{j=1}^{J} \dot{\phi}_j(T) q_j \tag{34a}$$

The reason for this expectation is that equation (34a) involves derivatives of the trial functions, ϕ_j, which can be more sensitive in convergence than ϕ_j itself. On the other hand, the formulation

$$\dot{u}(T) \simeq \lambda/M \tag{34b}$$

is not subject to these senstivities and represents more of a least-squares estimate of the final velocity.

A similar effect is present in the space domain for which it is well known that the summation of forces and moments on a beam is a much more accurate measure of stresses at an end than are the second and third derivatives of deflection at that end. Equation (31b), the special case of V(T) constrained by choice of ψ_i, shows this clearly. The extraction equation for λ (in this case separate from the solution for q) is expressed as a summation of external forces and internal momenta. Therefore, whether or not one explicitly invokes a Lagrange multiplier to enforce V(T) = 0, one should calculate $\lambda = P_T$ in order to obtain the most accurate estimate of $\dot{u}(T)$. In the case of multiple elements, this is extremely important. Thus, u(T) and P_T for a particular segment should be used directly as u(0) and P_0 for the next segment. Such a formulation is analogous to the mixed or hybrid finite-element method in space for which deflections and stresses are the state variables. It should be noted here that in the marching algorithm of Reference 8, P_T is moved to the left-hand side of the equation (along with u(T)) as an unknown. Thus, although v(T) is not formally set to zero, the numerical result is the same.

Once we have made the above observations, it is quite natural to extend this concept in order to obtain a better approximation for the momentum p(t) (i.e., for the velocity) at any point in the domain. Having

recognized that the Lagrange multiplier represents a momentum balance, we can write the momentum at time t as

$$P(t) = P_0 + \int_o^t (f - K\hat{u})dt \tag{35a}$$

or

$$p(t) = A_o - \langle \ldots\ldots B_{oj} \ldots\ldots \rangle \left\{ q_j \right\} \tag{35b}$$

where

$$A_o = P_0 + \int_o^t f dt \tag{35c}$$

$$B_{oj} = \int_o^t K\phi_j dt \tag{35d}$$

This is again analogous to the spatial problem, in which force equilibrium gives

$$F(x) = F_o + \int_o^x (K\hat{u} - f)dx \tag{35e}$$

One can easily prove that p(T) in equation (35b) is identically equal to $P_T = \lambda$ of the bilinear formulation, provided that v(t) = 1 can be exactly represented by a linear combination of the ψ_i's retained in the numerical results. This is almost certainly the case for any practical set of ψ_i's, and it is always the case as $n \to \infty$.

4.3 Example Problem

In this section, we apply two finite-element formulations to the flapping motion of a helicopter blade. The Lagrangian and virtual work for the flapping motion, once linearized and nondimensionalized, is written as

$$L_a = T_E - V_E = \frac{1}{2}\left(\overset{*}{\beta}^2 - p^2\,\beta^2\right), \quad \delta W = F_\beta\,\delta\beta \tag{35}$$

with ψ (the azimuth angle) taken as nondimensional time. The generalized force is F_β, which (when nondimensionalized) is written as

$$F_\beta = \frac{-\gamma}{8}\left(1 + \frac{4}{3}\mu\sin\psi\right)\overset{*}{\beta} - \frac{\gamma}{8}\left(\frac{4}{3}\mu\cos\psi + \mu^2\sin 2\psi\right)\beta \tag{36}$$

The final equation of motion is:

$$\overset{*}{\beta} + \frac{\gamma}{8}\left[1 + \frac{4}{3}\mu\sin\psi\right]\overset{*}{\beta} + \left[p^2 + \frac{\gamma}{8}\left(\frac{4}{3}\mu\cos\psi + \mu^2\sin 2\psi\right)\right]\beta = 0 \tag{37}$$

It should be noted that the differential equation resulting from the above development has periodic coefficients and its solution is perfectly smooth.

In order to study the stability of such systems, one needs to find the Floquet Transition Matrix [Q] which, for the above system, consists of the values of $\beta(2\pi)$ and $\overset{*}{\beta}(2\pi)$ due to unit initial displacement (with zero initial velocity) and to zero initial displacement (with unit initial velocity). In trying to calculate the Floquet transition matrix, we demonstrate the type of numerical instability associated with an improperly formulated finite-element method. The method is applied primarily to one element to show that the cause of instability is improper formulation and also to point out that violation of the rules that govern the stability of bilinear formulation can indeed result in numerical instability.

In the improperly-formulated application of Hamilton's Law (hereafter called Method H), we enforce both initial conditions <u>exactly</u> by

restricting the class of admissible functions. In the correct bilinear formulation (thereafter called Method B), we enforce only the initial displacement. The initial velocity approaches the exact value in a natural way. Results are given for two versions of method B. In B1, $\dot{u}(T)$ is obtained from the series, equation (34a). In B2, $\dot{u}(T)$ is obtained from the Lagrange multiplier, equation (34b).

5. Numerical Results

We now wish to compare numerical results from application of Hamilton's Law of Varying Action (Method H) with results from the new, bilinear formulation, (Methods B1 and B2). In the application of Hamilton's Law, we enforce both initial displacement and initial velocity, which results in constraints: $\delta\dot{u}(0)= 0$. These are enforced by Lagrange multipliers, λ_1, and λ_2, as in equation (33). This is in contrast to numerical application of the bilinear formulation, equation (29), in which $\dot{u}$ converges naturally. The basis functions for both ϕ_i and ψ_i are taken as Legendre polynomials over the range [-1, +1], unless otherwise noted in the results. We have tried results with other polynomials and, thus far, there is little effect of polynomial choice, as long as the polynomials are reasonably orthogonal.

5.1 Hover

For comparison purposes in the following results, we will consider $\beta(2\pi)$ and $\overset{*}{\beta}(2\pi)$ in response to the initial conditions $\overset{*}{\beta}(0) = 0$, $\beta(0) = 1$. These values are two of the four elements of the Floquet Transition Matrix; and relative comparisons with this element are representative of those for the other two elements and for the Floquet eigenvalues themselves. Figure 4 presents the results of Methods H and B as compared to an exact solution

for $\mu = 0$. The response, $\beta(2\pi)$, is plotted vs. n, the number of polynomials used in the series. At 6 polynomials, the error with Hamilton's Law is about 2%; and little improvement is obtained when the 7th polynomial is added. However, by 9 polynomial terms, the error has rapidly converged to less than 0.1%. With the bilinear formulation, the convergence is better; and only 8 polynomials are needed to reach 0.1% accuracy. At only 6 polynomials, however, the accuracy of the bilinear formulation is slightly inferior to that of Hamilton's Law. The reason for this cross-over is straightforward. In Hamilton's Law, one enforces $\dot{u}(0)$; and this is more accurate when fewer functions are used, provided it converges. However, as more terms are added, this advantage disappears. This is analagous to the advantage of Galerkin over Ritz methods when only a few comparison functions are used. However, once enough terms are used so as to converge on $\dot{u}(0)$, this difference is lost.

In Figure 5, we present the same data for $\overset{*}{\beta}(2\pi)$. In this figure, two curves are provided from the bilinear formulation. B1 is $\overset{*}{\beta}$ from the polynomial derivatives and B2 is $\overset{*}{\beta}$ from the Lagrange multiplier. Comparison of the H and B1 curves provides the same relative conclusions as in Figure 4. However, with B1, the convergence for $\overset{*}{\beta}$ is seen to be much slower than that for β. With B2, on the other hand, there is a dramatic improvement in $\overset{*}{\beta}$ convergence; and the accuracy of $\overset{*}{\beta}(2\pi)$ from λ rivals that of $\beta(2\pi)$ for accuracy. Thus, our original speculation on the convergence of the Lagrange multiplier is supported.

5.2 Forward Flight

Next, we move on to higher advance ratios, which introduces periodic coefficients into the equations. Figures 6-9 show the evolution of the

$\beta(2\pi)$ vs n curves as advance ratio is increased. No exact solutions are available, but the high-precision SSP results are taken as essentially exact. In Figure 6, at $\mu = 0.1$, we see a definite retardation in the convergence of Hamilton's Law, with 1% error still present at n = 10. (Note that Figure 6 has a compressed scale as compared to Figure 1.) The bilinear formulation, however, converges rapidly. At $\mu = 0.3$, Figure 7, a further degradation in Hamilton's Law is seen, and the results oscillate about the true solution as n is increased. The error is now 4% for n = 10. The bilinear formulation, on the other hand, still converges quickly with less than 0.1% error at n = 10. At $\mu = 0.5$, Figure 8, a greatly expanded scale is required to capture the large errors present in results with Hamilton's Law. At n = 12, the error is over 100%. In contrast, bilinear results are essentially converged at n = 11. Last, at $\mu = 0.7$ (Figure 9), the same scale shows a better, but still poor, result for Hamilton's Law; but convergence is achieved at n = 11 for the bilinear formulation.

Additional insight into the convergence problems of Hamilton's Law can be obtained by a cross-plot of this same data versus advance ratio for specified valves of n. Figure 10, for 10 basis functions, shows that the accuracy decreases with advance ratio and that the bilinear formulation has only 20% as much error as does Hamilton's Law. At 11 basis functions, Figure 11, we see that Hamilton's Law and the bilinear formulation each show improved convergence; but the bilinear form is essentially exact whereas Hamilton's Law has 10% error at $\mu = 0.9$. As we add one more basis function, n = 12, Figure 12, we see clearly the numerical difficulties encountered by Hamilton's Law. Although the error is maximum near $\mu = 0.5$, large errors still persist at all advance ratios greater than 0.5.

Interestingly, at 13 basis functions, Figure 13, the convergence anomaly disappears; and we return to a more uniform curve. Still, however, results with the bilinear formulation excel those with Hamilton's Law. Thus, we see that Hamilton's Law can sometimes yield spurious results despite the fact that it often does converge. Furthermore, for 7 basis functions or more, results with Hamilton's Law are always less accurate than those with the bilinear formulation.

5.3 Numerical Efficiency

Although a detailed discussion of the numerical efficiency of the bilinear formulation is beyond the scope of this paper, we would like to demonstrate that the method is competitive with conventional time-marching solutions. Figure 14 provides three plots of the error in flap damping in hover (calculated from the Floquet Transition Matrix) versus the required CPU time on a VAX 750 computer. One plot depicts the performance of Hamming's Modified Predictor-Corrector (from the IBM Scientific Subroutine Package). The second plot is the performance of B1, the bilinear formulation with velocity from $\dot{\hat{u}}$. The third plot is the performance of B2, the bilinear formulation with Lagrange multiplier. The predictor-corrector results, indicated by the squares, are calculated for 100 to 900 time steps in increments of 100. The bilinear results are calculated for 6 to 15 polynomials in increments of 1.

Several important conclusions can be drawn from this figure. First, at low CPU's (i.e., at larger errors), the predictor-corrector is much more

efficient than is the bilinear formulation. This is due to the relatively high cost of performing the required integrals. However, as the required error becomes more exacting (and CPU increases), the rate of convergence is quite different among the three methods. For the predictor-corrector, if one subtracts out the start-up CPU, the error decreases as CPU^{-5} (which is to be expected to a fourth-order method). For B1, however, the error decreases as CPU^{-13}; and, for B2, the error decreases as CPU^{-29}. We conclude, therefore, that the bilinear formulation with Lagrange multiplier is spectacularly better than the same method with velocity from $\dot{u}$. We also conclude that, at least for very small error bounds, the bilinear formulation can actually be more efficient than time marching.

Continuing numerical studies in the efficiency of the method are presently being conducted and will be reported at a later date. However, we can point out two preliminary conclusions at this time. First, Figure 14 is for a constant-coefficient case in which function evaluations are virtually free. As we add periodic coefficients, for which function evaluations become more expensive, the bilinear formulation becomes more and more competitive. Second, the competitiveness of the method can be enhanced by an optimum balance between number of elements (N) and the number of polynomials per element (n). Furthermore, when discontinuities occur either in the coefficients or in the forcing function, the bilinear formulation becomes even more attractive, since it allows one to place the nodes of elements at the discontinuities, Ref. 14.

5. Summary and Conclusions

The conclusions of this work are very clear:

1) The use of Hamilton's Law of Varying Action, as a basis for numerical solutions of time problems, is not always stable and can result in divergence and incorrect answers even as the number of polynomials is increased. This is demonstrated both mathematically and by numerical examples.

2) A new bilinear formulation of dynamics is introduced. In one of its special cases, it is a variational statement of dynamics which states that the variation of the Action plus the Virtual Action (taken over a space-time domain and crossing the space-time boundaries) must sum to zero.

3) The bilinear formulation can be used as a basis for numerical, finite-element solutions of time problems. These can be proved to be convergent, provided that the test functions are constrained in a very precise way depending on the problem. For example, for initial-value problems, one must have

$$\hat{v}(0) \neq 0, \ \hat{v}(T) = 0$$

4) Numerical results with the new formulation (and with the Lagrange multiplier used as an estimate of velocity) eliminate all previous numerical difficulties and display a computational efficiency competitive and often superior to that of time marching. This efficiency is enhanced by the optimum choice of the number of elements, which depends on the desired accuracy for a given problem.

5) The method, when applied to space-time problems (partial differential equations) provides a unified numerical approach to the complete dynamics solution.

6. References

1. Baily, C.D., "A New Look at Hamilton's Principle", Foundations of Physics, Vol. 5, No. 3, 1975, pp 433-451.

2. Hitzl, D.L. and Levinston, D.A., "Application of Hamilton's Law of Varying Action to the Restricted Three-Body Problem", Celestial Mechanics, 22, (1980), pp. 255-266.

3. Simkins, T.E., "Finite Elements for Initial Value Problems in Dynamics", AIAA Journal, Vol. 19, No. 10, October 1981, pp. 1357-1362.

4. Baruch, M. and Riff, R., "Hamilton's Principle, Hamilton's Law - 6^n Correct Formulation", AIAA Journal, Vol. 20, No. 5, May 1982, pp. 687-692.

5. Riff, R. and Baruch, M. "Stability of Time Finite Elements", AIAA Journal, Vol. 22, No., August 1984, pp. 1171-1173.

6. Baruch, M. and Riff, R., "Time Finite Element Discretization of Hamilton's Law of Varying Action", AIAA Journal, Vol. 22, No. 9, September 1984, pp. 1310-1318.

7. Borri, M., "Helicopter Rotor Dynamics by Finite Element Time Approximation", Special Issue of Computers and Mathematics with Applications, Vol. 12A, No. 1, 1986.

8. Borri, M., Lanz, M., and Nantegazza, P.", Comment on "Time Finite Element Discretization of Hamilton's Law of Varying Action", AIAA Journal, Vol. 23, No. 9, September, 1985, pp. 1457-1458.

9. Izadpanah, Amir, "Calculation of Floquet Stability by Generalization of Hamilton's Law to a Bilinear Formulation", Presented at the 40th Annual National Forum of the American Helicopter Society, Second-Place Winner in the Robert R. Lichten Competition, Arlington, Texas, May 1985.

10. Babuska, I. and Szabo, B., Finite Element Analysis, Book Manuscript, to be published.

11. Rektorys, K., Variational Methods in Science and Engineering, Second Edition, D. Reidel Publishing Co., Boston, 1980, pp. 114-116.

12. Aubin, Jean-Pierre, Applied Functional Analysis, John Wiley, New York, 1979, p. 66.

13. Brezzi, F., "On the Existence and Approximation of Saddle Point Problems arising from Lagrangian Multipliers", R.A.I.R.O., Vol. 8-R2, pp. 129-151 (1974)

14. Hodges, Dewey H. "Vibration and Response of Nonuniform Rotating Beams with Discontinuities," Journal of the American Helicopter Society, Vol. 24, No. 5, October 1979, pp. 43-50.

6. Acknowledgements

The authors would like to thank Professor Barna Szabo, Washington University in St. Louis, Professor I. Babuska, University of Maryland, and Professor M. Borri, University of Milano, for their valuable suggestions.

This research was sponsored by the United States Army Research Office, Grant Nos. DAAG-29-83-K-0133 and DAAG-29-85-K-0228, Dr. Gary Anderson, Technical Monitor. The view, opinions and/or findings contained in this paper are those of the authors and should not be construed as an official Department of the Army position, policy, or decision unless so designated by other documentation.

Figure Captions

Figure 1 Schematic of Beam

Figure 2 Schematic of Spring-Mass System

Figure 3 Space-Time Domain and Boundaries

Figure 4 Flapping at End of Period, $\mu = 0.0$

Figure 5 Flapping Velocity at End of Period, $\mu = 0.0$

Figure 6 Flapping at End of Period, $\mu = 0.1$

Figure 7 Flapping at End of Period, $\mu = 0.3$

Figure 8 Flapping End of Period, $\mu = 0.5$

Figure 9 Flapping at End of Period, $\mu = 0.7$

Figure 10 Flapping versus Advance Ratio , $n = 10$

Figure 11 Flapping versus Advance Ratio, $n = 11$

Figure 12 Flapping versus Advance Ratio, $n = 12$

Figure 13 Flapping versus Advance Ratio, $n = 13$

Figure 14 Per Cent Error vs. CPU, $\mu = 0.0$

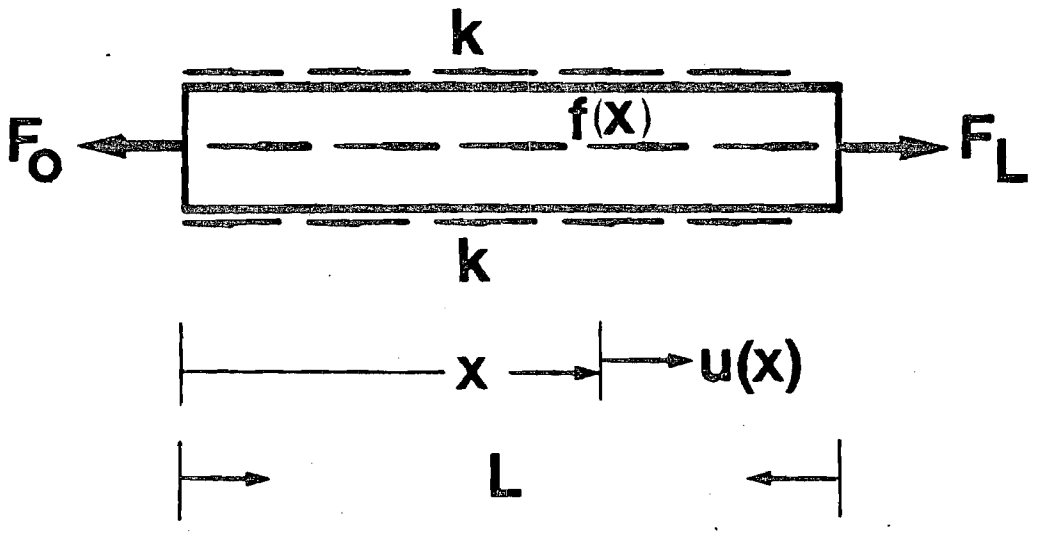

Figure 1. Schematic of Beam

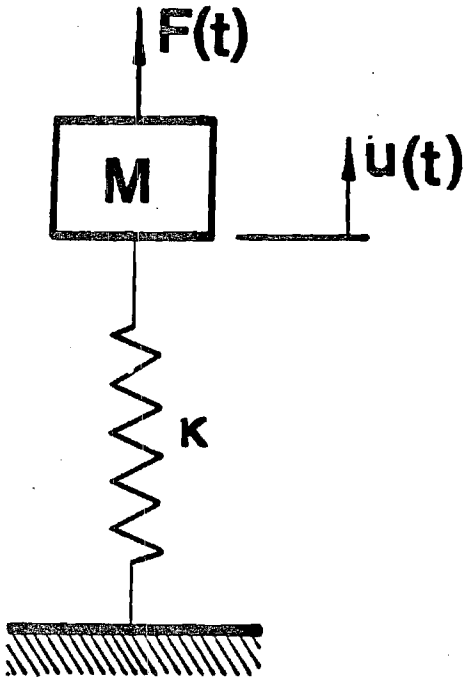

Figure 2. Schematic of Spring-Mass System

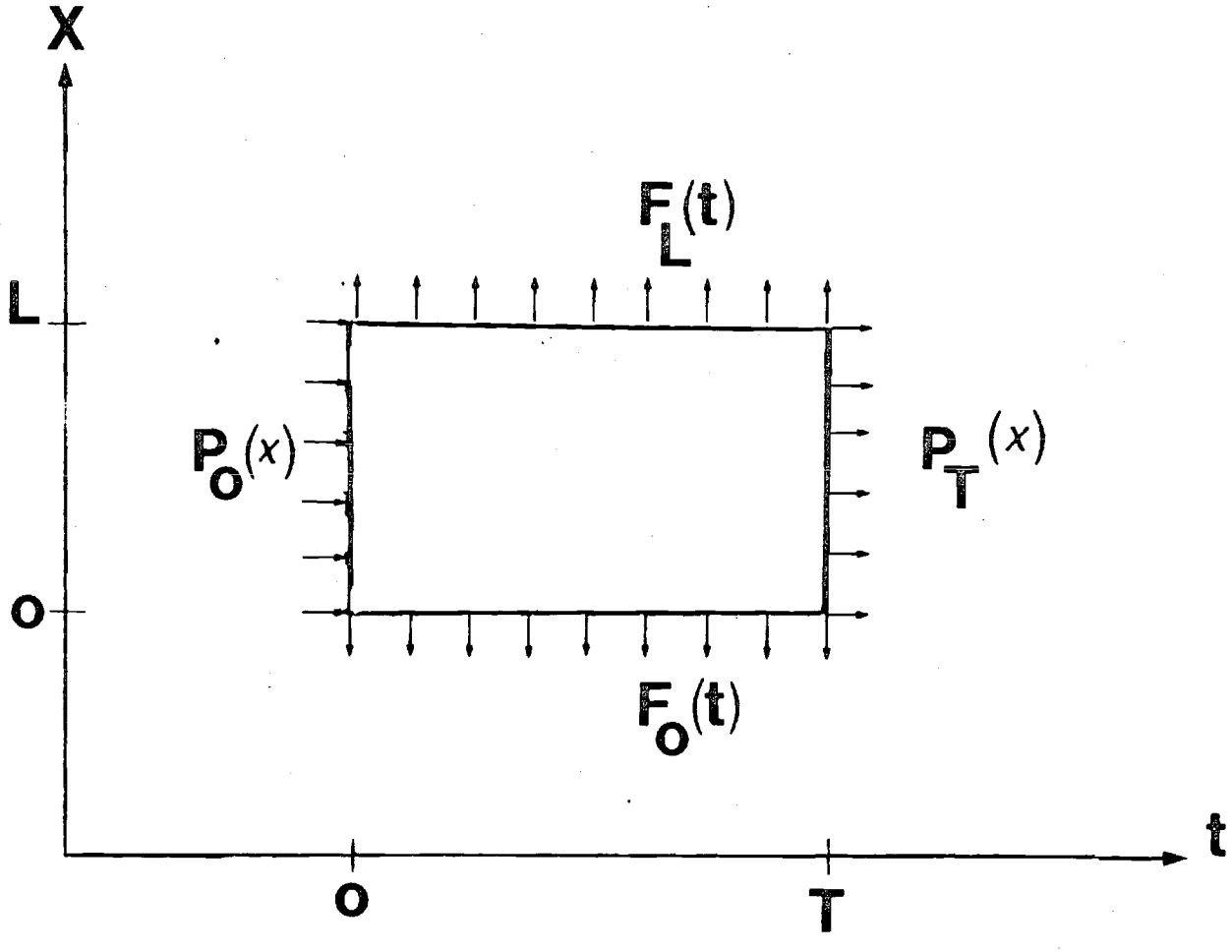

Figure 3. Space-Time Domain and Boundaries

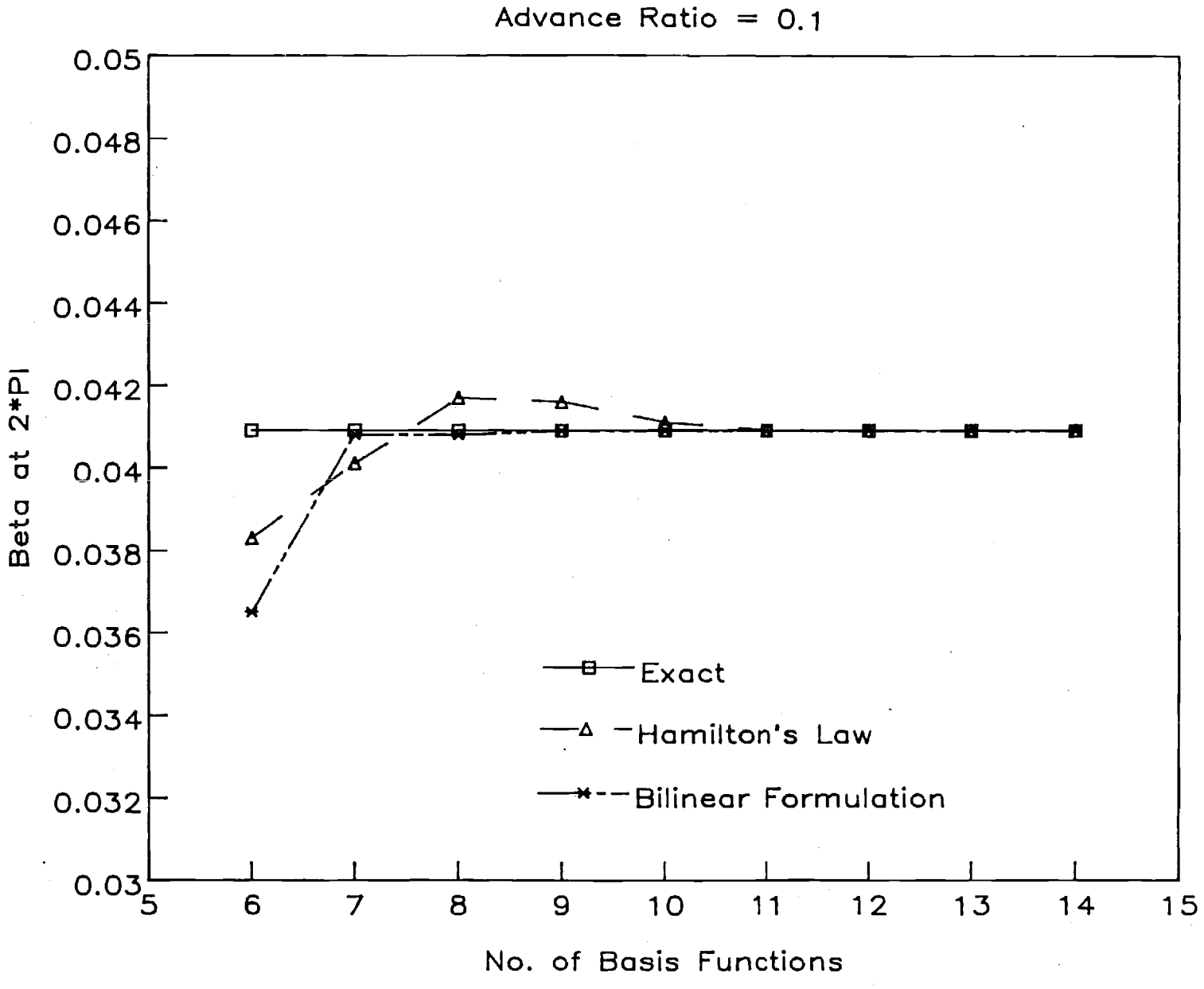

Figure 6. Flapping at End of Period, $\mu = 0.1$

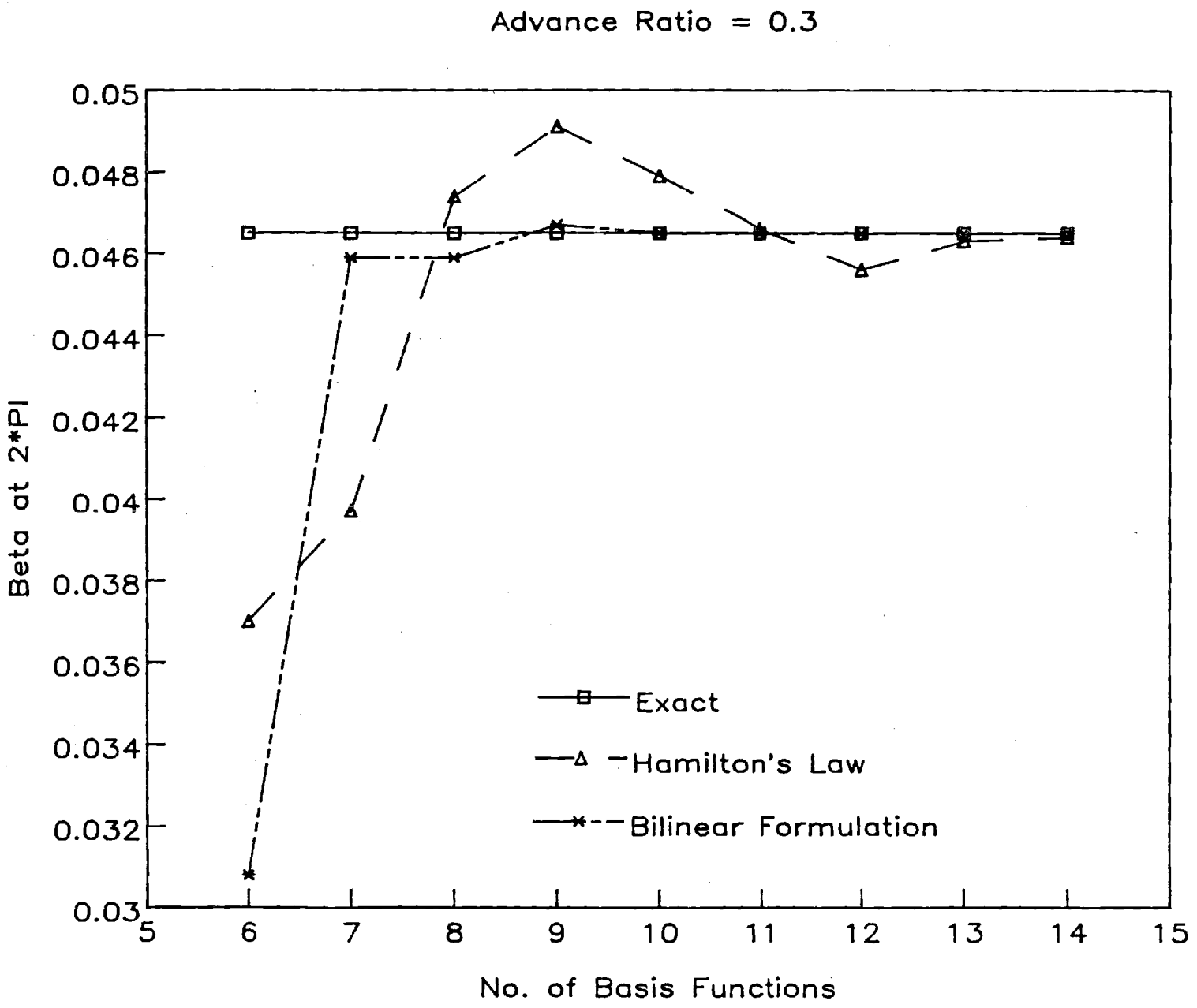

Figure 7. Flapping at End of Period, $\mu = 0.3$

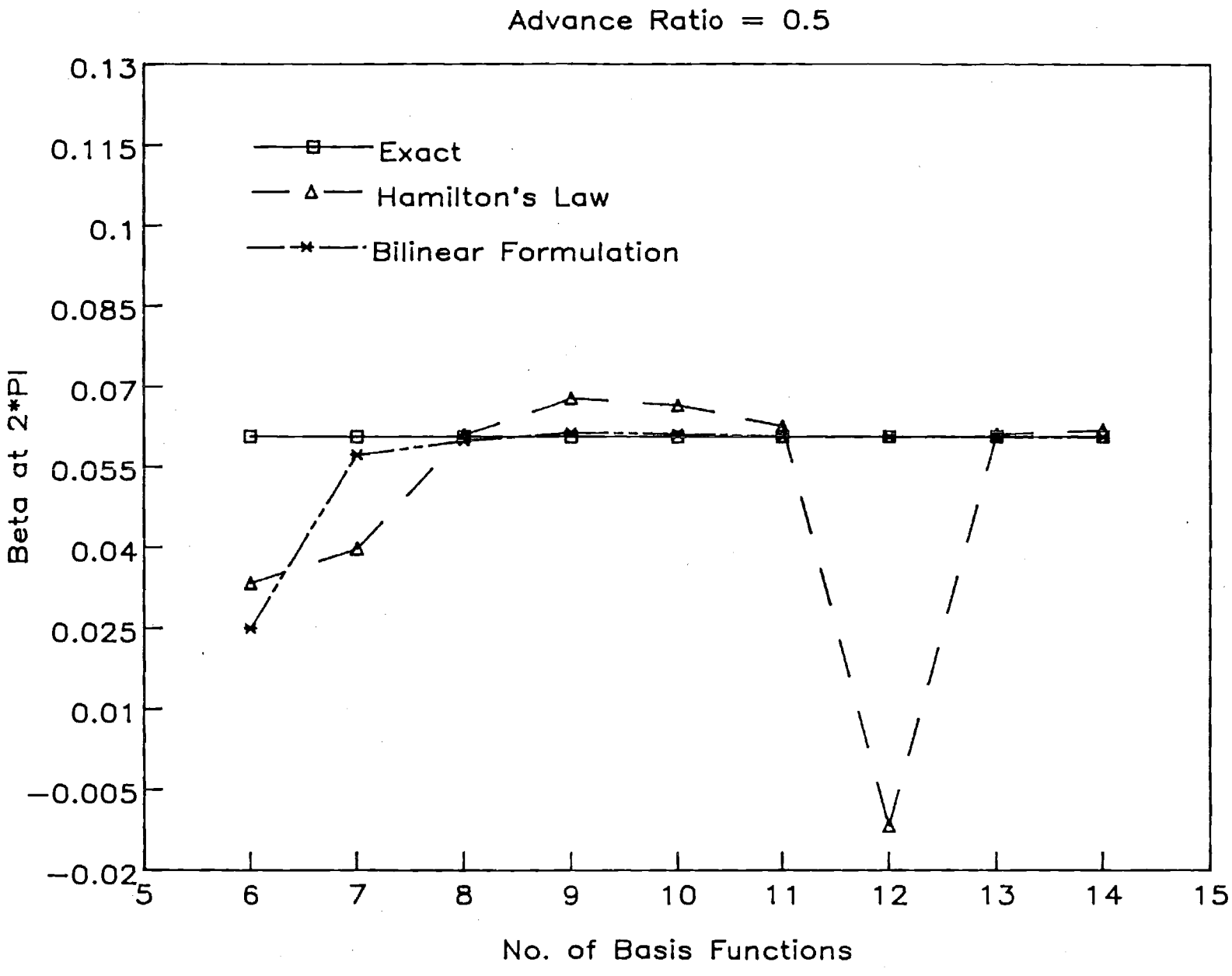

Figure 8. Flapping End of Period, $\mu = 0.5$

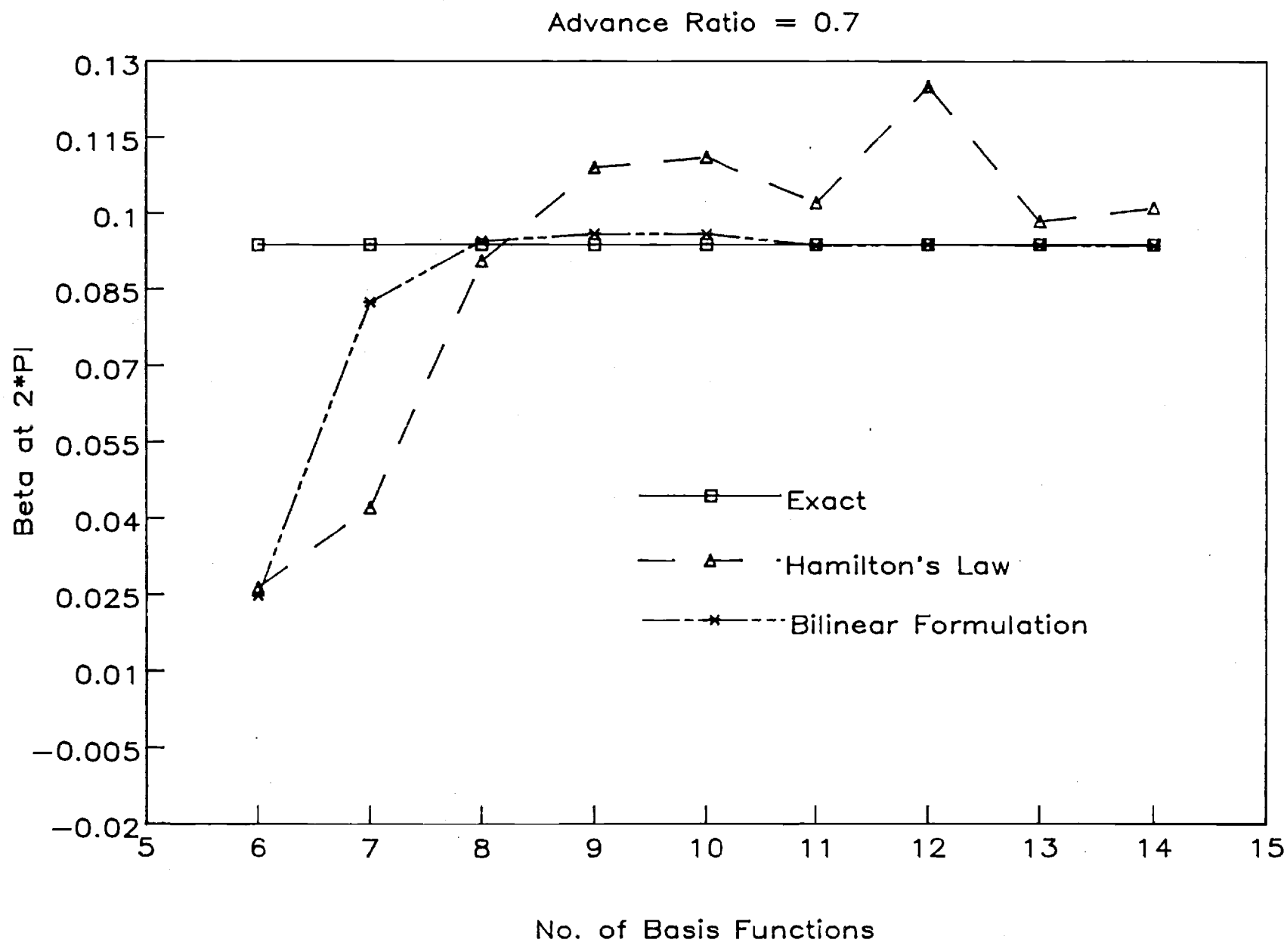

Figure 9. Flapping at End of Period, $\mu = 0.7$

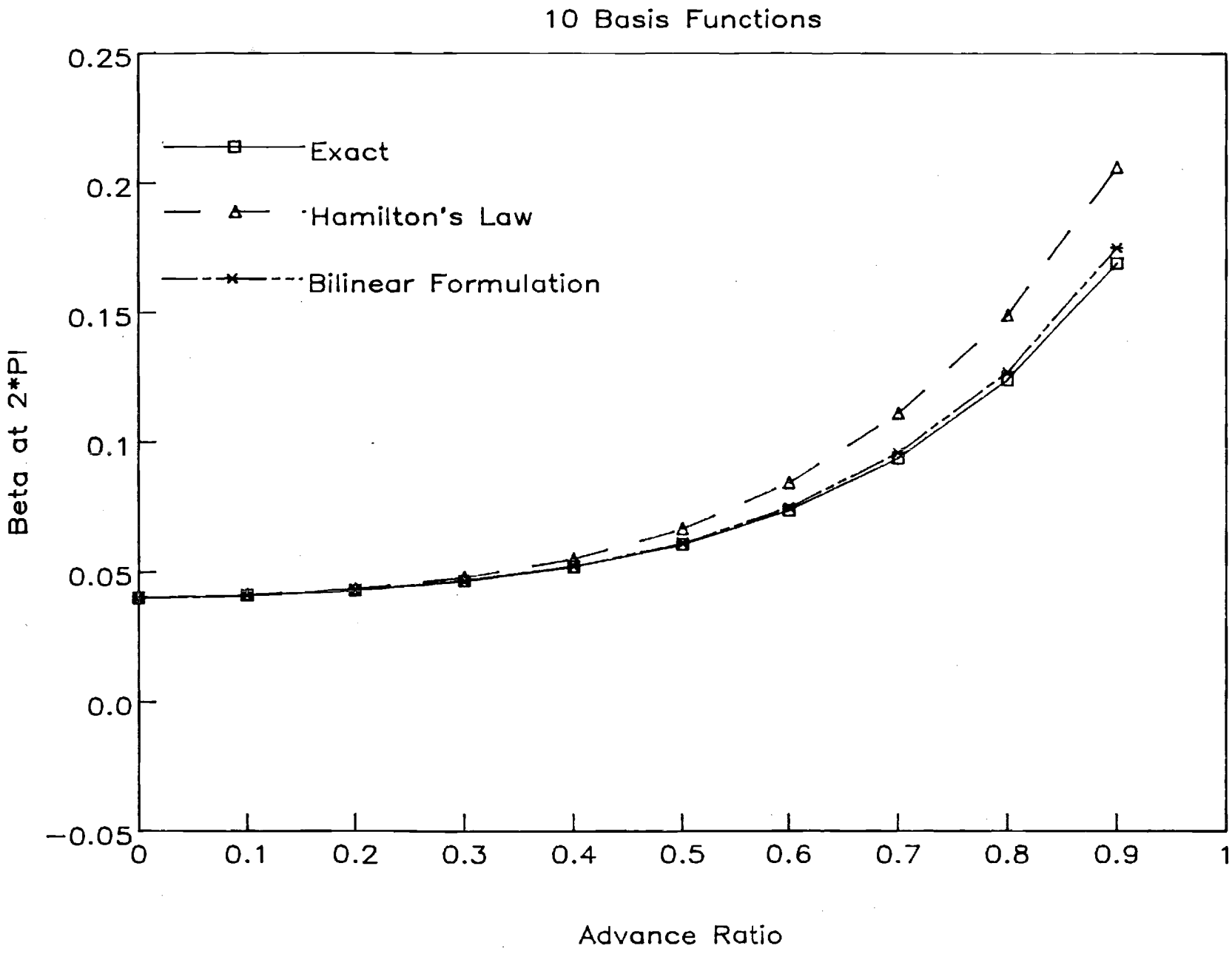

Figure 10. Flapping versus Advance Ratio, n = 10

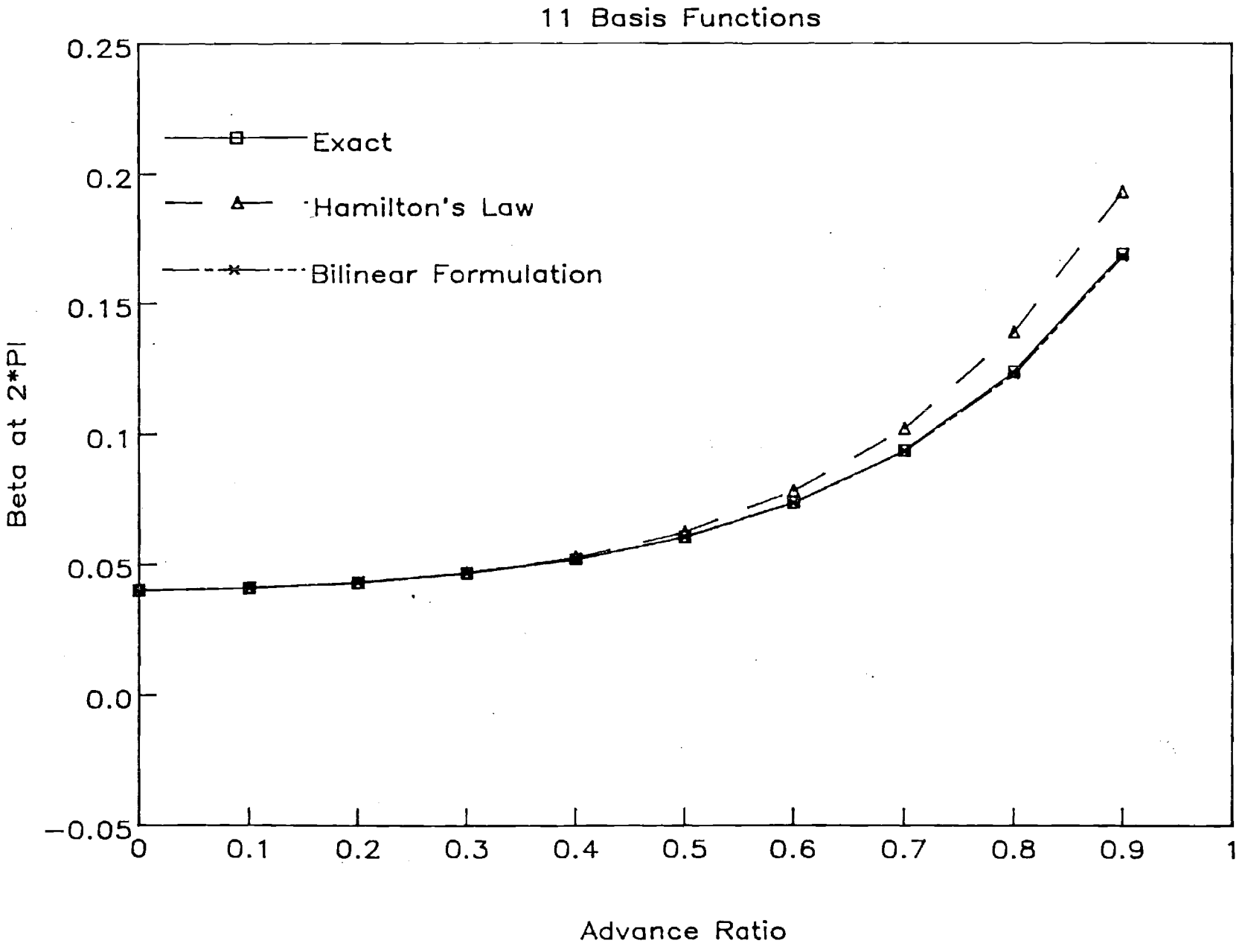

Figure 11. Flapping versus Advance Ratio, n = 11

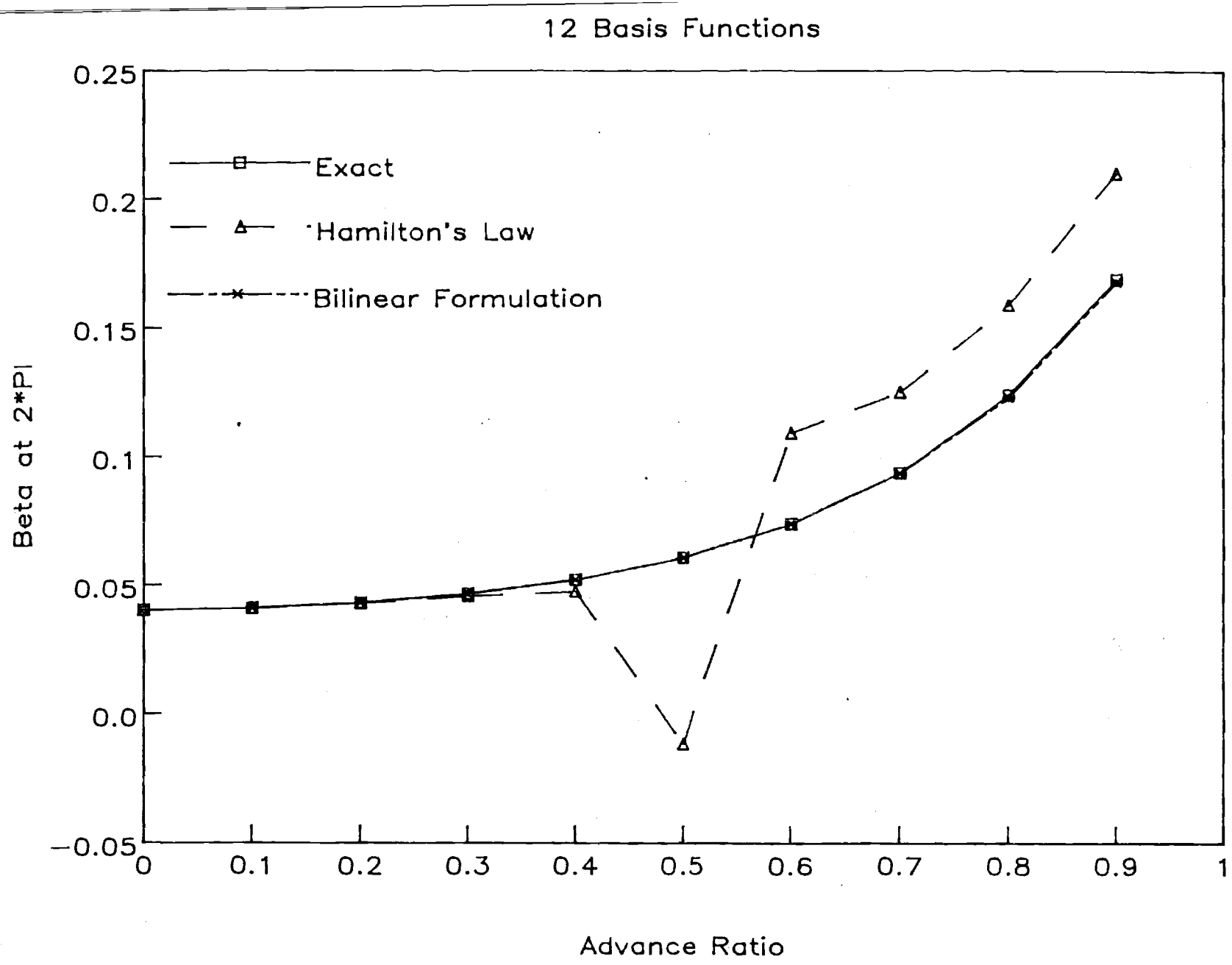

Figure 12. Flapping versus Advance Ratio, n = 12

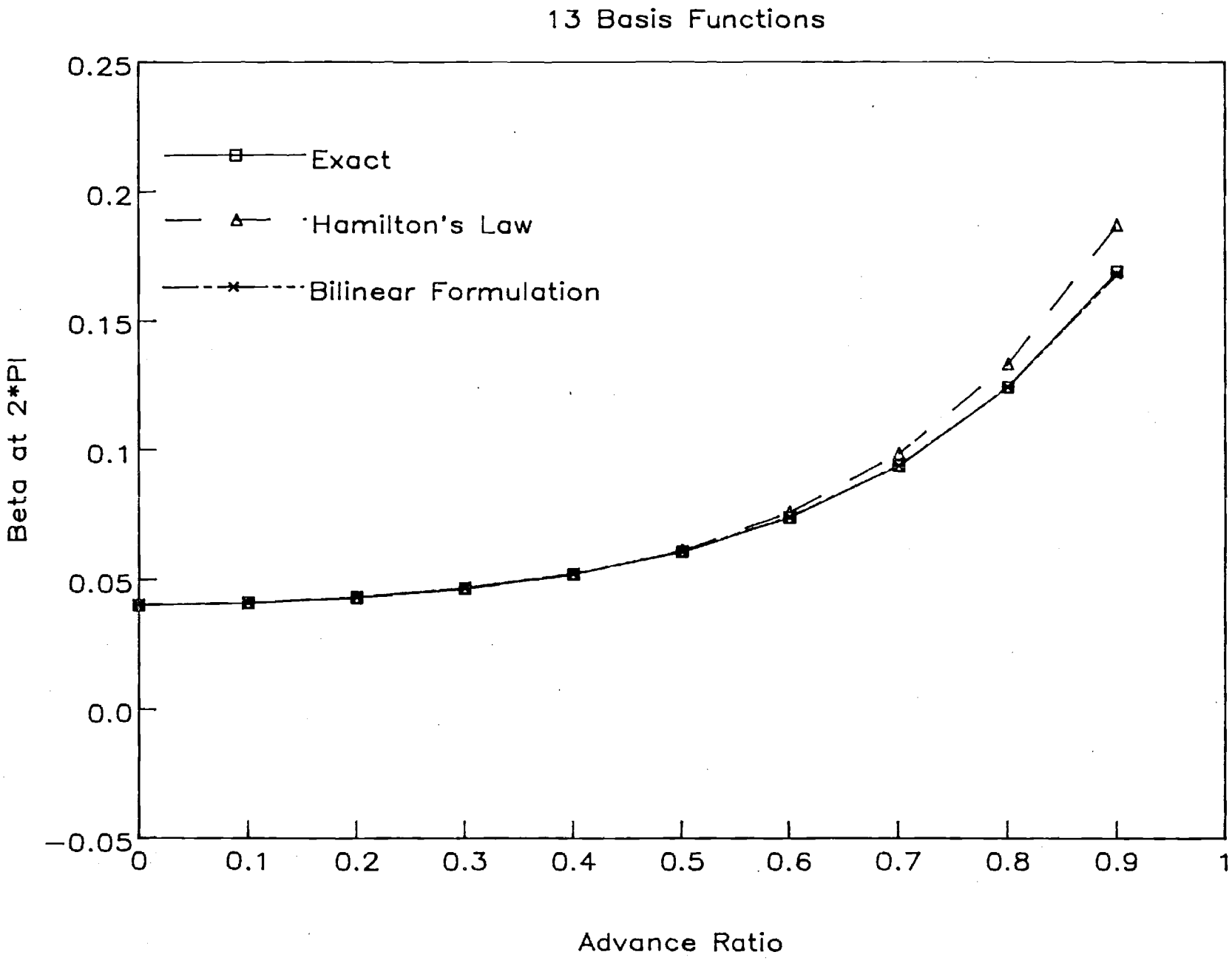

Figure 13. Flapping versus Advance Ratio, n = 13

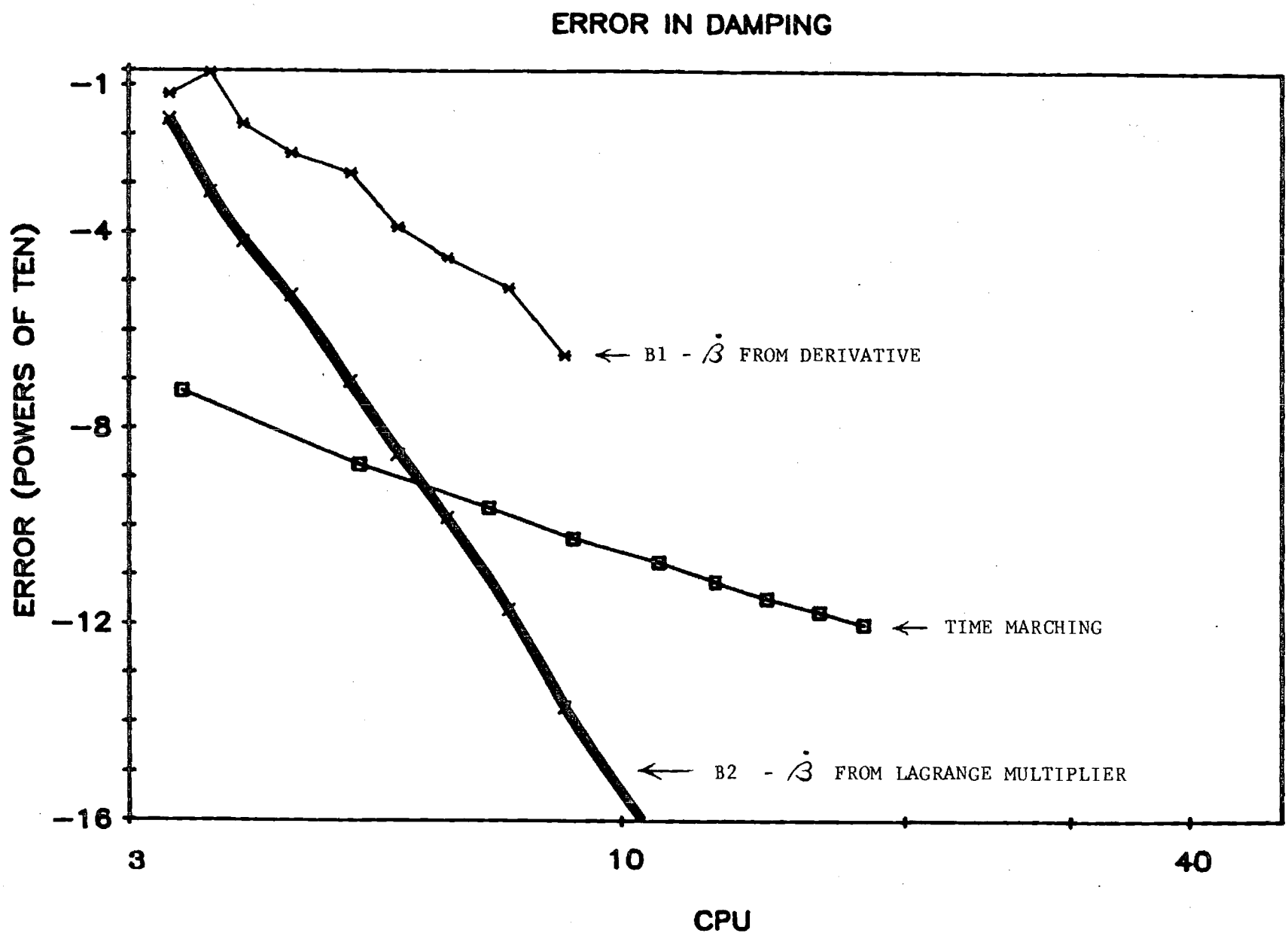

Figure 14. Per Cent Error vs. CPU, μ = 0.0

WASHINGTON UNIVERSITY

SEVER INSTITUTE OF TECHNOLOGY

EFFECT OF DYNAMIC STALL ON HELICOPTER TRIM AND FLAP-LAG RESPONSE

by

MNAOUAR CHOUCHANE

Prepared under the direction of Professor D. A. PETERS

A dissertation presented to the Sever Institute of
Washington University in partial fulfillment
of the requirements for the degree of

MASTER OF SCIENCE

August, 1986

Saint Louis, Missouri

WASHINGTON UNIVERSITY
SEVER INSTITUE OF TECHNOLOGY

ABSTRACT

EFFECT OF DYNAMIC STALL ON HELICOPTER TRIM AND FLAP-LAG RESPONSE

by Mnaouar Chouchane

ADVISOR: Professor D.A. Peters

August, 1986

Saint Louis, Missouri

A unified lift model is used in the derivation of elastic blade equations. The resultant mathematical model predicts the aerodynamic forces on the helicopter blade and the flap-lag response before and after stall occurs. An ordering scheme is applied during the derivation so that only important terms are retained. The time history solution is obtained using Galerkin's method. The results agree qualitatively with the linear model for small angles of attack, and give a reasonable prediction of the flap-lag response including stall.

TABLE OF CONTENTS

TABLE OF CONTENTS
(continued)

LIST OF TABLES

LIST OF FIGURES

LIST OF FIGURES
(continued)

EFFECT OF DYNAMIC STALL ON HELICOPTER TRIM AND FLAP-LAG RESPONSE

1. INTRODUCTION

1.1 PROBLEM STATEMENT

The helicopter blade, like any airfoil, is subjected to stall. However, stall on a rotor blade is different from that of a fixed wing. In forward flight, the advancing blade is moving at a faster speed than the retreating blade. This difference increases with the increase of cruise speed. As a result of this dissymetry of lift, the retreating blade must operate at a higher angle of attack to compensate for its low velocity with respect to the air. However, at high angles of attack, boundary layer separations have a major effect on the unsteady aerodynamics of the airfoil section so that lift is partially lost; but, due to the dynamic nature of the angle of attack, the loss of lift is much less than that predicted by static theory.

In general, airfoil stall occurs due to one of the following reasons:

- low speed
- high angle of attack
- heavy load applied on the blade or wing.

At first, stall is indicated by the significant vibration of the helicopter, which is a limiting factor by itself due to the sever working conditions of the aircraft as a result of vibration. If stall continues

the helicopter will pitch up. Furthermore, stall may result in a rapid growth of blade torsion and control-system loads. Accordingly, stall must be included in the analysis of helicopter performance, and should be considered in the aerodynamic and structural design of the helicopter and its control-systems. Because stall is a major constraint on the helicopter lift, speed, and maneuvering capability, a great effort has been oriented toward the development of analytic models to predict the aerodynamic lift and the pitching moment during dynamic stall. The present study is concentrated on the application of an analytical dynamic stall model in the prediction of blade motion and stability.

1.2 PREVIOUS WORK-AERODYNAMICS

Linearized aerodynamic theories are not always adequate for the case of a helicopter at high lift and high advance ratio. Thus, more advanced theories have been developed through the years. Most of these methods are based on computational algorithms that utilize tabulated data. In these tables, blade lift and moment are represented as functions of reduced pitch rate, reduced pitch acceleration, and angle of attack. In addition, an appropriate correction can be used for a change of Mach number or reduced frequency (1)*. Although this method has been widely used, it has been found that it presents the following major disadvantages:

- The data covers only the conditions experimentally measured.
- Difficulity of handling the interpolation and linearization.
- Inefficiency when applied with a computer simulation.
- Inability to formulate linearized, perturbation models

---

* The numbers in parentheses in the text indicate references in the Bibliography.

Other methods have been developed based on the use of a convolution integral and Wagner's function for the unstalled condition and then modified to account for stall. However, the necessity of a convolution integral computation is involved and does not allow linearized analysis for periodic coefficent cases (2).

An alternative analytical stall model was introduced recently (3), called the ONERA model, in which the dynamic stall is described by differential equations. The independant variables are the lift and pitching moment coefficients. The coefficients of the equations are defined by parameter identification and expressed as functions of the angle of attack only. Additional work in the field extended the ONERA model to include plunge, large angles of attack, and unsteady free stream. This model was simplified to be used for rotor dynamic stall of an oscillating airfoil and was applied to an individual blade section (4). Further investigation applied a modified ONERA model to an entire blade (5). Various interpretations of the model were analysed to select the best description. Further work extended the ONERA model to include large angles, reversed flow, and the distinction between angle of attack due to pitch and due to plunge (6).

1.3 PREVIOUS WORK-BLADE EQUATIONS

Helicopter rotor blade equations have been derived by various methods. In advanced research, the helicopter blade is considered elastic and can undergo inplane bending, vertical bending, and torsional degrees of freedom (7). These equations have been used in general in conjunction with aerodynamic models based on Greenberg's theory for fixed-wing aircraft, but modified to include some rotarywing effects. In the helicopter, unsteady aerodynamics play an important role during high forward speed and certain maneuvering conditions. An accurate aeroelastic model must include the dynamic stall effect on the airfoil lift and pitching moment. This idea is the objective of this research report.

1.4 PRESENT APPROACH

In previous research work, upon which this work is based (6), elastic blade equations were derived including quasi-steady aerodynamics. These equations give a reasonable description of the blade motions in low-lift cruise. However, at high advance ratios or high lift, the effect of unsteady aerodynamics is important and quasi-steady theory is not sufficient. As mentioned in section 2-2, however, there exists a unified lift model, expressed in terms of circulation (7). The aerodynamic forces of this model are described by two differential equations. One gives the linear quasi-steady aerodynamics, whereas the other predicts the change of lift as a result of stall effect. The actual lift is the sum of the two components. This is the model we use here.

As for the blade model used in this present research work, blade flap-lag only is considered. Torsion equations are not included. The number of equations for each degree of freedom is at least one, which corresponds to the rigid blade case, but higher modes can also be included. In addition, the aerodynamic lift depends on the position of the airfoil section from the hub axis. Thus, the span coordinate is a variable, even for rigid blade modes. For analysis purposes, the blade is divided into a certain number of segments. The lift is considered to have a constant value over each segment, but is allowed to vary from segment to segment. The magnitude of the resultant lift is the sum of the partial lift applied on each segment. Thus, the higher the number of segments chosen, the more accurate the result can be, although additional computational work is necessary.

The helicopter dynamic equations involve, in general, detailed algebra and a large number of terms. In order to avoid complications which give insignificant improvements, an ordering scheme is applied. The ordering of terms plays the role of a filter to segregate lower-order terms from higher-order terms. Structural parameters and elastic deflections are given an order of magnitude based on existing helicopter data. The final equations includes groups of terms with different orders. In this report, aeroelastic equations are presented in two forms, one with lower order terms only, and the other includes one level of higher order terms.

The flap-lag equations are non-linear partial differential equations with variable coefficients. To solve these equation, a modified Galerkin's method is applied by implementation of an approximate solution which satisfies the associated boundary conditions. Consequentely, the equations are brought to an ordinary form and solved through a numerical method to yield the time dependent solution, and thus, the final solution is found.

The present work is advanced over previous work in two ways:

- The aerodynamic model used is an extention of the ONERA model and includes, besides stall, the effects of plunge, unsteady free stream, and large angles of attack.

- The theoretical analysis tools used are based on results obtained in recent research work in autopilots (8) and are considered to be good steps toward a better understanding of the theory governing the aeroelastic behavior of the helicopter.

2. DERIVATION OF THE EQUATIONS OF MOTION

2.1 ELASTIC BLADE EQUATIONS

2.1.1 Introduction

Theoretical analysis is a very important tool in the helicopter field, especially in the preliminary design and trade-off decisions during the early stages of selection of the best configuration which satisfies certain requirements. In addition, rotorcraft analysis is necessary in order to predict the performance of the aircraft in each segment of the mission envelope (i.e specified maneuvering conditions).

In early analytical work, the blade was considered to be rigid with flap motion only (9). Other work adds a rigid-body inplane degree of freedom (10). Recently, the rotor blade has been considered to be elastic. It undergoes inplane bending, vertical bending, and torsional motions (7). These motions are coupled and result into nonlinearity. Authors in the field followed several methods to apply the fundamental principals of mechanics, and used various coordinate systems, in the derivation of blade equations. This research work here is based on the elastic blade equations presented in reference (7). These equations are derived by the energy method using a curvilinear coordinate system and tensor appoach. The important terms are retained by applying an ordering scheme to the equations.

2.1.2 Flap-Lag Equations

When the blade is treated as an elastic body, the center of gravity of each section encounters a longitudinal displacement u , an inplane displacement v , and a torsional deformation ϕ. A parameter (ε) is used as a scaling factor to find the order of each term and then write the equations up to the desired level of accuracy, without missing any important terms. (ε) has a magnitude of one tenth. Hence, (ε^2) has a magnitude of one percent. The dimensional form of the elastic blade equations presents the disadvantage of being related to a specific case. To find a solution, some basic parameters, such as, the rotor radius R , or the angular velocity Ω need to be specified. The equations must

be solved again completely whenever any one parameter is modified. In nondimensional form, however, many fewer independent parameters need to be considered. Furthermore, it is easier to apply solution methods to the nondimensional form of the equations. In consequence, all the equations are transformed into nondimensional form, and a solution is obtained for the general case.

We present here the inplane and vertical bending equations. The nondimensional form is obtained by dividing both sides of each equation by $m\Omega^2 R$.

Flap equation, the terms of order ε and ε^3 are retained:

$$-(Tw')' + (EI_{z'} - EI_{y'})(\theta + \phi)v'''' + \{EI_{y'} + (EI_{z'} - EI_{y'})(\theta + \phi)^2\}w'''' + \ddot{w} = L_w \tag{1a}$$

The nondimensional form

$$-(\tau \bar{w}^+)^+ + (\Lambda_5 - \Lambda_6)(\theta + \phi)\bar{v}^{++++} + \{\Lambda_6 + (\Lambda_5 - \Lambda_6)(\theta + \phi)^2\}\bar{w}^{++++} + \ddot{\bar{w}} = \bar{L}_w \tag{1b}$$

Lag equation, the terms of order ε^2 and ε^4 are retained:

$$-(Tv')' + \{EI_{z'} + (EI_{y'} - EI_{z'})(\theta + \phi)^2\}v'''' + (EI_{z'} - EI_{y'})(\theta + \phi)w''''$$

$$+ 2m\Omega\dot{u} + m\ddot{v} - m\Omega^2 v = l_v \tag{2a}$$

The nondimensional form:

$$-(\tau \bar{v}^+)^+ + \{\Lambda_5 + (\Lambda_6 - \Lambda_5)(\theta + \phi)^2\}\bar{v}^{++++} + (\Lambda_5 - \Lambda_6)(\theta + \phi)\bar{w}^{++++} + 2\dot{\bar{u}} + \ddot{\bar{v}} - \bar{v} = \bar{L}_v \tag{2b}$$

$$\dot{\bar{u}} = -\int_0^{\bar{x}} \bar{w}^+ \dot{\bar{w}}^+ d\bar{x} \tag{2c}$$

where

- $(')$: derivative with respect to space variable (x).
- $(.)$: derivative with respect to time variable (t).
- $(+)$: derivative with respect to nondimensional space variable $(\bar{x} = \frac{x}{R})$.
- $(*)$: derivative with respect to nondimensional time variable $(\psi = \Omega t)$.
- τ : nondimensional tension.

$$\tau = \frac{1 - x^2}{2}$$

The generalized aerodynamic forces per unit length in the inertial reference system L_v and L_w are expressed in terms of L_x and L_y , the aerodynamic forces per unit length in the deformed blade co-ordinate system. They are expressed (4) as follow

$$L_v = -\{L_x \cos(\theta + \phi) + L_y \sin(\theta + \phi)\}(1 - \frac{v'^2}{2}) \tag{3a}$$

$$L_w = \{-L_x \sin(\theta + \phi) + L_y \cos(\theta + \phi)\}(1 - \frac{w'^2}{2}) \tag{3b}$$

The nondimensional form is

$$\bar{L}_v = -\{\bar{L}_x \cos(\theta + \phi) + \bar{L}_y \sin(\theta + \phi)\}(1 - \frac{v^{+2}}{2}) \tag{4a}$$

$$\bar{L}_w = \{-\bar{L}_x \sin(\theta + \phi) + \bar{L}_y \cos(\theta + \phi)\}(1 - \frac{w^{+2}}{2}) \tag{4b}$$

In classical aerodynamic analyses of a helicopter blade,the quasi-steady approximation often is assumed. In this type of analyses, blade stall, compressibility, and reversed flow are neglected. Frequentely, the unsteady aerodynamic effect on a helicopter blade needs to be analysed in order

to obtain the blade response in certain flight conditions. To satisfy this requirement, some research studies have been concentrated on the development of mathematical methods to predict the aerodynamic forces and moments in a more general flight conditions (3), (6).

In the next two sections, two aerodynamic models are briefly introduced. These models are essentialy advanced with respect to the linear model in that the unsteady aerodynamics are included. The first model is the ONERA model. The second is a modified version and an extention to the first model, and called a unified lift model.

2.2 ONERA AERODYNAMIC MODEL

Tran and Petot recently introduced an analytical stall model (3) which consists of two differential equations relating the lift coefficients of a rotating airfoil to its angle of attack as follows

$$k\dot{C}_{z_1} + \lambda C_{z_1} = \lambda a\theta + (\lambda s + \delta)k\dot{\theta} + sk^2\ddot{\theta} \tag{5a}$$

$$k^2\ddot{C}_{z_2} + 2dwk\dot{C}_{z_2} + w^2(1 + d^2)C_{z_2} = -w^2(1 + d^2)\{\Delta C_z + ek\dot{\theta}\frac{\partial \Delta C_z}{\partial \theta}\} \tag{5b}$$

$$C_z = C_{z_1} + C_{z_2} \tag{5c}$$

In the above equations, the lift coefficient C_z is expressed as a sum of two components, C_{z_1} and C_{z_2} . C_{z_1}, is the lift coefficient associated with a linear model. C_{z_2} , however, is the deviation of the lift coefficient away from the linear value due to stall. The model is presented by differential equations which depend on ΔC_z , which is the difference between the linear static lift coefficient ($C_{z_l} = a\alpha$) and the actual stalled static lift coefficient C_{z_s} .

The coefficients λ, a, s, δ, d, w, and e depend on the angle of attack only, and are determined by parameter identification. In table 1, we present, for illustrative purposes, the numerical values of these coefficients determined from wind tunnel tests and parameter identification for an OA212 airfoil. In this table, u is the unit step function. It is equal to one for a positive argument and zero otherwise.

Table 1 - Identified Coefficents of Stall Equations

Parameter	Numerical Value	Physical description
λ	0.2	time delay parameter
$\bar{s}$	$\frac{5\pi}{180}$	apparent mass quantity
$\bar{\delta}$	$(\frac{\partial C_z}{\partial \theta} - \frac{4\pi}{180})(1 + 1.43\Delta C_z)$	relates lift coefficient to the pitch rate
w	$.10 + .023.(\lvert\theta\rvert - 13°)u(\lvert\theta\rvert - 13°)$	a damping factor
d	$\frac{.105}{w}$	stall natural frequency
e	$2 - 5.1 \tan^{-1}\{1.21(\lvert\theta\rvert - 13°)\}u(\lvert\theta\rvert - 13°)$	phase shift parameter

The static lift curve presented in Figure 1 for an OA212 airfoil is linear for angles of attack between $-10°$ and $10°$. For larger angles, the magnitude of the lift coefficients shows a deviation from linearity. C_{z_l} is the static lift coefficient in the linear region. C_{z_s} is the actual static lift. The static lift equation is defined for different angles of attack.(θ denotes the angle of attack in this section).
In the linear region,

$$C_{z_s} = C_{z_l} = 7.1\frac{\pi}{18}\theta \qquad -\theta_c < \theta < \theta_c \tag{6}$$

In the non linear region, the static lift coefficient is approximated by a seventh-degree polynomial.

$$C_{z_s} = \sum_{i=1}^{n} a_i(|\theta| - \theta_c)^i \qquad (\theta_c < \theta < 26°) \tag{7}$$

$$C_{z_s} = -\sum_{i=1}^{n} a_i(|\theta| - \theta_c)^i \qquad (-26° < \theta < -\theta_c) \tag{8}$$

θ_c , the critical angle of attack is approximately equal to $10°$ for the OA212 airfoil, the coefficents of the above polynomials are:

$$a_0 = 1.24$$

$$a_1 = 0.124$$

$$a_2 = -0.0630597$$

$$a_3 = 0.01395201 \tag{9}$$

$$a_4 = -0.0017390851$$

$$a_5 = 0.000124551913$$

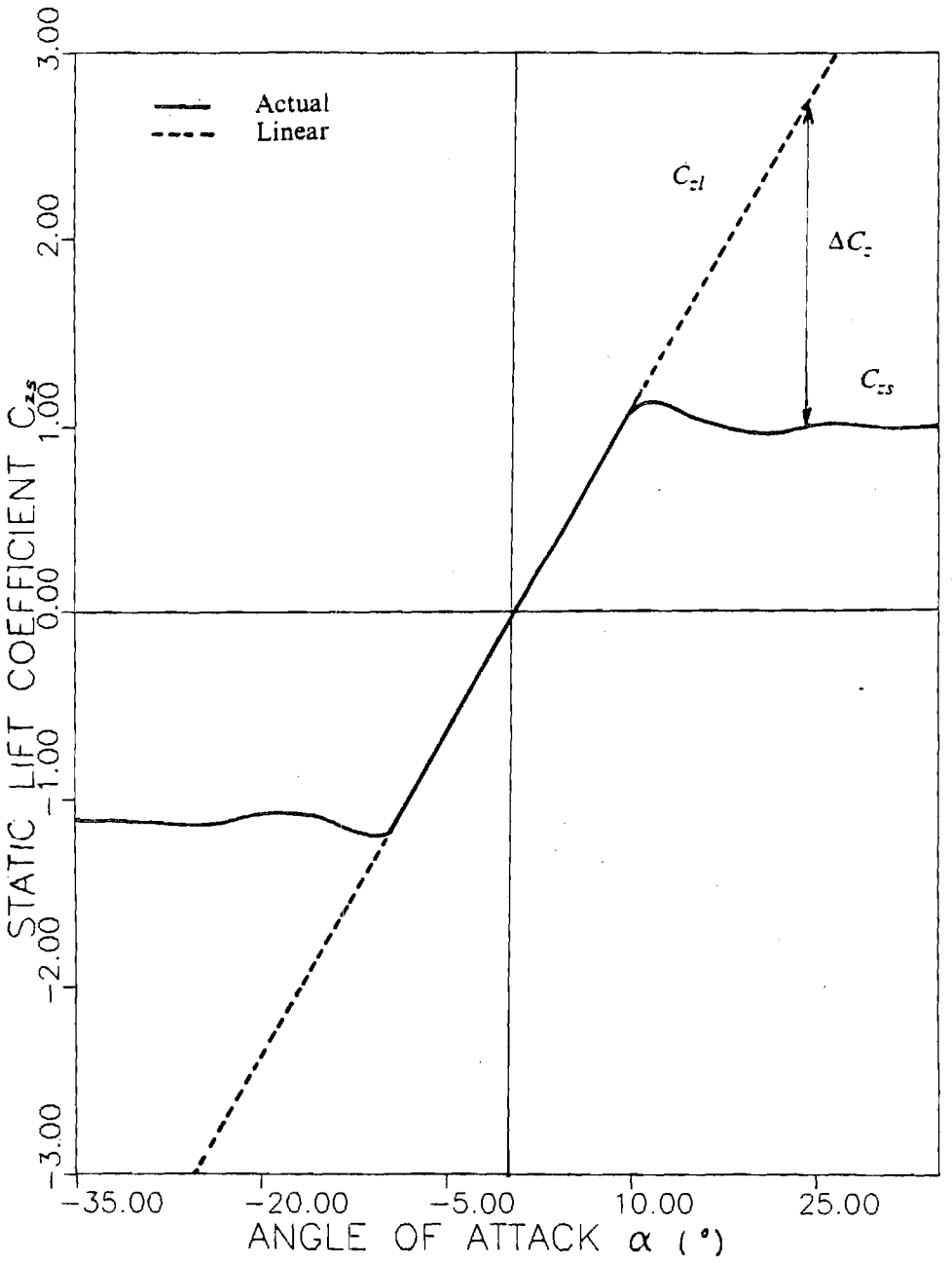

Figure 1. Static Lift Coefficient Versus Angle of Attack

OA212 Airfoil

$$a_6 = -4.6849257 \times 10^{-6}$$

$$a_7 = 7.087973 \times 10^{-8}$$

Since this polynomial diverges for large angles of attack. a constant value is used, for angles of attack greater than 26°.

$$C_{z_s} = 1.26 \qquad \theta > 26° \tag{10}$$

$$C_{z_s} = -1.26 \qquad \theta < -26° \tag{11}$$

Therefore, ΔC_z can be obtained as a difference between the extended linear static lift C_{z_l} and the actual static lift C_{z_s} computed by the above equations.

For analysis purposes, equations (5a-c) may equally be expressed in terms of the lift coefficients C_z, the normalized circulation per unit length $\bar{\Gamma}$, or the normalized lift per unit length $\bar{L}$ (7).

The final form of the equations in terms of nondimensional circulations is.

$$k\dot{\bar{\Gamma}}_1 + \lambda\bar{\Gamma}_1 = \lambda aU\theta + (\lambda s + \delta)Uk\dot{\theta} + sk^2U\ddot{\theta} \tag{12}$$

$$k^2\ddot{\bar{\Gamma}}_2 + 2dwk\dot{\bar{\Gamma}}_2 + w^2(1 + d^2)\bar{\Gamma}_2 = -w^2(1 + d^2)\{U_x\Delta C_z + e\bar{k}(\dot{U}_x + \frac{\partial \Delta C_z}{\partial \theta}\dot{U}_y)\} \tag{13}$$

In reference (5), it is shown that the circulation version of the ONERA aerodynamic model is the best suited among the three. It remains stable at or near the reversed flow. In addition, it produces physically reasonable results. Consequentely, the equations in terms of nondimensional circulation $\bar{\Gamma}$ were chosen as a basic model for further improvement which lead to a unified lift model.

2.3 UNIFIED LIFT MODEL

The unified lift model is an extension to the ONERA model. The latter is modified in order to include large angles of attack and reversed flow. Also, a distinction is made between angle of attack due to pitch motion and due to plunging motion.

The model is presented in reference (6). The simplified version, in which reversed flow is approximated and higher order terms in the $\bar{\Gamma}_2$ equation are neglected, is

$$\bar{k}\dot{\bar{\Gamma}}_1 + \lambda\bar{\Gamma}_1 = \lambda a U_y + \delta\bar{b}\dot{\bar{\varepsilon}} \tag{14a}$$

$$\bar{k}^2\ddot{\bar{\Gamma}}_2 + 2dw\bar{k}\dot{\bar{\Gamma}}_2 + w^2(1+d^2)\bar{\Gamma}_2 = -w^2(1+d^2)\{U_x\Delta C_z + e\bar{k}(\dot{U}_x\Delta C_z + \frac{\partial\Delta C_z}{\partial\theta}\dot{U}_y)\} \tag{14b}$$

where $\bar{k} \equiv \frac{b}{r}$ is an average of the reduced frequency of the freestream. The coefficients $\bar{\delta}$, w, d, e, are evaluated at the instantanoeus angle of attack, $\alpha = \tan^{-1}(\frac{U_y}{U_x})$,and ε^- is the rotation with respect to the air mass. This model is used later on to determine the aerodynamic forces applied on the blade. Although it does not present the perfect representation of stall, it is certainly more reasonable than the linear, quasi-steady theory presently used in stability analyses. In the unified model of Reference 6,

$$\Delta C_z = C_{zs} - a\tan\alpha \tag{14c}$$

However, in this thesis, we use the ONERA definition of ΔC_z. Although this is not completely consistent, it has little effect on numerical results.

2.4 GENERALIZED AERODYNAMIC FORCES

The right hand sides of equations (1b) and (2b), the aerodynamic forcing functions $\bar{L}_v$ and $\bar{L}_w$, are the horizontal and vertical components of the resultant forces in the undeformed blade coordinate. In figure 2 the aerodynamic forces in the deformed blade coordinate system are illustrated. The circulatory part (L_1) acts at the aerodynamic center, perpendicular to the free stream. The ap-

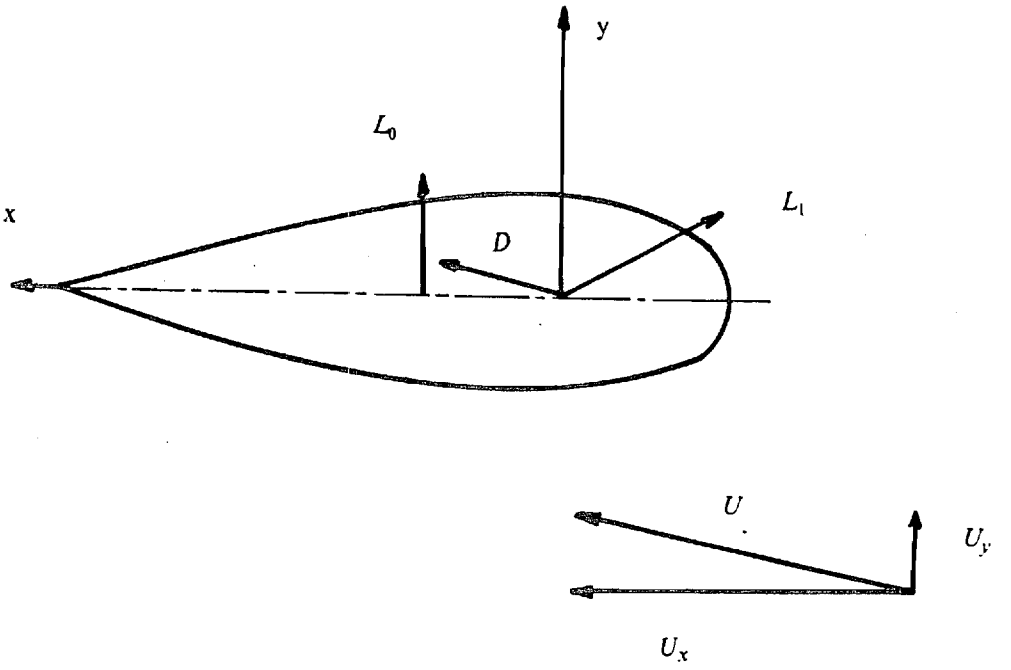

Figure 2. Aerodynamic Forces in the Deformed Blade Coordinate System.

parent mass lift (L_0) is acting at the midchord perpendicular to the chord. Finally, the profile drag (D) is parallel to the free stream and oriented in the same direction as the free stream. Their expressions are

$$\bar{L}_1 = U(\bar{\Gamma}_1 + \bar{\Gamma}_2) \tag{15}$$

$$\bar{D} = C_D(U_x^2 + U_y^2) \tag{16}$$

$$\bar{L}_0 = \bar{b}s\dot{U}_y \tag{17}$$

The vertical and horizontal components of these forces are

$$\bar{L}_{1x} = -U_y(\bar{\Gamma}_1 + \bar{\Gamma}_2) \tag{18a}$$

$$\bar{L}_{1y} = U_x(\bar{\Gamma}_1 + \bar{\Gamma}_2) \tag{18b}$$

$$\bar{L}_{0x} = L_0 = \bar{b}s\dot{U}_y \tag{19}$$

$$\bar{D}_x = C_D U_x \sqrt{U_x^2 + U_y^2} \tag{20a}$$

$$\bar{D}_y = C_D U_y \sqrt{U_x^2 + U_y^2} \tag{20b}$$

Therefore, the total components of lift in the x and y direction are

$$\bar{L}_x = -U_y(\bar{\Gamma}_1 + \bar{\Gamma}_2) + C_D U_x \sqrt{U_x^2 + U_y^2} \tag{21a}$$

$$\bar{L}_y = \bar{L}_0 + U_x(\bar{\Gamma}_1 + \bar{\Gamma}_2) + C_D U_y \sqrt{U_x^2 + U_y^2} \tag{21b}$$

(note here that the nondimensional forms of the equations (21-a) and (21-b) are obtained by dividing the original equations by $\rho b\Omega^2 R^2$.)

The velocity components included in the above equations, U_x and U_y, correspond to the deformed blade coordinate system. These components can be expressed as functions of the velocity components in the inertial system using a matrix transformation (4).

The nondimensional forms of the components parallel and perpendicular to blade chord are

$$\overline{U}_x(1, \varepsilon^2) = \bar{x} + \mu \sin\psi + \{\bar{v}^+ + \bar{w}^+(\theta + \phi)\}\mu \cos\psi +$$

$$\dot{\bar{v}} + \bar{u} - \frac{1}{2}(\theta + \phi)^2(\bar{x} + \mu \sin\psi) + (\overline{V}_i + \dot{\bar{w}})(\theta + \phi) \tag{22}$$

$$\overline{U}_y(\varepsilon, \varepsilon^3) = (\bar{x} + \mu \sin\psi)(\theta + \phi) - (\bar{w}^+ \mu \cos\psi + \overline{V}_i + \dot{\bar{w}}) + \frac{\bar{c}}{4}\dot{\alpha} +$$

$$\bar{w}^+(\dot{\bar{u}} - \bar{v}) + \dot{\bar{v}}(\theta + \phi)\mu \cos\psi + \frac{\bar{w}^+}{2}(\theta + \phi)^2 \mu \cos\psi + (\bar{x} + \mu \sin\psi)\int_0^{\bar{x}} \bar{v}^+ \bar{w}^{+\,+} d\bar{x} +$$

$$(\bar{u} + \dot{\bar{v}})(\theta + \phi) + (\overline{V}_i + \dot{\bar{w}})\{\frac{\bar{w}^{+2}}{2} + \frac{1}{2}(\theta + \phi)^2\} \tag{23}$$

The derivative of U_y with respect to the nondimensional time ψ is required in order to express the apparent mass term explicitly

$$\dot{\overline{U}}_y(\varepsilon, \varepsilon^3) = \{(\bar{x} + \mu \sin\psi)(\dot{\theta} + \dot{\phi}) + (\theta + \phi)(\mu \cos\psi) - (\dot{\bar{w}}^+ \mu \cos\psi - \bar{w}^+ \mu \sin\psi + \dot{\overline{V}}_i + \ddot{\bar{w}})\} +$$

$$+ \frac{\bar{c}}{4}\ddot{\alpha} + \dot{\bar{w}}^+(\dot{\bar{u}} - \bar{v}) + \bar{w}^+(\ddot{\bar{u}} - \dot{\bar{v}}) + \dot{\bar{v}}^+(\theta + \phi)\mu \cos\psi + \bar{v}^+(\dot{\theta} + \dot{\phi})\mu \cos\psi -$$

$$\bar{v}^+(\theta + \phi)\mu \sin\psi + \frac{\dot{\bar{w}}^+}{2}(\theta + \phi)^2 \mu \cos\psi + \bar{w}^+(\theta + \phi)(\dot{\theta} + \dot{\phi})\mu \cos\psi - \frac{\bar{w}^2}{2}(\theta + \phi)^2 \mu \sin\psi +$$

$$(\bar{x} + \mu \sin\psi)\int_0^{\bar{x}} \dot{\bar{v}}^+ \bar{w}^{+\,+} d\bar{x} + (\bar{x} + \mu \sin\psi)\int_0^{\bar{x}} \bar{v}\dot{\bar{w}}^{+\,+} d\bar{x} + \mu \cos\psi \int_0^{\bar{x}} \bar{v}^+ \bar{w}^{+\,+} d\bar{x} +$$

$$(\dot{\bar{u}} + \ddot{\bar{v}})(\theta + \phi) + (\bar{u} + \dot{\bar{v}})(\dot{\theta} + \dot{\phi}) + (\dot{\overline{V}}_i + \ddot{\bar{w}})\{\frac{\bar{w}^{+2}}{2} + \frac{1}{2}(\theta + \phi)^2\} +$$

$$(\overline{V}_i + \dot{\overline{w}})\{\overline{w}^{+}\dot{\overline{w}} + (\theta + \phi)(\dot{\theta} + \dot{\phi})\} \tag{24}$$

where $$\dot{\alpha} = \dot{\theta} + \dot{\phi} + \dot{\overline{w}} \tag{25}$$

Since the nondimensional blade chord is of the order ε , and the apparent mass coefficient s is approximately equal to π , the factor $\bar{b}s$ is considered to be of order ε , so that,

$$\overline{L}_0 = \bar{b}s\dot{U}_y(\varepsilon, \varepsilon^3) = \overline{L}_0(\varepsilon^2, \varepsilon^4) \tag{26}$$

On the other hand, U_x is of order $(1, \varepsilon^2)$ and U_y is of order $(\varepsilon, \varepsilon^3)$, so the lowest terms in U_y^2 are of order ε^2. As a result, U_y can be considered small relative to U_x and the resultant velocity can be approximated in the following manner

$$U = \sqrt{U_x^2 + U_y^2} \cong U_x + \frac{1}{2}\frac{U_y^2}{U_x} \tag{27}$$

Hence, equations (20a-b) can be written as follow

$$\overline{D}_x = C_D(U_x^2 + \frac{1}{2}U_y^2) \tag{28a}$$

$$\overline{D}_y = C_D(U_xU_y + \frac{1}{2}\frac{U_y^3}{U_x}) \tag{28b}$$

In a similar manner, the scaling procedure is applied to U_x^2 , U_y^2 and U_xU_y . Details are presented in Appendix 7-2.

Furthermore, the nondimensional circulations $\overline{\Gamma}_1$ and $\overline{\Gamma}_2$ should be scaled in order to determine the order of $\overline{L}_v$ and $\overline{L}_w$. $\overline{\Gamma}_1$ and $\overline{\Gamma}_2$ are of the form $\overline{\Gamma} = U\overline{C}_\Gamma$. It is shown above that lower-order terms of U are of order 1. By consulting the variation of C_Γ for a rotating airfoil (6), we can observe that C_Γ is , similarly, of order 1. Further, the nondimensional form of the aeroelastic equations is obtained by division of equations (1a) and (2a) by $m\Omega^2R$. However, the nondimensional forms of

the lift components $\bar{L}_x$ and $\bar{L}_y$ are obtained by division by $\rho b\Omega^2 R$. Accordingly. $\bar{L}_v$ and $\bar{L}_w$ should be multiplied by a factor of $(\frac{\gamma}{6a})$ in order to make both sides of the aeroelastic equations consistent. This factor is considered to be of order ε .

Thus far, we have found all the ingredients necessary to substitute into equations (4a) and (4b) and to define the order of each term. Therefore, the aerodynamic lift, $\bar{L}_v$ and $\bar{L}_w$, are

$$\bar{L}_v(\varepsilon^2, \varepsilon^4) = -\frac{\gamma}{6a}[(\bar{\Gamma}_1 + \bar{\Gamma}_2)(\bar{w}^+\mu\cos\psi + \bar{V}_i + \dot{\bar{w}}) + \frac{C_D}{a}(\bar{x} + \mu\sin\psi)^2] +$$

$$\frac{\gamma}{6a}(\bar{\Gamma}_1 + \bar{\Gamma}_2)[\frac{\bar{c}}{4}\dot{\alpha} + \bar{w}^+(\dot{\bar{u}} - \bar{v}) + \frac{\bar{w}^{+2}}{2}(\bar{V}_i + \dot{\bar{w}}) + \frac{1}{6}(\bar{x} + \mu\sin\psi)(\theta + \phi)^3] -$$

$$\bar{b}s\frac{\gamma}{6a}(\theta + \phi)\{(\bar{x} + \mu\sin\psi)(\dot{\theta} + \dot{\phi}) + (\theta + \phi)\mu\cos\psi - (\dot{\bar{w}}^+\mu\cos\psi - \bar{w}^+\mu\sin\psi + \dot{\bar{V}}_i + \ddot{\bar{w}})\} -$$

$$\frac{\gamma}{6a}\frac{C_D}{a}\{2(\dot{\bar{v}} + \bar{v}^+\mu\cos\psi + \bar{u})(\bar{x} + \mu\sin\psi) + \frac{1}{2}(\bar{w}^+\mu\cos\psi + \bar{V}_i + \dot{\bar{w}})^2\} \qquad (29a)$$

$$\bar{L}_w(\varepsilon, \varepsilon^3) = \frac{\gamma}{6a}(\bar{\Gamma}_1 + \bar{\Gamma}_2)(\bar{x} + \mu\sin\psi) + \frac{\gamma}{6a}(\bar{\Gamma}_1 + \bar{\Gamma}_2)\{\bar{v}^+\mu\cos\psi + \dot{\bar{v}} + \bar{u} - (\bar{x} + \mu\sin\psi)\frac{\bar{w}^{+2}}{2}\} +$$

$$\bar{b}s\frac{\gamma}{6a}\{(\bar{x} + \mu\sin\psi)(\dot{\theta} + \dot{\phi}) + (\theta + \phi)\mu\cos\psi - (\dot{\bar{w}}^+\mu\cos\psi - \bar{w}^+\mu\cos\psi + \dot{\bar{V}}_i + \ddot{\bar{w}})\} -$$

$$\frac{C_D}{a}\frac{\gamma}{6a}(\bar{x} + \mu\sin\psi)(\bar{w}^+\mu\cos\psi + \bar{V}_i + \dot{\bar{w}}) \qquad (29b)$$

The nondimensional blade tension τ is expressed as a function of span coordinate and displacements (4) as follows

$$\tau = \int_{\bar{x}}^{1}(\bar{x} + \bar{u} + 2\dot{\bar{v}} - \ddot{\bar{u}} + \bar{L}_u)d\bar{x} \qquad (30)$$

where $\bar{L}_u$ is the aerodynamic lift component in the blade span direction in the undeformed reference system.

In the above expression, only $\bar{x}$ is of order 1 , other terms are of order ε^2 and higher. Therefore, the lower order expression of τ is,

$$\tau = \frac{1 - x^2}{2} \tag{31}$$

Consequently, the important terms in the elastic blade equations have been determined. The aerodynamic circulations are given by equations (14a-b). Hence, to determine blade bendings and the aerodynamic lift in the vertical and inplane plans, a system of four partial nonlinear differential equations should be solved. This system includes two equations for vertical and inplane bendings, and two equations for the steady and unsteady aerodynamic circulations.In the next chapter we will apply approximate methods to solve these equations.

3. SOLUTION METHODS

In the previous chapter, flap and inplane bending are described by two nonlinear, partial-differential equations which are coupled together. Each equation consists of lower and higher order terms. Finding an analytical solution for this type of equations is not possible. However, these equations can be solved using approximate methods. These methods approximate a continuous system by an n-degree-of-freedom system. The selection of n is based on the accuracy desired of the solution. The solution is assumed to be a finite series of known functions multiplied by unknown coefficients. When the approximate solution methods are applied, the space and time dependent functions are decoupled, and the equations are formulated in a way that allows numerical solutions to be obtained.

In this chapter, approximate solution methods are applied to the aeroelastic equations(1b) and (2b), presented in the previous chapter, combined with equations (29a) and (29b). The aerodynamic circulations are expressed by equations(14-a-b). Only lower order terms of this equations are to be considered in the following analyses. This allows the investigation of the general trends of the result, without going into cumbersome computation with little improvement. In the following, we write the system of equations to be solved including lower-order terms only

Flap equation, order ε

$$-(\tau\bar{w}^{+})^{+}+\Lambda_6\bar{w}^{++++}+\ddot{\bar{w}}=\frac{\gamma}{6a}(\bar{\Gamma}_1+\bar{\Gamma}_2)(\bar{x}+\mu\sin\psi) \tag{32}$$

Lag equation, order ε^2

$$-(\frac{1-x^2}{2}\bar{v}^{+})^{+}+\Lambda_5\bar{v}^{++++}+(\Lambda_5-\Lambda_6)(\theta+\phi)\bar{w}^{++++}-2\int_0^{\bar{x}}\bar{w}^{+}\dot{\bar{w}}^{+}d\bar{x}+\ddot{\bar{v}}-\bar{v}=$$

$$-\frac{\gamma}{6a}(\bar{\Gamma}_1+\bar{\Gamma}_2)(\bar{w}^{+}\mu\cos\psi+\bar{V}_i+\dot{\bar{w}})-\frac{\gamma}{6a}C_D(\bar{x}+\mu\sin\psi)^2 \tag{33}$$

$\bar{\Gamma}_1$ equation, order 1

$$\bar{k}\dot{\bar{\Gamma}}_1 + \lambda\bar{\Gamma}_1 = \lambda a U_y + \delta\bar{b}\varepsilon^+ \tag{34}$$

$\bar{\Gamma}_2$ equation, order 1

$$\bar{k}^2\ddot{\bar{\Gamma}}_2 + 2dw\bar{k}\dot{\bar{\Gamma}}_2 + w^2(1+d^2)\bar{\Gamma}_2 = -w^2(1+d^2)[U_x\Delta C_z + e\bar{k}(\dot{U}_x\Delta C_z + \frac{\partial\Delta C_z}{\partial\theta}\dot{U}_y)] \tag{35}$$

It is interesting here to note that the terms of the lag equation are of higher order compared to the terms of the flap equation. Thus, to first order, flap drives lag in an important way, but lag has a lesser effect on flap.

3.1 APPROXIMATE SOLUTION USING GALERKIN'S METHOD

The flap, lag, and circulation equations presented above are non-linear partial differential equation with variable coefficents. The Ritz-Gallerkin's method is, in general, used in order to obtain an approximate solution. The method consists of assuming a solution of the problem in the form of a series composed of a linear combination of admissible functions , W_j for flap bending, and V_r for lag bending , multiplied by time dependent function , respectively q_j for flap,and p_r for lag

$$\bar{w} = \sum_{j=1}^{n} W_j(\bar{x})q_j(\psi) \tag{37}$$

$$\bar{v} = \sum_{r=1}^{n} V_r(\bar{x})p_r(\psi) \tag{34}$$

By substitution of the series of comparison functions in the differential equations, followed by premultiplication by the series, one can obtain a weighted error which represents the difference between right hand side and left hand side of the equation. The integral of the weighted error over the

domain must be zero. Galerkin's method consists of choosing the weighting functions exactly the same as the n comparison functions. The modified Galerkin's method includes virtual work of non-satisfied natural boundary conditions. Thus, it is equivalent to the Rayleigh-Ritz method.

The application of the above procedure transforms the flap, lag, and aerodynamic equations (32-35) to non-linear ordinary differential equations. The coefficients of the equations have integral forms which can be determined after selection of comparison functions. These coefficients are presented in Appendix 7-1 The equations are:

Flap equation

$$\sum_{j=1}^{n} I6_{ij}\ddot{q}_j + \sum_{j=1}^{n}(I10_{ij} + \Lambda_6 I8_{ij})q_j = \frac{\gamma}{6a}\sum_{l=1}^{m}(\overline{\Gamma}_{1l} + \overline{\Gamma}_{2l})(\mu \sin\psi I4_{il} + I5_{il}) \tag{38}$$

Lag equation

$$\sum_{i=1}^{n} I6'_{ij}\ddot{p}_j + \sum_{j=1}^{n}(I10'_{ij} - I6'_{ij} + \Lambda_5 I8'_{ij})p_j - 2\sum_{j=1}^{n}\sum_{k=1}^{n} I13'_{ijk}\dot{q}_k q_j + (\Lambda_5 - \Lambda_6)\theta\sum_{j=1}^{n} I8'_{ij}q_j =$$

$$-\frac{\gamma}{6a}\sum_{j=1}^{n}\sum_{l=1}^{m}(\overline{\Gamma}_{1l} + \overline{\Gamma}_{2l})[(I12'_{ijl}\mu\cos\psi q_j + I11'_{ijl})\dot{q}_j + \overline{V}_i I'_{il} A]$$

$$+ C_D\frac{\gamma}{6a}(I3'_i + 2\mu\sin\psi I2'_i + \mu^2\sin^2\psi I1'_i) \tag{39}$$

By selecting n comparison functions, it will be possible to compute the coefficients of the above equations. The flap and lag bendings will be represented by a 2n linear-differential equations. In equation (39) the lag displacement is coupled to the flap displacement.

3.2 COMPARISON FUNCTIONS

Energy methods, in general, use two classes of assumed mode functions: admissible functions, and comprison functions. Admissible functions are arbitrary functions satisfying all the geometric boundary conditions. On the other hand, comparison functions must satisfy both geometric and natural boundary conditions. In Galerkin's method, the assumed solution is a series of comparison functions. These functions can be trigonometric, power series, or polynomials. Among these choices, a modified form of the Duncan polynomials was successefully applied in reference (4) for bending of both hingless and articulated blades. The first three polynomials for bending are,

$$W_1 = x$$

$$W_2 = \frac{1}{11}(15x^2 - 5x^4 + x^6) \tag{40}$$

$$W_3 = \frac{1}{16}(-41x + 105x^3 - 63x^5 + 15x^7)$$

These polynomials are orthogonal and symmetric in the interval (-1 to +1) . Here, however, we use them on the interval (0 to +1). They satisfy both geometric and natural boundary conditions. In the next chapter, we use these polynomials as comparison functions for both flap and lag bendings. In a rigid blade analyses, the blade is considered to be a rigid body that has two degrees of freedom only, displacements in the vertical and inplane directions. The rigid blade mode is obtained when only the first polynomial is used in each summation. Thus, only W_1 is included in the expansion.

3.3 RIGID BLADE EQUATIONS

When the blade is considered to be rigid, a significant simplification is made to the problem. This assumption might be useful, especially, during preliminary design. In this stage, an approximate prediction of the performance and dynamic response should be sufficient. Such a simplified analysis can provide qualitative prediction of rotor response and trim.

The rigid blade equations may be obtained by expressions for $\bar{w}$ and $\bar{v}$ as follow,

$$\bar{w} = \bar{x}\beta \tag{41}$$

$$\bar{v} = \bar{x}\zeta \tag{42}$$

Substitution of the above equations into the lower-order flap and lag equations and application of Galerkin's method gives the rigid-blade equations.

Flap equation:

$$\ddot{\beta} + p^2\beta = \frac{\gamma}{2a}\sum_{l=1}^{m}(\bar{\Gamma}_{1l} + \bar{\Gamma}_{2l})(\mu \sin\psi I4''_l + I5''_l) \tag{43}$$

Lag equation

$$\ddot{\zeta} - 2\beta\dot{\beta} + \omega_\zeta^2\zeta + C_\zeta\dot{\zeta} = -\frac{\gamma}{2a}\sum_{l=1}^{m}\{(\bar{\Gamma}_{1l} + \bar{\Gamma}_{2l})(I4''_l\mu\beta\cos\psi + I11''_l)\dot{\beta} + \bar{V}_l I4''_l\}$$

$$+ C_D\frac{\gamma}{2a}(\frac{1}{4} + \frac{2}{3}\mu\sin\psi + \frac{1}{2}\mu^2\sin^2\psi) \tag{44}$$

If the last two equations are compared to classical rigid-blade equations (15), it is obvious that in equations (44) and (45), only the aerodynamic terms are different.

3.4 NUMERICAL SOLUTION

Several numerical methods can be used to solve equations (40) and (41) for an elastic blade, or equations (43) and (44) for a rigid blade mode. These methods require the differential equations to be written in the form $y' = f(x, y)$ .This is accomplished by using state variables so that a second-order differential equation, for example, is transformed into two first-order differential equations. For illustrative purposes, we express equations (43) and (44) in state variable form to yield a system of four first-order differential equations.

$$y(1) = \beta$$

$$y(2) = \dot{\beta}$$

$$\dot{y}(1) = y(2)$$

$$\dot{y}(2) = -y(1) + \frac{\gamma}{2a}\sum_{l=1}^{m}(\bar{\Gamma}_{1l} + \bar{\Gamma}_{2l})(\mu \sin\psi I4''_l + I5''_l)$$

$$y(3) = \zeta$$

$$y(4) = \dot{\zeta}$$

$$\dot{y}(3) = y(4)$$

$$\dot{y}(4) = 2y(1)y(2) - \frac{\gamma}{2a}\sum_{l=1}^{m}\{(\bar{\Gamma}_{1l} + \bar{\Gamma}_{2l})(I4''_l\mu y(1)\cos\psi + I11''_l y(2) + \bar{V}_i I4''_l\}$$

$$+ C_D\frac{\gamma}{2a}(\frac{1}{4} + \frac{2}{3}\mu\sin\psi + \frac{1}{2}\mu^2\sin^2\psi) \qquad (45)$$

This form is suitable to be used in conjunction with a numerical method. Equations (45), when integrated along with the stall equations, yield the dynamic response of a rigid rotor blade.

3.5 TRIM PROCEDURE

Any flight vehicule should be able to maintain equilibrium during flight conditions. In fixed wing aircraft, external aerodynamic surfaces (such as aelerons, elevators, and rudders) perform this function. Thus, by changing the elevator deflection, the airfoil camber is changed, and lift can be increased or decreased so that the aircraft is trimmed. In a helicopter, trim performed by variation of blade pitch angles on the advancing and retreating blade so that rolling and pitching of the aircraft is avoided.This is accomplished through pilot-controlled inputs of collective pitch (θ_0) and cyclic pitch (θ_s, θ_c).

The pitch mechanism produces the pitch setting for a helicopter trimmed condition, expressed as follows

$$\theta = \theta_0 + \theta_s \sin\psi + \theta_c \cos\psi \tag{46}$$

θ_0 , θ_s ,and θ_c are respectively, the collective, longitudinal, and lateral cyclic pitch angles. One must specify these angles in order to calculate rotor response. One way to do this is through approximate trim formulas such as those given in (16).

$$\theta_0 = (6\overline{C}_T + \frac{9}{8}\phi) + (15\overline{C}_T + \frac{19}{16}\phi)\mu^2 \tag{47}$$

$$\theta_s = -(16\overline{C}_T + \frac{3}{2}\phi)\mu - (16C_T - \frac{3}{4}\phi)\mu^3 \tag{48}$$

$$\theta_c = \frac{\gamma}{p^2}[(\overline{C}_T + \frac{1}{48}\phi)\mu - (\frac{5}{9}\overline{C}_T + \frac{1}{16}\phi)\mu^3] + \frac{4}{3}V_1 \tag{49}$$

$$\text{where} \quad \phi = \frac{4}{3}[\frac{1}{2}(\sqrt{C_T^2 + \mu^4} - \mu^2)]^{\frac{1}{2}} \text{ ,and} \quad \overline{C}_T = \frac{C_T}{a\sigma} \tag{50}$$

The above trim procedure was applied to determine the pitch settings in the stalled regime. However, these were found to be inadequate for the stalled conditions. Therefore, we introduce in

the next section another way of trimming the helicopter which consists of using automatic controllers.

3.6 AUTO-PILOT CONTROLS

An effective way of obtaining accurate pitch inputs is based on the use of an automatic feed-back system that can trim the helicopter. In reference (17), auto-pilot equations are developed and expressed as follow

$$\tau_0\ddot{\theta}_0 + \dot{\theta}_0 = A_0[\overline{C}_T - \frac{4}{3}\frac{p^2}{\gamma}\beta] \tag{51}$$

$$\tau_1\ddot{\theta}_s + \dot{\theta}_0 = A_1\frac{(p_0^2 - 1)}{\gamma}[\cos\psi - \frac{8(p^2 - 1)}{\gamma}\sin\psi]\beta \tag{52}$$

$$\tau_1\ddot{\theta}_c + \dot{\theta}_c = -A_1\frac{(p_0^2 - 1)}{\gamma}[\sin\psi + \frac{8(p^2 - 1)}{\gamma}\cos\psi]\beta \tag{53}$$

This automatic-feed-back system provides control to the helicopter for numerical purposes. It adjusts the pitch of the blade to maintain thrust, roll moment, and pitch moment. the parameters A_0 and A_1 are controller gains. The parameters τ_0 and τ_1 are time constants. The grouping $8\frac{(p^2 - 1)}{\gamma}$ is a coupling parameter giving the pitch-roll coupling of θ_s and θ_c. The grouping $\frac{4p^2\beta}{3\gamma}$ is an estimate of rotor thrust in the absence of an explicit C_T equation.

So far, we have introduced the aeroelastic blade equations using a unified lift model. In addition, we have modeled the rigid blade mode. Finally, we described some mathematical tools and numerical methods used to solve these equations. the results obtained are discussed in the next chapter.

4. RESULTS

In the previous chapter, aeroelastic equations (32-33) have been derived with a unified-stall aerodynamic model. In addition, approximate solution schemes based on a modified Galerkin's method have been used to separate variables and to transfer the partial-differential-equations (32-33) to linear ordinary-differential equations which must be solved for a time history. When state variables are introduced in equations (43-44), a system of first-order-differential equations is obtained (45). These equations can be solved simultaneously for specified initial conditions using a time-marching method. Nondimensional time is the independant variable of the equations. In this chapter, only rigid-blade modes are treated. An elastic blade may be treated in a similar manner, but more degrees of freedom would be included. Hence, the elastic blade case requires more than one assumed mode. The dependent variables include flap bending, lag bending, and pitch angles in the automatic-control cases.

Many numerical methods are available to solve ordinary differential equations. These methods may be divided into two categories, single-step methods and multi-step methods. The first type uses only the information from the last step to predict the value of the dependent variable in the current station. This type of method, which includes the Runge-Kutta method, is good to begin a solution; but it is inefficient for a large domain of integration. The second type of method takes advantage of the values of the dependent variable in more than one previous step. The solution can be corrected by one or several iterations until the desired order of accuracy is obtained. The present problem includes, in general, a time history of several revolutions which are needed to reach the steady state condition. Hence, the integration of the differential equation by a predictor-corrector method would reduce considerably the computational effort. In this research work, a subroutine based on Adams method is successefully used to solve the equations.

In the computational algorithm, input parameters define the basic aircraft configuration and flight conditions. The blade type is defined by its root stiffness, solidity, lock number, damping, and airfoil type. Flight conditions, on the other hand, are characterized by the advance ratio, and thrust coefficient. In Table 2, we present the common parameters used in the cases discussed in this

chapter. These parameters are selected from current helicopter data and used for illustration purposes.It is noted that we use only a constant value of C_D. In future work, we intend to include a variable C_D based on stall assumptions. Thus, the major study here is the effect of stall on lift but not on drag.

Vibration analysis includes flap and lag responses and their sensitivity to advance ratio and thrust coefficient. Torsion effect is neglected in this study. The variation of the automatic control settings required for trim is determined for a blade revolution in a steady state. In addition, the change of these settings as a response to blade stall is identified. Last, the vibration in the flap direction obtained from the stall model used in this research work is compared to results obtained when a linear aerodynamic model is used.

4.1 TRIM ANALYSIS

In order to determine the response of a helicopter blade, one must first determine the pilot controls (collective pitch, cyclic pitch, and shaft tilt) that are applied to the rotor. Earlier in this report, we introduced two alternative methods of doing this. One method was based on formulas derived by a harmonic balance of the equations without stall, equations(47-50). The other method, on automatic pilot was based on a controller to update the controls, equations(51-53). In either case, the purpose of the controller is to eliminate first harmonic moments (in the rotating frame) which come through (to the fixed frame) as steady pitching and rolling moments. In other words, "trim" implies (among other things) the balancing of these moments.

Figures 3-6 provide plots of the flapping response at $\bar{x} = 0.7$. Because this is a rigid blade with root spring, flap displacement, w, is a direct measure of root moment. The four figures show a variety of thrust coefficients and advance ratios, some with stall (high μ, high C_T), and others with little or no stall (low μ, low C_T). We see immediately that the approximate formulas give a large amount of 1/rev (i.e. $\sin\psi$, $\cos\psi$) in the response.

Table 2. Baseline Parameters

Parameter	Numerical Value	Physical Description
γ	6.63	Lock number
a	6.461	lift curve slope
C_D	.01	drag coefficient
Λ_5	.014	$\frac{EI_x}{m\Omega^2 R^4}$
Λ_6	.002	$\frac{EI_x}{m\Omega^2 R^4}$
$\bar{b}$	.05	$\frac{b}{R}$
P	1.03	flap frequency
f	.01	profile drag coefficient
σ	.1	solidity
K_β	.0203	stiffness of flap root
K_ζ	.02083	stiffness of lag root
C_ζ	.025	damping coefficent
τ_0	6.6	time constant
τ_1, τ_2	1.884	time constants
A_0	2.6	gain
A_1, A_2	3.6	gains

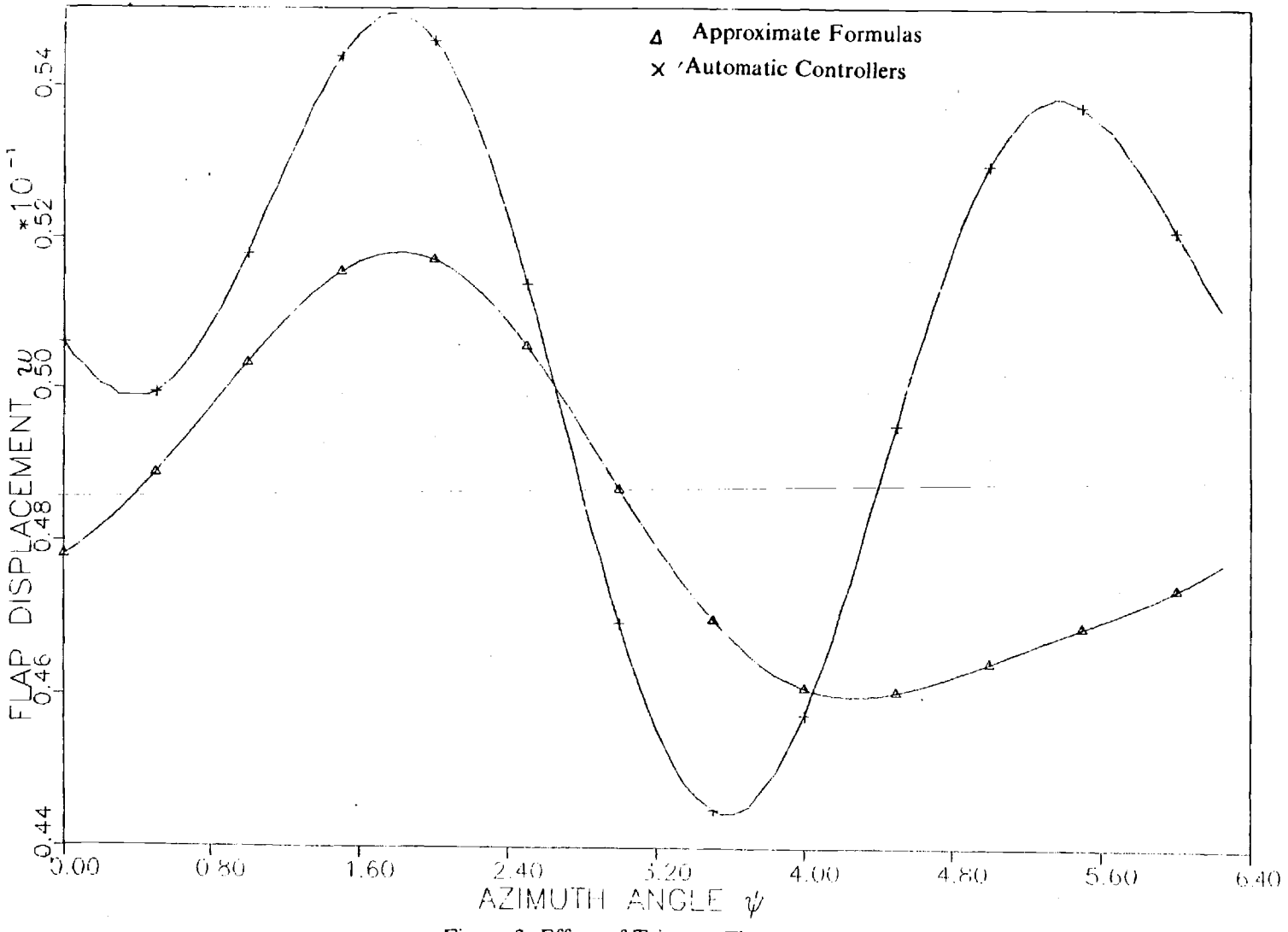

Figure 3. Effect of Trim on Flap Response

($C_T = 0.009$, $\mu = 0.10$)

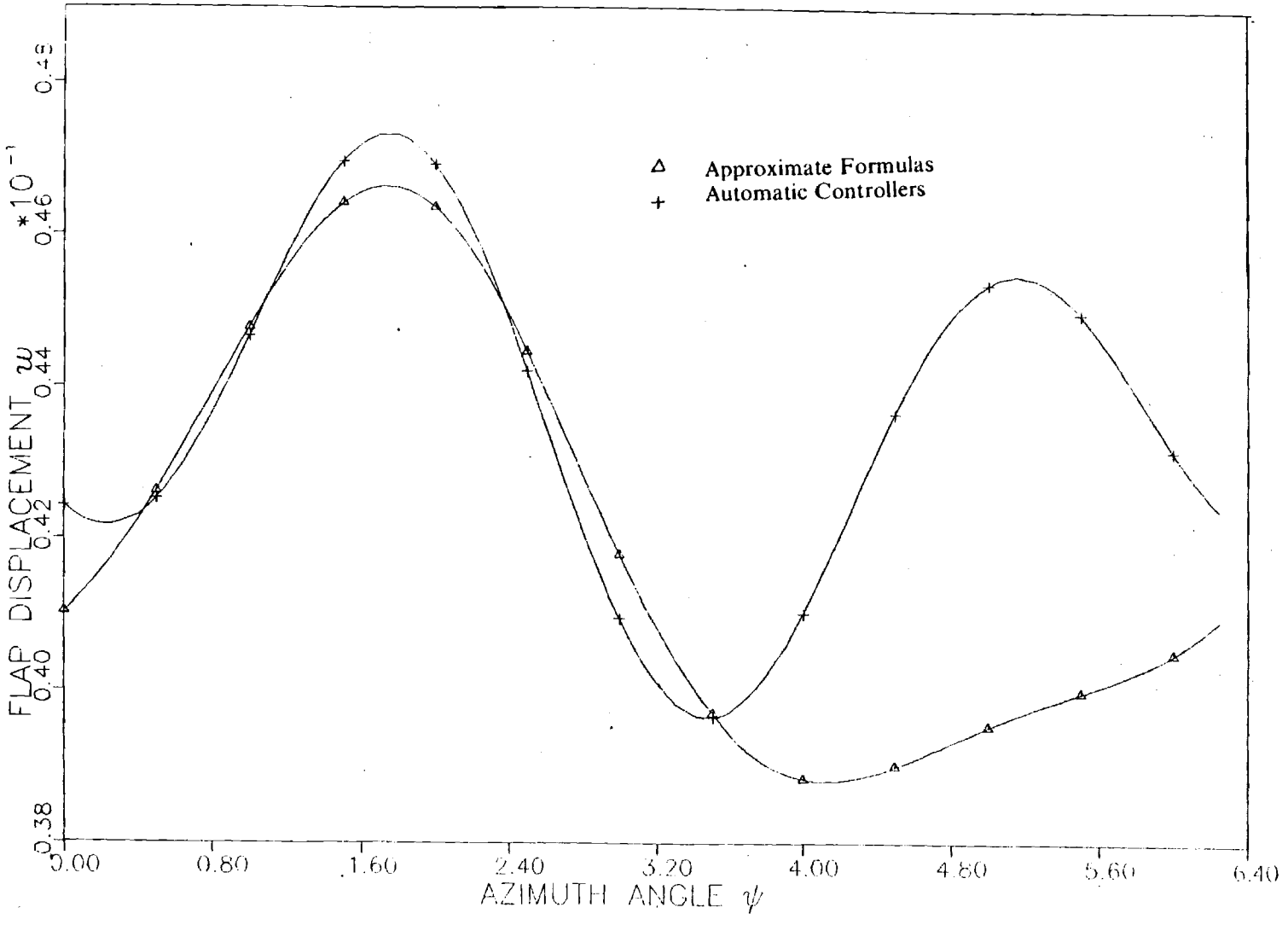

Figure 4. Effect of Trim on Flap Response

($C_T = 0.008$, $\mu = 0.15$)

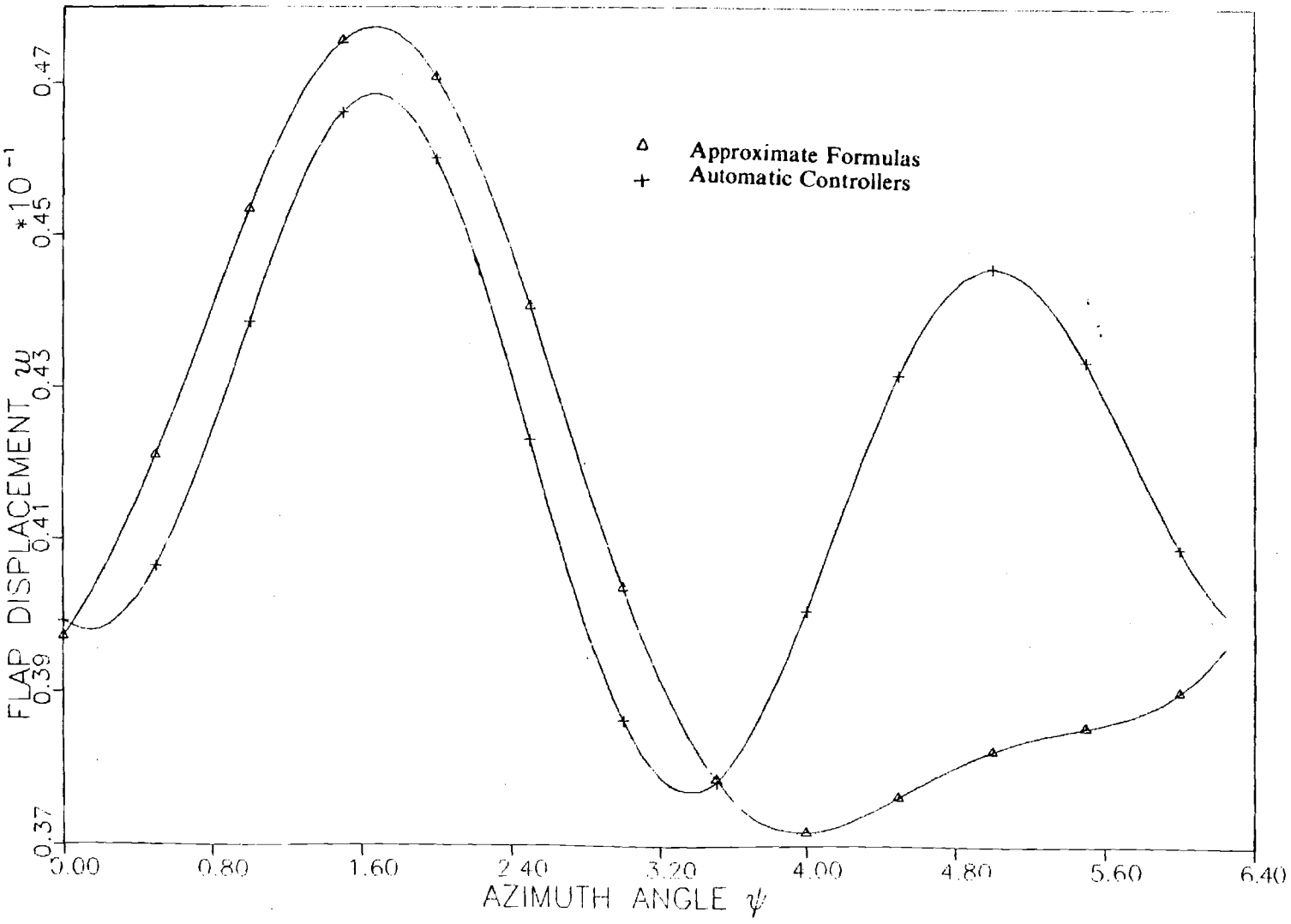

Figure 5. Effect of Trim on Flap Response

($C_T = 0.008$, $\mu = 0.20$)

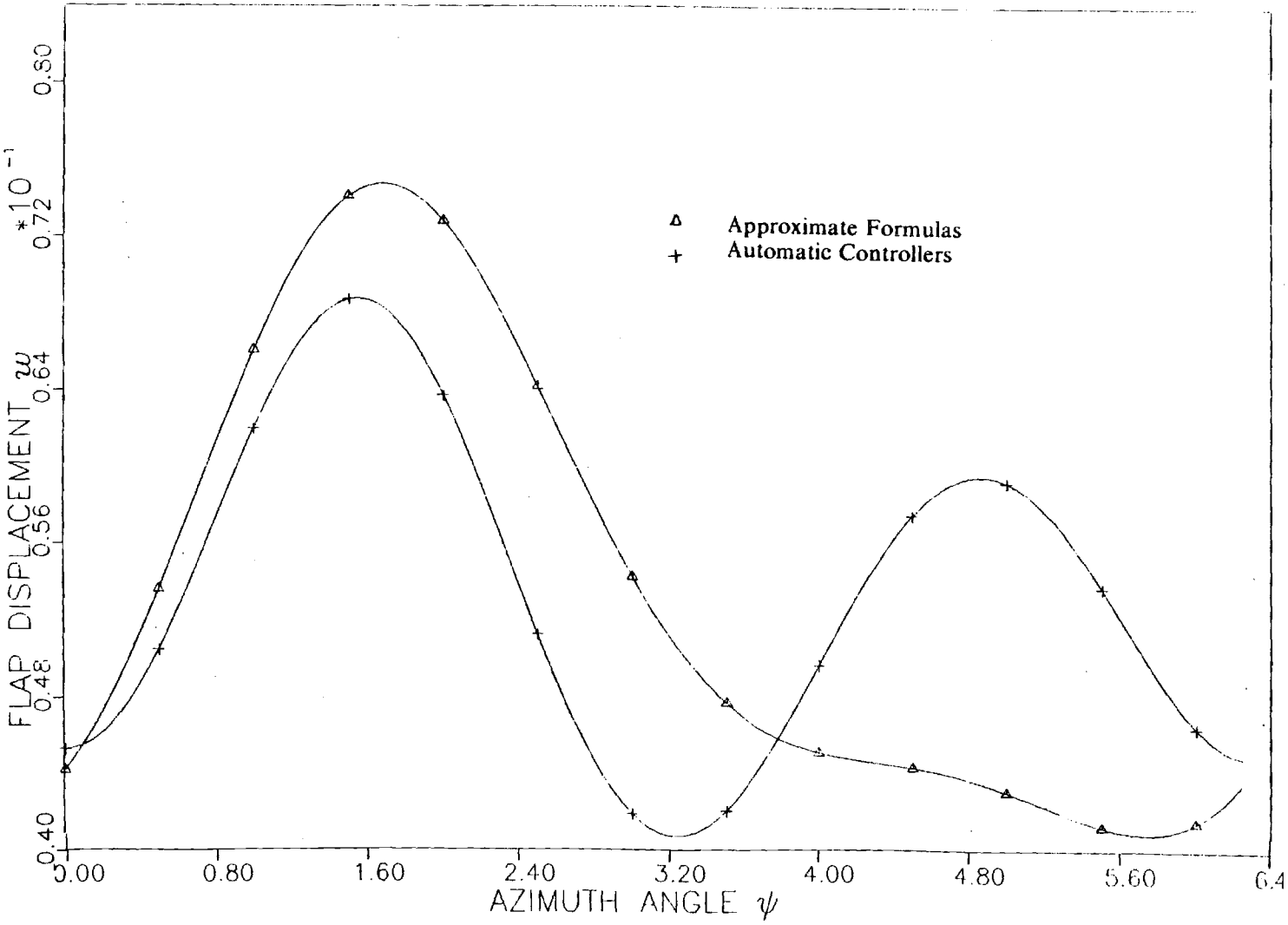

Figure 6. Effect of Trim on Flap Response

($C_T = 0.011$, $\mu = 0.3$)

Thus, they are not accurate due to the aspects of the model neglected in such formulas (inplane motion, unsteady aerodynamics, nonuniform inflow distribution, and stall). The results with the automatic pilot, however, show two peaks per cycle, indicative of little 1/rev, mostly 2/rev, and some 3/rev, which is indicative of trim.

It is interesting that most investigations in this area have had trouble obtaining a correct trim. For example, Figure 7 shows results at $\mu = 0.4$ from Reference (13). Two different iteration schemes are used for the two plots. Notice, however, that the results (although labelled as "propulsive trim") have a large 1/rev component very similar to that seen in our approximate-formula results of Figure 3. This is to be expected because only an approximate formula is used. Figure 8 presents other results from Reference (14). Here, we see a very large fore-to-aft 1/rev for a rotor supposely in "propulsive trim" at $C_T = 0.1, \mu = 0.2$, Furthermore, the curves show that the response is not even periodic, as the slopes do not match at $\psi = 0°$ and360°. In Figure 9, taken from Reference (15), the authors of Reference (14) attempt to correct the lack of trim found in Figure-8. The dashed curve is the old result (although in this paper it is corrected to be periodic), and the solid curve is the new result. In this new result, the trim solution is modified to include elastic twist. Notice, however, that although the 1/rev has been reduced by about 50%, it is still very much present. Furthermore, the solid curve is not at all periodic, with an error of over 100% in the slope betwween $\psi = 0°$ and $\psi = 360°$. This points out the difficulties in finding a good trim solution.

4.2 STEADY STATE RESPONSE

Steady state response corresponds to a state where all the transients have died out. In this instance, the response becomes periodic. The trim procedure supresses first harmonic vibrations in the flap response. Results will be presented for the twentieth revolution in which a steady state is achieved. The results will include flap response, $\bar{w}$; inplane response v, and lift coefficient. Also, cyclic pitch settings are evaluated in the automatic control flight regime.

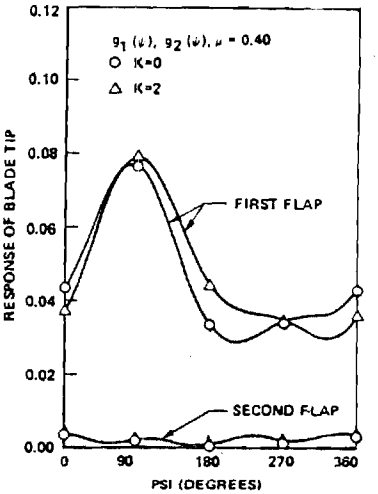

Fig. 7a Response of the soft-in-plane configuration, propulsive trim, $C_w = 0.005$

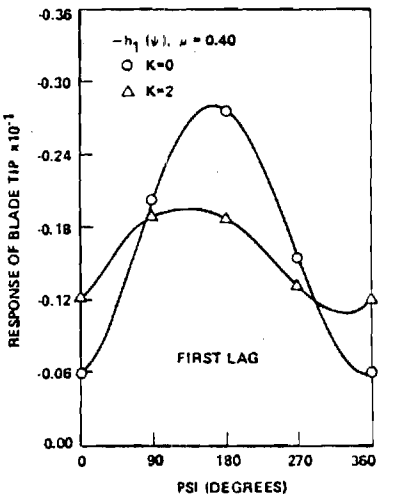

Fig. 7b Response of the soft-in-plane configuration, propulsive trim, $C_w = 0.005$

Figure 7. Flap, Lag, and Torsion Response
($C_T = 0.005$, $\mu = 0.40$)

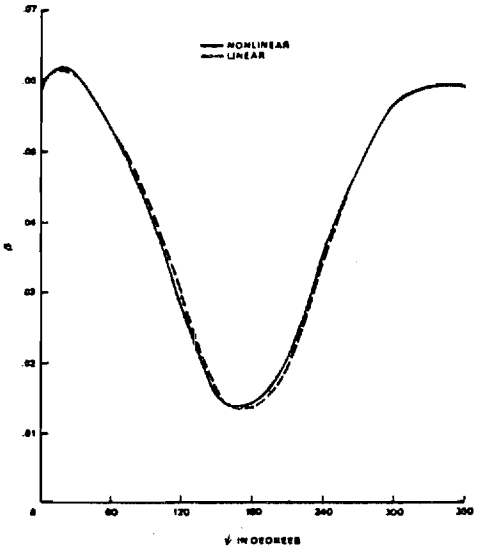

Figure 8a. Flap Equilibrium Angle

Figure 8b. Lag Equilibrium Angle

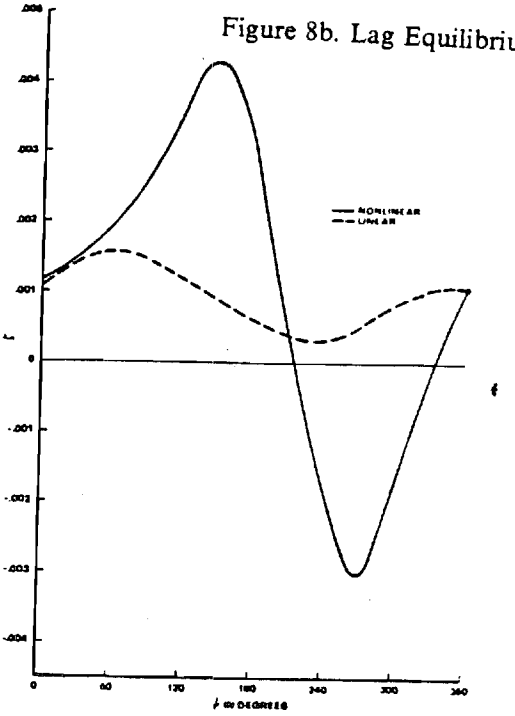

Figure 8. Flap-Lag Response

$(\frac{C_T}{\sigma} = 0.1, \mu = 0.20)$

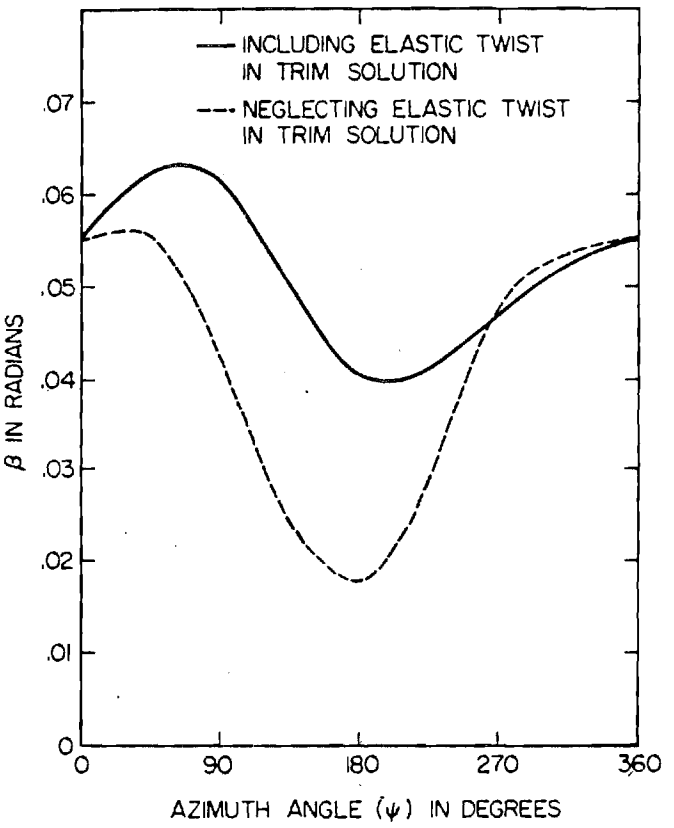

Figure 9. Flap-Lag Response

$(\frac{C_T}{\sigma} = 0.1\ ,\ \mu = 0.2)$

4.2.1 Effect of the Advance Ratio

Advance ratio is the normalized free stream velocity with respect to the blade tip speed. High advance ratio may lead to a stalled condition due to the fact that in the retreating side, the blade operates at higher angles of attack in order to compensate for a reduced free stream velocity. Three cases are analysed in which the advance ratio is varied for a constant thrust coefficient of $C_T = .01$, Figure 10. The flap response is trimmed up to an advance ratio of $\mu = .30$. However, some once-per-revolution type of oscillations begin to appear at $\mu = .30$. Higher advance ratios lead to a larger once-per-rev amplitudes of oscillation of the flap response and an inability to trim. The average bending in the flap direction is approximately constant for the three different advance ratios, but the amplitude of oscillations of the two-per-rev increases with speed . The constant value of w (average) is an indication of the thrust, $C_T = 0.01$, is being held constant. In the inplane direction, Figure 11, a once-per-revolution occurs because inplane is not trimmed in actual rotors. The amplitude of lag vibrations decreases from an advance ratio of .25 to an advance ratio of .29. And then begin to increase again for higher advance ratios. This is due to the effect of induced flow on inplane vibrations. The induced flow also decreases up to $\mu = 0.25$, and then increases due to shaft tilt. The dynamic stall also comes into play at $\mu = 0.25$; and this could contribute (via induced drag) to inplane response. Figure 12 presents the collective pitch controller at all three advance ratios. The collective pitch angle θ_0 increases with advance ratio up to $\mu = 0.25$ in order to generate more thrust. However, beyond this, θ_0 decreases to a lower value. This is attributed to the fact that less θ_0 (and more θ_s) is required to maintain the reasonable lift in the stalled regime. Consequently, the longitudinal collective pitch, θ_s (Figure.2) increases with advance ratio even into stall. Figure 13 represents the variation of the lateral cyclic pitch θ_c with azimuth angle. In this case, angles decrease with advance ratio (which is typical at high advance ratios); but the rate of decrease accelerates as stall becomes more pronounced at $\mu = 0.3$. The controllers, therefore, react to adjust the angle of attack so that 1/rev is reduced and aircraft trim is maintained. It is also interesting to note the 2/rev component in θ_0 and the 1/rev components in θ_s and θ_c. these are relatively small and are due to the fact that we are controlling only a single blade. Thus, the controller tries to compensate for 2/rev thrust and 1/rev moments. However, the controller has low-frequency response, and thus responds only slightly to these higher-harmonic inputs.

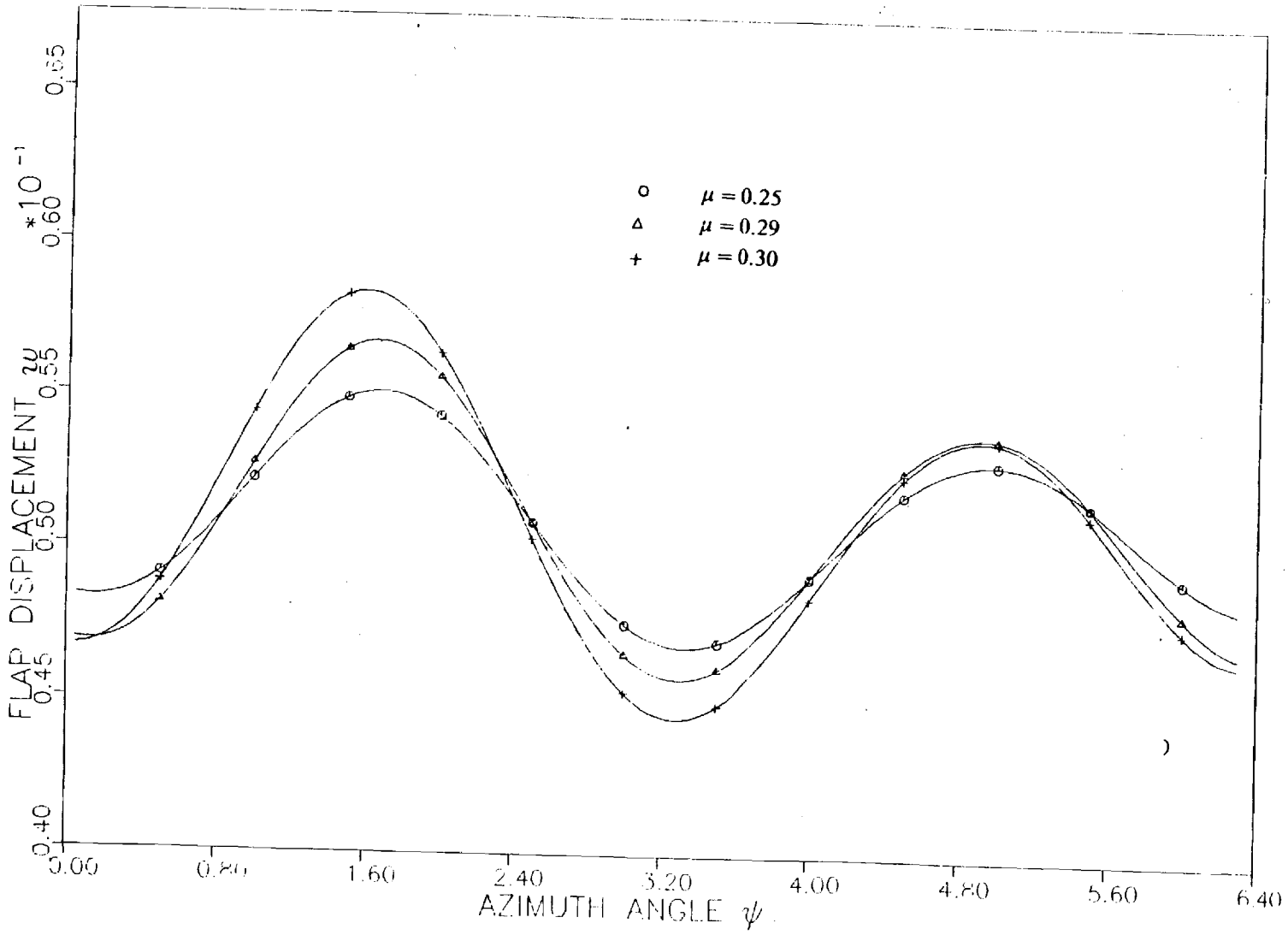

Figure 10. Flap Response for Constant Thrust Coefficient

$C_T = 0.01$

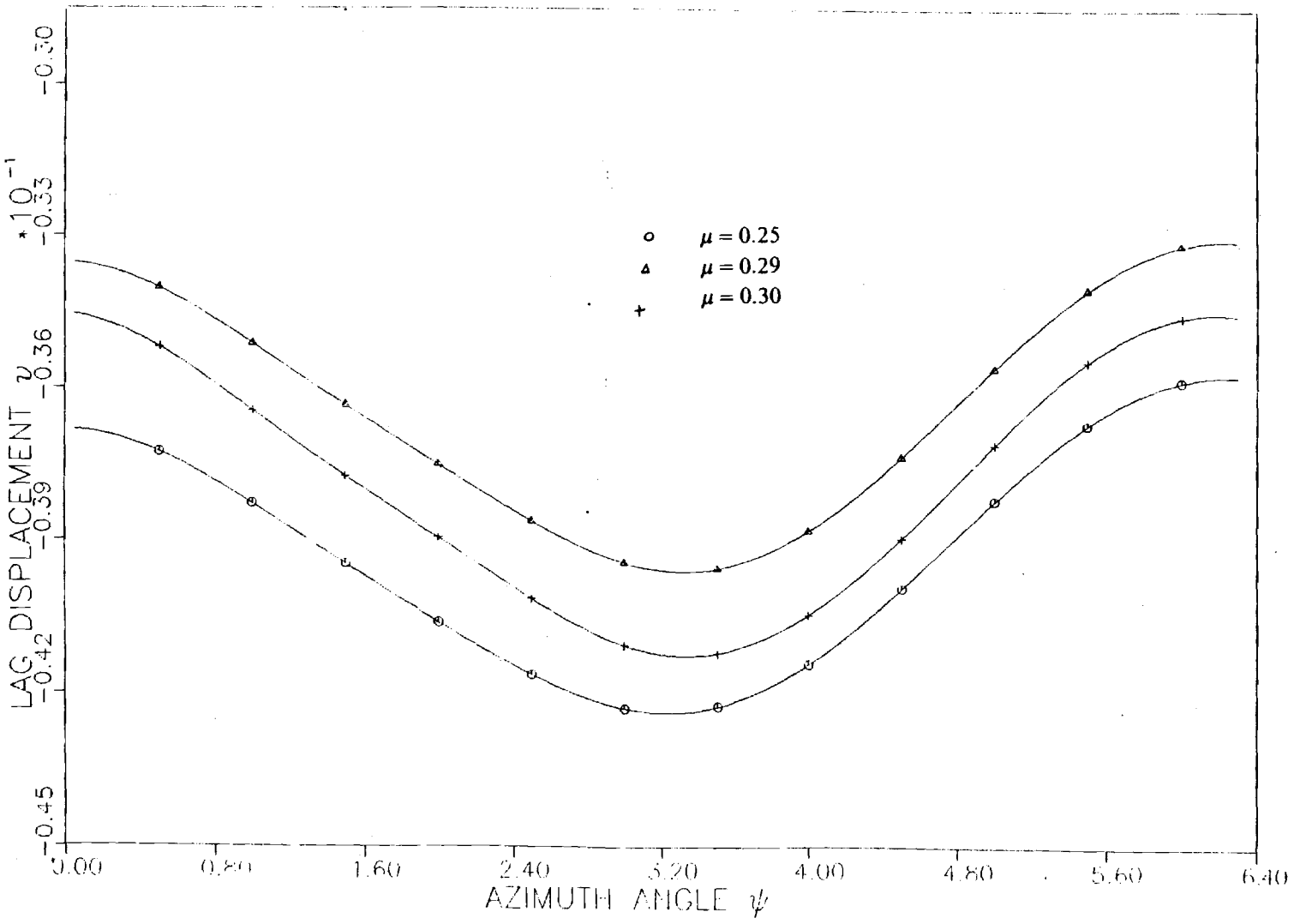

Figure 11. Lag Response for Constant Thrust Coefficient

$C_T = 0.01$

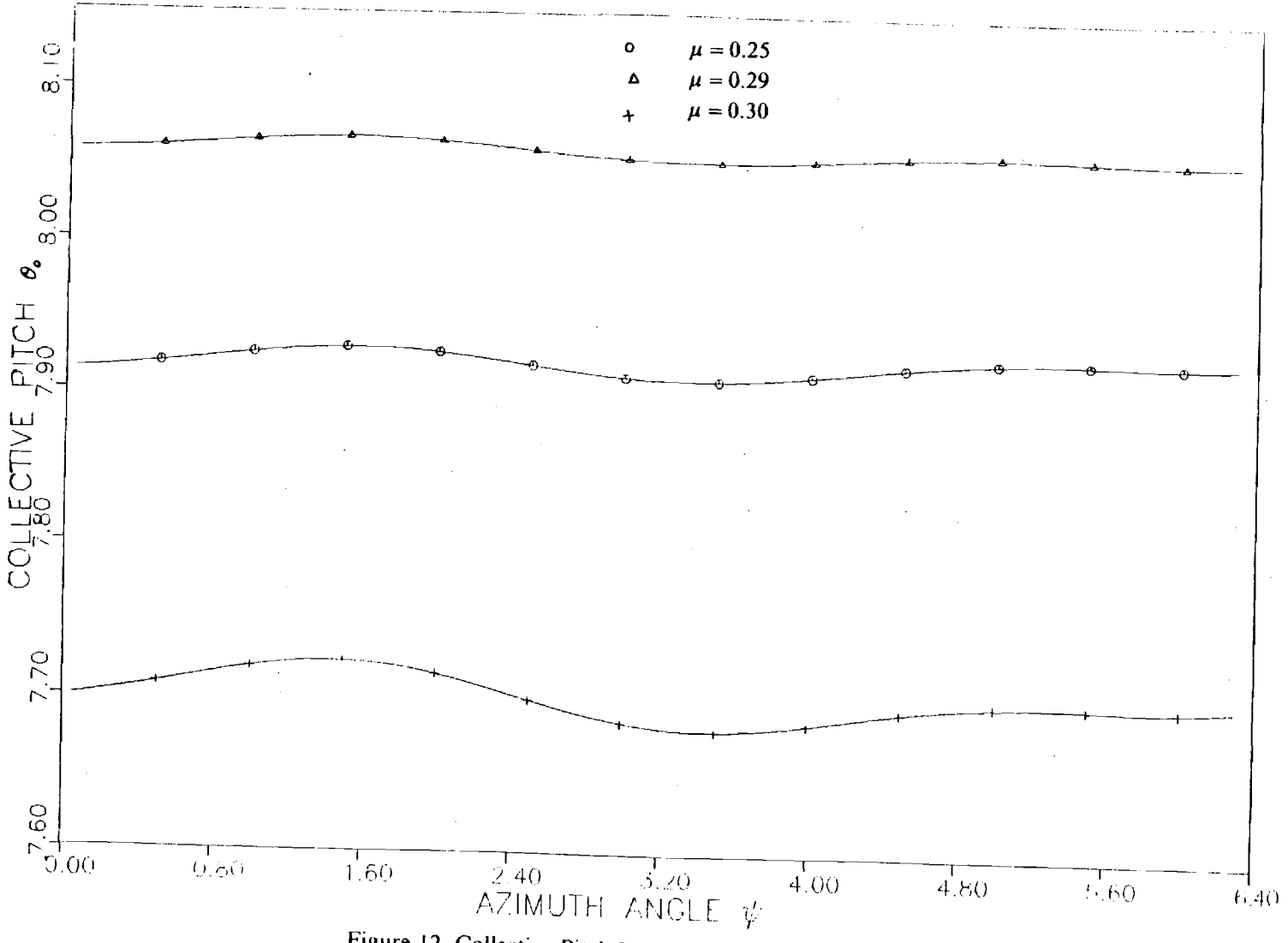

Figure 12. Collective Pitch Variationfor Constant Thrust

$C_T = 0.01$

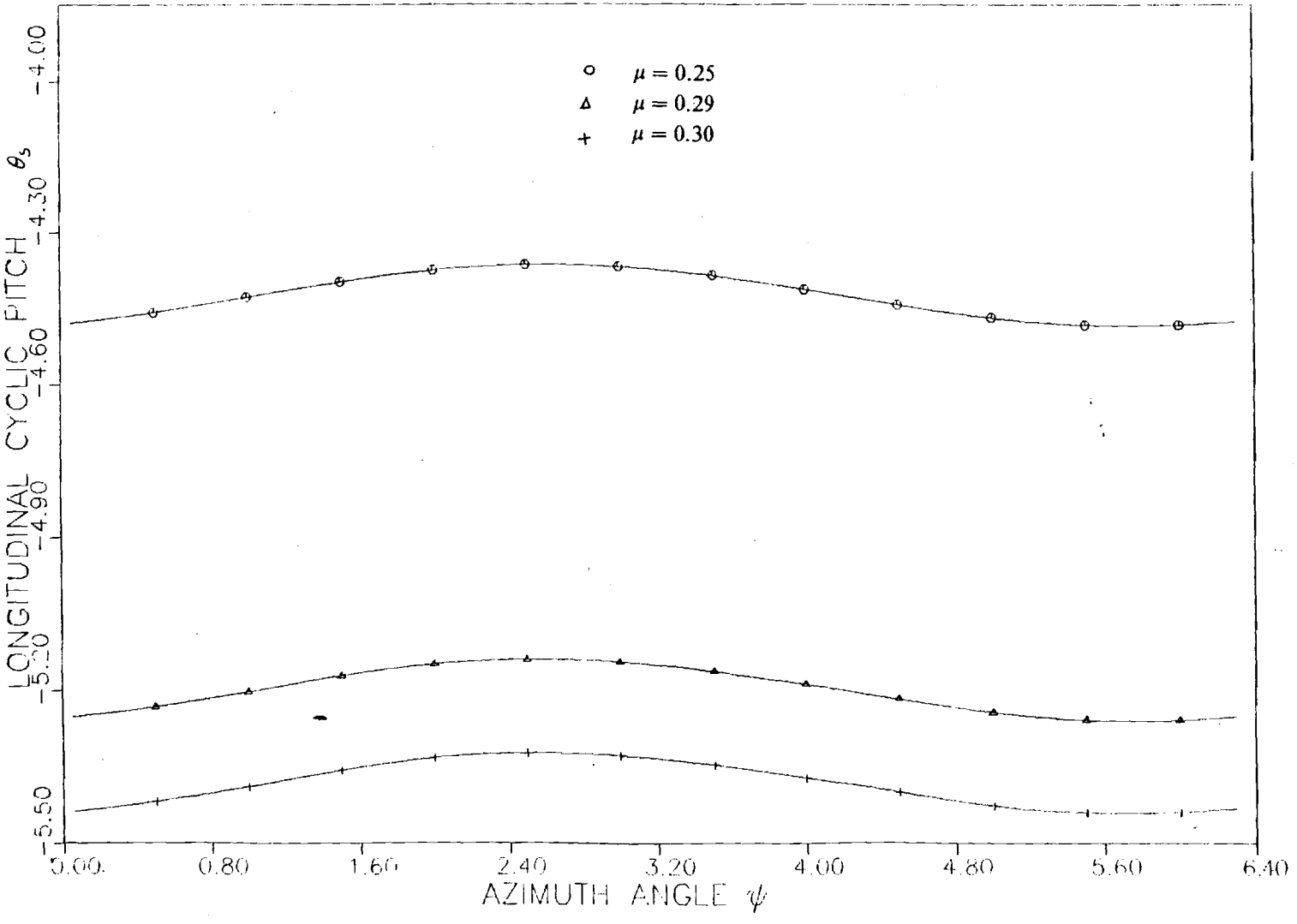

Figure 13. Longitudinal Cyclic Pitch for Constant Thrust

$C_T = 0.01$

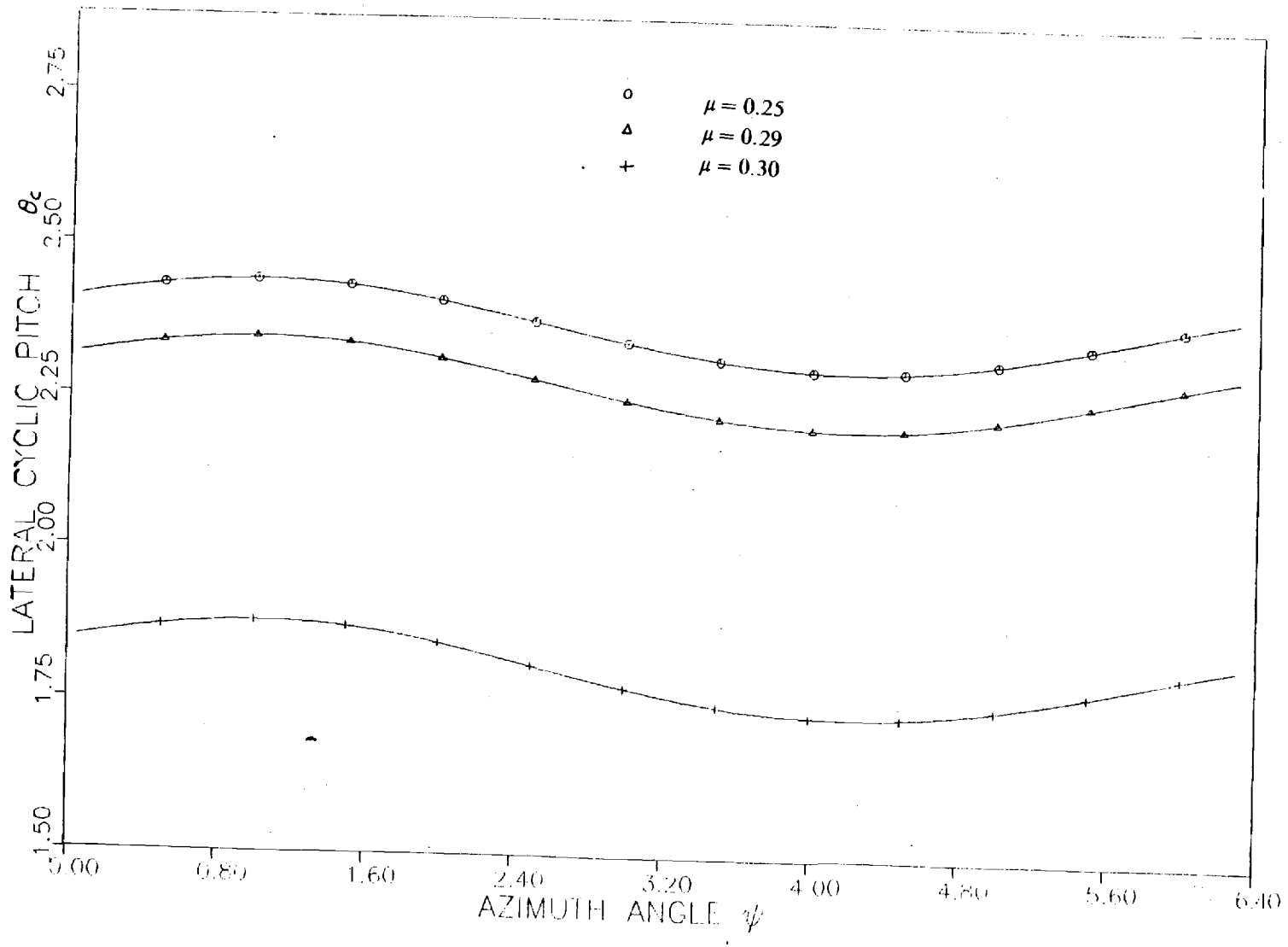

Figure 14. Lateral Cyclic Pitchfor Constant Thrust
$C_T = 0.01$

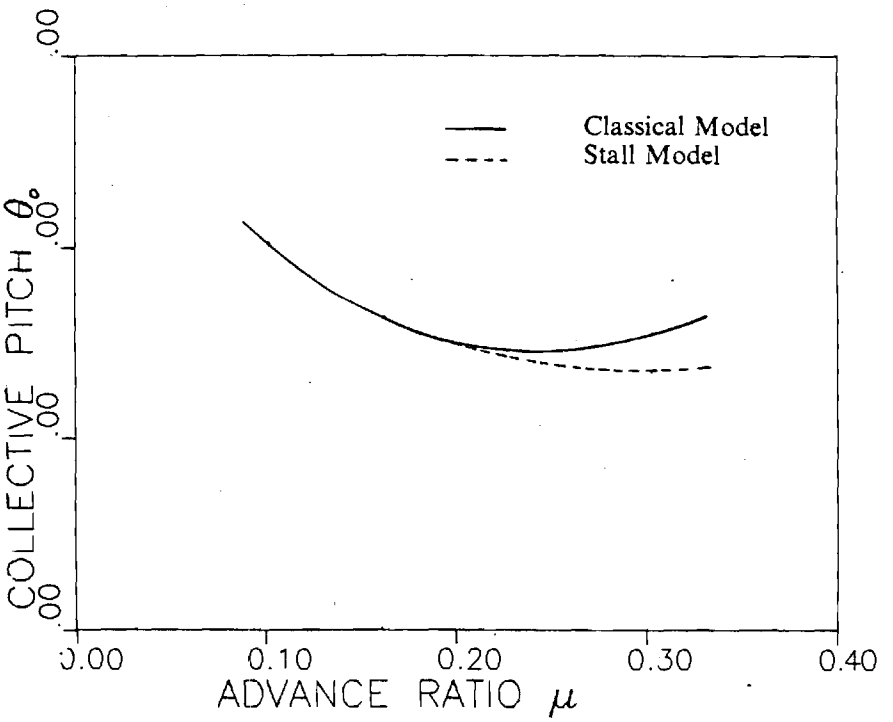

Figure 15. Collective Pitch, $C_T = 0.01$

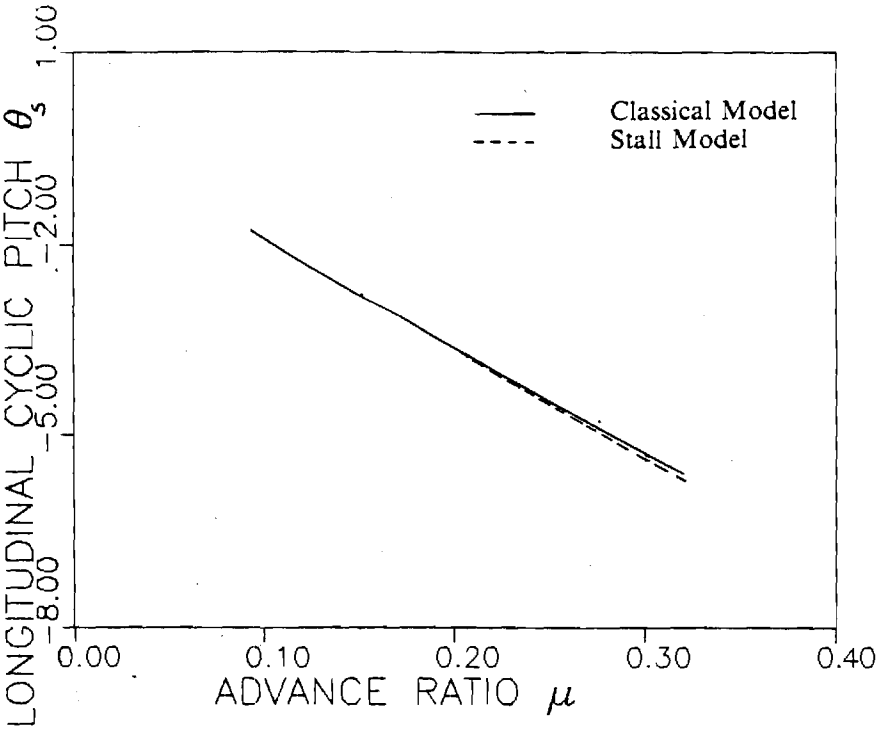

Figure 16. Longitudinal Cyclic Pitch, $C_T = 0.01$

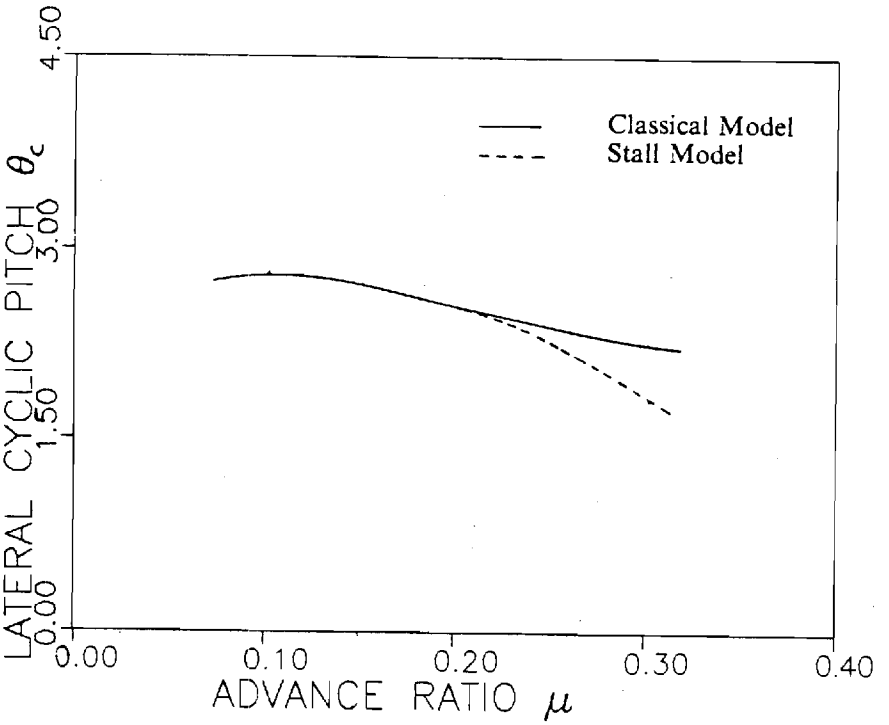

Figure 17. Lateral Cyclic Pitch, $C_T = 0.01$

In Figures 15-17, we cross-plot the control settings at various advance ratios and compare with and without stall. The magnitudes of the collective and lateral cyclic, (θ_0, and θ_c) decrease to a minimum and then increase again as the advance ratio reaches higher values, Figure 15-16. This variation is in conjuction with the typical variation of the power required with cruise speed. It is important to recall that a power curve for a helicopter starts, in general, at normal rated power in hover and then decreases until the minimum power is reached. This power corresponds to a flight for best endurance. The power curve increases again up to the highest cruise speed. Therefore, as required power changes, the collective and lateral cyclic react accordingly. On the other hand, longitudinal cyclic pitch, θ_s , Figure 16, increases in magnitude with advance ratio to account for the loss of free-speed velocity on the retreating blade. As more stall is present, the two former settings are decreased. However, the magnitude of θ_s continues to increases to take care of the effect of the increase of the advance ratio. Thus, with or without stall, the controls necessary to trim can vary in a complicated way.

4.2.2 Effect of Thrust

Rotor response may be effected considerably by stall either where the advance ratio increases or when the gross weight is increased for the same rotor. In Figures 18-22, the flap-lag responses and control settings are plotted at $\mu = 0.3$ for three values of thrust coefficient C_T (.009..01..011). We should point out that, because we do not include tip-losses, these C_T s are equivalent to a lower C_T in a real rotor. We begin with figure 18 . flap displacement. The average blade displacement increases approximately in proportion to the thrust coefficient. The same holds true for lag. Figure-19. This agrees qualitatively with physical results since the increase of load induces more bending in the flap and lag directions.

In contrast to the advance ratio sweeps discussed in the previous section, all control settings monotonically increase with thrust coefficient, Figure 20-22. They react to stall, however, by increasing in a higher rate as stall decreases the aerodynamic effectiveness (as will be shown in an other section of this chapter). Similar to that seen in the advance ratio effect, thrust increases the amplitude of vibrations in the flap and lag directions but within an acceptable limit. Had automatic

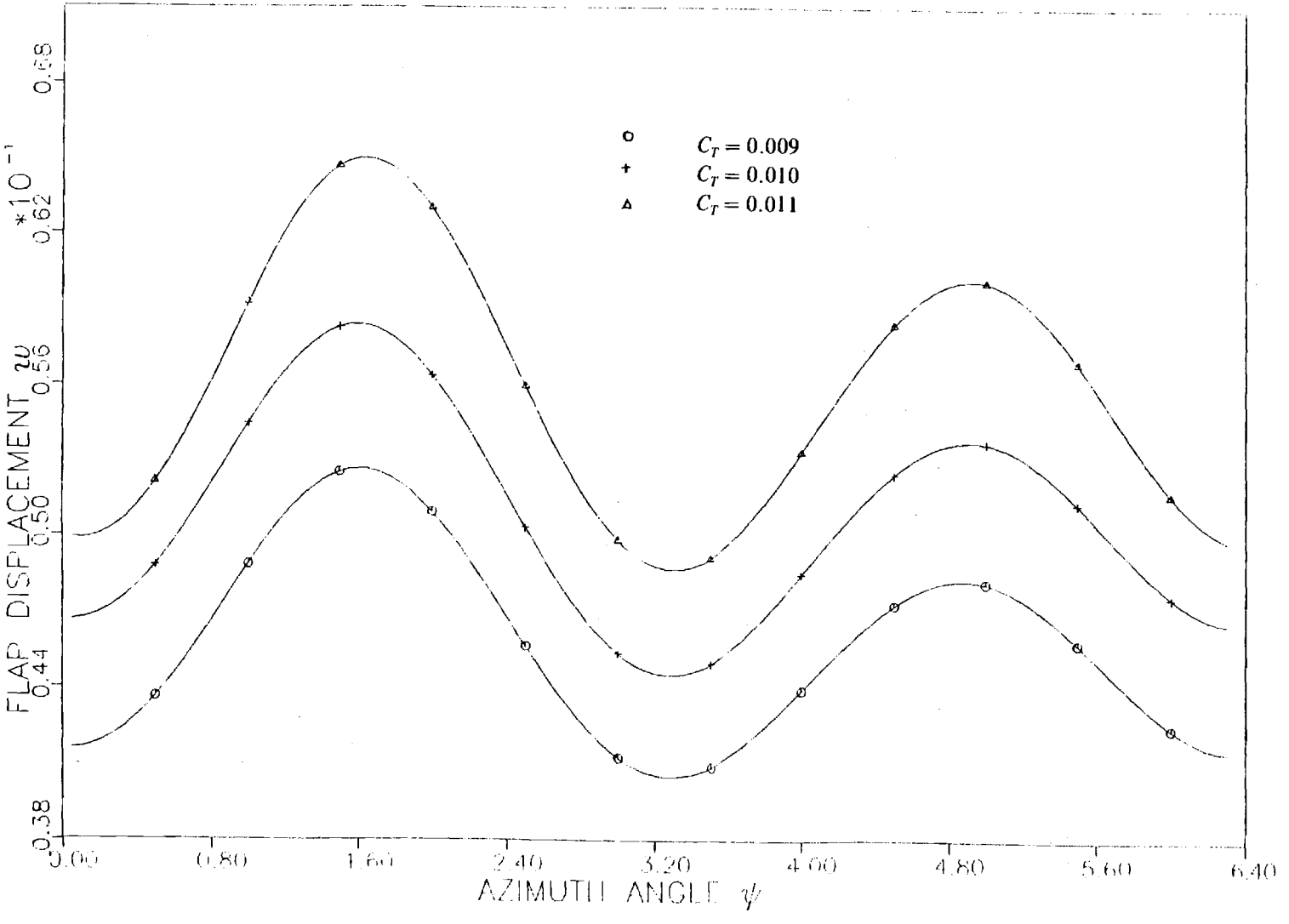

Figure 18. Flap Response for Constant Advance Ratio

$\mu = 0.3$

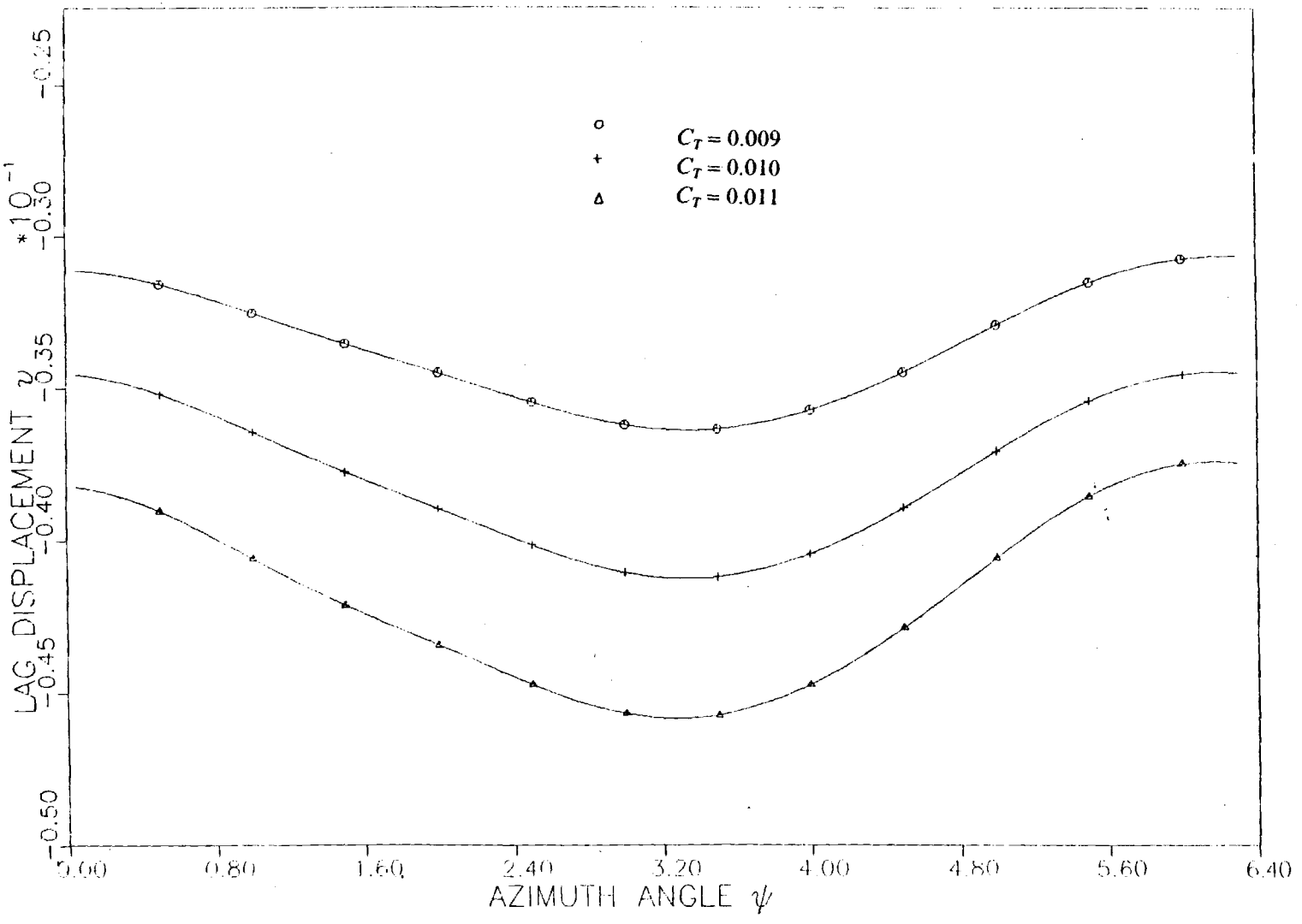

Figure 19. Lag Response for Constant Advance Ratio

$\mu = 0.3$

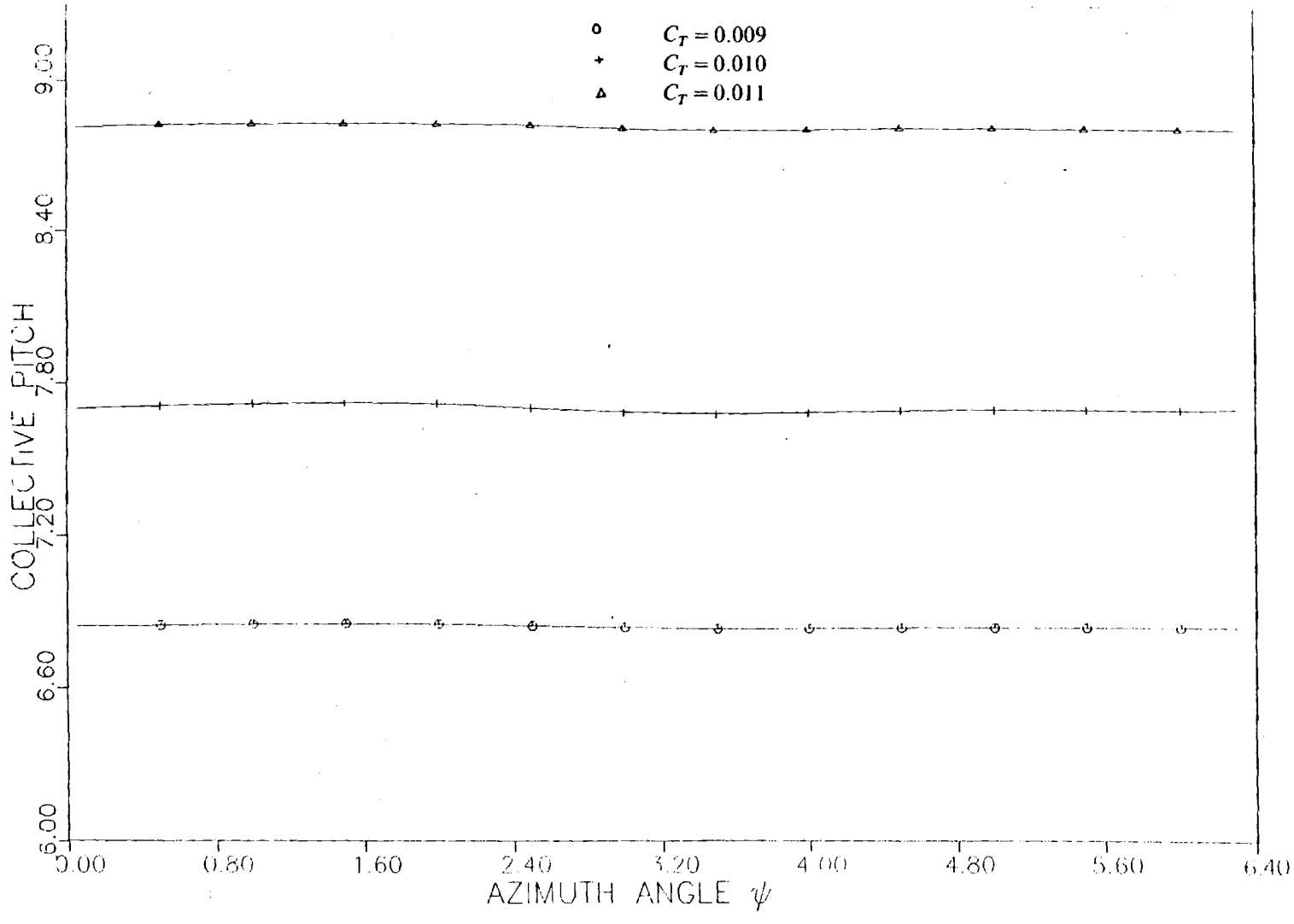

Figure 20. Collective Pitch for Constant Advance Ratio

$\mu = 0.3$

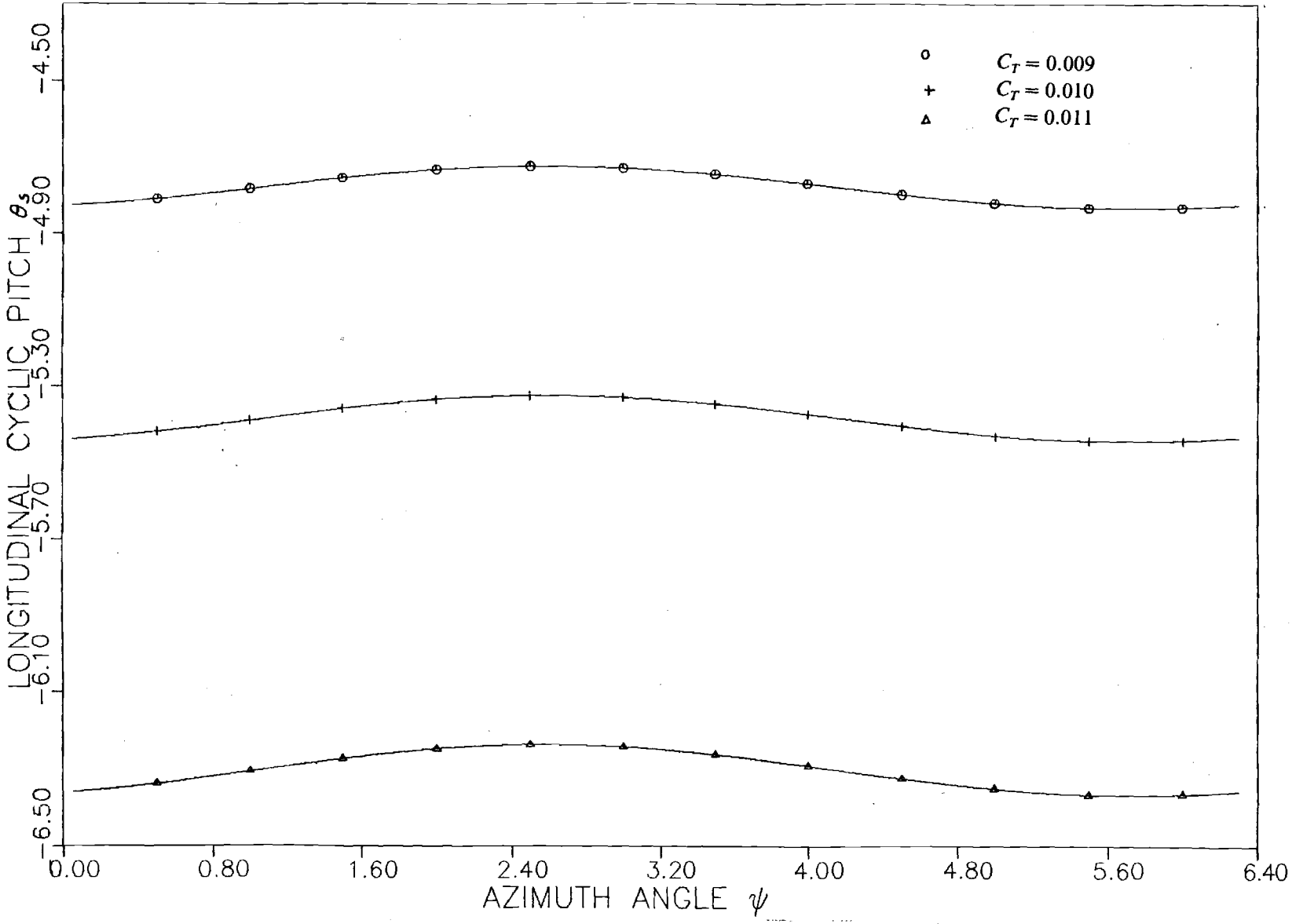

Figure 21. Longitudinal Cyclic Pitch for Constant Advance Ratio

$\mu = 0.3$

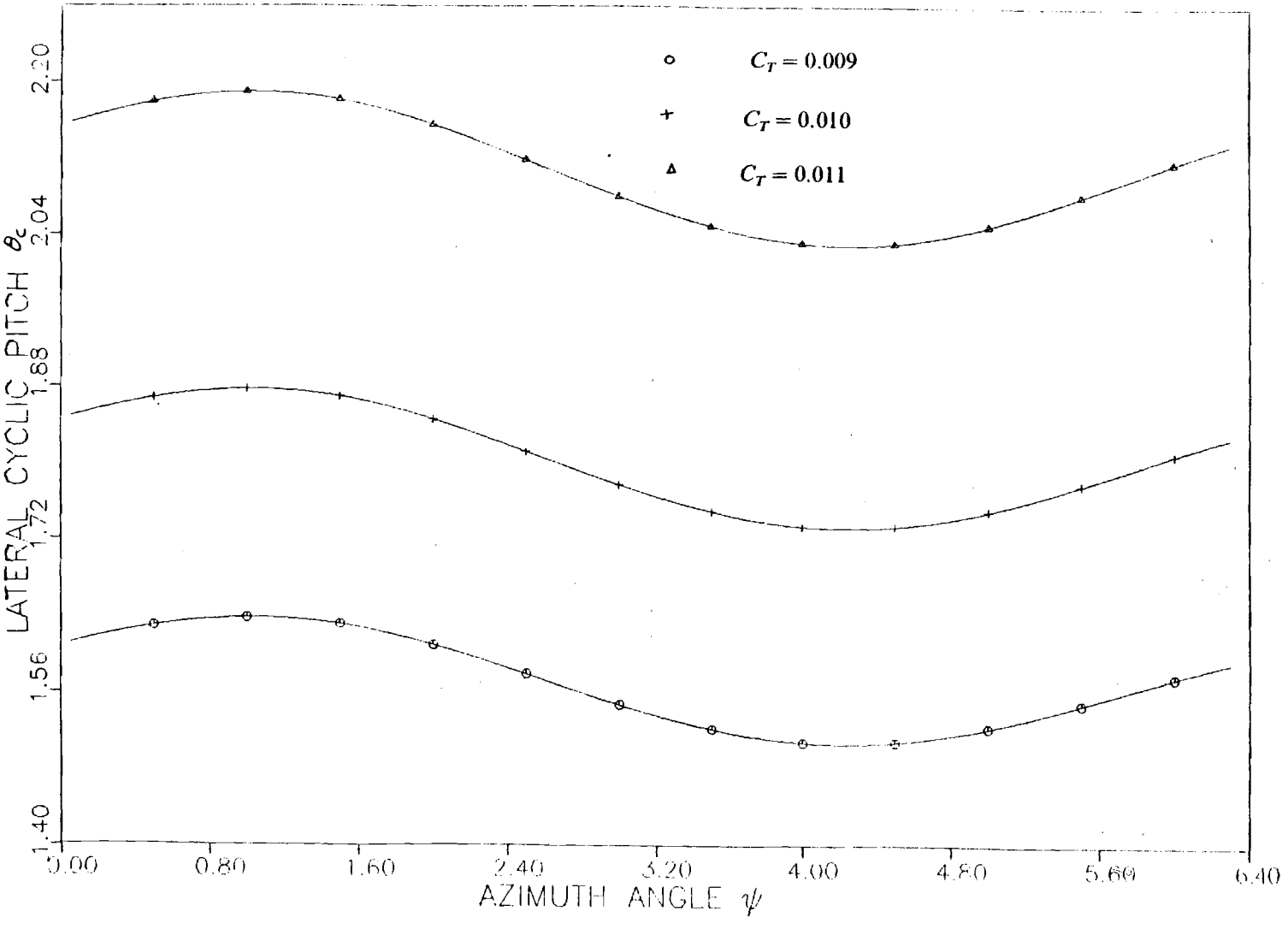

Figure 22. Lateral Cyclic Pitch for Constant Advance Ratio

$\mu = 0.3$

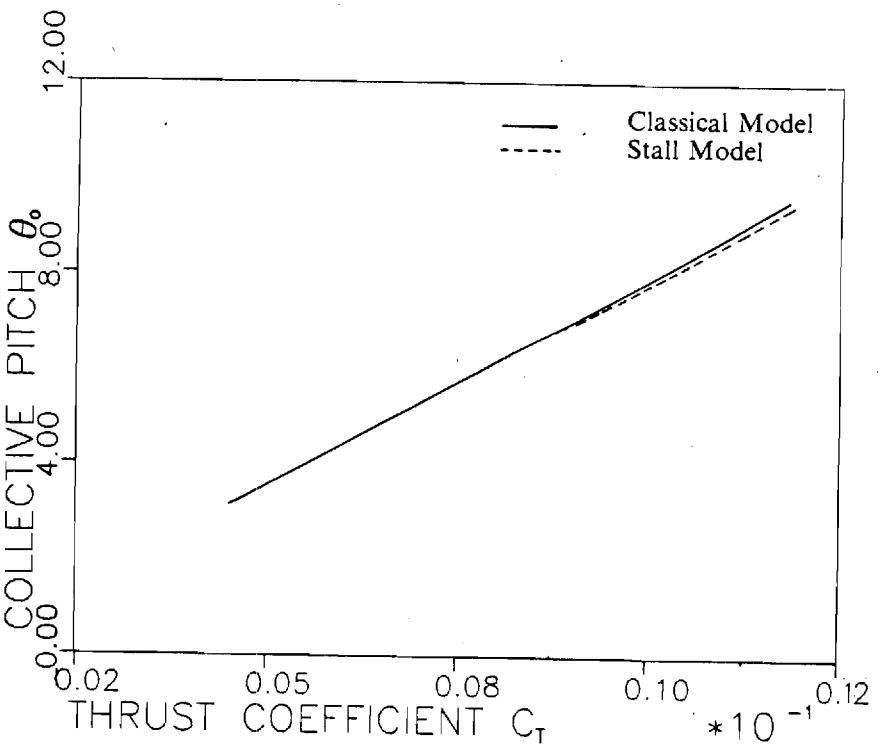

Figure 23. Collective Pitch, $\mu = 0.3$

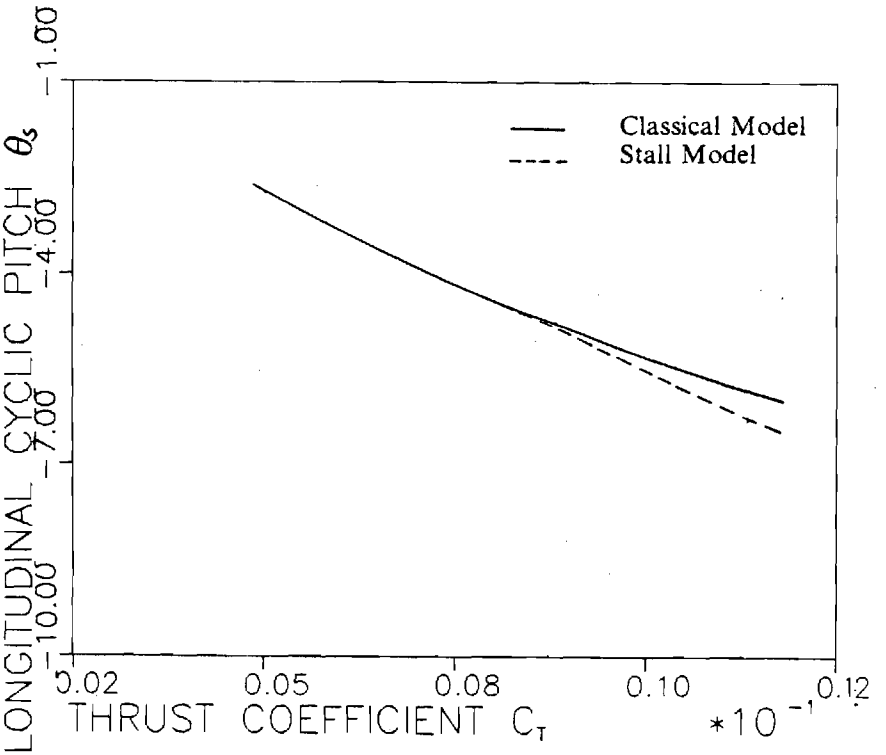

Figure 24. Longitudinal Pitch, $\mu = 0.3$

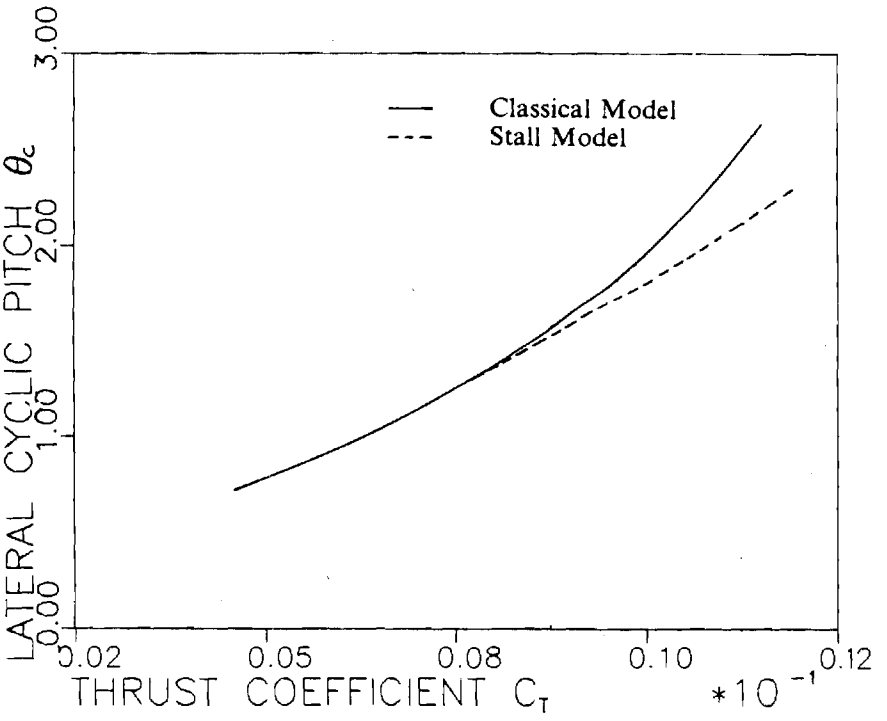

Figure 25. Lateral Pitch, $\mu = 0.3$

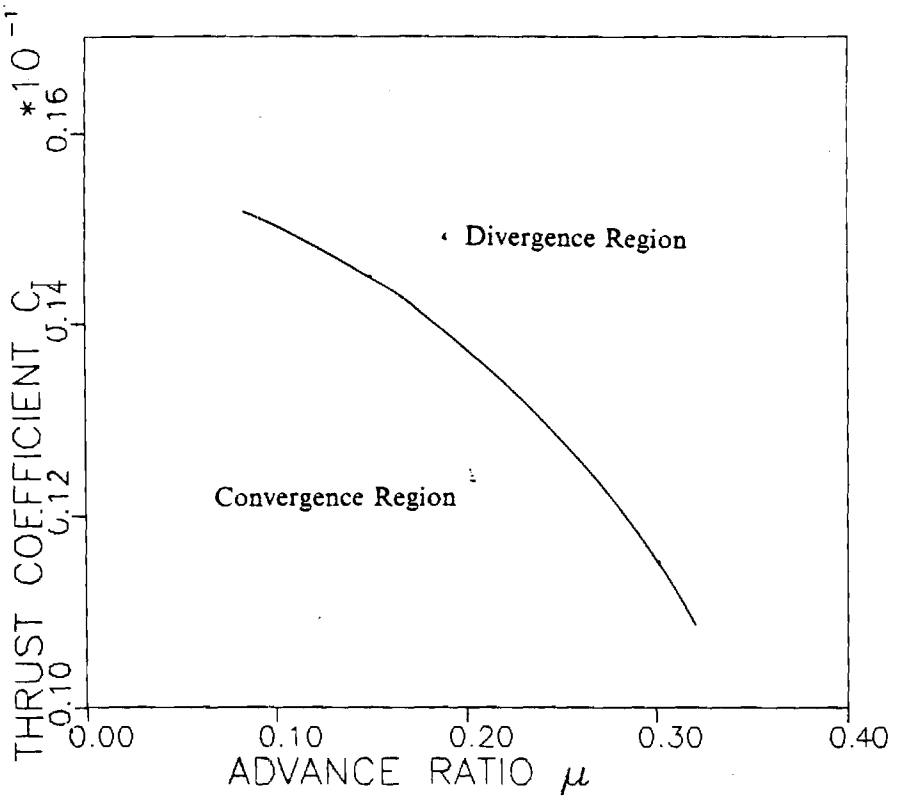

Figure 26. Stability Zone Limit

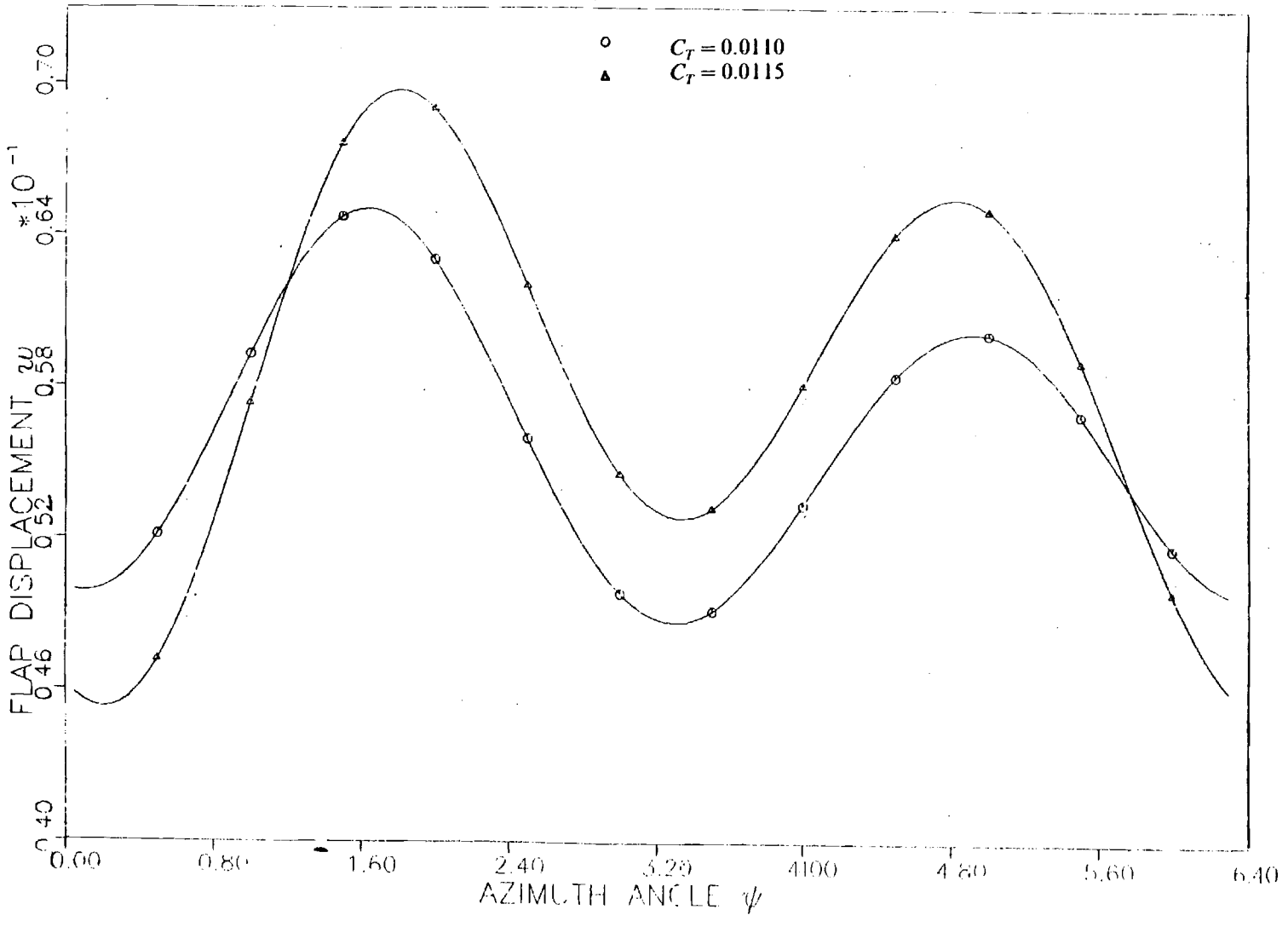

Figure 27. Trimming Boundary, $\mu = 0.3$

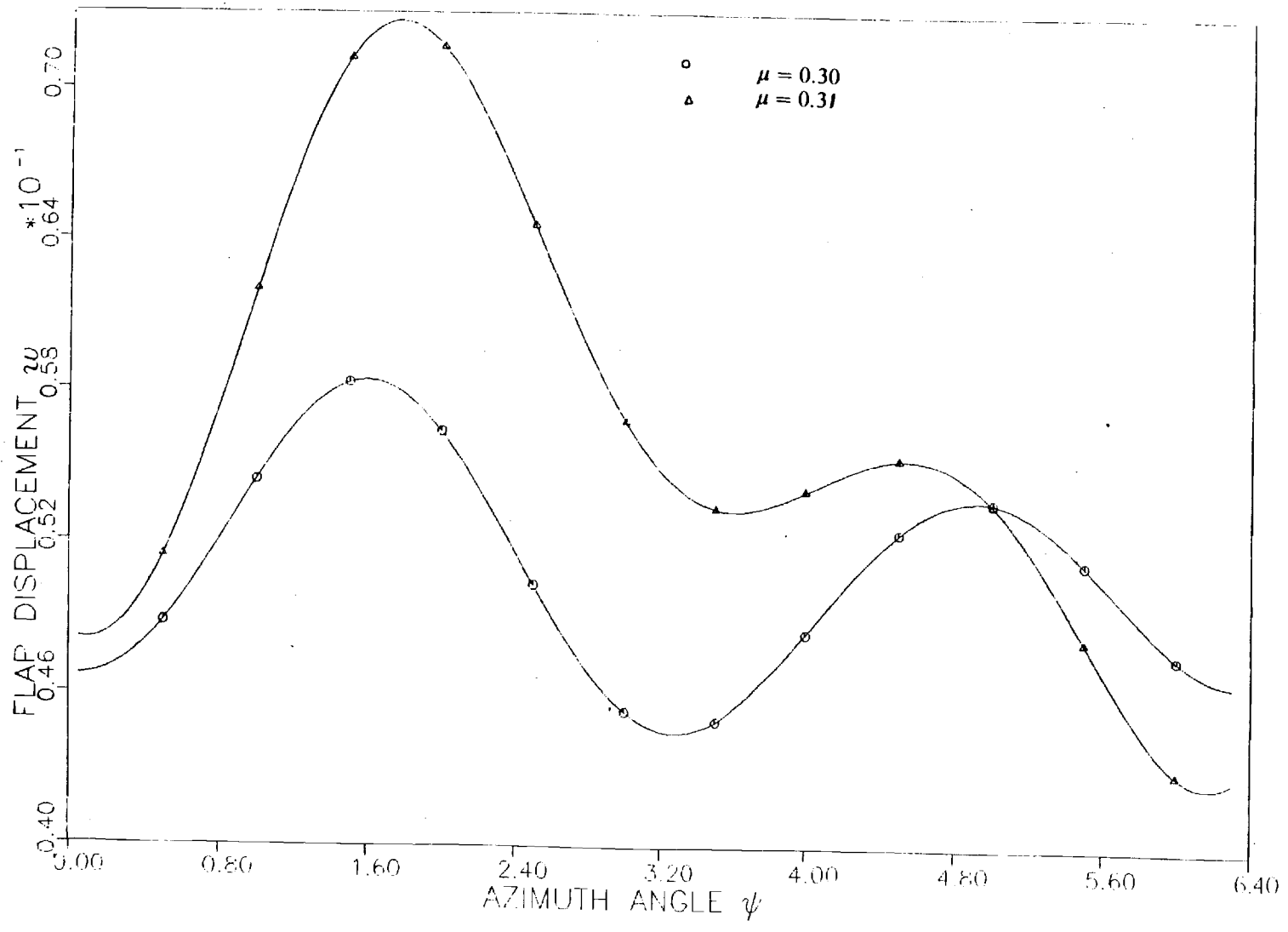

Figure 28. Trimming Boundary, $C_T = 0.1$

controllers not been used, the once-per-revolution vibration effect would have been more pronounced in the stalled region as was observed from Figures 3-5.

Figures 23-25 show a cross-plot of these results versus C_T . Control settings increase in a parabolic manner with the variation of thrust coefficient, since more power is required to maintain a constant cruise speed. When the stall limit is reached, controllers react to maintain aircraft stability. The collective and lateral pitch cyclics (θ_0, θ_c) decrease in magnitude. However, the lateral cyclic pitch θ_c reacts by increasing in magnitude. When we consider the fact that $\sin\psi$ is negative for the azimuth angles of the retreating side, we conlude that θ_c gives a positive contribution to the total pitch angle in order to maintain the angle of attack required for trim.

When the present automatic controller (with present gains and couplings) is applied to analyse highly stalled conditions, the method displays a lack of convergence. This is illustrated in Figure 26, which shows the unconvergence area. This numerical instability is probably due to the shift in pith-roll coupling that accompanies stall as well as the possible limit cycle that can occur when a blade oscillates in and out stall. Figures 27-28 show typical responses near the transition into the untrimmable region. Further work must be done to determine the exact cause and ultimate curve for this problem. (One possibility is an adaptive controller.) This is necessary in order to study stall at more extreme conditions.

4.3 EFFECT OF DYNAMIC STALL ON THE AERODYNAMIC LIFT

During blade rotation, cyclic pitch adjusts the blade angles of attack to maintain the trimmed state. The blade airfoil, therefore, oscillates in order to increase or decrease lift in different areas of the rotor disc. When the lift coefficient is plotted versus angle of attack for a blade in oscillation, closed curves are obtained, known as hysteresis loops. For a low advance ratio, $\mu = .25$, the lift increases and decreases almost linearly with angle of attack, Figure 29, with an elliptical shape due to lag effects. This confirms well that the linear theory and quasi-steady approximation is adequate at low μ. When the analysis is extended to higher advance ratios, Figure 30-32, the curves deviate from linearity for high angles of attacks. In Figure 29, lift curves with and without stall effect are

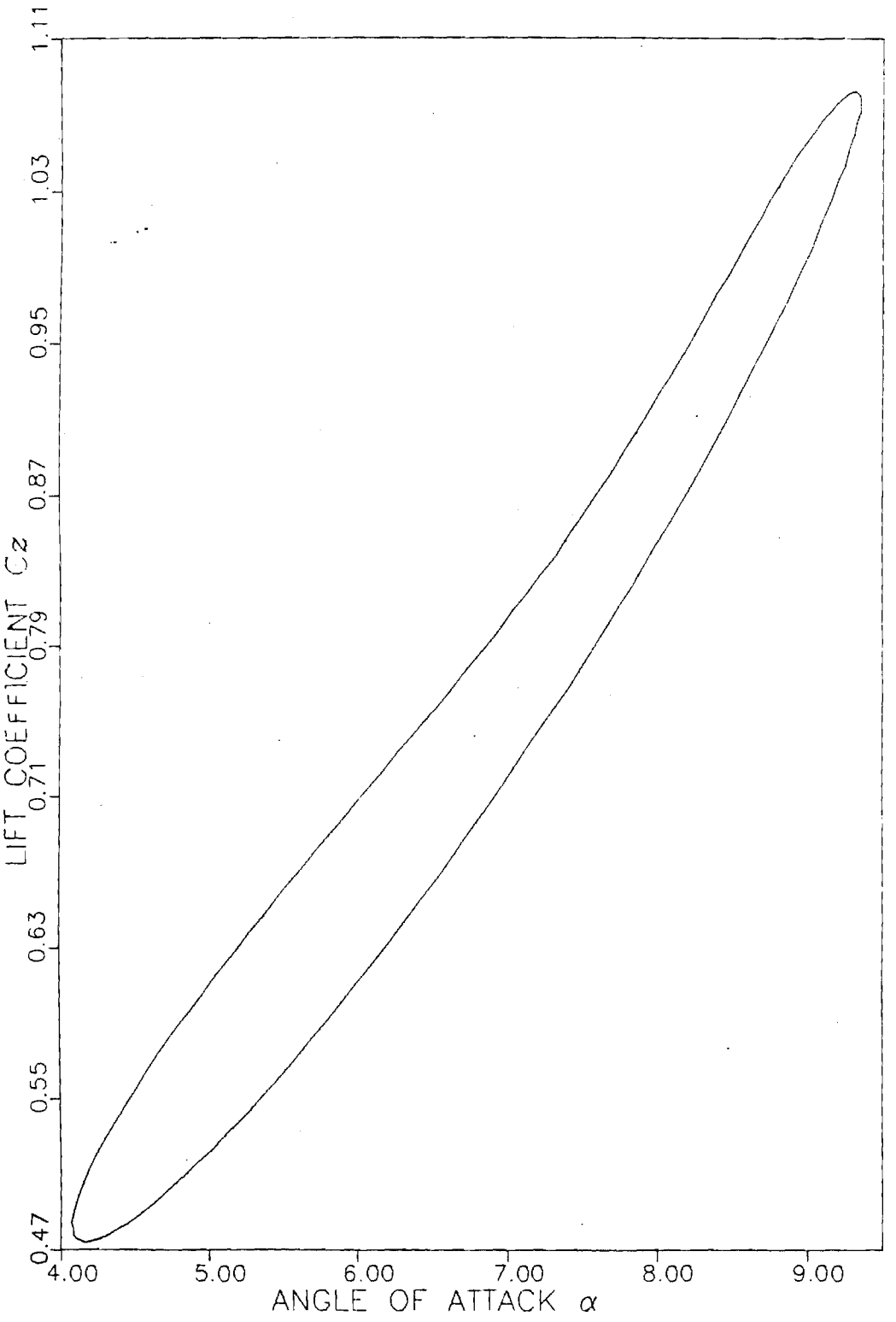

Figure 29. Lift Coefficient, $\mu = 0.20$, $C_T = 0.01$

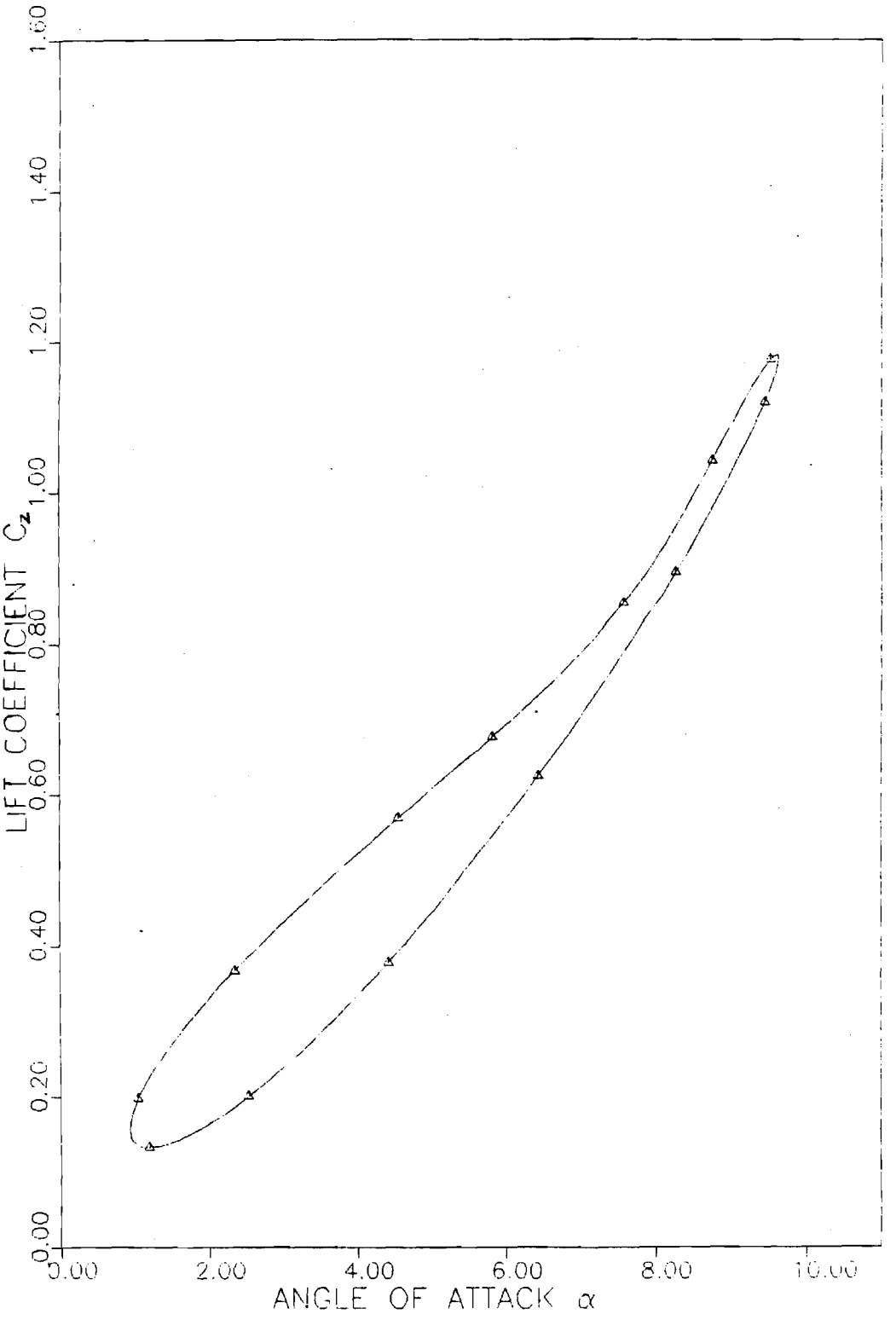

Figure 30. Lift Coefficient, $\mu = 0.3$, $C_T = 0.009$

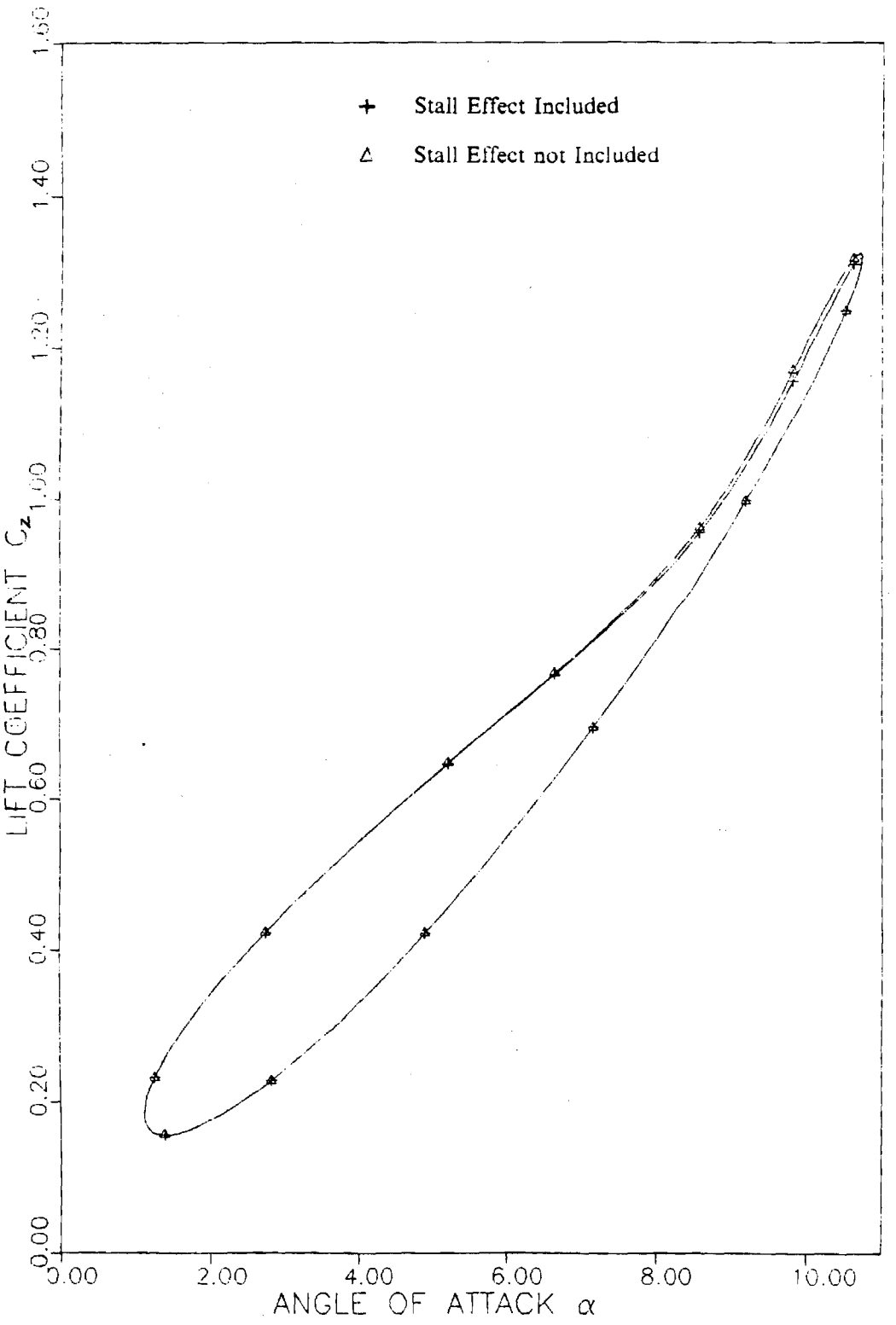

Figure 31. Lift Coefficient, $\mu = 0.3$, $C_T = 0.01$

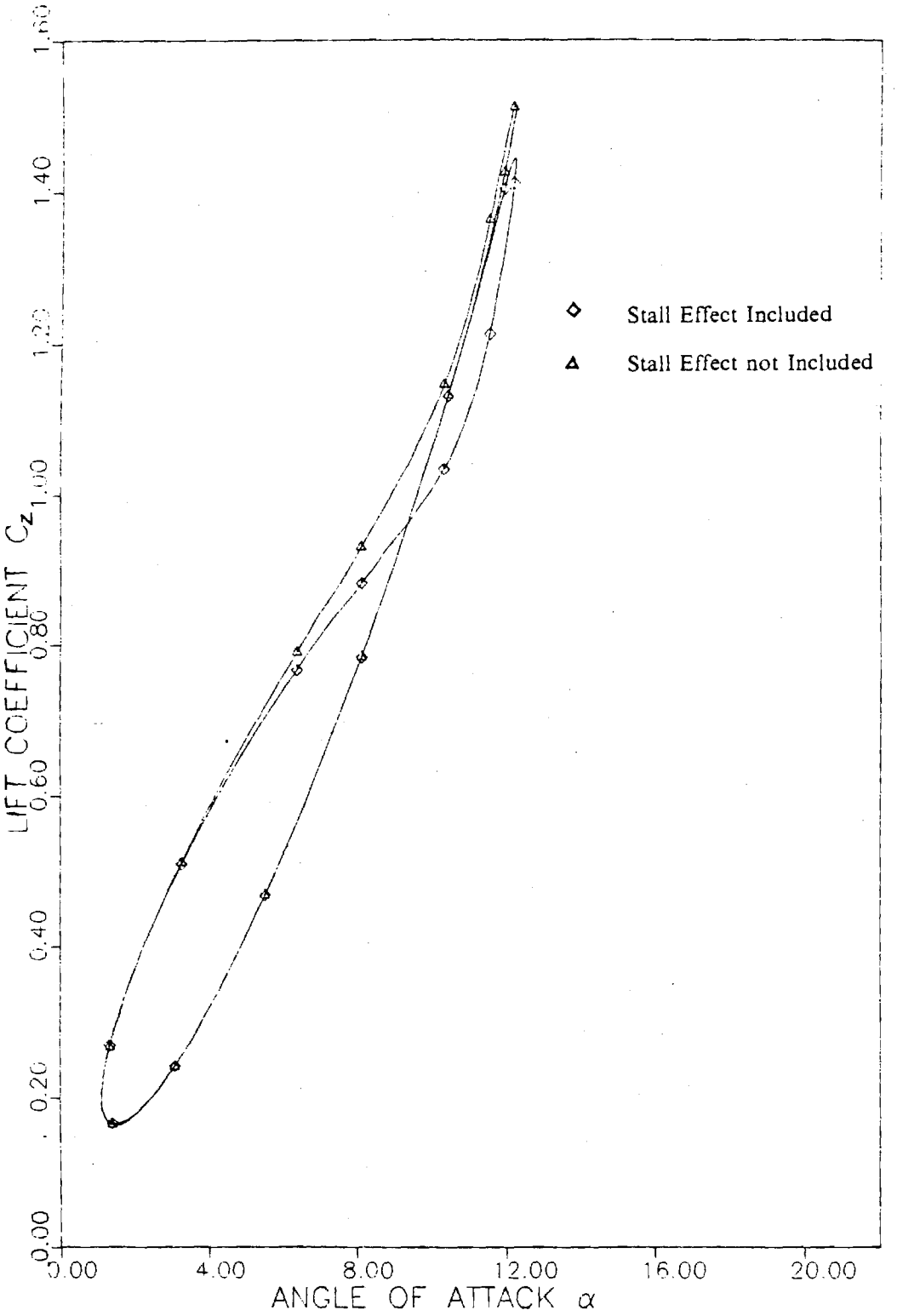

Figure 32. Lift Coefficient, $\mu = 0.3$, $C_T = 0.011$

identical because this case corresponds to an installed condition. When the thrust coefficient is incrased to a value of .010, lift curve including stall predictes a lower lift coefficient at high angles of attack than that which represents the case of a neglected stall effect, Figure 31. Figure 32 shows even a higher effect of stall. It is interesting to see (Figure 30-32) the increase in maximum angle of attack from 9.5° to 10.5° to 11.5° as C_T is varied from 0.009 to 0.010 to 0.011. The effect of stall increases accordingly. The stall can be seen to have a major effect and the classical theory does not lead to a right prediction at high angles of attack.

5. SUMMARY AND CONCLUSIONS

A unified-aerodynamic model has been introduced in the elastic-blade equations derived in Reference (7). This model is an extension of the ONERA lift model and includes plunge, unsteady free stream, and large angles of attack. An ordering scheme has been used to segregate the important terms from others. The elastic-blade equations are presented as lower-order terms and higher-order terms in the of flap, lag, and circulation equations. A solution method based on a modified Galerkin's method is used to separate the time and space variables in the differential equations. A numerical solution is obtained by solving the equations for time history. Two methods have been used for trimming purposes. Dynamic response has been conducted for a variety of thrust coefficients and advance ratios. Results lead to the following conclusions:

- The approximate method, in which pitch settings are approximated, gives large once-per-rev oscillations in the flap response.

- Automatic controllers eliminate the once-per-rev and are used successefully beyond stall limit.

- In highly stalled conditions, the automatic controllers displays a lack of convergence.

- The average bending in the flap direction is approximately independent of the advance ratio and increases in nearly-proportional manner with thrust coefficient. The 2/rev flap bending varies roughly as the advance ratio squared.

- The magnitude of inplane bendings increases up to a certain value of advance ratio and then begins to decrease. The amplitude of inplane bending vibrations is not effected by the speed change.

- The magnitude of inplane bending increases with the increase of the thrust coefficient. The amplitude of vibrations, however, maintains approximately a constant value.

Control settings depend on the advance ratio, thrust coefficient, and stall effects. For a constant thrust coefficent and variable advance ratio

- The collective and lateral pitch angles, θ_0, θ_c decrease to a minimum and then increase. Beyond stall boundaries, they decrease.

- The lateral cyclic pitch θ_c increases in magnitude with advance ratio. It continues to increase in the stalled conditions to account for the loss of lift in the retreating blade due to higher advance ratio.

For a variable thrust coefficient and constant advance ratio, the pitch settings vary as follow

- The magnitude of the three pitch cyclics, θ_0 , θ_s and θ_c increase in a nearly parabolic manner with thrust.

- They react beyond the stall boundaries similarly to the case of variable advance ratio.

The variation of lift coefficient agrees well with the linear theory for small angles of attack. At higher angles of attack, however, the model predicts a loss of lift due to stall effect.

In the future, more work is needed in order to investigate the trimming procedure. The approximate method based on constant cyclic pitch settings requires further investigation to account for nonuniform induced flow, large angles of attack, and stall effect. The present research may be extended to include the elastic-blade response and torsion effect.

6. ACKNOWLEDGEMENT

The author would like to thank Dr. David Peters for his guidance and moral support during this research.

This work was sponsored by the United States Army Research Office, Grant No. DAAG-29-80-C-0092. The view, opinions, and/or findings of this report are those of the author and should not be construed as an official Department of the Army position, policy, or decision, unless so designated by other documentation.

7. APPENDICES

APPENDIX 7.1

Galerkin Integrals

In section 3, Galerkin's method is used to obtain an approximate solution to the flap and lag equations. The coefficients of these equations have, in general, integral forms. The integrands consist of a product of comparison functions or their derivatives. The domain of integration is from 0 to 1 for hingless or centrally-hinged-articulated rotors, and from $\bar{e}$ to 1 for articulated rotor with a hinge offset e; where $\bar{e}$ is the nondimensional hinge offset, $\bar{e} = \frac{e}{R}$.

$$I1'_i = \int_0^1 V_i d\bar{x}$$

$$I2'_i = \int_0^1 \bar{x} W_i d\bar{x}$$

$$I3'_i = \int_0^1 \bar{x}^2 W_i d\bar{x}$$

$$I4_{il} = \int_{(l-x)\Delta\bar{x}}^{l\Delta\bar{x}} W_i d\bar{x}$$

$$I4'_{il} = \int_{(l-x)\Delta\bar{x}}^{l\Delta\bar{x}} V_i d\bar{x}$$

$$I4''_l = \int_{(l-x)\Delta\bar{x}}^{l\Delta\bar{x}} \bar{x} d\bar{x}$$

$$I5_{il} = \int_{(l-x)\Delta\bar{x}}^{l\Delta\bar{x}} \bar{x} W_i d\bar{x}$$

$$I6_{ij} = \int_0^1 W_i W_j d\bar{x}$$

$$I6'_{ij} = \int_0^1 V_i V_j d\bar{x}$$

$$I7_{ij} = \int_0^1 W_i^+ W_j^+ d\bar{x}$$

$$I8_{ij} = \int_0^1 W_i^{++} W_j^{++} d\bar{x}$$

$$I8'_{ij} = \int_0^1 V_i^{++} W_j^{++} d\bar{x}$$

$$I9_{ij} = \int_0^1 W_i W_j^+ d\bar{x}$$

$$I10_{ij} = \int_0^1 \frac{1}{2}(1 - x^2) W_i^+ W_j^+ d\bar{x}$$

$$I10'_{ij} = \int_0^1 \frac{1}{(1 - x^2)} V_i^+ V_i^+ d\bar{x}$$

$$I11_{ijl} = \int_{(l-1)\Delta\bar{x}}^{l\Delta\bar{x}} W_i W_j d\bar{x}$$

$$I11'_{ijl} = \int_{(l-1)\Delta\bar{x}}^{l\Delta\bar{x}} V_i W_j d\bar{x}$$

$$I11''_l = \int_{(l-1)\Delta\bar{x}}^{l\Delta\bar{x}} \bar{x}^2 d\bar{x}$$

$$I12_{ijl} = \int_{(l-1)\Delta\bar{x}}^{l\Delta\bar{x}} W_i W_j^+ d\bar{x}$$

$$I12'_{ijl} = \int_{(l-1)\Delta\bar{x}}^{l\Delta\bar{x}} V_i W_j^+ d\bar{x}$$

$$I13_{ijk} = \int_0^1 W_i \left(\int_0^{\bar{x}} W_j^+ W_k^+ d\bar{x} \right) d\bar{x}$$

In the above integrals, the prime mark indicates that the integral is a coefficient of the elastic lag equation. On the other hand, the double prime indicates that the integral is a coefficient of either the flap or lag equations in the rigid mode.

Appendix 7.2

Profile Drag Components

The profile drag force is applied on the aerodynamic center of the airfoil in the free stream direction. The quasi-steady expression is

$$\overline{D} = C_D(\theta)(U_x^2 + U_y^2)$$

The horizontal and vertical components are approximately

$$\overline{D}_x = C_B(U_x^2 + \frac{1}{2}U_y^2)$$

$$\overline{D}_y = C_D(U_xU_y + \frac{1}{2}\frac{U_y^3}{U_x})$$

The velocity components U_x and U_y are presented in section 2.4. In a similar manner the scaling procedure is applied to obtain U_x^2 , U_y^2 , and U_xU_y

$$U_x^2(1, \varepsilon^2) = (\overline{x} + \mu \sin\psi)^2$$

$$+ 2(\overline{x} + \mu \sin\psi)\{[\overline{v}^+ + \overline{w}^+(\theta + \phi)]\mu \cos\psi + \dot{\overline{v}} + \overline{u} - \frac{1}{2}(\theta + \phi)^2(\overline{x} + \mu \sin\psi) + (\overline{V}_i + \dot{\overline{w}})(\theta + \phi)\}$$

The other terms in U_x^2 expression are of order $\varepsilon^4$and higher.

$$U_y^2(\varepsilon^2) = (\overline{x} + \mu \sin\psi)^2(\theta + \phi)^2 + (\overline{w}^+\mu \sin\psi + \overline{V}_i + \dot{\overline{w}})^2 - 2(\overline{x} + \mu \sin\psi)(\theta + \phi)(\overline{w}^+\mu \cos\psi + \overline{V}_i + \dot{\overline{w}})$$

The other terms in U_y^2 expression are of order ε^4 and higher.

$$U_yU_x = (\overline{x} + \mu \sin\psi)[(\overline{x} + \mu \sin\psi)(thata + \phi) - (\overline{w}^+\mu \cos\psi + \overline{V}_i + \dot{\overline{w}})]$$

The other terms in $U_x U_y$ expression are of order ε^3 and higher. $\frac{U_y^3}{U_x}$ has terms of order higher or equal to ε^3 .

If we consider C_D of order ε , the x and y components of the nondimensional drag force of order lower or equal to ε^3 can be obtained by substitution of the appropriate components from the above equations.

8. NOMENCLATURE

a : airfoil lift curve slope, ($= 2\pi/radian$)

A_0, A_1 : gains

b : blade semi chord, $\frac{c}{2}$

c : blade chord, m

C_D : drag force coefficient

C_T : thrust coefficient

C_z : lift coefficent, $\frac{\bar{L}}{U^2}$

C_{zl} : static lift coefficient in the linear region

C_{zs} : static lift coefficient

d : stall damping parameter

e : phase shift parameter

D : airfoil profile drag per unit length, N/m

E : Young's modolus, N/m^2

$\bar{f}$: flat plate drag coefficient

F_x, F_y : aerodynamic forces per unit length in the deformed blade, N/m

$I_{y'}$, I_z : cross-sectional area moment of inertia, m^4

k : inverse of reduced velocity, $= \frac{\Omega b}{V} = \frac{\bar{b}}{(\bar{x} + \mu \sin \psi)}$

$\bar{k}$: average value of k, $\frac{\bar{b}}{\bar{x}}$

K_β : stiffness of flap root spring, $N - m/rad$

K_ζ : stiffness of lag root spring, $N - m/rad$

L : aerodynamic lift per unit length, N/m

L_a, L_N : circulatory and non circulatory lift respectively, N/m

L_u, L_v, L_w : generalized aerodynamic forces per unit length in the undeformed reference system, N/m^2

m : mass per unit length of the blade, kg/m

p : flap frequency, per revolution

R : blade length, m

s : apparent mass coefficient

t : time, sec

U : blade airfoil velocity with respect to air, *m/* sec

U_x : velocity component of blade airfoil parallel to the chord, *m/* sec

U_y : velocity component of the blade airfoil perpendicular to the chord, *m/* sec

u, v, w : elastic deformation in x, y, z directions respectively, *m*

V_i : induced downwash velocity, *m/* sec

$V(\bar{x}), W(\bar{x})$: comparison functions for bending

x : inertial coordinate system for undeformed blade, *m*

x, y, z : inertial coordinate system for undeformed blade

x', y', z' : inertial coordinate system for deformed blade

α : airfoil angle of attack, *rad*

β : rigid blade flap angle, *rad*

γ : Lock number

$\bar{\Gamma}$: nondimensional circulation, $\frac{\bar{L}}{U}$

ε : scaling parameter in the ordering scheme, (= .1)

ζ : rigid blade lag angle, *rad*

θ : blade pitch angle, *rad*

$\theta_0, \theta_c, \theta_s$: collective and cyclic pitch, *rad*

τ_0, τ_1 : time constants

σ : rotor solidity

ρ : air denstiy

ϕ : inflow angle,
elastic torsional deformation, *rad*

λ : time delay parameter

μ : advance ratio

ψ : nondimensional time, $\psi = \Omega t$

Ω : rotor blade angular velocity, $\frac{rad}{sec}$

$\dot{\bar{\varepsilon}}$: rate of rotation of the airfoil with respect to air mass taken with respect to nondimensional time, $\frac{rad}{\sec}$

$()_x, ()_y$: x and y components

$(\cdot)$: $\frac{\partial}{\partial \bar{t}}$

$(^+)$: $\frac{\partial}{\partial \bar{x}}$

$(^*)$: $\frac{\partial}{\partial \psi}$

$()_1, ()_2$: unstalled, stalled contributions

9. BIBLIOGRAPHY

1. Carta, F. O. and Carlson, R. G., "Determination of Airfoil and Rotor Blade Dynamic Stall Response," *Journal of the American Helicopter Society*, Vol. 18, No. 2, April 1973, pp.31-39.

2. Gangwani, S., "Prediction of Dynamic Stall and Unsteady Airloads for Rotor Blades," Proceedings of the 37th Annual National Forum of American Helicopter Society, New Orleans, May 1981, pp. 1-17.

3. Tran, C. T. and Petot, D., "Semi-Emperical Model for the Dynamic Stall of Airfoil in View of the Application to the Calculation of Responses of a Helicopter Blade in Forward Flight," *Vertica*, Vol. 6, 1982, pp. 219-239.

4. Rogers, J. P., "Application of an Analytic Stall Model to Dynamic Analysis of Rotor Blades," *Journal of the American Helicopter Society*, Vol. 29, No. 1, January 1984, pp. 25-33

5. Rudy, D. J., *"Comparison of Rotor Blade Flapping Response with Three Different Dynamic Stall Models,"* Master of Science Thesis, Washington University, May 1983.

6. Peters, D., "Toward a Unified Lift Model for Use in Rotor Blade Stability Analyses," *Journal of the American Helicopter Society*, Vol. 30, No. 3, July 1985, pp. 32-42

7. Karunamoorthy, S. N., *"Use of Hierarchical Elastic Blade Equations and Automatic Trim For Helicopter Vibration Analysis,"* Doctor of Science Thesis, Washington University, August 1985.

8. Peters, Kim, and Chen, S-Y, "Calculation of Trim Settings for a Helicopter Rotor by an Optimized Automatic Controller," *Journal of Guidance and Control*, Vol. 7, No. 1, Jan.-Feb. 1984, pp. 85-91

9. Wheatley, J. B., "An Analytical and Experimental Study of the effect of Periodic Blade Twist on the Thrust, Torque, and Flapping Motion of an Autogyro Rotor," NACA Rep. 591, 1937.

10. Wei, F-S and Peters, D. A. "Lag Damping in Autorotation by a Perturbation Method." Proceedings of the 34th Annual National Forum of the American Helicopter Society. Washington, D.C., May 1978.

11. Wei, F-S, *"Flap-Lag Stability of Helicopter and Windmill Rotor Blades in Powered Flight and Autorotation by a Perturbation Method,"* Doctor of Science Thesis, Washington University, 1978.

12. Kim, B. S., *"Control Settings for a Trimmed, Stalled Rotor by an Automatic Feedback System."* Master of Science Thesis, Washington University, 1980

13. Friedmann, P.P and Kottapalli, S-B-R, "Coupled Flap-Lag-Torsional Dynamics of Hingeless Rotor Blades in Forward Flight," *Journal of the American Helicopter Society*, Vol-27, No. 4, October 1982, pp. 28-36

14. Panda, Brahmananda and Chopra, Inderjit, "Flap-Lag-Torsion Stability in Forward flight." Proceedings of the 2nd Decennial Specialists' Meeting on Rotorcraft Dynamics, Ames Research Center, Moffett Field, California, Nov. 7-9, 1984, Paper No. 16.

15. Panda, Brahmanda and Chopra, Inderjit, "Flap-Lag-Torsion Stability in Forward Flight," *Journal of the American Helicopter Society*, Vol. 30, No. 4, October 1985, pp. 30-39

10. VITA

Biographical items on the author of the thesis, Mr. Mnaouar Chouchane.

1. Born October 5, 1960

2. Attended the Professional School of Higher Technical Education (E.N.S.E.T), University of Tunis, Tunisia from 1980 to 1984. Received a Bachelor of Science Degree in Mechanical Engineering in June 1984.

3. Part time High-school instructor of general mechanics and mechanical design from October 1983 to May 1984.

4. Awarded a national scholarship in 1984 for a graduate studies in the U.S.A.

5. Attended Washington University in Saint. Louis, Missouri from August 1984 to August 1985 as a full time student and from September 1985 to present as a part time student. Working on Master of Science Degree in Mechanical Engineering.

6. Attended the School of Aerospace Engineering, Georgia Institute of Technology in Atlanta, Georgia from September 1985 to present.

7. Member American Helicopter Society.

August, 1986

USE OF HIERARCHICAL ELASTIC BLADE EQUATIONS AND AUTOMATIC TRIM FOR ROTOR RESPONSE

Swami N. Karunamoorthy
Assistant Professor
Parks College of St. Louis University
Cahokia, Illinois

and

David A. Peters
Professor
School of Aerospace Engineering
Georgia Institute of Technology
Atlanta, GA 30332

Abstract

A unified approach has been developed to obtain the elastic blade equations in forward flight, when a blade undergoes flap, lag, and torsional motions. The mathematical model used in this analysis includes a tensor approach for strain components, a curvilinear coordinate system, a new and consistent ordering scheme, modified Greenberg's aerodynamic theory, and an optimized automatic controller for trim settings. These are the vital building blocks used to obtain the equations of motion. Although some of these features are found in the literature piecewise, the present analysis brings all of them together under one unified umbrella. The hierarchical nature of the elastic blade equations leads to the possibility of reducing them to various orders. A new family of orthogonal polynomials is developed for the purpose of applying a Galerkin time-history solution. The results show that this is a viable approach.

Nomenclature

A	:cross-sectional area of the blade, m^2
a	:airfoil lift curve slope, ($=2\pi$/radian)
c	:blade chord, m
c_{d_o}	:airfoil profile drag coefficient
D	:airfoil profile drag per unit length, N/m
e_{ij}	:strain tensor components
J	:torsional rigidity constant, m^4
k_A	:blade cross-section polar radius of gyration, m
k_m	:blade cross-section mass radius of gyration, m
k_{m_1}, k_{m_2}	:principal mass radii of gyration, m
L_u, L_v, L_w	:generalized aerodynamic forces per unit length in the undeformed blade, N/m
m	:mass per unit length of the blade, kg/m
M_ϕ	:generalized aerodynamic moment per unit length, N-m/m
p	:flap frequency, n/rev
R	:radius of the rotor disc, m
$\vec{r}_o$	:position vector of undeformed blade
$\vec{r}$	:position vector of deformed blade
T	:tension,N; also kinetic energy, kg - m^2/sec^2
U	:strain energy, N - m
u,v,w	:elastic deformations in x,y,z directions respectively, m
V_i	:induced downwash velocity, m/sec

x :blade axial coordinate, m

x,y,z :inertial coordinate system for undeformed blade;

α :warp amplitude in structural context

β :rigid blade flap angle

γ :Lock number

$\bar{\gamma}$:analogus Lock number ($\bar{\gamma} = 3\gamma$)

δ :variational operator, or first variation

ε :scaling parameter in the ordering scheme, (=.1)

ξ, η :blade cross-section principal axes coordinates; also ξ denotes rigid blade lag angle

θ_e :blade pre-twise, structural, rad

θ :blade pre-twist, aerodynamic or the pitch angle, rad

θ_0 :collective pitch angle, rad

θ_s :longitudinal cyclic angle, rad

θ_c :lateral cyclic pitch angle, rad

λ :warp function, nondimensional root spring = $\frac{RK\beta}{EI}$

Λ_5, Λ_6 :dimensionless bending stiffness

Λ_9 :dimensionless shear modulus

Λ_{11} :dimensionless radial stiffness

μ :advance ratio

τ :dimensionless tension

ϕ :elastic twist or torsional deformation

ϕ_0 :rigid blade torsional parameter

$\Phi(\bar{x})$:comparison functions for torsion

ψ :dimensionless time; also azimuth angle

Ω :rotor blade angular velocity, rad/sec

$(\bar{\ })$:nondimensional form

$(\ )'$:$\partial/\partial x$

$(\ )^{+}$:$\partial/\partial \bar{x}$

$(\dot{\ })$:$\partial/\partial t$

$(\check{\ })$:$\partial/\partial \Psi$

$(\vec{\ })$:denotes a vector

Introduction

In present-day developments of helicopter dynamics, the rotor blade is no longer treated as rigid. Dynamic response and load analysis depend on the flexibility of the blade. In general, a rotor blade undergoes inplane bending, vertical bending, and torsional motion which are know as lag, flap, and torsion (Figure 1). These bending and torsional motions couple with each other which leads to kinematical nonlinearity. Apart from these elastic and inertial forces, the shape of the blade and the free stream velocity give rise to aerodynamic forces. These forces are transmitted to the rotor hub as periodic forces and moments which, in turn, are transmitted to the fuselage through the rotorshaft and transmission. These forces may cause: (i) damage to the helicopter structure due to frequency coalescence, (ii) faulty readings in the instrument panel due to excessive vibration, or (iii) unpleasant noise and poor ride quality which can be uncomfortable for both the pilot and passengers.

To prevent these vibratory loads from developing and being transmitted to the fuselage, we need to know the exact magnitude of the forces acting on the blade. The prediction of these loads demands rigorous mathematical modeling and well-documented equations of motion. The derivation of the equations of motion for the complete helicopter needs to incorporate blade-to-blade and rotor-body couplings. However, the single-blade behavior is important and can be helpful in understanding the behavior of the complete system. Thus, the dynamics of a single blade forms an important fundamental building block in the study of helicopter dynamics.

In present helicopter technology, there is interest both in hingeless rotors and in articulated rotors. In hingeless rotors, the blades are attached directly the hub with flexures rather than through discrete flap or lead-lag hinges. This configuration is often preferred over conventional designs because of its reduced mechanical complexity and improved flying qualities. Therefore, an adequate set of equations should be applicable to both articulated and hingeless rotors.

Unlike fixed-wing aircraft, the helicopter undergoes two modes of flight, known as (i) hover, and (ii) forward flight. The equations for forward are cumbersome and an order of magnitude more complicated than the equations for hover. Of course, the equations for hover are a special case of the forward flight equations. It is forward flight, however, in which vibrations become important, Therefore, equations of motion adequate for vibrations must include forward flight.

Thus, the objectives of the present research work are (i) to develop a mathematical model for a single blade of a rotor in forward flight, (ii) to derive the nonlinear aeroelastic equations of motion, and (iii) to obtain the steady state response after all the transients die out.

Previous Work

The early analytical work shows a step-by-step advance in the analysis of rotor blades. First, only flapping motion was considered. In 1928, Glauert and Lock , Ref. 1, analysed the rigid flap model in hover. In 1937, Wheatley, Ref. 2, extended the analysis to forward flight. Elastic flap in hover was treated by Perisho, Ref. 3, in 1959. Peters and Ormiston, Ref. 4 have

investigated elastic flapping in forward flight in 1975. Later, lagging motion was included by Ormiston and Hodges, Ref. 5,6, in the case of hover. They investigated both rigid and elastic flap-lag dynamics during 1972 and 1973. In forward flight, rigid and elastic flap-lag cases were considered by Schrage and Eipe, Ref. 7,8, respectively during 1978-1979. In 1971, Miao, Ref. 9, included torsion in flap-lag dynamics of rigid blade in hover. In 1973, Peters, Ref. 10, analysed the problem in the case of forward flight. Elastic flap-lag-torsion in hover was investigated by Hodges and Dowell, Ref. 11, in 1974 and by Friedmann, Ref. 12, in 1977. The same problem in forward flight was considered by Freidmann and Kottapalli (Ref. 28) using the structural model developed in Ref. 13.

The addition of torsion to flapwise bending and chordwise bending (without aerodynamics) actually dates back to the early work of Houbolt and Brooks, Ref. 14, in 1958. That work, and the later work in References 11-13, add torsion via the use of Wagner's hypothesis which assumes that a beam consists of a group of straight fibres in the untwisted state that carry the axial stress. However, in the twisted state, the fibres no longer remain straight; and they twist with the cross section. The axial stress that is assumed to act along the fibres produces a couple about the neutral axis. However, Wagner's hypothesis does not strictly hold for a pretwisted beam, as pointed out by Hodges, Ref. 15. Moreover, when the rotor blade twists, the coordinate system becomes curved, which demands the use of a curvilinear coordinate system. Hodges has applied the curvilinear coordinate system in the investigation of tension-torsion, Ref. 15. Present work demonstrates its application to the coupling of torsion with vertical and inplane bending. The above literature pertains to the structural part of the problem and reveals an interesting fact, namely that much of the helicopter elasto-dynamics begin to develop after the year 1970.

Looking into the advancements of aerodynamics, the fundamental work dates back to the work of Theodorsen, Ref. 16. His classical theory, developed in 1935, included unsteady pitching motion and plunging motion of an airfoil. In 1947, Greenberg, Ref. 17, included unsteady free stream in addition to unsteady pitch and plunge. His model is based on potential flow theory and it forms a basis for most of the present literature. In 1957, Loewy, Ref. 18, formulated a model to accommodate the three-dimensional effects of blade rotation on the lift due to unsteady pitch and plunge. He suggests that lift and moment expressions used in the fixed-wing flutter theory may be used directly for the rotary-wing airfoil in harmonic motion, except that Theodorsen's function of reduced frequency, C(k), must be modified to include the effects of the number of blades in the rotor, the ratio of oscillatory frequency to rotational frequency, and the inflow ratio. In 1980, Johnson, Ref. 19, included the unsteady vertical velocity in Greenberg's model. In the same year, Tran and Petot, Ref. 20, implemented a dynamic stall model that includes unsteady pitch and plunge.

The present work is based on Greenberg's aerodynamic theory, and it is applied as recommended by Johnson. In this analysis, the equations are first modified to rotary-wing application through a suitable change of variable, and then a quasi-steady approximation is applied.

Scope of Work

The flap-lag-torsion equations in the available literature often suffer from: (i) inappropriate choice of coordinate system, (ii) inconsistent ordering scheme, and (iii) poor documentation. The present work includes:

1. Curvilinear coordinate system has been used.

2. Strain energy and strain components are obtained by a tensor approach.

3. The equations are well documented such that others can verify them.

4. A more consistent approach is used in the development of virtual work.

5. A rigorous, quasi-steady aerodynamic model has been formulated.

6. A new ordering scheme has been developed, and it is used consistently.

7. Inextensibility is automatically considered by the ordering scheme.

8. Nonlinear aeroelastic equations of motion are derived with flap, lag, and torsional degrees of freedom for an elastic blade in forward flight.

In the solution scheme, (i) Galerkin procedure is used to transform the nonlinear partial differential equations to nonlinear ordinary differential equations, (ii) A new family of orthogonal polynomials has been developed for the evaluation of Galerkin integrals, (iv) Hamming's predictor-corrector method is used to obtain the dynamic response, and (v) Auto-Pilot equations are incorporated to find the trim settings.

Formulation of Elasto-Dynamics

The equations of motion for a helicopter blade fall under the general category of elasto-dynamics. The development of these equations requires the choice of appropriate assumptions followed by consistent application of the laws of motion and elasticity. The assumptions used in the present analysis are, (i) the blade is flexible in flap, lag, and torsional directions, (ii)

the blade is sufficiently long and slender so that a uni-axial stress state is invoked, (iii) the blade is pretwisted and nonuniform, (iv) the cross section of the blade is symmetric about the chord and undergoes warping, (v) the warping function is antisymmetric, (vi) the blade is prismatic and has no pre-coning, and (vii) the elastic axis, inertia axis, and tensile axis are at the aerodynamic center of the blade cross-section.

To derive the appropriate expressions, we begin with the geometry of a generic cross-section. The position vector of an arbitrary point after deformation of blade is given by Ref. 21.

$$\vec{r} = x_1\vec{i} + y_1\vec{j} + z_1\vec{k}$$

$$\begin{aligned}\vec{r} = [x + u + \lambda\alpha - v'\{\eta\cos(\theta_e+\phi) - \zeta\sin(\theta_e+\phi)\} - w'\{\eta\sin(\theta_e+\phi) + \zeta\cos(\theta_e+\phi)\}]\vec{i} \\ +[v + \eta\cos(\theta_e+\phi) - \zeta\sin(\theta_e+\phi)]\vec{j} + [w + \eta\sin(\theta_e+\phi) + \zeta\cos(\theta_e+\phi)]\vec{k}\end{aligned} \tag{1}$$

By setting u,v,w,ϕ,α to zero, the position vector for the undeformed blade can be obtained as;

$$\vec{r}_0 = \vec{r}\big|_{u=v=w=\phi=\alpha=0}$$

$$\vec{r}_0 = x\vec{i} + (\eta\cos\theta_e - \zeta\sin\theta_e)\vec{j} + (\eta\sin\theta_e + \zeta\cos\theta_e)\vec{k} \tag{2}$$

The strain tensor can be expressed as Ref. 21,

$$e_{11} = u' + \lambda\alpha' - v''\{\eta\cos(\theta_e+\phi) - \varsigma\sin(\theta_e+\phi)\} - w''\{\eta\sin(\theta_e+\phi) + \varsigma\cos(\theta_e+\phi)\}$$
$$+(v'^2/2) + (w'^2/2) + (\eta^2+\varsigma^2)(\phi'^2/2) + \alpha\theta_e'(\varsigma\lambda_\eta - \eta\lambda_\varsigma) \quad (3)$$

$$2e_{12} = \lambda_\eta\alpha - \varsigma\phi' \quad (4)$$

$$2e_{13} = \lambda_\varsigma\alpha + \eta\phi' \quad (5)$$

where $\lambda_\eta = \partial\lambda/\partial\eta$; $\quad \lambda_\varsigma = \partial\lambda/\partial\varsigma$

Hamilton's Law

The next step in the derivation is to apply Hamilton's Law to obtain equations of motion. Hamilton's Law of Varying Action leads to Euler-Lagrange equations directly and it can be expressed as,

$$\int_{t_1}^{t_2}(\delta U - \delta T - \delta W)dt + (\partial T/\partial\dot{q}_i)\delta q_i\Big|_{t_1}^{t_2} = 0. \quad (6)$$

where, δU and δT are the variations in strain energy and kinetic energy and δW is the virtual work.

Ordering Scheme

In working out the nonlinear elastic blade equations, the algebra involved is very complex and leads to a large number of terms. To avoid over-complication in the equations, it is necessary to neglect the higher

order term. This requires some kind of scaling scheme to measure the order of the terms and to judge their importance in the given context. Epsilon (ε) is used as a scaling parameter which has the magnitude of one tenth and hence its square is equal to one percent. Now, the principle behind its application is that each term is assigned a certain order based on physical considerations and then terms of higher order are neglected.

The existing ordering schemes in the available literature are mainly for stability analysis. Also, they suffer from (i) lack of a strong basis for their development, and (ii) lack of efficiency in retaining all lower order terms. Therefore, a new ordering scheme has been developed from a vibration point of view, and it is based on physical data for two different typical helicopter rotors. The numerical values of certain structural parameters are given in Table 1, and the ordering of some dimensionless parameters is given in Table 2. It is interesting to observe that, despite the major differences in blade design, the two rotors have nearly that same nondimensional data.

The length of the rotor blade being significant, the elastic deformations u,v,w and their derivatives may not be of the same order over entire length of the blade. An illustrative problem has been solved for this purpose and the results show that the ordering of elastic deflections is different from that of their spatial derivatives over various regions of the blade, Ref. 21. These results are also used in ordering the equations.

As far as other implications of the ordering scheme, we should also mention that we have taken the advance ratio μ to be of the order $\varepsilon^{1/2}$. This implies that reversed flow terms, which are of the order $\frac{\gamma}{24}\mu^4$, are of order

ϵ^3 less than the leading terms. Thus, reversed flow is consistently neglected to all orders in this paper.

Quasi-Steady Aerodynamics

The assumptions made in the derivation of the aerodynamic forces and moments are, (i) the reduced frequency, k, is set equal to zero so that C(k)=1 which leads to quasi-steady approximation, (ii) blade stall, compressibility, and reversed flow are neglected, (iii) the flow is uniform and unsteady, (iv) radial flow is neglected, and (v) the airfoil undergoes unsteady pitching and plunging motion.

Considering the ordering of the aerodynamic terms, Lock number and the advance ratio are assumed to be of order unity. The pitching motion (Θ), and the rotational rate (α) are considered to be of order ϵ. The dimensionless chord and induced velocity are found to be of same order as the pitching motion. To summarize,

$$\frac{1}{6}\gamma, \quad \mu = O(1)$$

$$\alpha, \quad \theta, \quad \bar{V}_i, \quad \bar{c} = O(\epsilon)$$

$$\bar{c}(1/4), \quad \bar{c}^2, \quad (c_{d_o}/a) = O(\epsilon^2)$$

$$\bar{c}^2(1/16) = O(\epsilon^3)$$

Hierarchical Equations

The equations pertaining to lower order without any offsets and precone are given in this paper. The detailed equations of both lower and higher order with all the cross sectional offsets, precone, tip sweep and droop are given in Ref. 21.

Tension Equation $(1, \epsilon^2)$:

$$\underline{-\tau^+ - \bar{x} - \bar{u} - 2\breve{\bar{v}} + \breve{\breve{\bar{u}}}} = \bar{L}_u \tag{7}$$

Flap Equation (ξ, ϵ^3):

$$\underline{-(\tau\bar{w}^+)^+} + (\Lambda_5 - \Lambda_6)(\theta_e + \phi)\bar{v}^{++++} + \underline{\breve{\breve{\bar{w}}}}$$

$$+\{\Lambda_6 + (\Lambda_5 - \Lambda_6)(\theta_e + \phi)^2\}\bar{w}^{++++} = \bar{L}_w \tag{8}$$

Lag Equation (ξ^2, ϵ^4):

$$\underline{-(\tau\bar{v}^+)^+} + \{\Lambda_5 + (\Lambda_6 - \Lambda_5)(\theta_e + \phi)^2\}\bar{v}^{++++} + \underline{(\Lambda_5 - \Lambda_6)(\theta_e + \phi)\bar{w}^{++++}}$$

$$+\underline{\breve{\breve{\bar{v}}} - \bar{v}} - 2\underline{\int_0^x \bar{w}^+\breve{\bar{w}}^+} = \bar{L}_v \tag{9}$$

Torsion Equation (ξ^4, ϵ^6):

$$-[\tau(\bar{D}\theta_e^+ + \bar{k}_A^2\phi^+)]^+ + (\Lambda_5 - \Lambda_6)\{\bar{v}^{++}\bar{w}^{++} + (\bar{w}^{++})^2(\theta_e + \phi)\} - \underline{\Lambda_9 J\phi^{++}}$$

$$+\bar{k}_m^2\breve{\phi} + 2\breve{\bar{w}}^+\bar{k}_{m_1}^{-2} + (\bar{k}_{m_2}^{-2} - \bar{k}_{m_1}^{-2})(\theta_e + \phi) = \bar{M}_\phi \tag{10}$$

where, $\bar{D} = D/AR^2$. The tension, τ can be obtained from the equation (7) as,

$$\tau(1,\epsilon^2) = \int_x^1 \bar{x} + \int_x^1 (2\check{v} + \bar{u} - \overset{s}{\bar{u}} + \bar{L}_u) d\bar{x}$$

where,

$$\bar{u}(\epsilon^2) = \frac{1}{2}[\lambda_{11}^{-1}(\bar{x} - \frac{\bar{x}^3}{3}) - \int_0^x \bar{w}^{+^2} d\bar{x}]$$

$$\check{u} = -\int_0^x \bar{w}^+ \check{\bar{w}}^+$$

$$\overset{s}{\bar{u}} = -\int_0^x [\check{\bar{w}}^{+^2} + \bar{w}^+ \overset{s}{\bar{w}}^+] d\bar{x}$$

Therefore,

$$\tau(1) = \frac{1}{2}(1 - \bar{x}^2)$$

$$\tau(\epsilon^2) = \frac{\lambda_{11}^{-1}}{24}(1 - \bar{x}^2)(5 + \bar{x}^2) + \int_x^1 [2\check{v} - \frac{\gamma}{2}\bar{w}^+ \{(\bar{x} + \mu \sin\psi)^2(\theta + \phi)$$

$$-(\bar{x} + \mu \sin\psi)(\bar{V}_i + \check{\bar{w}} + \bar{w}^+ \mu \cos\psi)\}] d\bar{x} + \int_x^1 [\int_0^\xi \{\check{\bar{w}}^{+^2} + \bar{w}^+ \overset{s}{\bar{w}}^+ - \frac{1}{2}\bar{w}^{+^2}\} d\xi] d\bar{x}$$

where ξ is a dummy variable. It is interesting to observe that the lower order tension has only a constant term while the higher order has both a constant part and a variable part. The higher order tension contributes to higher order terms in flap and lag equations; however its contribution to the torsion equation may be ignored, because the terms are of very high order.

The lower order aerodynamic terms ($\bar{L}_u, \bar{L}_v, \bar{L}_w$, and $\bar{M}_\phi$) are given below:

$$L_u(\epsilon^2) = -\frac{\gamma}{2}(\bar{x} + \mu \sin\psi)\bar{w}^+[(\bar{x} + \mu \sin\psi)(\theta + \phi) - (\bar{V}_i + \check{\bar{w}} + \bar{w}^+ \mu \cos\psi)] \tag{11}$$

$$L_w(\epsilon) = \frac{\gamma}{2}[(\bar{x} + \mu \sin\psi)\{(\bar{x} + \mu \sin\psi)(\theta + \phi) - (\bar{V}_i + \check{\bar{w}} + \bar{w}^+ \mu \cos\psi)\}] \tag{12}$$

$$L_v(\epsilon^2) = \frac{\gamma}{2}[(\bar{V}_i + b\check{a}\bar{r}w + \bar{w}^+ \mu \cos\psi)^2 - (\theta + \phi)(\bar{x} + \mu \sin\psi)(\bar{V}_i + \check{\bar{w}} + \bar{w}^+ \mu \cos\psi)$$

$$-\frac{c_{d_o}}{a}(\bar{x} + \mu \sin\psi)^2] \tag{13}$$

$$\bar{M}_\phi(\epsilon^4) = \frac{\gamma}{2}[-\frac{\bar{c}^2}{16}\{(\bar{x} + \mu \sin\psi)\{2(\check{\theta} + \check{\phi}) + \bar{w}^+\} + (\theta + \phi)\mu \cos\psi + \bar{w}^+ \mu \sin\psi$$

$$-(\check{\bar{V}}_i + \check{\bar{w}} + \check{\bar{w}}^+ \mu \cos\psi)\}] \tag{14}$$

The higher order terms are given in Ref. 21.

Solution Technique

In solving the elastic flap, lag, and torsional equations, only the lower order terms in the hierarchy are considered. These equations are nonlinear, variable coefficient, partial differential equations. First, these equations are reduced to nonlinear ordinary differential equations by a modified Galerkin's procedure; which is equivalent to the Rayleigh-Ritz-method. Second, they are expressed in state variable form; and third, the solution is obtained through a numerical scheme. In the Galerkin or Ritz method, the dimensionless bending and torsional deflections are expressed in terms of a series of generalized coordinates and comparison functions. The various possibilities for assumed modes include trigonometric functions, power series, and polynomials. Among these, polynomials are a good choice, because any given mode shape can be approximated by a polynomial, and because polynomials simplify the calculation of Galerkin integrals.

The odd-numbered Legendre polynomials are sometimes used for the articulated blade because they are orthogonal and they satisfy the geometric boundary conditions. For hingeless blades, however, they do not satisfy the boundary conditions, whereas Duncan polynomials, Ref. 22, satisfy both geometric and natural boundary conditions. However, Duncan polynomials are neither orthogonal nor symmetric; and, hence, they may converge slowly. It is interesting to observe in the handbook, Ref. 23, that most of the available orthogonal polynomials are symmetric to the origin. This is what we would like for the Duncan polynomials.

In the present analysis, the Duncan polynomials are first modified to be symmetric functions on the interval -1 to +1. Second, they are orthogonalized by Gram-Schmidt orthogonalization process, Ref. 24; and third, they are normalized with respect to tip deflection.

The first five polynomials are given below:

Bending:

$$W_1 = x \tag{15}$$

$$W_2 = \frac{1}{11}(15x^2 - 5x^4 + x^6) \tag{16}$$

$$W_3 = \frac{1}{16}(15x^7 - 63x^5 + 105x^3 - 41x) \tag{17}$$

$$W_4 = 2.61x^8 - 10.1x^6 + 14x^4 - 5.51x^2 \tag{18}$$

$$W_5 = 10.23x^9 - 38.93x^7 + 52.98x^5 - 26.9x^3 + 3.62x \tag{19}$$

Torsion:

$$\Phi_1 = 1 \tag{20}$$

$$\Phi_2 = \frac{1}{2}(3x - x^3) \tag{21}$$

$$\Phi_3 = \frac{1}{8}(30x^2 - 15x^4 - 7) \tag{22}$$

$$\Phi_4 = \frac{1}{32}(290x^3 - 153x^5 - 105x) \tag{23}$$

$$\Phi_5 = \frac{1}{128}(2730x^4 - 1386x^6 - 1302x^2 + 86) \tag{24}$$

(21)

(22)

(23)

(24)

Some comments are in order here concerning the applicability of these polynomials to various types of rotor blades in the Rayleigh (or Modified Galerkin) framework. For a uniform articulated blade, the W_i functions all satisfy the geometric boundary condition w(o) = o. Thus, they are applicable in the Ritz method. In addition, all W_i's satisfy the two natural boundary conditions at the tip. Near the root, the convergence is affected by the fact that all odd-numbered W_i's have zero second derivative at x = 0, while all even-numbered W_i's have zero first and third derivatives at x = 0. Thus, the odd numbered polynomials are necessary in order to have good convergence of slope and shear force at the root; however, the even-numbered polynomials are not necessary unless one wishes w'''' to converge uniformly. If only odd polynomials are used, then the true Galerkin method would also apply since all boundary conditions would be fulfilled.

Now, if we add a finite root spring at x = 0 such that $K_\beta w(0) = EI\, w''(0)$, it turns out that modified W_i polynomials are still very applicable. Here, however, the natural boundary condition at the root is satisfied neither by even- nor odd-numbered polynomials. Thus, we must use either the Rayleigh-Ritz or the modified Galerkin method (modified by virtual work of nonfulfilled boundary loads); and we must include all W_i, even and odd. Still, the polynomials are very valuable due to their completeness and independence. It is also interesting to note that, in the limit as the root spring becomes very large, the multipliers of the odd-numbered W_i's (q_i's) will not go to zero, despite the fact that the odd W_i's have $w'(0) \neq 0$. The reason for this is clear. Were all the odd q_i's to vanish, the solution could have no root shear, $w'''(o)$ and therefore could not converge uniformly. What actually happens in the limit as $K_\beta \to \infty$ is that the odd q_i's adjust themselves in such a way to give $w'(0) = 0$. For example, if only 3 functions are used, then one will find $q_1 = \frac{41}{16} q_3$ as $K_\beta \to \infty$. This eliminates $w'(0)$ but does not eliminate $w'''(0)$, as would occur with $q_1 = q_3 = 0$.

However, if one wishes to solve explicitly for a purely cantilevered beam, the above polynomials would converge slowly to w. This is due to the fact that one would have to eliminate all odd-numbered W's a priori. The result is (and we have checked this) a good convergence to w, w', and w'' but a poor convergence to w''', especially near the root. Thus, one must take this into consideration when applying the polynomials. A similar discussion can be made of the torsional polynomials, Φ. In the limit as control-system stiffness becomes large, the odd-numbered Φ's will adjust themselves to maintain $\phi(0) = 0$. However, for explicitly infinite stiffness, poor convergence to $\phi''(0)$ can occur.

In order to decide further upon the validity of the new family of orthogonal polynomials and to choose the best combination of the polynomials, a test problem has been solved. The problem consists of a nonrotating beam with root spring. For various values of nondimensional root spring stiffness, λ, the equation of motion can be solved in closed form to obtain he mode shapes and frequencies. The first two bending mode shapes, for the cases of $\lambda = 0$ and $\lambda = \infty$, are plotted along with the polynomials in Figures 2-3. The comparison of mode shapes with the polynomials shows that the marriage between them is excellent. The odd-numbered polynomials closely approximate articulated blade modes ($\lambda = 0$), and the even-numbered polynomials approximate hingeless blade modes, $\lambda = \infty$. Similarly, the first two torsional mode shapes for the cases of $\lambda = 0$ and $\lambda = \infty$ are plotted with the polynomials in Figures 4-5. The comparison shows that the mode shapes closely agree with the torsional polynomials.

This close agreement of polynomials implies that we should obtain good frequency convergence over the entire range of hub types. Table 3 provides verification of this over the range $\lambda = 0$ (pinned) to $\lambda = 100$ (close to cantilevered). At $\lambda = 0$, the first two bending and torsion modes show good convergence with either 3 or 4 polynomials. Notice, however, that for the case in which the second polynomial is omitted, convergence to w is good despite the fact that the mode will have poor w" convergence near $x = 0$. As λ is increased, the 3 and 4 polynomial solutions continue to do well; but the case without polynomial #2 degrades in performance. Thus, we see that when a complete set of polynomials is used, we do very well over the entire range of flexure stiffnesses.

Trim Procedure

Two different approaches to rotor trim are considered in this study. In the first case, the control parameters are assumed to be known and are evaluated from empirical formulas, Ref. 25. In the second case, the control settings are assumed to be unknown; and, hence the parameters necessary to trim the rotor must be calculated simultaneously along with the generalized coordinates of elastic blade equations. This simulataneous trim solution is obtained through use of an autopilot. This is essentially a numerical controller (feedback system) used to trim the rotor.

The autopilot equations, Ref. 26 may be expressed as,

$$\tau\ddot{\theta}_s + \dot{\theta}_s = \frac{A(p_0^2 - 1)}{\gamma_0}[\cos\psi - \frac{8(p^2 - 1)}{\gamma}\sin\psi]\bar{w}_{tip} \tag{25}$$

$$\tau\ddot{\theta}_c + \dot{\theta}_c = -\frac{A(p_0^2 - 1)}{\gamma_0}[\sin\psi + \frac{8(p^2 - 1)}{\gamma}\cos\psi]\bar{w}_{tip} \tag{26}$$

where τ is the time constant and A is the gain. Excessively large values of the time constant leads to poor convergence while excessively small values will result in excessive oscillations of the controls. Similarly, the controller will give slow convergence for excessively small values of gain while, for excessively large values of gain, the controller could become

unstable. Hence, we need an optimum value for both the time constant and the gain. The parameters pertaining to an optimized automatic controller, Ref. 27 are given below:

$$\tau = 1.2\pi \tag{27a}$$

$$A = 2 \tag{27b}$$

$$p_0 = 1.12 \tag{27c}$$

$$\gamma_0 = 5 \tag{27d}$$

$$w_{tip} = \sum_{i=1}^{8} q_i \tag{27e}$$

Results and Discussions

The elastic blade equations are solved for two typical helicopter rotors: an articulated rotor and a hingeless rotor. The results are given in two sections. The first section describes the effect of autopilot on trimming, the second section summarizes the steady-state response of flap, lag and torsion.

Trimming Method

Trimming corresponds to helicopter control settings for a given flight condition. In the trimmed condition, the rotor is maintained at a fixed value of the thrust coefficient or, alternatively, at a fixed balue of Θ_0 with forward speed. The cyclic pitch is adjusted to suppress first harmonic cyclic flapping and therefore to approximately eliminate the rotor 1/rev hub moments. Among the flap, lag, and torsional motions of the blade, flapping has a more pronounced effect on steady hub moments. Hence, an emphasis is given to the trimming of flap motion alone.

In the first phase of computation, the control settings were assumed to be known, and they were evaluated by approximate trim formulas. This gave excellent results for rigid flapping with uniform flow; and the 1/rev response in flap motion is effectively suppressed. However, this method of trimming is inadequate in the presence of elastic flapping or in the case of a fore-to-aft inflow gradient. The results are sensitive to the inflow gradients, and the conventional trim approximations do not account for this. Essentially, it means that the trim values (i.e., the cyclic pitch parameters, Θ_s,Θ_c) must vary depending on the flight conditions. This may be accomplished by incorporating an autopilot, the automatic feedback system. Thus, all results presented in this paper are with the automatic controller. (See Ref. 21 for results with approximate formulas.)

Steady-State Response

Steady-state deflections of the rotor blade are necessary for the prediction of rotor loads; and hence, the determination of steady-state

response becomes essential. The numerical scheme is to numerically integrate the rotor blade equations in time until all the transients have died out. Then, the steady-state response of flap, lag, and torsion is obtained. The results are given in terms of dimensionless tip deflections as a function of dimensionless time. Two typical rotors, hingeless and articulated are investigated. The respective rotor parameters are given in Table 4.

Articulated Blade:

The equilibrium deflections of an articulated blade for flap, lag, and torsion are given in Figures 6-8. The response diagrams shown in the above figures are periodic. The computation is performed to thirteen revolutions of the rotor in order for all the transients to die out. Then, the results are plotted for one period; and the curves retain the same value of the amplitude and slope at both the ends of the period. Figure 6 describes the flap response with autopilot. The autopilot eliminates the one-per-rev oscillation in flap motion and hence the response has a fundamental two-per-rev oscillation. However, the autopilot does not trim the inplane and torsional motions; and, hence, the response of lag and torsion have one-per-rev oscillation.

The variations of lateral and longitudinal cyclic pitch parameters with respect to dimensionless time are sketched in Figures 9-10. It is evident from these figures that the variation has a one-per-rev oscillation. The oscillations of the cyclic pitch parameters come from the response of the control system to one-per-rev and two-per-rev hub forces. These are present because we have included only a single blade. If we include a higher number of blades, the sum of the oscillations over all the blades will average the

harmonics at the rotor hub and the harmonics that correspond to only the integer multiple of the number of blades will be present. For example, a three bladed rotor will have 3n-per-rev oscillations in Θ_s and Θ_c, where "n" is an integer; and these would be greatly reduced. The oscillations in Θ_s and Θ_c can also be eliminated either by use of larger values of τ or by filtering the signal.

For comparison purposes, the steady-state response of the articulated blade has been obtained for a blade undergoing flap motion only (Figure 11). In this case, the computation need be performed to only three revolutions of the rotor in order for all the transients to die out. The equilibrium deflection shown in the figure is periodic. For the case of zero advance ratio (hover), the blade undergoes constant flapping motion and hence the response is a straight line. The equilibrium deflection remains constant over the entire period. In the case of forward flight, the blade undergoes cyclic flapping and the trim settings alleviate the one-per-rev oscillation. Hence, we obtain two-per-rev response in the vertical plane. The average value of flapping is not much changed between Figure 6 and hover and forward flight in Figure 11. This is due to the fact that all cases have essentially the same thrust coefficient.

Hingeless Blade:

The steady-state responses of a hingeless blade for flap, lag, and torsion are given in Figures 12-14. It may be observed from the response diagrams that the results are similar to the case of an articulated blade. The responses is periodic and, hence, retains the same value of the amplitude and slope at both the ends of the period. Thirteen revolutions of rotor are

required, for all the transients to die out. Figure 12 gives the flap response with autopilot. The blade has a two-per-rev oscillation in flap motion. The lag and torsional responses are of one-per-rev type, similar to the articulated blade. The variations of cyclic pitch parameters are also similar to the case of articulated blade.

It is extremely interesting to compare the predominantly 2/rev response in Figures 6 and 12 with similar response plots of other investigators for "propulsive" or moment" trim. By definition, this type of trim must give zero 1/rev flapping. This is because propulsive force is trimmed by shaft tilt (not tip-path tilt), and 1/rev hub moments are set to zero. However, most work in this area has relied upon approximate trim formulas; and the results indicate that the blades were actually not trimmed. For example, Figures 2 and 5 of Reference 28 show a 1/rev flapping response equal to 30% to 50% of the steady coning at $\mu = 0.2$ and $\mu = 0.4$, respectively. Similarly, Figure 3 of Reference 29 shows a 1/rev flapping response equal to 60% of steady coning at $\mu = 0.2$. Reference 29 recognizes this lack of trim and attempts to correct the problem by including elastic twist in the trim formulation. The result, also shown in Figure 3 of Reference 29, is a reduction of the 1/rev to 20% of coning (still not trimmed). In addition, the "improved" response is not even periodic. These results point out the difficulty of finding a true trim. In the work presented have, we see the automatic pilot as a viable tool to obtain this otherwise difficult result.

Summary and Conclusions

The present investigation of elastic Flap-Lag-Torsion analysis leads to following results.

1. Nonlinear equations of motion for the elastic bending and torsion of a twisted, nonuniform blade have been derived by variational method, which includes use of a curvilinear coordinate system and tensor approach.

2. Modified Greenberg's aerodynamic theory proves to be a viable approach to obtain the aerodynamic forces. The quasi-steady approximation makes the aerodynamic model simple for research purposes. However, for a true loads analysis, an unsteady theory will be required.

3. The new ordering scheme (for vibrations only) is efficient to segregate the lower order terms from higher order terms and thus yield a hierarchy of equations (that is, a set of equations that can be taken to various orders).

4. The results present a new family of orthogonal polynomials that represent good comparison functions for the uncoupled nonrotating mode shapes of both articulated blades and blades with a root flexure. Also, the evaluation of Galerkin integrals is relatively simple with comparison functions that are polynomials.

5. Trim formulas are good for rigid blade equations with no inflow gradients; but they become inadequate for elastic blade equations. In order to eliminate this, it is necessary to include autopilot equations. This modification gives better results to elastic response computations, including the effective suppression of 1/rev flapping.

6. A logical extension of this analysis would be to include dynamic stall to the aerodynamic model and evaluate the rotor loads.

Acknowledgements

This work was sponsored by the United States Army Research Office, Grants No. DAAG-29-80-C-0092 and DAAG-29-85-K-0228. The view, opinions, and/or findings of this report are those of the authors and should not be construed as an official Department of the Army position, policy, or decision, unless so designated by other documentation.

References

1. Glauert, H., and Lock, C.N.H., "A Summary of the Experimental and Theoretical Investigations of the Characteristics of an Autogyro," Br. ARC Rep. and Memo. No. 11672, 1928.

2. Wheatley, J.B., "An Analytical and Experimental Study of the Effect of Periodic Blade Twist on the Thrust, Torque, and Flapping Motion of an Autogyro Rotor," NACA Rep. 591, 1937.

3. Perisho, C.H., "Analysis of the Stability of a Flexible Rotor Blade at High Advance Ratio," Journal of the American Helicopter Society, Vol. 4, No. 2, 1959.

4. Peters, D.A. and Ormiston, R.A., "Flapping Response Characteristics of Hingeless Rotor Blades by a Generalized Harmonic Balance Method," NASA TN D-7856, 1975.

5. Ormiston, R.A., and Hodges, D.H., "Linear Flap-Lag Dynamics of Hingeless Helicopter Rotor Blades in Hover," Journal of American Helicopter Society, Vol. 17, No. 2, 1972.

6. Hodges, D.H., and Ormiston, R.A., "Nonlinear Equations for Bending of Rotating Beams with Application to Linear Flap-Lag Stability of Hingeless Rotors," NASA TM X-2770, 1973.

7. Schrage, D.P., Effect of Structural Parameters on the Flap-Lag Forced Response of a Rotor Blade in Forward Flight, Doctor of Science Thesis, Washington University, 1978.

8. Eipe, A., Effect of Some Structural Parameters on Elastic Rotor Loads by an Iterative Harmonic Balance, Doctor of Science Thesis, Washington University, 1979.

9. Miao, W.L., "C-56 Program, Appendix-A," Boeing Vertol File 8-7453-1-2395, 1971.

10. Peters, D.A., "Flap-Lag Stability at Low Advance Ratios", presented at the Army Chief Investigators' Conference on Mathematicsl Analysis of Nonlinear Systems, Ames Research Center, March 20-21, 1975.

11. Hodges, D.H., and Dowell, E.H., "Nonlinear Equations of Motion for the Elastic Bending and Torsion of Twisted Nonuniform Rotor Blades," NASA TN D-7818, 1974.

12. Friedmann, P., "Influence of Modeling and Blade Parameters on the Aeroelastic Stability of a Cantilevered Rotor," AIAA Journal, Vol. 15, No. 2, Feb. 1977, pp. 149-152.

13. Rosen, Aviv, and Friedmann, P., "Nonlinear Equations of Equilibrium for Elastic Helicopter or Wind Turbine Blades Undergoing Moderate Deformation," NASA CR-159478, December 1978.

14. Houbolt, J.C., and Brooks, G.W., "Differential Equations of Motion for Combined Flapwise Bending, Chordwise Bending, and Torsion of Twisted Nonuniform Rotor Blades," NACA Rep. 1346, 1958.

15. Hodges, D.H., "Torsion of Pretwisted Beams due to Axial Loading," Journal of Applied Mechanics, Vol. 47, No. 2, 1980.

16. Theodorsen, T., "General Theory of Aerodynamic Instability and the Mechanism of Flutter," NACA Rep. 496, 1935.

17. Greenberg, J.M., "Airfoil in Sinusoidal Motion in Pulsating Stream," NACA TN 1326, 1947.

18. Loewy, R.G., "A Two-Dimensional Approximation to the Unsteady Aerodynamics of Rotary Wings," Journal of Aeronautical Sciences, Vol. 24, No. 2, 1957.

19. Johnson, W., "Application of Unsteady Airfoil Theory to Rotary Wings," Journal of Aircraft, Vol. 17, No. 4, 1980.

20. Tran, C.T., and Petot, D., "Semi-Empirical Model for the Dynamic Stall of Airfoils in View of the Application to the Calculation of Responses of a Helicopter Blade in Forward Flight," Vertica, Vol. 5, No. 1, 1981, pp. 35-53.

21. Karunamoorthy, S.N., "Use of Hierarchical Elastic Blade Equations and Automatic Trim for Helicopter Vibration Analysis, Doctor of Science Thesis, Washington University, 1985.

22. Duncan, W.J., "Galerkin's Method in Mechanics and Differential Equations," Aeronautical Research Council, Rep. and Memo. No. 1798, 1937.

23. Abramowitz, M., and Stegun, I.A., Handbook of Mathematical Functions With Formulas, Graphs, and Mathematical Tables, Dover Pub., 1965.

24. Jackson, D., Fourier Series and Orthogonal Polynomials, The Carus Mathematical Monographs, No. 6, The Mathematical Association of America, 1941.

25. Wei, F.S., and Peters, D.A., "Flap-Lag Damping in Autorotation by a Perturbation Method," 34th Annual National Forum, American Helicopter Society, 1978.

26. Kim, B.S., Control Settings for a Trimmed, Stalled Rotor by an Automatic Feedback System, Master of Science Thesis, Washington University, 1980.

27. Peters, D.A., Kim, B.S., and Chen, H.S., "Calculation of Trim Settings, for a Helicopter Rotor by an Optimized Automatic Controller," Journal of Guidance, Control, and Dynamics, Vol. 7, No. 1, 1984.

28. Panda, B. and Chopra, I., "Dynamic Stability of a Bearingless Circulation Control Rotor Blade in Hover," Journal of the American Helicopter Society, Vol. 30, No. 4, October 1985, pp. 40-47.

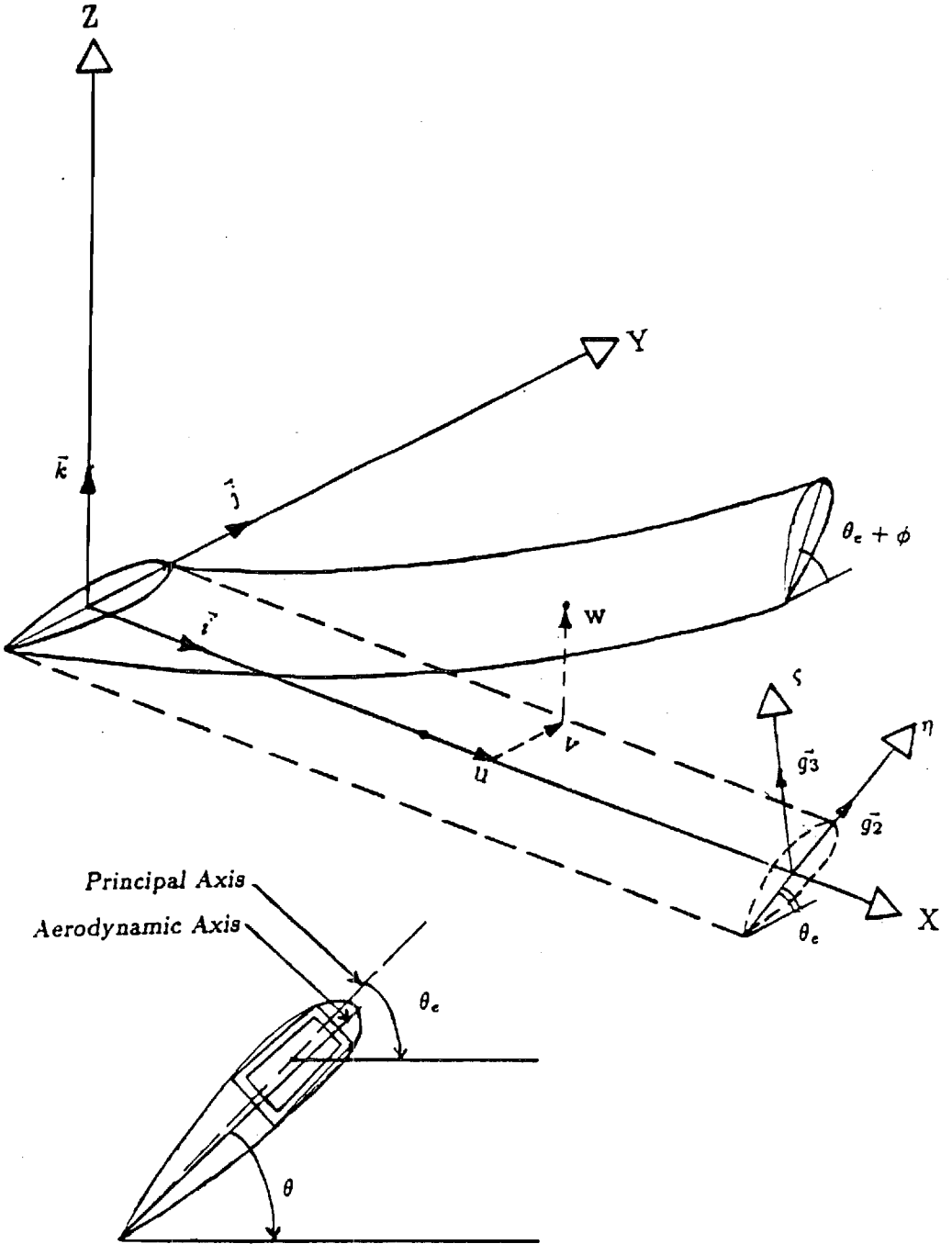

Figure 1. Rotor Blade Coordinate System

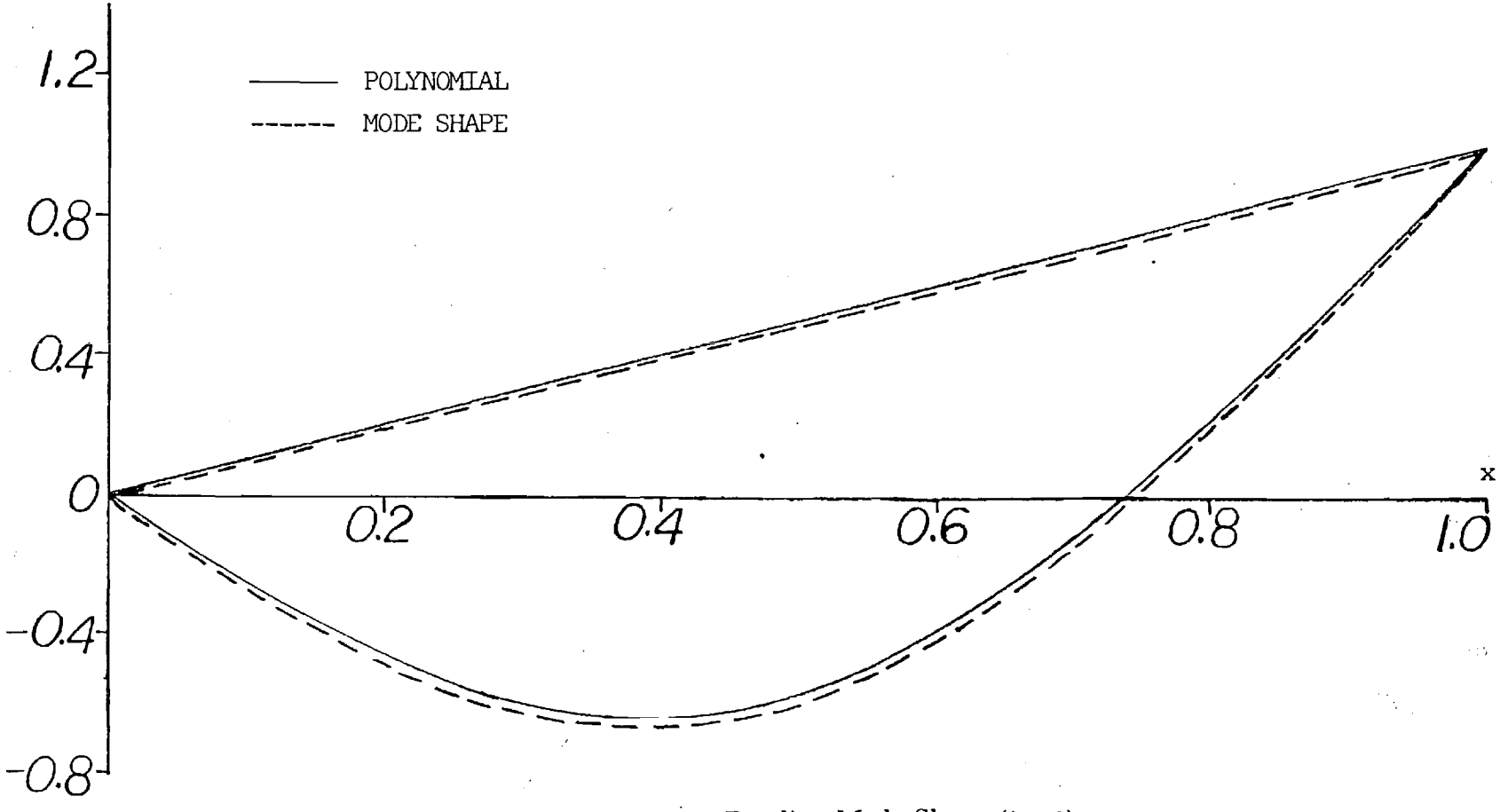

Figure 2 Bending Mode Shape ($\lambda = 0$)

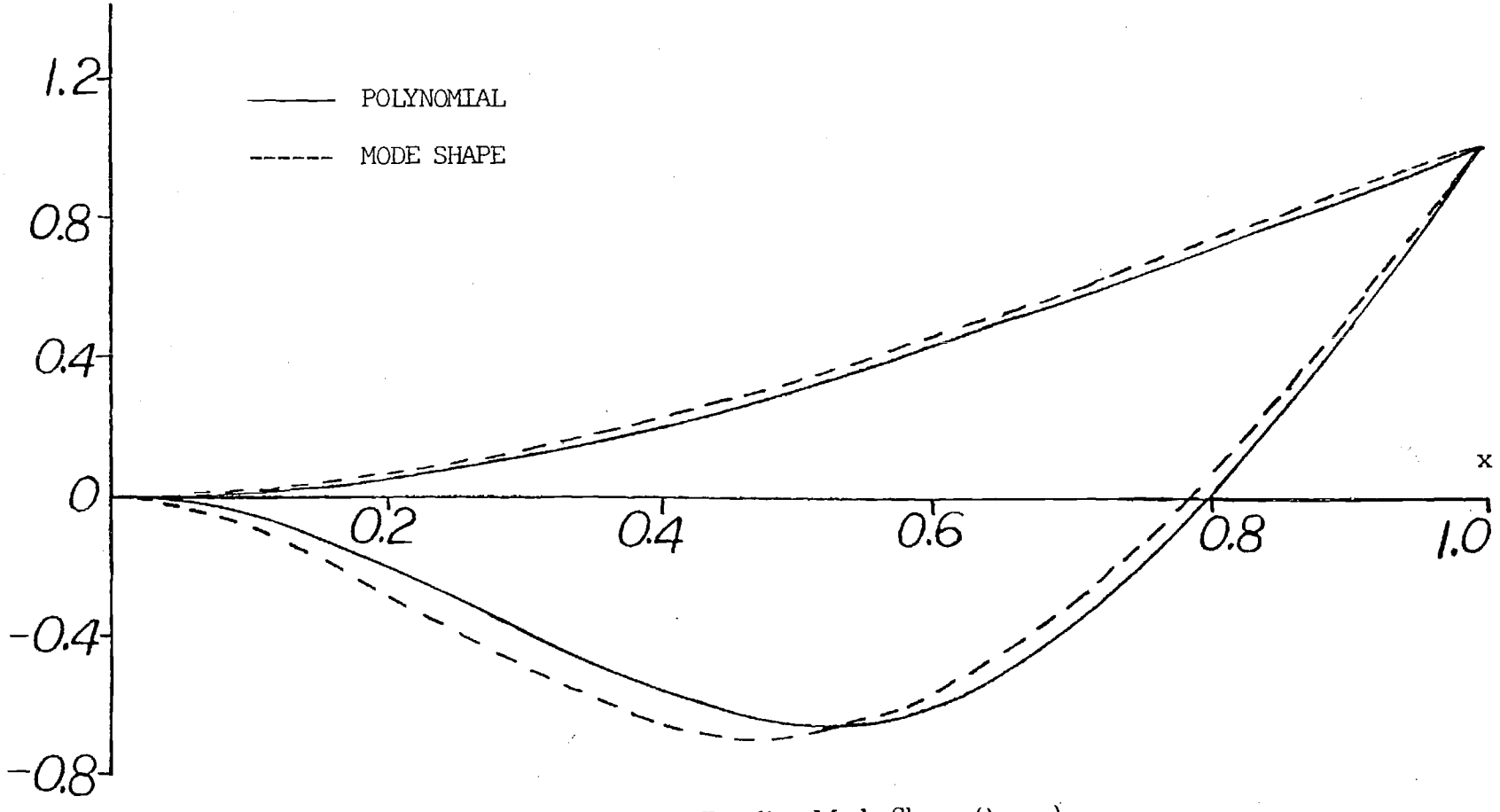

Figure 3 Bending Mode Shape ($\lambda = \infty$)

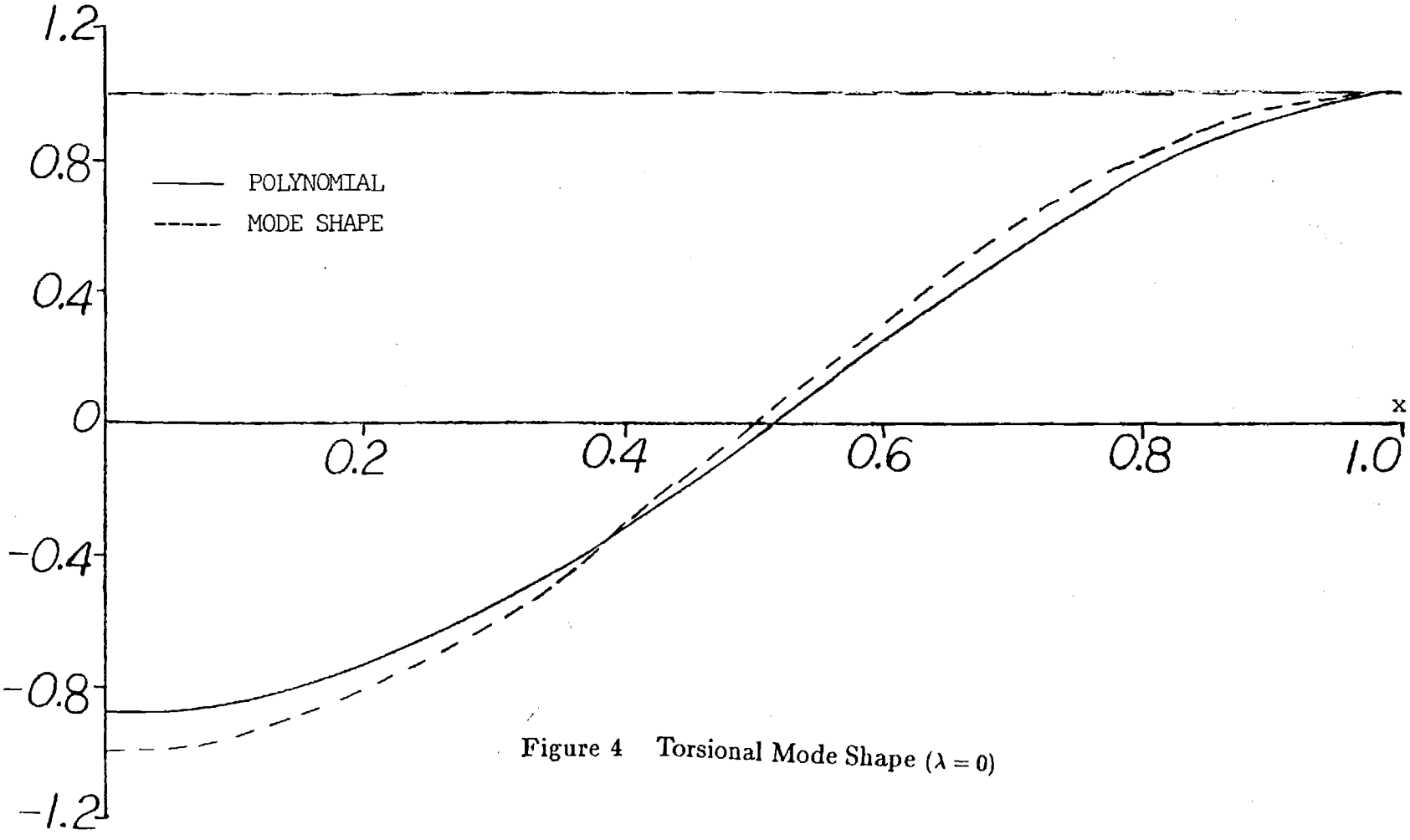

Figure 4 Torsional Mode Shape ($\lambda = 0$)

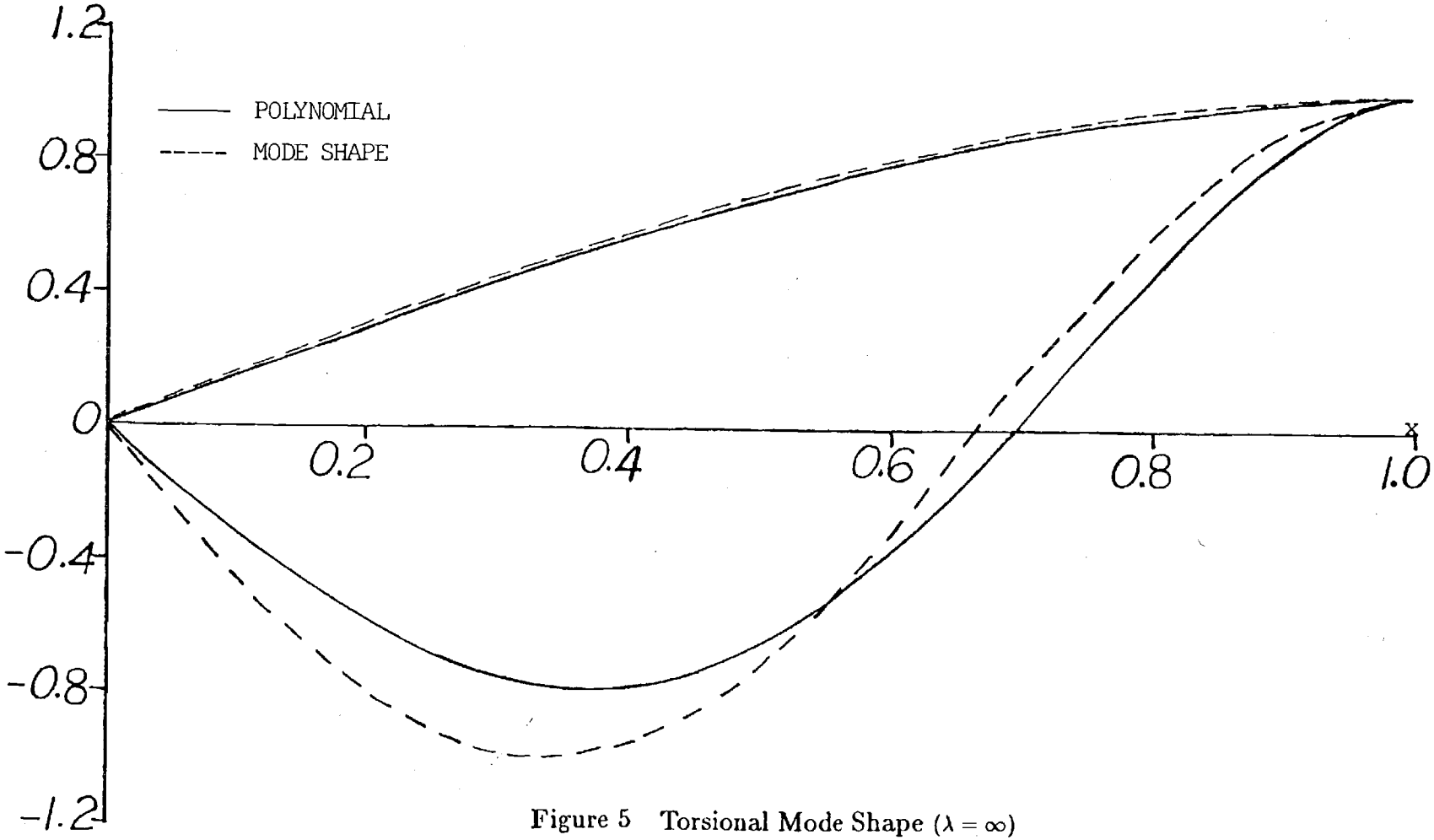

Figure 5 Torsional Mode Shape ($\lambda = \infty$)

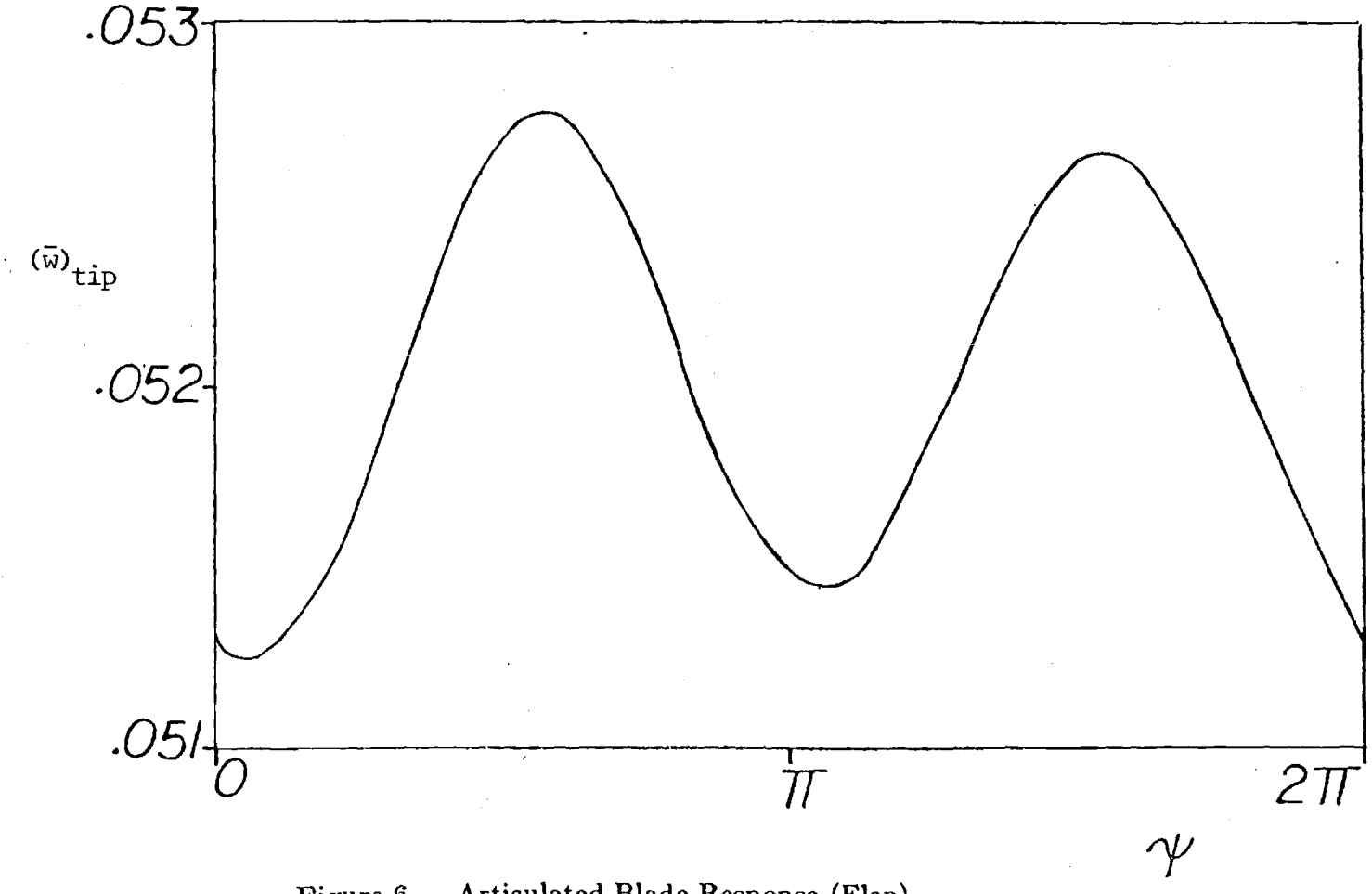

Figure 6 Articulated Blade Response (Flap)

(13th Revolution of Rotor)

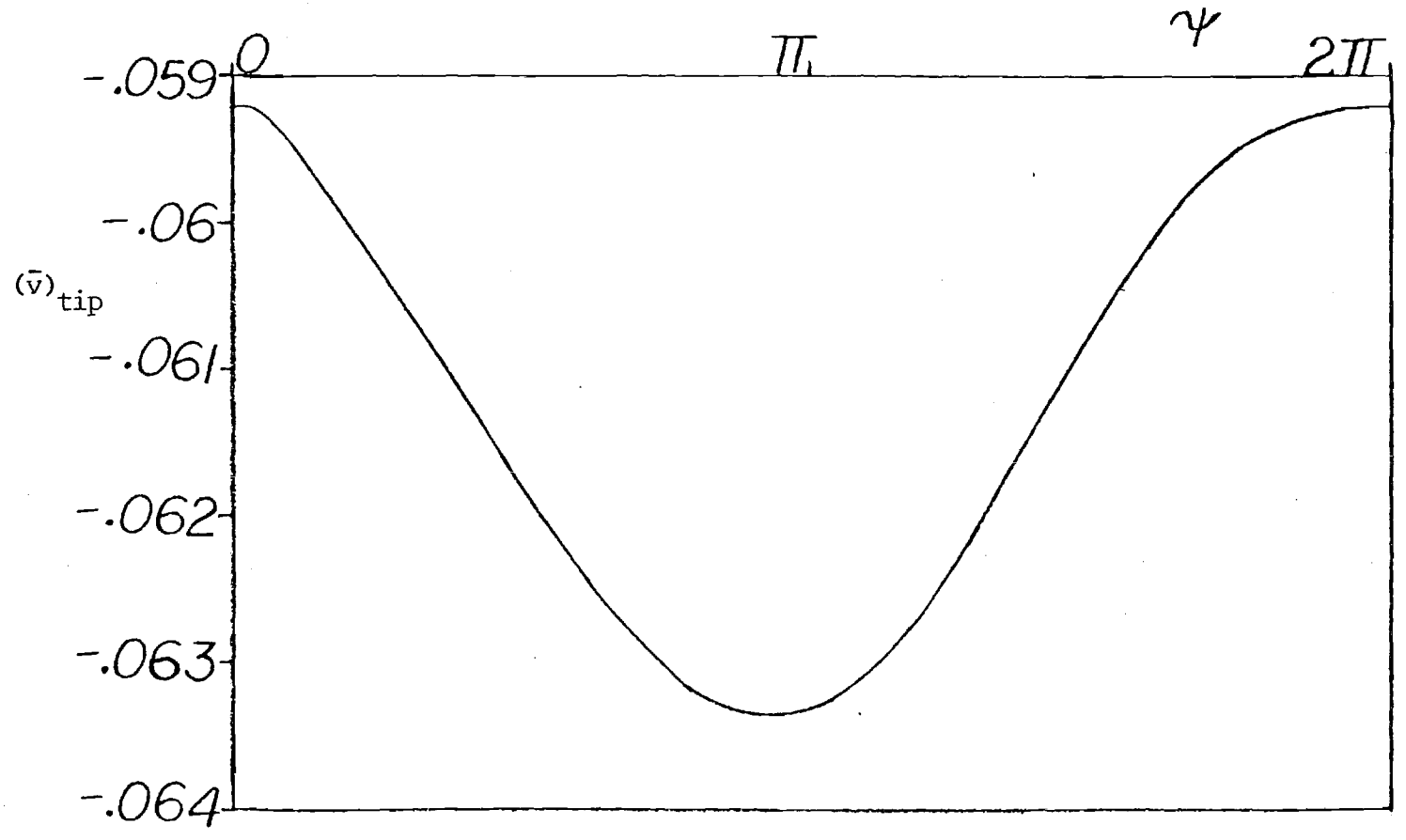

Figure 7 Articulated Blade Response (Lag)
(13th Revolution of Rotor)

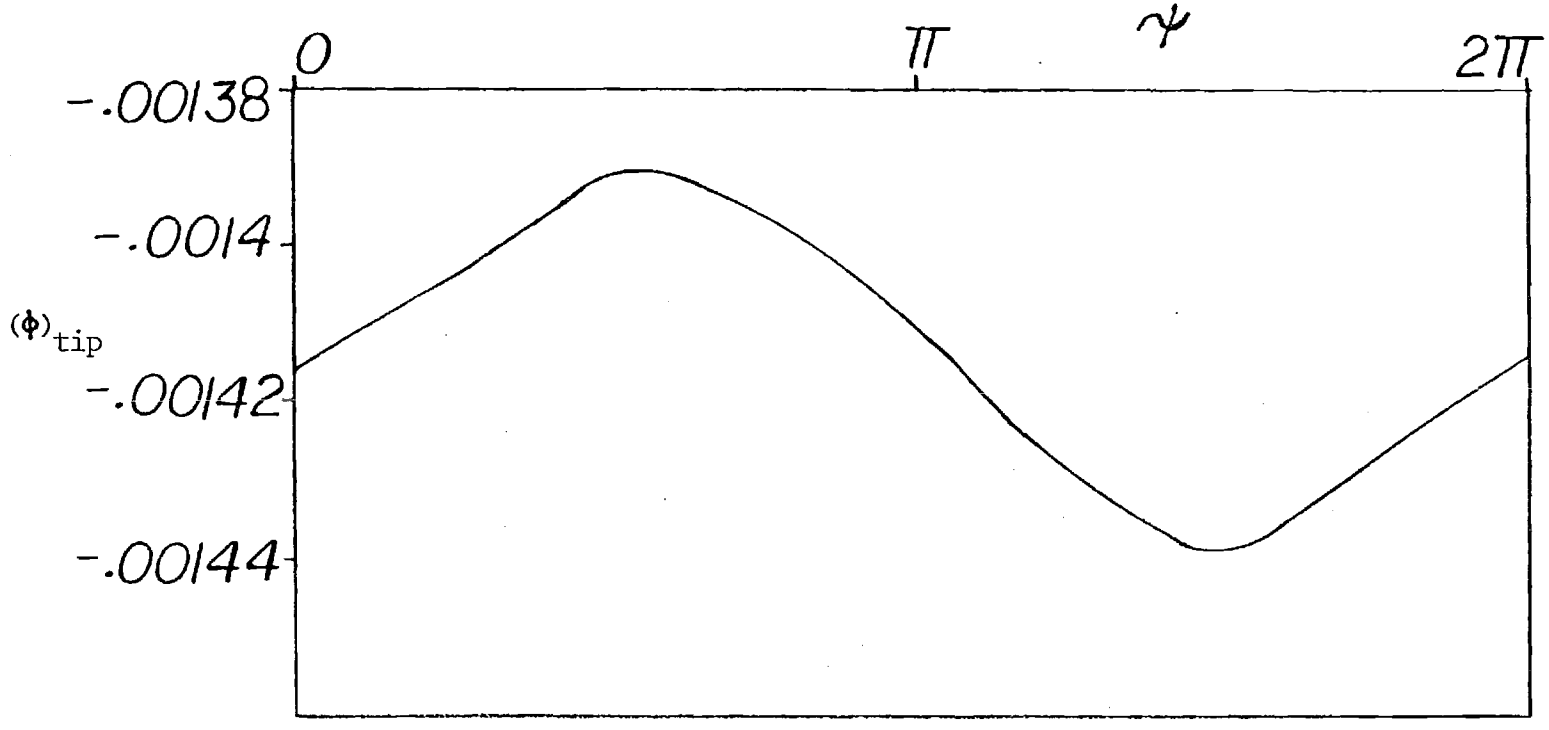

Figure 8 Articulated Blade Response (Torsion)
(13th Revolution of Rotor)

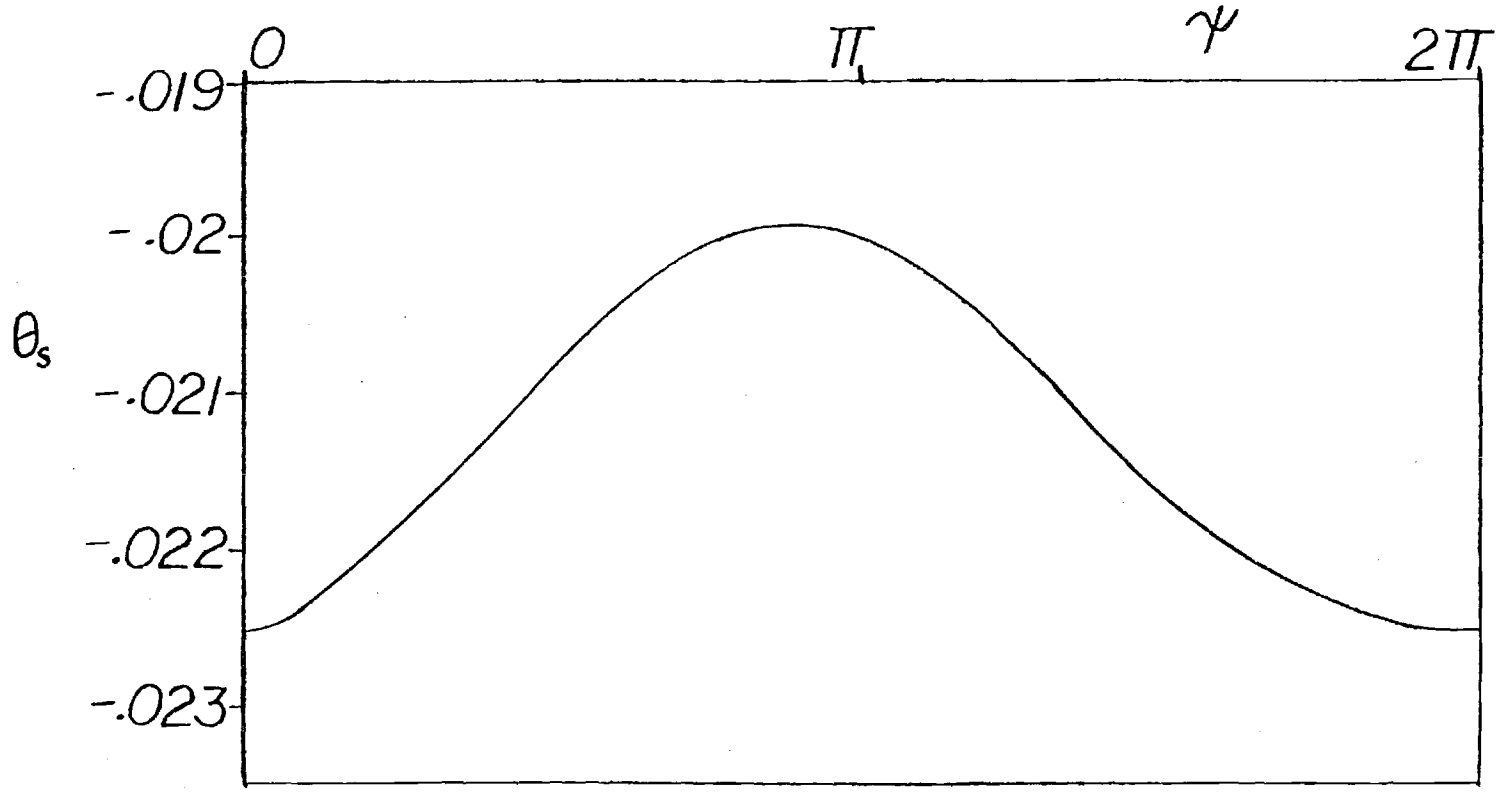

Figure 9 Longitudinal Cyclic Pitch, θ_s (Articulated)
(13th Revolution of Rotor)

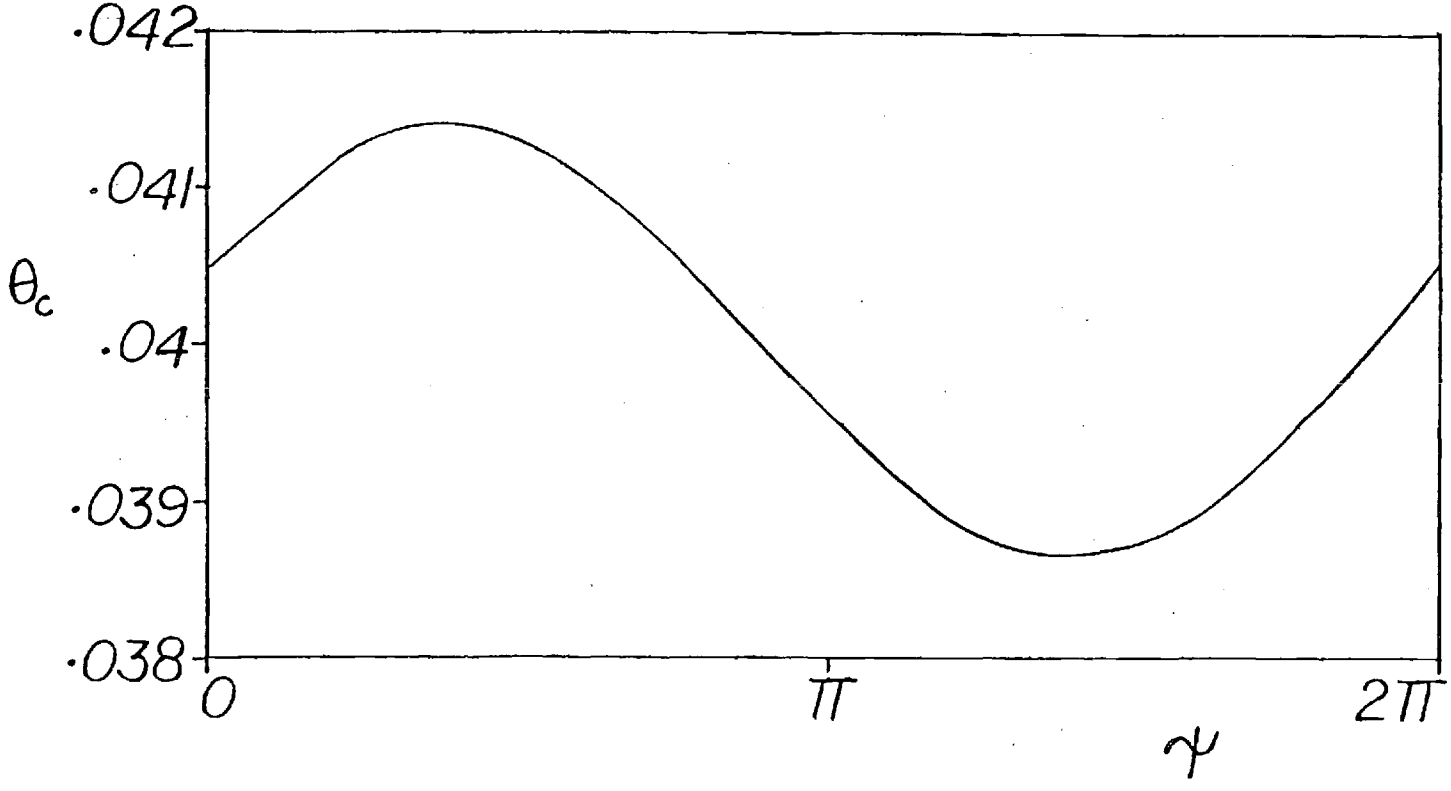

Figure 10 Lateral Cyclic Pitch, θ_c (Articulated)
(13th Revolution of Rotor)

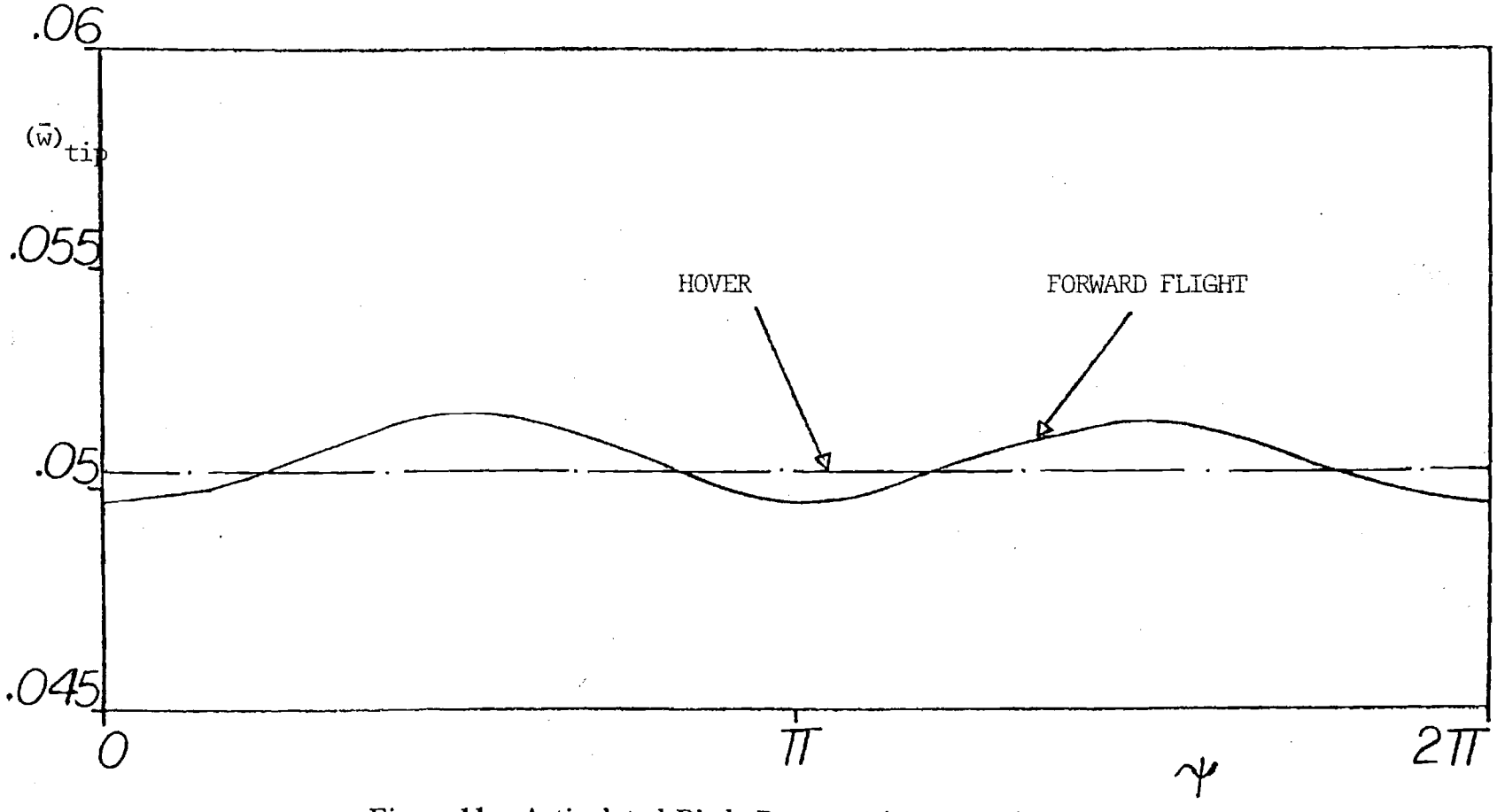

Figure 11 Articulated Blade Response (Flap Only)
(3rd Revolution of Rotor)

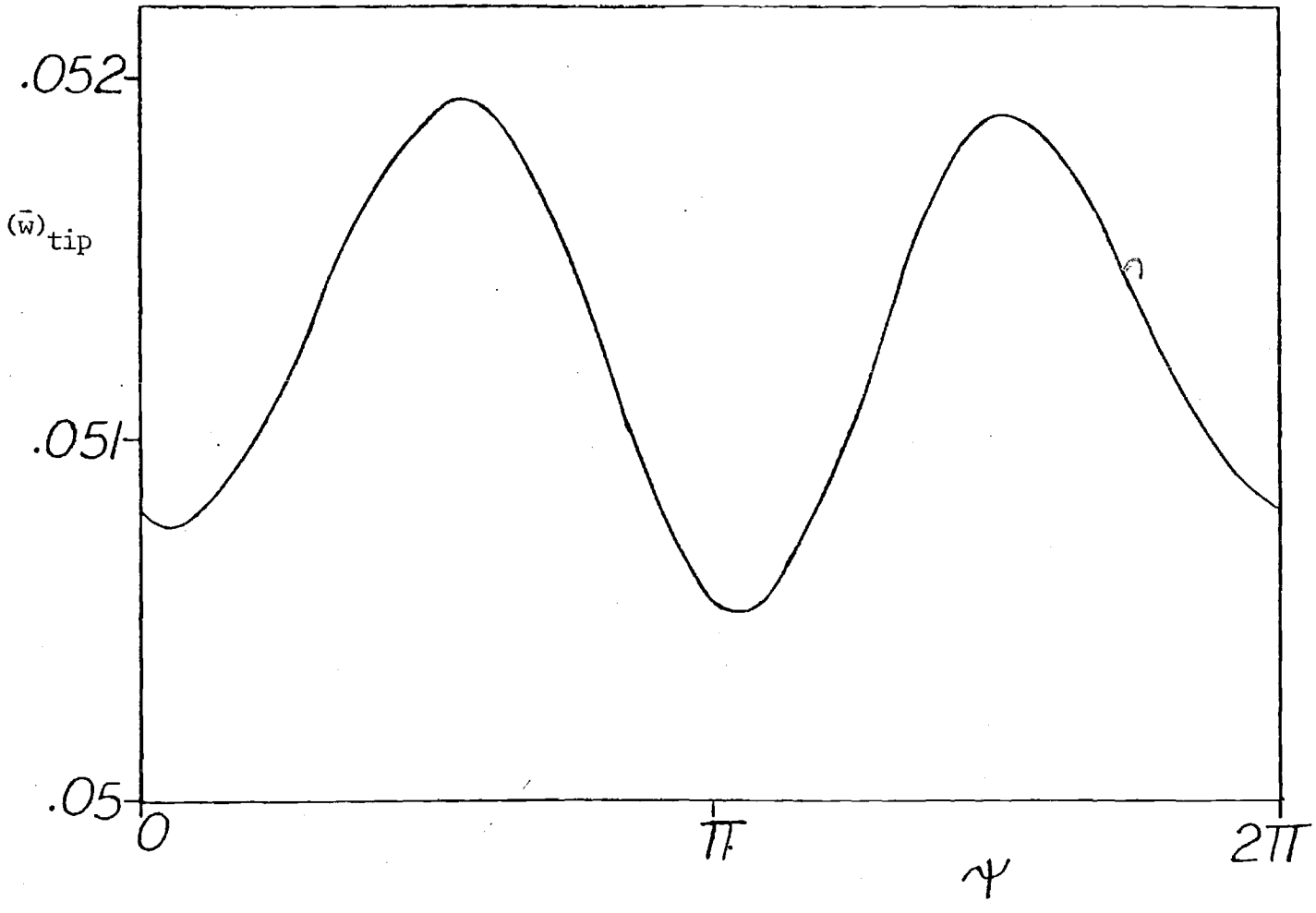

Figure 12 Hingeless Blade Response (Flap)
(13th Revolution of Rotor)

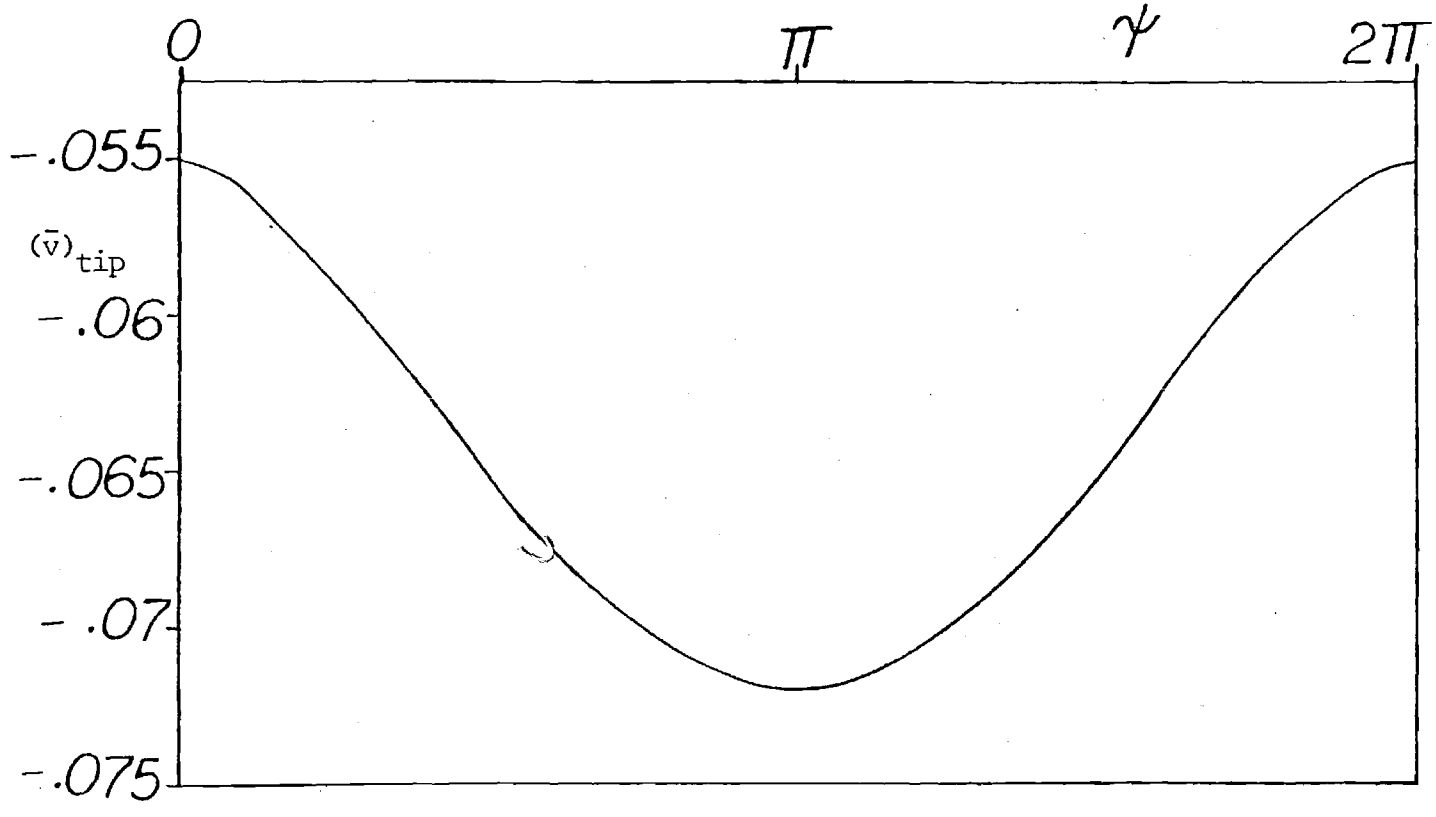

Figure 13 Hingeless Blade Response (Lag)
(13th Revolution of Rotor)

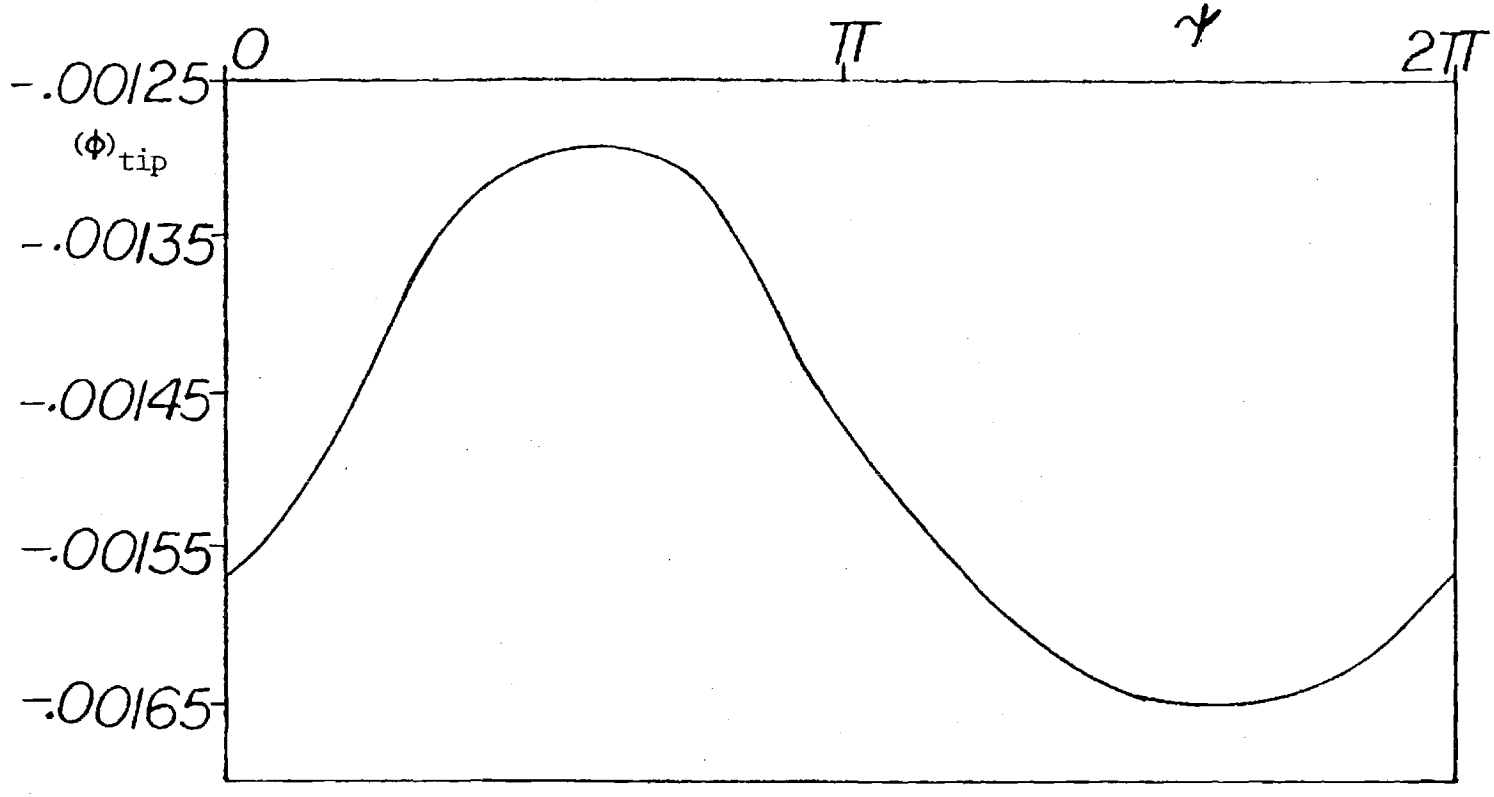

Figure 14 Hingeless Blade Response (Torsion)
(13th Revolution of Rotor)

Numerical Solutions of Induced Velocities by Semi-Infinite Tip Vortex Lines

by

Yihwan Danny, Chiu

Research Assistant

and

David A. Peters

Professor
School of Aerospace Engineering
Georgia Institute of Technology
Atlanta, Georgia

October 20, 1986

ABSTRACT

The method of Rand and Roson[9] (for improving convergence on computed axial induced velocity for a helical wake) is extended to include all velocity components, all points in the wake, and non-helical vortex lines (contraction). The method is based on finding upper and lower bounds on the truncated integral. Comparisons with other methods show that the present approach is efficient and accurate. Further, it avoids the errors associated with descretization of the vortex lines. Convergence occurs in only 3-5 revolutions, about 10% of the normal requirement.

NOTATION

A	=wake constant in radial coordinate equation, Eq. (24)
b	=number of blades
k_1, k_2	=parameters defining the average axial velocity of a tip vortex element
R	=blade radius
r	$=(x_i^2 + y_i^2)^{1/2}/R$, radius of the control point
U_{ij}, V_{ij}, W_{ij}	=components of induced velocity at the control point i
V_0	=axial free stream velocity
v_i	=average induced velocity for undistorted wake model or induced velocity at (x_0, y_0, z_0) at previous iteration for distorted and free-wake models
x_i, y_i, z_i	=coordinates of the control point
x_j, y_j, z_j	=coordinates of a segment of the trailing vortex line
x_0, y_0, z_0	=coordinates of the starting point of the trailing vortex line
x_j	$=\eta cos(\theta + \theta_n)$
y_j	$=\eta sin(\theta + \theta_n)$
z_i	$=\nu^{'}(\theta - \delta) + z_o$
η	$=(x_0^2 + y_0^2)^{1/2}/R$, radius of the trailing vortex line
$\eta^{'}$	$=d\eta/d\theta$, Eq. (25)
θ	=angle of turning of the blade
$\theta^{'}$	$=\theta_n + \theta$
θ_n	$=2\pi(n-1)/b$

δ $= tan^{-1}(y_0/x_0)$

ϕ $= tan^{-1}(y_i/x_i)$

λ =wake constant in radial coordinate equation, Eq. (24)

ν' $= (V_0 + v_i)/R\omega$, inflow ratio

ω = angular rotating velocity

INTRODUCTION

In order to calculate the local aerodynamic behavior of rotating blades (such as aircraft propellers, marine propellers, helicopter rotors, etc.), application of lifting-surface theory is required. This is especially true when one studies the flow around the tips of blades with low aspect ratio, for which the classical approach of lifting-line theory is not applicable. Some researchers employ the Panel Method (PM) or the Vortex Lattice Method (VLM) which amount to a Cauchy-type finite-element solution to lifting-surface problems. Many applications of the VLM and PM have been made with considerable success to problems of the aerodynamic analysis and design of fixed wings[1-3]. One reason for this success stems from the fact that the cost of computing the effect of the trailing vortex lines can be minimized (for the case of a wing) by use of efficient mathematical techniques. In the case of rotary wings, however, these fixed-wing techniques are not directly applicable. In the undistorted wake model, the calculation of induced velocities involves an integral with a semi-infinite limit, for which no closed-form analytic solution exists as in the case of a fixed wing. Therefore, these integrals must be calculated numerically. Different researchers have developed various methods to improve the efficiency of this trailing-vortex computation. Chang and Sullivan[4] terminate their calculations after 10 revolutions of the vortex helix. Baskin[5] carries out the numerical integration with an automatic selection of the upper limit, so that the absolute error of the obtained results does not exceed 10^{-4}. However, numerical results show that several thousand revolutions are required to obtain this accuracy. In the prescribed and free wake models, the so-called "far wake" also causes difficulty in the calculation of induced velocities. Summa[6] and Hess[7] replace the vortex line by a semi-infinite cylindrical wake from infinitely-many blades. Analytic solutions exist for the velocities induced by such a cylinder[8], and this allows an efficient treatment.

Recently, a numerical techinique has been developed by Rand and Rosen[9] to calculate

the axial velocity induced by semi-infinite helical vortex lines. Rosen and Garber[10] mention that they have extended this method to calculate radial velocites as well, and that a paper on the work has been submitted for publication. The purpose of this note is to extend their work to calculate all velocity components (including circumferential velocity) induced by semi-infinite helical lines. Further, this paper also extends the method to calculate all three veolcity components induced by non-helical vortex lines, provided the trajectory of these lines is known as a function of azimuth. For example, the method can be applied to the case of wake contraction. It should be noted that the calculation of induced velocity is not limited to points along the blade. The methods described herein apply to any point in the flowfield, the fact of which is important in PM.

THEORETICAL DERIVATION FOR HELICAL VORTEX LINES

As shown in Fig. 1, an (x,y,z) Cartesian coordinate system originates from the center of the hub. The axis system is defined by taking an x-axis through the trailing edge of the blade at the root, a z axis pointing to the positive down-wind direction, and a y axis that completes the right hand system. We define, u_{ij}, v_{ij}, w_{ij} as (x,y,z) components of induced velocity at a control point (x_i, y_i, z_i) and generated by a small helical vortex segment at the point (x_j, y_j, z_j) on the helical trailing vortex line that emanates from the point (x_0, y_0, z_0) with circulation equal to one. (The point (x_0, y_0, z_0) should lie on the trailing edge of the airfoil for the undistorted wake model or in the last point of the distorted vortex line in the near wake region for the prescribed or free wake model.) If we consider only the axial flight condition, the total nomalized induced-velocities induced by helical vortex lines (including those from other blades) U_{ij}, V_{ij}, W_{ij} can be determinted by use of the Biot-Savart law:

$$U_{ij}^{'} = \frac{1}{4\pi R} U_{ij} = \frac{1}{4\pi R} \int_0^\infty u_{ij} d\theta \tag{1}$$

$$V_{ij}^{'} = \frac{1}{4\pi R} V_{ij} = \frac{1}{4\pi R} \int_0^\infty v_{ij} d\theta \tag{2}$$

$$W_{ij}^{'} = \frac{1}{4\pi R} W_{ij} = \frac{1}{4\pi R} \int_0^\infty w_{ij} d\theta \tag{3}$$

$$u_{ij} = \sum_{n=1}^{b} \frac{\nu^{'}[\eta sin(\theta^{'} + \delta) - r sin(\phi) - (\theta + (z_0 - z_i)/\nu^{'})\eta cos(\theta^{'} + \delta)]}{[\eta^2 + r^2 - 2r\eta cos(\theta^{'} + \delta - \phi) + (\nu^{'}\theta + z_0 - z_i)^2]^{3/2}} \tag{4}$$

$$v_{ij} = \sum_{n=1}^{b} \frac{\nu^{'}[-\eta cos(\theta^{'} + \delta) + r cos(\phi) - (\theta + (z_0 - z_i)/\nu^{'})\eta sin(\theta^{'} + \delta)]}{[\eta^2 + r^2 - 2r\eta cos(\theta^{'} + \delta - \phi) + (\nu^{'}\theta + z_0 - z_i)^2]^{3/2}} \tag{5}$$

$$w_{ij} = \sum_{n=1}^{b} \frac{\eta^2 - r\eta cos(\theta^{'} + \delta - \phi)}{[\eta^2 + r^2 - 2r\eta cos(\theta^{'} + \delta - \phi) + (\nu^{'}\theta + z_0 - z_i)^2]^{3/2}} \tag{6}$$

We note here that, for $y_j = 0$, (U_{ij}, V_{ij}, W_{ij}) are radial, circumferential, and axial components, respectly. The expressions for U_{ij}, V_{ij}, W_{ij} are very similar to those of other references. See, for example, Ref. 9., App. 2., or Ref. 5, Eq. (8.11).

The problem considered here is how to compute Eqs. (1), (2), and (3) which do not have closed-form analytic solutions. Reference 9 uses a combination of numerical and analytic solutions to calculate W_{ij}. According to this method, the numerical intergration is carried only to a certain azimuth angle. Beyond this azimuth angle (to infinity), the integral is evalulated from the average of two analytic integrals that form lower and upper bounds of the real integrand. The purpose of this note is to discover if a similar approach can be developed for applications to both radial and circumferential velocities. Also, the

crux of the matter lies in assessing how to find lower and upper bounds of the real integrand for other cases.

1. Axial induced-velocity (along the z-axis direction)

As described in Ref. 9, w_{ij} is usually bounded by the functions w_1 and w_2 which are defined as follows:

$$w_1 = \sum_{n=1}^{b} \frac{\eta^2 - r\eta cos(\theta_n + \delta - \phi)}{\eta^2 + r^2 - 2r\eta cos(\theta_n + \delta - \phi) + (\nu'\theta + z_0 - z_i)^2} \tag{7}$$

$$w_2 = \sum_{n=1}^{b} \frac{\eta^2 - r\eta cos(\theta_n + \delta - \phi + \pi/b)}{\eta^2 + r^2 - 2r\eta cos(\theta_n + \delta - \phi + \pi/b) + (\nu'\theta + z_0 - z_i)^2} \tag{8}$$

For sufficiently high values of θ, it is possible to assume that

$$w_{ij} \approx \frac{1}{2}(w_1 + w_2) \tag{9}$$

Therefore, instead of Eq. (1), the following approximation may be used:

$$W_{ij} \approx \int_0^{\theta_m} w_{ij} d\theta + \frac{1}{2}[\int_{\theta_m}^{\infty} w_1 d\theta + \int_{\theta_m}^{\infty} w_2 d\theta] \tag{10}$$

The main advantage of Eq.(10) is that the two integrals in the parentheses have closed-form analytic solutions as follows:

$$\int_{\theta_m}^{\infty} w_1 d\theta = \sum_{n=1}^{b} \Bigg(\frac{\eta^2 - r\eta cos(\theta_n + \delta - \phi)}{[\eta^2 + r^2 - 2r\eta cos(\theta_n + \delta - \phi)]\nu'}$$

$$\times [1 - \frac{(\theta_m + (z_0 - z_i)/\nu')}{[(\theta_m + (z_0 - z_i)/\nu')^2 + \frac{\eta^2 + r^2 - 2r\eta cos(\theta_n + \delta - \phi)}{(\nu')^2}]^{1/2}}] \Bigg) \tag{11}$$

$$\int_{\theta_m}^{\infty} w_2 d\vartheta = \sum_{n=1}^{b} \Bigg(\frac{\eta^2 - r\eta cos(\theta_n + \delta - \phi + \pi/b)}{[\eta^2 + r^2 - 2r\eta cos(\theta_n + \delta - \phi + \pi/b)]\nu'}$$

$$\times [1 - \frac{(\theta_m + (z_0 - z_i)/\nu')}{[(\theta_m + (z_0 - z_i)/\nu')^2 + \frac{\eta^2 + r^2 - 2r\eta cos(\theta_n + \delta - \phi + \pi/b)}{(\nu')^2}]^{1/2}}] \Bigg) \qquad (12)$$

The above result may be found in Ref. 9.

2. Radial induced-velocity (along the x-axis direction)

We also find that the radial induced-velocity, u_{ij}, is usually bounded by the functions u_1 and u_2, which are defined as follows:

$$u_1 = \sum_{n=1}^{b} \frac{\nu'[\eta sin(\theta_n + \delta) - r sin(\phi) - (\theta + (z_0 - z_i)/\nu')\eta cos(\theta_n + \delta)]}{[\eta^2 + r^2 - 2r\eta cos(\theta_n + \delta - \phi) + (\nu'\theta + z_0 - z_i)^2]^{3/2}} \qquad (13)$$

$$u_2 = \sum_{n=1}^{b} \frac{\nu'[\eta sin(\theta_n + \delta + \pi/b) - r sin(\phi) - (\theta + (z_0 - z_i)/\nu')\eta cos(\theta_n + \delta + \pi/b)]}{[\eta^2 + r^2 - 2r\eta cos(\theta_n + \delta - \phi + \pi/b) + (\nu'\theta + z_0 - z_i)^2]^{3/2}} \qquad (14)$$

Therefore, we can find U_{ij} in a similar manner as:

$$U_{ij} \approx \int_0^{\theta_m} u_{ij} d\theta + \frac{1}{2}[\int_{\theta_m}^{\infty} u_1 d\theta + \int_{\theta_m}^{\infty} u_2 d\theta] \qquad (15)$$

where

$$\int_{\theta_m}^{\infty} u_1 d\theta = \sum_{n=1}^{b} \Bigg(\frac{\eta sin(\theta_n + \delta) - r sin(\phi)}{[\eta^2 + r^2 - 2r\eta cos(\theta_n + \delta - \phi)]}$$

$$\times [1 - \frac{(\theta_m + (z_0 - z_i)/\nu')}{[(\theta_m + (z_0 - z_i)/\nu')^2 + \frac{\eta^2 + r^2 - 2r\eta cos(\theta_n + \delta - \phi)}{(\nu')^2}]^{1/2}}]$$

$$- \frac{\eta cos(\theta_n + \delta)}{(\nu')^2[(\theta_m + (z_0 - z_i)/\nu')^2 + \frac{\eta^2 + r^2 - 2r\eta cos(\theta_n + \delta - \phi)}{(\nu')^2}]^{1/2}} \Bigg) \qquad (16)$$

$$\int_{\theta_m}^{\infty} u_2 d\theta = \sum_{n=1}^{b} \Bigg(\frac{\eta sin(\theta_n + \delta + \pi/b) - r sin(\phi)}{[\eta^2 + r^2 - 2r\eta cos(\theta_n + \delta - \phi + \pi/b)]}$$

$$\times [1 - \frac{(\theta_m + (z_0 - z_i)/\nu')}{[(\theta_m + (z_0 - z_i)/\nu')^2 + \frac{\eta^2 + r^2 - 2r\eta cos(\theta_n + \delta - \phi + \pi/b)}{(\nu')^2}]^{1/2}}]$$

$$- \frac{\eta cos(\theta_n + \delta + \pi/b)}{(\nu')^2 [(\theta_m + (z_0 - z_i)/\nu')^2 + \frac{\eta^2 + r^2 - 2r\eta cos(\theta_n + \delta - \phi + \pi/b)}{(\nu')^2}]^{1/2}} \Bigg) \qquad (17)$$

This is an original result of this work, although Ref. 10 mentions that they also have developed a similar formula.

3. Circumferential induced-velocity (along the y-axis direction)

Next, we find that the circumferential induced-velocity V_{ij} is generally bounded by the functions v_1 and v_2, which are defined as follows:

$$v_1 = \sum_{n=1}^{b} \frac{\nu' [-\eta cos(\theta_n + \delta + \pi/2b) + r cos(\phi) - (\theta + (z_0 - z_i)/\nu')\eta cos(\theta_n + \delta + \pi/2b)]}{[\eta^2 + r^2 - 2r\eta cos(\theta_n + \delta - \phi + \pi/2b) + (\nu'\theta + z_0 - z_i)^2]^{3/2}} \qquad (18)$$

$$v_2 = \sum_{n=1}^{b} \frac{\nu' [-\eta cos(\theta_n + \delta + 3\pi/2b) + r cos(\phi) - (\theta + (z_0 - z_i)/\nu')\eta cos(\theta_n + \delta + 3\pi/2b)]}{[\eta^2 + r^2 - 2r\eta cos(\theta_n + \delta - \phi + 3\pi/2b) + (\nu'\theta + z_0 - z_i)^2]^{3/2}} \qquad (19)$$

Therefore, we can find V_{ij} in a similar manner as:

$$V_{ij} \approx \int_0^{\theta_m} v_{ij} d\theta + \frac{1}{2} [\int_{\theta_m}^{\infty} v_1 d\theta + \int_{\theta_m}^{\infty} v_2 d\theta] \qquad (20)$$

where

$$\int_{\theta_m}^{\infty} v_1 d\theta = \sum_{n=1}^{b} \Bigg(\frac{-\eta cos(\theta_n + \delta + \pi/2b) + r cos(\phi)}{[\eta^2 + r^2 - 2r\eta cos(\theta_n + \delta - \phi + \pi/2b)]}$$

$$\times [1 - \frac{(\theta_m + (z_0 - z_i)/\nu')}{[(\theta_m + (z_0 - z_i)/\nu')^2 + \frac{\eta^2 + r^2 - 2r\eta cos(\theta_n + \delta - \phi + \pi/2b)}{(\nu')^2}]^{1/2}}]$$

$$-\frac{\eta sin(\theta_n+\delta+\pi/2b)}{(\nu^{'})^2[(\theta_m+(z_0-z_i)/\nu^{'})^2+\frac{\eta^2+r^2-2r\eta cos(\theta_n+\delta-\phi+\pi/2b)}{(\nu^{'})^2}]^{1/2}}\Bigg) \tag{21}$$

$$\int_{\theta_m}^{\infty} v_2 d\theta = \sum_{n=1}^{b}\Bigg(\frac{-\eta cos(\theta_n+\delta+3\pi/2b)+rcos(\phi)}{[\eta^2+r^2-2r\eta cos(\theta_n+\delta-\phi+3\pi/2b)]}$$

$$\times[1-\frac{(\theta_m+(z_0-z_i)/\nu^{'})}{[(\theta_m+(z_0-z_i)/\nu^{'})^2+\frac{\eta^2+r^2-2r\eta cos(\theta_n+\delta-\phi+3\pi/2b)}{(\nu^{'})^2}]^{1/2}}]$$

$$-\frac{\eta sin(\theta_n+\delta+3\pi/2b)}{(\nu^{'})^2[(\theta_m+(z_0-z_i)/\nu^{'})^2+\frac{\eta^2+r^2-2r\eta cos(\theta_n+\delta-\phi+3\pi/2b)}{(\nu^{'})^2}]^{1/2}}\Bigg) \tag{22}$$

This also is an original result of our work.

THEORETICAL DERIVATION WITH WAKE CONTRACTION

In this section, we extend this technique to the calculation of velocities induced by contracting vortex lines. First, the detailed trajectory of prescribed tip vortex lines (i.e., wake coordinate) are available in the hovering case. Two options[11-12] for high aspect ratio blades are verified by Tung[13] as follow: (1) Kocurek[11] wake and (2) Landgrebe[12] wake. In general, the wake coordinates derived from References 11-12 should be shifted by a transformation matrix according to the conning and offset-hinge coupling effect to determine the relative position of the wake to blades. However, in order to simplify this problem, we consider only the case for which the conning and offset-hinge coupling effect is neglected, and for which the tip vortex lines emanate from the trailing edge of airfoil, assumed to lie on the x axis. Also, only the Landgrebe wake is considered here.

As described in Ref. 12, the tip vortex from a single blade is approximated by the following geometric relations:

$$z_j = \begin{cases} k_1\theta & \text{for } 0 \leq \theta \leq 2\pi/b \\ (z_j)_{\theta=2\pi/b} + k_2(\theta - 2\pi/b) & \text{for } \theta \geq 2\pi/b \end{cases} \tag{23}$$

$$\eta = A + (1 - A)e^{-\lambda\theta} \tag{24}$$

$$\eta' = \lambda(A - 1)e^{-\lambda\theta} \tag{25}$$

The four parameters, (k_1, k_2, A, λ), are determined either from experimental tests or are taken as known functions of thrust coefficient and blade geometry[12]. The major difference between contracted-tip vortex lines and noncontracted-helical vortex lines is that η is not a costant in former case. Also, $y_0 = z_0 = \delta = 0$ holds true in the simplified assumption. Equtions (1) to (3) are still valid if we define u_{ij}, v_{ij}, v_{ij} as follows:

$$For\ \theta \leq 2\pi/b$$

$$u_{ij} = \sum_{n=1}^{b} \frac{k_1[\eta sin(\theta') - rsin(\phi) - (\theta - z_i/k_1)(\eta cos(\theta') + \eta' sin(\theta'))]}{[\eta^2 + r^2 - 2r\eta cos(\theta' - \phi) + (k_1\theta - z_i)^2]^{3/2}} \tag{26}$$

$$v_{ij} = \sum_{n=1}^{b} \frac{k_1[-\eta cos(\theta') + rcos(\phi) - (\theta - z_i/k_1)(\eta sin(\theta') - \eta' cos(\theta'))]}{[\eta^2 + r^2 - 2r\eta cos(\theta' - \phi) + (k_1\theta - z_i)^2]^{3/2}} \tag{27}$$

$$w_{ij} = \sum_{n=1}^{b} \frac{\eta^2 - r\eta cos(\theta' - \phi) - \eta' rsin(\theta' - \phi)}{[\eta^2 + r^2 - 2r\eta cos(\theta' - \phi) + (k_1\theta - z_i)^2]^{3/2}} \tag{28}$$

$$For\ \theta \geq 2\pi/b$$

$$u_{ij} = \sum_{n=1}^{b} \frac{k_2[\eta sin(\theta') - rsin(\phi) - ((k_1/k_2 - 1)2\pi/b + \theta - z_i/k_2)(\eta cos(\theta') + \eta' sin(\theta'))]}{[\eta^2 + r^2 - 2r\eta cos(\theta' - \phi) + (z_j - z_i)^2]^{3/2}} \tag{29}$$

$$v_{ij} = \sum_{n=1}^{b} \frac{k_2[-\eta cos(\theta') + rcos(\phi) - ((k_1/k_2 - 1)2\pi/b + \theta - z_i/k_2)(\eta sin(\theta') - \eta' cos(\theta'))]}{[\eta^2 + r^2 - 2r\eta cos(\theta' - \phi) + (z_j - z_i)^2]^{3/2}} \tag{30}$$

$$w_{ij} = \sum_{n=1}^{b} \frac{\eta^2 - r\eta cos(\theta' - \phi) - \eta' rsin(\theta' - \phi)}{[\eta^2 + r^2 - 2r\eta cos(\theta' - \phi) + (z_j - z_i)^2]^{3/2}} \tag{31}$$

Inspection of Eqns. (29)-(31) suggests corresponding formulas for the upper and lower bounds of (U_{ij}, V_{ij}, W_{ij}) including wake contraction. These functions are also constructed so as to have closed-form integrals.

where

$$w_1 = \sum_{n=1}^{b} \frac{\eta^2 - r\eta cos(\theta_n - \phi) - \eta' rsin(\theta_n - \phi)}{\eta^2 + r^2 - 2r\eta cos(\theta_n - \phi) + (z_j - z_i)^2} \tag{32}$$

$$w_2 = \sum_{n=1}^{b} \frac{\eta^2 - r\eta cos(\theta_n - \phi + \pi/b) - \eta' rsin(\theta_n - \phi + \pi/b)}{\eta^2 + r^2 - 2r\eta cos(\theta_n - \phi + \pi/b) + (z_j - z_i)^2} \tag{33}$$

$$\int_{\theta_m}^{\infty} w_1 d\theta = \sum_{n=1}^{b} \Bigg(\frac{\eta^2 - r\eta cos(\theta_n - \phi) - \eta' r sin(\theta_n - \phi)}{[\eta^2 + r^2 - 2r\eta cos(\theta_n - \phi)]k_2}$$

$$\times [1 - \frac{(\theta_m + (k_1/k_2 - 1)2\pi/b - z_i/k_2)}{[(\theta_m + (k_1/k_2 - 1)2\pi/b - z_i/k_2)^2 + \frac{\eta^2 + r^2 - 2r\eta cos(\theta_n - \phi)}{(k_2)^2}]^{1/2}}] \Bigg) \quad (34)$$

$$\int_{\theta_m}^{\infty} w_2 d\theta = \sum_{n=1}^{b} \Bigg(\frac{\eta^2 - r\eta cos(\theta_n - \phi + \pi/b) - \eta' r sin(\theta_n - \phi + \pi/b)}{[\eta^2 + r^2 - 2r\eta cos(\theta_n - \phi + \pi/b)]k_2}$$

$$\times [1 - \frac{(\theta_m + (k_1/k_2 - 1)2\pi/b - z_i/k_2)}{[(\theta_m + (k_1/k_2 - 1)2\pi/b - z_i/k_2)^2 + \frac{\eta^2 + r^2 - 2r\eta cos(\theta_n - \phi + \pi/b)}{(k_2)^2}]^{1/2}}] \Bigg) \quad (35)$$

$$u_1 = \sum_{n=1}^{b} \frac{k_2[\eta sin(\theta_n) - r sin(\phi) - ((z_j - z_i)/k_2)(\eta cos(\theta_n) + \eta' sin(\theta_n))]}{[\eta^2 + r^2 - 2r\eta cos(\theta_n - \phi) + (z_j - z_i)^2]^{3/2}} \quad (36)$$

$$u_2 = \sum_{n=1}^{b} \frac{k_2[\eta sin(\theta_n + \pi/b) - r sin(\phi) - ((z_j - z_i)/k_2)(\eta cos(\theta_n + \pi/b) + \eta' sin(\theta_n + \pi/b)]}{[\eta^2 + r^2 - 2r\eta cos(\theta_n - \phi + \pi/b) + (z_j - z_i)^2]^{3/2}} \quad (37)$$

$$\int_{\theta_m}^{\infty} u_1 d\theta = \sum_{n=1}^{b} \Bigg(\frac{\eta sin(\theta_n) - r sin(\phi)}{[\eta^2 + r^2 - 2r\eta cos(\theta_n - \phi)]}$$

$$\times [1 - \frac{(\theta_m + (k_1/k_2 - 1)2\pi/b - z_i/k_2)}{[(\theta_m + (k_1/k_2 - 1)2\pi/b - z_i/k_2)^2 + \frac{\eta^2 + r^2 - 2r\eta cos(\theta_n - \phi)}{(k_2)^2}]^{1/2}}]$$

$$- \frac{\eta cos(\theta_n) + \eta' sin(\theta_n)}{(k_2)^2[(\theta_m + (k_1/k_2 - 1)2\pi/b - z_i/k_2)^2 + \frac{\eta^2 + r^2 - 2r\eta cos(\theta_n - \phi)}{(k_2)^2}]^{1/2}} \Bigg) \quad (38)$$

$$\int_{\theta_m}^{\infty} u_2 d\theta = \sum_{n=1}^{b} \Bigg(\frac{\eta sin(\theta_n + \pi/b) - r sin(\phi)}{[\eta^2 + r^2 - 2r\eta cos(\theta_n - \phi + \pi/b)]}$$

$$\times [1 - \frac{(\theta_m + (k_1/k_2 - 1)2\pi/b - z_i/k_2)}{[(\theta_m + (k_1/k_2 - 1)2\pi/b - z_i/k_2)^2 + \frac{\eta^2 + r^2 - 2r\eta cos(\theta_n - \phi + \pi/b)}{(k_2)^2}]^{1/2}}]$$

$$-\frac{\eta cos(\theta_n+\pi/b)+\eta' sin(\theta_n+\pi/b)}{(k_2)^2[(\theta_m+(k_1/k_2-1)2\pi/b-z_i/k_2)^2+\frac{\eta^2+r^2-2r\eta cos(\theta_n-\phi+\pi/b)}{(k_2)^2}]^{1/2}}\Bigg) \quad (39)$$

$$v_1=\sum_{n=1}^{b}\frac{k_2[-\eta cos(\theta_n+\frac{\pi}{2b})+rcos(\phi)-((z_j-z_i)/k_2)(\eta sin(\theta_n+\frac{\pi}{2b})-\eta' cos(\theta_n+\frac{\pi}{2b})]}{[\eta^2+r^2-2r\eta cos(\theta_n-\phi+\frac{\pi}{2b})+(z_j-z_i)^2]^{3/2}} \quad (40)$$

$$v_2=\sum_{n=1}^{b}\frac{k_2[-\eta cos(\theta_n+\frac{3\pi}{2b})+rcos(\phi)-((z_j-z_i)/k_2)(\eta sin(\theta_n+\frac{3\pi}{2b})-\eta' cos(\theta_n+\frac{3\pi}{2b})]}{[\eta^2+r^2-2r\eta cos(\theta_n-\phi+\frac{3\pi}{2b})+(z_j-z_i)^2]^{3/2}} \quad (41)$$

$$\int_{\theta_m}^{\infty}v_1 d\theta=\sum_{n=1}^{b}\Bigg(\frac{-\eta cos(\theta_n+\frac{\pi}{2b})+rcos(\phi)}{[\eta^2+r^2-2r\eta cos(\theta_n-\phi+\frac{\pi}{2b})]}$$

$$\times[1-\frac{(\theta_m+(k_1/k_2-1)2\pi/b-z_i/k_2)}{[(\theta_m+(k_1/k_2-1)2\pi/b-z_i/k_2)^2+\frac{\eta^2+r^2-2r\eta cos(\theta_n-\phi+\frac{\pi}{2b})}{(k_2)^2}]^{1/2}}]$$

$$-\frac{\eta sin(\theta_n+\frac{\pi}{2b})-\eta' cos(\theta_n+\frac{\pi}{2b})}{(k_2)^2[(\theta_m+(k_1/k_2-1)2\pi/b-z_i/k_2)^2+\frac{\eta^2+r^2-2r\eta cos(\theta_n-\phi+\frac{\pi}{2b})}{(k_2)^2}]^{1/2}}\Bigg) \quad (42)$$

$$\int_{\theta_m}^{\infty}v_2 d\theta=\sum_{n=1}^{b}\Bigg(\frac{-\eta cos(\theta_n+\frac{3\pi}{2b})+rcos(\phi)}{[\eta^2+r^2-2r\eta cos(\theta_n-\phi+\frac{3\pi}{2b})]}$$

$$\times[1-\frac{(\theta_m+(k_1/k_2-1)2\pi/b-z_i/k_2)}{[(\theta_m+(k_1/k_2-1)2\pi/b-z_i/k_2)^2+\frac{\eta^2+r^2-2r\eta cos(\theta_n-\phi+\frac{3\pi}{2b})}{(k_2)^2}]^{1/2}}]$$

$$-\frac{\eta sin(\theta_n+\frac{3\pi}{2b})-\eta' cos(\theta_n+\frac{3\pi}{2b})}{(k_2)^2[(\theta_m+(k_1/k_2-1)2\pi/b-z_i/k_2)^2+\frac{\eta^2+r^2-2r\eta cos(\theta_n-\phi+\frac{3\pi}{2b})}{(k_2)^2}]^{1/2}}\Bigg) \quad (43)$$

With these formulas, the induced velocities may be estimated as per Eqns. (10), (15), and (20). Several things should be noted: 1.) θ_m should be greater that $2\pi/b$, 2.) tip vortex lines from other blades are included. 3.) η and η' are functions of θ, and 4.) the strength of the tip vortex is asusumed to be unity. Actually, the strength is equal to the maximun bound circulation.

NUMERICAL RESULTS

It is clear that, in general, the approximations of Eqs. (10), (15), and (20) improve as θ_m is increased. It is also clear that the accuracy of the approximation will be a function of $\nu^{'}, b, (x_i, y_i, z_i)$, and (x_0, y_0, z_0). Numerical results show that, if we select θ_m around 30π to 40π, the absolute error of the integral will not exceed 10^{-4} for the undistorted-wake model. A large value of $(z_0 - z_i)/\nu^{'}$ has the same effect for the distorted and free wake models as does an increase in θ_m for the helical wake. Therefore, an adequate θ_m should be a little bit less than 30π. Also, the accuracy is sensitive to the location of θ_m. The error as a function of θ_m oscilates about some average value for either the corrected or uncorrected methods. By selecting $\theta_m = m\pi$, where m is an integer, for U_{ij}, W_{ij} ; and $\theta_m = m\pi + \pi/(2b)$ for V_{ij}, we obtain values that are near this average for either case.

Figure 2 gives numerical results for the axial velocity, W_{ij}, at x_i/R=0.9 (on the rotor blade) due to two vortices (i.e., a two-bladed rotor) emanating from $x_0/R = \pm 0.6$. It is plotted as a function of θ_m, the maximum θ used in the integration. The circles are the values of the integral, Eq. (3), taken from 0 to θ_m and the squares are the values of the integral obtained by addition of the closed-form trailing terms to this result. This figure is, basically, a reproduction of results in Ref. 9. Several points are noteworthy. First, although the "approximation" is derived from approximate closed-form results, it should give the exact answer as $\theta_m \to \infty$. The value of the exact answer is 1.9×10^{-4}. (One can show that this velocity should be zero for the case of an infinite number blades because $x_0 < x_i$. However, the value of W_{ij} even for 2 blades is very small.) To obtain a similar accuracy level without the trailing corrections would require integration over 500 revolutions of the helix. At $\theta_m = 10\pi$ (5 revolution of numerical integration), the error of the numerical integral is 2.0; but, with the closed-form corrections, the error is only 0.005. Another way of viewing the results is that, for a certain error (e.g., $W_{ij} = 0.01$), the old

way requires 25 revolutions whereas the corrected method requires only 3 revolutions.

Figures 3 and 4 give similar results for the radial induced-velocity, U_{ij}, at the same point. Figure 3 illustrates the rapid convergence (with the closed-form correction) to the correct value of -10.8634. Figure 4, which gives percent error, illustrates in detail how much faster the convergence is. For example, 1% error requires 10 revolutions without the correction and only 3 revolutions with the corrections (a similar trend to W_{ij}). Figures 5 and 6 complete the velocity set with circumferential induced-velocity, V_{ij}. Figure 5 shows total velocity convergence. Figure 6 shows that, for a 1% error, we require 25 revolutions without the correction and only 3 revolutions with the correction. The sharp spike in the curve is an indication of an antinode (a place for which the approximate curve crosses the exact value, giving a temporary zero in error). The upper envelope of points, however, is the true convergence.

It is also interesting to compare rate of convergence (i.e., slopes) in Figures 2, 4, and 6. Table 1 gives the exponent N from error $\rightarrow (\theta_m)^{-N}$ for each case.

Table 1. slop of error curve, -N

Velocity	uncorrected	corrected
U_{ij}	2	5
V_{ij}	2	5
W^*_{ij}	2	6

*(Note: W_{ij} is not truly an error, but is nearly so because $W_{ij} \approx 0$.)

Thus, the corrected formulas average over twice the rate of convergence of the direct integrals.

In the previous figures, we have looked at the velocity on the blade. Now we turn to the velocity at 0.5 radii above the blade, $z_0/R = 0.5$ (which is equivalent to $z_0/R = 0, z_i/R = -0.5$). Figure 7 shows the result for the axial-induced velocity, W_{ij}. The rate of convergence is so slow without the correction that 40 revolutions still gives 1% error. However, with the correction, only 2 revolutions can give the same accuracy. Figures 8 and 9 are the results for radial and circumferential velocities of the same point. These results have the same trend of convergence as those of control points on the blades. If z_i is less than z_0 (i.e., the control is above the helical lines), numerical results confirm that the rate of convergence with the correction is always faster than those without the correction.

In order to check these formulas for control points below the rotor plane, we also look at the velocity at 0.5 radius below the blade, $z_0/R = -0.5$ (which is equivalent to $z_0/R = 0, z_i/R = 0.5$). Figure 10 shows the result for the axial-induced velocity, W_{ij}. There is a small region, over the first two revolutions, for which the "uncorrected" curve is better than the corrected curve due to an error cross-over. However, after θ_m passes through the first few revolutions, the corrected curve exhibits the typical rapid convergence. Figure 10 reveals that, for 1% error, we require 45 revolutions without the correction but only 5 revolutions with the correction.

Fig. 11 gives the result for the radial velocity, U_{ij}. Both corrected and uncorrected curves have a hump over the first few revolutions. The rate of convergence with the correction is faster than those without the correction. For example, for 1% error we require 15 revolutions without the correction and only 5 revolutions with the correction. Fig. 12 shows the result for the circumferential velocity, V_{ij}. Here, the rate of convergence with the correction is still faster than that without the correction. Also, for 1% error we require 15 revolutions without the correction and only 3 revolutions with the correction.

We now turn to numerical results with wake contraction. In the most common meth-

ods of analyses for this case, investigators use straight[12] or curved[6] vortex segments in order to descretize the computation. Normal lengths of these segments corresponding to azimuthal steps ranging from $\triangle\theta = 5^o$ to $\triangle\theta = 15^o$. Thus, there are two sources of error in such calculations. One is the truncation error, which results from truncation of the wake at some θ_m (as in the helical wake), and the other is the quadrature error that results from the descretization process (which is an approximation to the integral of vorticity). Very little work has been done on the effect of the quadrature error. In the method described in this paper, the vortex system is not broken into discrete filaments. Therefore, the error from the numerical integration is usually very small (normally 10^{-7} to 10^{-11}); and the truncation error dominates, although we try to minimize this truncation error by use of the closed-form correction. For conventional methods, however, both errors can be significant. Figure 13 illustrates these points. In the figure, the axial velocity, W_{ij}, is given at $x_i/R = 0.95$ (on the blade) due to 2 contracted tip-vortex lines with $k_1 = 0.175, k_2 = 0.0424, A = 0.78$, and $\lambda = 0.1936$ (from experimental data[12]).

First, let us compare numerical integration (0 to θ_m) with the method of vortex segments. Since both have the same truncation error, this will reveal the quaradure error. Vortex-segment results are given for both $\triangle\theta = 5^o$ and $\triangle\theta = 15^o$. In the range from π to 10π (0-5 revolutions), we see that the quadrature error is of opposite sign to truncation error and actually decreases the total error. Therefore, the 15^o segments (with more quadrature error) actually have less total error than do 5^o segments. As θ_m increases, the quadrature error (which is accumulated) increases while truncation error decreases. Thus, there comes a point for which the errors cancel (zero-error asymptotes on Figure). Beyond this, however, the quadrature error dominates; and 5^o segments become better than 15^o segments, although neither gives very good results. In contrast, the computation from the method in this paper shows good convergence throughout the range of θ_m. Figures 13 casts

doubts as to whether or not even 5^o segments ever converge.

Figures 14 and 15 show the corresponding plots for U_{ij} and V_{ij}. Here, the quadrature error does not cancel the truncation (they are at the same sign) and 5^o segments are more accurate than 15^o segments. For U_{ij}, 5^o segments seem to converge; but, for V_{ij}, even 5^o segments never give less than 2% error. Results from the approximate method give much greater accuracy with much less computer time than is required for discrete-vortex methodds.

CONCLUSIONS

1. A general method is offered in which the trailing portion of the integral for all three induced-velocity components can be found in closed form at any point in the flow field even with wake contraction.

2. The use of this closed-form correction greatly improves convergence such that only 5% to 30% of the normal computing time is required.

3. An upper limit of 15 rotor revolutions is sufficient for 10^{-4} accuracy, and 3-5 revolutions give 1% error accuracy.

4. The quadrature error in vortex-segment methods grows with number of revolutions and can dominate the error. This errror is negligible in the present method.

5. More work needs to be done to see if this approach is to be of benefit in forward flight.

REFERENCE

1. Lan, C., "A Quasi-Vortex-Lattice Method in Thin Wing Theory," Journal of Aircraft, Vol. 11, No. 9, 1974, pp. 518-527.

2. Margason, R. J. and Laman, J. E., "Vortex-Lattice Fortran Program for Estimating Subsonic Aerodynamic Characteristics of Complex Planforms," NASA TN D-6142, 1971.

3. Belotserkouskii, The Theory of Thin Wings in Subsonic Flow, Plenum Press, New York, 1967.

4. Chang, L. K., The Theoretical Performance of High Efficiency Propellers, Ph. D. Thesis, Purdue University, 1980.

5. Basin, V. E., et al., "Theory of the Lifting Aircrew," NASA TTF-823, 1976.

6. Summa, J. M. and Clark, D. R., "A Lifting-Surface Method for Hover/Climb Airloads", Presented at the 35th Annual National Forum of American Helicopter Society, Washington, D.C., May, 1979.

7. Hess, J. L. and Valarezo, W. O., "Calculation of Steady Flow about Propellers by Means of a Surface Panel Method," Presented at AIAA 23rd Aerospace Sciences Meeting, Reno, Nevada, January, 1985.

8. Hough, G. R. and Ordway, D. E., "The Generalized Actuator Disk," THERM Advanced Reseach Report No. TAR-TR6401, Jan. 1964.

9. Rand, O. and Rosen, A., "Efficient Method for Calculating the Axial Velocities Induced Along Rotating Blades by Trailing Helical Vorticity," Journal of Aircraft, Vol. 21, No. 6, June 1984, pp. 433-435.

10. Rosen, A. and Graber, A., "Free Wake Model of Hovering Rotors Having Straight or Curved Blades," International Conference on Rotorcraft Basic Research, Research Triangle Park, North Carolina, Feb., 1985.

11. J. D. Kocurek and J. L. Tangler "A Prescribed Wake Lifting Surface Hover Performance Analysis", Presented at the 32th Annual National Forum of American Helicopter Society, Washington, D.C., May, 1978.

12. Landgrebe, A. J, "The Wake Geometry of a Hovering Helicopter Rotor and Its Influence on Rotor Performance", Journal of Ameriacn Helicopter Society, Vol. 16, Oct. 1972, pp. 1-15.

13. C. Tung., et al., "The Structure of Trailing Vortices Generated by Model Rotor Blades", Vertica, Vol. 7, No. 1, pp. 33-43, 1983.

ACKNOWLEDGEMENT

This work was sponsored by the United States Army Research Office, Grant Nos. DAAG-29-83-K-0133 and DAAG-29-85-K-0228. The view, opinions, and/or findings contained in this report are those of the authors and should not be construed as an official Department of the Army position, policy, or decision, unless so designated by other documentation.

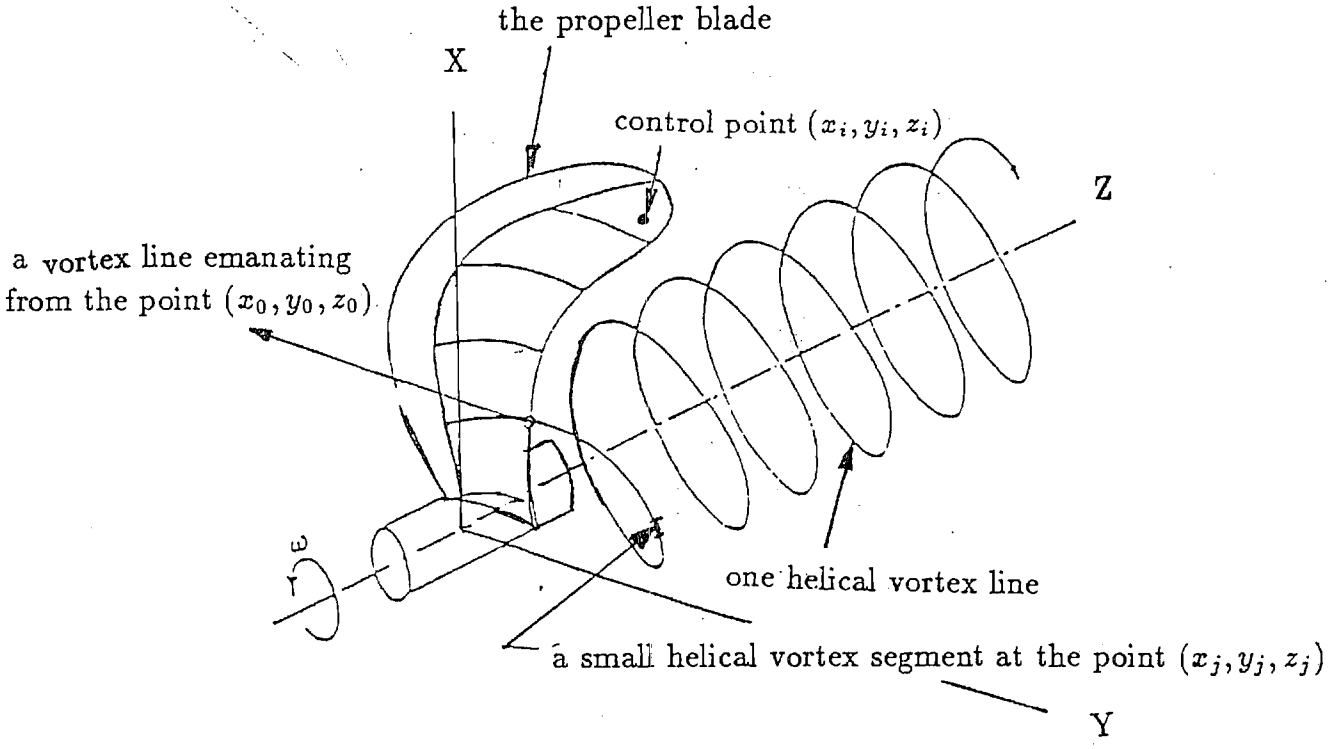

Figure 1. Vortex Coordinate System

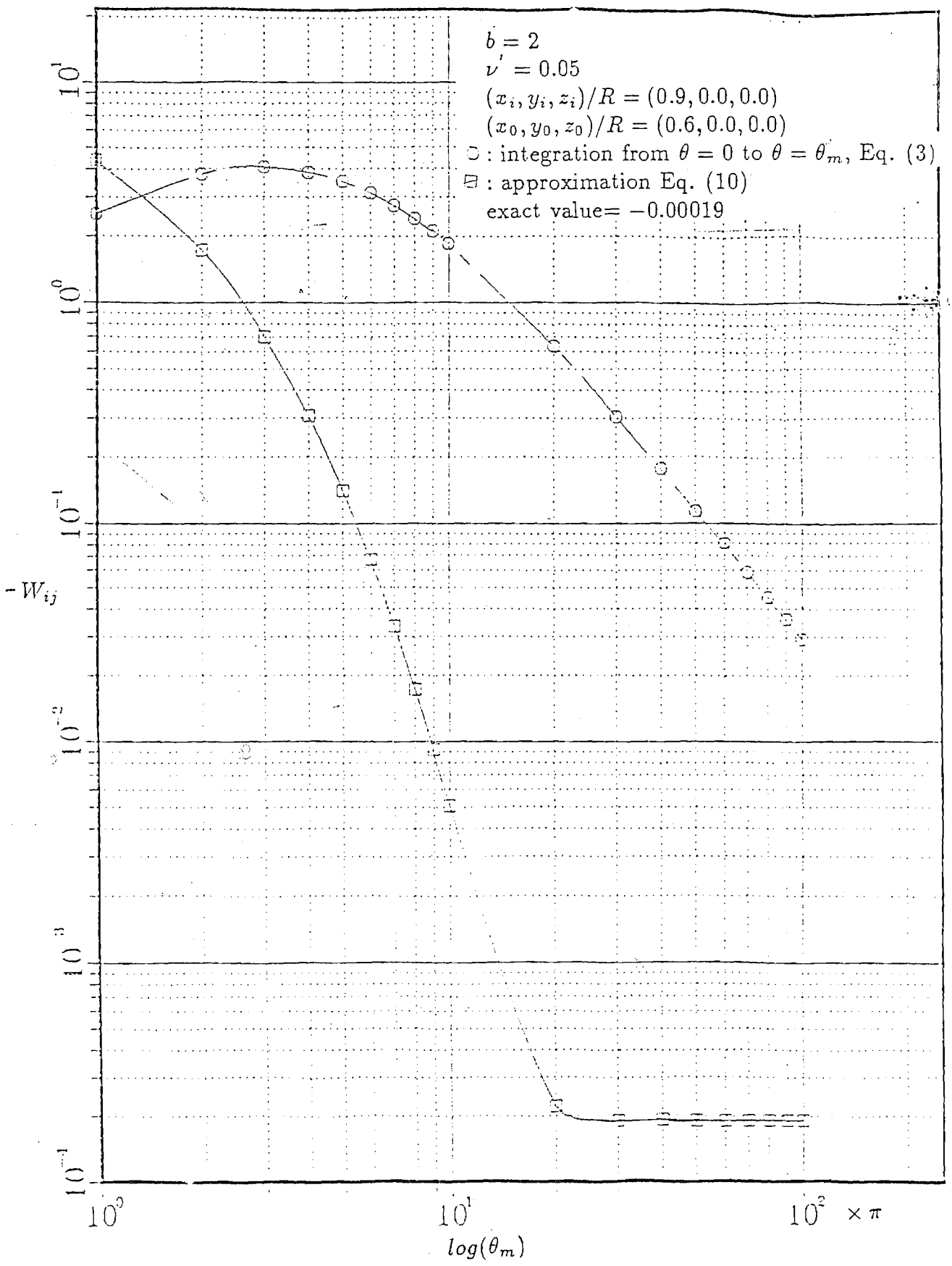

Figure 2. Comparison of Methods, W

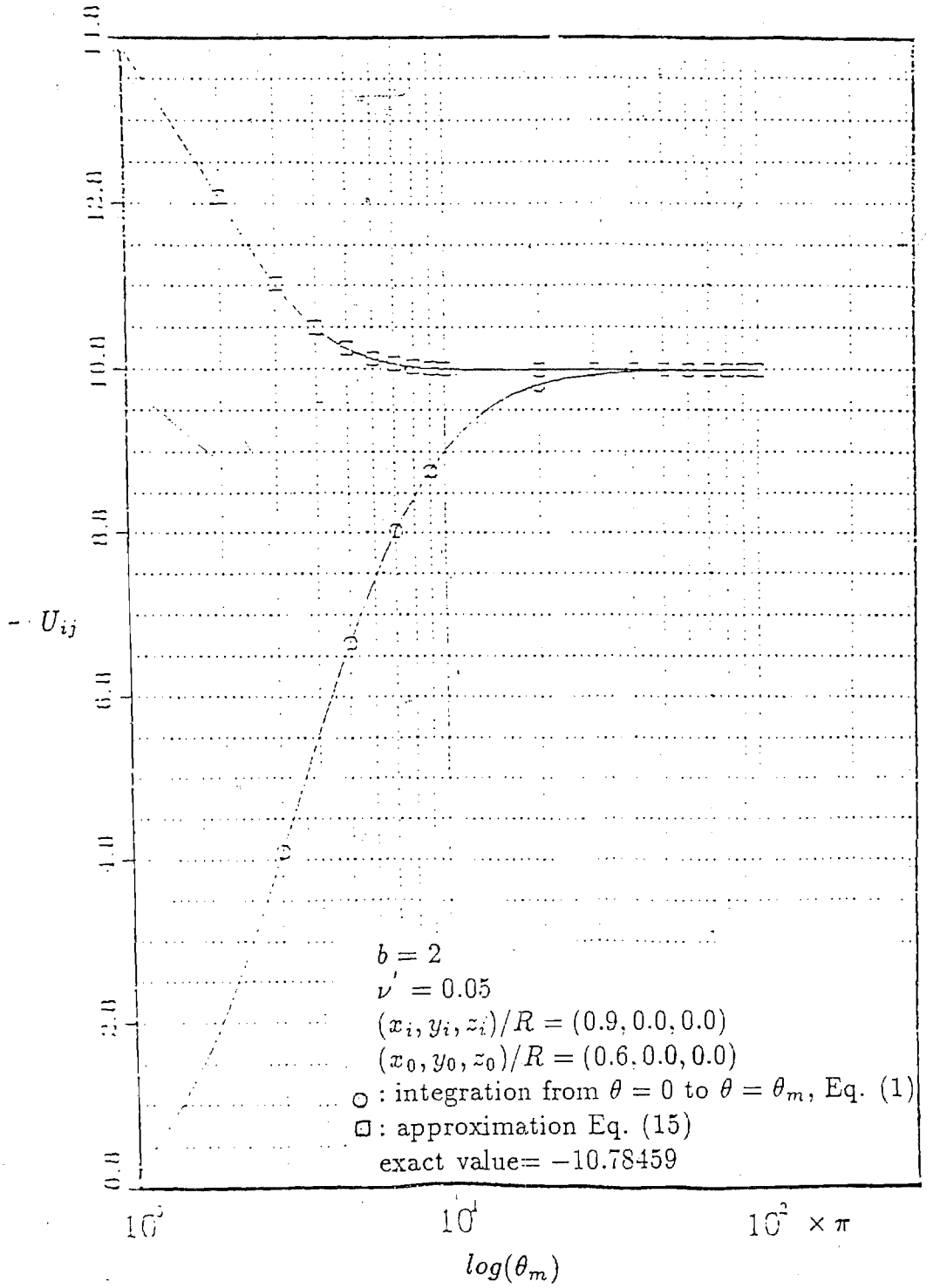

Figure 3. Comparison of Methods, U

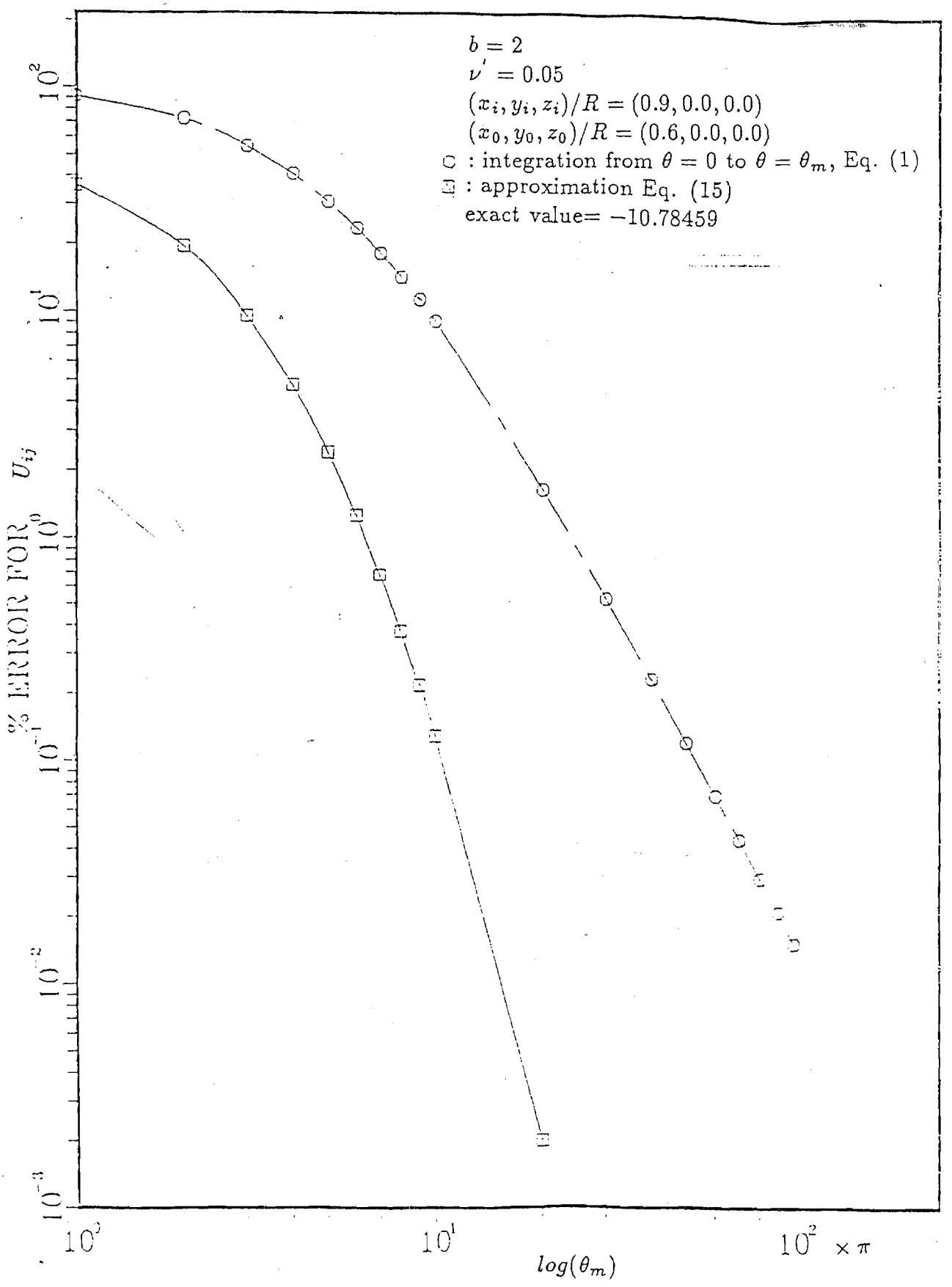

Figure 4. Comparison of Errors, U

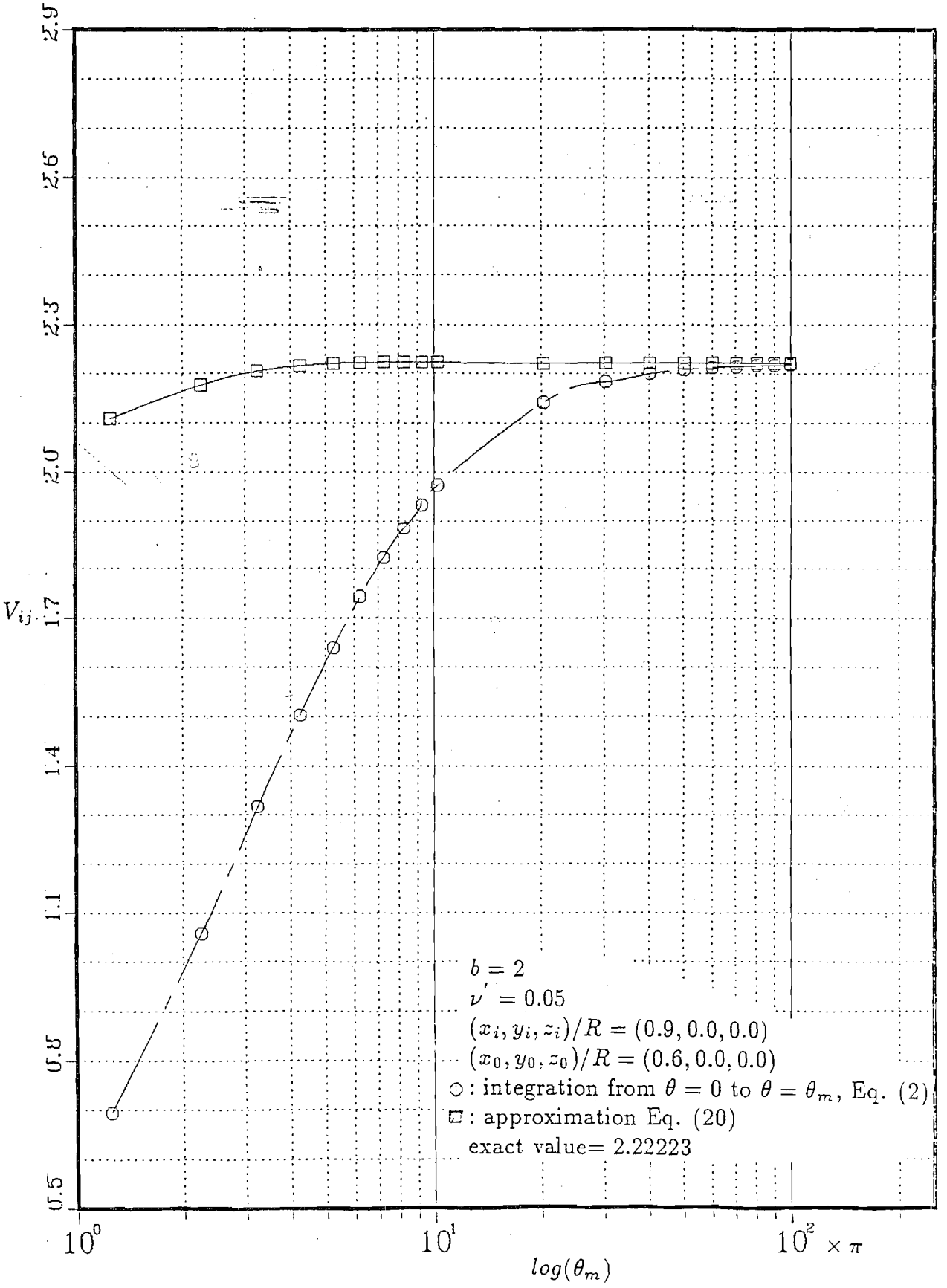

Figure 5. Comparison of Methods, V

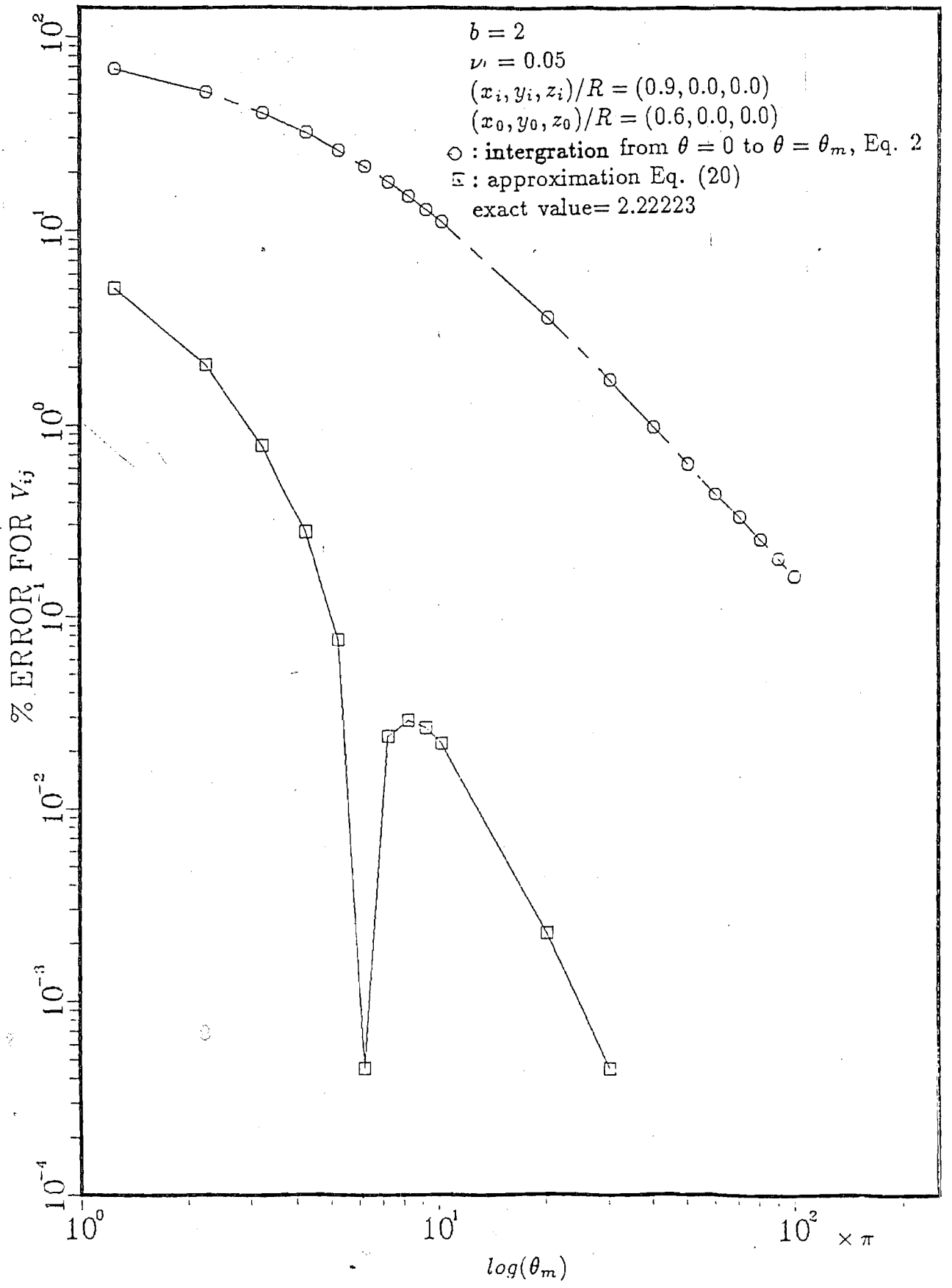

Figure 6. Comparison of Errors, V

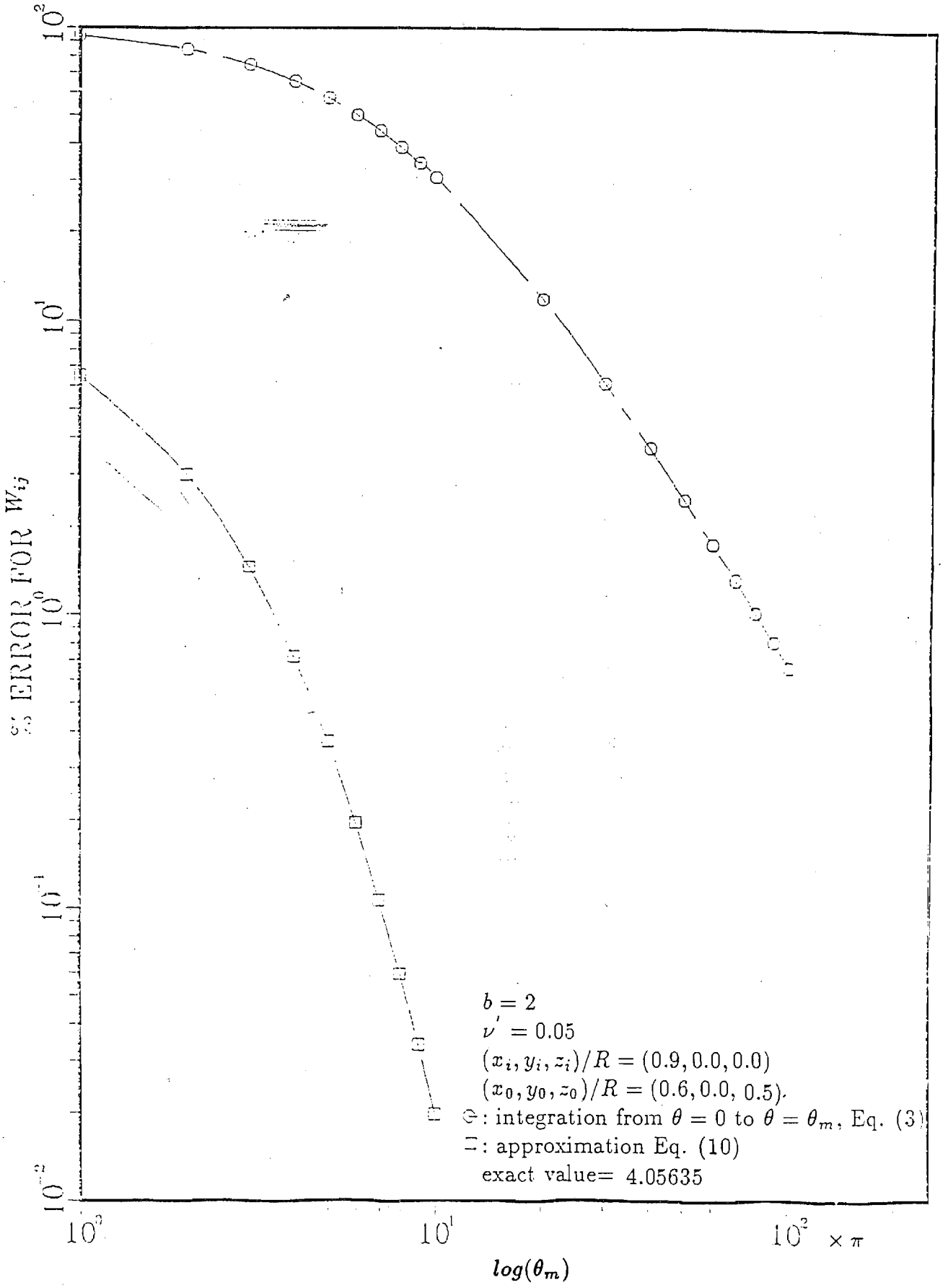

Figure 7. Errors above Rotor, W

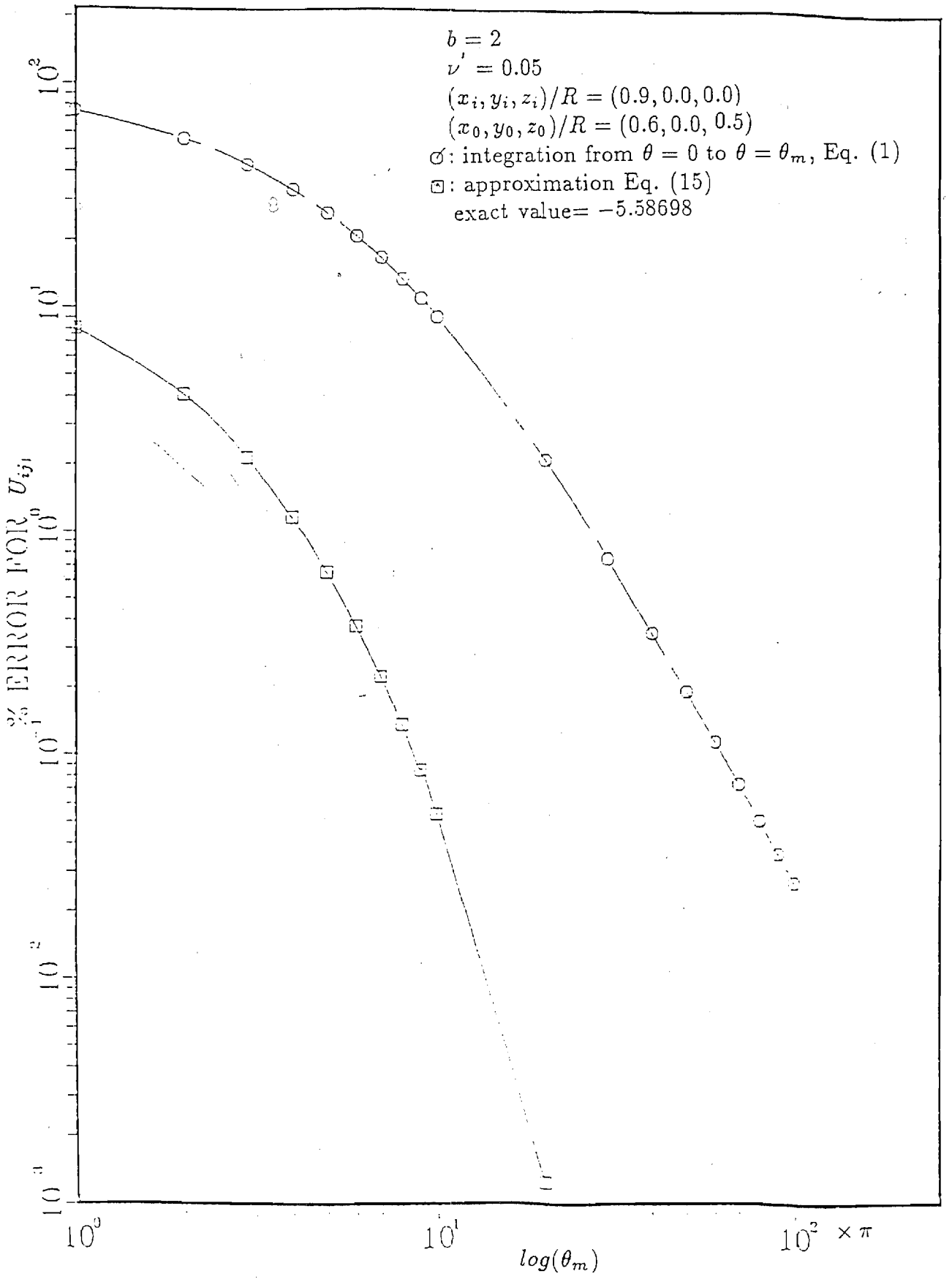

Figure 8. Errors above Rotor, U

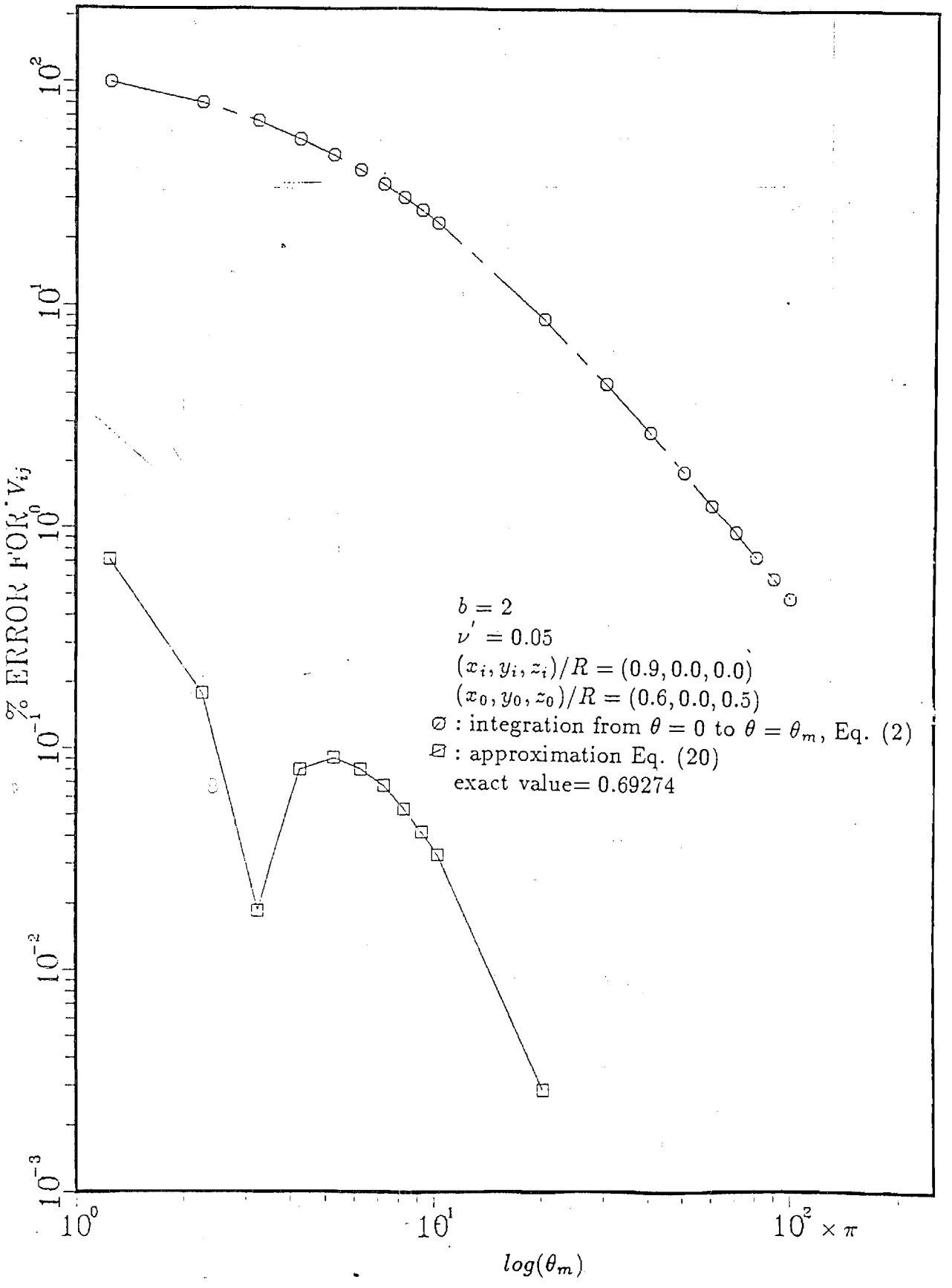

Figure 9. Errors above Rotor, V

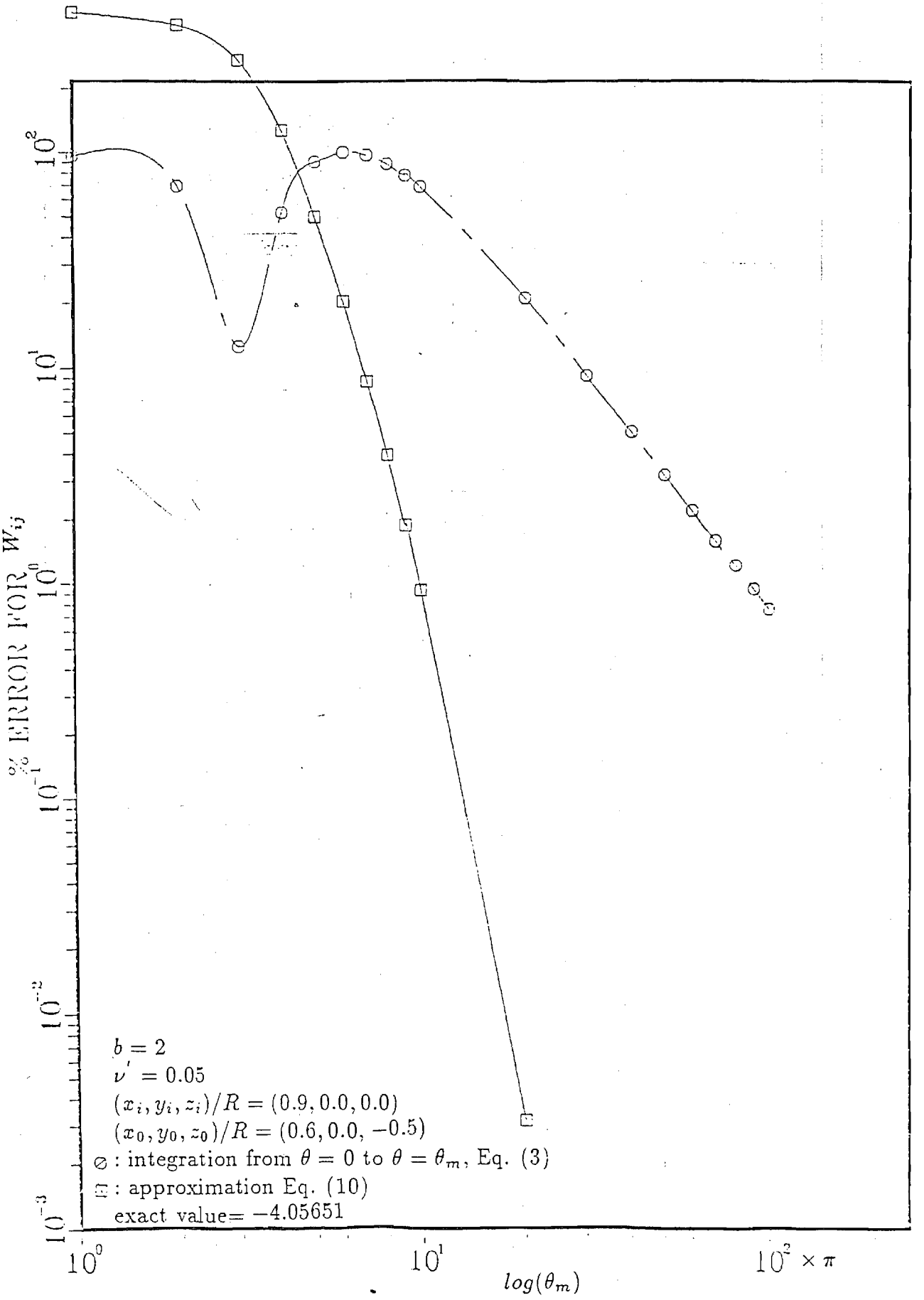

Figure 10. Errors below Rotor, W

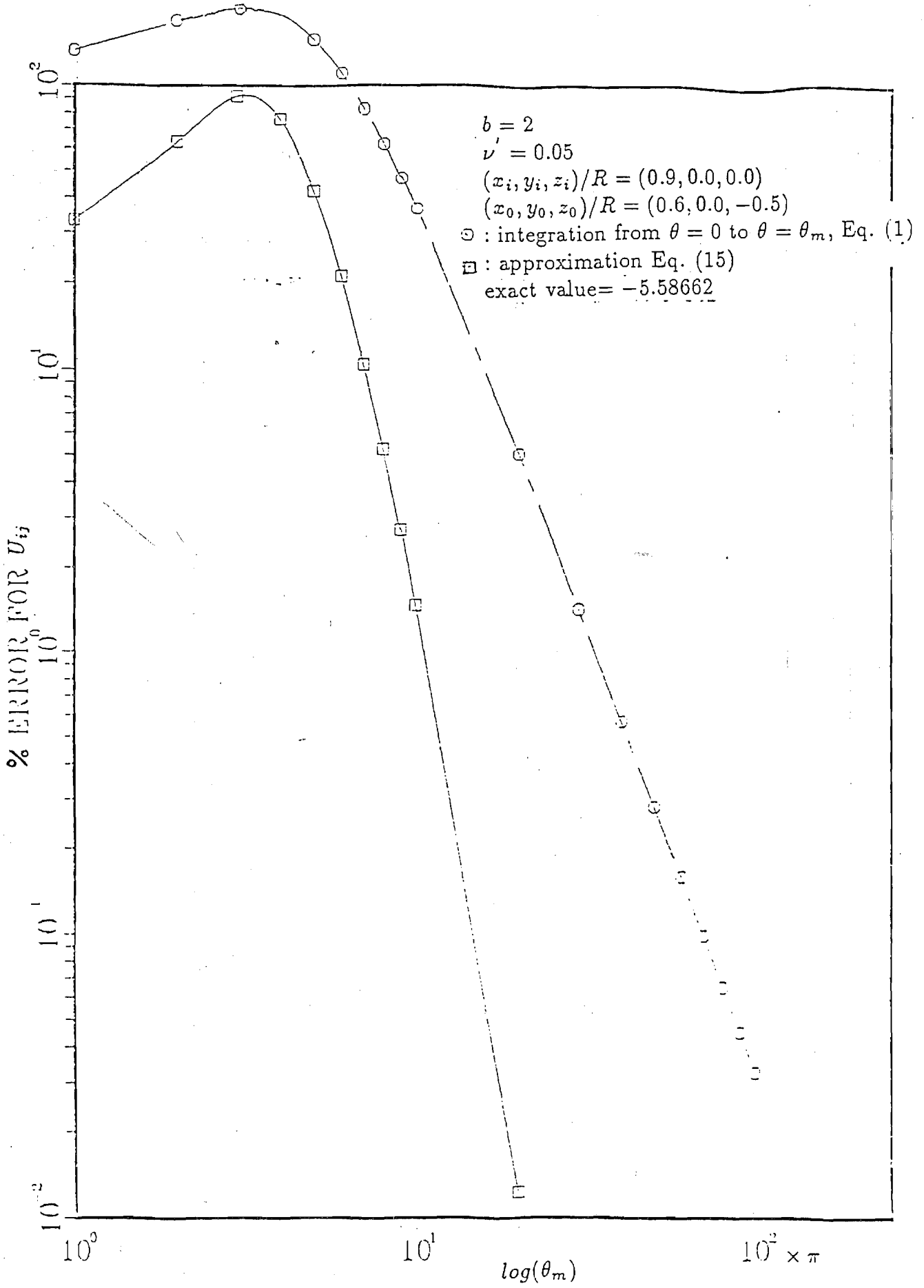

Figure 11. Errors below Rotor, U

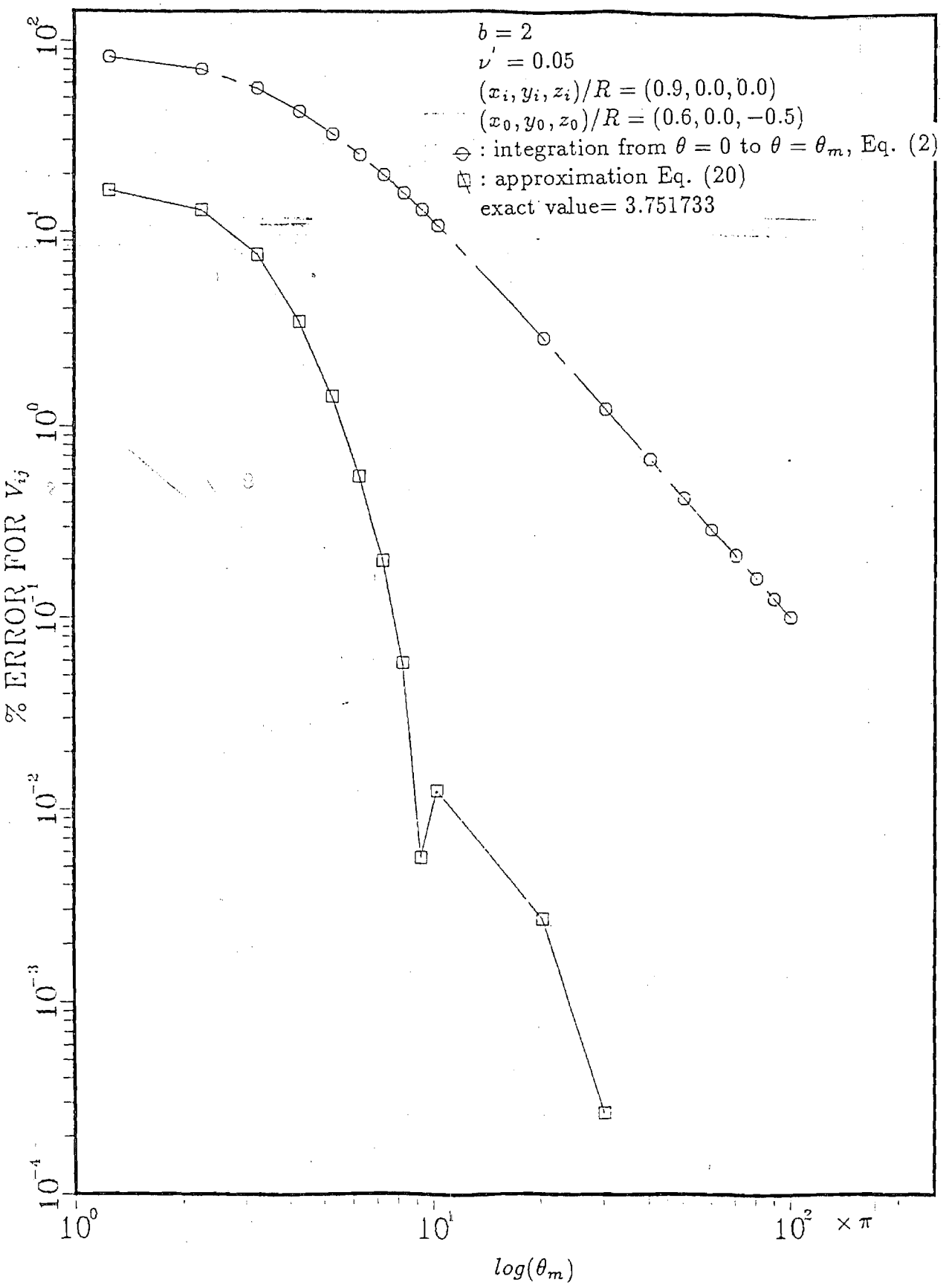

Figure 12. Errors below Rotor, V

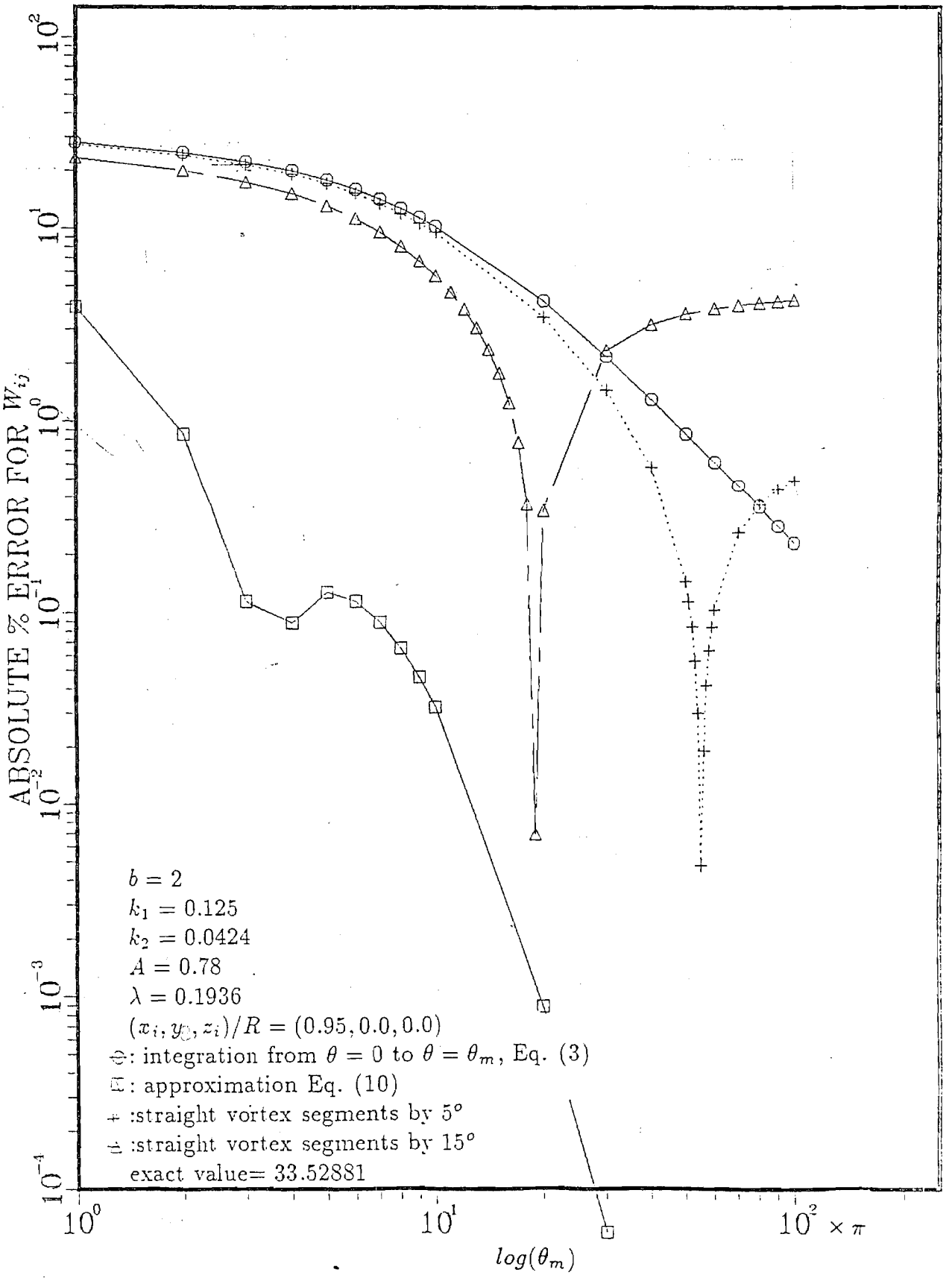

Figure 13. Comparison with Wake Contraction, W

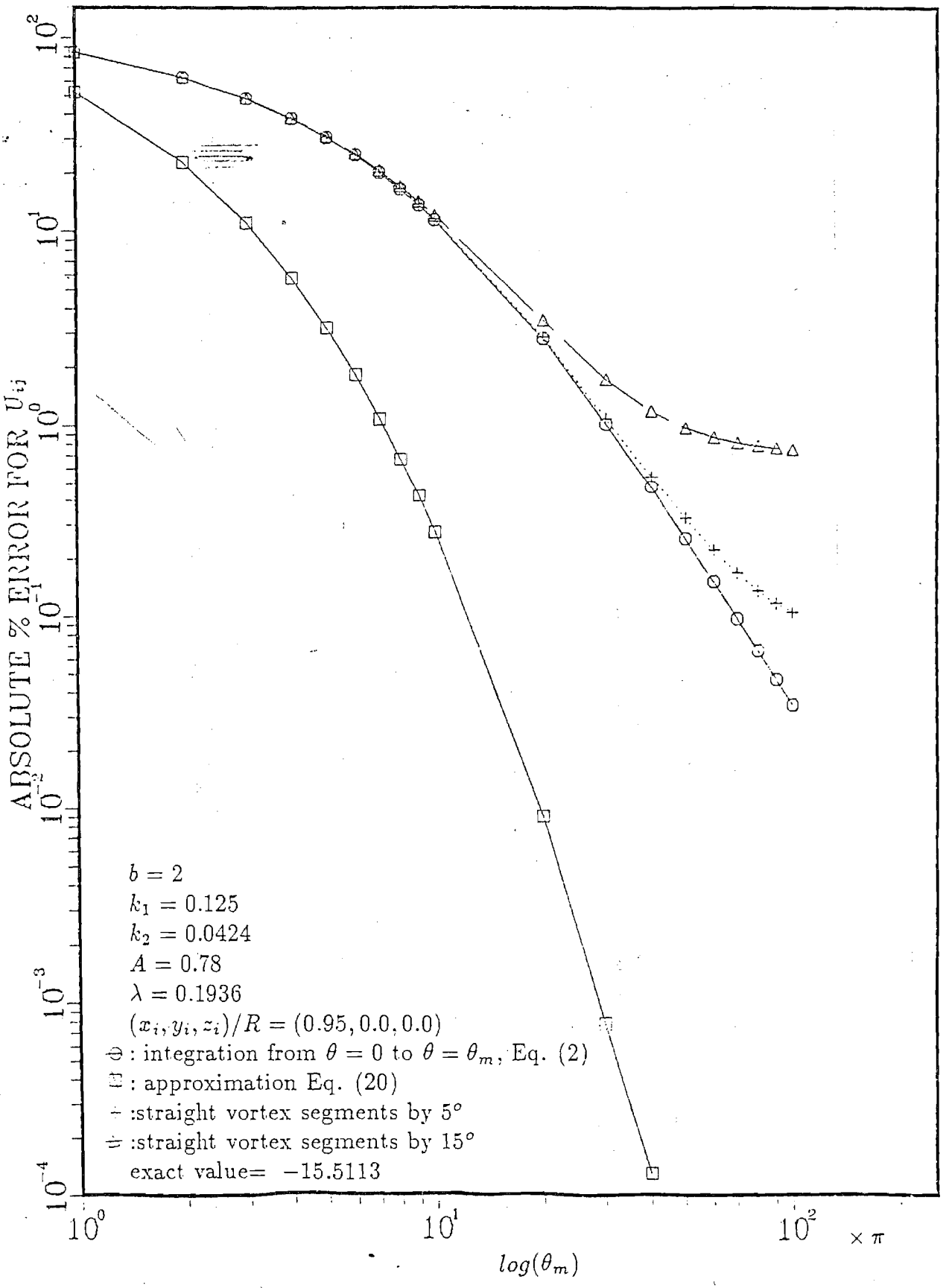

Figure 14. Comparison with Wake Contraction, U

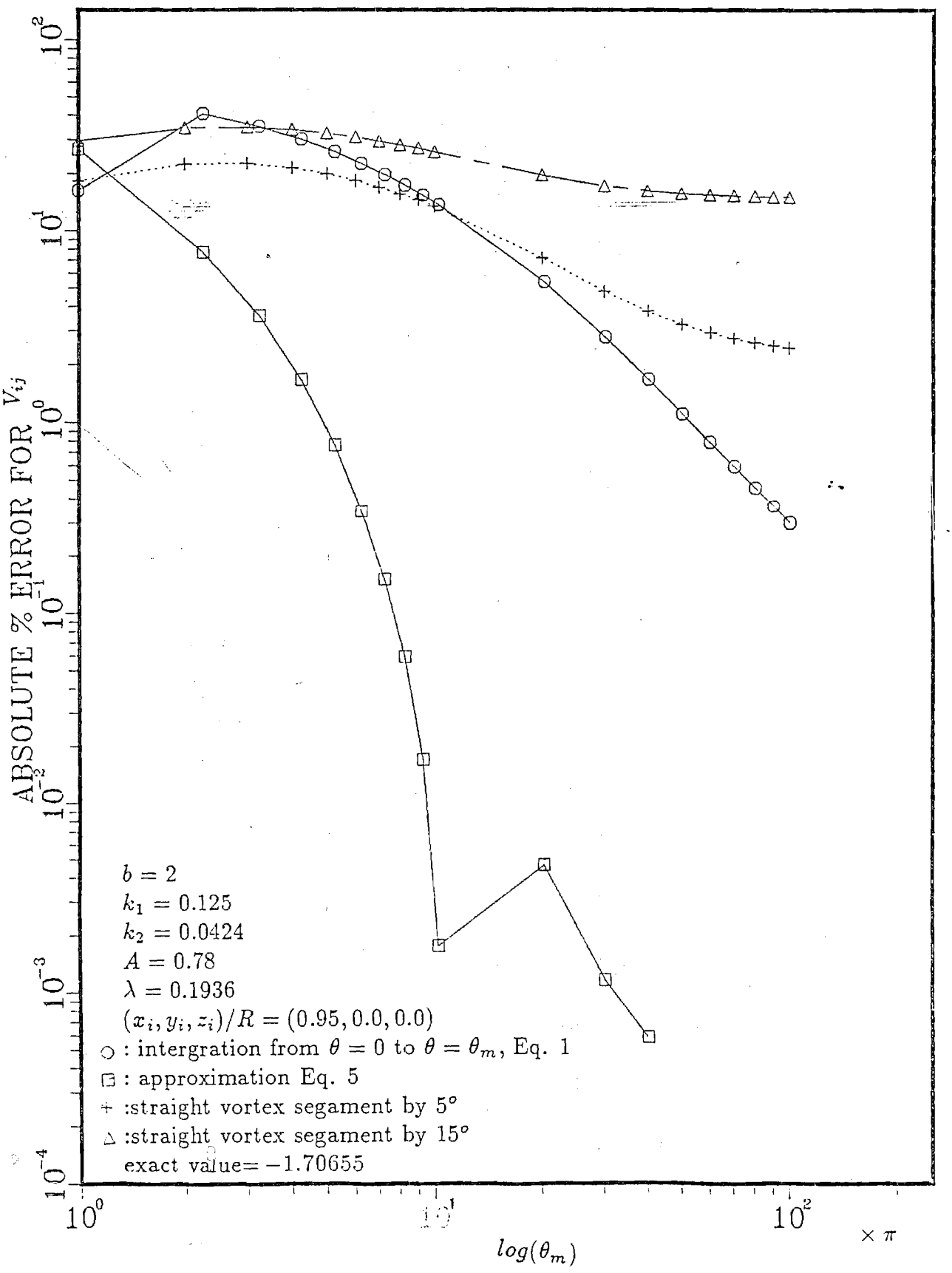

Figure 15. Comparison with Wake Contraction, V

E-16-620

A CLOSED-FORM UNSTEADY AERODYNAMIC THEORY FOR LIFTING ROTORS IN FORWARD FLIGHT

by

David A. Peters
Professor

and

Cheng-Jian He
Research Assistant

School of Aerospace Engineering
Georgia Institute of Technology
Atlanta, Georgia 30332

Submitted for Presentation at the 43rd Annual
National Forum of the American Helicopter Society

October 1, 1986

Extended Abstract

Nomenclature

a	-	slope of lift curve, rad^{-1}
A	-	denominator correction of C'
A_p, A_L	-	"A" due to present theory, Loewy theory
$\bar{b}$	-	semi-chord /R
B_n	-	time constant of nth harmonic @ V=1
C_T	-	thrust coefficient
C_L, C_M	-	roll moment and pitch moment
C'	-	lift deficiency function = $\frac{1}{1 + A}$
h	-	wake spacing over semichord
k	-	rotating reduced frequency
[L]	-	matrix of gains
[M]	-	apparent mass terms
M_q	-	root moment at qth blade, N-m.
m	-	blade passage number
n	-	harmonic number
P_{is}, P_{ic}	-	pressure harmonics
Q	-	number of blades
q	-	blade index
r	-	nondimensional radial station
R	-	blade radius, m
t	-	time, sec
V	-	mass-flow parameter
V_q	-	root shear of qth blade, N
W	-	Loewy wake-spacing function
μ	-	advance ratio

$\bar{\lambda}$	-	total steady inflow (free-stream + induced)
$\bar{\nu}$	-	induced steady inflow
$\lambda_{nc},\lambda_{ns}$	-	perturbation inflow harmonics
ρ	-	density of air, kg/m^3
σ	-	solidity = $2\bar{b}Q/\pi$
ψ	-	nondimensional time
$\bar{\psi}$	-	spatial location
ω	-	frequency per rev
ω_{NR}	-	nonrotating ω
ω_R	-	rotating ω
Ω	-	rotor speed, rad/sec

Introduction

Presently, the only closed-form theory for the unsteady aerodynamics of rotors (as opposed to fixed wings) is the work of Loewy, done 30 years ago, Ref. 1. That theory is both elegant and useful with several experimental verifications, Ref. 2. However, it also has several disadvantages. First, it is a two-dimensional strip theory (with vortex layers to simulate the 3-D effect). This creates a singularity (i.e., discontinuity) at $\omega_R = 0$ and causes the theory to be inaccurate in the frequency range of flight dynamics and rigid-blade flapping (ω_R<2/rev). Second, the theory is for a nonlifting climb and is not applicable, for example, to pure hover or to forward flight. Third, the theory is set in the frequency domain as a complex lift-deficiency function. This implies that it is applicable only in the context of linear aerodynamics (no stall) and that it cannot be used in time-domain analyses. Although the time-domain deficiency can be overcome by numerical extraction of a state-space model, Ref. 3, such a model is still limited by the other drawbacks mentioned above; and the states have no physical interpretation. The only serious competitor to Loewy theory is that of Miller, Ref. 2. Although the Miller theory is three-dimensional, closed-form results exist only at integer-multiple frequencies. Thus, it cannot be used for transient blade dynamics (only for airloads).

What we offer in this paper is a closed-form alternative to Loewy theory. This theory is based on three-dimensional potential-flow theory for an actuator disc. However, the pressure on a finite number of blades is represented by discrete pressure spikes, Fig. 1, which can change magnitude with time and which revolve around the disk with frequency Ω. When such a discrete pressure distribution is analyzed according to the theory of Ref. 4,

the result is a closed form relationship between inflow and lift that is applicable in hover and forward flight. The mass flow correction of Ref. 5 also allows inclusion of steady blade lift (i.e., wake contraction). This new theory is in the time domain (although a frequency-domain version can be obtained) and it is independent of the blade-element theory used. In other words, it can be applied in conjunction with stall models or with other high-reduced-frequency lift models. Furthermore, this approach completely captures the dynamic inflow theory of Ref. 6, including the impressive correlation with experimental data at $\omega < 2/\text{rev}$. Finally, the theory provides agreement with Loewy theory for frequencies $> 2/\text{rev}$ and reduced frequencies < 0.3.

Implementation

The unsteady aerodynamic theory proposed here is a finite-state model. However, it is not synthesized from some other theory. It comes from first principles. Furthermore, the states have direct physical significance as induced-flow distributions. We write the perturbation induced flow of the rotor disk as

$$\lambda(r,\psi) = \lambda_{oc} + \sum_{n=1}^{N} \lambda_{nc} r^n \cos(n\bar{\psi}) + \lambda_{ns} r^n \sin(n\bar{\psi}) \qquad (1)$$

where $\bar{\psi}$ is the spatial azimuth variable; and λ_o, λ_{ns}, λ_{nc} are the inflow states (functions of nondimensional time $\psi = \Omega t$). Other radial distributions can be added (as will be outlined in the paper); but Refs. 2 and 4 find r^n, the single term, very convenient. Here, N can be taken as large as you please; but the theory is probably not accurate for $N > 21$.

The equations for the inflow coefficients are written in terms of blade loadings, P.

$$\left[M_i\right]\left\{\dot{\lambda}_{ic}\right\} + \left[L_c^{-1}\right]\left\{\lambda_{ic}\right\} = \left\{P_{ic}\right\} \qquad i = 0, N \tag{2a}$$

$$\left[M_i\right]\left\{\dot{\lambda}_{is}\right\} + \left[L_s^{-1}\right]\left\{\lambda_{is}\right\} = \left\{P_{is}\right\} \qquad i = 1, N \tag{2b}$$

The blade loadings in Equation (2) can be defined in several ways (as we will outline in the paper). However, one very convenient way is to define them in terms of the the root shear, V_q, and root moment, M_q, of the qth blade, q = 1, Q.

$$P_{oc} = \frac{1}{\rho\pi\Omega^2R^4} \sum_{q=1}^{Q} V_q \tag{3a}$$

$$P_{ns} = \frac{1}{\rho\pi\Omega^2R^5} \frac{n+3}{2n+2} \sum_{q=1}^{Q} M_q \sin(n\bar{\psi}_q) \tag{3b}$$

$$P_{nc} = \frac{1}{\rho\pi\Omega^2R^5} \frac{n+3}{2n+2} \sum_{q=1}^{Q} M_q \cos(n\bar{\psi}_q) \tag{3c}$$

P_{oc}, P_{1s}, and P_{1c} are C_T, $-C_L$, and $-C_M$ respectively. The other P_n values can be identified with higher harmonic disc loadings. The V_q and M_q in Equations (3) may come from any blade-lift theory. Thus, they can include stall, Theordorsen type variations, reversed flow, etc.

The M-matrix in Equation (2) is a diagonal matrix composed of apparent mass terms, M_i, which can be written in terms of time constants, B_i.

$$M_o = 2B_o \tag{4a}$$

$$M_n = B_n/(n+1) \qquad n > 0 \tag{4b}$$

Several alternative formulas exist for B_n (as will be discussed in the paper). A typical one, called the "geometric mean", is given by

$$B_n = \frac{2}{\pi}\sqrt{\frac{2}{n+5}}\ \frac{(2n)!!}{(2n+1)!!} \tag{5}$$

B_n is dependent on lift distribution.

The L-matrix of Equation (2) is not strongly dependent on lift distribution and is derived assuming

$$\text{Lift} \sim r^{n+1}\sqrt{1-r^2} \tag{6}$$

Presently, we have worked out the first 3x3 portion of L_c and 2x2 portion of L_s in closed form for forward flight; and we hope to have the remainder done by the Forum. In hover, however, L and L^{-1} are diagonal matrices known completely in closed form.

$$L_{oc} = \frac{1}{2v} \tag{7a}$$

$$L_{nc} = L_{ns} = \frac{n+1}{V} \tag{7b}$$

In forward flight, of course, L_s and L_c are full matrices. The parameter, V, is the mass-flow parameter that accounts for rotor thrust, $\bar{\nu}$.

$$V = \frac{\mu^2+\bar{\lambda}(\bar{\lambda}+\bar{\nu})}{\sqrt{\mu^2+\bar{\lambda}^2}} \tag{8}$$

The upper 2x2 of M and L_c and the upper 1x1 of L_s comprise classical dynamic inflow theory.

Comparison with Loewy Theory

In order to verify that the above model captures Loewy theory, we can express our model for the special case of frequency response in a nonlifting climb ($V = \bar{\lambda}$ = climb rate), which is the Loewy assumption. If we further assume blade-element theory, we can write a lift-deficiency function for our model of the form

$$C' = \frac{1}{1+A} \tag{9}$$

$$A = A_p = \frac{\sigma a}{8} \sum_{m=-M}^{+M} \frac{1}{V + B_n(\omega_{NR} - mQ)i} \tag{10}$$

where Q is the number of blades, ω_{NR} is the nonrotating frequency, and n is the wave number of the inflow harmonic excited by mQ, (Details will be given in the final paper).

Collective Mode: $(\omega_R = \omega_{NR})$	$n = \lvert mQ \rvert$	(11a-d)
Regressing Cyclic: $(\omega_R = \omega_{NR} + 1)$	$n = \lvert mQ + 1 \rvert$	
Progressing Cyclic: $(\omega_R = \omega_{NR} - 1)$	$n = \lvert mQ - 1 \rvert$	
Differential Mode: $(\omega_R = \omega_{NR} \pm \frac{Q}{2})$	$n = \lvert mQ \pm \frac{Q}{2} \rvert$	

For rotors with more than 4 blades, the higher-harmonic rotor modes, of the form $\cos(p\bar{\psi})$ and $\sin(p\psi)$, have $\omega_R = \omega_{NR} \pm p$ and $n = \lvert mQ \pm p \rvert$ for regressing and progressing modes. Notice, then, that every value of n can be excited by some rotor mode.

For comparison, we can write the Loewy lift-deficiency function for small k (Ref. 7) in the same form as Equation (9) with

$$A = A_L = \pi k\left(\frac{1}{2} + w\right) = \frac{\pi k}{2} \quad \frac{e^{kh}\, e^{\frac{2\pi i}{Q}\omega_{NR}} + 1}{e^{kh}\, e^{\frac{2\pi i}{Q}\omega_{NR}} - 1} \tag{12}$$

where k is the reduced frequency based on semichord.

$$k = \frac{\bar{b}}{r}\,|\omega_R| \tag{13}$$

and with ω_R given as in Equation (11). Notice that, although k is assumed small, kh (reduced frequency based on wake spacing) and ω_{NR} (per/rev frequency) are <u>not</u> assumed small.

Although Equations (10) and (12) look entirely different and are derived from entirely different theories, they are actually nearly identical. To illustrate this, we expand Equation (12) in an exact Laurent's series about the poles $\sigma_m = mQ + Vk/\bar{b}i$.

$$A_L = \pi k\left(\frac{1}{2} + w\right) = \frac{\sigma a}{8} \sum_{m=-\infty}^{+\infty} \frac{1}{V + \frac{\bar{b}}{k}\,(\omega_{NR} - mQ)i} \tag{14}$$

where we have used $a = 2\pi$, $h = 4V/\sigma$, and $\sigma = 2\bar{b}Q/\pi$. Equation (14) is an exact representation of A_L (despite the fact that k can depend on ω_{NR}), and we have verified this numerically.

The similarity between Equation (10) and Equation (14) is amazing when one considers the former is from actuator-disk theory and the latter is from lifting-line theory. Even the differences are small. First, we notice that the apparent-mass coefficients of actuator-disc theory are nearly identical to the corresponding coefficients of Loewy theory when ω_R is near n.

$$B_n = \frac{2}{\pi}\sqrt{\frac{2}{n+5}}\,\frac{(2n)!!}{(2n+1)!!} \approx \frac{.80}{(2.8+n)} = \frac{.80}{n}\,\Big|_{\substack{N \\ \text{Large } n}} \tag{15a}$$

$$B_n^L \text{ (Loewy)} = \frac{\bar{b}}{k} = \frac{r}{|\omega_R|} = \frac{r}{n} \tag{15b}$$

In other words, the coefficients from actuator-disk theory are nearly identical to those of Loewy at the 80% radius for large n. Therefore, if we assume that C' and A are dominated by the pole nearest to ω_{NR}, then B_n should become important only when ω_{NR} is near mQ (ω_R near n). Thus, the two theories should give similar results for C'.

It is important to note, however, that our B_n is not equal to B_n^L except except as $n \to \infty$ ($n > 30$). At lower values of n, the 2-dimensional Loewy theory overestimates the apparent mass of the flow. In fact, the Loewy result give 3 times the actuator-disk apparent mass for n=1 (cyclic) and an infinite apparent mass at n = 0, collective. Figure 2 illustrates the difference in apparent mass between the two theories in more detail. The dashed line is the theory of Equation (5), the shaded area is a range of realistic values (for various assumptions on lift distribution) and the solid line is the Loewy value at r = .75, which goes to infinity as $n \to 0$. It is important to note here that B_o and B_1 have been identified very accurately from experimental data, Refs. 5 and 7. These show that $.375 \leq B_o \leq .425$ and $.22 \leq B_1 \leq .24$. Clearly, the 3-D potential flow results agree with experiments ($B_o = .42$, $B_1 = .24$); while the 2-D vortex results do not ($B_o = \infty$, $B_1 = .75$).

The physical reason for this overprediction by Loewy theory is that, in the 2-dimensional theory, vortex strength from a single oscillation is actually counted more than once in apparently different vortex layers below, Figure 3. Although these multiple accountings average out in the quasisteady case, they give far too much kinetic energy in the unsteady flow. The most dramatic numerical result of this overprediction is in the collective mode

($\omega_R = \omega_{NR} = \omega$, $n = mQ$) near $\omega = 0$. The Loewy function has a discontinuity (due to the infinite apparent mass) which is clearly evident either from a numerical plot of Equation (12), Figure 4, or from an examination of the m=0 term, equation (14).

$$A_L\ (\omega = 0) = \frac{1}{V + ri\ \frac{\omega_R}{|\omega_R|}} = \frac{1}{V \pm ri} \qquad (16)$$

There is a discontinuity in this function at $\omega = 0$. Thus, our new theory not only captures the Loewy theory at low k; but it <u>improves</u> it at lower ω's by giving 3-dimensional estimates of apparent mass.

Numerical Results

Many numerical results will be given in the paper, and these will show (among other things) that the actuator-disc theory with the Loewy B_n^L almost identically matches the Loewy function. In this abstract, however, we compare ReC' and ImC' for Loewy theory with that of our new model with B_n from Equation (5). Figure 4 is for a collective excitation, Figures 5-6 are for progressive and regressive cyclic excitations, and Figure 7 is for a differential excitation (ω in rotating system). Several points are noteworthy.

1. The new model captures Loewy theory at higher frequencies.
2. At lower frequencies, the new model captures dynamic inflow results but deviates from Loewy theory.
3. The Loewy function has discontinuities at $\omega = 0$ in the rotating system (collective $\omega = 0$, cyclic $\omega = 1$).

4. The largest differences in the theories are in the real part of the collective mode and in the imaginary parts of all modes at frequencies less than 2/rev.

Therefore, the new model (which is in the time domain and applicable in forward flight) substantially recovers Loewy theory with improvements at low k. Further, it can be used with dynamic stall, Theordorsen theory, or other 2-D models of lift.

References

1. Loewy, Robert G., "A Two-Dimensional Approximation to the Unsteady Aerodynamics of Rotary Wings", Journal of the Aeronautical Sciences, Vol. 24, No. 2, Feb. 1957, pp. 81-92.

2. Miller, R.H. "Rotor Blade Harmonic Air Loading", AIAA Journal, Vol. 2, No. 7, July 1964, pp. 1254-1269.

3. Friedmann, P. and Venkatesan, C., "Finite State Modelling of Unsteady Aerodynamics and its Application to a Rotor Dynamic Problem", Eleventh European Rotorcraft Forum, London, Sept. 10-13, 1985, Paper No. 72.

4. Pitt, Dale M., Rotor Dynamic Inflow Derivatives and Time Constants from Various Inflow Models, D.Sc. Dissertation, Washington University, St. Louis, December 1980.

5. Pitt, Dale M. and Peters, David A., "Theoretical Prediction of Dynamic-Inflow Derivatives", Vertica, Vol. 5, 1981, pp. 21-34.

6. Banerjee, D., Crews, S.T., Hohenemser, K.H., and Yin, S.K., "Identification of State Variables and Dynamic Inflow From Rotor Model Dynamic Tests", Journal of the American Helicopter Society, Vol. 22, No. 2, April 1977, pp. 28-36.

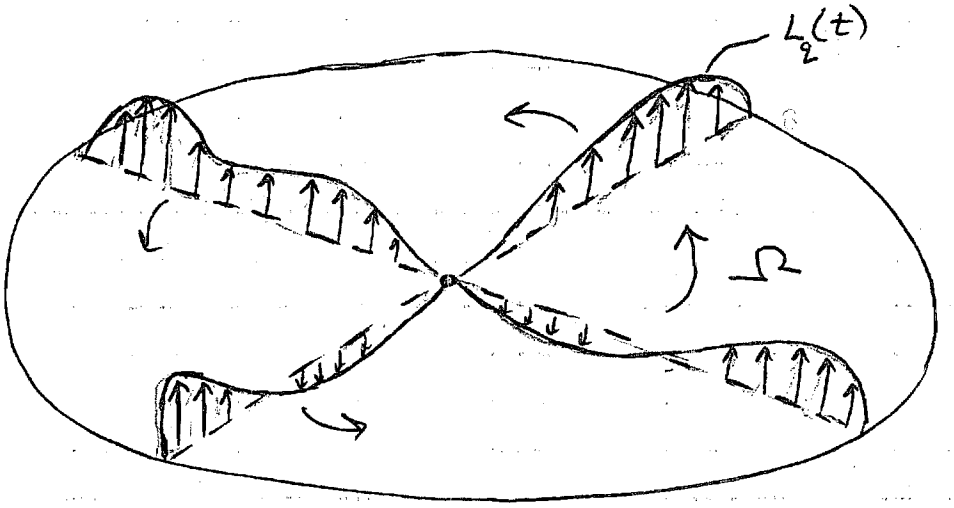

Figure 1 Discrete Blade Loading

Figure 2. Comparison of Time Constants for nth Harmonic

B_n

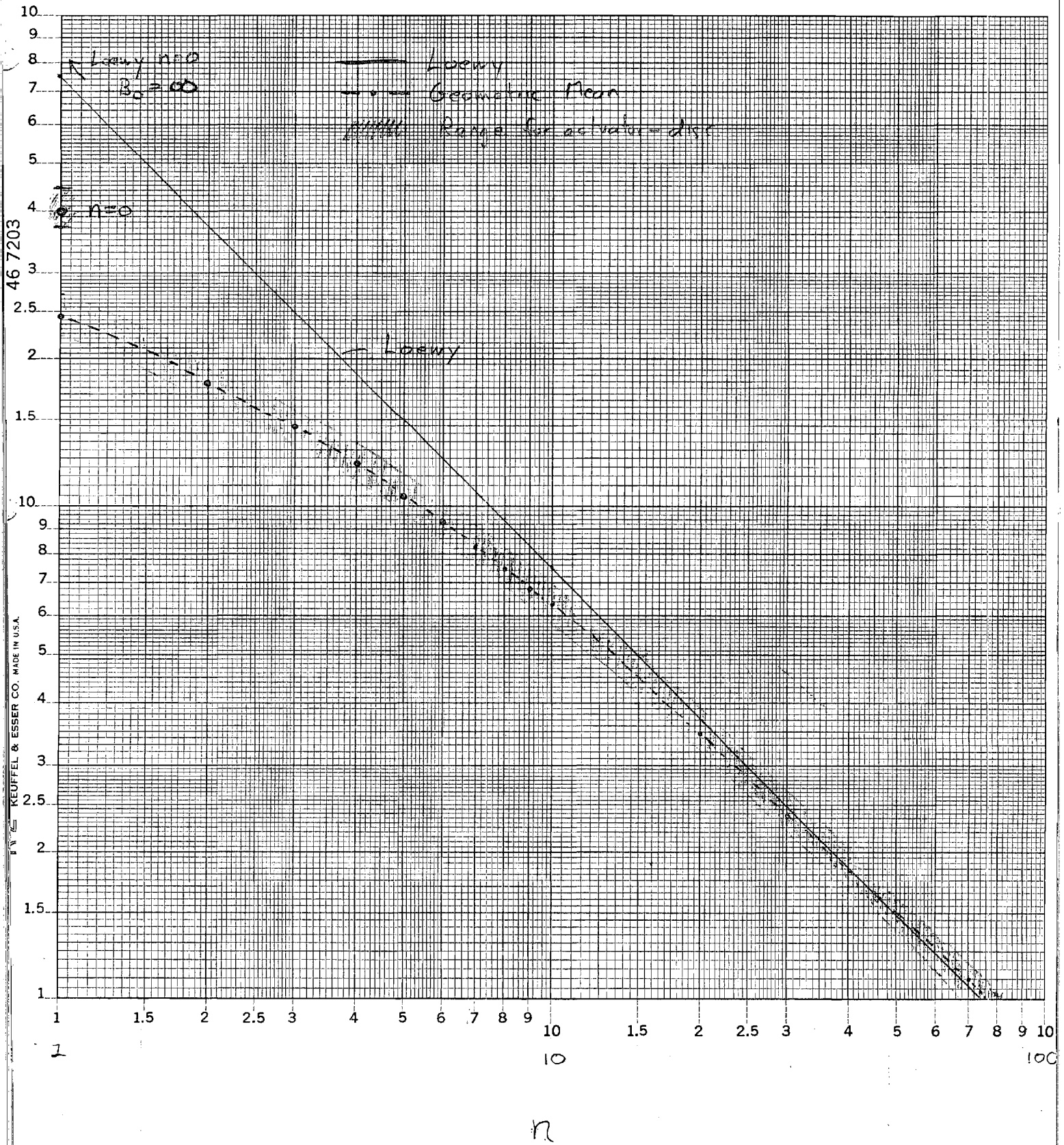

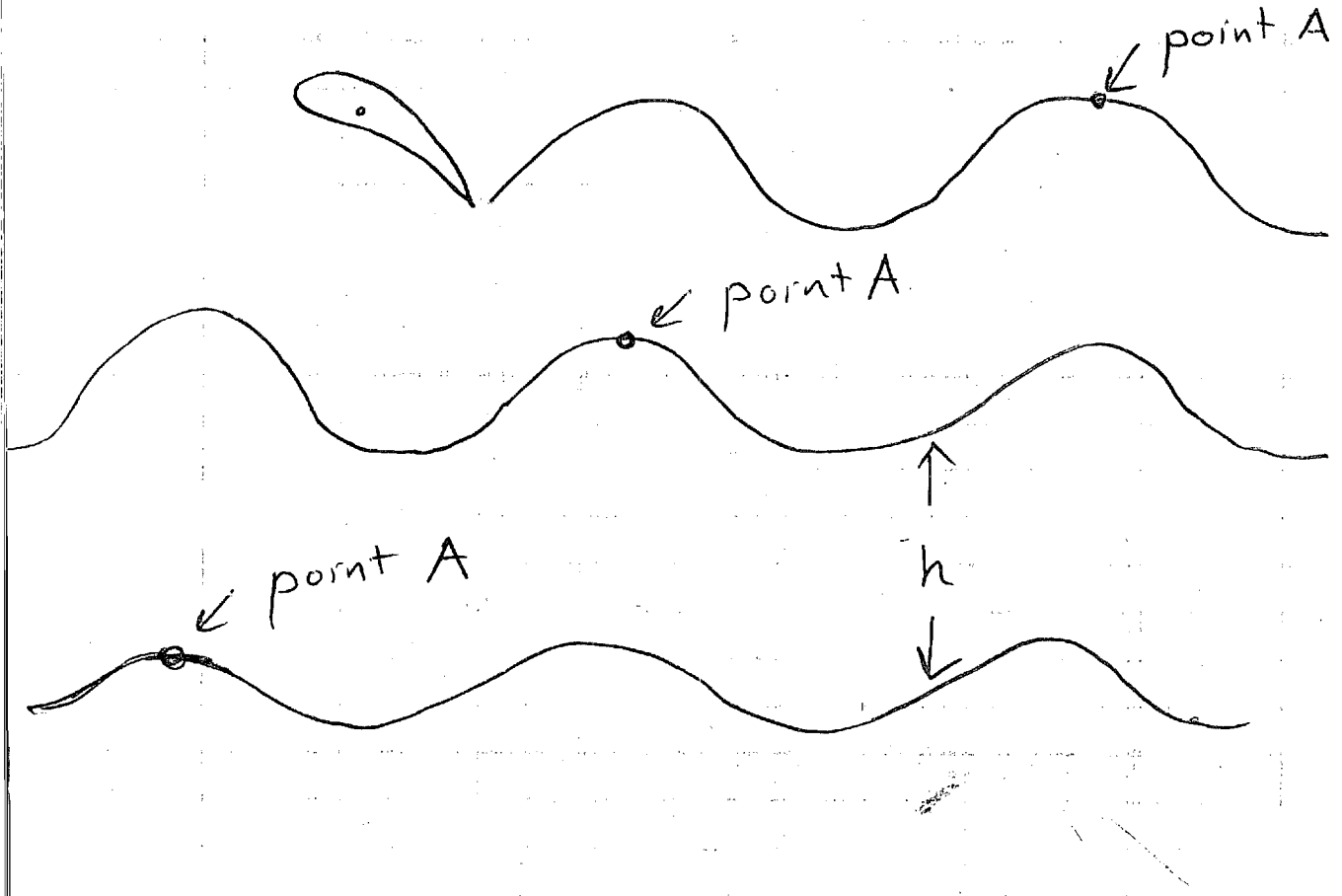

Fig. 3 2-D Approximation
(1/rev)

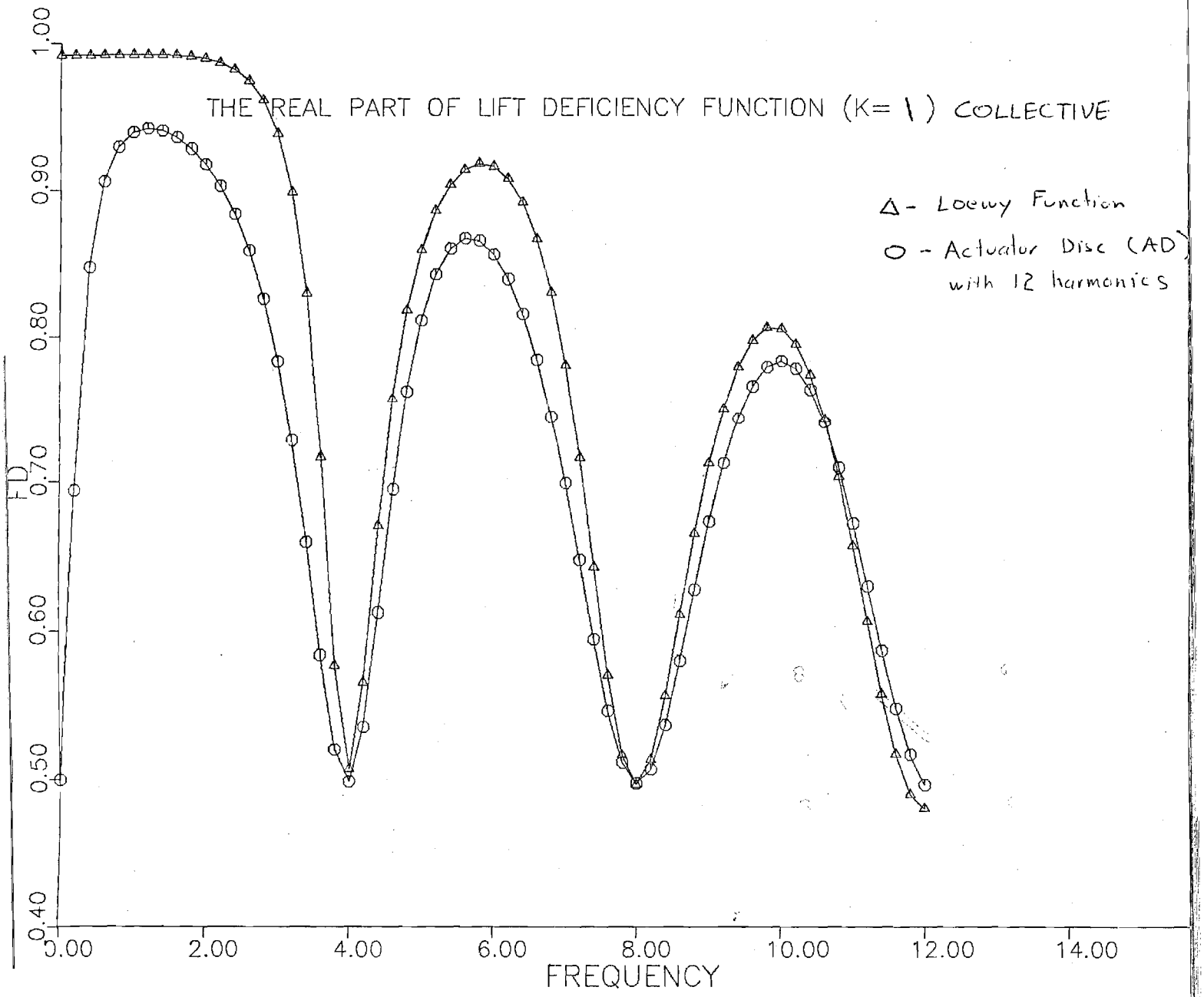
THE REAL PART OF LIFT DEFICIENCY FUNCTION (K= 1) COLLECTIVE
Δ - Loewy Function
O - Actuator Disc (AD) with 12 harmonics
FD
1.00
0.90
0.80
0.70
0.60
0.50
0.40
0.00
2.00
4.00
6.00
8.00
10.00
12.00
14.00
FREQUENCY

Figure 4a

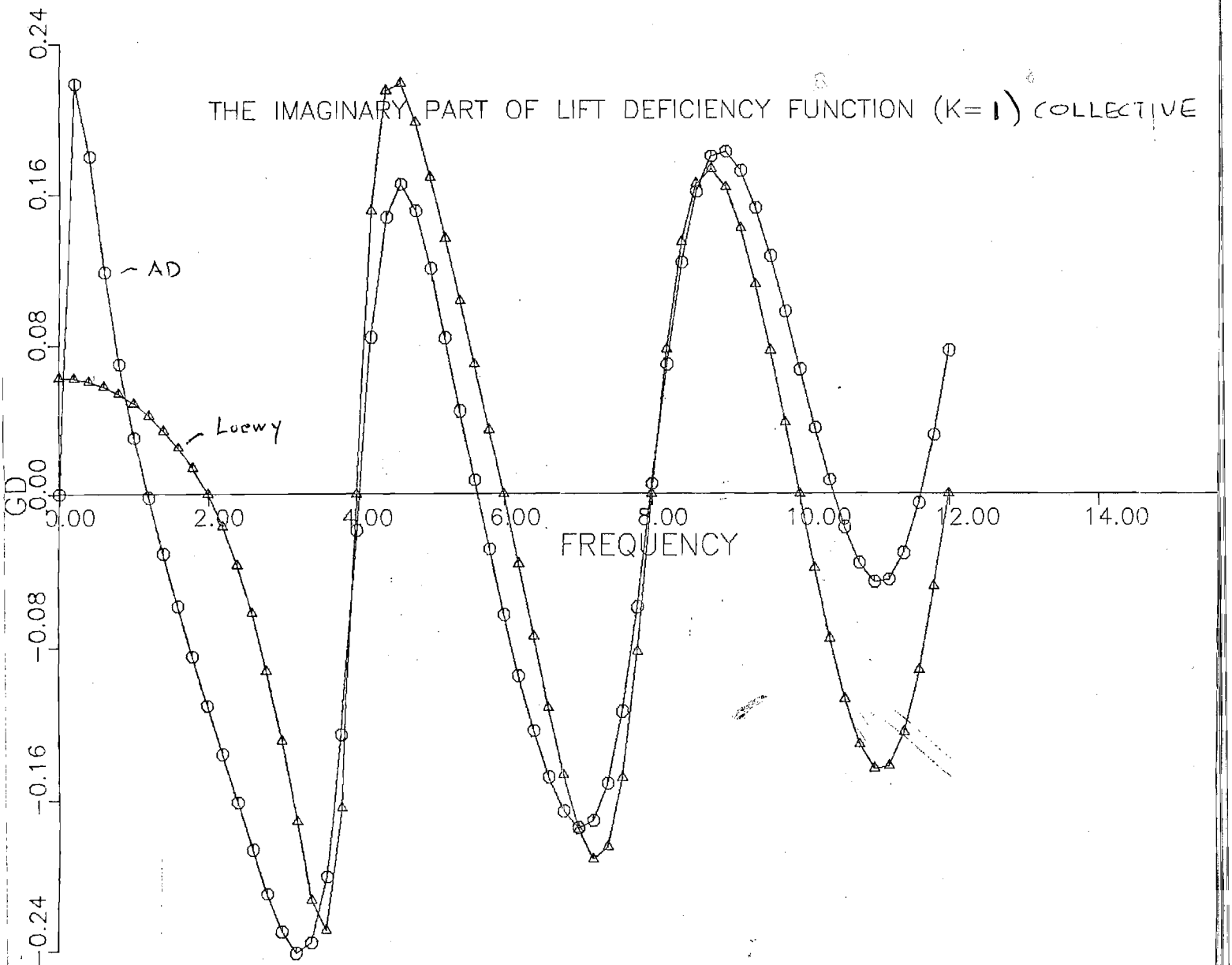
THE IMAGINARY PART OF LIFT DEFICIENCY FUNCTION (K=1) COLLECTIVE
0.24
0.16
0.08
0.00
-0.08
-0.16
-0.24
GD
AD
Loewy
0.00
2.00
4.00
6.00
8.00
10.00
12.00
14.00
FREQUENCY

Figure 4b

Regressive Mode

13 harmonics

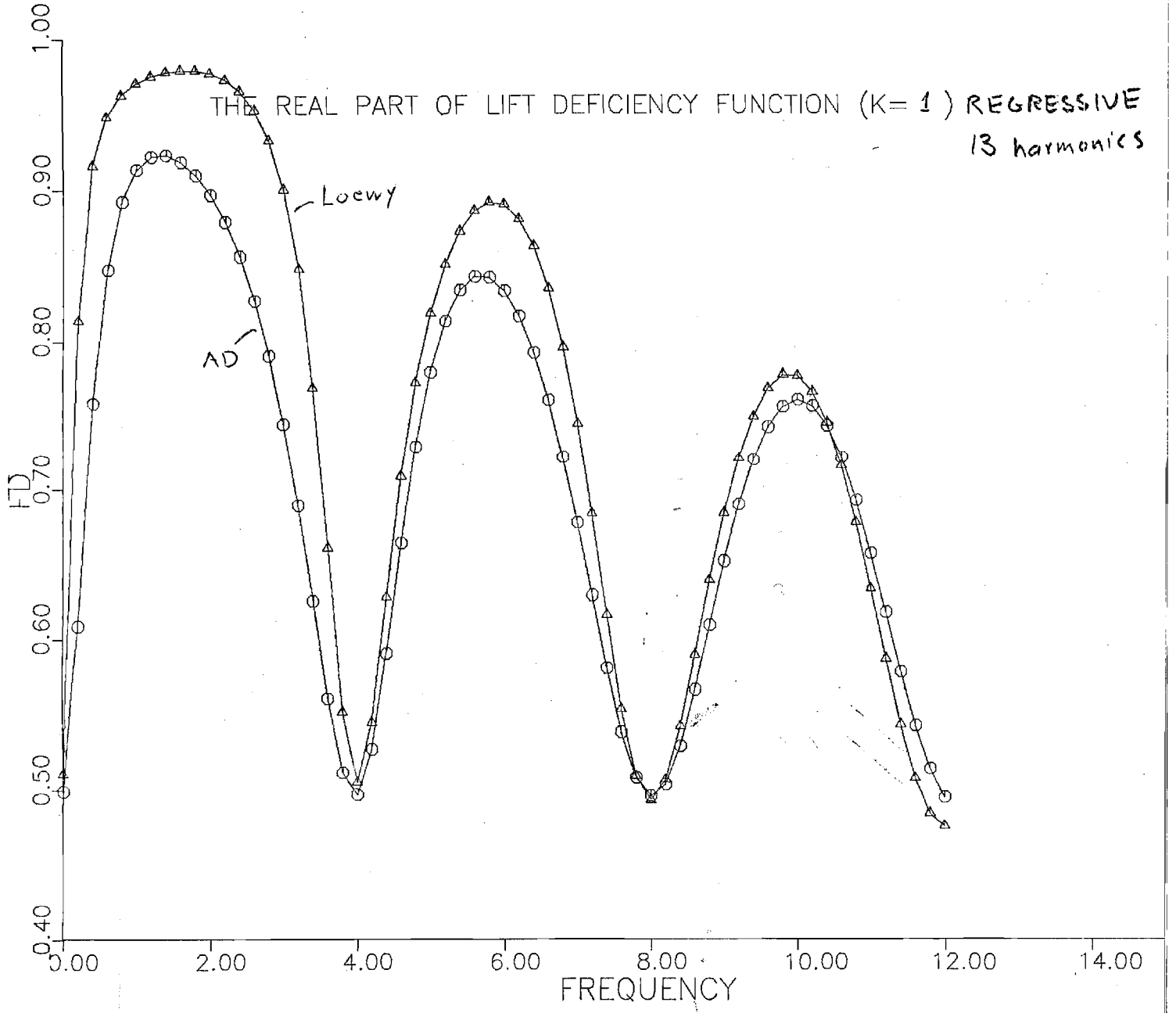

Figure # 5a

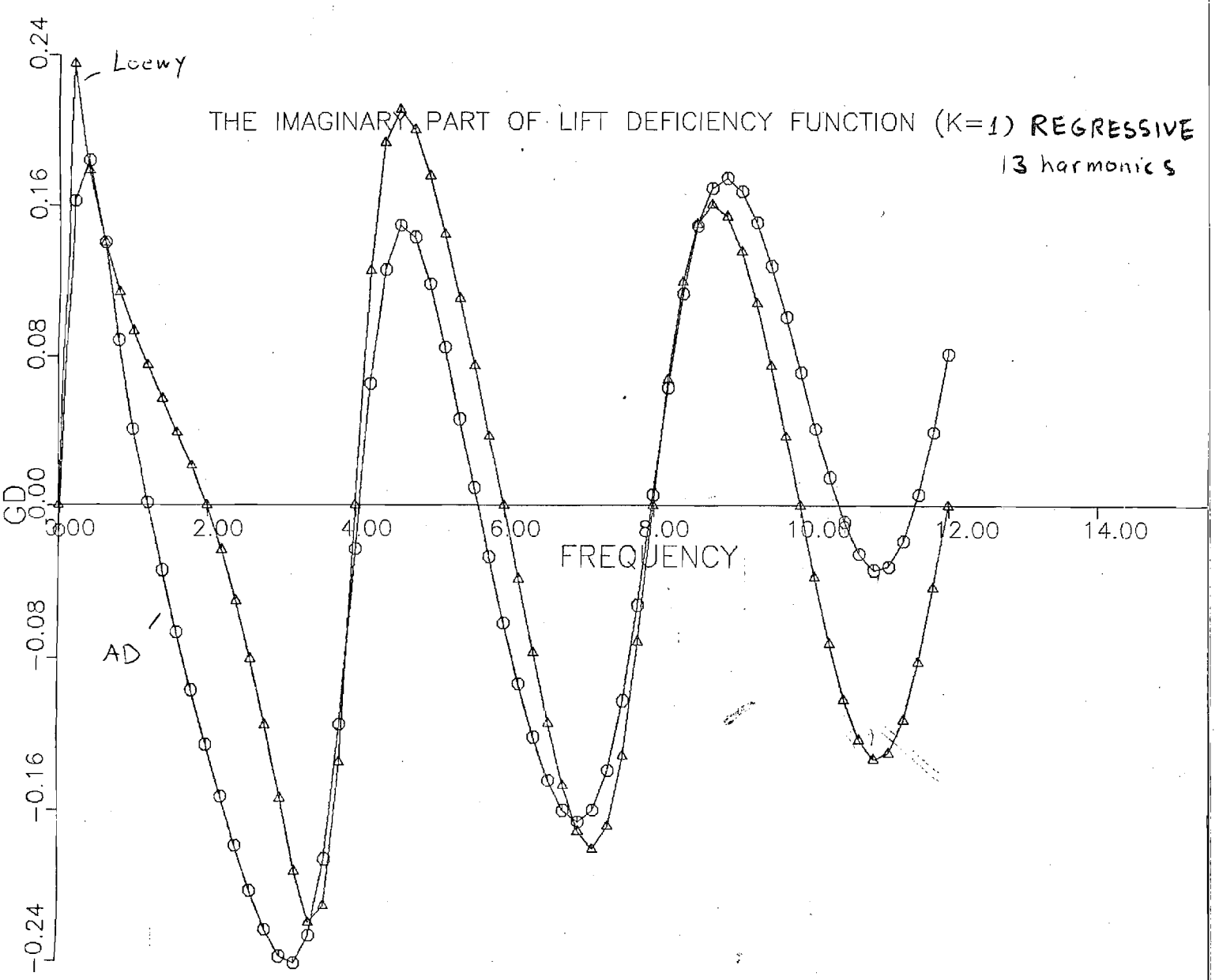
THE IMAGINARY PART OF LIFT DEFICIENCY FUNCTION (K=1) REGRESSIVE
13 harmonics
Loewy
AD
GD
FREQUENCY
0.24
0.16
0.08
0.00
-0.08
-0.16
-0.24
2.00
4.00
6.00
8.00
10.00
12.00
14.00

Figure 5b

progressive Mode :

K=1 : Geometric Me

K=2 : $\frac{3}{4m}$

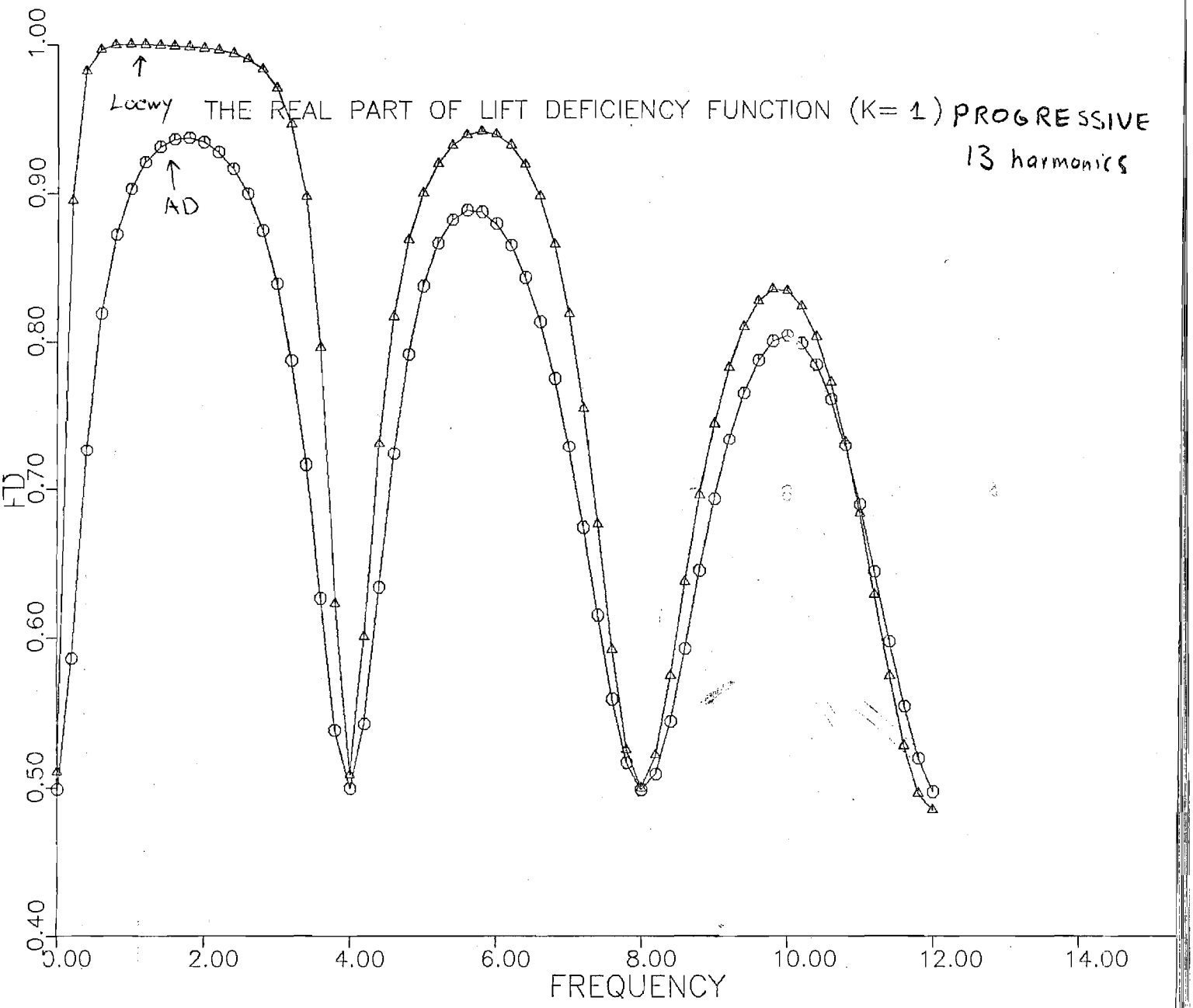

Figure 6a

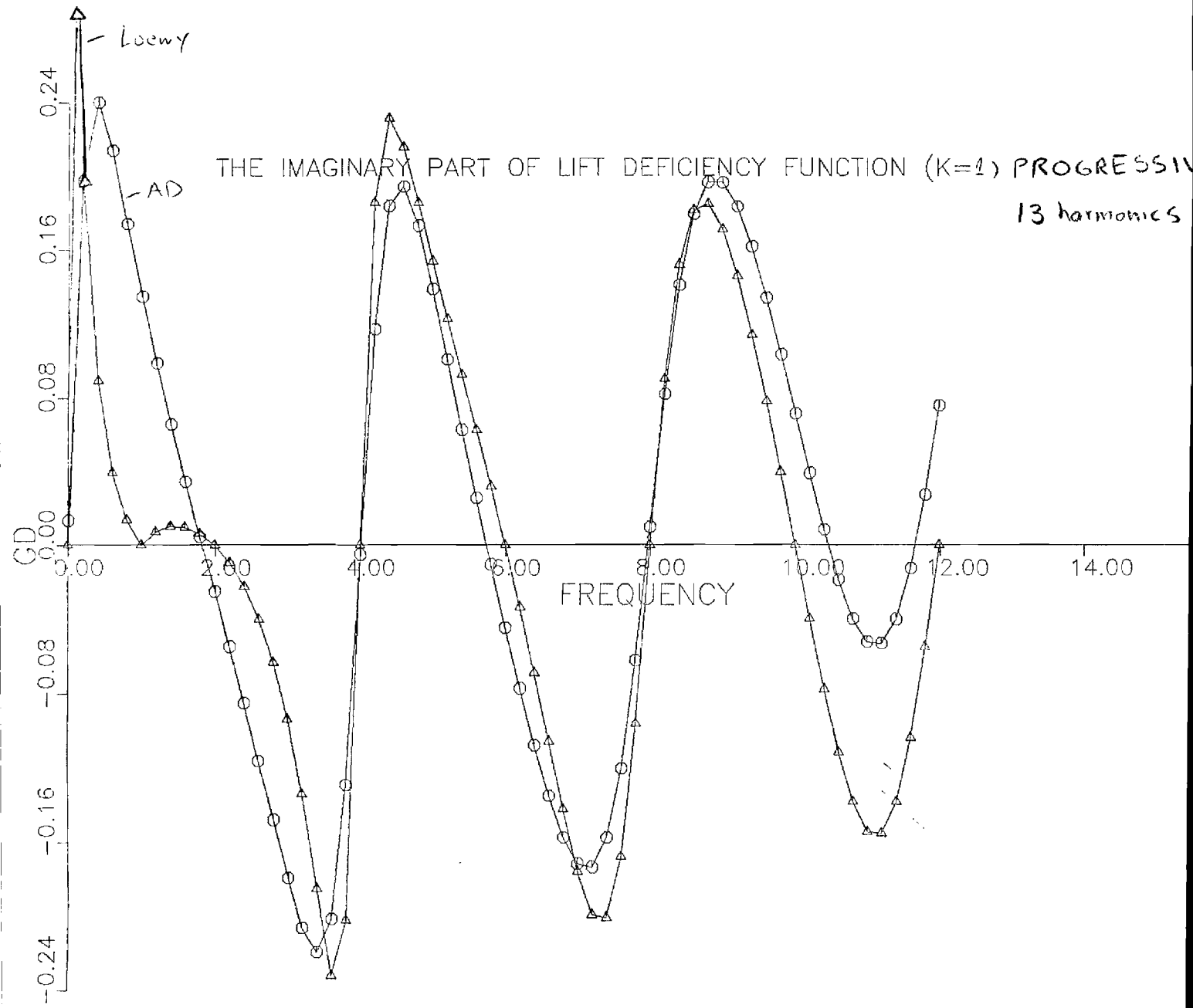
Loewy
AD
THE IMAGINARY PART OF LIFT DEFICIENCY FUNCTION (K=1) PROGRESSIV
13 harmonics
0.24
0.16
0.08
0.00
-0.08
-0.16
-0.24
(D)
0.00
2.00
4.00
6.00
8.00
10.00
12.00
14.00
FREQUENCY

Figure 6b

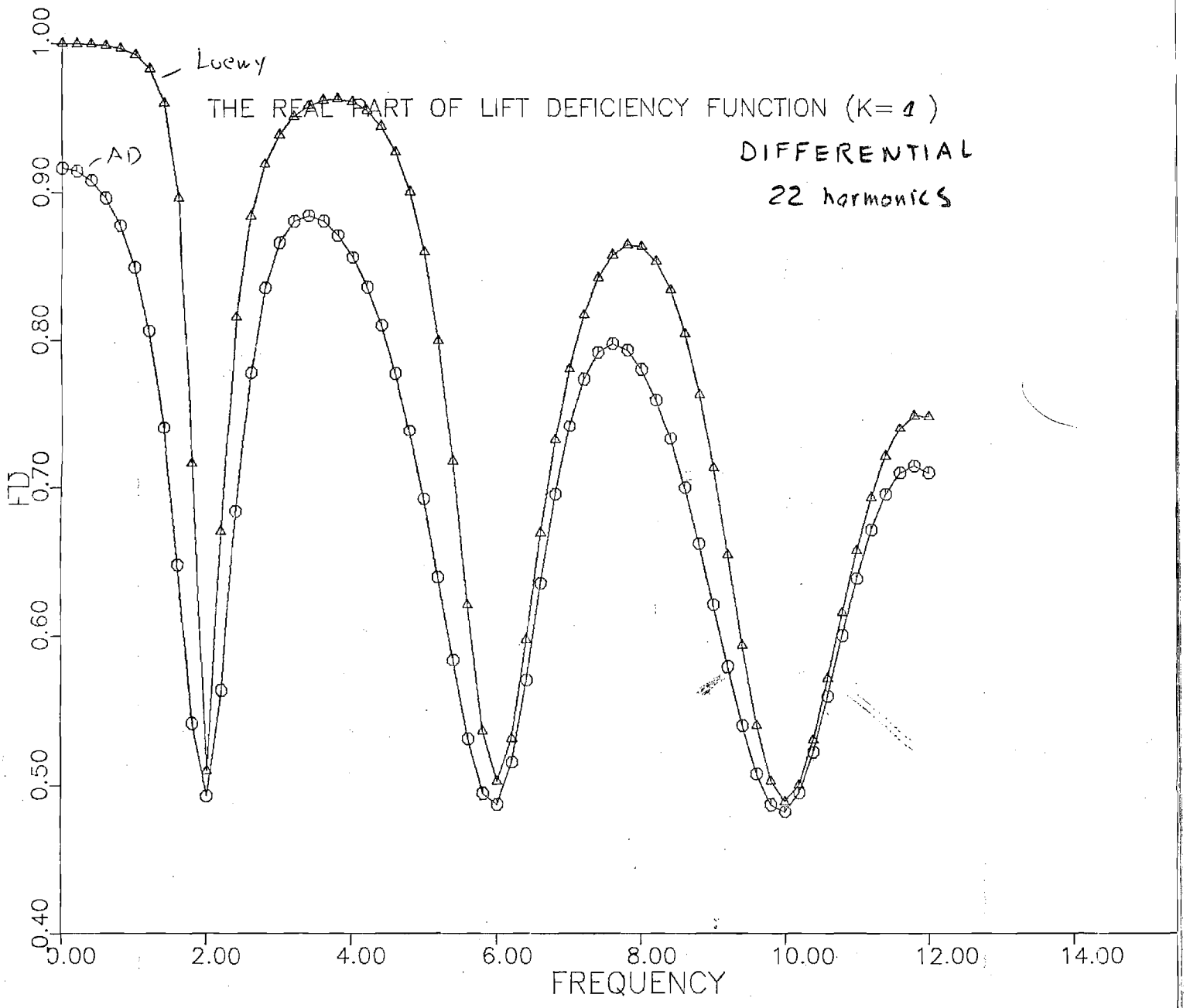
THE REAL PART OF LIFT DEFICIENCY FUNCTION (K= 1)
DIFFERENTIAL
22 harmonics
Loewy
AD
FD
1.00
0.90
0.80
0.70
0.60
0.50
0.40
0.00
2.00
4.00
6.00
8.00
10.00
12.00
14.00
FREQUENCY

Figure 7a

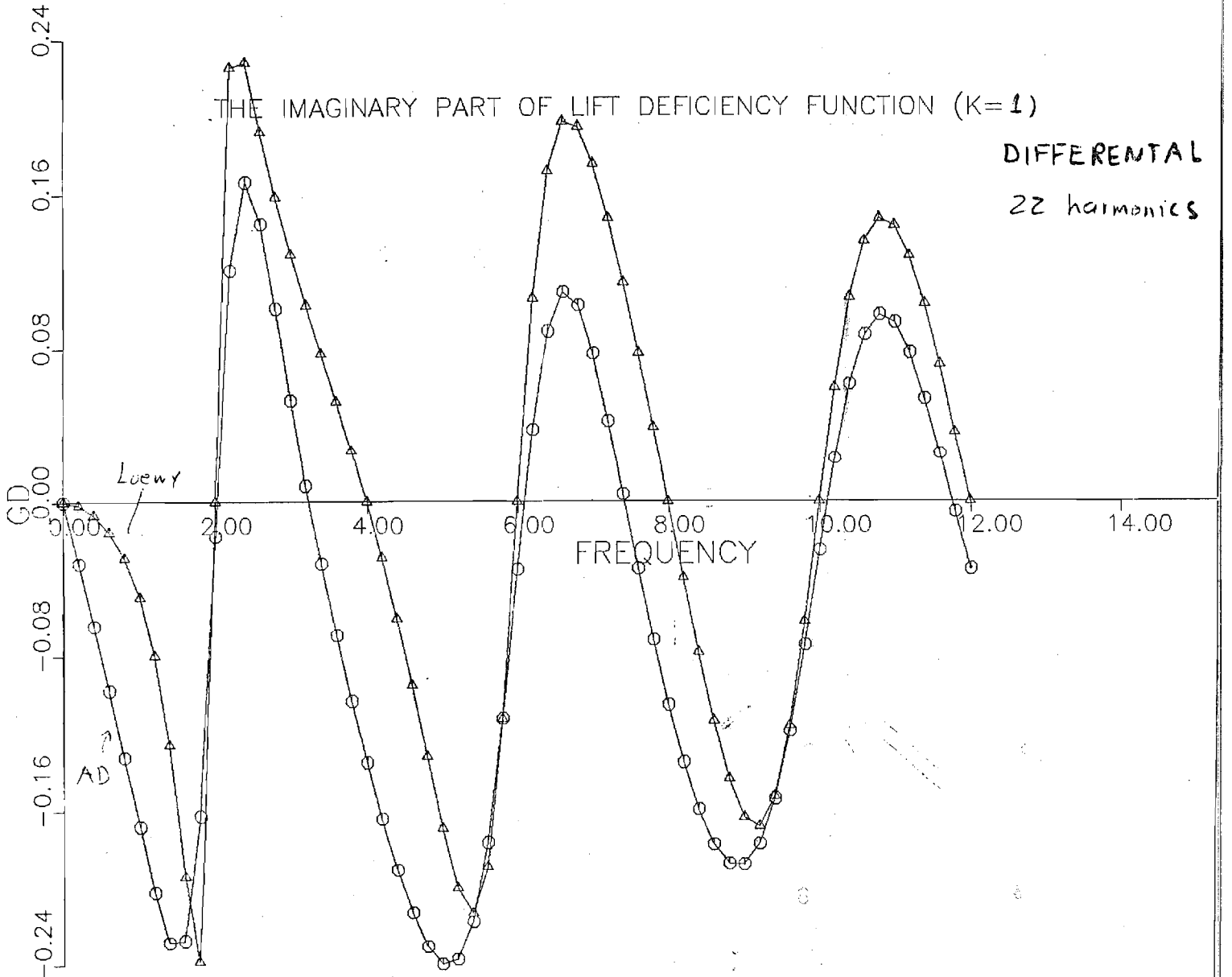
THE IMAGINARY PART OF LIFT DEFICIENCY FUNCTION (K=1)
DIFFERENTAL
22 harmonics
GD
FREQUENCY
Loewy
AD
0.24
0.16
0.08
0.00
-0.08
-0.16
-0.24
0.00
2.00
4.00
6.00
8.00
10.00
12.00
14.00

Figure 7b

GEORGIA INSTITUTE OF TECHNOLOGY
ATLANTA, GEORGIA 30332

SCHOOL OF
AEROSPACE ENGINEERING

404-894-3000

DANIEL GUGGENHEIM SCHOOL
OF AERONAUTICS

January 19, 1986

Dr. Robert R. Singleton
U.S. Army Research Office
P.O. Box 1221
Research Triangle Park, NC 27709-2211

Dear Dr. Singleton:

Please find enclosed 20 copies of the first semi-annual progress report for ARO Grant NO. DAAG29-85-K-0228. This is a very exciting time for us in that every research task seems to be opening new insights for us.

Yours truly,

David A. Peters.

cc: Dewey Hodges
Robert Heallund

PROGRESS REPORT

TWENTY COPIES REQUIRED

1. ARO PROPOSAL NUMBER: 23322-EG

2. PERIOD COVERED BY REPORT: 1 July 1985 - 31 December 1965

3. TITLE OF PROPOSAL: Effect of Dynamic Stall and Elastic Parameters on the Fundamental Mechanisms of Helicopter Vibrations

4. CONTRACT OR GRANT NUMBER: DAAG29-85-K-0228

5. NAME OF INSTITUTION: Georgia Institute of Technology

6. AUTHORS OF REPORT: [redacted]

7. LIST OF MANUSCRIPTS SUBMITTED OR PUBLISHED UNDER ARO SPONSORSHIP DURING THIS REPORTING PERIOD, INCLUDING JOURNAL REFERENCES:

1. Peters, David A., "Determination of the Mass-Flow Parameter of Dynamic Inflow from Existing Experimental Data", submitted to the JAHS.

2. Karunamoorthy, Swami and Peters, David, "Use of Hierarchical Elastic Blade Equations and Automatic Trim for Helicopter Vibration Analysis", accepted for presentation at the 42nd Annual National Forum of the American Helicopter Society, Washington, D.C., June 2-4, 1986.

8. SCIENTIFIC PERSONNEL SUPPORTED BY THIS PROJECT AND DEGREES AWARDED DURING THIS REPORTING PERIOD:

Person	Man-Month of Effort	Degree Sought
Mnaour Chouchane	- *	M.S.
Robert Longabaugh	1.33	M.S.
David A. Peters	.72	-
Ming-Sheng Huang	1.33	Ph.D.
Danny Chiu	1.33	Ph.D.

David A. Peters
School of Aerospace Engineering
Georgia Institute of Technology
Atlanta, GA 30332

* Worked on project but supported by other sources

BRIEF OUTLINE OF RESEARCH FINDINGS

This progress report covers the first four months of our grant. Actually, this period begins the third year of a three-year effort that began at Washington University and that is continuing here at Georgia Tech. Although we have experienced some temporary delays (due to the change in computer systems, etc.) we have also received some excellent aids to our research, however, by interactions with the Center of Excellence for Rotary-Wing*. Thus, our research is proceeding very nicely. Below is a brief synopsis of our progress in each area.

In the area of our application of Hamilton's Law, we greatly benefited by the recent ARO workshop held at Georgia Tech and the interactions with Dr. Dewey Hodges (Aeroflight dynamics lab) and Prof. Borri (University of Milan). It turns out that Prof. Borri's method is a special case of ours; but in trying to prove this equivalence, we discovered that our Lagrange multiplier can be used to greatly improve the convergence of blade velocity. We have also successfully implemented the multi-element version of our method. Therefore, we are now in the phase of detailed convergence studies with variations in the method. Everything, however, looks very good.

For our second task, rotor-body vibrations, we have experienced a serious setback. Ming-Sheng Huang, the graduate research assistant doing this work, was struck by a car and suffered serious head injuries. However, he has astounded the doctors by his remarkable recovery and is now back at Tech working on his program. Nevertheless, the work has experienced significant delay; and we will not be able to finish it by the end of the grant period.

Our third task is the addition of dynamic-stall lift to elastic flap-lag vibrations. This task is proceeding rather well. The computer code is completed, and we are now in the stage of documentation. Once we have verified the model on some test cases, we will add trim capability and begin detailed calculations of the effect of stall. Basically we are looking for two effects: 1) the effects of stall due to movement of the trim point, and 2) the direct effect of stall on oscillations about trim.

Another area of significant progress has been in our tip-loss research. Here, we have greatly benefited from the aerodynamic community at Georgia Tech. Because of this, we have been able to improve our lifting-surface code for fixed surfaces. Also, we have been able to obtain more example calculations (with known results) to better test our new methods. All of these results consistently show improved convergence with our optimized mesh choice. Now, we are in the process of utilizing some of the vortex-wake codes at Georgia Tech by application of our mesh choice in their programs.

The final area to be discussed is that of improved multi-blade coordinates. In the past four months, we have successfully implemented our new version of 4-bladed multi-blade coordinates. Thus, we can now model 2 or 4 bladed rotors by both old and new methodologies. Our next step is to compare all of these with Floquet results to understand the advantages and possible deficiencies of the method.

*Advanced Technology

PROGRESS REPORT

TWENTY COPIES REQUIRED

1. ARO PROPOSAL NUMBER: 23322-EG

2. PERIOD COVERED BY REPORT: 1 July 1985 - 31 December 1985

3. TITLE OF PROPOSAL: Effect of Dynamic Stall and Elastic Parameters on the Fundamental Mechanisms of Helicopter Vibrations

4. CONTRACT OR GRANT NUMBER: DAAG29-85-K-0228

5. NAME OF INSTITUTION: Georgia Institute of Technology

6. AUTHORS OF REPORT: [signature]

7. LIST OF MANUSCRIPTS SUBMITTED OR PUBLISHED UNDER ARO SPONSORSHIP DURING THIS REPORTING PERIOD, INCLUDING JOURNAL REFERENCES:

1. Peters, David A., "Determination of the Mass-Flow Parameter of Dynamic Inflow from Existing Experimental Data", submitted to the JAHS.

2. Karunamoorthy, Swami and Peters, David, "Use of Hierarchical Elastic Blade Equations and Automatic Trim for Helicopter Vibration Analysis", accepted for presentation at the 42nd Annual National Forum of the American Helicopter Society, Washington, D.C., June 2-4, 1986.

8. SCIENTIFIC PERSONNEL SUPPORTED BY THIS PROJECT AND DEGREES AWARDED DURING THIS REPORTING PERIOD:

Person	Man-Month of Effort	Degree Sought
Mnaour Chouchane	- *	M.S.
Robert Longabaugh	1.33	M.S.
David A. Peters	.72	-
Ming-Sheng Huang	1.33	Ph.D.
Danny Chiu	1.33	Ph.D.

David A. Peters
School of Aerospace Engineering
Georgia Institute of Technology
Atlanta, GA 30332

* Worked on project but supported by other sources

BRIEF OUTLINE OF RESEARCH FINDINGS

This progress report covers the first four months of our grant. Actually, this period begins the third year of a three-year effort that began at Washington University and that is continuing here at Georgia Tech. Although we have experienced some temporary delays (due to the change in computer systems, etc.) we have also received some excellent aids to our research, however, by interactions with the Center of Excellence for Rotary-Wing*. Thus, our research is proceeding very nicely. Below is a brief synopsis of our progress in each area.

In the area of our application of Hamilton's Law, we greatly benefited by the recent ARO workshop held at Georgia Tech and the interactions with Dr. Dewey Hodges (Aeroflight dynamics lab) and Prof. Borri (University of Milan). It turns out that Prof. Borri's method is a special case of ours; but in trying to prove this equivalence, we discovered that our Lagrange multiplier can be used to greatly improve the convergence of blade velocity. We have also successfully implemented the multi-element version of our method. Therefore, we are now in the phase of detailed convergence studies with variations in the method. Everything, however, looks very good.

For our second task, rotor-body vibrations, we have experienced a serious setback. Ming-Sheng Huang, the graduate research assistant doing this work, was struck by a car and suffered serious head injuries. However, he has astounded the doctors by his remarkable recovery and is now back at Tech working on his program. Nevertheless, the work has experienced significant delay; and we will not be able to finish it by the end of the grant period.

Our third task is the addition of dynamic-stall lift to elastic flap-lag vibrations. This task is proceeding rather well. The computer code is completed, and we are now in the stage of documentation. Once we have verified the model on some test cases, we will add trim capability and begin detailed calculations of the effect of stall. Basically we are looking for two effects: 1) the effects of stall due to movement of the trim point, and 2) the direct effect of stall on oscillations about trim.

Another area of significant progress has been in our tip-loss research. Here, we have greatly benefited from the aerodynamic community at Georgia Tech. Because of this, we have been able to improve our lifting-surface code for fixed surfaces. Also, we have been able to obtain more example calculations (with known results) to better test our new methods. All of these results consistently show improved convergence with our optimized mesh choice. Now, we are in the process of utilizing some of the vortex-wake codes at Georgia Tech by application of our mesh choice in their programs.

The final area to be discussed is that of improved multi-blade coordinates. In the past four months, we have successfully implemented our new version of 4-bladed multi-blade coordinates. Thus, we can now model 2 or 4 bladed rotors by both old and new methodologies. Our next step is to compare all of these with Floquet results to understand the advantages and possible deficiencies of the method.

*Advanced Technology

E-16-620

23322-EG

PROGRESS REPORT

1. ARO PROPOSAL NUMBER: 23322-EG

2. PERIOD COVERED BY REPORT: 1 January 1986 - June 1986

3. TITLE OF PROPOSAL: Effect of Dynamic Stall and Elastic Parameters on the Fundamental Mechanisms of Helicopter Vibrations

4. CONTRACT OR GRANT NUMBER: DAAG29-85-K-0228

5. NAME OF INSTITUTION: Georgia Institute of Technology

6. AUTHORS OF REPORT: David A. Peters, Principal Investigator

7. LIST OF MANUSCRIPTS SUBMITTED OR PUBLISHED UNDER ARO SPONSORSHIP DURING THIS REPORTING PERIOD, INCLUDING JOURNAL REFERENCES:

   1. Gaonkar and Peters, "Effectiveness of Current Dynamic-Inflow Models in Hover and Forward Flight," Journal of the American Helicopter Society, Vol. 31, No. 2, April 1986, pp. 47-57.

   2. Gaonkar and Peters, "Review of Dynamic Inflow Modeling for Rotorcraft Flight Dynamics," presented at the AIAA 27th SDM meeting, San Antonio, May 1986.

   3. Peters and Izadpanah, "P-Version Finite Elements for the Space-Time Domain," submitted to Computational Mechanics, June 1986.

   4. Chouchane, Mnaouar, Effect of Dynamic Stall on Helicopter Trim and Flap-Lag Response, Master of Science Thesis, Washington University, May 1986.

   5. Peters and Chouchane, "Effect of Dynamic Stall on Helicopter Trim and Flap-Lag Response," submitted to Fluids and Structures, June 1986

   6. Karunamoorthy and Peters, "Use of Hierarchical Elastic Blade Equations and Automatic Trim for Helicopter Vibration Analysis," submitted to Vertica, May 1986.

8. SCIENTIFIC PERSONNEL SUPPORTED BY THIS PROJECT AND DEGREES AWARDED DURING THIS REPORTING PERIOD:

Person	Man-Months of Effort	Degree Sought
Manouar Chouchane	2.00*	M.S.**
Robert Longabaugh	2.00	M.S.
Ming-Sheng Huang	2.00	Ph.D.
Danny Chiu	2.00	Ph.D.
Amir Izadpanah	2.00	Ph.D.
Chen-Jian He	1.00	Ph.D
David Peters	1.08	Ph.D.

* Worked on project but supported by other source
** Degree Awarded, June 1986

David A. Peters
School of Aerospace Engineering
Georgia Institute of Technology
Atlanta, GA 30332

BRIEF OUTLINE OF RESEARCH FINDINGS

As we are nearing the end of our present grant, each area of research is nearing important milestones for conclusion and documentation. In the area of dynamic stall, we have completed the addition of trim to the model and have performed response calculations. Mr. Chouchane, the research assistant working in this area, has finished his M.S. degree; and we have submitted a paper on his work to Fluids and Structures. In working the trim problem, we discovered that none of the previous work on flap-lag (or flap-lag-torsion) response has achieved anywhere near an effective trim, even without stall. Our work has led us to new insights on how to apply automatic pilot equations to trim complicated dynamic systems.

In our work with multiblade coordinates, researched by Bob Longabaugh, we have discovered that the new approach, while offering significant improvement for 2-bladed rotors, creates unacceptable anomalies for 4-bladed rotors. As a result, we have formulated a second alternative. We have also proven that these two are the only possibilities in this context, and we are continuing comparisons with Floquet theory to assess the reasons for this unexpected behavior.

In the area of Rotor-Body Coupling, Mr. Huang has now extended his programming effort to include the difficult nonlinearities in the harmonic balance. These nonlinearities not only greatly complicate the equations, but they also are forcing to make new innovations in our solution strategy. Until now, we had utilized impedance matching. However, the nonlinearities imply new methods of implementation in order to capitalize on the advantages of impedance matching for a nonlinear system. In a related area, we have submitted a a paper on hub-fixed vibrations to Vertica.

A third aspect of our research, tip aerodynamics, is also proceding well. Danny Chiu, the research assistant, has successfully passed his qualifying exams, and we are preparing a technical note on one of the spin-offs of our work. We hope by the end of the summer to have our tip-loss computational programs completely operational and to have provided important numerical results.

One of the most exciting aspects of our research, finite elements in time, is nearing a major milestone. One paper, on the theoretical basis of the method, has already been submitted to Computational Mechanics. This paper outlines the variational formulation, interpretation in terms of "least action", and proof of numerical convergence. A second paper, in preparation, deals with our most recent findings on numerical convergence and numerical stability. These really "close the book" on the linear problem in terms of mathematical basis, stability, and optimum choice of polynomial number. Mr. Izadpanah, the research assistant on this project, is preparing to defend his Ph.D. thesis this summer.

Finally, our work in dynamic inflow has been rekindled due to several recent developments. First, new experimental data by Chen at NASA Ames has renewed interest in some of assumptions of actuator-disk theory when the "disk" (i.e., the rotor plane) is not stationary. Second, in attempting to use dynamic inflow as a source of higher-harmonic airloads, we have uncovered a strong connection between actuator-disk theory and Loewy theory. Presently, we are working with

Peretz Friedmann on a paper that outlines this connection. Furthermore, Mr. Chen-Jian He, a new student at Georgia Tech, has begun preliminary studies of how the apparent mass terms of Loewy theory relate to those of actuator-disk theory. Professor Gaonkar, of Florida Atlantic University, is also working with us on a survey paper of our past work; and this will soon be submitted to the AIAA Journal.

E-16-620

FINAL REPORT

EFFECT OF DYNAMIC STALL AND ELASTIC PARAMETERS ON THE FUNDAMENTAL MECHANISMS OF HELICOPTER VIBRATIONS

David A. Peters

Prepared for

U.S. Army Research Office
P.O. Box 12211
Research Triangle Park, NC 27709-2211

Under

Contract No. DAAG29-85-K

November 1986

GEORGIA INSTITUTE OF TECHNOLOGY
A UNIT OF THE UNIVERSITY SYSTEM OF GEORGIA
SCHOOL OF AEROSPACE ENGINEERING
ATLANTA, GEORGIA 30332

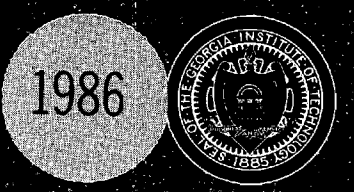

UNCLASSIFIED

SECURITY CLASSIFICATION OF THIS PAGE *(When Data Entered)*

REPORT DOCUMENTATION PAGE		READ INSTRUCTIONS BEFORE COMPLETING FORM
1. REPORT NUMBER 1	2. GOVT ACCESSION NO. NA	3. RECIPIENT'S CATALOG NUMBER NA
4. TITLE *(and Subtitle)* Effect of Dynamic Stall and Elastic Parameters on the Fundamental Mechanisms of Helicopter Vibrations		5. TYPE OF REPORT & PERIOD COVERED Final Report Sept. 1, 1985 to Sept.30,1986 6. PERFORMING ORG. REPORT NUMBER
7. AUTHOR*(s)* David A. Peters		8. CONTRACT OR GRANT NUMBER*(s)* DAAG29-85-K
9. PERFORMING ORGANIZATION NAME AND ADDRESS School of Aerospace Engineering Georgia Institute of Technology Atlanta, Georgia 30332		10. PROGRAM ELEMENT, PROJECT, TASK AREA & WORK UNIT NUMBERS NA
11. CONTROLLING OFFICE NAME AND ADDRESS U. S. Army Research Office P. O. Box 12211 Research Triangle Park, NC 27709-2211		12. REPORT DATE Nov. 1, 1986 13. NUMBER OF PAGES
14. MONITORING AGENCY NAME & ADDRESS*(if different from Controlling Office)*		15. SECURITY CLASS. *(of this report)* UNCLASSIFIED 15a. DECLASSIFICATION/DOWNGRADING SCHEDULE

16. DISTRIBUTION STATEMENT *(of this Report)*

Approved for public release; distribution unlimited.

17. DISTRIBUTION STATEMENT *(of the abstract entered in Block 20, if different from Report)*

NA

18. SUPPLEMENTARY NOTES

The view, opinions and/or findings contained in this report are those of the author(s) and should not be construed as an official Department of the Army position, policy, or decision, unless so designated by other documentation.

19. KEY WORDS *(Continue on reverse side if necessary and identify by block number)*

Helicopter, Vibration, Stall

20. ABSTRACT *(Continue on reverse side if necessary and identify by block number)*

This research has dealt with the modeling and solution of rotary-wing dynamics. In the modeling area, it deals with elastic-blade models, ways to introduce rotor-body coupling, aerodynamic behavior near blade-tips, and the modeling of dynamic stall. In solution strategies, we have concentrated on new and improved Floquet methods, on innovative trim methodologies (such as auto-pilot and periodic shooting), on efficient formulation of equations, and on lifting-line and lifting-surface meshes. We have awarded 1 Master of Science and 1 Doctor of Philosophy degree to persons working on the project.

DD FORM 1 JAN 73 1473 EDITION OF 1 NOV 65 IS OBSOLETE 10

UNCLASSIFIED

SECURITY CLASSIFICATION OF THIS PAGE *(When Data Entered)*

20. ABSTRACT CONTINUED

EFFECT OF DYNAMIC STALL AND ELASTIC PARAMETERS ON THE FUNDAMENTAL MECHANISMS OF HELICOPTER VIBRATIONS

Final Technical Report

by

David A. Peters
Principal Investigator

1 November 1986

U.S. Army Research Office
Grant No: DAAG-29-83-K-0133

Georgia Institute of Technology
School of Aerospace Engineering
Atlanta, GA 30332

Table of Contents

1. Introduction

This final report covers 1 year of ARO-sponsored research into the fundamental behavior of rotor dynamics. The original proposal was for 3 years, but the first two years were done under a separate grant. Thus, this report covers only a portion of the originally-proposed work. In this final report, we will summarize the work done, including publications and scientific personnel; and we will provide pertinent technical descriptions of each major area we have pursued.

The philosophy of our research has been to increase the fundamental understanding of those dynamic and aerodynamic phenomena associated with the helicopter. Our approach has been to follow three intertwining lines of research. The first of these is the line of mathematical modeling. Here, we wish both to synthesize and refine mathematical models for various, isolated rotorcraft phenomena, and to learn to couple them together in a systematic way. This is the building-block approach we have followed. The second line of inquiry has been in the development of solution methodologies for these equations. Here, certain solution strategies work better for certain models; and some modeling techniques require new solution strategies. We look specifically at methods that magnify our insight, are computationally efficient, and that can be extended to large-scale systems.

This leads, then, to the third thread of research: basic physical insight. Of course, because we deal with isolated components or with simplified couplings, we do not intend to be able to make predictions on helicopter stability and response that would be applicable to detailed design studies. On the other hand, we do expect our methods to be predictive of the behavior of simplified research models, such as those used by the Army Research and Technology Laboratories. Furthermore, we believe our results give qualitative insight into the physical phenomena present in production rotors. Thus, we try to involve all three elements in our research effort.

2. Statement of Problem

The objectives and scope of this work are as follows:

1) To discover the basic relationships between blade structural parameters and the flap-lag-torsion airloads that result.

2) To determine the extent to which rotor-body coupling affects inplane loads and overall helicopter vibrations.

3) To develop our basic trim procedures to the point at which they can be applied to large, state-of-the-art rotor response program.

4) To determine the effect of dynamic stall on the rotor airloads and on the basic trimming methods.

5) To investigate other methods of obtaining time histories of rotor response, including Hamilton's Law of Varying Action.

Before proceeding to the details of each objective, it is informative to outline the scope in each task. With the exception of item 3, the above objectives are not aimed at the quantitative prediction of helicopter response. They are aimed at obtaining fundamental insight into how rotor vibrations develop and into how they can be efficiently calculated. Thus, in item 1 we consider a simple elastic-blade model with elastic flap, lag, and torsion. Although other, more sophisticated flap-lag-torsion models certainly exist, they have not been obtained under the same assumptions nor with the same purpose in mind as ours. Thus, we have proceeded slowly and carefully to make sure we understand the physical processes at each step.

In item 2, we are looking at a fuselage with 5 rigid body modes and 4 elastic modes (as in our prior work) but with a more detailed rotor model. Naturally, a true fuselage will have many more elastic modes; but we look at a generic frequency sweep that could be representative of several potential modes. Since we have already found that flapping motions drive inplane motions (while inplane effects flapping much less) we make several simplifying assumptions to increase the productivity (and physical interpretations) of the work.

Item 3 is the only area in which we approach the area of applications. These trim procedures are now fairly well understood in terms of theory, and the advancements now come through more sophisticated applications. Therefore, we have reformulated the trim procedures.

Item 4 is a new area of research that developed out of our dynamic-stall work. It is not in our scope to develop any dramatically new dynamic stall procedures. We merely take existing methodologies, investigate how they should be modified to be useful for simplified vibration analyses, and study the resultant effects on the types of calculations we are making.

Item 5 is also a new area of research which developed out of our prior trim investigations. For nearly linear systems, the trim method of periodic shooting is equivalent to finding and inverting the Floquet transition matrix. (An earlier solution method in our research also relied on Floquet theory for vibration analysis.) Thus, it is natural to look for more efficient means of finding the transition matrix. One possibility is the use of Hamilton's Law of Varying Action with comparison functions in time. In this research we study Hamilton's Law in detail with respect to convergence and efficiency.

3. Scientific Personnel and Degrees

Below is a tabulation of those who worked on this project during the past two years along with the degree they have pursued.

Personnel	Man-Months Effort	Degree Sought
David A. Peters	2.2	
Huang Ming-Sheng	4.3	Ph.D
Danny Chiu	4.3	Ph.D
Amir Izadpanah	4.0	Ph.D.*
Robert Longabaugh	4.0	M.S.
Mnaouar Chouchane	-	M.S.**
Cheng-Jian He	2.0	Ph.D.

* Awarded by Georgia Institute of Technology, Sept. 1986

**Awarded by Washington University, Aug. 1986

4. Publications and Reports

1. Karunamoorthy, Swami and Peters, David, "Use of Hierarchical Elastic Blade Equations and Automatic Trim for Helicopter Vibration Analysis", presented at the 42nd Annual National Forum of the American Helicopter Society, Washington, D.C., June 2-4, 1986, Vertica, special issue, 1986.

2. Gaonkar and Peters, "Effectiveness of Current Dynamic Inflow Models in Hover and Forward Flight", Journal of the American Helicopter Society, Vol. 31, No. 2, April 1986.

3. Gaonkar and Peters, "Review of Dynamic Inflow Modeling for Rotorcraft Flight Dynamics", presented at the AIAA 27th SDM meeting, San Antonio, Texas, May 1986.

4. Peters and Chouchane, "Effect of Dynamic Stall on Helicopter Trim and Flap-Lag Response", Fluids and Structures, Vol. I, No. 1, 1986.

5. Izadpanah, Amir, p-Version Finite Elements for the Space-Time Domain with Application to Floquet Theory, Ph.D. Dissertation, Georgia Institute of Technology, Sept. 1986.

6. Chouchane, Mnaouar, Effect of Dynamic Stall on Helicopter Trim and Flap-Lag Response, Master of Science Thesis, Washington University, August 1986.

7. Peters, David and Izadpanah, Amir, "hp-Finite Elements for the Space-Time Domain with Proof of Convergence", presented at the First World Congress on Computational Mechanics, Austin, Texas, Sept. 22-25, 1986, submitted to Computational Mechanics.

8. Huang, Ming-Sheng and Peters, David, "Coupled Elastic Rotor/Body Vibrations with Inplane Degrees of Freedom", ARO workshop on Dynamics and Aeroelastic Modeling of Rotor Systems, Georgia Tech, December 4-5, 1985.

5. Summary of Results

In this section, we summarize the results of our research for this one-year effort. However, (the first two years were performed at Washington University in St. Louis), we will also refer to how this third year completes the work begun in the first two years. Reference numbers refer to publication in Section 4.

5.1 Finite Elements in Time

Recently, much attention has been give to numerical application of Hamilton's Law of varying action. Hamilton's Law is a variational statement about "action" which provides, for the time domain, what variation of work provides in the space domain. Thus, these applications of Hamilton's Law result in finite elements over the time domain; and these can be either p-version, h-version, or a combination of the two (depending on the choice of test functions). However, numerical applications of Hamilton's Law have sometime resulted in solutions that do not converge as the number of elements (i.e., polynomials) is increased. In this research, a convergence proof was found, based on the bilinear formulation, which demonstrates that some formulations are not truly bilinear and may not converge. The proof also leads to an alternate, bilinear formulation of Hamilton's Law for which convergence is assured. The bilinear formulation also leads to an alternative statement about dynamics. In particular, the "virtual action" plus the variation of action over a space-domain must always sum to zero.

Numerical application of the correct bilinear formulation leads to Lagrange multiplier with the physical connotation of an end momentum (which is the analogy of end force in spatial problems). Thus, initial velocity is treated as a "natural" rather than as "geometric" boundary condition; and the Lagrange multiplier converges to the unknown momentum (i.e., velocity) at the end of the time period. Thus, the bilinear formulation is a "mixed method". Accuracies of solutions with the Lagrange multiplier are an order of magnitude better than those which use the derivative of shape functions for velocity.

In the limit as one takes many elements with only a few polynomials each, this formulation reduces to a classical time-marching method, (an h-version finite element) similar to Euler, Runge-Kutta, or predictor correctors. In the limit as many polynomials are used per element, but with only a few elements, the method becomes similar to a Ritz-Galerkin procedure in time (a p-version finite element). Results show that, for any given problem (as characterized by the computational cost of a function evaluation), there is an optimum choice of polynomial number in order to meet any error criterion with minimum computational effort. Similarly, depending on the problem, a particular choice of polynomial number may or may not be more efficient than conventional time-marching methods. In general, finite elements in time become more efficient than marching as the desired accuracy becomes exacting and as function evaluations become computationally expensive.

The details of this work can be found in References 5 and 7. Figures 1-5, taken from Reference 5, summarize the major conclusions of the work. Figure 1 shows the blade flapping angle, β, at the end of one rotor revolution as calculated both by Hamilton's Finite Elements and by our new, bilinear formulation. One can see that, for Hamilton's Law, β fails to converge uniformly as the number of basis functions is increased. Figure 2 further shows that this divergence is not restricted to a certain advance ratio. Results with Hamilton's Law can be in error over 100% even with 12 basis functions at $\mu = 0.5$. The new formulation, on the other hand, converges in all cases.

Figure 3 provides hp-optimization information. The figure gives $\log_{10}$ of the error as a function of the number of floating-point multiplications required in the computation, M. The straight-lines are for various number of polynomials per element, n, with the step size being a running parameter along the lines. One can see that, for any given error tolerance, there is a minimum M given by the interior of optimum curve formed by the locus of straight lines. The x's are results from Hammings predictor-corrector. For this case (C=16 implies 3 to 4 sine or cosine functions in each coefficient), the hp finite elements are always superior to conventional time marching.

Another interesting result of our research can be seen in plots, like Figure 4, which show error on the interior of a large, p-version element. The error norm is zero at t=0 (due to known initial values). It goes through some erratic oscillations (due to truncation errors near x=0), but settles down over the rest of the element. The <u>minimum</u> error, however, is found at $t=\tau$, the end of the period. The values at the end of the period are exactly what is needed for Floquet theory. Thus, finite elements in time (when correctly formulated) are ideal for Floquet applications.

Finally, we consider numerical stability when finite elements are used to march indefinitely, Figure 5. The values ρ and σ are the system frequency and damping multiplied by the element length, Δt. The exterior of the large semi-circles (as well as the interior of the small semi-circles on the ρ axis) are conditions of numerical instability. "n" is the number of polynomials per element. To put this in perspective, typical radii of convergence for other methods are near 2 = 1.4, smaller than even the n=2 result. At n = 6, a step size equal to two periods ($r=3\pi$) is required before instability occurs. From Figure 3, however, we see that such a large step size would result in very large errors with or without the instability. No optimal point on Figure 3 is unstable.

5.2 Dynamic Stall

A major portion of our research has dealt with the introduction of a modified ONERA model (for dynamic stall) into rotor elastic-blade analysis. In this research, reported in References 4 and 6, flap and inplane bending are described by two nonlinear, partial-differential equations which are coupled together as derived in Reference 1. Each equation consists of lower and higher order terms. Approximate solution methods are applied to these aeroelastic equations. The aerodynamic circulations are expressed by our unified theory. Only lower order terms of the equations in Ref. 1 are considered in the analyses. This allows the investigation of the general trends of the result without going into cumbersome computation with little

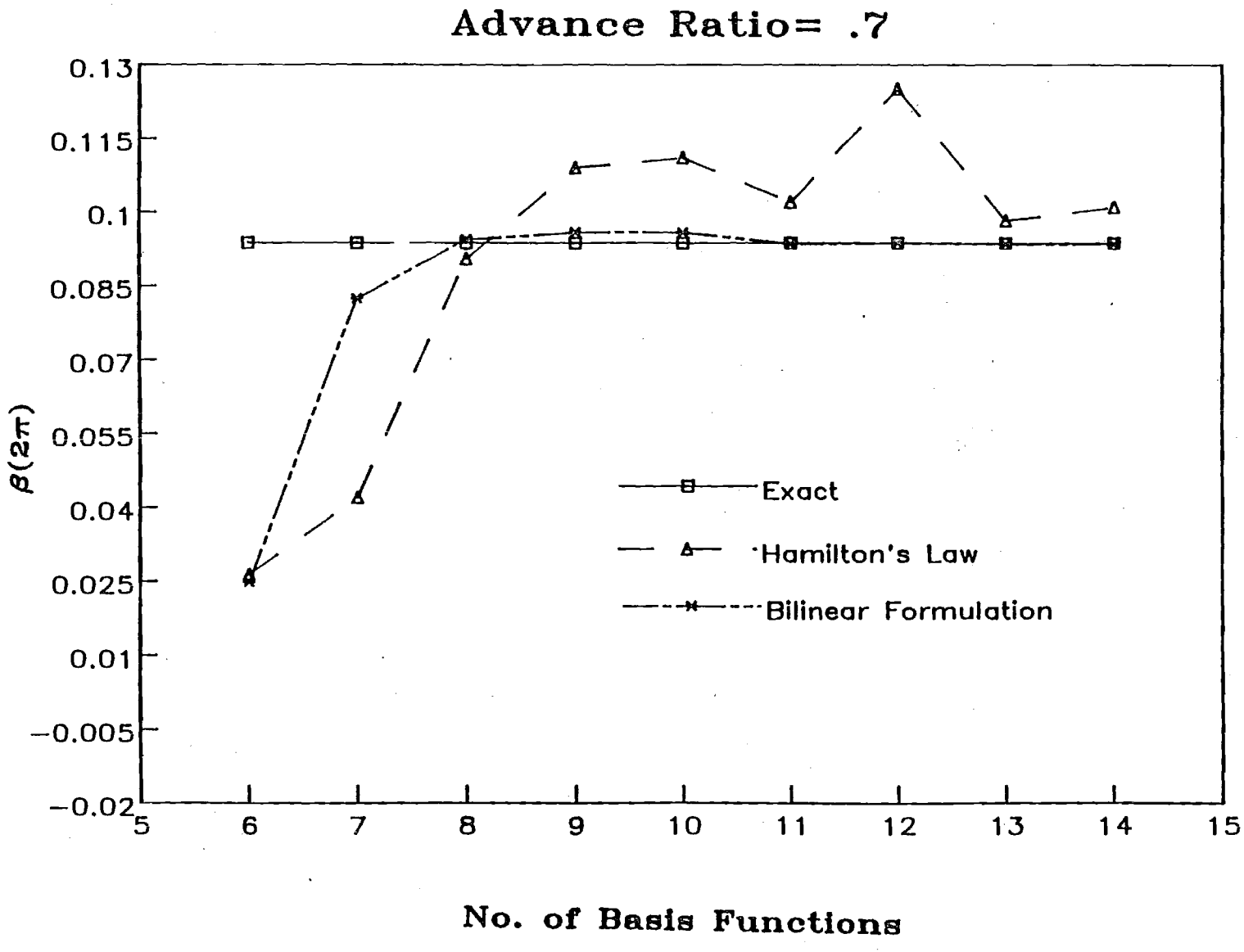

Figure 1. Flapping at the End of Period, $\mu = 0.7$

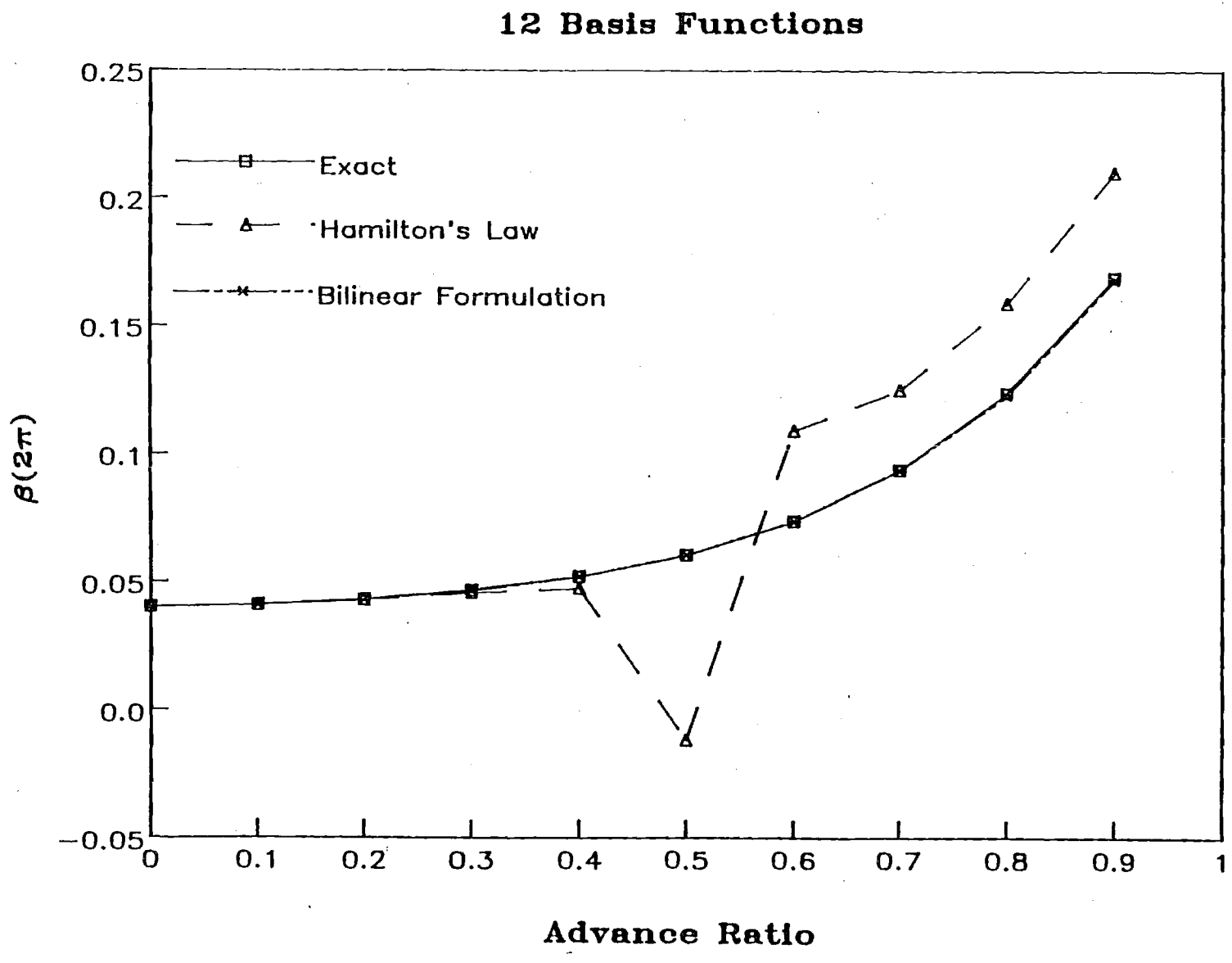

Figure 2. Flapping versus Advance Ratio, n=12

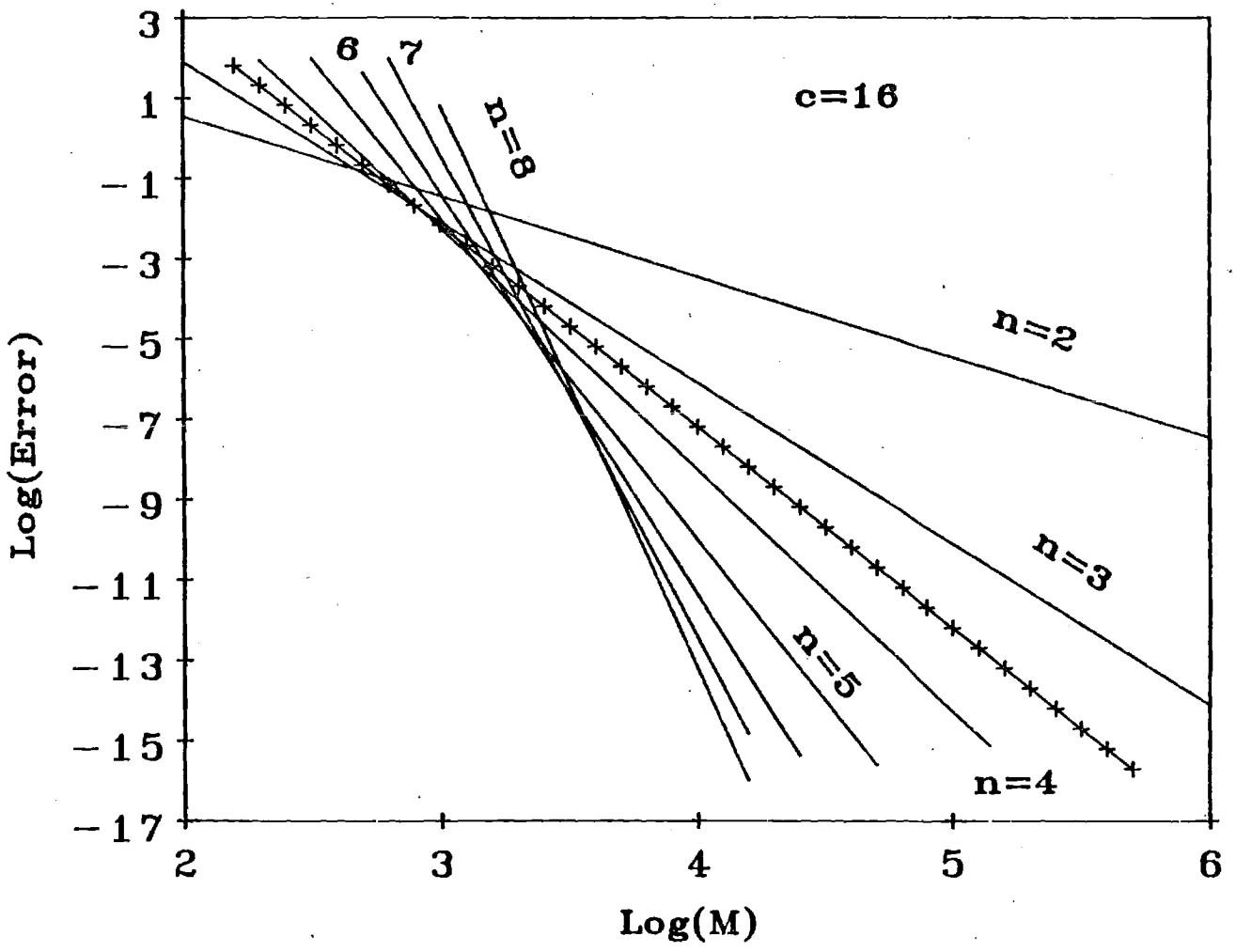

Figure 3. Error as Function of Floating-point Multiplications, c=16

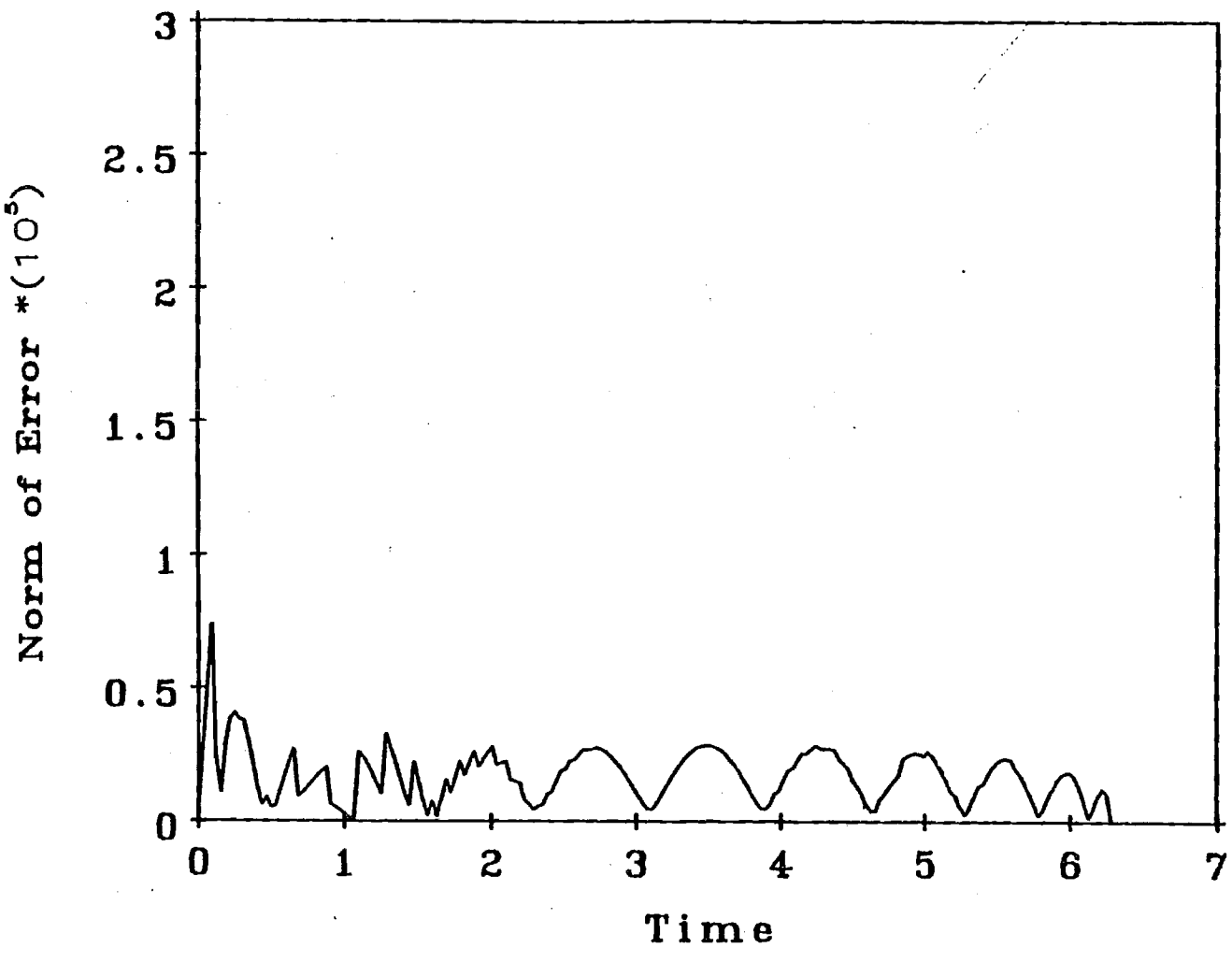

Figure 4 : Norm of Error Using Lagrange Multiplier to find $\hat{\beta}$

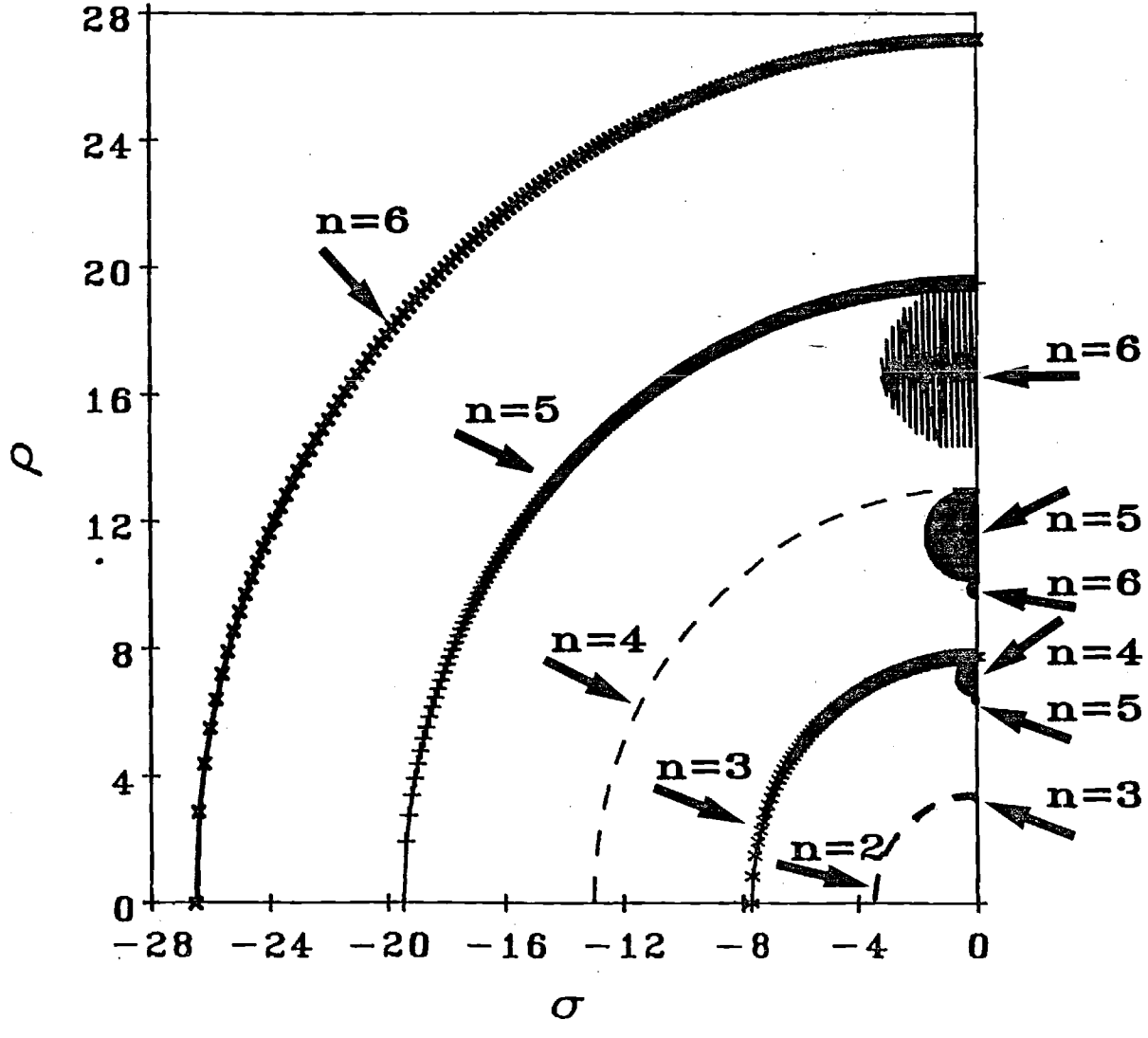

Figure 5 : Stability Boundaries of 2-6 Basis Functions

improvement. In the following, we write the system of equations to be solved including lower-order terms only

Flap equation, order ε

$$-(\tau\bar{w}^{+})^{+}+\Lambda_6\bar{w}^{++++}+\ddot{\bar{w}}=\frac{\gamma}{6a}(\bar{\Gamma}_1+\bar{\Gamma}_2)(\bar{x}+\mu\sin\psi) \tag{1}$$

Lag equation, order ε^2

$$-(\frac{1-x^2}{2}\bar{v}^{+})^{+}+\Lambda_5\bar{v}^{++++}+(\Lambda_5-\Lambda_6)(\theta+\phi)\bar{w}^{++++}-2\int_0^{\bar{x}}\bar{w}^{+}\dot{\bar{w}}^{+}d\bar{x}+\ddot{\bar{v}}-\bar{v}=$$

$$-\frac{\gamma}{6a}(\bar{\Gamma}_1+\bar{\Gamma}_2)(\bar{w}^{+}\mu\cos\psi+\bar{V}_i+\dot{\bar{w}})-\frac{\gamma}{6a}C_D(\bar{x}+\mu\sin\psi)^2 \tag{2}$$

$\bar{\Gamma}_1$ equation, order 1

$$\bar{k}\dot{\bar{\Gamma}}_1+\lambda\bar{\Gamma}_1=\lambda aU_y+\delta\bar{b}\varepsilon^{+} \tag{3}$$

$\bar{\Gamma}_2$ equation, order 1

$$\bar{k}^2\ddot{\bar{\Gamma}}_2+2dw\bar{k}\dot{\bar{\Gamma}}_2+w^2(1+d^2)\bar{\Gamma}_2=-w^2(1+d^2)[U_x\Delta C_z+e\bar{k}(\dot{U}_x\Delta C_z+\frac{\partial\Delta C_z}{\partial\theta}\dot{U}_y)] \tag{4}$$

It is interesting here to note that the terms of the lag equation are of higher order compared to the terms of the flap equation. Thus, to first order, flap drives lag in an important way, but lag has a lesser effect on flap.

An effective way of obtaining accurate pitch inputs is based on the use of an automatic feed-back system that can trim the helicopter. The auto-pilot equations are developed and expressed as follows:

$$\tau_0\ddot{\theta}_0 + \dot{\theta}_0 = A_0[\bar{C}_T - \frac{4}{3}\frac{p^2}{\gamma}\beta] \tag{5}$$

$$\tau_1\ddot{\theta}_s + \dot{\theta}_0 = A_1\frac{(p_0^2 - 1)}{\gamma}[\cos\psi - \frac{8(p^2 - 1)}{\gamma}\sin\psi]\beta \tag{6}$$

$$\tau_1\ddot{\theta}_c + \dot{\theta}_c = -A_1\frac{(p_0^2 - 1)}{\gamma}[\sin\psi + \frac{8(p^2 - 1)}{\gamma}\cos\psi]\beta \tag{7}$$

This automatic-feed-back system provides control to the helicopter for numerical purposes. It adjusts the pitch of the blade to maintain thrust, roll moment, and pitch moment. The parameters A_0 and A_1 are controller gains. The parameters τ_0 and τ_1 are time constants. The grouping $8\frac{(p^2-1)}{\gamma}$ is a coupling parameter giving the pitch-roll coupling of θ_s and θ_c. The grouping $\frac{4p^2\beta}{3\gamma}$ is an estimate of rotor thrust in the absence of an explicit C_T equation.

In the computational algorithm, input parameters define the basic aircraft configuration and flight conditions. The blade type is defined by its root stiffness, solidity, Lock number, damping, and airfoil type. Flight conditions, on the other hand, are characterized by the advance ratio, and thrust coefficient. In Table 1, we present the common parameters used in the cases discussed in this report. These parameters are selected from current helicopter data and used for illustration purposes. It is noted that we use only a constant value of C_D. In future work, we intend to include a variable C_D based on stall assumptions. Thus, the major study here is the effect of stall on lift but not on drag.

Vibration analysis includes flap and lag responses and their sensitivity to advance ratio and thrust coefficient. The torsion effect is neglected in this study. The variation of the automatic control settings required for trim is determined for a blade revolution in a steady state. In addition, the change of these settings as a response to blade stall is identified. Last, the vibration in the flap direction obtained from the stall model used in this research work is compared to results obtained when a linear aerodynamic model is used.

Table 1 Baseline Parameters

Parameter	Numerical Value	Physical Description
γ	6.63	Lock number
a	6.461	lift curve slope
C_D	.01	drag coefficient
Λ_5	.014	$\frac{EI_y}{m\Omega^2 R^4}$
Λ_6	.002	$\frac{EI_x}{m\Omega^2 R^4}$
$\bar{b}$	.05	$\frac{b}{R}$
P	1.03	flap frequency
f	.01	profile drag coefficient
σ	.1	solidity
K_β	.0203	stiffness of flap root
K_ζ	.02083	stiffness of lag root
C_ζ	.025	damping coefficent
τ_0	6.6	time constant
τ_1, τ_2	1.884	time constants
A_0	2.6	gain
A_1, A_2	3.6	gains

In order to determine the response of a helicopter blade, one must determine the pilot controls (collective pitch, cyclic pitch, and shaft tilt) that are applied to the rotor. There are two primary methods of doing this. One method is based on formulas derived by a harmonic balance of the equations without stall. In the other method, an automatic pilot is implemented to update the controls, equations (5-7). In either case, the purpose of the controller is to eliminate first harmonic moments (in the rotating frame) which come through (to the fixed frame) as steady pitching and rolling moments. In other words, "trim" implies (among other things) the balancing of these moments.

Figures 6-9 provide plots of the flapping response at $\bar{x} = 0.7$. Because this is a rigid blade with root spring, flap displacement, w, is a direct measure of root moment. The four figures show a variety of thrust coefficients and advance ratios, some with stall (high μ, high C_T), and others with little or no stall (low μ, low C_T). We see immediately that the approximate formulas for trim give a large amount of 1/rev (i.e., sin ψ) in the response. Thus, they are not accurate due to the aspects of the model neglected in such formulas (inplane motion, unsteady aerodynamics, nonuniform inflow distribution, and stall). The results with the automatic pilot, however, show two peaks per cycle, indicative of little 1/rev, mostly 2/rev, and some 3/rev, which is indicative of trim.

It is interesting that most investigations in this area have had trouble obtaining a correct trim. For example, Figure 10 shows results at $\mu = 0.4$ from Friedmann. Two different iteration schemes are used for the two plots. Notice, however, that the results (although labelled as "propulsive trim") have a large 1/rev component very similar to that seen in our approximate-formula results of Figure 6. This is to be expected because only an approximate formula is used. Figure 11 presents other results from Chopra. Here, we see a very large fore-to-aft 1/rev for a rotor supposedly in "propulsive trim" at $C_T = 0.1$, $\mu = 0.2$. Furthermore, the curves show that the response is not even periodic, as the slopes do not match at $\psi = 0°$ and 360°. In Figure 12 taken from a later Chopra reference, the authors attempt to correct the lack of trim found in Figure 11. The dashed curve is the old result (although in this paper it is corrected to be periodic), and the solid curve is the new result. In this new result, the trim solution is modified to include elastic twist. Notice, however, that although the 1/rev has been reduced by about 50%, it is still very much present. Furthermore, the solid curve is not all periodic, with an error of over 100% in the slope between $\psi = 0°$ and $\psi = 360°$. This points out the difficulties in finding a good trim solution with elastic-blade equations. The autopilot aids greatly in this regard.

In summary, unified-aerodynamic model has been introduced in the elastic-blade equations. This model is an extension of the ONERA lift model and includes plunge, unsteady free stream, and large angles of attack. An ordering scheme has been used to segregate the important terms from others. The elastic-blade equations are presented as lower-order terms and higher-order terms in the flap, lag, and circulation equations. A solution method based on a modified Galerkin's method is used to separate the time and space variables in the differential equations. A numerical solution is

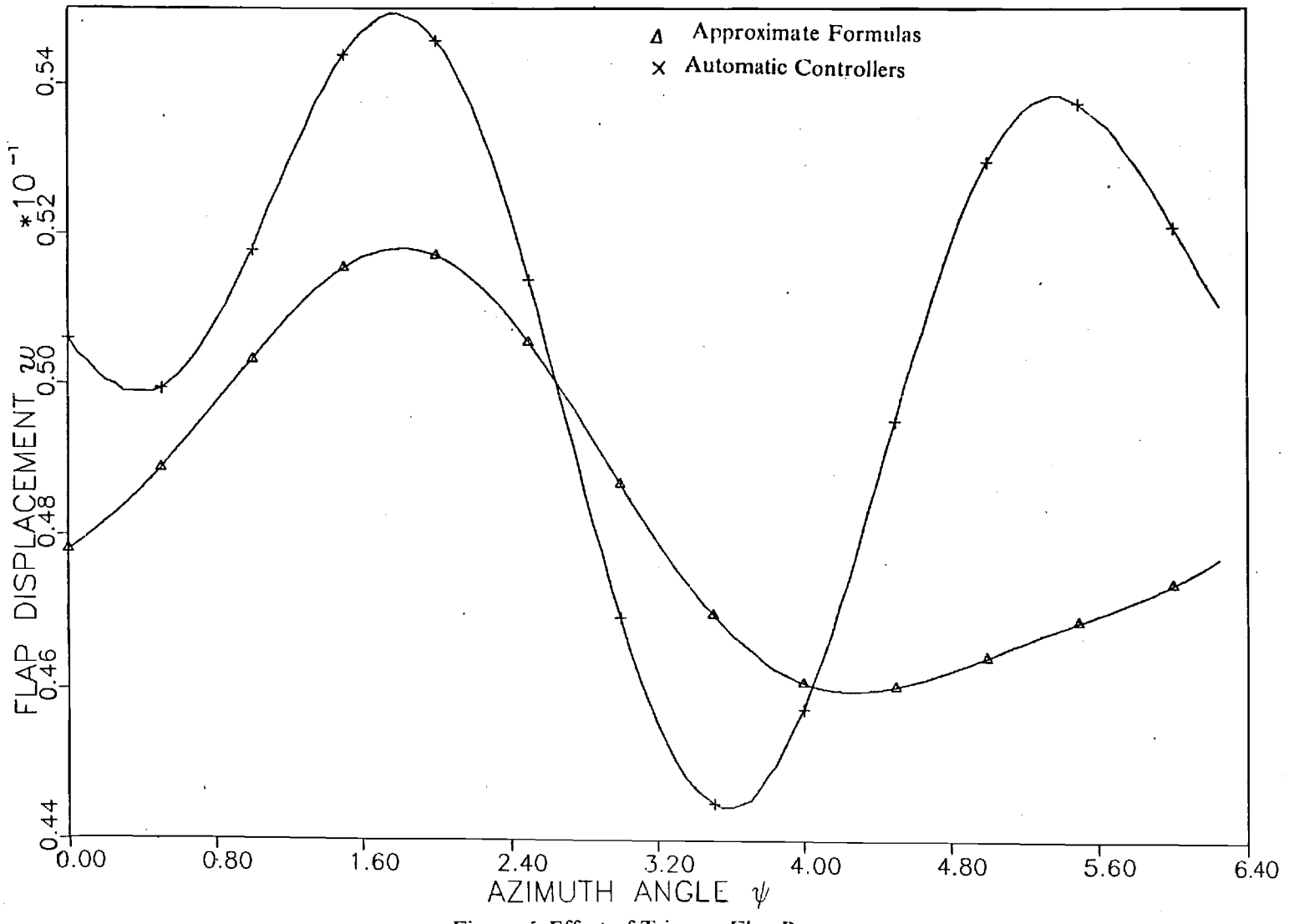

Figure 6. Effect of Trim on Flap Response

($C_T = 0.009$, $\mu = 0.10$)

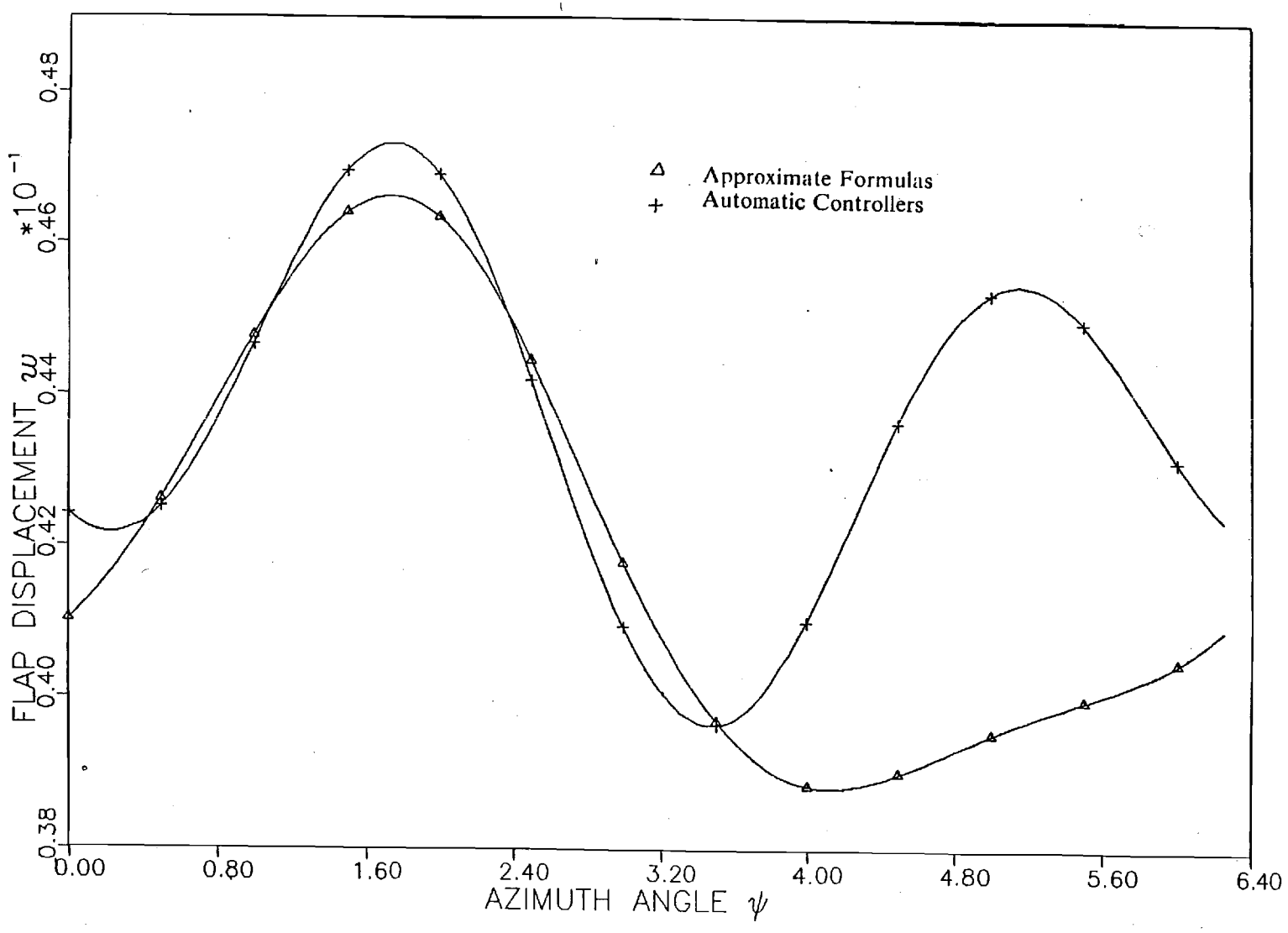

Figure 7 Effect of Trim on Flap Response

($C_T = 0.008$, $\mu = 0.15$)

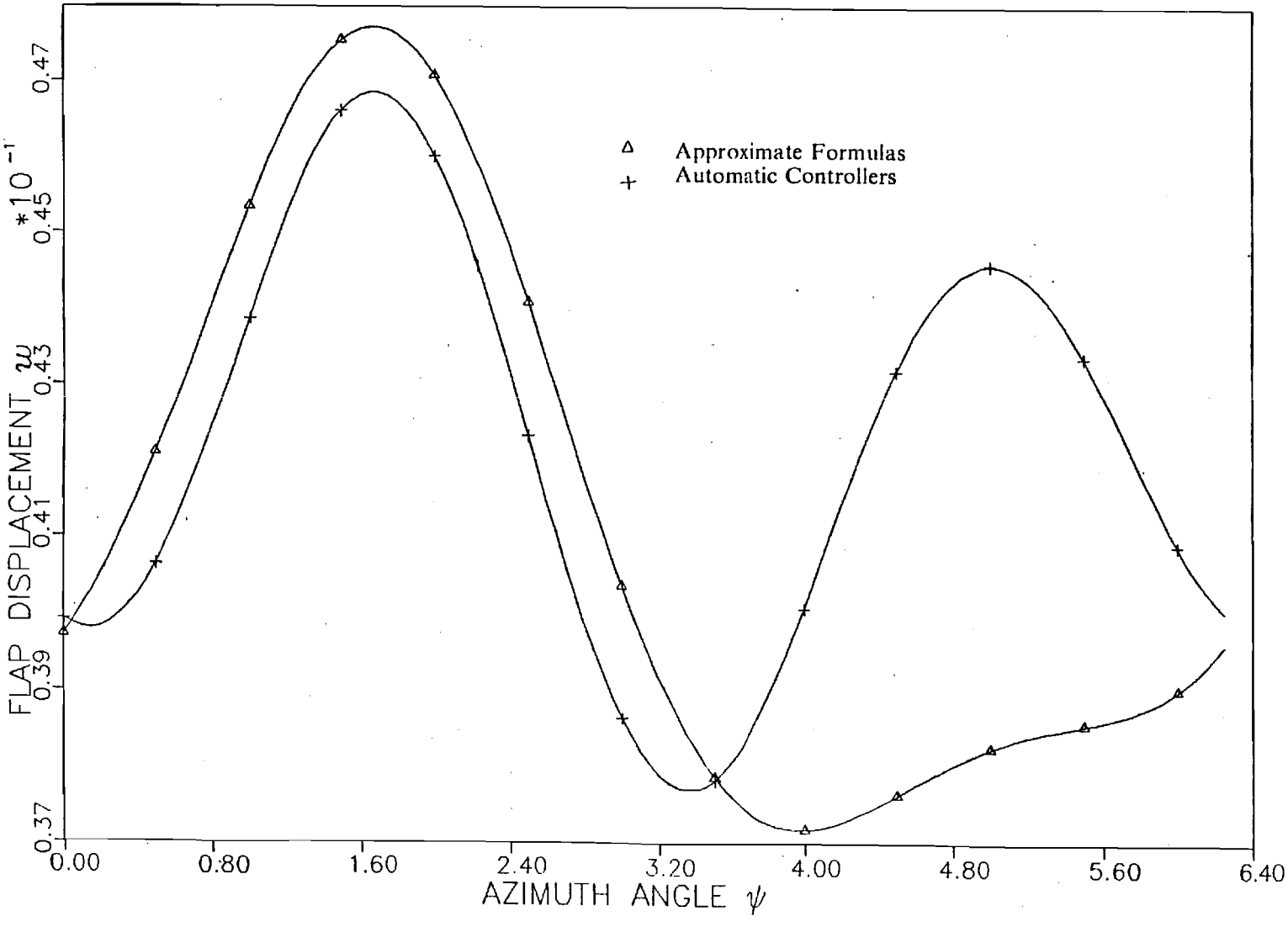

Figure 8 Effect of Trim on Flap Response

($C_T = 0.008$, $\mu = 0.20$)

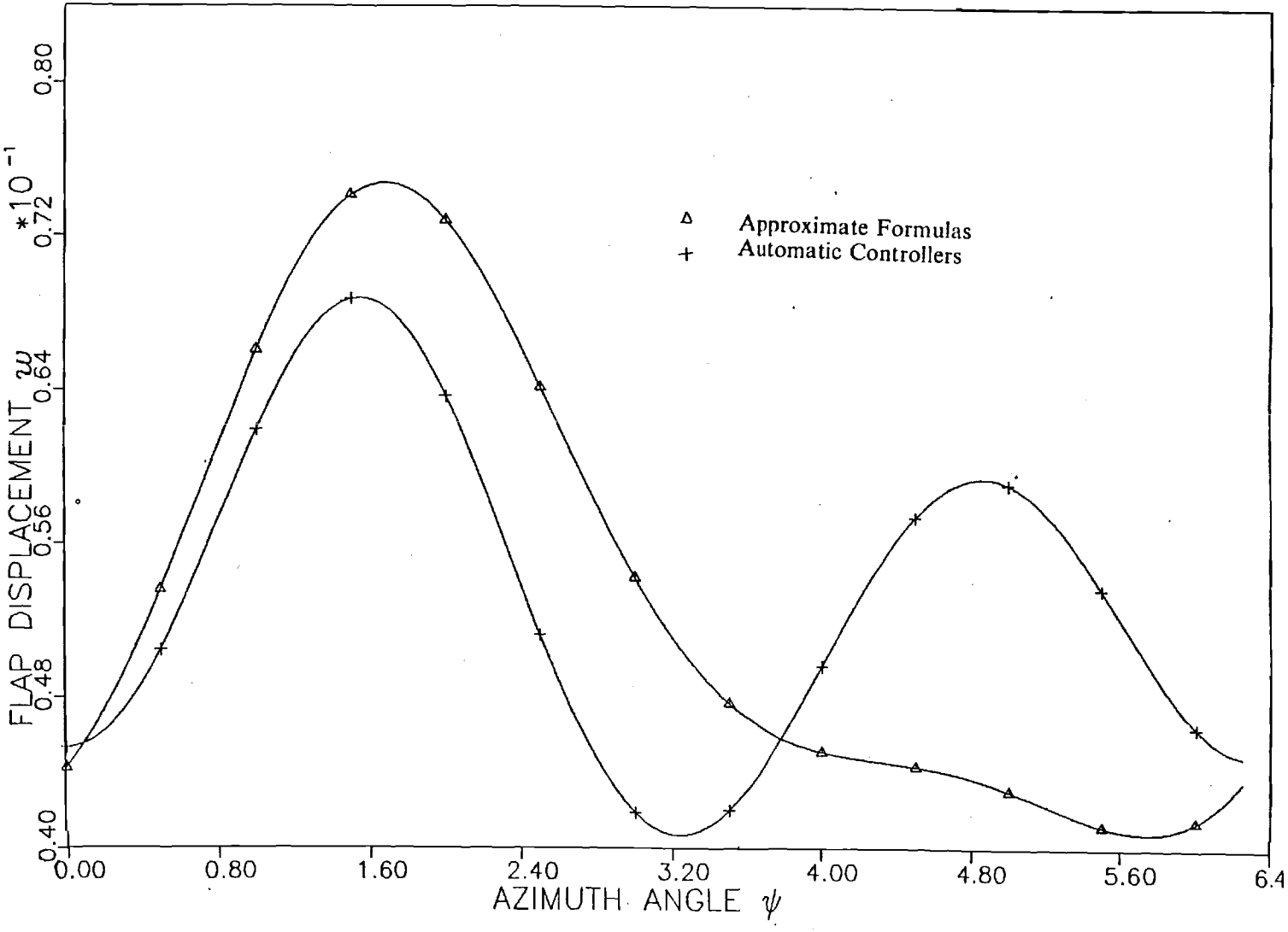

Figure 9. Effect of Trim on Flap Response

($C_T = 0.011$, $\mu = 0.3$)

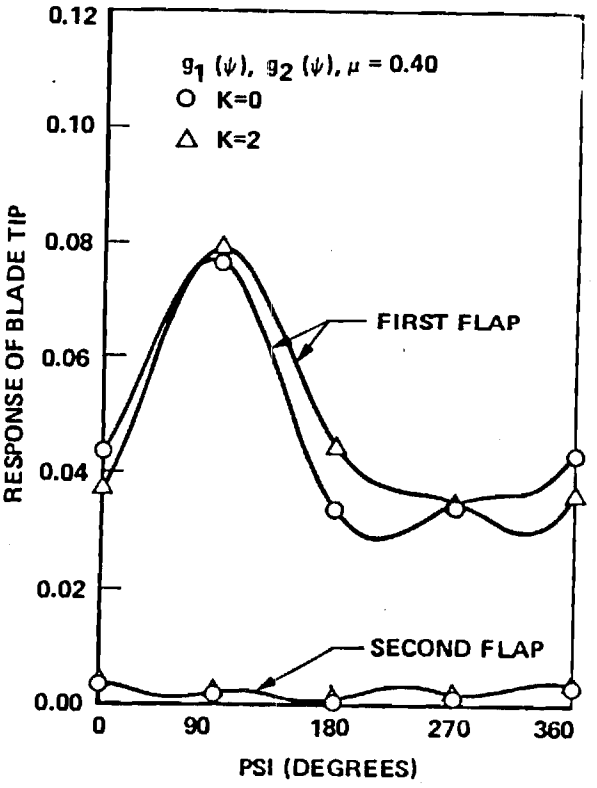

Figure 10. Soft-in-Plane Configuration, Propulsive Trim, C_T = .005, Ref.13.

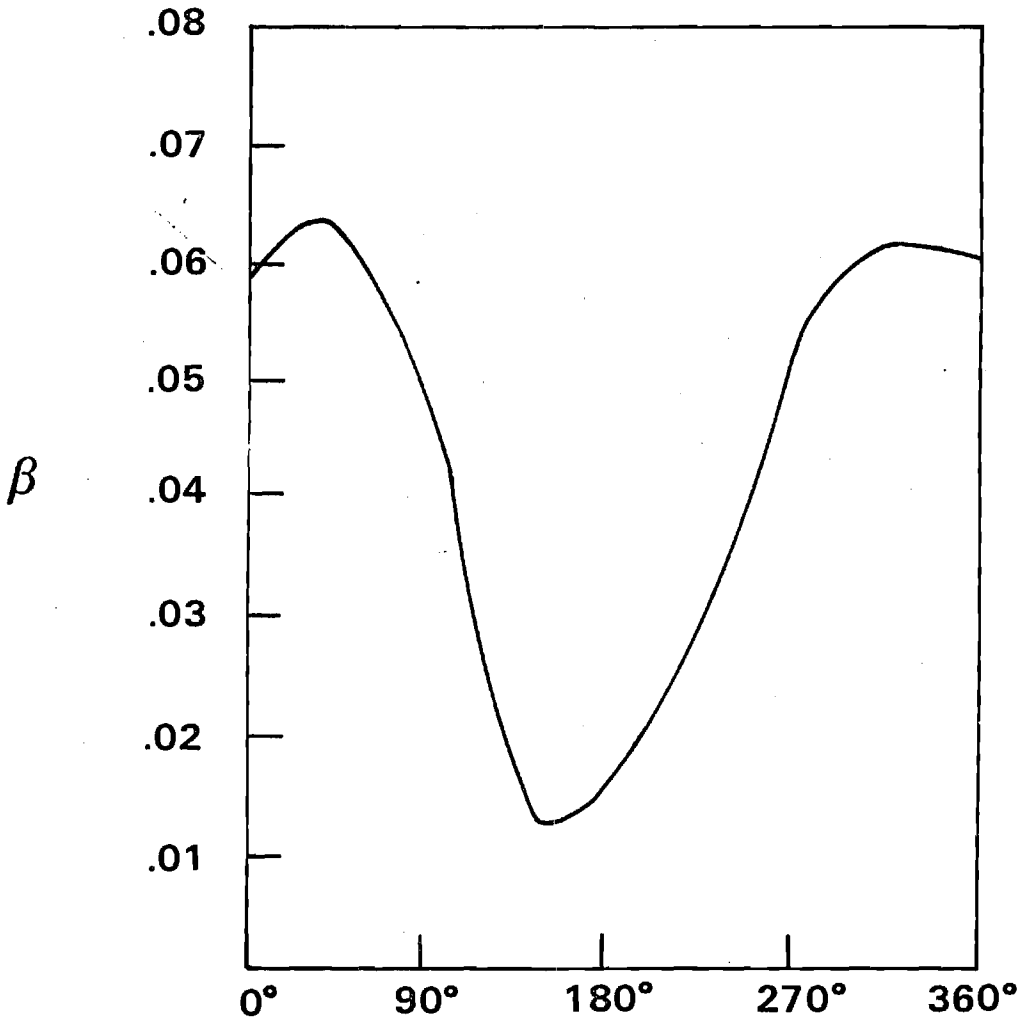

Figure 11. Flap-Lag Response, $C_T/\sigma = 0.1$, $\mu = 0.2$, Ref. 14.

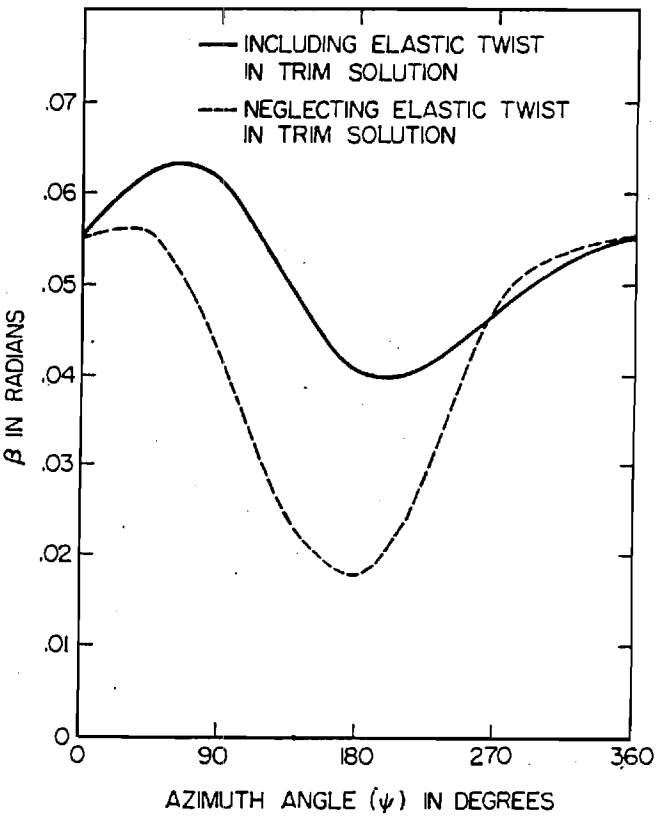

Figure 12 Flap-Lag Response

$(\frac{C_T}{\sigma} = 0.1\ ,\ \mu = 0.2)$

obtained by solving the equations for time history. Two methods have been used for trimming purposes. Dynamic response has been conducted for a variety of thrust coefficients and advance ratios. Results lead to the following conclusions:

1) The approximate method, in which pitch settings are approximated, gives large once-per-rev oscillations in the flap response.
2) Automatic controllers eliminate the once-per-rev and are used successfully beyond stall limit.

5.3 Tip-Loss Aerodynamics

In this area, we have made two very important contributions to the understanding of tip loss. First, we have developed methods to optimize the lifting-surface mesh. This optimization not only improves accuracy but also guarantees convergence, something that cannot be said of conventional mesh choices. Second, we have developed closed-form estimates of the far-wake contributions to induced velocity even with wake contraction. This improves convergence on velocity computations by a factor of 10. These two methods together from the nucleus of our tip-loss computer code which is now being utilized. Because neither of these developments has yet been published (although papers are now in review), we attach to this report an extended abstract which outlines the developments in mesh choice; and, under separate cover, we have sent to ARO a manuscript on the far-wake methodology, which has been submitted to the Journal of Aircraft.

5.4 Rotor-Body Coupling

Our research in rotor-body coupling has been severely hampered by a tragic accident involving Huang Ming-Sheng, the graduate research assistant involved in this work. Reference 8, attached to this report summarizes the basic theory behind the work, which was developed by Mr. Huang prior to his accident. Since recovering from these injuries, he has undertaken the task of coding this theory. That work is now completed. Due to the loss of time, we are not now able to deliver extensive numerical calculations as we had hoped. We will, however, continue this research (hopefully under future ARO funding).

5.5 Dynamic Inflow

We have made considerable progress in this grant toward achieving more widespread use of the theory of dynamic inflow. Reference 2 provides the ultimate correlation between our ARO-sponsored inflow model and wind-tunnel test data in the Ames 7x10 wind tunnel. Reference 3 gives a review of the past 30 years of dynamic inflow modeling including the present state of the art and current research interests. Current research interests which we have pursued in this grant are: 1) role of tip-path dynamics on actuator-disk assumptions, 2) effect of hub motions on dynamic inflow and 3) relationships between higher-harmonic dynamic inflow and unsteady aerodynamics. In the first item, we now believe that tip-path dynamics should not alter the momentum statement of dynamic-inflow theory. In the second area, hub motions can effect the formulation of linearized dynamic inflow. We have worked out

the details in Ref. 3. In item 3, we have uncovered some very strong relationships between Loewy theory and dynamic-inflow theory. Those may allow us to develop a 3-dimensional, unified theory of unsteady aerodynamics that is applicable to rotary-wing problems. An extended abstract concerning this new theory has been submitted to the AHS Forum and has been sent to ARO under separate cover.

5.6 Multiblade Transform

One of the smaller tasks in our research effort has been the study of a modified multiblade transform designed to put the differential mode into the nonrotating system. This work is essentially complete, although the student involved has not yet finished writing his M.S. thesis. The major conclusions are as follows:

1) The new transform for 2-bladed rotors does provide improvement over the conventional 2-bladed transform. In particular, it captures the essentials of the 1/rev instability at high μ.

2) For rotors with an even number of blades greater than 2(e.g., 4,6,8,etc.), there are two possible alternate transforms. One provides some improvement in the transient analysis but degrades accuracy of the forced response. The other improves forced response but degrades transients. Therefore, it is doubtful that either transform will be of general use in dynamics analyses.

3) As a spin-off of the study, we have developed matrix-manipulation algorithms that can perform the multi-blade transformation (either conventionally or in one of our new ways). These algorithms offer a simple way to make this important change of variable, and they are superior to computer algebra, numerical analysis, or fourth-order tensor approaches used by other investigators.

6. Summary of Results

In summary, we can say that our research has been very successful. It has resulted in improved analysis tools and in improved understanding of rotor vibrations. Many of these tools have been (and are being) integrated into production rotor codes.

Optimum Choice of Panel Size and Collocation Points for Rapid Convergence of Lifting-Line and Lifting-Surface Theories as Applied to Both Fixed and Rotating Aerodynamics Surfaces

by

Yihwan Danny, Chiu

Research Assistant

and

David A. Peters

Professor

School of Aerospace Engineering

Georgia Institute of Technology

Atlanta, Georgia

An Abstract Submitted to the Aerodynamics Committe of the American Helicopter Society For Presentation at the 1986 Annual National Forum.

Oct. 15, 1985

ABSTRACT

Researchers often use lifting-line and lifting-surface (or panel) theories to obtain lift and drag of fixed and rotating wings. The choice of panels, line segments, and control points within panels (i.e., collation points) is usually performed on an ad hoc basis based on engineering judgement. The results of this research show that often-used methods such as: 1) placing control points at mid-span of the panel, 2) placing large panels near the blade root and small panels near the wing tip, and 3) using equally-spaced panels near the blade tip, all result in order-unity errors in the calculation; and these errors **do not** decrease with refined mesh even as the number of panels and the number of significant digits is increased without bound. They are non-vanishing residuals.

The work reported here describes both how to eliminate these residual errors through proper choice of panel size and control points, and how to optimize the mesh size to give the maximum rate of convergence as the number of panels is increased. Comparisons with experimental data, with other lifting-line and lifting-surface results, and with a classical Fourier solution, demonstrate the superiority of the new procedure over conventional mesh-choice methods.

INTRODUCTION

It is commonly agreeed that the key to accurate calculation of the rotor aerodynamic behavior is the correct modeling of the rotor wake. McCroskey[1] concluded that lifting-line calculations (for rotary-wings) are in error, regardless of the wake model. The prescribed-wake method of calculation also gives errors in spanwise loading distribution, regardless of which representation is used for the surface of the blade. Even with the complicated free-wake models, lifting-surface codes still fail to predict adequately some cases with highly nonlinear twist distribution. It has been proposed that a major part of these observed discrepancies is due to improper selection of collocation points, (i.e., the possibility of running into mathematical singularities that have no physical counterpart[2]).

Most present-day rotor analyses employ a Kernel-function (in the Mangler sense), which contains a higher-order singularity and is diffcult to handle. Some researchers, however, employ the Vortex Lattice Method (VLM) which amounts to a Cauchy-type finite-element solution to both lifting-surface and lifting-line problems. Many applications of the VLM have been made to problems of the aerodynamic analysis and design of wings with considerable sucess.[3-6] However, the prediction of the detailed aerodynamic performance of a rotary wing is more difficult than that of a fixed wing. In the latter, the wake trails back from the wing in a relatively straight path to downstream infinity. The effect of the trailing vortex on the calculation can be minimized by use of certain mathematical techniques or by use of a free-wake model, which automatically allows wake roll-up. In the case of a rotary wing, the blades pass directly over their own wakes as well as those of other blades as they rotate. Furthermore, a given element has a longer residence time in the immediate vicinity of the rotor plane compared with that of a fixed-wing vortex element. Many computational efforts has been performed to reduce the error caused by wake vortex elements of rotary wings. These include the numerical integration technique[7] (for the prescribed-wake models), curved-vortex elements [8] (for free-wake models), and division of the wake into three separate regions with each computed separately.[9]

The intention of this research is to discover if a simple, systematic, optimized VLM approach can be developed for application to both fixed and rotary wings (especially for helicopter blades), despite criticisms of the VLM, which continue. These criticisms contend either that the lattics are laid out in a preconceived manner to give some desired answer or that too many lattices are required for adequate convergence of the computed loading. The present work is to derive systematically an optimized vortex-lattice layout which overcomes these objections and which can be applied to a wide variety of configuration, including rotary wings.

RECENT DEVELOPEMENTS AND SCOPE OF WORK

(A) 2-D thin airfoil theory:

In the conventional VLM, a thin airfoil is divided into a number of element panels, N, and a horseshoe vortex is placed at the 1/4 quarter-chord of each panel. The control point is located at the 3/4 quarter-chord of each panel. The results agree with Jame's[10] analysis that the first prediction-value (vortex strength) is consistently 11.4% too low for a variety of cambers. Furthermore, increasing the number of elements does not help acurracy. But C_l (lift coeff.) and C_m (pitching moment coeff.) are always exact for N greater than 2. This is the reason that the majority of aerodynamists use conventional VLM. Lan[3] developed the so-called "semi-circle rule" to select collocation points and obtain the essentially exact C_l, C_m and vortex strenth. Kocurate[11] used a Doublet-Vortex method to find the local circulation in this 2-D case and applied it to the lifting-surface performance analysis for hovering rotors. His panel spacing is biased by a cosine distribution, but control points are located at the midpoint of each panel. The method does converge as N is increased, but the rate of convergence is still too slow. Results in this paper show that the semi-circle rule can be applied to both panel size and collocation points to obtain essentially exact values of C_l, C_m, and vortex strength.

(B) Lifting line theory:

Glauert[12] solved Prandtl's lifting-line formula by using a Fourier Series method. Dejarnet[13] applied Multhopp's intepolation technique to obtain the same result as Glauert.

The conventional VLM divides the entire wing span into a number of panels, M. Also, the trailing point is located at the boundary of each panel; and the the control point is placed at the midpoint of each panel. The 1/4-3/4 rule is also used by Hough[14] to afford a singnificant reduction in computational costs. Dejoung[15] has proved that there is mathematical convergence of the VLM to the exact answer, when the 1/4-3/4 rule is used as M (or N, in 2-D case) approaches infinity. The crux of the matter lies in assessing how fast the verified 1/4-3/4 rule improves the convergence and if it is an optimized-choice. Actually, the 1/4-3/4 rule is a special case of the Finite-Difference method, for which locations presumably can be chosen arbitrarily. In this paper, however, we show that if the collocation points are laid out according to a special shape function, which has the same shape as the desired unknow circulations, then the VLM generates the fastest convergence. These shape functions must have quadradic behavior near the wing tip to match the asymptotic tip behavior[16]. Both parabolic and semi-circle functions are valid for this requirement at the tip, and these functions result in an unequally-spaced Finite-Difference technique. Results from different shape functions, compared with the classic solution for a elliptical wing, confirm the rapid convergence of the new method. A mathematical proof (of the optimality of the correct shape function) will be included in the final paper.

Basin[17] derived the mathematic equation of lifting-line theory for a rotary wing (in the prescribed-wake sense). Rosen[7] extended it to curved blades. Both of these use 10 equally-spaced meshes, but the results are not particularly accurate. Part of reason stems from the fact that M is not large enough due to poor selection of collation points. By using a semi-circle or quater-circle to select collation points, we can guarantee rapid convergence. Also included in this paper is an extension of Multhopp's interpolation technique to Prandtl's lifting formula for rotary-wing problems. This technique proves to be equivalent in accuracy to use of the "Fourier Series" method. Although based on a 3-D, rigid-wake concept, an example is given for lightly-loaded hovering blades, calculated by both Finite-Difference and Fourier Series techniques. These are compared with the experimental data[18], and both give excellent correlation.

(C) Lifting-surface theory:

The conventional VLM layout for lifting-surface theory is to use uniformly-spaced panels for both chordwise and spanwise directions over the whole wing. The 1/4-3/4 rule is also used by Hough[14] for the spanwise direction and by Belotserkovskii[6] for the chordwise direction. A reviews of these results[3-6] reveals that (M,N) should be at least (40,2) to give good convergence for typical fixed wings. Dejarnette[13] also applied Multhopp's interpolation technique to the lifting-surface formula with smaller computation time; but the method can be used only for rectangular wings. Some criteria, developed from combination of lifting-line and thin-airfoil theory, can be applied in order to select collocation points. Results in this paper show that a mesh size of only (10,2) can give excellent convergence to exact values when one uses the semi-circle rule to select panels. For rotary wings, Rosen[19] and Chang[20] use only (10,1) equally-spaced panels to calculate aerodynamics; and the results seem to be doubtful. Proper selection, made by the semi-circle or quarter-circle rule, should improve the convergence. These criteria are valid not only for VLM but also for the Double Lattice method, which is an extention of VLM.[21] For example, in the case of the propeller analysis by Murray[22], an increase in outboard unequally-spaced panels actually appears to have a detrimental effect on convergence. Thus, meshes cannot be selected or refined arbitrarily. Finally, one can reformulate the problem to solve for induced drag and pitching moment as well as for lift.

CONCLUDING REMARKS

We have reviewed the conventional VLM literature with respect to selection of collocation points and the corresponding results. These generally show a low rate of convergence. A new criteria for choice of these points is derived from lifting-line theory. A mathematical proof is provided to show that this is the optimum choice. In summary, the optimum choice of collocation points can be done as follows:

1. The choice of points in finite-difference lift calculations should be made on the

basis of equal vortex strength between points, not on equal spacing. Ideally, this would require an adaptive mesh which could change at each iteration; but practical results show this is not necessary, and a quasi-optimum mesh can be used.

2. The size of each panel must smoothly transition from large increments to small increments, moving along the direction in which the rapid change of vortex stregth occurs, and following a smooth shape function. This function must be quadratic near the tip.

3. One way to choose the points in a quasi-optimum manner is to map the spanwise and chordwise interval according to a function which has the approximate properities of criterion 1 and 2, such as a semi-circle. Both panel boundaries and collocation points must be chosen in a smooth manner according to this function.

4. A easy way to map the interval for rotary-wings in subsonic flow is to use the "Semi-circle rule". An advantage of this mapping is that integrals over the vortex strength, can often be reduced to closed form. Sevsral semi-circles can be used if several discontinuities occur.

Multhopp's interpolation technique is also specified as a semi-circle rule for unequally-spaced Finite Differences, which yields the same error as the Fourier Series method and can be applied for rotary wings. The results for wing problems by the Finite Difference technique (unequally-spaced mesh) are found to compare well with experimental data, but with smaller computational times, improved accuracy, and simplfied mathematical derivation, as compared with other continuous loading methods.

REFERENCE

1. McCroskey, W. J., "Special Opportunities in Helicopter Aerodynamics," NASA TM 84396, 1983.

2. Stepniewski, W. Z., Rotory-Wing Aerodynamics, Volume 1, Dover Publications, New York, 1981.

3. Lan, C. E., "A Quasi-Vortex-Lattice Method in Thin Wing Theory," J. Aircraft, Vol. 11, No. 9, 1974, pp. 518-527.

4. Margason, R. J. & Laman, J. E., "Vortex-Lattice Fortran Program for Estimating Subsonic Aerodynamic Characteristics of Complex Planforms," NASA TN D-6142, 1971.

5. Lamar, J. E., "A Modified Multhopp Approach for Predicting Lifting Pressures and Camber Shape for Composite Planforms in Subsonic Flow, "NASA TN D-4427, 1968.

6. Belotserkouskii, The Theory of Thin Wings in Subsonic Flow, Plenum Press, New York, 1967.

7. Rand, O. & Rosen A., "The Aerodynamics of Helicopter Rotors in Hovering and Axial Flight Using Lifting-Line Models," AE No. 485, Haifa, Israel, 1982.

8. Bliss D. B., et al., "A New Methodology For Helicopter Free Wake Analysis," 39th Annual Forum of AHS, St. Louis, May, 1983.

9. Suma, J. M. & Maskew, B., "New Methods for the Calculation of Hover Airloads," 5th European Rotorcraft and Powered Lift Aircraft Forum. Amsterdam, the Netherlands, 1979.

10. James, R. M., "On the Remarkable Accuraey for the Vortex Lattice Discretization in Thin Wing Theory," Rept DAC-67211, Douglas Aircraft Co., Long Beach, California, 1969.

11. Kocurek, J. D., A Lifting Surface Performance Analysis with Circulation Coupled Wake for Advanced Configuration Hovering Rotors, Ph. D. Thesis, Texas A&M University, May, 1978.

12. Mises, R., Theory of Flight, Dover, New York, 1959.

13. Dejarnette, F. R., "Arrangement of Vortex Lattice on Subsonic Wings," Vortex-Lattice

Utilization, NASA SP-405, 1976.

14. Hough, G. R., "Lattice Arrangements for Rapid Covergence," Vortex-Lattice Utilization, NASA SP-405, 1976.

15. Deyoung, J., "Optimum Lattice Arrangement Developed from a Rigorous Analysis Basis," Vortex-Lattice Utilization, NASA SP-405, 1976.

16. Chiu, Y. W., An Investigation of Loss of Lift and Increased Drag Near Wings Tips, M. S. Thesis, Washington University, St. Louis, May, 1984.

17. Basin, V. E., Theory of Lifting Aircrew, NASA TTF-823, 1976.

18. Meyer, J. R. & Falabella, G., "An Investigation of the Experimental Aerodynamic Loading on a Model Helicopter Rotor Blades," NASA TN 2953, 1953.

19. Rosen, A. & Graber, A., "Free Wake Model of Hovering Rotors Having Straight or Curved Blades," International Conference on Rotorcraft Basic Research, Research Triangle Park, North Carolina, Feb., 1985.

20. Chang, L. K., The Theoretical Performance of High Efficiency Propellers, Ph. D. Thesis, Purdue University, 1980.

21. Albano, E. & Rosen, W. P., "A Doublet-Lattice Method for Calculating Lift Distribution on Oscillating Surface in Subsonic Flows," AIAA Journal, Vol 7, 1969, pp. 279-285.

22. Murray, J. C. & Carta, F. O., "Lifting Surface Theory for Statically Operating Propellers," Technical Report AFAPL-TR-72-100, 1972.

COMPARISON OF 2-D THIN AIRFOIL VORTEX DISTRIBUTION WITH STRAIGHT-LINE CAMBER

$$1 = W(x) = \frac{1}{2\pi} \int_0^1 \frac{\gamma(x_1)\,dx_1}{x - x_1}$$

ERROR PERCENTAGE %		
Nth POINT	V.L.M.	CURRENT
1.	11.363	0.0
2.	0.897	0.0
3.	0.274	0.0003
4.	0.112	0.0001
5.	0.039	0.0001
6.	0.013	0.0001
7.	0.070	0.0006
8.	0.174	0.0001
9.	0.466	0.0005
10.	2.314	0.0034
Cl	0.0	0.0
Cm	0.0	0.0

* (10 meshes and codes)

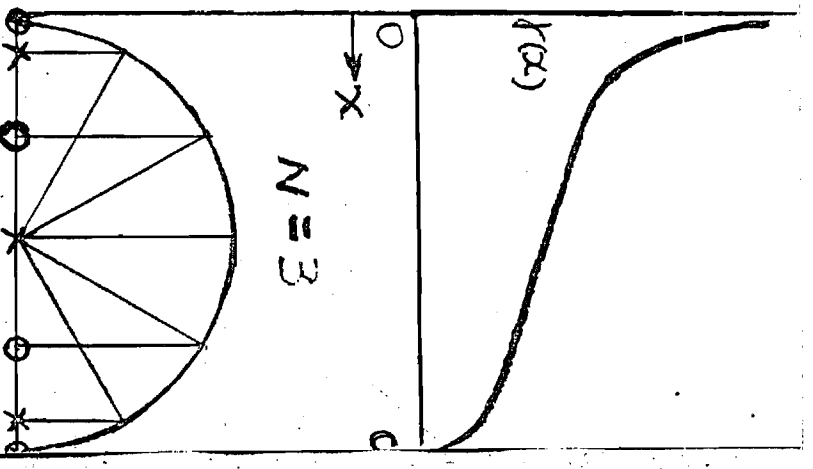

COMPARISON OF 2-D THIN AIRFOIL VORTEX DISTRIBUTION WITH PARABOLIC CAMBER

$$0.5(x-0.5) = W(x) = \frac{1}{2\pi}\int_0^1 \frac{\gamma(x_1)dx_1}{x-x_1}$$

ERROR PERCENTAGE %		
Nth POINT	V.L.M.	CURRENT
1.	11.363	0.0028
2.	0.897	0.0003
3.	0.274	0.0002
4.	0.112	0.0003
5.	0.039	0.0001
6.	0.013	0.0001
7.	0.070	0.0004
8.	0.174	0.0001
9.	0.466	0.0008
10.	2.314	0.0020
Cl	0.0	0.0
Cm	0.0	0.0

* (10 meshes and codes)

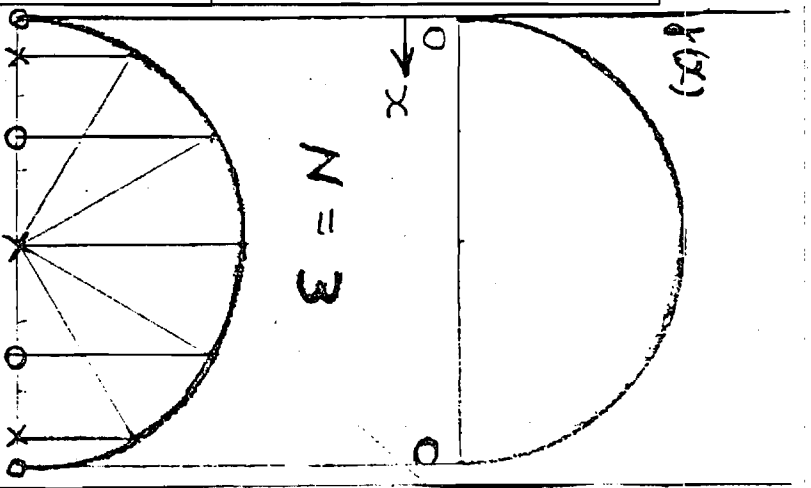

COMPARISON OF PREDICTED VORTEX DISTRIBUTIONS FOR AN AIRFOIL WITH 30% FLAP CHORD AND 30° FLAP DEFLECTION

ERROR PERCENTAGE		
NO. POINT	V.L.M.	CURRENT
1.	15.92	0.26
2.	6.25	0.29
3.	6.10	0.37
4.	6.80	0.88
5.	-9.15	13.58
6.	18.24	7.38
7.	7.59	0.02
8.	11.59	0.07
Cl	4.07	0.17
Cm	2.25	0.025

* (8–(5;3)– meshes and codes)

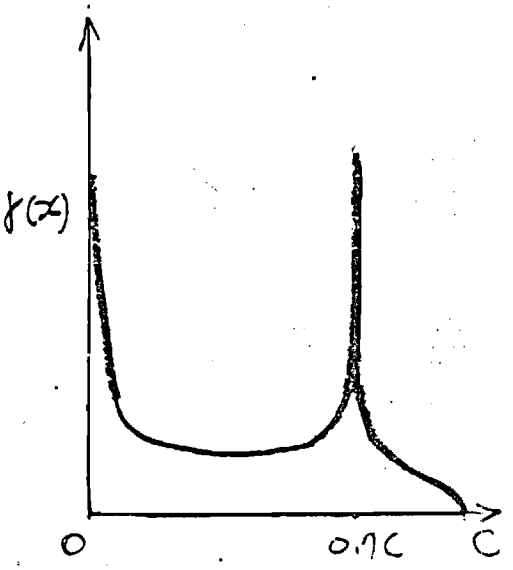

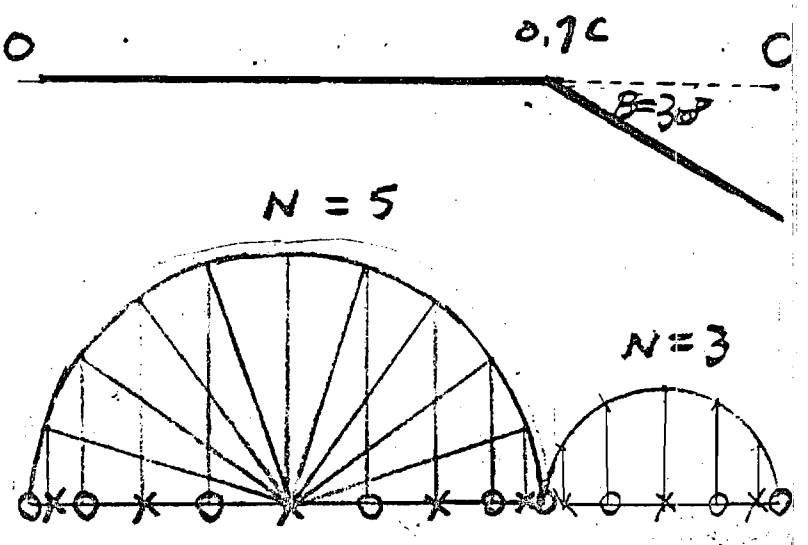

FIG. ACCURACY OF CL FOR UNTWISTED ELLIPTIC WINGS(AR=20)

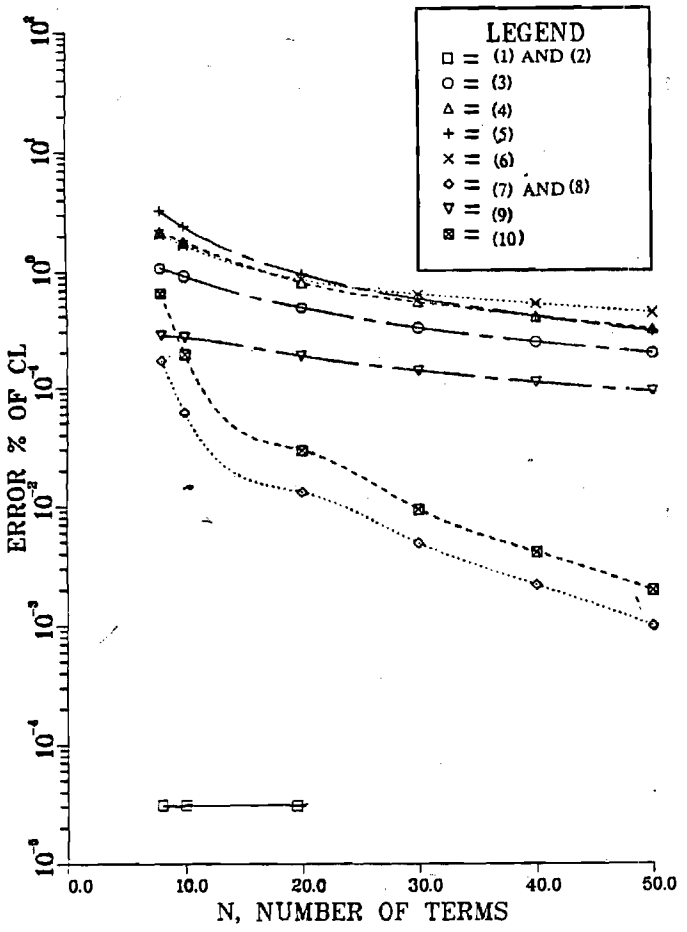

(1) FOURIER SERIES METHOD, REF 12

(2) MULTHOPP'S INTERPOLATION, REF 13

(3) Panel spacing is biased by a parabolic distribution, but control points are located at the midpoint of each panel. Also, wing tips are specified as boundary points.

(4) Panel spacing is biased by a cosine distribution, but control points are located at the midpoint of each panel. Also, wing tips are specified as boundary points.

(5) Both control and trailing points are selected according to equally-spaced panels and wing tips are specified as boundary points.

(6) Panel spacing is biased by an elliptic distribution, but control points are located at the midpoint of each panel. Also, wing tips are specified as boundary points.

(7) Both control and trailing points are selected according to the parabolic function and wing tips are specified as boundary points.

(8) Both control and trailing points are selected according to semi-circle rule and wing tips are specified as boundary points.

(9) Both control and trailing points are selected according to equally-spaced panels and wing tips are specified as trailing points.

(10) Both control and trailing points are selected according to the parabolic function and wing tips are specified as trailing points.

COMPARISON OF VORTEX DISTRIBUTION FOR A RECTANGULAR WING WITH EXPERMENTAL TESTS (Cl per degree)

AR=1.13		
METHOD	TYPE	ERROR %
MULTHOPP(20)*	L-LINE	37.00
" (10;1)*	L-SURFACE	1.80
" (10;2)*	L-SURFACE	<< 0.10
FINITE(10;2)**	L-SURFACE	0.41

AR=2.13		
METHOD	TYPE	ERROR %
MULTHOPP(20)*	L-LINE	19.00
" (10;1)*	L-SURFACE	3.90
" (10;2)*	L-SURFACE	2.30
FINITE(10;2)**	L-SURFACE	1.90

* : ref. 13

**: Current Method

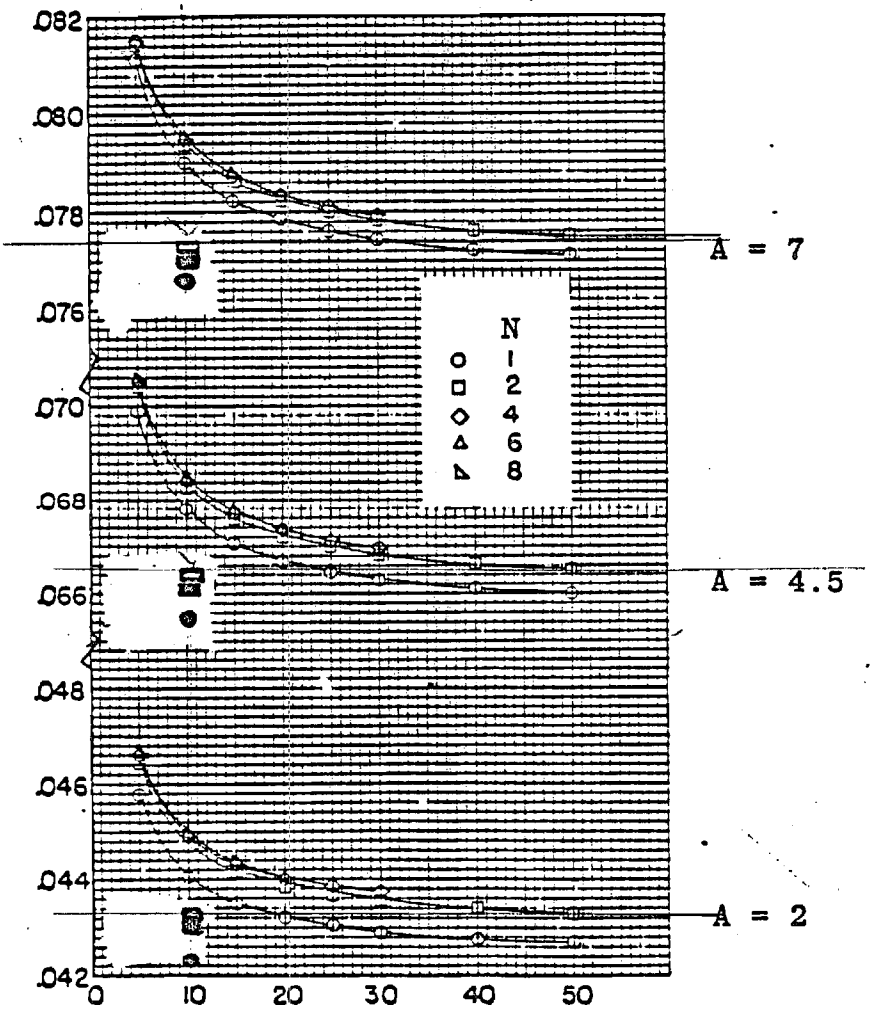

. Effect of vortex-lattice arrangement for rectangular planforms.

A : Aspect Ratio

▭ : Current Method, (M,N)=(10,2)

▬ : ref. 13, (M,N)=(10,2)

● : ref. 13, (M,N)=(10,1)

——— : three conventional VLM. ref. 4

FIG. SPANWISE AERODYNAMIC LOADING

NACA0015(TN2953)

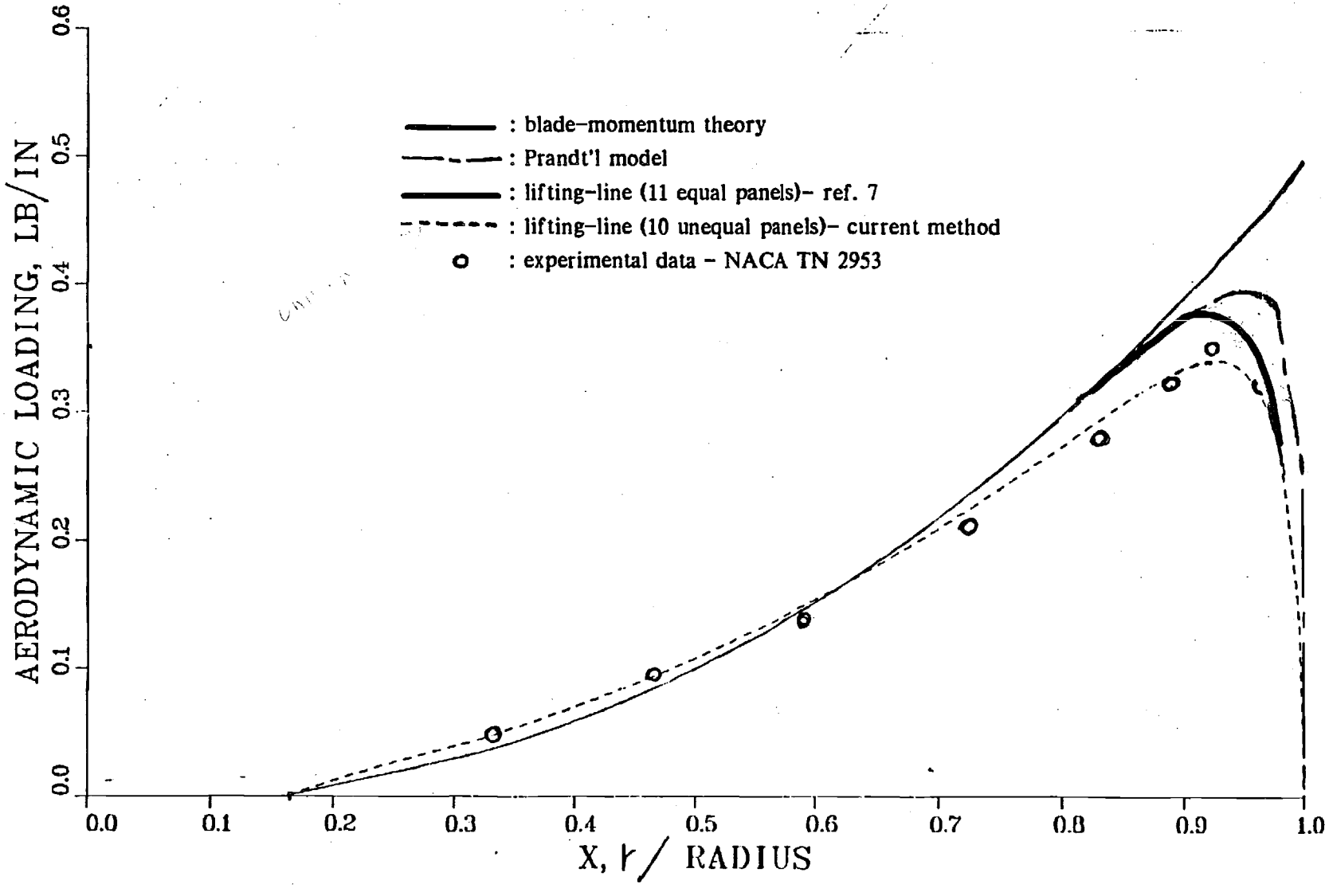

COUPLED ELASTIC ROTOR/BODY VIBRATIONS WITH INPLANE DEGREES OF FREEDOM (Work in Progress)

by

Ming-Sheng Huang
Research Assistant

and

David A. Peters
Professor of Aerospace Engineering
Georgia Institute of Technology
Atlanta, Georgia 30332

Presented at the ARO Workshop on
Dynamics and Aeroelastic Modeling
of Rotor Systems

December 4-5, 1985

INTRODUCTION

1.1 BACKGROUD

Helicopter vibration reduction is important as well as useful. With less vibration, a helicopter can survive much longer and can provide a comfortable environment for passengers. However, unlike conventional fixed-wing aircraft, the helicopter suffers an intrinsic, severe vibration source in the main rotor, which contains elastic blades and is connected flexibly to the fuselage by a hub-pylon system. So, the problem is rather sophisticated. It is well known that the fuselage motions due to rotor vibrations will cause the hub to move in all degrees of freedom. This hub motion can cause the hub loads to be different from those calculated for a fixed-hub condition. This alteration can often be an order-of-magnitude change. Therefore, in studying the effect of hub motions on hub loads, we are actually studying a feedback system.

1.2 PREVIOUS WORK

The concept of performing a coupled rotor/airframe vibration analysis by impedance matching was pointed out in 1964, Reference 1, which indicates two important facts. First, a coupled rotor/airframe analysis can be performed in a rigorous maner by separate calculation of rotor and fuselage impedances followed by a matching of forces and displacements at the hub. Second, the rotor impedance need only be calculated for a single blade and then appropriately transformed to apply to any number of blades.

In 1974, Staley and Sciarra treated the vertical vibrations of a coupled rotor and fuselage, including the effect of vertical hub motions. They used a lumped mass for rotor impedance and showed that hub motions could create order-of-magnitude changes in hub loads. In Reference 3, Hohenemser and Yin further investigate the effects of rotor-body coupling. Their model for rotor impedance is based on a rotor representation that includes two masses(each equal to one-half of the total rotor mass) connected by a spring to represent the first flapping

frequency. Reference 3 presents some very interesting conclusions that pertain to fuselage design. Particularly, it notes that under certain conditions it may be desirable to tune a fuselage frequency to the blade passage frequency in ordor to eliminate hub loads. Also, it outlines a method of computing the complete rotor impedance by finite elements and transfer matrices. Other work on the importance of hub impedance may be found in References 4-6.

Since rather crude models have been used for hub impedance (rigid mass, no aerodynamics, etc.), one might wonder why more sophisticated models were not used. The answer is straightforward. These were only the initial investigations into this effect. Furthermore, although most analysts realized the importance of detailed blade modeling for fixed hub loads (blade modes, unsteady aerodynamics, periodic coefficients, etc.), it was not clear in the beginning which of these effects would be important for finding the role of hub motion on loads. Because of the high frequencies involed (4/rev, 8/rev), many felt that inertial terms would dominate.

Reference 7 offers a sophisticated (but linear) rotor flapping model that allows for a detailed investigation of both loads and impedance (even in the presence of periodic coefficients). The method, generalized harmonic balance, involves a computer-bassed manipulation of equations that allows many degrees of freedom, many modes, and many harmonics. In Reference 8, Hsu and Peters apply this method to a flexible rotor and then use impedance matching to include plunge, pitch, and roll of the hub. This combined technique proves to be very efficient on two counts. First, the calculation for only one blade can be used for n-blades (as in Reference 1). Second, wholesale changes in fuselage properties can be made without a requirement to recalculate rotor properties. It is interesting that other investigators who began with a full-blown, coupled analysis later changed to the impedance matching technique, Reference 9-10.

For inplane vibrations with a fixed hub, Reference 8 sets up the rotor equations with rigid blades, and Reference 12 treats the same problem but with elastic blades.

In Reference 13, a fuselage model with offsets and 9 degrees of freedom is considered, coupled with a rigid inplane blade model. There is an important conclusion in reference 13 which will be very useful for further nonlinear analysis. It is that the addition of inplane degrees of freedom does not significantly affect the plunge vibrations for the cases considered, and these cases are for resonable configurations.

1.3 SCOPE OF WORK

In order to predicate the helicopter coupled vibration much better, the rotor with elastic blades should be considered. The scope of this research is to continue the previous efforts in the study of inplane coupled rotor-body vibrations. To do so, first, the dynamic partial differential equations of elastic blades including hub motions should be derived. Second, hub loads equations should be derived. Third, the fuselage equations are taken to be the same as those in Reference 13. The major goal of this research is to investigate if higher frequencies of the elastic blades will affect the coupled rotor-body vibrations.

2. ELASTIC BLADE EQUATIONS

The equations of motion for a flexible hingeless rotor blade in forward flight, as derived in Reference 12, are the starting point for this analysis. The present analysis, however, expands the previous work in following way. The hub motions (including plunge, longitudinal and lateral displacements, pitch and roll angles, and their first and second derivatives) are added to the equations.

2.1 COORDINATES AND THEIR TRASFORMATIONS

The coordinate systems used in the present analysis are shown in Figure 1. The triplet X,Y,Z represents a fuselage fixed coordinate system; and the triplet x,y,z represents a rotating coordinate system. Between the Z and z axes there is a precone angle. The deflection components of the elastic axis of the deformed blade (u, v, and w) are taken in the x,y,z coordinate system. The final set of axes, x', y', z' are taken along the deformed axes.

There are transformations among these coordinates. Figure 2 shows the pitch angle α_c and roll angle α_s; and, Figure 3 indicates azimuth angle ψ and precone angle β_{pc}. With these angles, one can trasform any vector, say $\vec{F}$, from the fixed coordinate X,Y,Z to the undeformed rotating coordinate x,y,z. We have:

$$\begin{pmatrix} F_x \\ F_y \\ F_z \end{pmatrix} = [T_R] \begin{pmatrix} F_X \\ F_Y \\ F_Z \end{pmatrix} \tag{1}$$

where,

$$[T_R] = \begin{pmatrix} \begin{pmatrix} \cos\beta_{pc}\cos\alpha_c\cos\psi \\ +\sin\beta_{pc}\sin\alpha_c \end{pmatrix} & \begin{pmatrix} -\cos\beta_{pc}\cos\psi\sin\alpha_c\sin\alpha_s \\ +\cos\beta_{pc}\sin\psi\cos\alpha_s \\ +\sin\beta_{pc}\cos\alpha_c\sin\alpha_s \end{pmatrix} & \begin{pmatrix} -\cos\beta_{pc}\cos\psi\sin\alpha_c\cos\alpha_s \\ -\cos\beta_{pc}\sin\psi\sin\alpha_s \\ +\sin\beta_{pc}\cos\alpha_c\cos\alpha_s \end{pmatrix} \\ (-\sin\psi\cos\alpha_c) & \begin{pmatrix} \sin\psi\sin\alpha_c\sin\alpha_s \\ +\cos\psi\cos\alpha_s \end{pmatrix} & \begin{pmatrix} \sin\psi\sin\alpha_c\cos\alpha_s \\ -\cos\psi\sin\alpha_s \end{pmatrix} \\ \begin{pmatrix} -\sin\beta_{pc}\cos\psi\cos\alpha_c \\ +\cos\beta_{pc}\sin\alpha_c \end{pmatrix} & \begin{pmatrix} \sin\beta_{pc}\cos\psi\sin\alpha_c\sin\alpha_s \\ -\sin\beta_{pc}\sin\psi\cos\alpha_s \\ +\cos\beta_{pc}\cos\alpha_c\sin\alpha_s \end{pmatrix} & \begin{pmatrix} \sin\beta_{pc}\cos\psi\sin\alpha_c\cos\alpha_s \\ +\sin\beta_{pc}\sin\psi\sin\alpha_s \\ +\cos\beta_{pc}\cos\alpha_c\cos\alpha_s \end{pmatrix} \end{pmatrix} \tag{2}$$

The transformation from undeformed coordinates to deformed coordinates is given by

$$\begin{pmatrix} F_{x'} \\ F_{y'} \\ F_{z'} \end{pmatrix} = [T_d] \begin{pmatrix} F_x \\ F_y \\ F_z \end{pmatrix} \tag{3}$$

where,

$$[T_d] = \begin{pmatrix} 1 & v^+ & w^+ \\ -\theta w^+ - v^+ & 1 & \theta \\ -w^+ + \theta v^+ & -\theta - w^+ v^+ & 1 \end{pmatrix} \tag{4}$$

With these transformations, we can transfer the vectors to any coordinates needed. Other, kinematic contributions to θ are treated as pitch-lag coupling.

2.2 HAMILTON'S LAW

The next step in the derivation is to apply Hamilton's Law to obtain equations of motion. The Hamilton's Law can be expressed as

$$\int_{t_1}^{t_2} (\delta U - \delta T - \delta W)\, dt + \frac{\partial T}{\partial \dot{q}_i} \delta q_i \Big|_{t_1}^{t_2} = 0 \tag{5}$$

where, δU and δT are the variations in strain energy and kinetic energy, and δW is the virtual work. 'q_i' is the generalized coordinate. To apply equation (5), δU, δT and δW must be formulated in terms of the generalized coordinates.

2.2.1 STRAIN ENERGY

The strain energy can be expressed as follows:

$$U = \frac{1}{2} \int_0^R \iint_A E \epsilon_{xx}^2 dA\, dx \tag{6}$$

then,

$$\delta U = \int_0^R \iint_A E \epsilon_{xx} \delta \epsilon_{xx}\, dA\, dx \tag{7}$$

where,

$$\epsilon_{xx} = u' + \frac{v'^2}{2} + \frac{w'^2}{2} - v''[\eta \cos\theta_e - \varsigma \cos\theta_e] - w''[\eta \sin\theta_e + \varsigma \cos\theta_e] \tag{8}$$

and

$$\theta_e = R_e\theta \tag{9}$$

Therefore, δU can be fuether expressed as

$$\delta U = \int_0^R \Big\{ V_{x'}[\delta u' + v'\delta v' + w'\delta w'] + [M_{z'} + M_{y'}R_e\theta]\delta V'' + [M_{z'}R_e\theta - M_{y'}]\delta W'' \Big\}\, dx \tag{10}$$

where,

$$V_{x'} = EA\left\{ u' + \frac{v'^2}{2} + \frac{w'^2}{2} \right\} \tag{11}$$

$$M_{y'} = EI_{y'}[v''R_e\theta - w''] \tag{12}$$

$$M_{z'} = EI_{z'}[v'' + w''R_e\theta] \tag{13}$$

Integration by parts of δU gives the following result:

$$\delta U = \int_0^R \left(\bar{Y}_u\delta u + \bar{Y}_v\delta v + \bar{Y}_w\delta w\right) dx + b(U) \tag{14}$$

where,

$$\bar{Y}_u = -(V_{x'})' \tag{15}$$

$$\bar{Y}_v = [M_{z'} + M_{y'}R_e\theta]'' - (V_{x'}v')' \tag{16}$$

$$\bar{Y}_w = [M_{z'}R_e\theta - M_{y'}]'' - (V_{x'}w')' \tag{17}$$

and the boundary condition is

$$b(U) = V_{x'}\delta u\Big|_0^R + \Big\{ V_{x'}v' - [M_{z'} + M_{y'}R_e\theta]' \Big\}\delta v\Big|_0^R + [M_{z'} + M_{y'}R_e\theta]\delta v'\Big|_0^R + \Big\{ V_{x'}w - [M_{z'}R_e\theta - M_{y'}]' \Big\}\delta w\Big|_0^R + [M_{z'}R_e\theta - M_{y'}]\delta w'\Big|_0^R \tag{18}$$

2.2.2. KINETIC ENERGY

The kinetic energy can be expressed as

$$T = \frac{1}{2}\int_0^R \iint_A \rho \vec{V} \cdot \vec{V}\, d\eta\, d\zeta\, dx \tag{19}$$

and the variation is

$$\delta T = \int_0^R \iint_A \rho \vec{V} \cdot \delta\vec{V}\, d\eta\, d\zeta\, dx \tag{20}$$

where the velocity vector is

$$\begin{aligned}
\vec{V} = \vec{i}\Big\{ & \dot{x}_1 + \dot{\alpha}_s z_1 \sin\psi + \dot{\alpha}_c z_1 \cos\psi - \dot{\alpha}_s y_1 \beta_{pc} \cos\psi \\
& + \dot{\alpha}_c y_1 \beta_{pc} \sin\psi - \Omega y_1 - \dot{X}\cos\psi + \dot{Y}\sin\psi - \dot{Z}\beta_{pc} \Big\} \\
+ \vec{j}\Big\{ & \dot{y}_1 + \dot{\alpha}_s z_1 \cos\psi - \dot{\alpha}_c z_1 \sin\psi - \Omega z_1 \beta_{pc} + \dot{X}\sin\psi \\
& + \dot{\alpha}_s x_1 \beta_{pc} \cos\psi - \dot{\alpha}_c x_1 \beta_{pc} \sin\psi + \Omega x_1 + \dot{Y}\cos\psi \Big\} \\
+ \vec{k}\Big\{ & \dot{z}_1 - \dot{\alpha}_s y_1 \cos\psi + \dot{\alpha}_c y_1 \sin\psi + \Omega y_1 \beta_{pc} - \dot{\alpha}_s x_1 \sin\psi \\
& - \dot{\alpha}_c x_1 \cos\psi + \dot{X}\beta_{pc}\cos\psi - \dot{Y}\beta_{pc}\sin\psi - \dot{Z} \Big\}
\end{aligned} \tag{21}$$

and where,

$$\begin{aligned}
x_1 &= x + u - v'[\eta\cos\theta - \zeta\sin\theta] - w'[\eta\sin\theta + \zeta\cos\theta] \\
y_1 &= v + \eta\cos\theta - \zeta\sin\theta \\
z_1 &= w + \eta\sin\theta + \zeta\cos\theta
\end{aligned} \tag{22}$$

After integration over the blade cross section, the variation of kinetic energy becomes:

$$\delta T = \int_0^R \left(\bar{Z}_u \delta u + \bar{Z}_v \delta v + \bar{Z}_w \delta w + \bar{Z}_{v'} \delta v' + \bar{Z}_{w'} \delta w'\right) dx \tag{23}$$

where,

$$\begin{aligned}
\bar{Z}_u = m\big[& \ddot{u} - \dot{\alpha}_s \dot{w}\sin\Omega t + 2\Omega\dot{v} + \ddot{X}\cos\Omega t - \ddot{Y}\sin\Omega t - \Omega\dot{\alpha}_c\dot{w}\sin\Omega t \\
& + 2\Omega\dot{\alpha}_s\beta_{pc}x\cos\Omega t - 2\Omega\dot{\alpha}_c\beta_{pc}x\sin\Omega t + \Omega\dot{\alpha}_s\dot{w}\cos\Omega t
\end{aligned}$$

$$+\Omega^2 x - \dot{\alpha}_s \dot{w} \sin\Omega t + \dot{\alpha}_s{}^2 x + 2\dot{\alpha}_s \dot{\alpha}_c x \cos\Omega t \sin\Omega t$$

$$- \dot{\alpha}_c \dot{w} \cos\Omega t - \ddot{Z}\beta_{pc} + \dot{Z}\dot{\alpha}_s \sin\Omega t + \dot{Z}\dot{\alpha}_c \cos\Omega t]$$

$$+ m(w + e\sin\theta)[-\ddot{\alpha}_s \sin\Omega t - \Omega\dot{\alpha}_s \cos\Omega t - \Omega^2 \beta_{pc}] \tag{24}$$

$$\bar{Z}_v = m[-\ddot{v} + 2\dot{\alpha}_c \dot{w} \sin\Omega t + \Omega\beta_{pc}\dot{w} - \ddot{\alpha}_s \beta_{pc} x \cos\Omega t + \dot{\alpha}_s \Omega \beta_{pc} x \sin\Omega t$$

$$+ \ddot{\alpha}_c \beta_{pc} x \sin\Omega t + \dot{\alpha}_c \beta_{pc} x \cos\Omega t - \ddot{X}\sin\Omega t - \ddot{Y}\cos\Omega t - 2\dot{\alpha}_s \dot{w}\cos\Omega t$$

$$+ \dot{\alpha}_s{}^2 x \sin\Omega t \cos\Omega t - \dot{\alpha}_c \dot{alpha}_s(\cos^2\Omega t - \sin^2\Omega t) - \dot{\alpha}_c{}^2 x \sin\Omega t \cos\Omega t$$

$$+ \Omega\beta_{pc}\dot{w} - \Omega\dot{\alpha}_s \beta_{pc} x \sin\Omega t - \Omega\dot{\alpha}_c \beta_{pc} x \cos\Omega t + \dot{Z}\dot{\alpha}_s \cos\Omega t - \dot{Z}\dot{\alpha}_c \sin\Omega t]$$

$$+ m\Omega^2(v + e\cos\theta) - 2\Omega m\dot{u} + 2me\Omega(\dot{v}'\cos\theta + \dot{w}'\sin\theta)$$

$$+ m(w + e\sin\theta)[-\ddot{\alpha}_s \cos\Omega t + \ddot{\alpha}_c \sin\Omega t] \tag{25}$$

$$\bar{Z}_w = m[-\ddot{w} + 2\dot{\alpha}_s \dot{v}\cos\Omega t - 2\dot{\alpha}_c \dot{v}\sin\Omega t - 2\Omega\beta_{pc}\dot{v} + \ddot{\alpha}_s x \sin\Omega t + 2\dot{\alpha}_s \Omega x \cos\Omega t$$

$$+ \ddot{\alpha}_c x \cos\Omega t - 2\Omega\dot{\alpha}_c x \sin\Omega t + \dot{Y}\dot{\alpha}_s + \ddot{X}\beta_{pc}\cos\Omega t - \ddot{Y}\beta_{pc}\sin\Omega t$$

$$- \ddot{Z} - \ddot{X}\dot{alpha}_c - \Omega^2 \beta_{pc} x - 2\Omega\ddot{X}\beta_{pc}\sin\Omega t - 2\Omega\dot{Y}\beta_{pc}\cos\Omega t$$

$$+ m(v + e\cos\theta)[\ddot{\alpha}_s \cos\Omega t - 2\Omega\dot{\alpha}_s \sin\Omega t - \ddot{\alpha}_c \sin\Omega t - 2\Omega\dot{\alpha}_c \cos\Omega t] \tag{26}$$

$$\bar{Z}_{v'} = me\cos\theta[\ddot{Y}\sin\Omega t - \ddot{X}\cos\Omega t - \Omega^2 x - 2\Omega\dot{v}] \tag{27}$$

$$\bar{Z}_{w'} = me\sin\theta[\ddot{Y}\sin\Omega t - \ddot{X}\cos\Omega t - \Omega^2 x - 2\Omega\dot{v}] \tag{28}$$

in which,

$$m = \iint_A \rho\, d\eta\, d\zeta \tag{29}$$

$$me\cos\theta = \iint_A \rho(y_1 - v)\, d\eta\, d\zeta \tag{30}$$

$$me\sin\theta = \iint_A \rho(z_1 - w)\, d\eta\, d\zeta \tag{31}$$

Integration by parts again gives

$$\int_0^R \bar{Z}_{v'}\delta v'\, dx = \int_0^R \bar{Z}_{v'}\delta(\delta v)$$

$$= \bar{Z}_{v'}\delta v\Big|_0^R - \int_0^R \bar{Z}'_{v'}\delta v\, dx \tag{32}$$

and

$$\int_0^R \bar{Z}_{w'}\delta w'\,dx = \bar{Z}_{w'}\delta w\Big|_0^R - \int_0^R \bar{Z}'_{w'}\delta w\,dx \tag{33}$$

Finally, the variation of kinetic energy can be expressed as

$$\delta T = \int_0^R [\bar{Z}_u\delta u + (bar\,Z_v - \bar{Z}'_{v'})\delta v + (\bar{Z}_w - \bar{Z}'_{w'})\delta w]\,dx + b(T) \tag{34}$$

where the boundary condition is

$$b(T) = \bar{Z}_{v'}\delta v\Big|_0^R + \bar{Z}_{w'}\delta w\Big|_0^R \tag{35}$$

2.2.3 VIRTUAL WORK

The final step necessary to compute the equations is the computation of virtual work. The virtual work, δW, is mainly due to the nonconservative external forces which come from the theory of aerodynamics. The virtual work can be expressed as

$$\delta W = \int_0^R (L_u\delta u + L_v\delta v + L_w\delta w)\,dx \tag{36}$$

where L_u, L_v, L_w are forces acting along x,y,z directions.

2.2.4 GENERAL EQUATIONS

The functional of Hamilton's Law has three variables u, v, and w. This will lead to three Euler-Lagrange equations which are the required equations of motion. Later, u can be eliminated which will reduce the system of equations to only two. The basic equations come from Equation (5). If we ignore the trailing terms that are cancelled by

$$\delta q_i\Big|_{t_1}^{t_2} = 0 \tag{37}$$

then we have

$$\int_{t_1}^{t_2} (\delta U - \delta T - \delta W)\,dt = 0 \tag{38}$$

Therefore,

$$\delta U - \delta T - \delta W = 0 \tag{39}$$

with trailing terms dropped. In the case considered, we have

$$\int_0^R \left\{(\bar{Y}_u - \bar{Z}_u - L_u)\delta u + [\bar{Y}_v - (\bar{Z}_v - \bar{Z}'_{v'}) - L_v]\delta v + [\bar{Y}_w - (\bar{Z}_w - \bar{Z}'_{w'}) - L_w]\delta w\right\} dx + b(U) - b(T) = 0 \quad (40)$$

From the principles of variational calculus, the equations of motion and boundary conditions can be obtained from Equation (40).

δU equations:

$$\bar{Y}_u - \bar{Z}_u = L_u \quad (41)$$

δV equations:

$$\bar{Y}_v - (\bar{Z}_v - \bar{Z}'_{v'}) = L_v \quad (42)$$

δW equations:

$$\bar{Y}_w - (\bar{Z}_w - \bar{Z}'_{w'}) = L_w \quad (43)$$

and boundary condition:

$$b(U) - b(T) = 0 \quad (44)$$

2.2.5 BASIC EQUATIONS

With the help of the ordering scheme in Reference 12, but keeping flapping equations o(ϵ), lead-lag equation o(ϵ^2), and eliminating axial deflection from δU equation, we obtain flapping and lead-lag equations in nondimensional form as follows:

Flapping equation:

$$\begin{aligned}&\Lambda_1^2\bar{w}^{++++} + (\Lambda_2^2 - \Lambda_1^2)R_e\theta\bar{v}^{++++} - \tau^+\bar{w}^+ - \tau\bar{w}^{++} + \bar{w}^{**} - 2\bar{v}^{*+} - \alpha_s^{**}\bar{x}\sin\psi \\ &- 2\alpha_s^*\bar{x}\cos\psi - \alpha_c^{**}\cos\psi + 2\alpha_c^*\bar{x}\sin\psi + \bar{X}^{**}\beta_{pc}\cos\psi - \bar{Y}^{**}\beta_{pc}\sin\psi - \bar{Z}^{**} + \beta_{pc}\bar{x} \\ &= L_w \end{aligned} \quad (45)$$

Lead-lag equation

$$\begin{aligned}&\Lambda_2^2\bar{v}^{++++} + (\Lambda_2^2 - \Lambda_1^2)R_e\theta bar{w}^{++++} - \tau^+\bar{v}^+ - \tau\bar{v}^{++} - \bar{v} - 2\int_0^{\bar{x}} \bar{w}^+\bar{w}^{*+}\,d\bar{x} \\ &+ \bar{v}^{**} - \alpha_c^{**}\beta_{pc}\sin\psi - \alpha_c^{**}\bar{x}\bar{w}\sin\psi + \alpha_c^{*2}\bar{x}\sin\psi\cos\psi - 2\alpha_c^*\bar{w}^*\sin\psi + 2\bar{Z}^*\alpha_c^*\sin\psi \\ &+ \alpha_s^{**}\bar{x}\beta_{pc}\cos\psi + \alpha_s^{**}\bar{w}\cos\psi - \alpha_s^{*2}\bar{x}\sin\psi\cos\psi + 2\alpha_s^*\bar{w}^*\cos\psi - 2\bar{Z}^*\alpha_s^*\cos\psi \\ &+ \alpha_s^*\alpha_c^*\bar{x}(\cos^2\psi - \sin^2\psi) - 2\beta_{pc}\bar{w}^* + \bar{X}^{**}\sin\psi + \bar{Y}^{**}\cos\psi \\ &= L_v \end{aligned} \quad (46)$$

2.3 AERODYNAMIC FORCES

In deriving the aerodynamic forces, the following assumptions are made

1. Linear, quasi-steady aerodynamics
2. Blade stall, compressibility and reversed flow are neglected.
3. Uniform induced flow

Figure 4 shows the free airflow passing through the helicopter. And, Figure 5 shows the blade element geometry. The total velocity with respect to air mass in forward flight will be

$$\vec{U}_T = \vec{U}_{air} - \vec{U} \tag{47}$$

where,

$$\vec{U}_{air} = v_\infty \vec{I} - (V + v)\vec{K} \tag{48}$$

and $\vec{U}$ is the velocity obtained in Equation (21). Using the transformation $[T_R]$ and $[T_d]$ in Equations (2) and (4), We obtain the required velocity components in deformed coordinate with dimensionless form as follows:

$$\begin{aligned}
\bar{U}_{y'} = & -\theta\bar{w}^+\mu\cos\psi - \bar{v}^+\mu\cos\psi - \mu\sin\psi - \bar{v}^* - barx - \bar{u} \\
& - \alpha_s^*\bar{w}\cos\psi + \alpha_c^*\bar{w}\sin\psi + \bar{w}\beta_{pc} - \alpha_s^*\bar{x}\beta_{pc}\cos\psi \\
& + \alpha_c^*\beta_{pc}\bar{x}\sin\psi - \bar{X}^*\sin\psi - \bar{Y}^*\cos\psi - \theta\lambda \\
& - \theta\beta_{pc}\mu\cos\psi + \theta\alpha_c\mu - \theta\bar{w}^* + \theta\alpha_s{}^*\bar{x}\sin\psi \\
& + \theta\alpha_c^*\bar{x}\cos\psi + \theta\bar{Z}^* - \lambda\alpha_c\sin\psi + \lambda\alpha_s\cos\psi
\end{aligned} \tag{49}$$

$$\begin{aligned}
\bar{U}_{z'} = & -\bar{w}^+\mu\cos\psi - \bar{w}^+\bar{X}^*\cos\psi + \bar{w}^+\bar{Y}^*\sin\psi - \lambda \\
& + \theta\mu\sin\psi + \theta\bar{x} + \bar{X}^*\theta\sin\psi + \bar{Y}^*\theta\cos\psi \\
& - \mu\beta_{pc}\cos\psi + \mu\alpha_c - \bar{w}^* + \alpha_s^*\bar{x}\sin\psi \\
& + \alpha_c^*\bar{x}\cos\psi - \bar{X}^*\beta_{pc}\cos\psi + \bar{Y}^*\beta_{pc}\sin\psi + \bar{Z}^*
\end{aligned} \tag{50}$$

In the deformed coordinate, the dimensionless aerodynamic forces can be expressed as

$$\bar{F}_{x'} = 0 \tag{51}$$

$$\bar{F}_{y'} = \frac{\gamma}{6}[\bar{U}_{z'}^2 - \frac{C_{d_o}}{a}\bar{U}_{y'}^2] \tag{52}$$

$$\bar{F}_{x'} = -\frac{\gamma}{6}[\bar{U}_{z'}\bar{U}_{y'}] \tag{53}$$

Then, we can transfer the aerodynamic forces above to undeformed rotating coordinates, which are

$$\begin{pmatrix} \bar{F}_x \\ \bar{F}_y \\ \bar{F}_z \end{pmatrix} = [T_d]^T \begin{pmatrix} \bar{F}_{x'} \\ \bar{F}_{y'} \\ \bar{F}_{z'} \end{pmatrix} \tag{54}$$

Then, the external aerodynamic forces are

$$\bar{L}_w = \bar{F}_z \tag{55}$$

$$\bar{L}_v = \bar{F}_y \tag{56}$$

2.4 FINAL EQUATIONS

Combining Equation (45), (46) and Equation (55), (56), we obtain the complete flapping and lead-lag equations as follows:

FLAPPING EQUATION

$$\begin{aligned}
&\Lambda_1^2 \bar{w}^{++++} + (\Lambda_2^2 - \Lambda_1^2) R_e \theta \bar{v}^{++++} - \tau^+ \bar{w}^+ - \tau \bar{w}^{++} + \bar{w}^{**} - 2\bar{v}^{*+} - \alpha_s^{**} \bar{x} \sin\psi \\
&- 2\alpha_s^* \bar{x} \cos\psi - \alpha_c^{**} \bar{x} \cos\psi + 2\alpha_c^* \bar{x} \sin\psi + \bar{X}^{**} \beta_{pc} \cos\psi - \bar{Y}^{**} \beta_{pc} \sin\psi - \bar{Z}^{**} + \beta_{pc} \bar{x} \\
&= \frac{\gamma}{6} \Big\{ \theta\mu^2 \sin^2\psi + \theta \bar{x}^2 + 2\theta\mu \bar{x} \sin\psi + \mu^2 \alpha_c \sin\psi + \mu \alpha_s^* \bar{x} \sin^2\psi + \mu \alpha_c^* \bar{x} \sin\psi \cos\psi \\
&\quad + \mu \bar{Z}^* \sin\psi + \mu \alpha_c \bar{x} - \bar{w}^* \bar{x} + \alpha_s^* \bar{x}^2 \sin\psi + \alpha_c^* \bar{x}^2 \cos\psi - \bar{w}^+ \mu^2 \sin\psi \cos\psi + \bar{z}^* \bar{x} \\
&\quad - \mu\lambda \sin\psi - \lambda \bar{x} - \mu^2 \beta_{pc} \sin\psi \cos\psi - \mu \bar{w}^* \sin\psi - \bar{w}^+ \bar{x} \cos\psi - \mu \beta_{pc} \bar{x} \cos\psi \Big\}
\end{aligned} \tag{57}$$

LEAD-LAG EQUATION

$$\begin{aligned}
&\Lambda_2^2 \bar{v}^{++++} + (\Lambda_2^2 - \Lambda_1^2) R_e \theta \bar{w}^{++++} - \tau^+ \bar{v}^+ - \tau \bar{v}^{++} - \bar{v} \\
&- 2 \int_0^{\bar{x}} \bar{w}^+ \bar{w}^{*+} \, d\bar{x} + \bar{v}^{**} - \alpha_c^{**} \beta_{pc} \sin\psi - \alpha_c^{**} \bar{x} \bar{w} \sin\psi \\
&+ \alpha_c^{*2} \bar{x} \sin\psi \cos\psi - 2\alpha_c^* \bar{w}^* \sin\psi + 2\bar{Z}^* \alpha_c^* \sin\psi + \alpha_s^{**} \bar{x} \beta_{pc} \cos\psi \\
&+ \alpha_s^{**} \bar{w} \cos\psi - \alpha_s^{*2} \bar{x} \sin\psi \cos\psi + 2\alpha_s^* \bar{w}^* \cos\psi - 2\bar{Z}^* \alpha_s^* \cos\psi \\
&+ \alpha_s^* \alpha_c^* \bar{x} (\cos^2\psi - \sin^2\psi) - 2\beta_{pc} \bar{w}^* + \bar{X}^{**} \sin\psi + \bar{Y}^{**} \cos\psi
\end{aligned}$$

$$= \frac{\gamma}{6}\Big\{ \bar{w}^{+2}\mu^2\cos^2\psi + \lambda^2 + \mu^2\beta_{pc}{}^2\cos^2\psi + \mu^2\alpha_c^2$$

$$+ \bar{w}^{*2} + \bar{Z}^{*2} + \alpha_s^{*2}\bar{x}^2\sin^2\psi + \alpha_c^{*2}\bar{x}^2\cos^2\psi$$

$$- \bar{w}^{+}\theta\mu^2\cos\psi\sin\psi - \bar{w}^{+}\theta\mu\bar{x}\cos\psi + 2\lambda\bar{w}^{+}\mu\cos\psi$$

$$+ 2\bar{w}^{+}\mu^2\beta_{pc}\cos\psi - 2\bar{w}^{+}\mu^2\alpha_c\cos\psi + 2\bar{w}^{+}\bar{w}^{*}\mu\cos\psi$$

$$- 2\bar{w}^{+}\alpha_s^{*}\mu\bar{x}\cos\psi\sin\psi - 2\bar{w}^{+}\alpha_c^{*}\mu\bar{x}\cos^2\psi - 2\bar{w}^{+}\bar{Z}^{*}\mu\cos\psi$$

$$- \theta\lambda\mu\sin\psi - \theta\mu^2\beta_{pc}\sin\psi\cos\psi + \theta\mu^2\alpha_c\sin\psi$$

$$- \bar{w}^{*}\theta\mu\sin\psi + \theta\alpha_s^{*}\mu\bar{x}\sin^2\psi + \theta\alpha_c^{*}\mu\bar{x}\sin\psi\cos\psi$$

$$+ \theta\bar{Z}^{*}\mu\sin\psi - \theta\lambda\bar{x} - \theta\mu\beta_{pc}\bar{x}\cos\psi + \theta\mu\alpha_c\bar{x} - \theta\bar{w}^{*}\bar{x}$$

$$+ \theta\bar{Z}^{*}\bar{x} + \theta\alpha_s^{*}\bar{x}^2\sin\psi + \theta\alpha_c^{*}\bar{x}^2\cos\psi + 2\lambda\mu\beta_{pc}\cos\psi$$

$$- 2\lambda\mu\alpha_c + 2\lambda\bar{w}^{*} - 2\lambda\alpha_s^{*}\bar{x}\sin\psi - 2\lambda\alpha_c^{*}\bar{x}\cos\psi - 2\lambda\bar{Z}^{*}$$

$$- 2\mu^2\beta_{pc}\alpha_c\cos\psi + 2\bar{w}^{*}\mu\beta_{pc}\cos\psi - 2\alpha_s^{*}\beta_{pc}\mu\bar{x}\sin\psi\cos\psi$$

$$- 2\alpha_c^{*}\beta_{pc}\mu\bar{x}\cos^2\psi - 2\bar{z}^{*}\mu\beta_{pc}\cos\psi - 2\bar{w}^{*}\mu\alpha_c + 2\alpha_c\alpha_s^{*}\bar{x}\sin\psi$$

$$+ 2\alpha_c^{*}\alpha_s\mu\bar{x}\cos\psi + 2\bar{Z}^{*}\mu\alpha_c - 2\bar{w}^{*}\alpha_s^{*}\bar{x}\sin\psi - 2\bar{w}^{*}\alpha_c^{*}\bar{x}\cos\psi$$

$$- 2\bar{Z}^{*}\bar{w}^{*} + 2\alpha_s^{*}\alpha_c^{*}\bar{x}^2\sin\psi\cos\psi + 2\bar{Z}^{*}\alpha_s^{*}\bar{x}\sin\psi + 2\bar{Z}^{*}\alpha_c^{*}\bar{x}\cos\psi$$

$$- \frac{C_{d_s}}{a}[\bar{x}^2 + \mu^2\sin^2 + 2\mu\bar{x}\sin\psi + 2\mu\bar{x}^{*}\sin^2\psi$$

$$+ 2\bar{x}\bar{X}^{*}\sin\psi + 2\mu\bar{Y}^{*}\sin\psi\cos\psi + 2\bar{x}\bar{Y}^{*}\cos\psi]\Big\} \qquad (58)$$

THE BOUNDARY CONDITION

$$V_{x'}\delta u\Big|_0^R + \{V_{x'}v' - [M_{z'} + My'R_e\theta]'\}\delta v\Big|_0^R + [M_{z'} + M_{y'}R_e\theta]\delta v'\Big|_0^R$$

$$+ \{V_{x'}w - [M_{z'}R_e\theta - M_{y'}]'\}\delta w\Big|_0^R + [M_{z'}R_e\theta - M_{y'}]\delta w'\Big|_0^R$$

$$- me\cos\theta[\ddot{\bar{Y}}\sin\Omega t - \ddot{\bar{X}}\cos\Omega t - \Omega^2 x - 2\Omega\dot{v}]\delta v\Big|_0^R$$

$$- me\sin\theta[\ddot{\bar{Y}}\sin\Omega t - \ddot{\bar{X}}\cos\Omega t - \Omega^2 x - 2\Omega\dot{v}]\delta w\Big|_0^R$$

$$= 0 \qquad (59)$$

It may be noted that for a rigid blade (for which $w = \beta x$ and $v = \zeta x$, the flapping Equation (57) and the lead-lag Equation (58) reduce to those of Reference 13 with the exception of nonlinear higher-order terms.

3. HUB LOAD EQUATIONS

The hub loads including the shears and moments, in both rotating and fixed coordinate systems, are shown in Figure 6. C_x, C_y, and C_z are radial, lead-lag, and flap shear components; and C_u, C_v, C_w are torsional, in-plane and out-of-plane moment components in the rotating coordinate system. C_Z, C_X, and C_Y are the vertical thrust, forward drag, and side force components in the fixed coordinate system. The loads with respect to the rotating system are called rotating loads and those corresponding to the fixed system are called nonrotating loads. They are derived in detail below.

3.1 ROTATING LOADS

The expressions for the root shear and moment components in the rotating coordinate system are formed by spanwise integration of the aerodynamic and inertia loads as follows:

$$C_x = \frac{3}{\gamma}\int_0^1 \bar{F}_x \, d\bar{X} - \frac{3}{\gamma}\int_0^1 \bar{a}_{ox}\, d\bar{x} \tag{60}$$

$$C_y = \frac{3}{\gamma}\int_0^1 \bar{F}_y \, d\bar{x} - \frac{3}{\gamma}\int_0^1 \bar{a}_{oy} d\bar{x} \tag{61}$$

$$C_z = \frac{3}{\gamma}\int_0^1 \bar{F}_z \, d\bar{x} - \frac{3}{\gamma}\int_0^1 \bar{a}_{oz}\, d\bar{x} \tag{62}$$

$$C_w = \frac{3}{\gamma}\int_0^1 \bar{F}_z \bar{x}\, d\bar{x} + \frac{3}{\gamma}\int_0^1 \bar{a}_{oz}\bar{x}\, d\bar{x} + \frac{3}{\gamma}\int_0^1 \bar{F}_x \bar{w}\, d\bar{x} - \frac{3}{\gamma}\int_0^1 \bar{a}_{ox}\bar{w}\, d\bar{x} \tag{63}$$

$$C_u \approx 0 \tag{64}$$

$$C_v \approx 0 \tag{65}$$

where the aerodynamic forces are obtained in Equation (54), and the dimentionless accelerations are as follows:

$$\begin{aligned}\bar{a}_{ox} = {} & \bar{u}^{**} - 2\alpha_s^*\bar{w}^* \sin\psi + 2\alpha_c^*\bar{w}^*\cos\psi - 2\bar{v}^* - \alpha_s^{*2}\bar{x}\sin^2\psi \\ & - \alpha_c^{*2}\bar{x}\cos\psi + 2\alpha_s^*\alpha_c^*\bar{x}\sin\psi\cos\psi - 2\alpha_s^*\beta_{pc}\bar{x}\cos\psi \\ & + 2\alpha_c^*\beta_{pc}\bar{x}\sin\psi - \bar{x} - \bar{u} + \beta_{pc}\bar{w} - \alpha_s^{**}\bar{w}\cos\psi\end{aligned}$$

$$+ \alpha_c^{**}\bar{w}\cos\psi + \bar{X}^{**}\cos\psi + \bar{Y}^{**}\sin\psi \tag{66}$$

$$\begin{aligned}\bar{a}_{oy} = {} & \bar{v}^{**} + 2\bar{u}^{*} - 2\alpha_s^{*}\bar{w}^{*}\cos\psi - 2\alpha_c^{*}\bar{w}^{*}\sin\psi - 2\beta_{pc}\bar{w}^{*} \\ & - \alpha_s^{*}\bar{w}\sin\psi + \alpha_c^{*}\bar{w}\cos\psi - \bar{v} - \alpha_s^{*2}\bar{x}\sin\psi\cos\psi \\ & - \alpha_c^{*}\alpha_s^{*}\bar{x}\sin^2\psi + \alpha_s^{*}\alpha_c^{*}\bar{x}\cos^2\psi + \alpha_s^{*}\beta_{pc}\bar{x}\sin\psi \\ & + \alpha_c^{*2}\bar{x}\sin\psi\cos\psi + \alpha_s^{**}\beta_{pc}\bar{x}\cos\psi - \alpha_c^{**}\beta_{pc}\bar{x}\sin\psi \\ & - \alpha_s^{**}\bar{w}\cos\psi + \alpha_s^{*}\bar{w}\sin\psi - \alpha_c^{**}\bar{w}\sin\psi - \alpha_c^{*}\bar{w}\cos\psi \\ & - \bar{X}^{**}\sin\psi + \bar{Y}^{**}\cos\psi \end{aligned} \tag{67}$$

$$\begin{aligned}\bar{a}_{oz} = {} & \bar{w}^{**} + 2\alpha_s^{*}\bar{x}\cos\psi + 2\alpha_c^{*}\bar{x}\sin\psi + \beta_{pc}\bar{x} \\ & + \alpha_s^{**}\bar{x}\sin\psi - \alpha_c^{**}\bar{x}\cos\psi + \bar{Z}^{**}\end{aligned} \tag{68}$$

3.2 NON-ROTATING LOADS

The shear and moment components in the fixed coordinate system are formed from the load components in the rotating coordinate system. They can be simply expressed as

$$C_X = C_x\cos\psi - C_y\sin\psi \tag{69}$$

$$C_Y = C_x\sin\psi + C_y\cos\psi \tag{70}$$

$$C_Z = C_z \tag{71}$$

$$C_L = -C_w\sin\psi \tag{72}$$

$$C_M = C_w\cos\psi \tag{73}$$

They can be put into matrix form as done in Reference 13. It is:

$$\begin{pmatrix} C_M \\ C_L \\ C_X \\ C_Y \\ C_Z \end{pmatrix} = \left[\Phi(\psi)\right] \begin{pmatrix} \theta_o \\ \theta_s \\ \theta_c \\ \lambda \\ \beta \\ \beta_{pc} \\ \frac{C_{d_o}}{a} \\ \bar{\alpha}_c \end{pmatrix} + \left[A(\psi)\right] \begin{pmatrix} \alpha_c \\ \alpha_s \\ \bar{X} \\ \bar{Y} \\ \bar{Z} \end{pmatrix} + \left[B(\psi)\right] \begin{pmatrix} \alpha_c^{*} \\ \alpha_s^{*} \\ \bar{X}^{*} \\ \bar{Y}^{*} \\ \bar{Z}^{*} \end{pmatrix} + \left[D(\psi)\right] \begin{pmatrix} \alpha_c^{**} \\ \alpha_s^{**} \\ \bar{X}^{**} \\ \bar{Y}^{**} \\ \bar{Z}^{**} \end{pmatrix}$$

$$+ \left\{\vec{F}\left(\bar{w}, \bar{w}^{+}, \bar{w}^{*}, \bar{w}^{*+}, \bar{w}^{**}, \bar{w}^{++}, \bar{w}^{*++}, \bar{v}, \bar{v}^{*}, \bar{v}^{**}\right)\right\} \tag{74}$$

Again, Equation (74) matches the similar equation in Reference 13 very well, except for the additional nonlinear terms.

4.FUSELAGE EQUATIONS

In this research, the same model as in Reference 13 is used for fuselage, except that X and Y axes have opposite positive directions. Figure 7 shows the fuselage model in the longitudinal and pitch directions.

This model includes 9 degrees of freedom. These are:

1) vertical rigid-body;

2) rigid-body pitch;

3) rigid-body roll;

4) rigid lateral;

5) rigid longitudinal;

6) elastic vertical;

7) elastic lateral;

8) elastic pylon in pitch;

9) elastic pylon in roll.

The model also includes vertical offsets between the fuselage center of mass, the pylon focus, the pylon center of mass, and the rotor center.

The fuselage is modeled as a uniform beam with a lumped mass M_c added at the center. The mass of the pylon is separated from the fuselage, which is connected to the fuselage through pitch and roll torsional springs. The fuselage equations of motion are the same as those in Reference 13, except that the X and Y axes are reversed.

5. SOLUTION METHOD

5.1 GALERKIN METHOD

The flap-lag equations of motion, Equation (57) and (58), are nonlinear, variable coefficient, integro-partial differential equations. First, these equations can be reduced to nonlinear ordinary differential equations in terms of the generalized coordinates by use of the modal form $w = \phi_j q_j$ and $v = \phi_l p_l$, and the Galerkin method as below:

$$\begin{pmatrix} M_{ij} & M_{il} \\ M_{kj} & M_{kl} \end{pmatrix} \begin{pmatrix} \ddot{q}_j \\ \ddot{p}_l \end{pmatrix} + \begin{pmatrix} C_{ij} & C_{il} \\ C_{kj} & C_{kl} \end{pmatrix} \begin{pmatrix} \dot{q}_j \\ \dot{p}_l \end{pmatrix} + \begin{pmatrix} K_{ij} & K_{il} \\ K_{kj} & K_{kl} \end{pmatrix} \begin{pmatrix} q_j \\ p_l \end{pmatrix} = \begin{pmatrix} F_i \\ F_k \end{pmatrix} \tag{75}$$

Where M, C, and K are functions of q, p, and their derivatives and where

$i, j = 1, \ldots$ m number of flap degrees of freedom;

and

$k, l = 1, \ldots$ n number of lead-lag degrees of freedom.

5.2 HARMONIC BALANCE

As done in Reference 13, fuselage equations can be transformed into a set of linear, algebraic equations by a harmonic balance which is formulated in matrix notation for a linear, multi-degree-of-freedom system in Reference 7. In our case, the equations are nonlinear. Therefore, an important conclusion obtained in Reference 13 can be used. As mentioned before, it says that the addition of inplane degrees of freedom does not significantly affect the plunge vibrations for the cases considered, and these cases are for resonable configurations. Figure 8 and 9 shows the comparison of plunge vibration with or without inplane degrees of freedom.

Therefore, we can first solve the plunge-pitch-roll problem with inplane parameters eliminated. To do this, the flapping equation is expressed as below:

$$\begin{pmatrix} M_{11} & \cdots & M_{1i} \\ \vdots & \ddots & \vdots \\ M_{i1} & \cdots & M_{ij} \end{pmatrix} \begin{pmatrix} q_1^{**} \\ \vdots \\ q_j^{**} \end{pmatrix} + \begin{pmatrix} C_{11} & \cdots & C_{1i} \\ \vdots & \ddots & \vdots \\ C_{i1} & \cdots & C_{ij} \end{pmatrix} \begin{pmatrix} q_1^{*} \\ \vdots \\ q_j^{*} \end{pmatrix} + \begin{pmatrix} K_{11} & \cdots & K_{1i} \\ \vdots & \ddots & \vdots \\ K_{i1} & \cdots & K_{ij} \end{pmatrix} \begin{pmatrix} q_1 \\ \vdots \\ q_j \end{pmatrix}$$

$$= \left[\bar{Q}(\psi)\right] \begin{pmatrix} \theta_o \\ \theta_s \\ \theta_c \\ \lambda \\ \bar{\beta} \\ \beta_{pc} \\ \frac{C_{d_0}}{a} \\ \bar{\alpha}_c \end{pmatrix} + \left[\bar{A}(\psi)\right] \begin{pmatrix} \alpha_c \\ \alpha_s \\ \bar{Z} \end{pmatrix} + \left[\bar{B}(\psi)\right] \begin{pmatrix} \alpha_c^* \\ \alpha_s^* \\ \bar{Z}^* \end{pmatrix} + \left[\bar{D}(\psi)\right] \begin{pmatrix} \alpha_c^{**} \\ \alpha_s^{**} \\ \bar{Z}^{**} \end{pmatrix} \tag{76}$$

and the load equation (74) becomes

$$\begin{pmatrix} \tilde{C}_M \\ \tilde{C}_L \\ \tilde{C}_Z \end{pmatrix} = \left[\tilde{\Phi}(\psi)\right] \begin{pmatrix} \theta_o \\ \theta_s \\ \theta_c \\ \lambda \\ \bar{\beta} \\ \beta_{pc} \\ \frac{C_{d_0}}{a} \\ \bar{\alpha}_c \end{pmatrix} + \left[\tilde{A}(\psi)\right] \begin{pmatrix} \alpha_c \\ \alpha_s \\ \bar{Z} \end{pmatrix} + \left[\tilde{B}(\psi)\right] \begin{pmatrix} \alpha_c^* \\ \alpha_s^* \\ \bar{Z}^* \end{pmatrix} + \left[\tilde{D}(\psi)\right] \begin{pmatrix} \alpha_c^{**} \\ \alpha_s^{**} \\ \bar{Z}^{**} \end{pmatrix}$$

$$+ \left[\tilde{E}(\psi)\right] \begin{pmatrix} q_1 \\ \vdots \\ q_j \end{pmatrix} + \left[\tilde{F}(\psi)\right] \begin{pmatrix} q_1^* \\ \vdots \\ q_j^* \end{pmatrix} + \left[\tilde{G}(\psi)\right] \begin{pmatrix} q_1^{**} \\ \vdots \\ q_j^{**} \end{pmatrix} \tag{77}$$

For the fuselage equations, we have eliminated $\bar{X}$, $\bar{Y}$, and $\bar{Y}_F$, and their derivatives. Now, these equations are linear ordinary differential equations with peoriodic coefficients. They are easily solved by harmonic balance technique and impedance matching. The control vector components θ_o, θ_s, θ_c, λ, $\bar{\beta}$, β_{pc}, $\frac{C_{d_0}}{a}$, and $\bar{\alpha}_c$ can be

obtained from a trim procedure.

For the next step, we go to Equation (75) with $q_1 \ldots q_j$ and α_c, α_s, and $\bar{Z}$ and their derivitives as knowns. The flap-lag Equations (75) can be further expressed as

$$\begin{pmatrix} M_{ij} & M_{il} \\ M_{kj} & M_{kl} \end{pmatrix} \begin{pmatrix} \ddot{q}_j \\ \ddot{p}_l \end{pmatrix} + \begin{pmatrix} C_{ij} & C_{il} \\ C_{kj} & C_{kl} \end{pmatrix} \begin{pmatrix} \dot{q}_j \\ \dot{p}_l \end{pmatrix} + \begin{pmatrix} K_{ij} & K_{il} \\ K_{kj} & K_{kl} \end{pmatrix} \begin{pmatrix} q_j \\ p_l \end{pmatrix}$$

$$= \left[\hat{Q}(\psi)\right] \begin{pmatrix} \theta_o \\ \theta_s \\ \theta_c \\ \lambda \\ \bar{\beta} \\ \beta_{pc} \\ \frac{C_{d_o}}{a} \\ \bar{\alpha}_c \end{pmatrix} + \left[\hat{A}(\psi)\right] \begin{pmatrix} \alpha_c \\ \alpha_s \\ \bar{X} \\ \bar{Y} \\ \bar{Z} \end{pmatrix} + \left[\hat{B}(\psi)\right] \begin{pmatrix} \alpha_c^* \\ \alpha_s^* \\ \bar{X}^* \\ \bar{Y}^* \\ \bar{Z}^* \end{pmatrix} + \left[\hat{D}(\psi)\right] \begin{pmatrix} \alpha_c^{**} \\ \alpha_s^{**} \\ \bar{X}^{**} \\ \bar{Y}^{**} \\ \bar{Z}^{**} \end{pmatrix} \tag{78}$$

and the load Equations (74) can be further expressed as

$$\begin{pmatrix} C_M \\ C_L \\ C_X \\ C_Y \\ C_Z \end{pmatrix} = \left[\Phi(\psi)\right] \begin{pmatrix} \theta_o \\ \theta_s \\ \theta_c \\ \lambda \\ \bar{\beta} \\ \beta_{pc} \\ \frac{C_{d_o}}{a} \\ \bar{\alpha}_c \end{pmatrix} + \left[A(\psi)\right] \begin{pmatrix} \alpha_c \\ \alpha_s \\ \bar{X} \\ \bar{Y} \\ \bar{Z} \end{pmatrix} + \left[B(\psi)\right] \begin{pmatrix} \alpha_c^* \\ \alpha_s^* \\ \bar{X}^* \\ \bar{Y}^* \\ \bar{Z}^* \end{pmatrix} + \left[D(\psi)\right] \begin{pmatrix} \alpha_c^{**} \\ \alpha_s^{**} \\ \bar{X}^{**} \\ \bar{Y}^{**} \\ \bar{Z}^{**} \end{pmatrix}$$

$$+ \left[E(\psi)\right] \begin{pmatrix} q_j \\ p_l \end{pmatrix} + \left[F(\psi)\right] \begin{pmatrix} q_j^* \\ p_l^* \end{pmatrix} + \left[G(\psi)\right] \begin{pmatrix} q_j^{**} \\ p_l^{**} \end{pmatrix} \tag{79}$$

Then, using flap-lag Equations (78), load Equations (79) and complete fuselage equations, we can finally solve the inplane problem.

6. STATEMENT OF WORK

In helicopter preliminary design stage, it is very important for designers to determine the helicopter structure dynamic parameters. Besides getting a stable system, we hope that helicopter vibrations can be reduced as much as possible in the helicopter flight envelope. Since different combinations of fuselage and rotor parameters can cause quite different vibration levels, we should study them carefully. As is well known, most hingeless rotors can be considered as relatively soft flapwise, except the ABC blade which is stiff flapwise. So, we will choose a soft flapwise rotor system as done in Reference 7 and Reference 13. For the inplane direction, soft inplane and stiff inplane both are common. Therefore, this investigation includes both soft inplane and stiff inplane rotors. In brief, we will change fuselage dynamic parameters (the fuselage first bending natural frequencies in vertical and lateral directions, and the pylon torsional natural frequencies in pitch and roll directions) to match two categories of rotor systems, which are soft flapwise, and both soft inplane and stiff inplane. Also, the fuselage layout will affect the dynamic response significantly, as obtained in Reference 13, the configurations without or with offsets are concerned.

In order to finally solve the Equations (78) and (79) with different dynamic parameters described above, the detailed procedure are as follows. At first, Equations (76) and (77) should be solved in order to obtain the generalized coordinates $q_1 \ldots q_j$ and α_c, α_s, and $\bar{Z}$ and their first and second derivatives as knowns. To do so, three nonrotating out-of-plane bending modes are used, which are the same as those in Reference 8. Also, the baseline parameters are chosen as the same as those in Reference 8 for comparison purposes. The baseline parameters are as follows:

Rotor:	4 blades	$\gamma = 8$	$\mu = .3$
	$p = 1.12$	$\omega_2 = 2.5$	$\omega_3 = 4.5$
Fuselage	$\bar{r}_{gm} = .37$	$\bar{r}_{gL} = .14$	
	$\bar{\omega}_{fv} = 1.53$	$\bar{\omega}_{fm} = 2.58$	$\bar{\omega}_{fL} = 1.18\bar{\omega}_{fm}$
	$\bar{\omega}_{fv}/\bar{\omega}_{cv} = 1.45$	$\bar{\omega}_{fm}/\bar{\omega}_{cm} = 10.0$	$\bar{\omega}_{fL}/\bar{\omega}_{cL} = 4.47$
	$g_v = g_m = g_L = .02$	$\bar{h} = \bar{d}_F = \bar{d}_p = 0.0$	
Trim Condition:	$\lvert\bar{C}_Z\rvert = .0144$	$\lvert\bar{C}_L\rvert = \lvert\bar{C}_M\rvert = 0.0$	
	$\alpha_c = -.0715$	$\lambda = .03187$	

Next, we add three nonrotating blade inplane bending modes. In order to study the dynamic response for both soft-inplane and stiff-inplane rotors, two sets of three nonrotating blade inplane bending modes are used to correspond to different rotors. For the comparison purposes, the first inplane nonrotating bending frequencies corresponding to soft inplane and stiff inplane rotors are the same as those in Reference 13, which are $\omega_\zeta = .7$ and $\omega_\zeta = 1.4$, respectively. Also, we need both lateral damping coeffecients of the fuselage and the steady portion of side forces, which are $g_y = .02, .002$, and $|\bar{C}_X| = |\bar{C}_Y| = 0.0$, the same as those in Reference 13.

The last step is to study the effects of offsets. The same parameters, $h = .4$, $d_p = 0.0$, and $d_F = .2$ as those in Reference 13, are used for both soft inplane and stiff inplane cases. Thus, we can obtain all responses for different possible situations.

At the present point in our research we are transfering our computer codes from the VAX system at Washington University to the CDC system at Georgia Institute of Technology. When this work is completed, we will be able to continue the numerical work and should have our first answer shortly. The first runs will be validation runs to ensure that we can repeat the results of References 8, 12, and 13. Then we will procede to studies of parameter variations.

7. NOMENCLATURE

a	= slope of lift curve, 1/rad
A	= ratio of rotor mass to moment of inertia, $M\bar{x}R/I_y$
b	= number of blades
C_{d_o}	= blade profile drag coefficient
$\hat{C}_Z$	= conventional thrust coefficient, thrust$/\rho\pi\Omega^2R^4$
C_X, C_Y, C_Z, C_M, C_L	= vibratory portion of nondimensional longitudinal force, lateral force, thrust, pitch and roll moment over σa
$\bar{C}_X, \bar{C}_Y, \bar{C}_Z, \bar{C}_M, \bar{C}_L$	= steady portion of coefficients
d_F	= offset between focus and center of pylon, divided by R
d_p	= offset between focus and center of pylon, divided by R
d_r	= offset between hub and center of pylon, divided by R
e	= mass centroid offset from elastic axis of a blade
EI	= beam cross-section bending stiffness
$\{\vec{F}\}$	= vector of forces
g	= nondimensional acceleration of gravity, g/Ω^2R
g_z, g_y, g_m, g_l	= plunge, lateral, pitch and roll structural damping, $\approx 2\zeta/\omega_n$
h	= offset between hub and focus, divided by R
$[H]$	= fuselage receptance
$[I]$	= identity matrix
I_{y_1}	= pitch inertia moment of pylon, divided by M_pR^2
I_{x_1}	= roll inertia moment of pylon, divided by M_pR^2
I_{y_2}	= pitch inertia moment of fuselage, divided by M_FR^2
I_{x_2}	= roll inertia moment of fuselage, divided by M_FR^2
l	= length of the beam, m

m = mass per unit beam length, kg/m

M_c = lumped mass on the center of fuselage, kg

M_p = mass of pylon, kg

M_F = mass of fuselage, $M_c + ml$, kg/m

M_f = mass of whole fuselage, $M_c + ml + M_p$, kg

q_i = generalized coordinates

$\bar{r}_{pm}, \bar{r}_{pl}$ = radius of gyration of pylon in pitch, roll, divided by R

$\bar{r}_{Fm}, \bar{r}_{FL}$ = radius of gyration of fuselage in pitch, roll, divided by R

R = rotor radius, m

R_v = beam mass divided by whole airframe mass, $ml/(ml + M_c + M_p)$

$[T_d]$ = transformation matrix, Equation (4)

$[T_R]$ = transformation matrix, Equation (2)

U = blade airfoil velocity with respect to the air mass, m/sec
also strain energy, N-m

U_p, U_T = velocity components of blade airfoil section, perpendicular and parallel to the chord respectively, m/sec

u, v, w = elastic deformation in x, y, z directions respectively, m

V = velocity vector of a arbitrary point on deformed blade, m/sec

δW = virtual work, N-m

$\bar{x}$ = distance along fuselage, nose to tail, or distance along radius of rotor, root to tip, divided by R

x, y, z = rotating coordinates fixed on the blade

x', y', z' = deformed coordinates fixed on the blade

X, Y, Z = fixed fuselage coordinates

$\bar{Y}_F, \bar{Z}_F$ = dimensionless fuselage elastic degree of freedom in vertical and lateral directions

α_c = pitch angle of hub, fuselage, positive nose up, rad

α_s = roll angle of hub, fuselage, positive advancing side up, rad

$\bar{\beta}$ = equilibrium flapping angle, rad

$\beta_o + \beta_s \sin\psi + \beta_c \cos\psi$

β_o = coning angle, rad

β_s = lateral cyclic flap angle, rad

β_c = longitudinal cyclic flap angle, rad

β_{pc} = pre-cone angle

γ = Lock number

δ = first variation

ϵ = scaling parameter, (=.1)

ζ, η = blade cross-section principal axes coordinates

$\{\vec{\theta}\}$ = vector of control variables

$\bar{\theta}$ = equilibrium pitch angle,

$\theta_o + \theta_s \sin\psi + \theta_c \cos\psi + \theta_\beta(\bar{\theta} - \beta_{pc}) + \theta_\zeta \bar{\zeta}$

$\theta_o, \theta_s, \theta_c$ = collective and cyclic pitch, rad

λ = inflow ratio

μ = advance ratio

μ_p = ratio of mass of pylon to mass of fuselage, $M_p/(ml + M_c)$

μ_c = ratio of lumped mass to the uniformly distributed mass, M_p/ml

ρ = air density, kg/m^3

σ	= rotor solidity
σ_{ij}	= stress tensor components, N/m^2
τ	= dimensionless tenssion
ψ	= blade azimuth angle, nondimensional time
$\bar{\omega}$	= natural frequency of fuselage, divided by Ω
$\bar{\omega}_{xy}$	= frequency of "y" motion with "x" boundary condition, divided by Ω; y = z,y,m,L plunge, lateral, pitch, roll, x = c, f cantilevered,free
Ω	= rotor speed, rad/sec
$()^*$	= $d( )/d\psi$
$\dot{()}$	= $d( )/dt$
$()^+$	= $d( )/d\bar{x}$
$()'$	= $d( )/dx$

8. REFERENCES

(1) Gestenberger, Walter and Wood, Edward R., "Analysis of Hilecopter Aeroelastic Characteristics in High-Speed Flight", AIAA Journal, Vol. 1, No. 10, October 1964.

(2) Staley, J. A. and Sciarra, J. J., "Coupled Rotor/Airframe Vibration Predication methods", Rotorcraft Dynamics, NASA SP-352, 1974.

(3) Hohenemser, Kurt H. and Yin, Sheng-Kuang, "The Role of Rotor Impedance in the Vibration Analysis of Rotorcraft", Fourth European Powered Lift Aircraft Forum, Stressa, Italy, September 1978.

(4) Kato, Kanichiro and Yamane, Takaski, "Calculation of Rotor Impedance for Hovering Articulated-Rotor Helicopters", AIAA Journal, Vol. 16, No. 1, January 1979.

(5) Kuczynski, W. A. and Sissingh, G. J., "Characteristics of Hingeless Rotors with Hub Moment Feedback Controls Including Experimental Rotor Frequency Response", NASA CR 114427, January 1972.

(6) Viswanthan, S. P. and Meyers, A. W., "Reduction of Helicopter Vibration through Control of Hub Impedance", Journal of the American Helicopter Society, Vol. 25, No. 4, October, 1980, pp. 5-12

(7) Peters, David A. and Ormiston, Robert A., "Flapping Response Characteristics of Hingeless Rotor Blades by a Generalized Harmonic Balance Method", NASA TN D-7856, February 1975.

(8) Hsu, T-K and Peters, David A., "Coupled Rotor/Airframe Vibration Analysis by a combined Harmonic-Balance, Impedance-Matching Method", Journal of American Hilecopter Society, Vol. 27, No. 1, January 1982, pp. 25-34

(9) Kuns, D., "Effects of Rotor-Body Coupling in a Linear Rotorcraft Vibration Modal", Proceedings of the 36th Annual Forum of the American Helicopter Society, Washington, DC, May 1980.

(10) Kuns, D., "A Nonlinear Response Analysis and Solution Method for Rotorcraft Vibration", Journal of the American Helicopter Society, Vol. 28, No. 1, January 1983.

(11) Schrage, Daniel P., "Effect of Structural Parameters on Elastic Flap-Lag Forced Response of a Rotor Blade in Forward Flight", Doctor of Science thesis, Washington University in St. Louis, May, 1978.

(12) Eipe, Abraham, "Effect of Some Structural Parameters on Elastic Rotor Loads by an Iterative Harmonic Balance", Doctor of Science Thesis, Washington University in St. Louis, December, 1979.

(13) Huang, Ming-Sheng, "Coupled Rotor-Airframe Vibrations with Elastic Fuselage and Inplane Degrees of Freedom", Master of Science Thesis, Washington University in St. Louis, June, 1983.

9. ACKNOWLEDGEMENT

The work was sponsored by the United States Army Research Office, Grant No. ARO-DAAG-29-80-C-0092. The view, opinions, and/or findings contained in this report are those of the authors and should not be construed as an official department of the Army position, policy, or decision, unless so designated by other documentation.

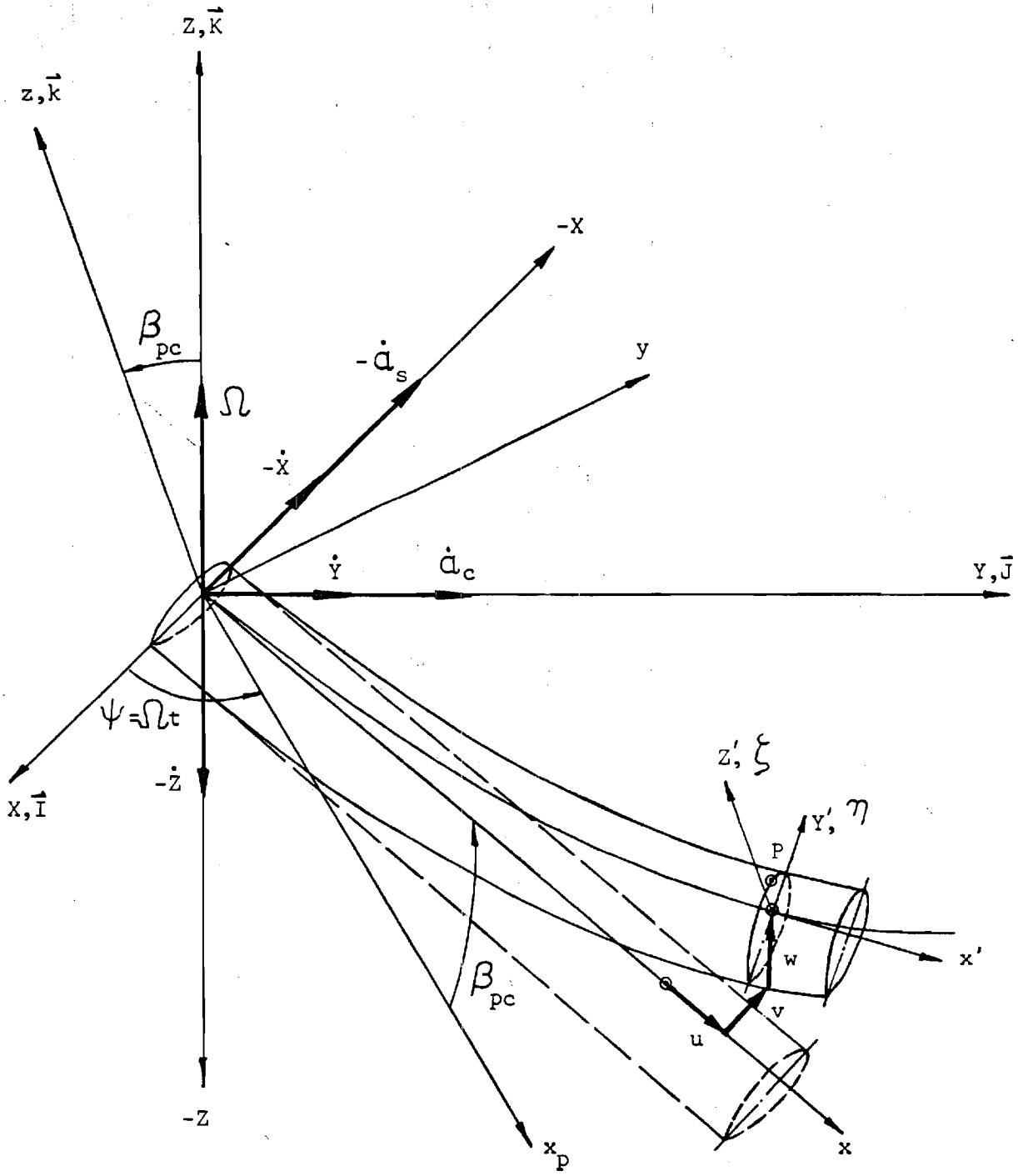

Figure 1 Fixed, rotating and deformed Coordinate systems of an elastic blade

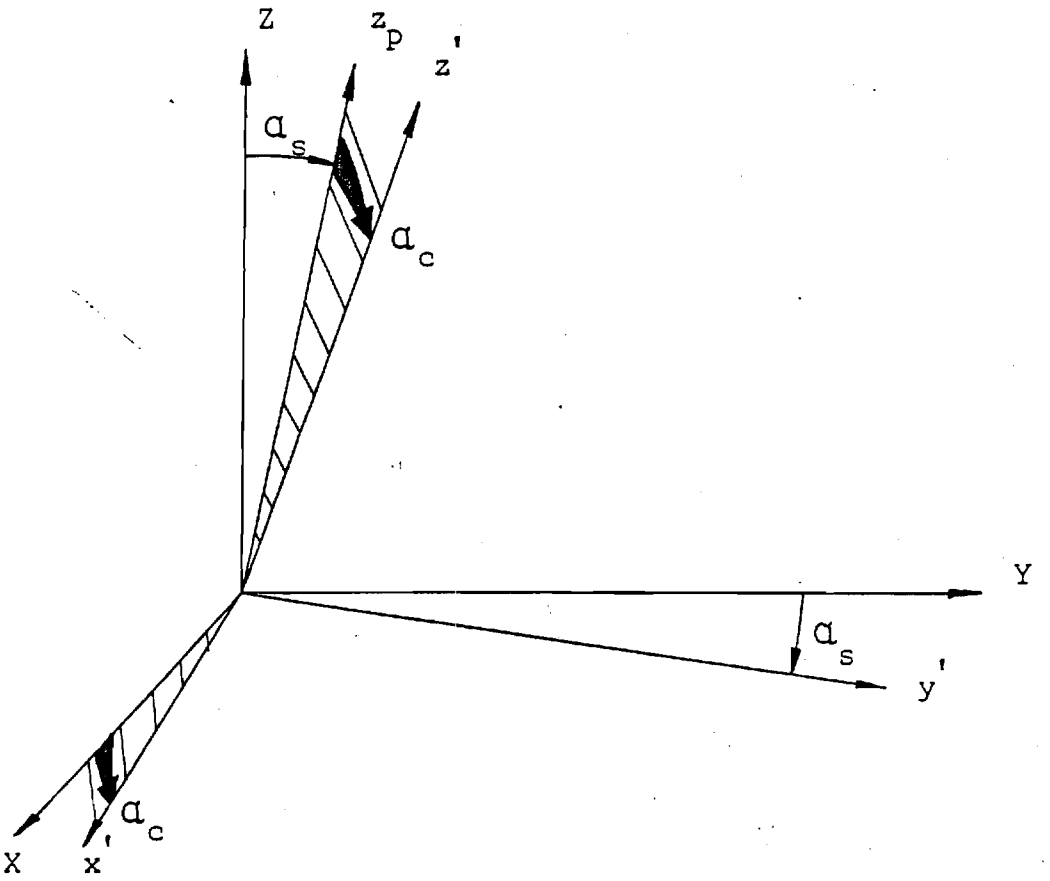

Figure 2 Considering pitching and rolling angles

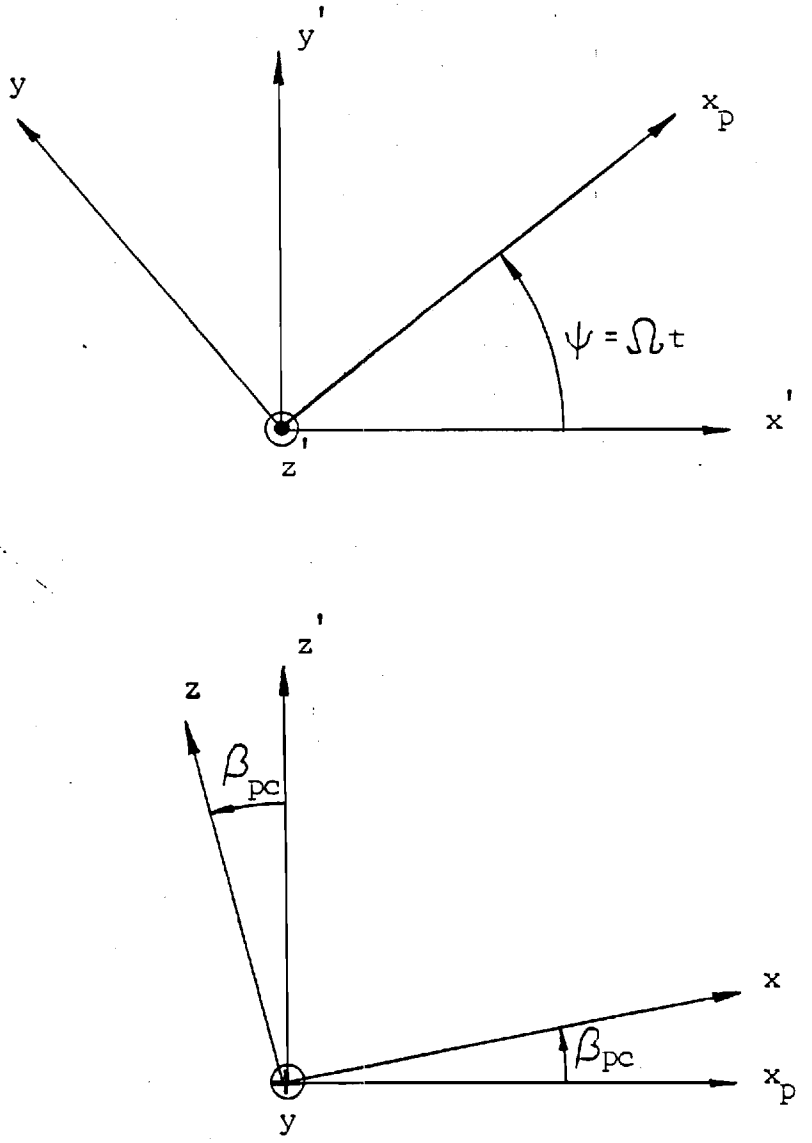

Figure 3 Considering azimuth and pre-cone angles

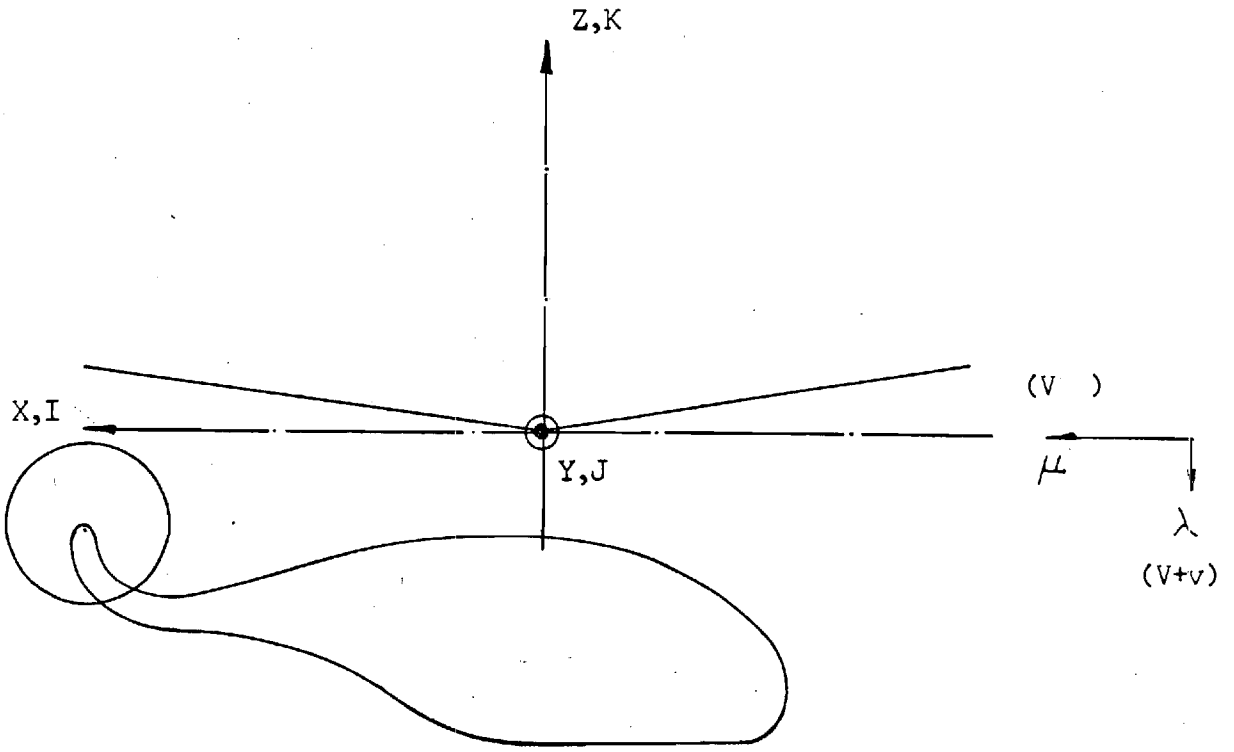

Figue 4 Free airflow passing through the helicopter

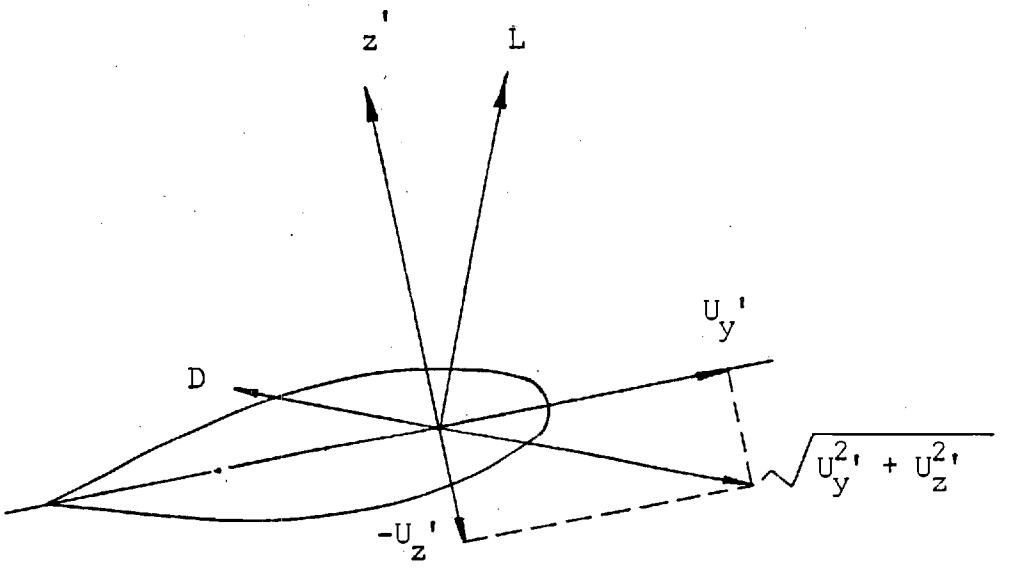

Figure 5 Blade element geometry

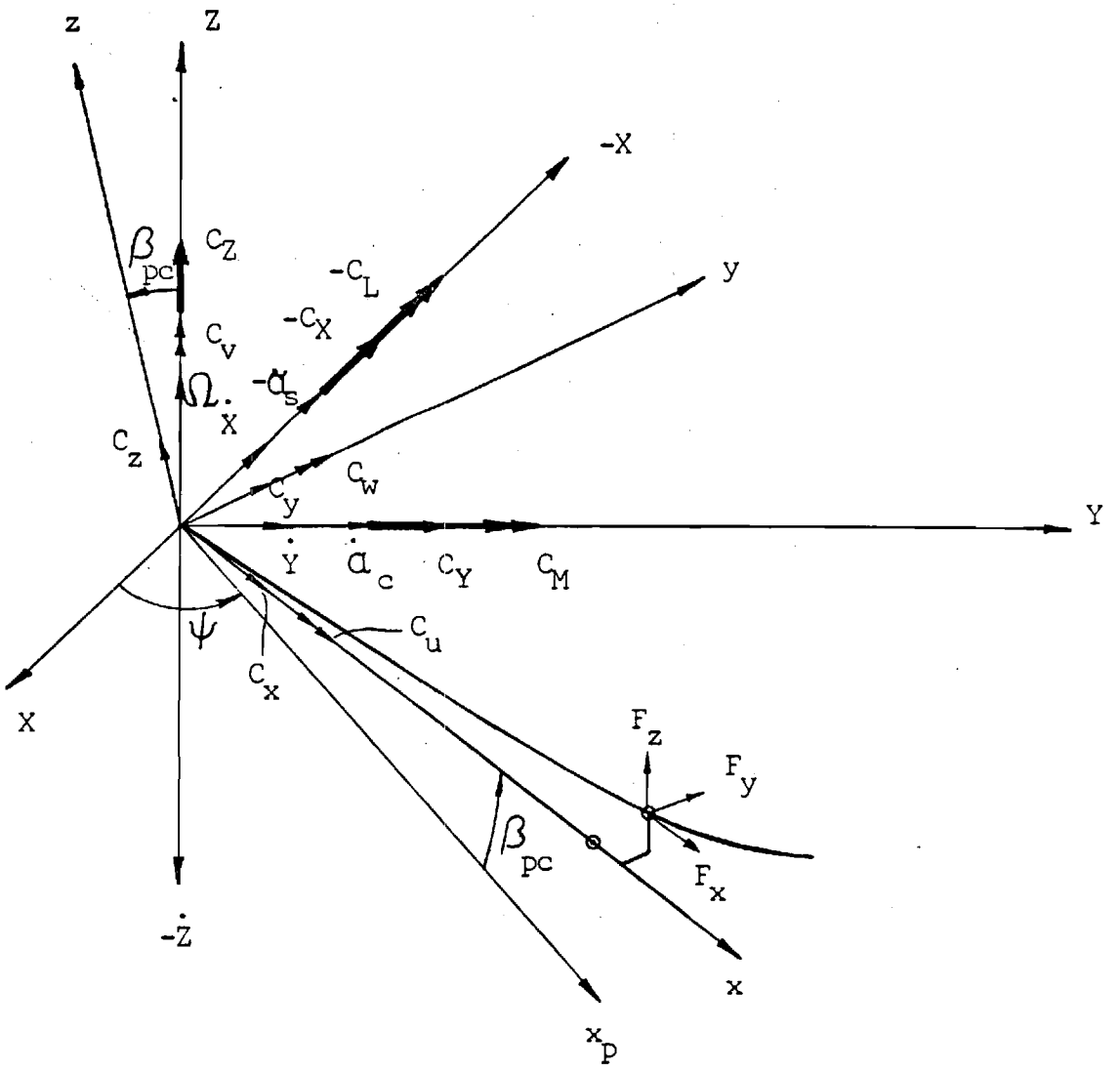

Figure 6 Hub loads

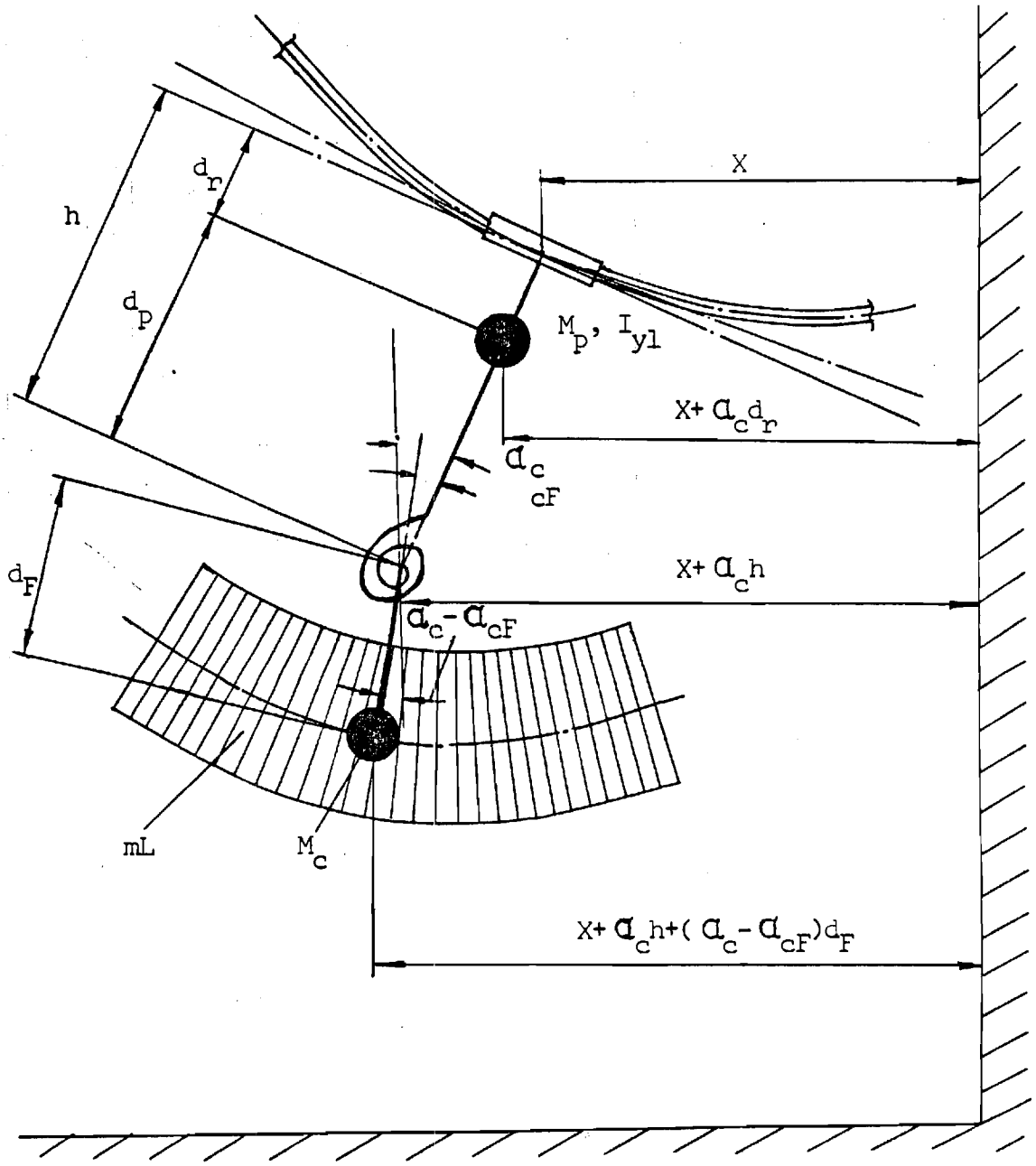

Figure 7 Fuselage model in longitudinal and pitch direction